A ghostly tail of the Hoyle state and its breathing-mode excitation

by

Kevin Ching Wei Li

Dissertation presented for the degree of Doctor of Philosophy in Nuclear Physics in the Faculty of Science at Stellenbosch University

Supervisors: Prof P. Papka
iThemba Laboratory for Accelerator Based Sciences
Department of Physics, University of Stellenbosch

Dr F.D. Smit
iThemba Laboratory for Accelerator Based Sciences

Dr R. Neveling
iThemba Laboratory for Accelerator Based Sciences

Dr P. Adsley
iThemba Laboratory for Accelerator Based Sciences
Department of Physics, University of the Witwatersrand

2020

Declaration

By submitting this dissertation electronically, I declare that the entirety of the work contained therein is my own, original work, that I am the sole author thereof (save to the extent explicitly otherwise stated), that reproduction and publication thereof by Stellenbosch University will not infringe any third party rights and that I have not previously in its entirety or in part submitted it for obtaining any qualification.

Date: March 2020

Abstract

A ghostly tail of the Hoyle state and its breathing-mode excitation

K.C.W. Li

Department of Physics,
University of Stellenbosch,
Private Bag X1, Matieland 7602, South Africa.

Dissertation: PhD (Nuclear Physics)

2020

^{12}C is almost exclusively produced in stars from a combination of ^{4}He and unstable ^{8}Be which form an excited three-alpha resonance named the Hoyle state, located just above the 3α separation energy at $E_x = 7.65407(19)$ MeV. Whilst this resonance is understood to be the archetypal α-cluster state, ^{12}C is understood to straddle the region between the shell-model and collective pictures as its ground state presents with a large overlap with shell-model states. The significant work by the nuclear physics community to theoretically describe ^{12}C is therefore of both astrophysical and structural significance. An indication that an unlisted source of monopole strength may manifest at $E_x \approx 9$ MeV was given by the peak-fitting and Multipole Decomposition Analysis (MDA) of M. Itoh *et al.* which suggested a double-peaked, broad monopole structure in the excitation-energy region of $E_x \approx$ 8-13 MeV just above the Hoyle state. Some recent theoretical works which employ formalisms such as AMD, 3α OCM and GCM suggest that this unestablished origin of monopole strength may be understood as the breathing-mode excitation of the 0^+_2 Hoyle state, corresponding to a low-energy fragment of the isoscalar giant monopole resonance (ISGMR). The primary motive of this thesis was to search for any unidentified sources of monopole strength in the $E_x \approx$ 7-16 MeV excitation-energy region and investigate if they exhibit strong collectivity. A new measurement of the ^{14}C$(p,t)^{12}$C reaction at $\theta_{\text{lab}} = 0^\circ$ was performed with the K600 magnetic spectrometer and the CAKE array to detect coincident charged-particle decay. This data was combined previous datasets of ^{14}C$(p,t)^{12}$C at 21° and ^{12}C$(\alpha,\alpha')^{12}$C at $\theta_{\text{lab}} = 0^\circ(\times 2)$, 6°, 8.5° and 10° to be simultaneously analysed with a new multilevel multichannel R-matrix analysis fitting code. A total of 6 hypotheses were explored and the best quality model corresponded to the monopole

structure in the $E_x \approx$ 7-16 MeV excitation-energy region being modeled by a two-level approximation with coherent interference and an additional 0^+ resonance at $E_x = 9.270(14)$ MeV with a width of $\Gamma_{\text{tot}} = 1581(58)$ MeV. The extracted parameters for this resonance are in excellent agreement with both the aforementioned measurement by M. Itoh *et al.* as well as various theoretical predictions. There is particularly good agreement with the OCM calculation by C. Kurokawa and K. Katō which yielded a resonance energy of $E_x \approx 8.95$ MeV and a width of $\Gamma_{\text{tot}} = 1.48$ MeV for the 0_3^+ state [1]. The angular distribution of α_0 decay in the associated interval of 8.5 MeV $< E_x <$ 9.0 MeV was found to exhibit isotropy which implies that the strength is predominantly monopole. The identification of this new source of monopole strength may play a significant role in the 3α rate in certain astrophysical conditions.

Uittreksel

A ghostly tail of the Hoyle state and its breathing-mode excitation

("A ghostly tail of the Hoyle state and its breathing-mode excitation")

K.C.W. Li

Departement van Fisika,
Universiteit van Stellenbosch,
Privaatsak X1, Matieland 7602, Suid Afrika.

Proefskrif: PhD (Nuclear Physics)

2020

^{12}C word in sterre geproduseer deur die absorpsie van 'n ^{4}He kern deur 'n onstabiele ^{8}Be kern om die opgewekte drie-alfa resonans toestand in ^{12}C, die sogenaamde Hoyle toestand, te vorm. Hierdie toestand bestaan by E_x = 7.65407(19) MeV wat net bokant die opbreek drumpel na drie alfas gelëe is. Alhoewel die Hoyle toestand die klassieke voorbeeld van 'n alpha-toestand is, dek 12C die gebied tussen die skilmodel en kollektiewe-model beskrywing aangesien dat die grond toestand tog 'n groot oorvleuling met skilmodel toestande het. Die beduidende werk wat deur die fisika gemeenskap gedoen is om 12C teoreties te beskryf is derhalwe vir beide astrofisika en kernstruktuur studies van belang. Daar bestaan aanduidings van 'n ongelyste toestand met moontlike monopool eienskappe wat by $E_x \approx 9$ MeV voorkom, soos getoon in die werk van Itoh et al. In hul navorsing het Itoh et al. deur middel van piek passings en multipool dekomposisie 'n breë 0^+ dubbelpiek struktuur in die energie gebied $E_x \approx$ 8-13 MeV geidentifiseer, net bokant die Hoyle toestand. In teoretiese berekeninge wat onlangs verskyn het en wat van verskeie formalismes soos AMD, 3α OCM en GCM gebruik gemaak het, is daar aanduidinge dat die oorsprong van hierdie monopool sterkte moontlik verklaar kan word as 'n sg. opgewekte asemhalings variante van die Hoyle toestand, wat in dieselfde energie gebied voorkom as die lae-energie fragment van die Reuse Isoskalare Monopool Resonansie (ISGMR). Die primere motivering van hierdie tesis was om vir ongeidentifiseerde bronne van monopool sterkte in die $E_x \approx$ 7-16 MeV opwekkingsenergie gebied te soek wat sterk kollektiewe eienskappe het. 'n

Nuwe meting by $\theta_{\text{lab}} = 0^\circ$ met die $^{14}\text{C}(p,t)^{12}\text{C}$ reaksie is met die K600 magnetiese spektrometer gemaak in koinsidensie met die CAKE detektor ten einde gelaaide verval deelties waar te neem. Daarna is hierdie data met voorheen gemete $^{14}\text{C}(p,t)^{12}\text{C}$ data by 21°, $^{12}\text{C}(\alpha,\alpha')^{12}\text{C}$ data by $\theta_{\text{lab}} = 0^\circ$ (twee stelle), 6°, 8.5° en 10° gekombineer en gelyktydig met 'n nuwe multivlak, multikanaal R-matriks analiese kode gepas. Daar is ses hypotesise getoets vir passings in die $E_x \approx$ 7-16 MeV gebied. Die beste model is 'n dubbele 0^+ toestand sisteem met koherente interferensie tussen die toestande, waar die laagste toestand by $E_x = 9.270(14)$ MeV gevind is met 'n wydte van $\Gamma_{\text{tot}} = 1581(58)$ MeV. Dit is in goeie ooreenstemming met die $E_x = 8.95$ MeV, $\Gamma_{\text{tot}} = 1.48$ MeV, tot nou toe ongelyste 0^+ toestand soos voorspel deur C. Kurokawa and K. Katō. Die hoekverdeling van die verval wat geassosieer is met die interval in opwekkings energie 8.5 MeV $< E_x <$ 9.0 MeV is isotroop wat impliseer dat die opgewekte toestand oorwegend monopool is. Die bevestiging en positiewe identifikasie van hierdie nuwe bron van monopool sterkte mag 'n beduidende rol speel in die 3α reaksie tempo onder astrofisiese toestande.

Acknowledgements

This work would not have been possible without the excellent work of the accelerator team and workshop staff at iThemba LABS.

Thank you to Dr. Evgenii Nikolskii for your significant contribution to the primary experiment performed for this thesis. Your steady hands were crucial in handling the precious ^{14}C target that I would prefer not to even blink near (lest the gust severs the last millimetre that holds the target together).

Thank you to Prof. M.N. Harakeh for his guidance with regards to the DWBA calculations in this work. Your patience and generosity with your time has been most appreciated.

Thank you to Dr. F. Nemulodi and Dr. L. Pelligri for your advice with regards to the reaction calculations performed for this thesis.

Thank you to Dr. L.M. Donaldson, thank you for your assistance in organising and participating in the practices for the defence presentation.

To Dr. Ricky Smit, aside from feeding me at the lab for many years whenever my blood sugar drops (I think I owe you a paycheck's worth of snacks), your gentle guidance and sage wisdom have been a blessing. I'm very grateful for the steady stream of references in my inbox and your reminders to expand my views in research. It has also been great to have a supervisor that shamelessly enjoys puns.

To Dr. Retief Neveling, thank you for constantly believing me when I say that a call or meeting will be a "quick two minutes", only to consistently engage in an intense half-hour discussion. It has been a blessing to have your expertise to call upon.

To Dr. Phil Adsley, your self-less patience and guidance has been a blessing, thank you. Beyond your wide range of knowledge, I'm immensely grateful for your ability to bring life and enthusiasm to any research we discuss.

To Prof. Paul Papka, in many senses this entire journey began with you in the small third-year laboratory during my undergraduate degree. Whilst much has changed since then, the core spirit of our work together has endured. Whenever I have a challenge, whether it's about physics or life in general (don't worry, nothing...), I always know who I can call upon for guidance. Your infectious passion has guided me not only as a researcher, but as a person. I am indebted to the kindness that the Papka family have shown Suzette and

me.

To my supervisors, beyond your guidance, I wish to thank you for the trust you have placed in me these past few years. Indeed, that trust has given me great encouragement and self-belief during the many moments of doubt. It is somewhat uncommon for a student to be under the guidance of the same four supervisors for six years (including my Masters). The mentorship I received from you all during these years has been a privilege.

To my extended family, your encouragement and support has been a foundation in my life these past few years. To my sister May, your pride in my work always brings me great encouragement.

To my loving wife Suzette Li, your unrelenting support and encouragement has been the bedrock upon which I've been free to grow. Your belief in me, which extends far beyond my own, colours everything that I do.

To my mother Irene Y.P. Chu and my father Colin P.J. Li, it goes without saying that I owe you everything. I'm constantly aware that the opportunity to study, never mind the privilege of studying what one loves, is something your younger selves could only dream of. I've tried to honour your sacrifices with unrelenting hard work.

Dedications

To my family

Greater love hath no man than this,
that a man lay down his life for his friends.
John 15:13

Contents

List of Figures

List of Tables

Chapter 1

Introduction

Clustering is a phenomenon that transcends length scales to manifest in both atomic and cosmic regimes, with examples such as molecular clustering and galaxy clusters, respectively [2, 3]. In the subatomic domain, light nuclei have garnered great interest as they are postulated to manifest cluster structures with notable properties such as dilute densities and may even present as Bose Einstein Condensate (BEC) states in nuclear matter, whereby a system of bosonic α-particle subunits simultaneously occupies the lowest-energy quantum state [4, 5]. Alpha-conjugate nuclei, which are exactly composed of α-particle subunits, are of particular interest since they are currently amongst the best candidates to exhibit α-clustering structures. Historically, the concept of α clustering in nuclei was pioneered by L.R Hafstad and E. Teller [6] who observed the linear correlation between the total binding energy of α-conjugate nucleui and the corresponding number of nearest-neighbour bonds between the α-particle subunits, as shown in Figure 1.1.

The 0^+ structure of ^{12}C in the $E_x \approx$ 7-16 MeV excitation-energy region is of great interest, not least because the $J^\pi = 0_2^+$ Hoyle state at $E_x = 7.65407(19)$ MeV is the archetypal α-cluster state which also plays a preeminent role in nucleosynthesis [8, 9]. The challenge of explaining the entire monopole structure therefore provides a crucial test for the current understanding of both ^{12}C and of α-clustering as a whole. The first well-known source of monopole strength corresponds to the Hoyle state which exhibits a narrow peak located at $E_x = 7.65407(19)$ MeV and a high-energy tail known as the ghost anomaly, which exhibits a local maximum at $E_x \approx 9$ MeV and resembles a second resonance. This phenomenon originates from the dynamics for the α decay mode of the Hoyle state. The second prominent source of monopole strength is the broad 0^+ resonance at $E_x \approx 10$ MeV. The NNDC lists two 0^+ resonances situated at $E_x = 9.930(30)$ and 10.3(3) MeV, with widths of $\Gamma = 2.710(80)$ and 3.0(7) MeV, respectively [10]. The 10.3(3) MeV resonance energy corresponds to a measurement of the $^{12}\mathrm{C}(\alpha, \alpha')^{12}\mathrm{C}$ reaction with $E_{beam} = 120$ MeV at $0^\circ < \theta_{\alpha'} < 4^\circ$, presented in an unpublished KVI annual report (1983) [11]. The close proximity of these two resonance energies

with respect to their relatively large widths (which agree within error) strongly suggests that these two listed resonances are one and the same [12]. A relatively recent study by M. Itoh *et al.* [13] introduced an unlisted broad 0^+ resonance at $E_x \approx 9$ MeV in order to fit the data (with rudimentary Gaussian lineshapes) from $^{12}\mathrm{C}(\alpha,\alpha')^{12}\mathrm{C}$ measurements, as shown on panel (a) of Figure 1.2. A more recent multipole decomposition analysis (MDA) [14] performed

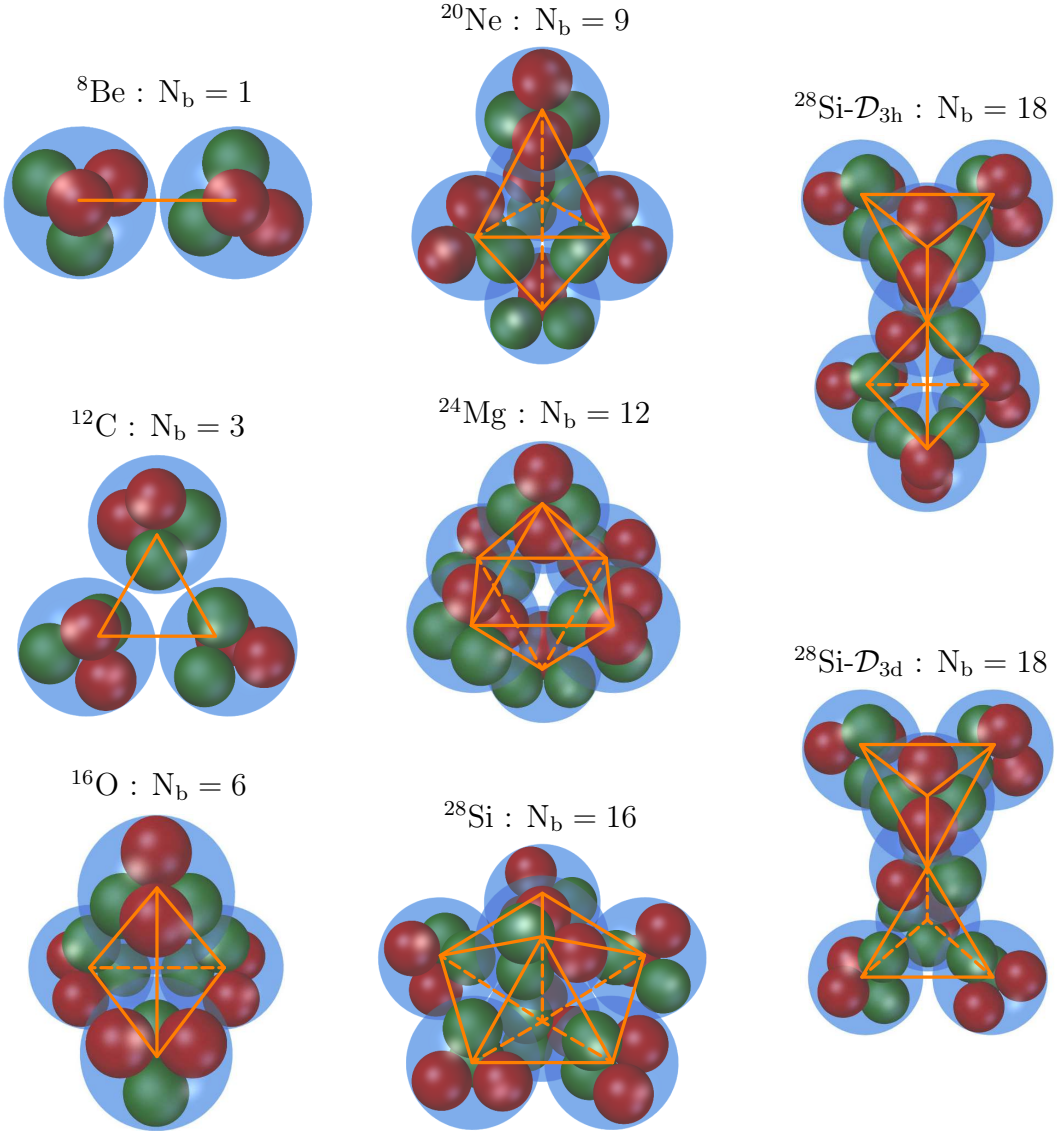

Figure 1.1: Schematic representation of possible geometric configurations for the six lightest α-conjugate nuclei. The configurations labelled ^{8}Be, ^{12}C, ^{16}O, ^{20}Ne, ^{24}Mg and ^{28}Si were predicted by D.M. Brink and E. Boeker [7], whilst ^{28}Si-$\mathcal{D}_{3h}$ and ^{28}Si-$\mathcal{D}_{3d}$ label the possible configurations that correspond to values of N_b suggested by L.R. Hafstad and E. Teller [6]. The number of nearest-neighbour bonds between α clusters, N_b, is displayed for each configuration.

by the same group revealed the strength at $E_x \approx 8$ MeV to be dominated by a 0^+ contribution, as shown on panel (b) of Figure 1.2. Several calculations have been performed to describe the broad monopole structure above the Hoyle state, with formalisms such as Antisymmetrized Molecular Dynamics (AMD), Fermionic Molecular Dynamics (FMD), the 3α Orthogonality Condition Model (OCM) and the Generator Coordinate Method (GCM). Some of these calculations yielded two distinct sources of broad monopole strength above the Hoyle state, where the higher-lying 0^+ resonance is postulated to correspond to the broad 0^+ resonance currently listed on the NNDC at $E_x \approx 10$ MeV. Notably, several theories indicated that the lower-lying broad monopole strength corresponded to the breathing-mode excitation of the Hoyle state may be understood as the breathing-mode excitation of the 0^+_2 Hoyle state, corresponding to a low-energy fragment of the isoscalar giant monopole resonance (ISGMR). This can be pictured as the in-phase radial oscillation of the constituent α-particle clusters for the triangular configuration of ^{12}C depicted in Figure 1.1.

The primary objective of this work was to attempt to identify new sources of monopole strength in ^{12}C in the excitation-energy region of $E_x \approx$ 7-16 MeV and in particular, investigate whether an unlisted 0^+ resonance is necessary to reproduce the data at $E_x \approx 9$ MeV. In order to identify a collective breathing-mode excitation, two different probes were employed: the $^{12}\mathrm{C}(\alpha,\alpha')^{12}\mathrm{C}$ and $^{14}\mathrm{C}(p,t)^{12}\mathrm{C}$ reactions. Inelastic α scattering is understood to be the best probe to populate ISGMR strength and it was measured at $0°(\times 2)$, $6°$, $8.5°$ and $10°$ with various incident beam energies. In contrast, the $^{14}\mathrm{C}(p,t)^{12}\mathrm{C}$ reaction is understood to be selective against the population of the ISGMR as it should not access excitations which are of 1p-1h nature [12]. Instead, the $^{14}\mathrm{C}(p,t)^{12}\mathrm{C}$ is rather suggested to be selective towards giant pairing vibrations [15]. The combination of these two vastly different reaction mechanisms is presumed to

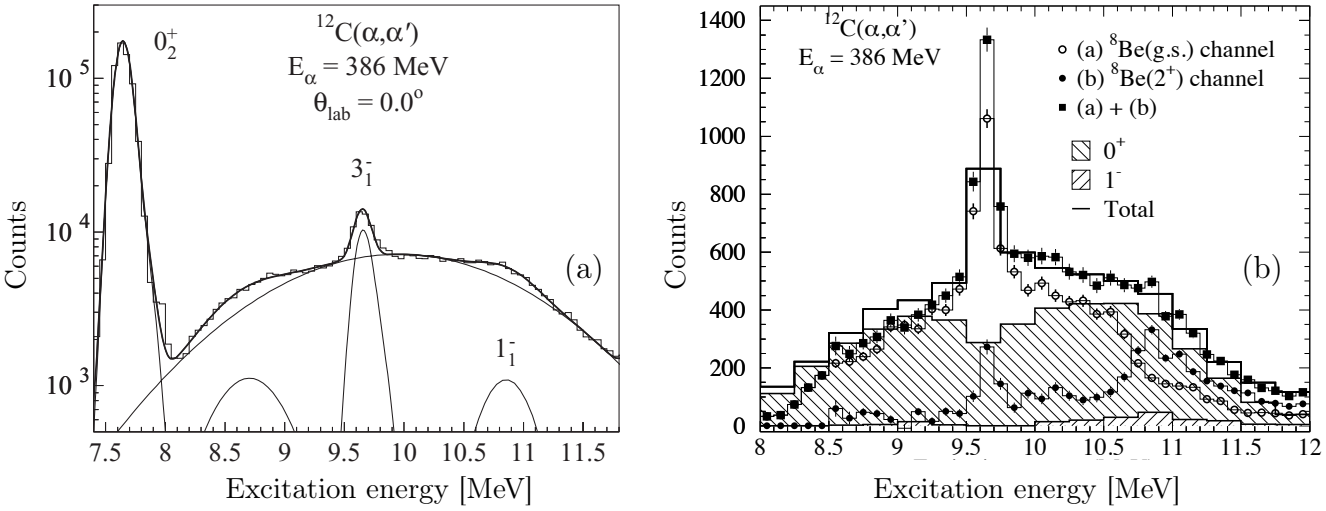

Figure 1.2: The peak-fitting and multipole decomposition analyses of ^{12}C by M. Itoh *et al.* from Refs. [13, 14].

augment the differences in population between static monopole excitations, such as the Hoyle state, and a dynamic breathing-mode excitation.

In comparison to simplistic peak-fitting procedures, the analysis of this work employs a new multilevel multichannel R-matrix analysis code which is specialised for fitting direct nuclear reactions. Such an analysis would enable an advanced treatment of the coherent interference between the monopole resonances in the excitation-energy region of $E_x \approx$ 7-16 MeV and investigate whether this can account for the excess monopole strength observed by M. Itoh *et al.* at $E_x \approx 9$ MeV. This unique multilevel multichannel analysis, which simultaneously fits the unique combination of ^{12}C$(\alpha,\alpha')^{12}$C and ^{14}C$(p,t)^{12}$C data to provide a consistent analysis, may provide insight into the monopole structure of ^{12}C and test our ability to model the structure of ^{12}C. Moreover, the presence of an addition monopole resonance just above the Hoyle will have serious repercussions on the astrophysically-significant 3α reaction rate.

Chapter 2

Theory

The structure of ^{12}C is of great interest as it straddles the region between the shell-model and collective pictures. Whilst the shell model can reproduce the 0^+_1 ground state, it fails to do so for the 0^+_2 Hoyle state which exhibits a highly α-clustered structure. The ability to theoretically describe the Hoyle state has been a *tour de force* of the nuclear physics community, with various α-cluster formalisms such as Antisymmetrized Molecular Dynamics (AMD), Fermionic Molecular Dynamics (FMD) and many others [16]. Notably, the Hoyle state and other low-lying states in ^{12}C have also been reproduced with state-of-the-art *ab initio* calculations [17]. Despite this progress, the current understanding of the comprehensive monopole structure in ^{12}C is still uncertain. One of the challenges of the data analysis in this region is that if multiple overlapping 0^+ resonances contribute, the resonances can no longer be analysed in isolation and must be modeled as a single 0^+ entity which may exhibit non-negligible interference effects.

Resonances such as the Hoyle state present as variations in cross section as a function of nuclear excitation energy and are characterised by their total angular momentum (J), parity (π), resonance energy (E_R), observed width (Γ) and branching ratios of decay (BR). In the $E_x \approx$ 7-16 MeV excitation-energy region of interest for ^{12}C, the Hoyle state contributes to the total monopole strength both through its primary peak with $\Gamma = 9.3(9)$ eV width and its high-energy tail. This high-energy tail, otherwise known as the ghost anomaly, is unusual as it exhibits a local maximum and resembles a second resonance. This phenomenon originates from the dynamics of the dominant α decay mode of the Hoyle state. The second prominent source of monopole strength is the broad 0^+ resonance at $E_x \approx 10$ MeV. As mentioned in Chapter 1, the two 0^+ resonances listed on the NNDC at 9.930(30) and 10.3(3) MeV, with respective widths of 2.710(80) and 3.0(7) MeV, are understood to correspond to the same resonance [12]. A more recent study of this monopole strength, populated through the β-decay from ^{12}N and ^{12}B, was performed with a multilevel multi-channel R-matrix analysis which also supports the existence of this resonance [18]. Notably, it was found that in the multilevel formalism, the interpretation

of the resonance energy is complicated due to the coherent interference between states may longer be a reliable indicator of an observed local maximum. The resonance energy for this state determined (by the best-fitting model) to be situated at 11.01 MeV with a width of 1.31 MeV which agrees relatively well with the calculated resonance energy of 11.3 MeV which is calculated by R. Álvarez-Rodríguez *et al.* [19]. This analysis did not introduce an unlisted 0^+ resonance at $E_x \approx 9$ MeV to describe the data.

A third, unestablished source of monopole strength has postulated to manifest between the Hoyle state and the aforementioned 0^+ resonance listed at 10.3(3) MeV. The study of the $^{12}\mathrm{C}(\alpha,\alpha')^{12}\mathrm{C}$ reaction at $\theta_{\mathrm{lab}} = 0°$ with multipole decomposition analysis (MDA) by M. Itoh *et al.* [13] indicated a double-peaked broad 0^+ structure in the $E_x \approx$ 7-16 MeV excitation-energy region of interest. It was found that to fit the data, an additional peak was necessary at $E_x \approx 9$ MeV: a region that the MDA indicates is dominated by monopole strength. The results indicate the 0^+_3 resonance to be located at $E_x = 9.04(9)$ MeV with a width of $\Gamma = 1.45(18)$ MeV whilst the 0^+_4 state is situated at 10.56(6) MeV with a similar width of $\Gamma = 1.42(8)$ MeV. It is understood that the latter resonance corresponds to the aforementioned broad 0^+ state that is currently incorrectly listed on the NNDC as two distinct 0^+ states at $E_x \approx 10$ MeV [10]. It was found that for the newly-introduced 0^+_3 state, the $^{12}\mathrm{C} \rightarrow^8 \mathrm{Be}_{0^+} + \alpha$ (S-wave) decay channel dominates whilst for the 0^+_4 state, the $^{12}\mathrm{C} \rightarrow^8 \mathrm{Be}_{2^+} + \alpha$ (D-wave) channel dominates.

Some recent theoretical calculations suggest that this unestablished source of monopole strength may be understood as the breathing-mode excitation of the 0^+_2 Hoyle state. This resonance may correspond to a low-energy fragment of the isoscalar giant monopole resonance (ISGMR) which is microscopically described as a coherent superposition of 1p-1h excitations and in particular, the $1p_{3/2}$-$2p_{3/2}$ and $1p_{1/2}$-$2p_{1/2}$ excitations. Such a collective excitation of the Hoyle state can be pictured as the in-phase radial oscillation of the constituent α-particle clusters for the triangular configuration of ^{12}C depicted in Figure 1.1. The properties of giant resonances and the methods to study them are introduced in Section 2.1. Some of the formalisms which are able to reproduce the 0^+_2 Hoyle state and the higher-lying broad 0^+_3 and 0^+_4 states are introduced in Sections 2.2 - 2.5.

2.1 Giant Resonances

In contrast to resonances which can be parameterised by the simple binary model of R-matrix theory, giant resonances are collective excitations that involve most, if not all of the nucleons and can be macroscopically envisioned as *en masse* vibrations of the nucleus. The introduction to giant resonances presented in this section predominantly largely based on the works of M.N. Harakeh and A. van der Woude [20] and E. Khan [21]. Giant resonances cor-

respond to transitions between two states as opposed to being the final states themselves and are therefore sometimes also referred to as responses to clarify this difference [22, 23, 24, 25]. Giant resonances are characterised by their total angular momentum (J_R), orbital angular momentum (L_R), spin (S_R), parity (π_R) and isospin (T_R). For the initial and final state denoted by i and f, respectively, the conservation of momentum, parity and isospin yields the following relations:

$$\vec{J}_f = \vec{J}_i + \vec{J}_R, \tag{2.1}$$

$$\pi_f = \pi_i \pi_R = \pi_i (-1)^{L_R}, \tag{2.2}$$

and

$$\vec{T}_f = \vec{T}_i + \vec{T}_R \tag{2.3}$$

where the total angular momentum and parity of the giant resonance are given by

$$\vec{J}_R = \vec{L}_R + \vec{S}_R, \tag{2.4}$$

and

$$\pi_R = (-1)^{L_R}. \tag{2.5}$$

For a giant resonance built upon a state with 0^+ spin and parity, the $\vec{J}_R$ and π_R values are identical to that of the final state. Experimental data indicates that giant resonances can be microscopically described as a coherent superposition of particle-hole excitations built upon the mean-field ground state. Since nucleon particles and their corresponding holes exhibit spins of

$$\vec{s}_p = \frac{\vec{1}}{2} \quad \text{and} \quad \vec{s}_h = \frac{\vec{1}}{2}, \tag{2.6}$$

it follows that the spin of a giant resonance is given by

$$\vec{S}_R = \vec{s}_p + \vec{s}_h = \vec{0} \text{ or } \vec{1}, \tag{2.7}$$

Similarly, given the isospin of particles and holes:

$$\vec{t}_p = \frac{\vec{1}}{2} \quad \text{and} \quad \vec{t}_h = \frac{\vec{1}}{2}, \tag{2.8}$$

the isopin of a giant resonance is given by

$$\vec{T}_R = \vec{t}_p + \vec{t}_h = \vec{0} \text{ or } \vec{1} \tag{2.9}$$

Giant resonances with isospin $\vec{T}_R = 0$ are denoted as being isoscalar and correspond to protons and neutrons which oscillate in phase. In contrast, giant

resonances with $\vec{T}_R = 1$ are denoted as isovector, corresponding to out-of-phase oscillations between protons and neutrons. An isovector resonance is additionally dependent on a quantity: T_3, which is the projection of the isospin on the third axis in isospin space, i.e. $T_3 = \frac{1}{2}$ for neutrons and $-\frac{1}{2}$ for protons. Spins of $\vec{S}_R = 0$ and 1 correspond to electric and magnetic resonances, respectively. Magnetic excitation modes correspond to the oscillation of nucleons with spin $\uparrow$ against those with spin $\downarrow$ whilst for electronic modes, there is no distinction between the spins of the nucleons. An example of various excitations of giant resonances are presented on Figure 2.1. Electric ($\Delta S = 0$) isoscalar ($\Delta T = 0$) vibrations correspond to the in-phase oscillation of protons and neutrons which is defined by the ΔL between the initial and final states. Isoscalar giant monopole resonances (which exhibit $\Delta S = 0$, $\Delta T = 0$ and $\Delta L = 0$) correspond to the radial in-phase oscillation of protons and neutrons and are also referred to as breathing or compressional modes. For a nucleus with mass A, the ISGMR is typically located at $E_x \approx 80A^{-1/3}$, however for lighter nuclei with $A < 58$, the ISGMR is generally fragmented over a wide excitation-energy range unlike for heavier nuclei which typically a single, well-defined compressional mode [26]. The newly-introduced 0^+ strength introduced by M. Itoh *et al.* $E_x \approx 9$ MeV is suggested by several formalisms (see Sections 2.2 - 2.5) to present as a breathing-mode excitation of the Hoyle state, corresponding to low-energy fragment of the ISGMR strength in ^{12}C.

To study a particular excitation mode, the populating probe can be appropriately chosen. For the case of inelastic scattering using a probe q with isospin T_q and isospin projection T_{3q}, the reaction is of the form

$$A + q \rightarrow A^* + q, \tag{2.10}$$

where A and A^* represent the nucleus of interest in its initial (i) and excited final state (f). The conservation laws for T and T_z yield:

$$\vec{T}_i + \vec{T}_q = \vec{T}_f + \vec{T}_q, \tag{2.11}$$

and

$$\begin{aligned} \vec{T}_{3i} + \vec{T}_{3q} &= \vec{T}_{3f} + \vec{T}_{3q} \\ \Rightarrow \qquad \vec{T}_{3i} &= \vec{T}_{3f}. \end{aligned} \tag{2.12}$$

Given the definition for the giant resonance isospin in Equation 2.10, it follows that

$$\vec{T}_i + \vec{T}_R = \vec{T}_f, \tag{2.13}$$

and

$$\vec{T}_{3i} + \vec{T}_{3R} = \vec{T}_{3f} \tag{2.14}$$

$$\Rightarrow \qquad \vec{T}_{3R} = 0. \tag{2.15}$$

Equations 2.11 and 2.16 ultimately yield the relation

$$0 \leq T_R \leq 2T_q. \tag{2.16}$$

This implies that a probe with T_q can be selected to limit the maximum T_R of a populated giant resonance. The primary objective of this work is to investigate the presence of an ISGMR in ^{12}C which is predicted by some of the theories introduced in this chapter. The best probe to selectively populate ISGMR strength is inelastic α scattering which populate giant resonances with a maximum isospin of $T_R = 0$ since α-particles exhibit $T_q = 0$. In conjunction with inelastic α scattering, probes which are selective against the population of ISGMRs can also provide a useful tool for their identification. An example of such a probe is the (p, t) which entails the pickup of a pair of neutrons and should not excite the ISGMR which is of one-particle one-hole (1p-1h) nature and in particular, the $1p_{3/2}$-$2p_{3/2}$ and $1p_{1/2}$-$2p_{1/2}$ excitations [12]. Instead, the (p, t) reaction is suggested to be selective towards giant pairing vibrations [15]. The combination of the ^{12}C$(\alpha, \alpha')^{12}$C and ^{14}C$(p, t)^{12}$C measurements analysed for this work therefore provides an ideal tool to identify ISGMR strength.

2.2 Antisymmetrized Molecular Dynamics

In the framework of AMD [28, 29, 30, 31, 32, 33], a wavefunction for the A-nucleon system is described by a Slater determinant $|\Phi\rangle$ of single-particle states φ_i as

$$|\Phi\rangle = \frac{1}{\sqrt{A!}} \det\left\{|\varphi_1\rangle, ..., |\varphi_A\rangle\right\}, \tag{2.17}$$

where the i^{th} single-particle wavefunction is composed of a spatial component $|\phi_i\rangle$, spin component $|\chi_i\rangle$ and isospin component $|\tau_i\rangle$ as

$$|\varphi_i\rangle = |\phi_i\rangle\,|\chi_i\rangle\,|\tau_i\rangle\,. \tag{2.18}$$

The spatial component $|\phi_i\rangle$ is given by a Gaussian wave packet centered at $\boldsymbol{Z_i}/\sqrt{\nu}$ as

$$\langle \boldsymbol{r}|\phi_i|\boldsymbol{r}|\phi_i\rangle = \frac{2\nu}{\pi}^{\frac{3}{4}} \exp\left[-\nu\left(\boldsymbol{r} - \frac{\boldsymbol{Z_i}}{\sqrt{\nu}}\right)^2 + \frac{1}{2}\boldsymbol{Z_i^2}\right] \tag{2.19}$$

$$|\chi_i\rangle = \xi_{i\uparrow}\,|\uparrow\rangle + \xi_{i\downarrow}\,|\downarrow\rangle \tag{2.20}$$

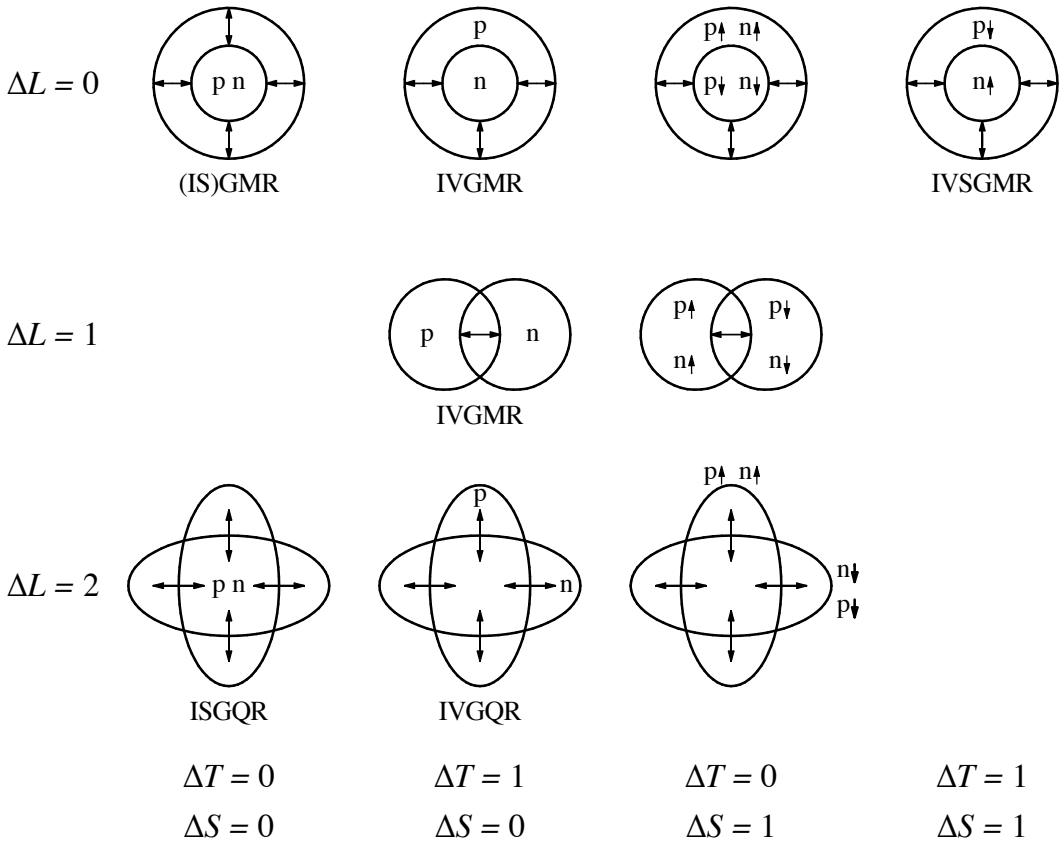

Figure 2.1: Schematic representation of collective excitation modes, adapted from Refs. [20, 27]

$$|\tau_i\rangle = |p\rangle \text{ or } |n\rangle \tag{2.21}$$

For AMD calculations, all Gaussian wave packets share the same inverse width, ν, which is a real external parameter which is optimised for each nucleus. This drawback is particularly relevant for ^{12}C as shell-model-like states typically prefer different widths with respect to cluster states. A related formalism that does not fix the inverse width is the FMD model (see Section 2.3).

Y. Kanada-En'yo investigated isoscalar monopole (ISM) and isoscalar dipole (ISD) excitations in ^{12}C with the shifted AMD plus 3α-cluster generator coordinate method [30]. Small-amplitude vibration modes, which are described by coherent 1p-1h excitations, were incorporated by small variations of the single-particle wavefunction in the ground-state wavefunction whereas large-amplitude α-cluster modes were accounted for by superposing 3α-cluster wave functions in the generator coordinate method (see Section 2.5). The calculation yields low-energy ISM strength with an energy-weighted sum rule (EWSR) value of 26% which is consistent with the 0^+_2 Hoyle state and the broad 0^+ at

listed at 10.3(3) MeV, however the properties of the higher lying broad ISGMR in ^{12}C are not reproduced.

2.3 Fermionic Molecular Dynamics

A formalism related to AMD is the Fermionic Molecular Dynamics (FMD) model pioneered by H. Feldmier [34, 35, 36, 37]. The wavefunction for A-nucleon system is given by a Slater determinant $|Q\rangle$ of single-particle states $|q_i\rangle$, given by

$$|Q\rangle = \mathcal{A}\{\, |q_1\rangle \otimes ... \otimes |q_A\rangle \,\}. \tag{2.22}$$

The single-particle wavefunctions are described by Gaussian wave packets of the form

$$\langle \boldsymbol{x}|q\rangle = \sum_i c_i \exp\left\{-\frac{(\boldsymbol{x}-\boldsymbol{b}_i)^2}{2a_i}\right\} |\chi_i\rangle \otimes, |\xi\rangle \tag{2.23}$$

and the equation of motion is obtained from the variational principle. In the framework of FMD, the inverse width a is treated as a complex time-dependent variational parameter which can be unique for each single-particle state whereas for AMD, it is a real external parameter that is shared for all single-particle states.

FMD calculations by M. Chernykh *et al.* reproduce both the Hoyle state and a 0^+_3 resonance in ^{12}C at $E_x = 10.33$ which may correspond to the broad 0^+ state listed at 10.3(3) MeV on the NNDC [38, 10]. Whilst the ground state of ^{12}C presents with a large overlap with shell-model states, both the calculated 0^+_2 Hoyle state and the higher-lying broad 0^+ state are dominated by α-cluster configurations (with a non-negligible component of shell-model nature).

Time-dependent fermionic molecular dynamics (FMD) calculations by T. Furuta *et al.* produce two broad 0^+ resonances in this excitation-energy region, each of which correspond to a different vibration mode [39]. Figure 2.3 presents results for the monopole excitations. The peak at higher frequencies is associated with the time variation of the widths (which cannot be calculated with AMD) and corresponds to the coherent vibration of the constituent α clusters which is similar to a breathing-mode excitation, as depicted in (a) of Figure 2.2. The peak at lower frequency/energy corresponds to an oscillation of the positions of three α clusters around the center of the nucleus, as depicted in (b) of Figure 2.2.

2.4 3α Orthogonality Condition Model

The orthogonality condition model (OCM) is suited towards the study of state near and above the particle threshold energy [40, 41, 42]. The Hamiltonian of

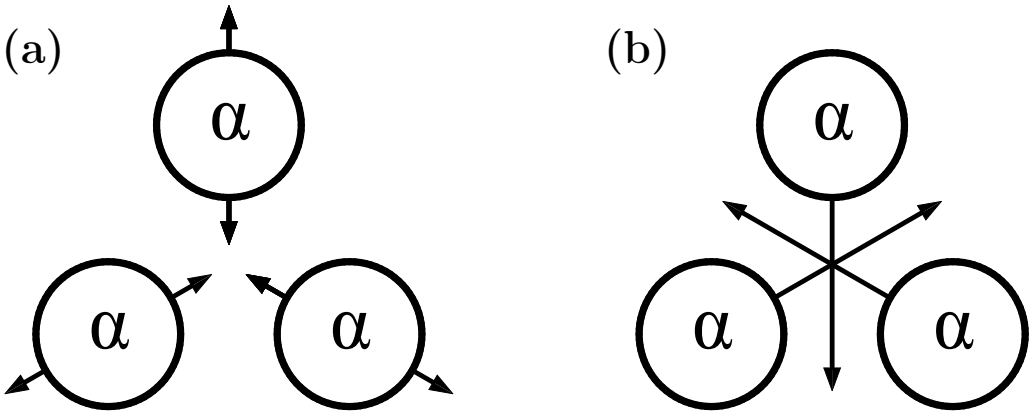

Figure 2.2: Adapted from T. Furuta *et al.* [39]. Schematics (a) and (b) respectively depict the possible small- and large-amplitude oscillation modes for the GMR in ^{12}C.

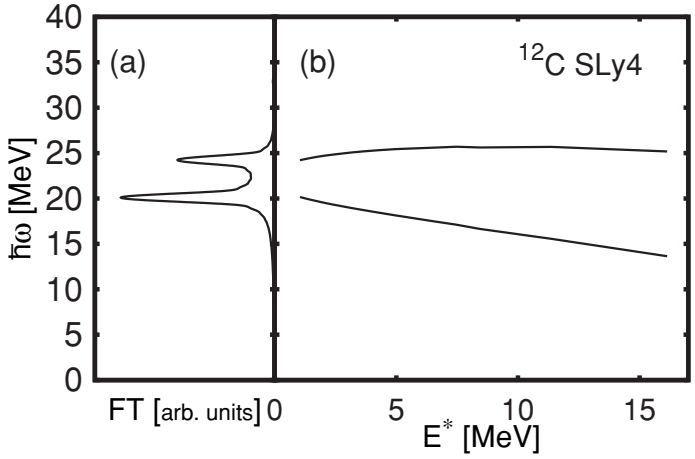

Figure 2.3: Courtesy of T. Furuta and F. Gulminelli *et al.* [39]. Panel (a) presents the oscillation frequencies of the root-mean-square radius are plotted against the spectral function (Fourier component) FT[r](ω) for the small amplitude limit. Panel (b) presents the same oscillation frequencies plotted as a function of the oscillation amplitude (excitation energy given by the initial amplitude).

the 3α OCM has the following form

$$H = \sum_{i=1}^{3} t_i - T_G + \sum_{i=1}^{3} V_{\alpha\alpha}(\xi_i) + V_{3\alpha}(\xi_1, \xi_2, \xi_3) + \sum_{i=1}^{3} V^i_{\text{Pauli}} \tag{2.24}$$

where the t_i and T_G operators correspond to the kinetic energies of the i^{th} α-particle and the centre-of-mass motion, respectively. The $V_{\alpha\alpha}$ potential corresponds to the α-α interaction and is chosen to simultaneously reproduce α-α

scattering data as well as the 3α threshold. V_{Pauli} is a pseudo potential representing the Pauli principle between α clusters. $V_{3\alpha}$ is the repulsive 3α potential which is sometimes introduced to reproduce the ground state rotational band.

Some calculations with the 3α OCM model [40, 41, 42] with the CSM method [43, 44] predict two broad 0^+ structures above the Hoyle state: the work of S. Ohtsubo *et al.* predicted the 0_3^+ state to be situated at 8.09 MeV with a width of $\Gamma = 1.68$ MeV whilst the 0_4^+ state is predicted to be situated at 11.89 MeV with a width of $\Gamma = 1.0$ MeV. OCM calculations by C. Kurokawa and K. Katō [1] predict the 0_3^+ state at 8.95 MeV with a width of $\Gamma = 1.48$ MeV whilst the 0_4^+ state is predicted to be situated at 11.87 MeV with a width of $\Gamma = 1.1$ MeV. The 0_4^+ state is suggested to correspond to a bent-arm-like structure of 3 α particles whilst the 0_3^+ state is predicted to share similar properties to the 0_2^+ Hoyle state (with a larger r.m.s. width.) and exhibit a 2α-α reduced width amplitude with a nodal number that is greater than the Hoyle state. Both sets of calculations yield parameter for the 0_3^+ and 0_4^+ states that are in relatively good agreement with the measurement by M. Itoh *et al.* which yielded a newly-introduced 0_3^+ resonance at 9.04 MeV and a 0_4^+ resonance at 10.56 MeV with respective widths of $\Gamma = 1.45(18)$ and $\Gamma = 1.42(8)$ MeV[14].

2.5 Generator Coordinate Method

The generator coordinate method (GCM) calculation by E. Eugaki *et al.* has been successful in reproducing the 0_1^+ ground state as well as the 0_2^+ Hoyle state [45]. Additionally, a higher-lying broad 0^+ state was predicted at $E_x = 11.7$ MeV with a considerable component of the $^{12}\text{C} \rightarrow ^8\text{Be}_{2^+} + \alpha$ (D-wave) configuration. This predicted broad state should correspond to the aforementioned 0_4^+ state observed by M. Itoh *et al.* which was shown to decay primary through the $^{12}\text{C} \rightarrow ^8\text{Be}_{2^+} + \alpha$ (D-wave) channel [13].

The Hamiltonian of the GCM is given by

$$\hat{H} = \sum_{i=1}^{4N} \hat{t}_i + \sum_{i<j}^{4N} \hat{v}_i(r_{ij}) + \sum_{i<j}^{4N} \hat{v}_C(r_{ij}) - \hat{t}_{cm}, \tag{2.25}$$

where $\hat{t}_i$ and $\hat{t}_{cm}$ correspond to the kinetic energies of the nucleons and the centre of mass. The $\hat{v}_N$ operator corresponds to the effective nucleon-nucleon interaction whilst $\hat{v}_C$ denotes the Coulomb interaction.

GCM calculations by B. Zhou *et al.* [46], which employed $2\alpha + \alpha$ Tohsaki-Horiuchi-Schuck-Röpke (THSR) wavefunctions, also predict broad 0_3^+ and 0_4^+ states located at 9.38 and 11.7 MeV, respectively. The GCM-THSR results for the four lowest-lying 0^+ states in ^{12}C are shown in Figure 2.4 where the excitation energies of the states are presented as a function of the number of THSR wavefunction bases. Calculations for different values of R_{cut}, an upper-limiting cutoff parameter for the radius, are shown. Using R-matrix theory [47] (see

Section 2.6), the α_0 ($^{12}\mathrm{C} \rightarrow^{8} \mathrm{Be}_{0^+} + \alpha\,(S\text{-wave})$) partial widths for the 0_2^+, 0_3^+ and 0_4^+ states were determined as 7.39 eV, 0.92 MeV and 0.66 MeV, respectively. These results are in relatively good agreement with the aforementioned measurement of M. Itoh *et al.* which yielded a newly-introduced 0_3^+ resonance at 9.04 MeV and a 0_4^+ resonance at 10.56 MeV with respective widths of $\Gamma = 1.45(18)$ and $\Gamma = 1.42(8)$ MeV. The monopole transition strength between the 0_2^+ Hoyle state and the 0_3^+ state was calculated to be much larger than other monopole transitions. The 0_3^+ state was also determined to exhibit a much larger radius (> 5 fm) than the Hoyle state. Consequently, the calculated 0_3^+ state was determined to be the breathing-mode excitation of the Hoyle state.

GCM calculations by R. Imai *et al.* [48], which employed the Brink-Bloch wavefunction comprised of $(0s)^4$ α clusters, also predict broad 0_3^+ and 0_4^+ states above the Hoyle state. It was found that both the Hoyle state and the predicted 0_3^+ state exhibit considerable monopole transition strength from the ground state due to their dilute natures. However, the monopole transition strength for the 0_3^+ state was determined to be smaller than for the Hoyle state as it is primarily composed of $4\hbar\omega$ configurations which are not accessible by the $2\hbar\omega$ monopole operator. Similarly to the calculation by B. Zhou *et al.*, it was also found that the monopole transition strength from the 0_2^+ Hoyle state to the 0_3^+ state is considerable (6.2 WU) and it was concluded that the 0_3^+ state is a $2\hbar\omega$ excitation of the Hoyle state, i.e. the breathing mode.

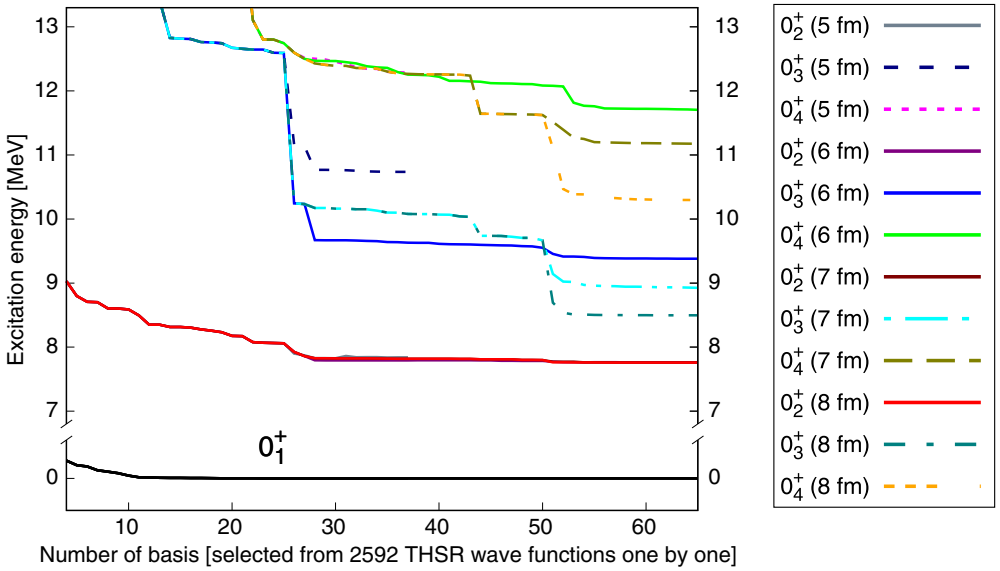

Figure 2.4: Courtesy of B. Zhou *et al.* from Ref. [46]. Excitation-energies of the four lowest-lying 0^+ states in ^{12}C as a function of the number of THSR wavefunction bases and for different values of R_{cut}. See text for details.

2.6 R-matrix Theory

A prominent formalism to analyse nuclear resonances is R-matrix theory, first introduced by Wigner and Eisenbud in 1947 [49] and is comprehensively described in the seminal paper A.M. by Lane and R.G. Thomas [47] and in a more recent review by P. Descouvemont and D. Baye [50]. The calculable R-matrix theory produces the resonance energies and reduced widths from basis functions whereas for phenomenological R-matrix, these parameters are fitted to data. This parameterisation is particularly useful for fields such as astrophysics which requires the extrapolation of data to unmeasured regions. The R-matrix formalism is fundamentally a scattering theory with a number of fundamental of assumptions such as

- The applicability of non-relativistic quantum mechanics. This is justified by the low kinetic energies of the nucleons within the nucleus with respect to the rest mass energy.
- The absence or unimportance of all processes in which more than two product nuclei are formed. This implies that the theory pertains to the energy range where three-body breakup is energetically inhibited or negligible.
- The absence or unimportance of all creation or destruction processes. This is primarily disregard photons in the formalism.
- For any pair of nuclei, there exists a radial separation distance beyond which neither nucleus experiences a nuclear potential field from the other.

The formalism was developed to describe the population of unbound states formed through the elastic scattering of two nuclei of the form:

$$A + a \rightarrow C \rightarrow A + a, \tag{2.26}$$

where C is an intermediate compound nucleus which decays independently of the reaction channel, according to the Bohr independence hypothesis [51, 52]. The resonances appear as peaks in the cross section as a function of the excitation-energy of the nucleus C (or equivalently, as a function of the beam energy E_a) [53].

The decay of the Hoyle state is dominated by pair decay and in particular, the α_0 decay mode to the ground state of ^{8}Be. Indeed, the population of the Hoyle state in stars occurs precisely through the inverse of this decay whereby an α-particle fuses to a preformed ^{8}Be nucleus. Since the ^{8}Be nucleus is inherently unbound, the population of the Hoyle state through resonance scattering with α-particles is not experimentally feasible with stable beams. Instead, the Hoyle state has been experimentally investigated through a host of alternative

populating reactions such a β decay, transfer reactions and inelastic scattering with the seminal measurement performed with the $^{12}\mathrm{N}(d,\alpha)^{12}\mathrm{C}$ reaction [54, 55]. The compound nucleus assumption essentially decouples the populating reaction channel from the intrinsic decay characteristics of the nucleus

The following section presents a brief pedagogical introduction to R-matrix theory which provides context for the more advanced R-matrix results that are implemented for the analysis [56, 57, 58]. The time-independent Schrödinger equation which describes the relative motion of the two nuclei is given by

$$\hat{H}\psi(R,\theta,\phi) = \left[\hat{T} + V - E\right]\psi(R,\theta,\phi) = 0. \tag{2.27}$$

The kinetic-energy operator $\hat{T}$ is given by

$$\begin{aligned}\hat{T} &= -\frac{\hbar^2}{2\mu}\nabla_R^2 \\ &= \frac{\hbar^2}{2\mu}\left[\frac{1}{R^2}\frac{\partial}{\partial R}\left(R^2\frac{\partial}{\partial R}\right) + \frac{\hat{L}^2}{R^2}\right],\end{aligned} \tag{2.28}$$

where the L^2 angular-momentum operator is given by

$$\hat{L}^2 = -\hbar^2\left[\frac{1}{\sin^2\theta}\frac{\partial^2}{\partial\phi^2} + \frac{1}{\sin\theta}\frac{\partial}{\partial\theta}\left(\sin\theta\frac{\partial}{\partial\theta}\right)\right], \tag{2.29}$$

If both the target and projectile nuclei are unpolarised, the potential $V = V(R)$ must be spherically symmetric and corresponds to a central force. The wavefunction of the projectile must be cylindrically symmetric and takes the form of a plane wave: e^{ikz}.

Given the commutation relations between the L^2 operator and L:

$$[L_x, L_y] = \mathrm{i}\hbar L_z, \quad [L_y, L_z] = \mathrm{i}\hbar L_x, \quad [L_z, L_x] = \mathrm{i}\hbar L_y, \tag{2.30}$$

where axis of quantisation for the angular momentum is chosen to be $\hat{z}$ (beam) axis and the z-component of the angular momentum is given by the operator

$$\hat{L}_z = \frac{\hbar}{\mathrm{i}}\frac{\partial}{\partial\phi}. \tag{2.31}$$

it can be shown that $[\hat{L}^2, \hat{L}] = 0$, implying that simultaneous eigenstates exist between these two operators. This implies that cylindrical symmetry is also preserved for the outgoing wavefunction and the time-independent Schrödinger equation 2.27 can be simplied to

$$\left[\hat{T} + V(R) - E\right]\psi(R,\theta) = 0. \tag{2.32}$$

The Legendre polynomials are a suitable basis as they commute with both $\hat{L}^2$ and $\hat{L}$ and form an orthogonal and complete basis on the interval $0 \geq \theta \geq \pi$, with an associated inner product defined as

$$\int_0^\pi P_L(\cos\theta) P_{L'}(\cos\theta) \sin\theta \mathrm{d}\theta = \frac{2}{2L+1}\delta_{LL'}. \tag{2.33}$$

The full wave function, which depends upon the radius R and the polar angle θ can therefore be expanded as

$$\psi(R,\theta) = \sum_{L=0}^{\infty}(2L+1)\mathrm{i}^L P_L(\cos\theta)\frac{1}{kR}\chi_L(R), \tag{2.34}$$

where the radial and angular dependencies of the wavefunction have been decoupled and $\frac{1}{kR}\chi_L(R)$ contains the radial dependency. Substitution of this wavefunction into Equation 2.32 yields

$$\sum_{L=0}^{\infty}\left[-\frac{\hbar^2}{2\mu}\left(\frac{\mathrm{d}^2}{\mathrm{d}R^2} - \frac{L(L+1)}{R^2}\right) + V(R) - E\right]\chi_L(R)P_L(\cos\theta) = 0. \tag{2.35}$$

Equation 2.35 can be multiplied $P_{L'}(\cos\theta)$ and integrated over 0 to π, the inner product of Equation 2.33 yields

$$\begin{aligned}\int_0^\pi \sum_{L=0}^{\infty}\left[-\frac{\hbar^2}{2\mu}\left(\frac{\mathrm{d}^2}{\mathrm{d}R^2} - \frac{L(L+1)}{R^2}\right) + V(R) - E\right]\chi_L(R)P_{L'}(\cos\theta)P_L(\cos\theta)\mathrm{d}\theta \\ = \sum_{L=0}^{\infty}\left[-\frac{\hbar^2}{2\mu}\left(\frac{\mathrm{d}^2}{\mathrm{d}R^2} - \frac{L(L+1)}{R^2}\right) + V(R) - E\right]\chi_L(R)\frac{2}{2L+1}\delta_{LL'} = 0.\end{aligned} \tag{2.36}$$

It can therefore be concluded that the following equation, known as the partial wave equation, must hold for each $\chi_L(R)$ term of the partial wave expansion:

$$\left[-\frac{\hbar^2}{2\mu}\left(\frac{\mathrm{d}^2}{\mathrm{d}R^2} - \frac{L(L+1)}{R^2}\right) + V(R) - E\right]\chi_L(R) = 0. \tag{2.37}$$

As previously mentioned, a fundamental assumption of R-matrix theory is that for any pair of nuclei, there exists a radial separation distance beyond which the nuclear interaction is negligible. This external radius, a, is a chosen parameter and not fitted to data. The challenge of solving the partial wave equation can be partitioned into an internal region ($R \leq a$), where the both the nuclear and Coulomb interactions must be accounted for, and an external region ($R \geq a$) where only the Coulomb potential persists.

For the external region ($R \geq a$), only the Coulomb potential is considered and each term of the partial wave equation can be shown to be of the form:

$$\left[\frac{\mathrm{d}^2}{\mathrm{d}\rho^2} - \frac{L(L+1)}{\rho^2} - \frac{2\eta}{\rho} + 1\right] \chi_L(\eta, \rho) = 0, \tag{2.38}$$

which is known as the Coulomb wave equation and describes the relative motion of particles under the Coulomb potential. The dimensionless Sommerfeld parameter, η, is given by

$$\eta = \frac{Z_1 Z_2 e^2}{\hbar v} = \frac{Z_1 Z_2 e^2}{\hbar} \left(\frac{\mu}{2E}\right)^2, \tag{2.39}$$

where Z_1 and Z_2 are the charges of the two decay product nuclei, μ is the reduced mass, E is the centre of mass energy, and e is the elementary unit of charge [59]. Two linearly independent solutions to this second-order differential equation are the regular and irregular Coulomb wavefunctions [60], respectively denoted as $F(\eta, \rho)$ and $G(\eta, 0)$, which exhibit the characteristics:

$$F(\eta, 0) = 0 \quad \text{and} \quad G(\eta, 0) \neq 0. \tag{2.40}$$

The Coulomb functions cannot be expressed in terms of elementary functions and are related through the Wronskian

$$G_L(\eta, \rho)\frac{\mathrm{d}F_L(\eta, \rho)}{\mathrm{d}\rho} - F_L(\eta, \rho)\frac{\mathrm{d}G_L(\eta, \rho)}{\mathrm{d}\rho} = 1 \tag{2.41}$$

Given the linear independence of $F(\eta, \rho)$ and $G(\eta, \rho)$, the external wavefunction solution $\chi_L(R)$ of the Coulomb wave equation can always be expressed as a linear combination

$$\chi_L(R) = C_1 G(\eta, \rho) + C_2 F(\eta, \rho), \tag{2.42}$$

where C_1 and C_2 are constants. It has been shown that the incident plane wave can be expressed in terms of the regular Coulomb functions [61]:

$$e^{ikz} = \sum_{L=0}^{\infty} (2L+1) i^L P_L(\cos\theta) \frac{1}{kR} F_L(0, kR). \tag{2.43}$$

The Coulomb Hankel functions, which are constructed from the regular and irregular Coulomb functions, are also linearly independent solutions and are given by

$$H_L^{\pm}(\eta, \rho) = G_L(\eta, \rho) \pm i F_L(\eta, \rho). \tag{2.44}$$

The plane wave can therefore be equivalently expressed in terms of the Coulomb Hankel Functions as

$$e^{ikz} = \sum_{L=0}^{\infty} (2L+1) \mathrm{i}^L P_L(\cos\theta) \frac{1}{kR} \frac{\mathrm{i}}{2} \left[H_L^-(0, kR) - H_L^+(0, kR)\right], \tag{2.45}$$

and the radial function $\chi_L^{\text{ext}}(R)$ is given by

$$\chi_L^{\text{ext}}(R) = A_L \left[H_L^-(0, kR) - \mathbf{S}_L H_L^+(0, kR) \right], \tag{2.46}$$

where A_L and $\mathbf{S}_L$ are complex constants. The S-matrix element for each partial wave is equivalently described by a phase shift δ_L through the relation:

$$\mathbf{S}_L = e^{2i\delta_L}. \tag{2.47}$$

The S-matrix elements $\mathbf{S}_L$ (or the related phase shifts) are uniquely determined by the potential and ultimately define the measured cross section.

For the internal region ($R \leq a$), $V(R)$ is composed of both the Coulomb and nuclear potentials. For a trial wavefunction, $u_L(R)$, the terms of the partial wave equation can be expressed as

$$u_L''(R) = \left[\frac{L(L+1)}{R^2} + \frac{2\mu}{\hbar^2} \left(V(R) - E \right) \right] u_L(R). \tag{2.48}$$

A numerical integration scheme is typically employed to solve for $u_L(R)$ and the actual radial wavefunction solution $\chi_L(R)$ is related to the trial wavefunction by some complex constant B

$$\chi_L(R) = B u_L(R). \tag{2.49}$$

For the external region ($R >= a$), the wavefunction must agree with the external form given in Equation 2.45. To determine S_L, the internal and external solutions and their respective derivatives are matched at $R = a$. A mathematical object that is convenient for matching derivatives is the inverse logarithmic derivative, known as the R-matrix element:

$$\mathbf{R}_L = \frac{1}{a} \frac{\chi_L(a)}{\chi_L'(R)} = \frac{1}{a} \frac{u_L(a)}{u_L'(R)}. \tag{2.50}$$

The R-matrix element enables the matching of $u_L(R)$ with its derivative and is independent of the complex factor B. The R-matrix element is used to determine the aforementioned S-matrix elements $\mathbf{S}_L$ to ultimately determine the reaction cross section (see Equation 2.47).

2.6.1 Important Results of R-matrix Theory

The following results are used for the R-matrix analyses for this work and are quoted without derivation. A seminal paper on the subject by A.M. Lane and R.G. Thomas [47] is recommended for in-depth derivations and discussions whilst a study by P. Descouvemont and D. Baye provides a more modern reference [50].

2.6.1.1 Cross section

For a scattering reaction of the form:

$$A + a \rightarrow C \rightarrow B + b, \tag{2.51}$$

which proceeds through N levels with the same spin and parity of the compound nucleus C, the cross section σ_{ab} can be expressed as

$$\sigma_{ab} = \frac{\pi g_J}{k_a^2} \sum_{sls'l'} \left| 2P_a^{\frac{1}{2}} P_b^{\frac{1}{2}} \sum_{\lambda,\mu=1}^{N} \gamma_{\lambda a}\gamma_{\mu b} A_{\lambda\mu} \right|^2, \tag{2.52}$$

where $A_{\lambda\mu}$ are the elements of the level matrix [47]. The reduced width amplitude $\gamma_{\lambda a}$ describes the populating reaction whilst $\gamma_{\mu b}$ pertains to the intrinsic decay properties of the levels in the compound nucleus C [62]. The square of the reduced width amplitudes are referred to as the reduced widths. The sum is over the channel spin s and relative orbital angular momentum l of both the populating reaction and the decay. In the case where the channel spin s and relative orbital angular momentum l is unique for both the populating reaction and the decay, the cross section reduces to

$$\sigma_{ab} = \frac{\pi g_J}{k_a^2} \left| 2P_a^{\frac{1}{2}} P_b^{\frac{1}{2}} \sum_{\lambda,\mu=1}^{N} \gamma_{\lambda a}\gamma_{\mu b} A_{\lambda\mu} \right|^2. \tag{2.53}$$

The elements of the level matrix depend on the eigenenergies e_λ, the level widths $\Gamma_{\lambda\mu}$:

$$\Gamma_{\lambda\mu} = \sum_c \Gamma_{\lambda\mu c}, \quad \text{where} \quad \Gamma_{\lambda\mu c} = 2P_c\gamma_{\lambda c}\gamma_{\mu c}, \tag{2.54}$$

and the level shifts $\Delta_{\lambda\mu}$, given by

$$\Delta_{\lambda\mu} = \sum_c \Delta_{\lambda\mu c}, \quad \text{where} \quad \Delta_{\lambda\mu c} = -(S_c - B_c)\gamma_{\lambda c}\gamma_{\mu c}, \tag{2.55}$$

where B_c are the boundary condition constants. The shift function, $S(E)$ is defined as

$$S(E) = ka\frac{\dot{F}(\eta,\rho)F(\eta,\rho) + \dot{G}(\eta,\rho)G(\eta,\rho)}{F_l(\eta,\rho)^2 + G_l(\eta,\rho)^2}, \tag{2.56}$$

where the derivatives, $\dot{F}(\eta,\rho)$ and $\dot{G}(\eta,\rho)$, are with respect to ρ:

$$\dot{F}(\eta,\rho) = \frac{dF(\eta,\rho)}{d\rho}, \quad \dot{G}(\eta,\rho) = \frac{dG(\eta,\rho)}{d\rho}. \tag{2.57}$$

If the shift function can be assumed to be slowly varying, the boundary condition parameter can be chosen to be $B_c = S_c(e_\lambda)$ so that the resonance energy

(eigenenergy) e_λ corresponds directly to the location parameter of a standard Lorentzian lineshape. This approximation is known as the natural boundary condition and is implemented in the R-matrix analyses for this work.

2.6.1.2 Penetrability

The penetrability, $P_l(E)$, encapsulates the effect of the Coulomb interaction between the pair of nuclei. For the decay channel with wavenumber k and with external radius $R = a$, and orbital angular momentum of decay l, the penetrability with centre-of-mass energy E is given by

$$P_l(E) = ka\left|\frac{u_l(\infty)}{u_l(a)}\right|^2, \tag{2.58}$$

where $u_l(R)$ is the radial wavefunction which can be expressed in terms of Coulomb Hankel functions (see Equation 2.45). which asymptotically reduce to plane waves given the asymptotic form of the Coulomb functions:

$$G_L(0,\rho) \sim \cos(\rho - L\pi/2), \tag{2.59}$$

and

$$H_L^{\pm}(0,\rho) \sim e^{\pm i(\rho - L\pi/2)} = \mathrm{i}^{\mp} e^{\pm \mathrm{i}\rho}. \tag{2.60}$$

The penetrability can then be expressed in terms of the regular and irregular Coulomb functions as

$$\begin{aligned} P_l(E) &= ka\left|\frac{e^{\mathrm{i}ka}}{\mathrm{i}F_L(\eta,ka) + G_L(\eta,ka)}\right|^2 \\ &= \frac{ka}{F_l(\eta,ka)^2 + G_l(\eta,ka)^2}. \end{aligned} \tag{2.61}$$

For the 0_2^+ Hoyle state, the observed lineshape is dependent on the penetrability for the α_0 decay mode: $^{12}\mathrm{C} \rightarrow {}^{8}\mathrm{Be}_{\mathrm{g.s.}} + \alpha$. The primary peak of the Hoyle state is situated at $E_x = 7.65407(19)$, just above the α separation energy of 7.36659(4) MeV where the α_0 penetrability drastically rises. It is precisely this strong excitation-energy dependence that gives rise to the aforementioned ghost of the Hoyle state.

2.6.1.3 Observed partial widths, total widths and branching ratios

The observed partial width of the i^{th} decay channel, with orbital angular momentum of decay l and with a centre-of-mass energy E is given by

$$\Gamma_i(E) = 2\gamma_i^2 P_l(E), \tag{2.62}$$

where the excitation-energy of the recoil nucleus is related through the Q value of the decay as $E_x = E - Q$. The total width of the resonance Γ (sometimes denoted as Γ_{tot}), which is a experimental observable and is given by the sum of the partial widths across all channels:

$$\Gamma = \sum_i \Gamma_i. \tag{2.63}$$

The branching ratio of the i^{th} decay channel can be determined from the ratio of the associated partial width and the total width of the resonance:

$$B_i = \Gamma_i/\Gamma. \tag{2.64}$$

2.6.1.4 Wigner limit

In a seminal paper by Wigner [63], the principle of causality is invoked in the derivation of a lower-limit for the energy derivative of the phase shift $\frac{\mathrm{d}\delta}{\mathrm{d}E}$ (see Equation 2.47). Given the interpretation of the phase shift derivative as a time delay by Eisenbud [64], this lower-limit can be interpreted as: "the scattered particle cannot leave the scatterer before it arrives". This limit corresponds to a weak/uniform potential which gives rise to the extreme case of a uniform radiall wavefuction, i.e. $w(R)/R \equiv \text{constant} \implies w(R) \propto R$. With the normalisation over the interval $0 \geq R \geq a$ given by

$$\begin{aligned} &\int_0^a \left|\frac{w(R)}{R}\right|^2 R^2 dR = 1, \\ \implies &w(R) = 3^{1/2} a^{-3/2} R. \end{aligned} \tag{2.65}$$

this limiting case translates to an upper limit on the reduced width γ_i^2 of a decay channel known as the Wigner limit, given by

$$\gamma_W^2 = \frac{\hbar}{2\mu a}|w(a)|^2 = \frac{3\hbar^2}{2\mu a^2}. \tag{2.66}$$

Implicitly, the Wigner limit also imposes an upper limit upon the observed width of a decay channel. Whilst the Wigner limit is clearly dependent upon the chosen parameter a, it is well-documented that the resulting limit upon the observed width is relatively independent of the chosen radius as the penetrability is also directly dependent on a (see Equation 2.61) [**?**].

The ratio between reduced widths and and Wigner limit is known as the Wigner ratio, given by

$$\theta_W^2 = \frac{\gamma^2}{\gamma_W^2}. \tag{2.67}$$

A large Wigner ratio for a particular decay into nuclei $B+b$ is indicative that the structure for the excited level in compound nucleus C exhibits a large content for the $B+b$ configuration.

2.6.1.5 One-Level Approximation

For the one-level approximation, the resonance in question is considered as isolated level which corresponds to a single term in the level matrix (see Equation 2.52). The cross section is given by

$$\begin{aligned}\sigma_{ab} &= \frac{\pi g_J}{k_a^2}\frac{\Gamma_{1a}\Gamma_{1b}}{\left[e_1+\Delta_1-E\right]^2+\frac{1}{4}\Gamma_1^2} \\ &= \frac{\pi g_J}{k_a^2}\frac{\Gamma_{1a}\Gamma_{1b}}{\left[\overline{E}_1-E\right]^2+\frac{1}{4}\Gamma_1^2}.\end{aligned} \tag{2.68}$$

where e_1 is eigenenergy (resonance energy) and Δ_1 is the level shift and $\overline{E}_1 = e_1+\Delta_1$. With the natural boundary condition described in Section 2.6.1.1, the fitted location parameter of the Lorentzian lineshape coresponds directly to the resonace energy (eigenenergy), i.e. $\overline{E}_1 = e_1$.

2.6.1.6 Two-Level Approximation

For two overlapping levels of the same spin and parity, the levels should not be analysed in isolation, but rather as a single anomaly. For the two-level approximation, there are four terms in the level matrix with relations given in Ref. [47] as:

$$\begin{aligned}A_{11} &= \epsilon_2/D \\ &= \left(e_2+\Delta_2-E+\tfrac{i}{2}\Gamma_2\right)/D \\ &= \left(\overline{E}_2-E+\tfrac{i}{2}\Gamma_2\right)/D,\end{aligned} \tag{2.69}$$

$$A_{22} = \epsilon_1/D \tag{2.70}$$

and

$$A_{12} = A_{21} = \xi_{12}/D, \tag{2.71}$$

where

$$\epsilon_1 = e_1+\Delta_1-E+\frac{i}{2}\Gamma_1 = \overline{E}_1-E+\frac{i}{2}\Gamma_1, \tag{2.72}$$

$$\xi_{12} = -\Delta_{12}-\frac{i}{2}\Gamma_{12}, \tag{2.73}$$

and

$$D = \epsilon_1\epsilon_2 - \xi_{12}^2, \tag{2.74}$$

which can be expanded as

$$D^2 = \left[(\overline{E}_1 - E)(\overline{E}_2 - E) + \tfrac{1}{4}(\Gamma_{12}^2 - \Gamma_1\Gamma_2)\right]^2 + \tfrac{1}{4}\left[\Gamma_1(\overline{E}_2 - E) + \Gamma_2(\overline{E}_1 - E)\right]^2. \tag{2.75}$$

With Equation 2.52, the cross section for the two-level approximation is given by

$$\sigma_{ab}(E) = \frac{\pi g_J}{k_a^2}\sum_{sls'l'}\frac{\left[(\overline{E}_2 - E)\Gamma_{1a}^{\frac{1}{2}}\Gamma_{1b}^{\frac{1}{2}} + (\overline{E}_1 - E)\Gamma_{2a}^{\frac{1}{2}}\Gamma_{2b}^{\frac{1}{2}} - \Delta_{12}\left(\Gamma_{1a}^{\frac{1}{2}}\Gamma_{2b}^{\frac{1}{2}} + \Gamma_{2a}^{\frac{1}{2}}\Gamma_{1b}^{\frac{1}{2}}\right)\right]^2 + \frac{1}{4}\left[\sum_c \Pi_{ca}\Pi_{cb}\right]^2}{\left[(\overline{E}_1 - E)(\overline{E}_2 - E) + \frac{1}{4}(\Gamma_{12}^2 - \Gamma_1\Gamma_2)\right]^2 + \frac{1}{4}\left[\Gamma_1(\overline{E}_2 - E) + \Gamma_2(\overline{E}_1 - E)\right]^2}. \tag{2.76}$$

With the natural boundary condition (described in Section 2.6.1.1), this expression for the cross section is simplified to

$$\sigma_{ab}(E) = \frac{\pi g_J}{k_a^2}\sum_{sls'l'}\frac{\left[(\overline{E}_2 - E)\Gamma_{1a}^{\frac{1}{2}}\Gamma_{1b}^{\frac{1}{2}} + (\overline{E}_1 - E)\Gamma_{2a}^{\frac{1}{2}}\Gamma_{2b}^{\frac{1}{2}}\right]^2 + \frac{1}{4}\left[\sum_c \Pi_{ca}\Pi_{cb}\right]^2}{\left[(\overline{E}_1 - E)(\overline{E}_2 - E) + \frac{1}{4}(\Gamma_{12}^2 - \Gamma_1\Gamma_2)\right]^2 + \frac{1}{4}\left[\Gamma_1(\overline{E}_2 - E) + \Gamma_2(\overline{E}_1 - E)\right]^2}. \tag{2.77}$$

In the first term of the numerator, the $(\overline{E}_2 - E)\Gamma_{1a}^{\frac{1}{2}}\Gamma_{1b}^{\frac{1}{2}}$ and $(\overline{E}_1 - E)\Gamma_{2a}^{\frac{1}{2}}\Gamma_{2b}^{\frac{1}{2}}$ components are analagous to the numerator of the single-level approximation. The primary difference is the $(\overline{E}_2 - E)$ and $(\overline{E}_1 - E)$ prefactors which suppress the "resonance" term of a particular level near the eigenenergy of the other level (and vica versa). The cross term between these components corresponds to the interference which is constructive if $\gamma_{1a}\gamma_{1b}$ and $\gamma_{2a}\gamma_{2b}$ have the opposite signs and is destructive for the converse. It is observed that the individual signs of the reduced width amplitudes cannot be individually determined, however the relative signs between $\gamma_{1a}\gamma_{1b}$ and $\gamma_{2a}\gamma_{2b}$ can be measured.

2.6.1.7 Three-Level Approximation

For three overlapping levels of the same spin and parity, the levels should not be analysed in isolation, but rather as a single anomaly For the three-level approximation, there are a total of nine terms in the level matrix, 6 of which are unique, and their relations given in Ref. [47] as:

$$DA_{11} = \epsilon_2\epsilon_3 - \xi_{23}^2, \tag{2.78}$$

$$DA_{22} = \epsilon_1\epsilon_3 - \xi_{13}^2, \tag{2.79}$$

$$DA_{33} = \epsilon_1\epsilon_2 - \xi_{12}^2, \tag{2.80}$$

$$DA_{12} = DA_{21} = -\xi_{12}\epsilon_3 - \xi_{13}\xi_{23}, \tag{2.81}$$

$$DA_{13} = DA_{31} = -\xi_{13}\epsilon_2 - \xi_{12}\xi_{23}, \tag{2.82}$$

$$DA_{23} = DA_{32} = -\xi_{23}\epsilon_1 - \xi_{12}\xi_{13}, \tag{2.83}$$

where

$$D = \epsilon_1\epsilon_2\epsilon_3, \tag{2.84}$$

$$\epsilon_1 = e_1 + \Delta_1 - E + \frac{i}{2}\Gamma_1 = \overline{E}_1 - E + \frac{i}{2}\Gamma_1, \tag{2.85}$$

and

$$\xi_{12} = -\Delta_{12} - \frac{i}{2}\Gamma_{12}. \tag{2.86}$$

Equations 2.78 and 2.81 can be expanded as

$$\begin{aligned} DA_{11} = {} & (\overline{E}_1 - E)(\overline{E}_2 - E) + \tfrac{1}{4}(\Gamma_{23}^2 - \Gamma_2\Gamma_3) - \Delta_{23}^2 \\ & + \tfrac{i}{2}\left[\Gamma_2(\overline{E}_3 - E) + \Gamma_3(\overline{E}_2 - E) - 2\Delta_{23}\Gamma_{23}\right], \end{aligned} \tag{2.87}$$

and

$$\begin{aligned} DA_{12} = {} & \Delta_{12}(\overline{E}_3 - E) - \Delta_{13}\Delta_{23} + \tfrac{1}{4}(\Gamma_{12}\Gamma_{23} - \Gamma_{12}\Gamma_3) \\ & + \tfrac{i}{2}\left[\Gamma_3\Delta_{12} + \Gamma_{12}(\overline{E}_3 - E) - \Gamma_{23}\Delta_{13} - \Gamma_{13}\Delta_{23}\right]. \end{aligned} \tag{2.88}$$

With some algebraic manipulation, the expression for the three-level approximation is determined as:

$$\sigma_{ab} = \frac{\pi g_J}{k_a^2 D^2} \sum_{sls'l'} \Bigg\{ \Bigg\langle \Gamma^{\frac{1}{2}}_{1a}\Gamma^{\frac{1}{2}}_{1b}\left[(\overline{E}_2 - E)(\overline{E}_3 - E) + \tfrac{1}{4}\left(\Gamma^2_{23} - \Gamma_2\Gamma_3\right) - \Delta^2_{23}\right] \tag{2.89}$$
$$+ \Gamma^{\frac{1}{2}}_{2a}\Gamma^{\frac{1}{2}}_{2b}\left[(\overline{E}_1 - E)(\overline{E}_3 - E) + \tfrac{1}{4}\left(\Gamma^2_{13} - \Gamma_1\Gamma_3\right) - \Delta^2_{13}\right]$$
$$+ \Gamma^{\frac{1}{2}}_{3a}\Gamma^{\frac{1}{2}}_{3b}\left[(\overline{E}_1 - E)(\overline{E}_2 - E) + \tfrac{1}{4}\left(\Gamma^2_{12} - \Gamma_1\Gamma_2\right) - \Delta^2_{12}\right]$$
$$+ \left(\Gamma^{\frac{1}{2}}_{1a}\Gamma^{\frac{1}{2}}_{2b} + \Gamma^{\frac{1}{2}}_{2a}\Gamma^{\frac{1}{2}}_{1b}\right)\left[\Delta_{12}(\overline{E}_3 - E) - \Delta_{13}\Delta_{23} + \tfrac{1}{4}\left(\Gamma_{13}\Gamma_{23} - \Gamma_{12}\Gamma_3\right)\right]$$
$$+ \left(\Gamma^{\frac{1}{2}}_{1a}\Gamma^{\frac{1}{2}}_{3b} + \Gamma^{\frac{1}{2}}_{3a}\Gamma^{\frac{1}{2}}_{1b}\right)\left[\Delta_{13}(\overline{E}_2 - E) - \Delta_{12}\Delta_{23} + \tfrac{1}{4}\left(\Gamma_{12}\Gamma_{23} - \Gamma_{13}\Gamma_2\right)\right]$$
$$+ \left(\Gamma^{\frac{1}{2}}_{2a}\Gamma^{\frac{1}{2}}_{3b} + \Gamma^{\frac{1}{2}}_{3a}\Gamma^{\frac{1}{2}}_{2b}\right)\left[\Delta_{23}(\overline{E}_1 - E) - \Delta_{12}\Delta_{13} + \tfrac{1}{4}\left(\Gamma_{12}\Gamma_{13} - \Gamma_{23}\Gamma_1\right)\right]\Bigg\rangle^2$$
$$+ \frac{1}{4}\Bigg\langle \left(\Gamma^{\frac{1}{2}}_{1a}\Gamma^{\frac{1}{2}}_{1b}\right)\left[\Gamma_2(\overline{E}_3 - E) + \Gamma_3(\overline{E}_2 - E) - 2\Delta_{23}\Gamma_{23}\right]$$
$$+ \left(\Gamma^{\frac{1}{2}}_{2a}\Gamma^{\frac{1}{2}}_{2b}\right)\left[\Gamma_1(\overline{E}_3 - E) + \Gamma_3(\overline{E}_1 - E) - 2\Delta_{13}\Gamma_{13}\right]$$
$$+ \left(\Gamma^{\frac{1}{2}}_{3a}\Gamma^{\frac{1}{2}}_{3b}\right)\left[\Gamma_1(\overline{E}_2 - E) + \Gamma_2(\overline{E}_1 - E) - 2\Delta_{12}\Gamma_{12}\right]$$
$$+ \left(\Gamma^{\frac{1}{2}}_{1a}\Gamma^{\frac{1}{2}}_{2b} + \Gamma^{\frac{1}{2}}_{2a}\Gamma^{\frac{1}{2}}_{1b}\right)\left[\Gamma_3\Delta_{12} + \Gamma_{12}(\overline{E}_3 - E) - \Gamma_{23}\Delta_{13} - \Gamma_{13}\Delta_{23}\right]$$
$$+ \left(\Gamma^{\frac{1}{2}}_{1a}\Gamma^{\frac{1}{2}}_{3b} + \Gamma^{\frac{1}{2}}_{3a}\Gamma^{\frac{1}{2}}_{1b}\right)\left[\Gamma_2\Delta_{13} + \Gamma_{13}(\overline{E}_2 - E) - \Gamma_{12}\Delta_{23} - \Gamma_{23}\Delta_{12}\right]$$
$$+ \left(\Gamma^{\frac{1}{2}}_{2a}\Gamma^{\frac{1}{2}}_{3b} + \Gamma^{\frac{1}{2}}_{3a}\Gamma^{\frac{1}{2}}_{2b}\right)\left[\Gamma_1\Delta_{23} + \Gamma_{23}(\overline{E}_1 - E) - \Gamma_{12}\Delta_{13} - \Gamma_{13}\Delta_{12}\right]\Bigg\rangle^2\Bigg\},$$

where

$$D^2 = \Big[(\overline{E}_1 - E)(\overline{E}_2 - E)(\overline{E}_3 - E) - \tfrac{1}{4}\left\{\Gamma_1\Gamma_2(\overline{E}_3 - E) + \Gamma_2\Gamma_3(\overline{E}_1 - E) + \Gamma_1\Gamma_3(\overline{E}_2 - E)\right\}\Big]^2$$
$$+ \tfrac{1}{4}\Big[\Gamma_2(\overline{E}_1 - E)(\overline{E}_3 - E) + \Gamma_1(\overline{E}_2 - E)(\overline{E}_3 - E) + \Gamma_3(\overline{E}_1 - E)(\overline{E}_2 - E) - \tfrac{1}{4}\Gamma_1\Gamma_2\Gamma_3\Big]^2. \tag{2.90}$$

Under the natural boundary condition described in Section 2.6.1.1, the cross section can be simplified to

$$\begin{aligned}
\sigma_{ab} = \frac{\pi g_J}{k_a^2 D^2} \sum_{sls'l'} \Bigg\{ \Bigg\langle & \quad \Gamma^{\frac{1}{2}}_{1a}\Gamma^{\frac{1}{2}}_{1b}\left[(\overline{E}_2 - E)(\overline{E}_3 - E) + \tfrac{1}{4}\left(\Gamma^2_{23} - \Gamma_2\Gamma_3\right)\right] \\
& + \Gamma^{\frac{1}{2}}_{2a}\Gamma^{\frac{1}{2}}_{2b}\left[(\overline{E}_1 - E)(\overline{E}_3 - E) + \tfrac{1}{4}\left(\Gamma^2_{13} - \Gamma_1\Gamma_3\right)\right] \\
& + \Gamma^{\frac{1}{2}}_{3a}\Gamma^{\frac{1}{2}}_{3b}\left[(\overline{E}_1 - E)(\overline{E}_2 - E) + \tfrac{1}{4}\left(\Gamma^2_{12} - \Gamma_1\Gamma_2\right)\right] \\
& + \tfrac{1}{4}\left(\Gamma^{\frac{1}{2}}_{1a}\Gamma^{\frac{1}{2}}_{2b} + \Gamma^{\frac{1}{2}}_{2a}\Gamma^{\frac{1}{2}}_{1b}\right)\left(\Gamma_{13}\Gamma_{23} - \Gamma_{12}\Gamma_3\right) \\
& + \tfrac{1}{4}\left(\Gamma^{\frac{1}{2}}_{1a}\Gamma^{\frac{1}{2}}_{3b} + \Gamma^{\frac{1}{2}}_{3a}\Gamma^{\frac{1}{2}}_{1b}\right)\left(\Gamma_{12}\Gamma_{23} - \Gamma_{13}\Gamma_2\right) \\
& + \tfrac{1}{4}\left(\Gamma^{\frac{1}{2}}_{2a}\Gamma^{\frac{1}{2}}_{3b} + \Gamma^{\frac{1}{2}}_{3a}\Gamma^{\frac{1}{2}}_{2b}\right)\left(\Gamma_{12}\Gamma_{13} - \Gamma_{23}\Gamma_1\right)\Bigg\rangle^2 \\
+ \frac{1}{4}\Bigg\langle & \left(\Gamma^{\frac{1}{2}}_{1a}\Gamma^{\frac{1}{2}}_{1b}\right)\left[\Gamma_2(\overline{E}_3 - E) + \Gamma_3(\overline{E}_2 - E)\right] \\
& + \left(\Gamma^{\frac{1}{2}}_{2a}\Gamma^{\frac{1}{2}}_{2b}\right)\left[\Gamma_1(\overline{E}_3 - E) + \Gamma_3(\overline{E}_1 - E)\right] \\
& + \left(\Gamma^{\frac{1}{2}}_{3a}\Gamma^{\frac{1}{2}}_{3b}\right)\left[\Gamma_1(\overline{E}_2 - E) + \Gamma_2(\overline{E}_1 - E)\right] \\
& + \left(\Gamma^{\frac{1}{2}}_{1a}\Gamma^{\frac{1}{2}}_{2b} + \Gamma^{\frac{1}{2}}_{2a}\Gamma^{\frac{1}{2}}_{1b}\right)\Gamma_{12}(\overline{E}_3 - E) \\
& + \left(\Gamma^{\frac{1}{2}}_{1a}\Gamma^{\frac{1}{2}}_{3b} + \Gamma^{\frac{1}{2}}_{3a}\Gamma^{\frac{1}{2}}_{1b}\right)\Gamma_{13}(\overline{E}_2 - E) \\
& + \left(\Gamma^{\frac{1}{2}}_{2a}\Gamma^{\frac{1}{2}}_{3b} + \Gamma^{\frac{1}{2}}_{3a}\Gamma^{\frac{1}{2}}_{2b}\right)\Gamma_{23}(\overline{E}_1 - E)\Bigg\rangle^2\Bigg\}, \qquad (2.91)
\end{aligned}$$

2.6.1.8 Feeding factors for Direct Reactions

As previously mentioned, the formalism of R-matrix theory was initially developed in the context of elastic resonance scattering of the form in Equation 2.26 and provided expressions for the cross sections and phase shifts. Such resonances can also be studied through nuclear reactions of the form

$$D + d \rightarrow C + c \qquad (C \rightarrow B + b), \qquad (2.92)$$

where D and d are the target and projectile, respectively. C and c are the recoil and ejectile nuclei and under the single-channel approximation, C is assumed to only decay through the breakup into particles $A + a$. The work of F.C. Barker investigated how the parameters to describe the nucleus should be consistent between such reactions and the aforementioned elastic resonance scattering [53, 62]. For scattering of the form in Equation 2.26, the cross section for a single level is given in Equation 2.68. For a direct of the form in Equation 2.92, the cross section for a single level can be expressed as

$$\sigma_{dcb}(E) \propto \frac{G_{1dc}\Gamma_{1b}}{\left[E - e_1 - \Delta_1\right]^2 + \frac{1}{4}\Gamma_1^2}, \tag{2.93}$$

where G_{1dc} is a real positive feeding factor that typically varies slowly with excitation energy. The form of this cross section is analagous to Equation 2.68 where feeding channel width Γ_{1a} is replaced by the feeding factor G_{1dc}. For scattering of the form in Equation 2.51, the feeding channel width contributes to both the total width Γ_{tot} and the level shifts Δ, however they do not contribute for direct reactions of the form in Equation 2.92. All the nuclear reaction measurements analysed for this work predominantly proceed through direct-reaction mechanism. Consequently, this formalism for analysing direct reactions was implemented for the single-level, two-level and three-level approximations used by the R-matrix analysis code (see Section 4.10).

2.6.2 Penetrabilities with finite-width daughter states

The penetrability $P_l(E)$ expresses the relative probability of decay for a particular decay channel with orbital angular momentum l. This decay occurs between states in the parent and daughter nuclei which have excitation energies of E_x and E', respectively. The use of this form of the penetrability implicitly assumes that the final state of the daughter nucleus can be approximated to be infinitely narrow. For the $E_x \approx$ 7-16 MeV excitation-energy region of interest in ^{12}C, the only relevant decay modes are α_0 and α_1 decay to the 0_1^+ ground state and 2_1^+ excited state of ^{8}Be, respectively. This assumption is not appropriate for both the α_0 and α_1 decay modes since the ground state of the corresponding ^{8}Be daughter nucleus is inherently unbound by 91.84(4) keV. Similar to the Hoyle state, the 0_1^+ ground state of ^{8}Be, with a width of 5.57(25) eV, is understood to manifest a secondary peak known as the ghost anomaly given the close proximity of the resonance energy above the α-separation energy [65, 66]. The α_0 decay channel to the ground state is often used for the simplified single-channel R-matrix parameterisation of the Hoyle state. Whilst the penetrability is typically calculated directly to the 0.0 MeV resonance energy of the ^{8}Be ground state, it has been previously postulated that the α_0 decay mode to the ghost of the ^{8}Be ground state may not be negligible [8]. For α_1 decay, the significantly larger width of 1.513(15) MeV for the 2_1^+ 3.030(10) MeV excited state of ^{8}Be is also incompatible with the aforementioned approximation of the daughter state being infinitely narrow [10]. In order to account for the finite width of a daughter state, a modified penetrability $\mathcal{P}_l(E)$ is introduced as

$$\mathcal{P}_l(E) = \frac{\int_{E_0}^{E} P_l(E - E')\rho(E')\,dE'}{\int_{E_0}^{E} \rho(E')\,dE'}, \tag{2.94}$$

where $\rho(E')$ is the intrinsic nuclear lineshape of the daughter state, E' is the excitation energy of the daughter nucleus and E is the centre-of-mass energy of the decay, given by

$$E = E_x + Q, \tag{2.95}$$

where the Q value corresponds to the decay. The normalisation factor in the denominator of Equation 2.94 is dependent on the centre-of-mass energy E as for a parent nucleus with $E_x = E - Q$, the highest excitation energy of the daughter nucleus that is accessible through the corresponding decay is $E' = E$. The lower limit of the integrals, E_0, is the minimum excitation energy of the daughter-state nucleus. For bound nuclei $E_0 = 0$, but in the case of ^{8}Be, $E_0 = -91.84(4)$ keV as the ground state resonance has been relatively defined to be situated at 0 keV. The integration range can therefore extend to negative values for E' as the intrinsic lineshape of the daughter state can in general extend to negative excitation energies if the daughter nucleus is

unbound, as is the case for α_0 decay from ^{12}C to the ground state of ^{8}Be which exhibits a width of 5.57(25) eV. This means that for daughter nuclei which are inherently unbound, it is possible that $\mathcal{P}_l(0) > 0$, although this effect is negligible as the intrinsic lineshape $\rho(E')$ typically vanishes rapidly as E' approaches the lower integration limit E_0. For the ground state of ^{8}Be, the intrinsic lineshape falls below 1% of the peak maximum at just 30 eV below the peak maximum situated at 0 MeV (see Figure 2.6).

Other forms of penetrability have been implemented by S. Hyldegaard et al. [67] which corresponds to a formula from the work of A.M. Lane and R.G. Thomas [47], given by

$$\mathcal{P}_l(E) = \int_0^{E_{max}} P_l(E - E')\rho(E')/\pi \, dE', \tag{2.96}$$

where E_{max} is the upper integration limit for the excitation-energy of ^{8}Be which was chosen so that the 0_1^+ and 2_1^+ states dominate within the integration interval. The associated normalisation is given by

$$\int_0^{\infty} \rho(E') \, dE' = \pi. \tag{2.97}$$

Another alternative penetrability suggested by L. Buchmann [68] is more similar to version used in this work and is given by

$$\mathcal{P}_l(E) = \frac{\int_0^{\infty} P_l(E + Q - E')\rho(E') \, dE'}{\int_0^{\infty} \rho(E') \, dE'}. \tag{2.98}$$

For completeness, Ref. [67] quotes Ref. [68] as having a slightly different form:

$$\mathcal{P}_l(E) = \frac{\int_0^{\infty} P_l(E - E')\rho(E') \, dE'}{\int_0^{\infty} \rho(E') \, dE'}. \tag{2.99}$$

A common issue with these alternative forms for $\mathcal{P}_l(E)$ in Equations 2.96, 2.98 and 2.99 is that they they do not integrate below $E' = 0$. For the case of α_0 decay from ^{12}C to the ground state of ^{8}Be, the lower integration limit of 0 means that approximately half of the primary peak for ground state is erroneously omitted from the weighted average. Furthermore, the normalisation for the penetrability in Equation 2.96 violates energy-conservation. For a particular centre-of-mass decay energy E, the maximum excitation energy that can be accessed for the daughter nucleus is $E' = E$. The intrinsic lineshape of the daughter state $\rho(E')$, which acts as the probability density function for the weighted average, should therefore only be normalised up to E and not infinity as in Equation 2.97. A final note on the penetrabilities given by Equations 2.96, 2.98 and 2.99 is that the upper limit of integration for the numerator does not have to extend to infinity as $P_l(E^*) = 0$ for $E^* \leq 0$.

To reliably determine the intrinsic nuclear lineshapes of the 0_1^+ ground state and the 2_1^+ excited state of ^{8}Be, an R-matrix analysis of the ^{8}Be excitation-energy spectrum was performed using literature values. The ^{12}C$(p, p\alpha)^8$Be measurement performed by J. Mabiala *et al.* at iThemba LABS was reanalysed and presented in Figure 2.5 [69]. The three resonances that contribute to the ^{8}Be excitation-energy spectrum below 15 MeV are the 0_1^+ ground state and the 2_1^+ and 4_1^+ excited states. Since all three resonances exhibit different spin, a one-level formalism can be used to describe the lineshape for each resonance. Given the large proton separation energy for ^{8}Be of 17.25440(4) MeV, the only relevant decay mode for the displayed excitation-energy range is α decay. Moreover, since ^{4}He can be considered inert for these energies as its first excited state is situated at > 20 MeV, each of the aforementioned lineshapes can be further simplified to only consider a single channel of α_0 decay. In order to be consistent with literature, the resonance energies and observed widths for the R-matrix lineshapes are fixed to the values listed on the NNDC [10]. The observed lineshapes are all convolved with both Gaussian and Landau distributions (with the same optimised parameters for all resonances) to approximate the experimental resolution and target-related energy loss, respectively. This analysis independently shows that the NNDC parameters provide a satisfactory parameterisation of the ^{8}Be excitation-energy spectrum. The intrinsic lineshapes of the 0_1^+ ground state and the 2_1^+ excited state of ^{8}Be are presented on Figure 2.6. The maximum of the primary peak of the 0_1^+ ground state is out of the displayed range with the maximum value at approximately 1.5×10^6 times the maximum of the ghost anomaly which is located at approximately 0.46 MeV. The yield within the primary peak is approximately 4.7 times that of the ghost anomaly.

The P_l and $\mathcal{P}_l$ penetrabilities for the α_0 decay mode of ^{12}C are displayed on Figures 2.7 and 2.8 for $l = 0, 1, 2, 3$ and 4. It is observed that at lower excitation energies, the P_l and $\mathcal{P}_l$ penetrabilities are functionally identical since the α_0 decay mode is dominated by the transition into the narrow primary peak of the 0_1^+ ^{8}Be ground state, which can be well approximated by an infinitely narrow peak. As the excitation energy increases, the P_l and $\mathcal{P}_l$ penetrabilities diverge as their is sufficient centre of mass energy for the α_0 decay mode to access the transition to the ghost anomaly. Since α_0 decays to the ghost anomaly have less centre of mass kinetic energy compared with decays to the narrow primary peak, the $\mathcal{P}_l$ penetrability becomes lower than P_l. For higher excitation energies beyond $E_x \approx 18$ MeV, the energy dependence between P_l and $\mathcal{P}_l$ converges, as can be seen on Figure 2.9. This is because at such energies, the kinematics of α_0 decay to the primary peak and the ghost anomaly also converge.

The P_l and $\mathcal{P}_l$ penetrabilities for the α_1 decay mode of ^{12}C are displayed on Figures 2.10 for $l = 0, 1, 2, 3$ and 4. These α_1 penetrabilities require a more thorough analysis and the penetrabilities for $l = 0, 1, 2, 3$ and 4 are displayed on Figures 2.11 - 2.15, respectively. An arbitrary threshold of 0.01 has been

used to indicate the excitation energies beyond which the P_l and $\mathcal{P}_l$ penetrabilities are non negligible and the excitation energy at which P_l and $\mathcal{P}_l$ intersect is also shown. It is observed that at lower excitation energies below this intersection point, the modified $\mathcal{P}_l$ penetrability is considerably larger than P_l. This is because the modified $\mathcal{P}_l$ penetrability permits α_1 decays to ^{8}Be excitation energies below the 3.030(10) MeV resonance energy of the 2^+_1 excited state. Since these transitions are not accounted for by the P_l penetrability, the excitation energy at which P_l becomes non-negligible is significantly larger. Equivalently, the observed α_1 partial width associated with $\mathcal{P}_l$ begins to play an important role at approximately 2 MeV lower in the excitation energy with respect to the α_1 partial width predicted by P_l. Beyond the point of intersection between P_l and $\mathcal{P}_l$, the modified $\mathcal{P}_l$ penetrability is suppressed with respect to P_l. Analagous to α_0 decay, this is because α_1 decays to the high-energy tail of the 2^+_1 excited state of ^{8}Be have less centre of mass kinetic energy compared with decays to the singular resonance energy of 3.030(10) MeV. For higher excitation energies beyond $E_x \approx 25$ MeV, the energy dependence between P_l and $\mathcal{P}_l$ converges, as can be seen on Figure 2.16. At such energies, the kinematics of α_1 decay to the high-energy tail of the 2^+_1 excited state and the singular 3.030(10) MeV resonance energy converge.

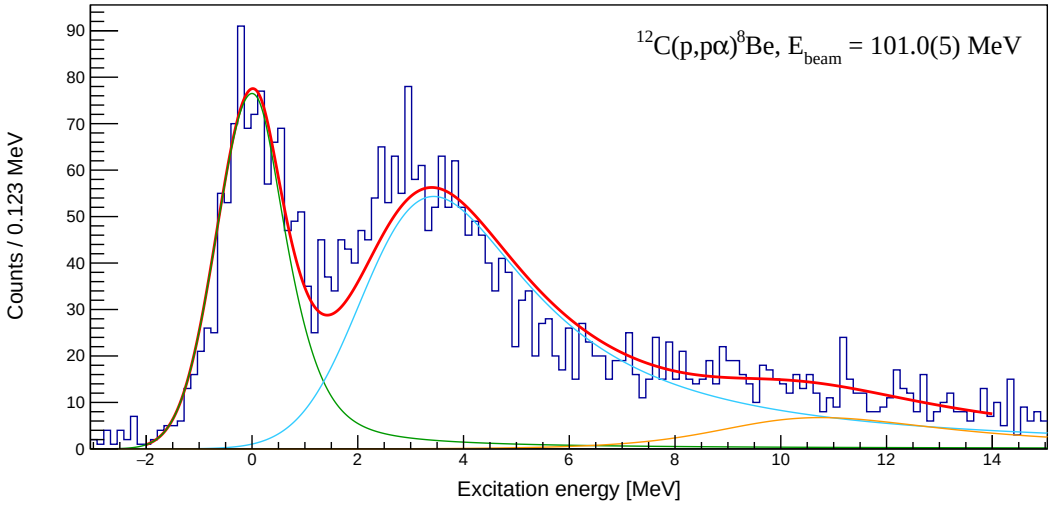

Figure 2.5: The excitation-energy spectrum of ^{8}Be from the $^{12}\mathrm{C}(p, p\alpha)^8\mathrm{Be}$ measurement with $E_{\mathrm{beam}} = 101.0(5)$ MeV, performed by J. Mabiala *et al.* at iThemba LABS [69].

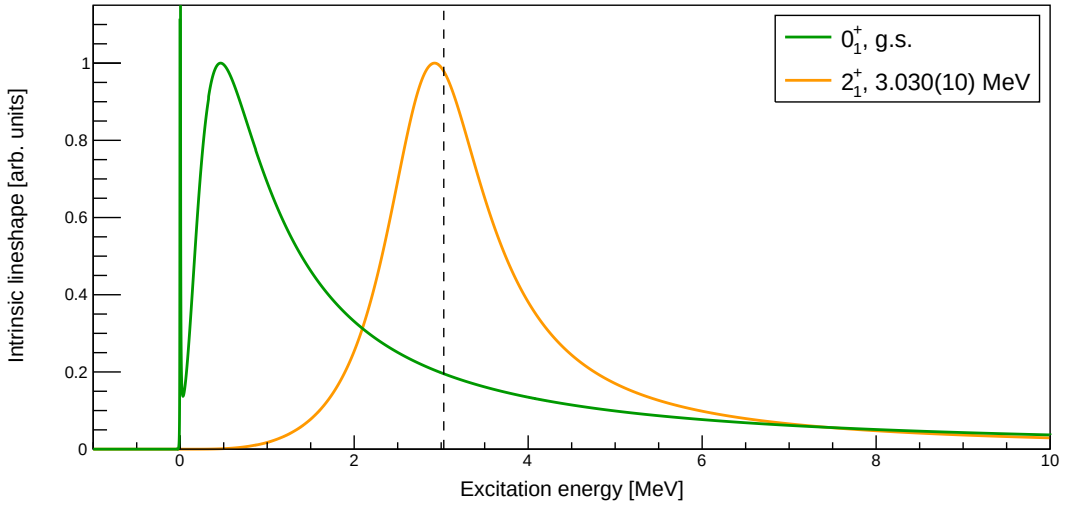

Figure 2.6: The intrinsic lineshapes of the 0^+_1 ground state and the 2^+_1 excited state of ^{8}Be, according to the values listed on the NNDC [10]. The vertical dashed line indicates the 3.030(10) MeV resonance energy of the 2^+_1 state.

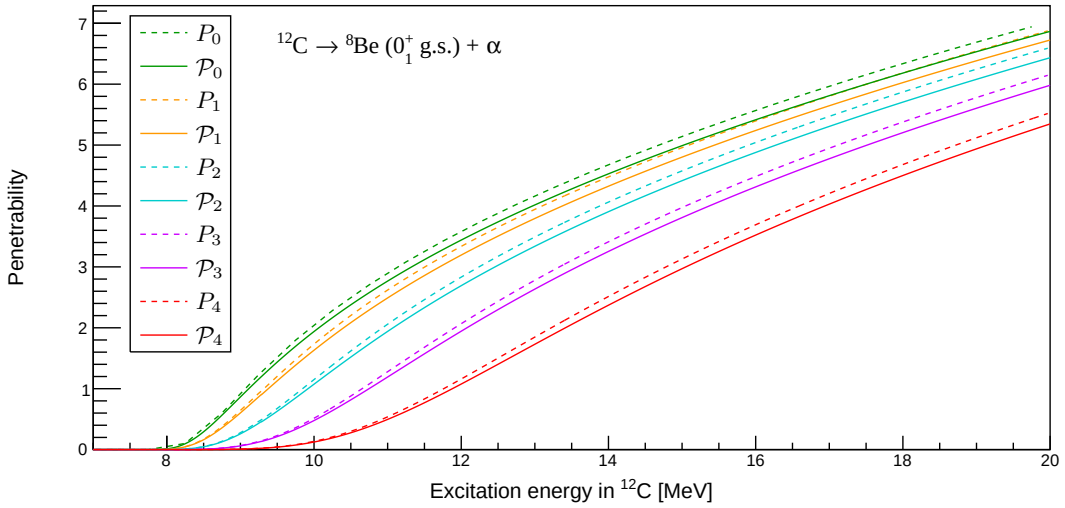

Figure 2.7: The P_l and $\mathcal{P}_l$ penetrabilities for the α_0 decay mode of ^{12}C for $l = 0, 1, 2, 3$ and 4.

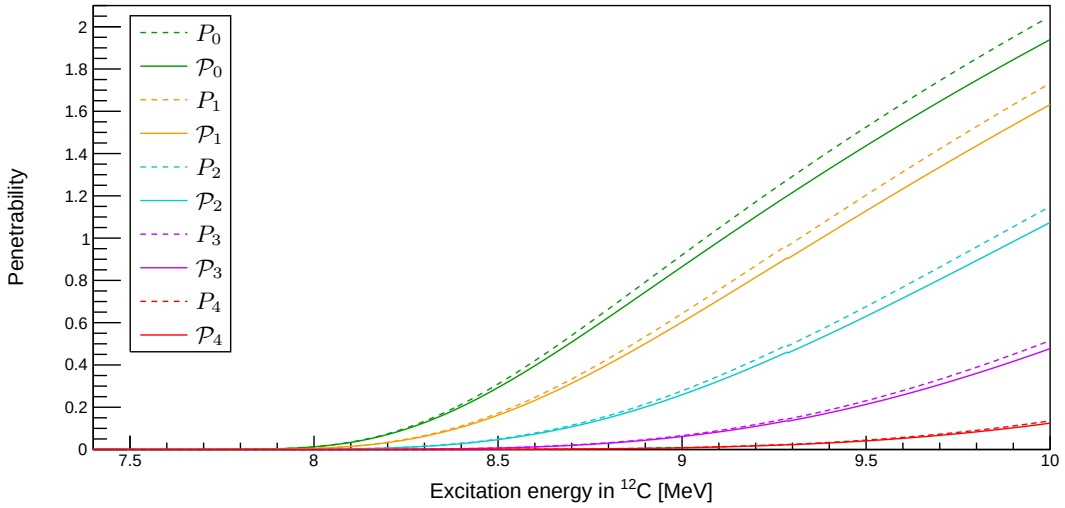

Figure 2.8: The P_l and $\mathcal{P}_l$ penetrabilities for the α_0 decay mode of ^{12}C for $l = 0, 1, 2, 3$ and 4, zoomed in on the divergence between P_l and $\mathcal{P}_l$.

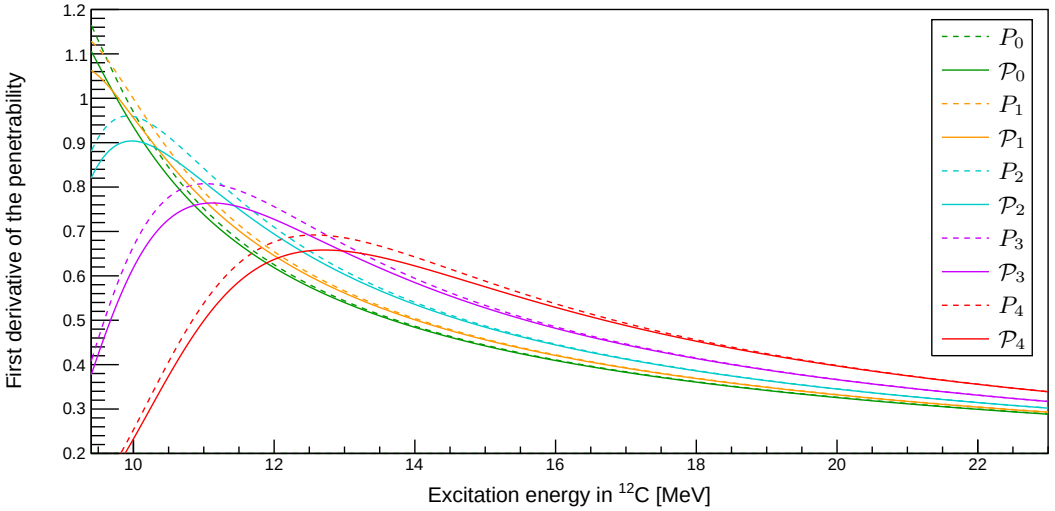

Figure 2.9: The first derivative of the P_l and $\mathcal{P}_l$ penetrabilities for the α_0 decay mode of ^{12}C for $l = 0, 1, 2, 3$ and 4.

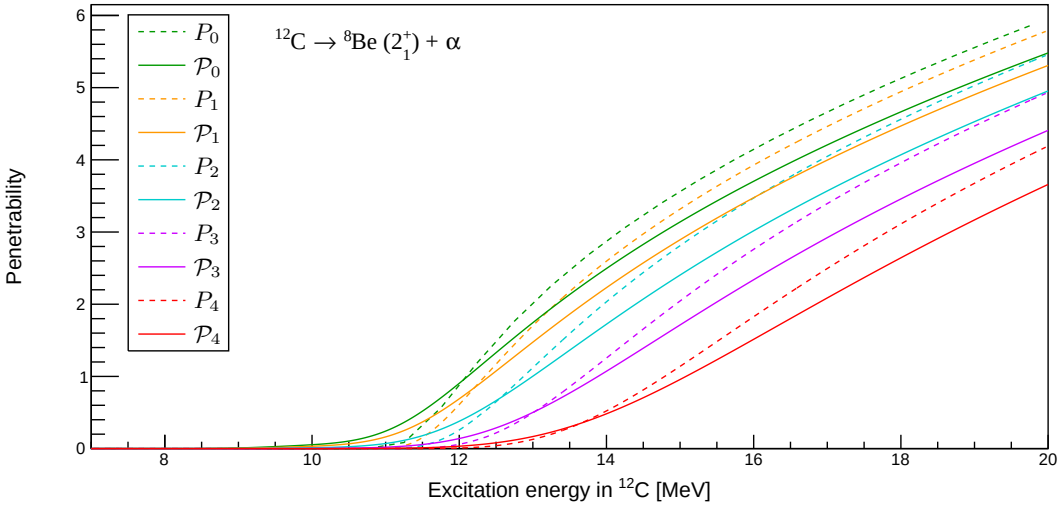

Figure 2.10: The P_l and $\mathcal{P}_l$ penetrabilities for the α_1 decay mode of ^{12}C for $l = 0, 1, 2, 3$ and 4.

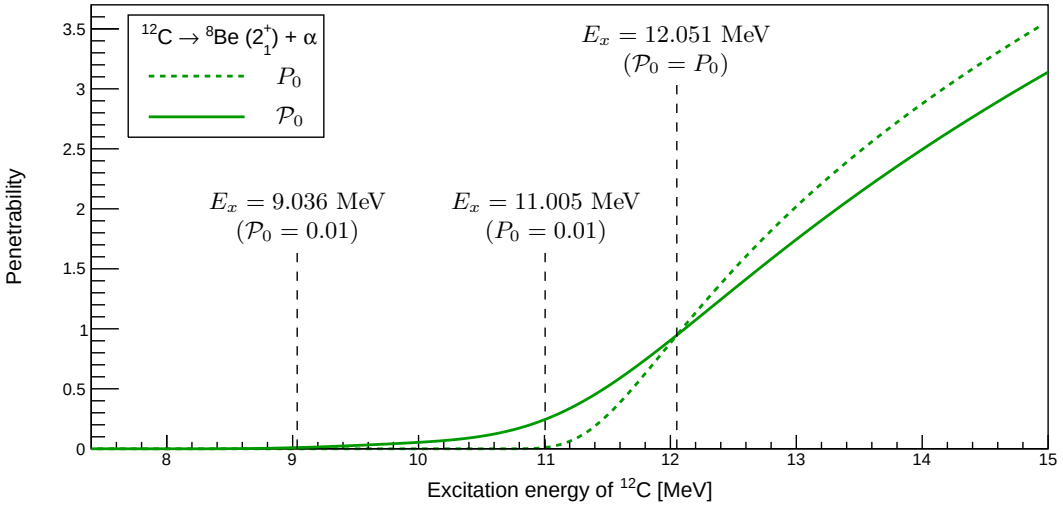

Figure 2.11: The P_0 and $\mathcal{P}_0$ penetrabilities for the α_1 decay mode of ^{12}C.

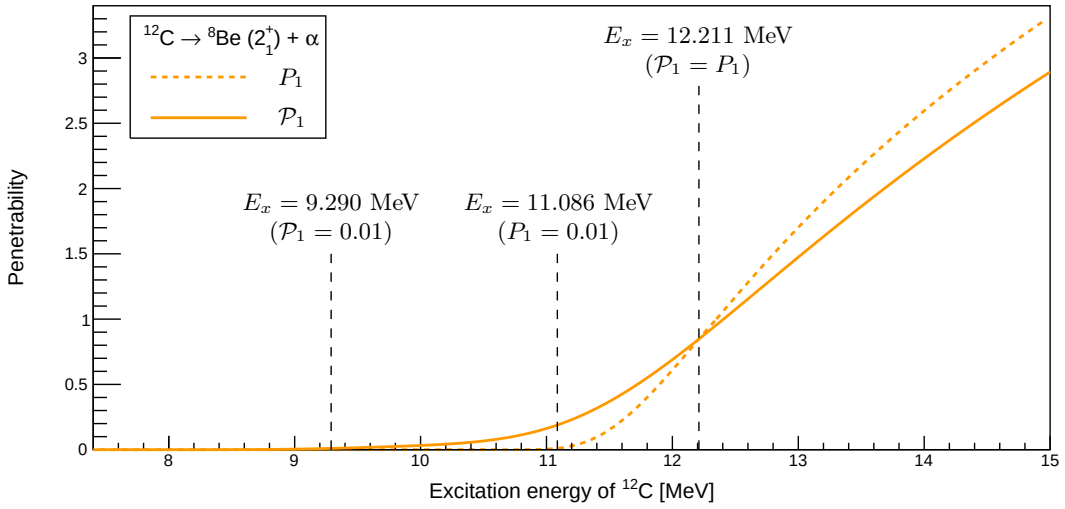

Figure 2.12: The P_1 and $\mathcal{P}_1$ penetrabilities for the α_1 decay mode of ^{12}C.

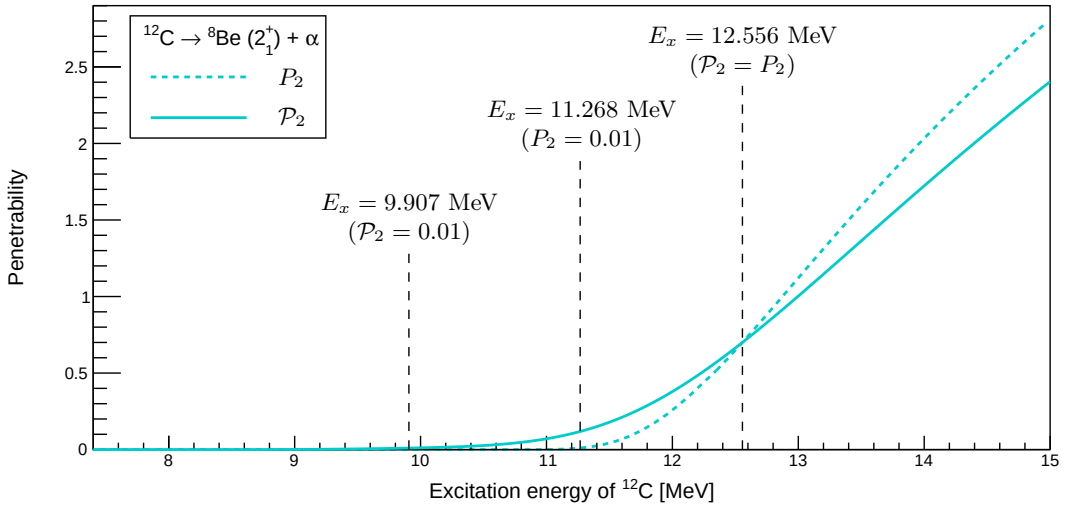

Figure 2.13: The P_2 and $\mathcal{P}_2$ penetrabilities for the α_1 decay mode of ^{12}C.

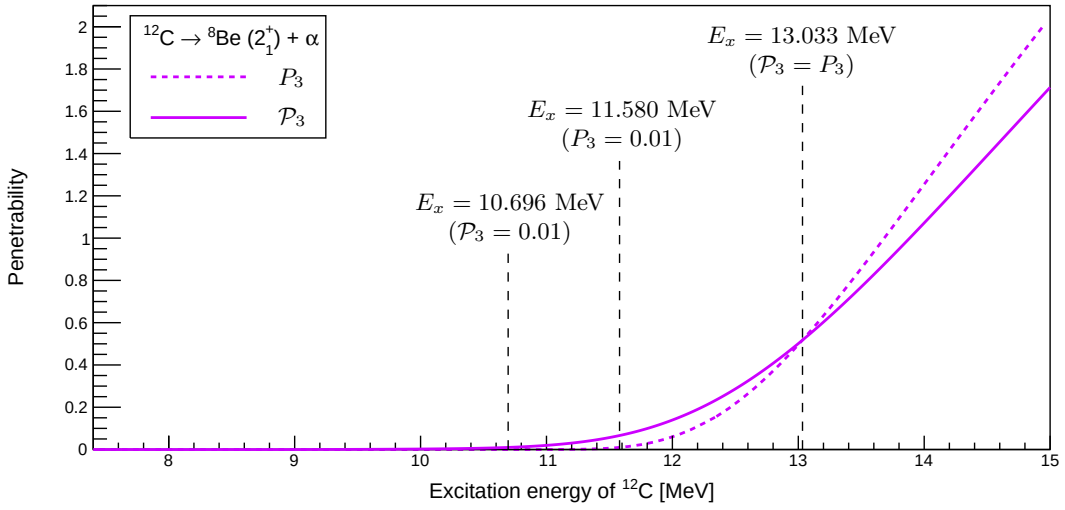

Figure 2.14: The P_3 and $\mathcal{P}_3$ penetrabilities for the α_1 decay mode of ^{12}C.

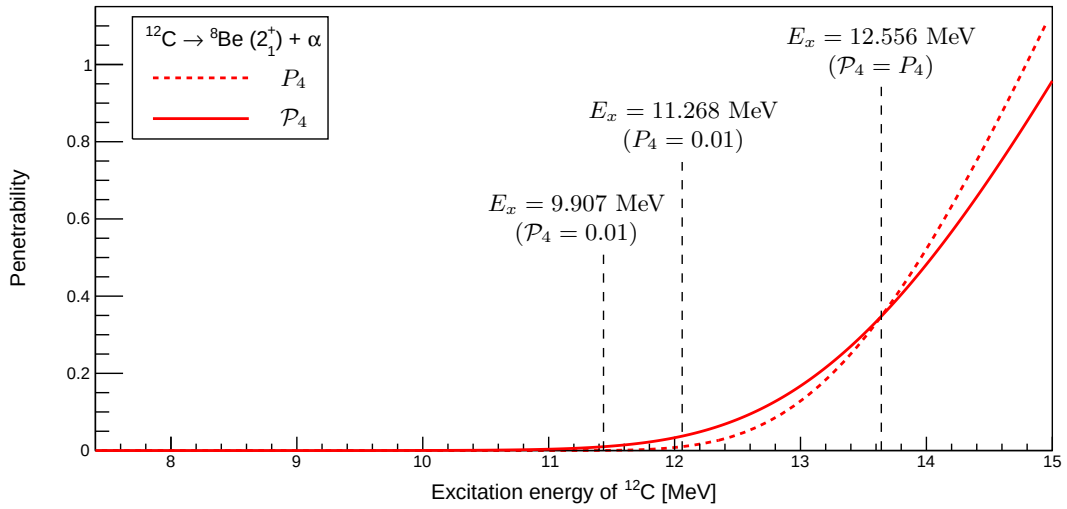

Figure 2.15: The P_4 and $\mathcal{P}_4$ penetrabilities for the α_1 decay mode of ^{12}C.

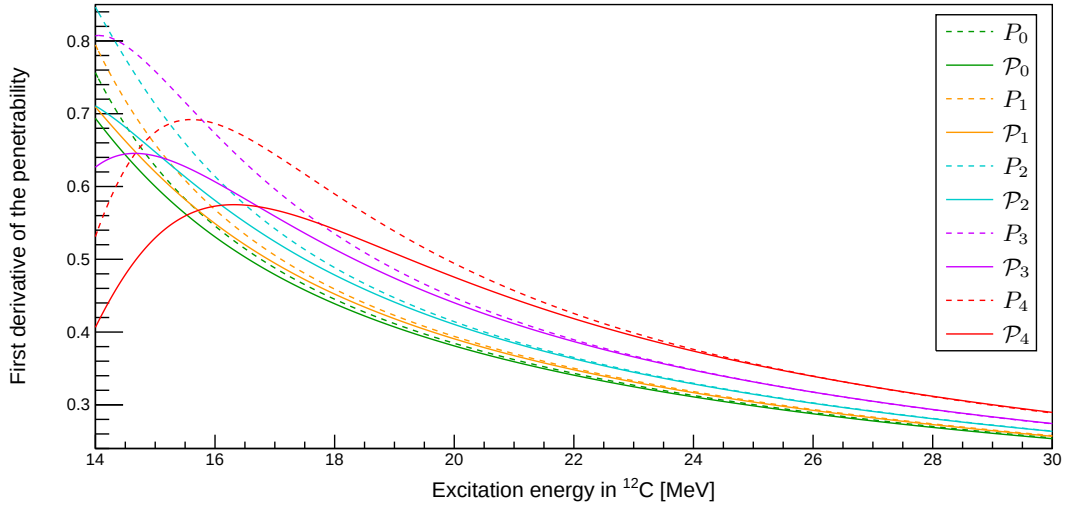

Figure 2.16: The first derivative of the P_l and $\mathcal{P}_l$ penetrabilities for the α_1 decay mode of ^{12}C for $l = 0, 1, 2, 3$ and 4.

2.7 Reaction Channels

In general, the observed lineshape of a populated resonance is dependent on both the intrinsic structure of the nucleus and the populating reaction channel. In order to consistently analyse the $^{12}\mathrm{C}(\alpha, \alpha')^{12}\mathrm{C}$ and $^{14}\mathrm{C}(p, t)^{12}\mathrm{C}$ measurements for this thesis on an even footing, the excitation-energy dependence of each populating reaction must be determined.

The formulation of R-matrix theory is typically presented in the context of resonant scattering, whereby the centre-of-mass energy of the projectile

and target nuclei is equal to the excitation-energy of the resonance [47, 57]. The projectile and target nuclei form a compound nucleus through successive interactions over a timescale of $10^{-18} - 10^{-16}$ s. The successive interactions are localised within the interior of the nucleus and the energy is shared amongst the nucleons of the system. The evaporation of particles from the compound nucleus is consequently uncorrelated to the population channel. For such resonance-scattering measurements, the beam energy is typically varied to determine an excitation function. The projectile is captured and undergoes a time delay before being emitted as the decay particle. A resonance, which presents as a change in the excitation function, corresponds to a rise in the phase shift $\delta(E)$ that can be expressed as

$$\delta(E) = \delta_{bg}(E) + \delta_{res}(E), \tag{2.100}$$

where δ_{bg} and δ_{res} are the elastic background and resonance phase shifts, respectively. In general, resonance-scattering reactions may introduce a non-zero background phase shifts which result in observed lineshapes that depart significantly from the Breit-Wigner lineshape [56]. In contrast to resonance scattering, direct reactions typically occur at higher centre-of-mass energies [70]. The direct reaction mechanism typically occurs through a single interaction in contrast to the successive interactions of the compound nucleus. Direct reactions occur through a single step over a shorter timescale that is related to the traversal time of the projectile with respect to the size of the target nucleus. Consequently, direct reactions are understood to predominantly probe the periphery of the nucleus and excite simple nucleon configurations which are similar to that of the ground state. The direct-reaction is the dominant reaction mechanism that occurs for all the ^{12}C$(\alpha,\alpha')^{12}$C and ^{14}C$(p,t)^{12}$C measurements analysed for this thesis, although intermediate reactions with successive interactions do contribute. In these two cases of inelastic α scattering and two-neutron transfer, the ejectile is distinct from the decay particle of the resonance of interest. The background elastic phase shift that is present for resonance scattering does not play a role and consequently, the observed lineshape of a single-level resonance is populated as a pure Breit-Wigner resonance. This simplifies the observed lineshape, however as previously mentioned, the direct populating reaction may still exhibit dependence on the excitation-energy of the recoil nucleus. This is accounted for by the feeding factors discussed in Section 2.6.1.8. In order to consistently analyse ^{12}C excitation-energy spectra that are populated through different reactions and measured under different experimental conditions, the feeding factors for the various population reactions must be determined. The calculations for the excitation-energy dependence of the ^{12}C$(\alpha,\alpha')^{12}$C and ^{14}C$(p,t)^{12}$C reactions are presented in this chapter.

In order to calculate the feeding factors of a particular direct reaction in lab frame, the differential cross section for a particular excitation energy is first calculated with in the centre-of-mass inertial reference frame with CHUCK3

[71]. For the two-body reaction:

$$A + B \rightarrow C + D, \tag{2.101}$$

the optical-potentials used to describe the initial/final systems are of the form

$$U_{opt}(r) = U_C(r) + U_{vol}(r) + U_{surf}(r) + U_{so}. \tag{2.102}$$

The coulomb potential term, $U_C(r)$, is taken to be the interaction of a point charge with a uniformly charged sphere of radius R_C, given by

$$U_C(r) = \begin{cases} \left(\frac{3}{2} - \frac{r^2}{2R_C^2}\right) Z_P Z_T e^2/R_C & \text{if } r \leq R_C \\ Z_P Z_T e^2/r & \text{if } r > R_C, \end{cases} \tag{2.103}$$

where Z_P and Z_T are the charges for the projectile and target, respectively. The volume term, $U_{vol}(r)$, has both real and imaginary components

$$U_{vol}(r) = V_v f_v(r_R) + iW_v f_{wv}(r_I), \tag{2.104}$$

where r_R/r_I is the real/imaginary component of the radius parameter r. The real and imaginary depths of the volume term, respectively given by V_v and W_v, must both be negative for an attractive real and absorptive imaginary potential. The Wood-Saxon form factors, $f(r)$, are given as

$$f_i(r) = \frac{1}{1 + \exp\left(\frac{r - R_i}{a_i}\right)}, \tag{2.105}$$

where a_i and R_i are the associated diffuseness and radius parameters, respectively. These radii are typically parameterised as a function of the reduced radii r_i as

$$R_i = r_i M_T^{1/3}, \tag{2.106}$$

where M_T is the mass of the target. The surface term, $U_{surf}(r)$, is given as

$$U_{surf}(r) = V_s g_{vs}(r_R) + iW_s g_{ws}(r_I), \tag{2.107}$$

where V_s and W_s are the real and imaginary depths, respectively, and $g_i(r)$ is the derivative of the Wood-Saxon potential given by

$$g_i(r) = \frac{\mathrm{d}f_i(r)}{\mathrm{d}r}. \tag{2.108}$$

The spin-orbit term, $U_{so}(r)$, is given as

$$U_{so}(r) = \left(-V_{so}\frac{1}{r}\frac{\mathrm{d}f(r_R)}{\mathrm{d}r} - iW_{so}\frac{1}{r}\frac{\mathrm{d}f(r_I)}{\mathrm{d}r}\right) \mathrm{L} \cdot \mathrm{s} \tag{2.109}$$

The optical-model potential (OMP) parameters used for this work are summarised in Table 2.1. The OMP parameters to describe the $^{12}\mathrm{C}+\alpha$ systems of experiments PR166, PR194 and PR251 are from the method of M. Nolte, H. Machner and J. Bojowald [72]. The OMP parameters to describe the $^{14}\mathrm{C}+p$ and $^{12}\mathrm{C}+t$ systems from the work of M. Yasue *et al.* are taken from Ref. [73]. The OMP parameters to describe the $^{14}\mathrm{C}+p$ systems of experiments PR195 and PR240 are from the method of D.G. Madland [74]. The OMP parameters to describe the $^{12}\mathrm{C}+t$ systems of experiments PR195 and PR240 are from the method of D.Y. Pang *et al.* [75]. A programme to calculate the form factors for isoscalar dipole and monopole transitions M.N. Harakeh [76].

A coupled-channels nuclear reactions code written by P.D. Kunz, CHUCK3, was used to calculate the differential cross section for the ejectile (C) in the centre-of-mass inertial reference frame of the reaction. In order to determine the feeding factors corresponding to a particular measurement, these differential cross sections must be transformed to the inertial reference frame of the laboratory with the relation

$$\frac{\mathrm{d}\sigma_C}{\mathrm{d}\Omega_L}\,\mathrm{d}\Omega_L = \frac{\mathrm{d}\sigma_C}{\mathrm{d}\Omega}\,\sin\theta\,\mathrm{d}\Omega, \tag{2.110}$$

or

$$\frac{\mathrm{d}\sigma_C}{\mathrm{d}\Omega_L}\,\sin\theta_L\,\mathrm{d}\theta_L\,\mathrm{d}\phi_L = \frac{\mathrm{d}\sigma_C}{\mathrm{d}\Omega}\,\sin\theta\,\mathrm{d}\theta\,\mathrm{d}\phi, \tag{2.111}$$

where θ and ϕ are the polar and azimuthal angles of particle C in the centre-of-mass inertial reference frame [77]. The corresponding laboratory angles θ_L and ϕ_L are obtained through Lorentz transformation to yield

$$\frac{\mathrm{d}\sigma_C}{\mathrm{d}\Omega_L} = \frac{(1+\gamma^2+2\gamma\cos\theta)^{\frac{3}{2}}}{1+\gamma\cos\theta}\frac{\mathrm{d}\sigma_C}{\mathrm{d}\Omega} \tag{2.112}$$

where γ corresponds to the relativistic momentum of the initial scattering particles, $A+B$, in the laboratory inertial reference frame.

After the differential cross-section in the labaratory reference frame has been calculated, the cross section measured for a particular experiment, σ_C, can be calculated through

$$\sigma_C = \int \epsilon(\theta_L,\phi_L)\cdot\frac{\mathrm{d}\sigma_C}{\mathrm{d}\Omega_L}\,\mathrm{d}\Omega_L, \tag{2.113}$$

where $\epsilon(\theta_L,\phi_L)$ is the detector efficiency for the outgoing ejectile C. Since all the differential cross sections relevant for this work exhibit azimuthal symmetry, the ϕ_L dependence can be integrated out to yield

$$\sigma_C = \int_0^{\pi} \epsilon(\theta_L)\cdot\frac{\mathrm{d}\sigma_C}{\mathrm{d}\theta_L}\,\sin\theta_L\,\mathrm{d}\theta_L. \tag{2.114}$$

The efficiency for the measurement of the ejectile, $\epsilon(\theta_L)$, can be assumed to be directly proportional to the solid angle of the collimator if the efficiency of the focal-plane detector system is relatively constant across the measurement range. The collimator solid angles for all analysed experiments are presented in Figure 2.17.

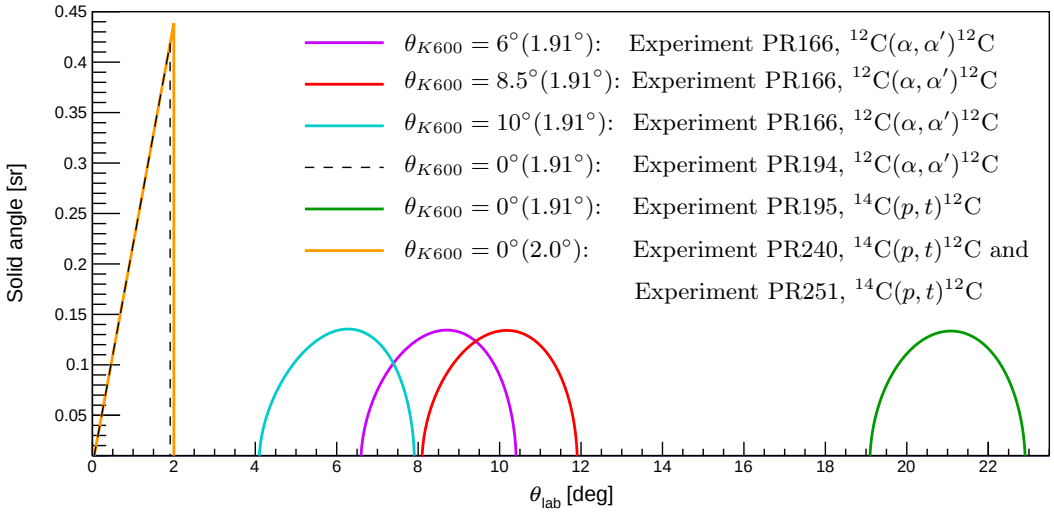

Figure 2.17: The solid angles subtended by the collimator of the K600 spectrometer as a function of θ_{lab}. The angles in brackets are the opening angles of the corresponding circular collimators.

Experiment	System	E_{beam}	V_v	r_v	a_v	W_v	r_{wv}	a_{wv}	V_s	r_{vs}	a_{vs}	W_s	r_{ws}	a_{ws}	V_{so}	r_{vso}	a_{vso}	W_{so}	r_{wso}	a_{wso}	r_c
PR166	$^{12}\text{C}+\alpha$	196	-79.96	1.245	0.801	-42.42	1.57	0.646	—	—	—	—	—	—	—	—	—	—	—	—	1.25
PR194	$^{12}\text{C}+\alpha$	160	-88.92	1.245	0.801	-42.21	1.57	0.646	—	—	—	—	—	—	—	—	—	—	—	—	1.25
PR194	$^{12}\text{C}+\alpha$	118	-99.37	1.245	0.801	-41.95	1.57	0.646	—	—	—	—	—	—	—	—	—	—	—	—	1.25
M. Yasue	$^{14}\text{C}+p$	40.3	-47.2	1.102	0.626	-41.95	1.57	0.646	—	—	—	6.46	1.108	0.60	-5.83	1.102	0.626	—	—	—	1.20
et al.	$^{12}\text{C}+t$		-164.3	1.20	0.72	-16.85	1.4	0.88	—	—	—	—	—	—	-2.5	1.20	0.72	—	—	—	1.30
PR195	$^{14}\text{C}+p$	67.5	-35.6	1.19	0.70	-6.3	1.49	0.44	—	—	—	—	—	—	-5.2	0.99	0.69	—	—	—	1.20
	$^{12}\text{C}+t$		-110.0	1.10	0.84	-5.68	1.26	0.84	—	—	—	—	—	—	-12.72	1.26	0.84	—	—	—	1.30
PR240	$^{14}\text{C}+p$	140	-23.1	1.25	0.72	-9.1	1.31	0.62	—	—	—	—	—	—	-2.9	0.99	0.69	—	—	—	1.20
	$^{12}\text{C}+t$		-100.5	1.10	0.82	-15.72	1.26	0.84	—	—	—	—	—	—	-8.13	1.26	0.84	—	—	—	1.30

Table 2.1: The optical-model potential parameters for the $^{12}\text{C}(\alpha,\alpha')^{12}\text{C}$ and $^{14}\text{C}(p,t)^{12}\text{C}$ reactions studied for this work.

2.7.1 The $^{12}C(\alpha,\alpha')^{12}C$ reaction

The angular momentum conservation that governs two-body scattering between projectile and target nuclei (denoted as particles 0 and 1, respectively) yields:

$$j_0 + j_1 + l = j_2 + j_3, \tag{2.115}$$

where l denotes the transferred orbital angular momentum and j_i is the total angular momentum of the i^{th} particle. The ejectile and the recoil nuclei are denoted as particles 2 and 3, respectively. For the $^{12}C(\alpha,\alpha')^{12}C$ and $^{14}C(p,t)^{12}C$ measurements analysed for this thesis, the ejectiles can be assumed to remain in their ground states.

For the $^{12}C(\alpha,\alpha')^{12}C$ reaction, the 0^+ ground state of the α-particle (ejectile) greatly simplifies the angular-momentum selection rules for the recoil nucleus, given by:

$$j_3 = |j_1 - l|, |j_1 - l| + 1, \ldots, j_1 + l. \tag{2.116}$$

Since ^{12}C exhibits a 0^+ ground state, it follows that if inelastic α-particle scattering on ^{12}C occurs through a single-step mechanism, the transferred orbital angular momentum is equal to the total angular momentum of the recoil nucleus. For all inelastic α-scattering reactions studied for this work, the incident α-particles carry approximately 30-50 MeV/u of kinetic energy or greater which justifies the single-step approximation. Under such an approximation, only natural parity states in ^{12}C can be excited, according to the relation

$$j_3 = l, \tag{2.117}$$

$$\pi_3 = (-1)^l, \tag{2.118}$$

The differential cross sections for the population of a 0^+, 1^-, 2^+, 3^- and 4^+ state at $E_x = 10$ MeV through the $^{12}C(\alpha,\alpha')^{12}C$ reaction are shown for experiments PR166, PR194 and PR251 in Appendix C. The calculated feeding factors for all the $^{12}C(\alpha,\alpha')^{12}C$ measurements studied for this work are presented in Figures 2.18 and 2.19. Panel (c) of Figure 2.19 presents a summary of the calculated feeding factors for 0^+ resonances for all the $^{12}C(\alpha,\alpha')^{12}C$ measurements which are normalised to unity at the associated resonance energy of $E_x = 7.65407(19)$ MeV. It is observed that in general, the feeding factors for 0^+ resonances excited through inelastic α scattering decrease with increasing excitation energy. This can be understood in terms of transferred orbital angular momentum l: semi-classically, as the excitation energy of the recoil nucleus increases, the energy of the outgoing α ejectile decreases and thus carries less angular momentum, resulting in a worse l-matching and a diminished cross section. These feeding factors are used for the R-matrix analysis of the $^{12}C(\alpha,\alpha')^{12}C$ measurements presented in Chapter 5.

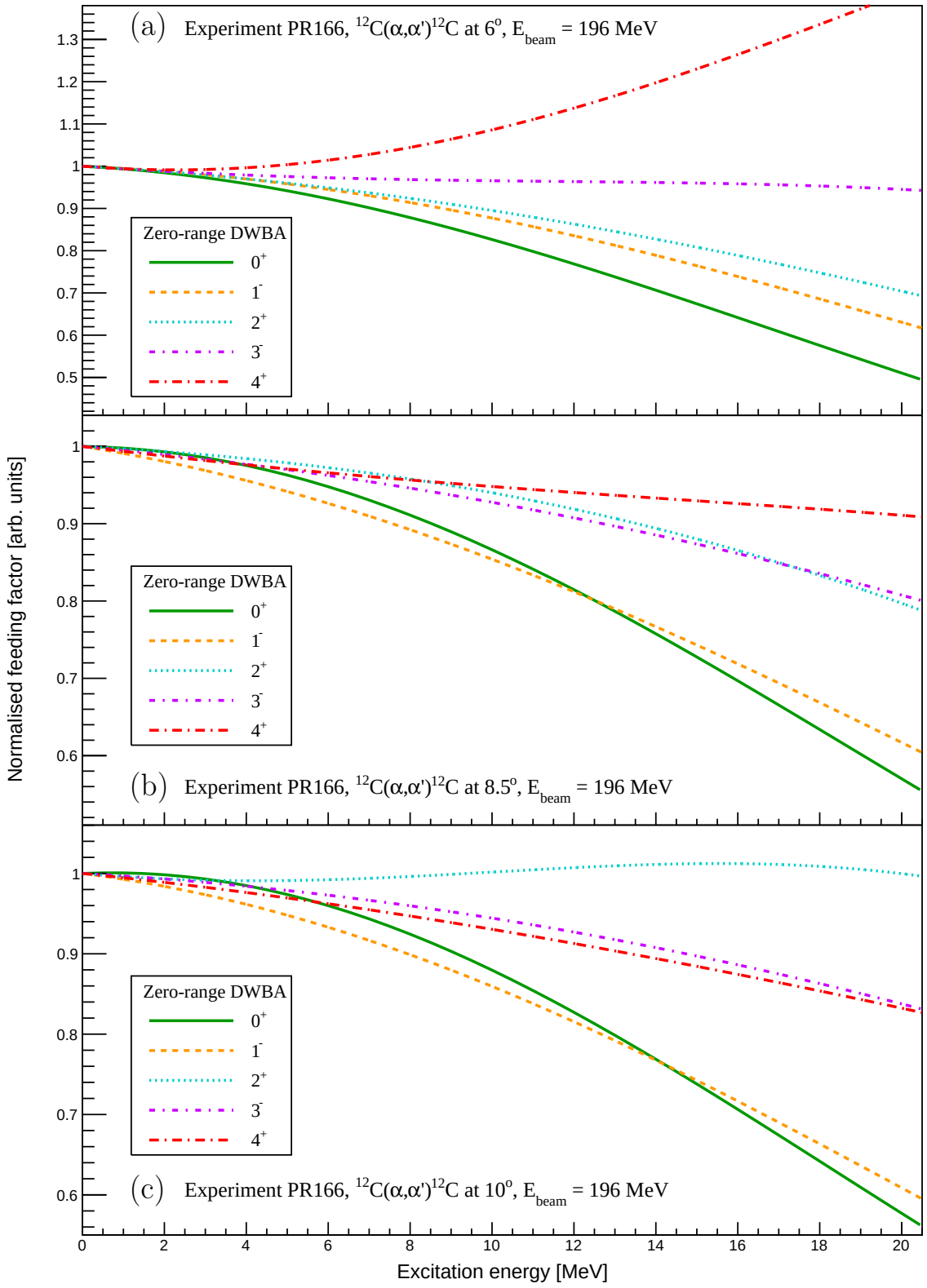

Figure 2.18: The normalised feeding factors for the $^{12}\mathrm{C}(\alpha,\alpha')^{12}\mathrm{C}$ reactions of experiments PR166 at $\theta_{\mathrm{lab}} = 6°$ (a), 8.5° (b) and 10° (c). The feeding factors have been normalised to unity at $E_x = 0$ MeV.

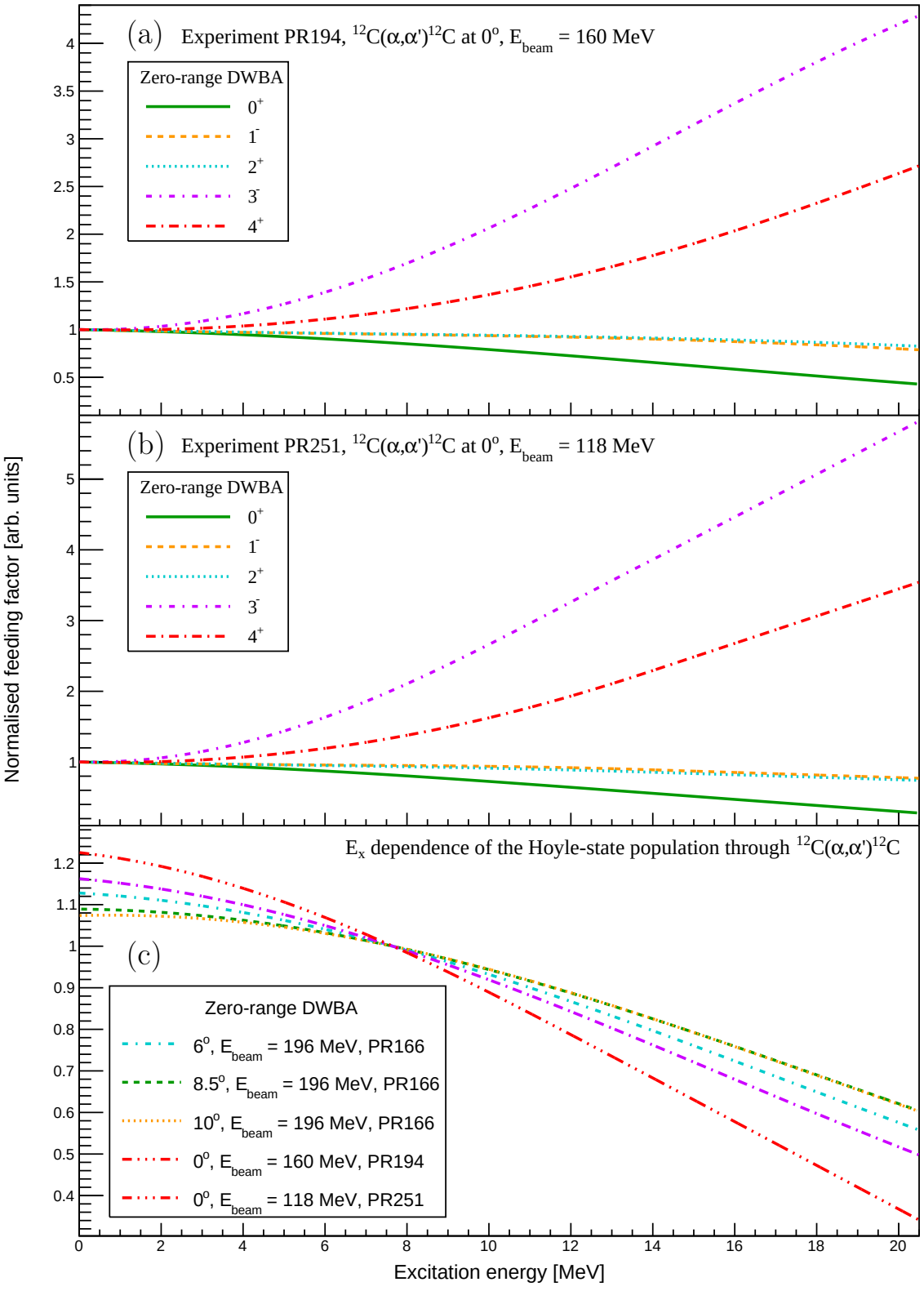

Figure 2.19: The normalised feeding factors for the $^{12}C(\alpha,\alpha')^{12}C$ reactions of experiments PR194 (a) and PR251 (b), normalised to unity at $E_x = 0$ MeV. Panel (c) presents a summary of the feeding factors for the Hoyle state from all analysed $^{12}C(\alpha,\alpha')^{12}C$ measurements, normalised to unity at the associated resonance energy of $E_x = 7.65407(19)$ MeV.

2.7.2 The $^{14}C(p,t)^{12}C$ reaction

For the $^{14}C(p,t)^{12}C$ reaction, the angular momentum of the $1/2^+$ proton (ejectile) ground state couples with the transferred orbital angular momentum for two-different values of angular-momentum values of the reaction, j_r:

$$j_r = j_0 + j_1 + l = l - \frac{1}{2}, l + \frac{1}{2}, \tag{2.119}$$

where j_0 and j_1 are the total angular momentum of projectile and target nuclei, respectively. The angular-momentum selection rules for the ejectile and recoil nucleus, respectively given by j_2 and j_3, are consequently given by:

$$j_3 = |j_r - j_2|, |j_r - j_2| + 1, \ldots, j_r + j_2, \tag{2.120}$$

The angular-momentum combinations for the $^{14}C(p,t)^{12}C$ reaction are summarised below in Table 2.2. Whilst these combinations show that the $^{14}C(p,t)^{12}C$ reaction may be able to populate both natural- and unnatural-parity states, if the two neutrons picked up by the proton are assumed to both be p-wave, i.e. from the $p_{1/2}$ and $p_{3/2}$ orbitals, then a direct single-step pickup can only excite 0^+, 1^+ and 2^+ states in ^{12}C.

j_p	+	$j_{^{14}C}$	+	l_p		$\longrightarrow$	j_t	+	$j_{^{12}C}$
$1/2^+$		0^+		0	$(j_r = 1/2)$		$1/2^+$		$0^+, 1^+$
				1	$(j_r = 1/2)$				$0^-, 1^-$
					$(j_r = 3/2)$				$1^-, 2^-$
				2	$(j_r = 3/2)$				$1^+, 2^+$
					$(j_r = 5/2)$				$2^+, 3^+$
				3	$(j_r = 5/2)$				$2^-, 3^-$
					$(j_r = 7/2)$				$3^-, 4^-$
				4	$(j_r = 7/2)$				$3^+, 4^+$
					$(j_r = 9/2)$				$4^+, 5^+$
				5	$(j_r = 9/2)$				$4^-, 5^-$
					$(j_r = 11/2)$				$5^-, 6^-$
				$\vdots$	$\vdots$				$\vdots$

Table 2.2: The angular-momentum combinations for the $^{14}C(p,t)^{12}C$ reaction, applicable for experiments PR195 and PR240.

The $^{14}C(p,t)^{12}C$ reaction was studied by M. Yasue *et al.* [73] with an incident beam energy of $E_{\text{beam}} = 40.3$ MeV over the excitation energy range of $E_x = 0$-19 MeV and performed exact-finite-range and zero-range DWBA calculations to fit the differential cross sections. It was found that the multi-step $^{14}C(p,t)^{12}C(t,t')^{12}C^*$ reaction was crucial to reproduce the differential cross section of the 0_2^+ Hoyle state and in particular, through the 2_1^+ 4.43982(21) MeV state with a coupling of $\beta_2 = -0.15$. Due to time constraints, only these two dominant forms of channel couplings were studied and the $^{14}C(p,d)^{13}C(d,t)^{12}C$ sequential transfer reaction was ignored. It was assumed that at the relatively higher beam energies employed for this work (experiments PR195 and PR240), the two-step sequential transfer contribution is relatively suppressed. In the $E_x \approx 7$-16 MeV excitation-energy region of interest, the main contributing resonance contributions are from the 0_2^+ Hoyle state and the broad ghost anomaly tail, the 2_1^+ state and the broad 0^+ resonance situated at $E_x \approx 10$ MeV. The feeding factors for these broad and dominating contributions are of primary interest and the feeding factors for the broad 0^+ resonance is expected to be proportional to that of the Hoyle state. The 3_1^- state situated at 9.641(5) MeV is ignored as the observed lineshape of this resonance through $^{14}C(p,t)^{12}C$ is less affected by the direct feeding factor due to its relatively narrower width of 46(3) keV.

In order to determine the feeding factors associated with the $^{14}C(p,t)^{12}C$ reactions for experiments PR195 and PR240, the differential cross sections were calculated with CHUCK3. The coupling parameters were determined with the same data studied by M. Yasue *et al.* with the coupling scheme presented on Figure 2.20. This coupling scheme indicates the intra and inter couplings of the ground state and β-bands of ^{12}C which includes the 2_1^+ rotational state of the Hoyle state which has been established to be situated at $E_x = 9.870(60)$ MeV in the period following the work of M. Yasue *et al.* published in 1990. In previous work by R. De Leo *et al.*, the 2_1^+ rotational state of the Hoyle state was assumed to be situated at 10.3 MeV [78]. The spectroscopic amplitudes for the 0_1^+, 2_1^+ and 0_2^+ states in ^{12}C presented by the work of M. Yasue *et al.* have been used for this work (see Table 2.3). The spectroscopic amplitudes for the 2_1^+ rotational state of the Hoyle state are fitted to the data.
To determine the coupling parameters from the data studied by M. Yasue *et*

^{14}C		^{12}C		Spectroscopic amplitudes		
E_x	J^π	E_x	J^π	$(p_{1/2})^{-2}$	$(p_{1/2}p_{3/2})^{-1}$	$(p_{3/2})^{-2}$
0.0	0^+	0.0	0^+	0.7061	—	0.4476
		4.44	2^+	—	1.3061	0.5196
		7.65	0^+	−0.6004	—	0.3094

Table 2.3: The spectroscopic amplitudes for the 0_1^+, 2_1^+ and 0_2^+ states in ^{12}C from Ref. [73].

al., an optimisation code was implemented with some noteworthy constraints on the parameter space. Firstly, the oblate nature of the ground state implies that the quadrupole coupling between the 0^+_1 ground state and the 2^+_1 state situated at 4.43982(21) MeV should be relatively large and negative. The coupling was fixed at $\beta_2 = -0.588$ for the optimisation. This oblate nature was recently confirmed by the work of M. Kumar Raju *et al.* [79]. Secondly, since the cross couplings between the ground-state and Hoyle-state bands should be the same, the β_2 quadrupole coupling between the 0^+_1 ground state and the 9.870(60) MeV 2^+_2 state (d) shares the same optimisation parameter as the β_2 between the 0^+_2 Hoyle state and the 4.43982(21) MeV 2^+_1 state (e). Thirdly, the β_2 quadrupole coupling (g) between the 0^+_2 Hoyle state and the 9.870(60) MeV 2^+_2 state should be the same as the reorientation term (h) and as such, the optimisation parameter is shared. The final constraint concerns the oblate nature of the ground state which is in contrast to the 0^+_2 Hoyle state which is understood to be prolate [80] and as such, the β_2 quadrupole coupling between the 0^+_2 Hoyle state and its 2^+_1 rotational state at 9.870(60) MeV (g) should be large and positive. The fit to the ^{14}C$(p,t)^{12}$C differential cross sections from M. Yasue *et al.* yielded two sets of optimised parameters for the spectrscopic amplitudes of the 9.870(60) MeV 2^+_2 state and the aforementioned couplings, as summarised in Table 2.4. The first set of optimised parameters, referred to as coupling scheme (1), corresponds to the restriction of the quadrupole coupling (g) to be larger in magnitude than the quadrupole coupling (a) between the 0^+_1 ground state and the 4.43982(21) MeV 2^+_1 state which is fixed to $\beta_2 = -0.588$. The corresponding fits for coupling scheme (1) are presented in Figure 2.21. The second set of optimised parameters, referred to as coupling scheme

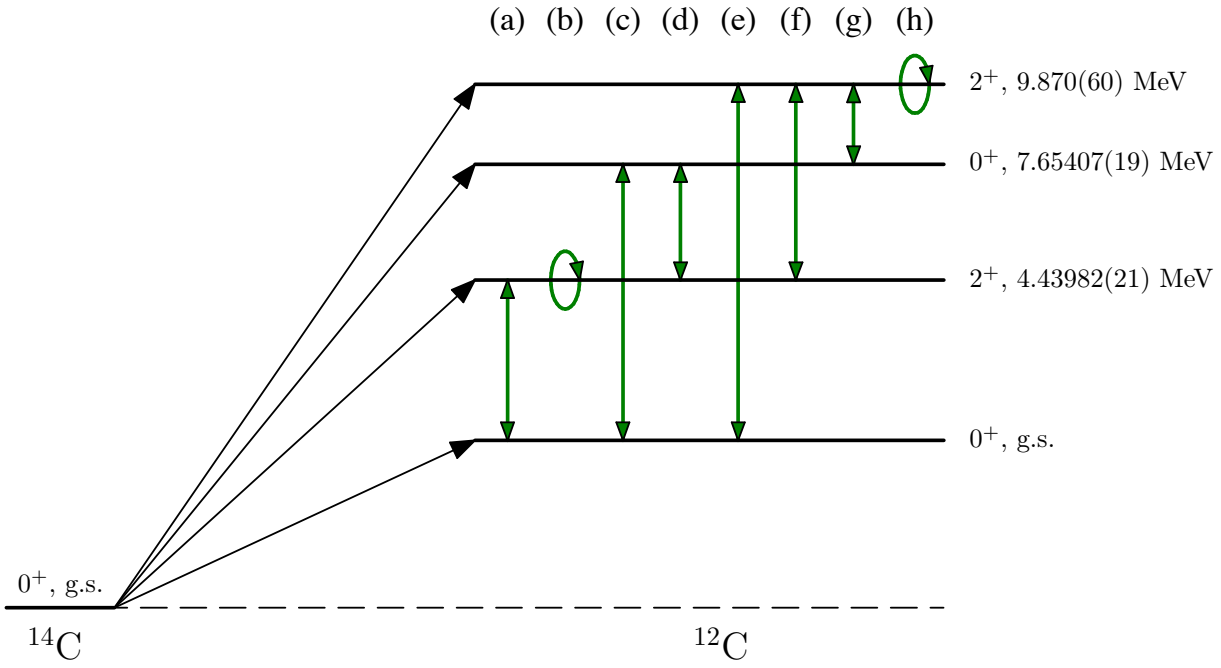

Figure 2.20: The ^{14}C$(p,t)^{12}$C coupling scheme for the zero-range coupled-channels DWBA calculation with CHUCK3. The green arrows represent the ^{12}C$(t,t')^{12}$C couplings.

(2), corresponds to the extension of the parameter space to allow quadrupole coupling (g) to be smaller in magnitude than the aforementioned fixed value of $\beta_2 = -0.588$ (a), yielding a better goodness of fit compared to coupling scheme (1). The corresponding fits for coupling scheme (2) are presented in Figure 2.22. Whilst the differential cross section for the Hoyle state is reproduced better with coupling scheme (2), it was decided that coupling scheme (1) would be used as it was assumed that the quadrupole coupling (g) between the 0_2^+ Hoyle state and the 9.870(60) MeV 2_2^+ state should be larger in magnitude than the fixed $\beta_2 = -0.588$ quadrupole coupling (a) between the 0_1^+ ground state and the 4.43982(21) MeV 2_1^+ state.

The feeding factors for the 0_2^+ Hoyle state and the 9.870(60) MeV 2_1^+ state are calculated using both coupling schemes for experiments PR195 and PR240, as presented on Figure 2.23. On panels (a) and (c), it is observed that the feeding factors for the 0_2^+ Hoyle state are very similar between coupling schemes (1) and (2). It is observed that the feeding factors calculated with only the direct $^{14}\mathrm{C}(p,t)^{12}\mathrm{C}$ term vary more strongly with excitation energy in comparison to the $^{14}\mathrm{C}(p,t)^{12}\mathrm{C}(2_1^+)(t,t')^{12}\mathrm{C}^*$ coupling described by M. Yasue *et al.* and the two aforementioned coupling schemes, (1) and (2). For the $^{14}\mathrm{C}(p,t)^{12}\mathrm{C}$ measurements of experiment PR195 and PR240, it is observed that the feeding factors for the 0_2^+ Hoyle state increase with excitation energy over the $E_x \approx$ 7-16 MeV range of interest. This is in contrast to the feeding factors for the $^{12}\mathrm{C}(\alpha,\alpha')^{12}\mathrm{C}$ measurements which all decrease with increasing excitation energy (see Figure 2.19). This can be understood in terms of semi-classical l-matching: the proton projectile carries less angular momentum with respect to the triton ejectile with approximately the same kinetic energy. As greater excitation energy is imparted to the recoil nucleus, the kinetic energy of the triton decreases, resulting in less angular momentum, better l-matching and an increased cross section. On panels (b) and (d), it is observed that the feeding factors for the 9.870(60) MeV 2_2^+ state are less similar between coupling schemes (1) and (2). This is because the difference in the coupling schemes pertains directly to the β_2 quadrupole coupling (g) between the 0_2^+ Hoyle state and the 9.870(60) MeV 2_2^+ state as well as the reorientation term (h).

Whilst a study by A.C. Dreyfuss *et al.* has found that the Hoyle state is better described through deformed prolate collective modes rather than vibrational modes, the coupling scheme used for this work is a valid first approximation to determine the feeding factors [80]. These feeding factors are used for the R-matrix analysis of the $^{14}\mathrm{C}(p,t)^{12}\mathrm{C}$ measurements presented in Chapter 5. The differential cross sections of the 0_1^+, 2_1^+, 0_2^+ and 2_1^+ $^{12}\mathrm{C}$ states with coupling scheme (1) are presented in Appendix C for experiments PR195 and PR240.

#	$(p_{1/2})^{-2}$	$(p_{3/2})^{-2}$	(a)	(b)	(c)	(d)	(e)	(f)		(g)	(h)
			β_2	β_2	β_0	β_2	β_2	β_0	β_2	β_2	β_2
1	−2.3661	−2.8208	−0.588*	−0.588*	0.0331	−0.1965	−0.1965	0.0331	0.1231	0.8073	0.8073
2	−0.3624	1.4217	−0.588*	−0.588*	0.1090	−0.2546	−0.2546	0.1090	0.3051	0.2604	0.2604

Table 2.4: The spectroscopic amplitudes for the 0_1^+, 2_1^+ and 0_2^+ states in ^{12}C from Ref. [73].

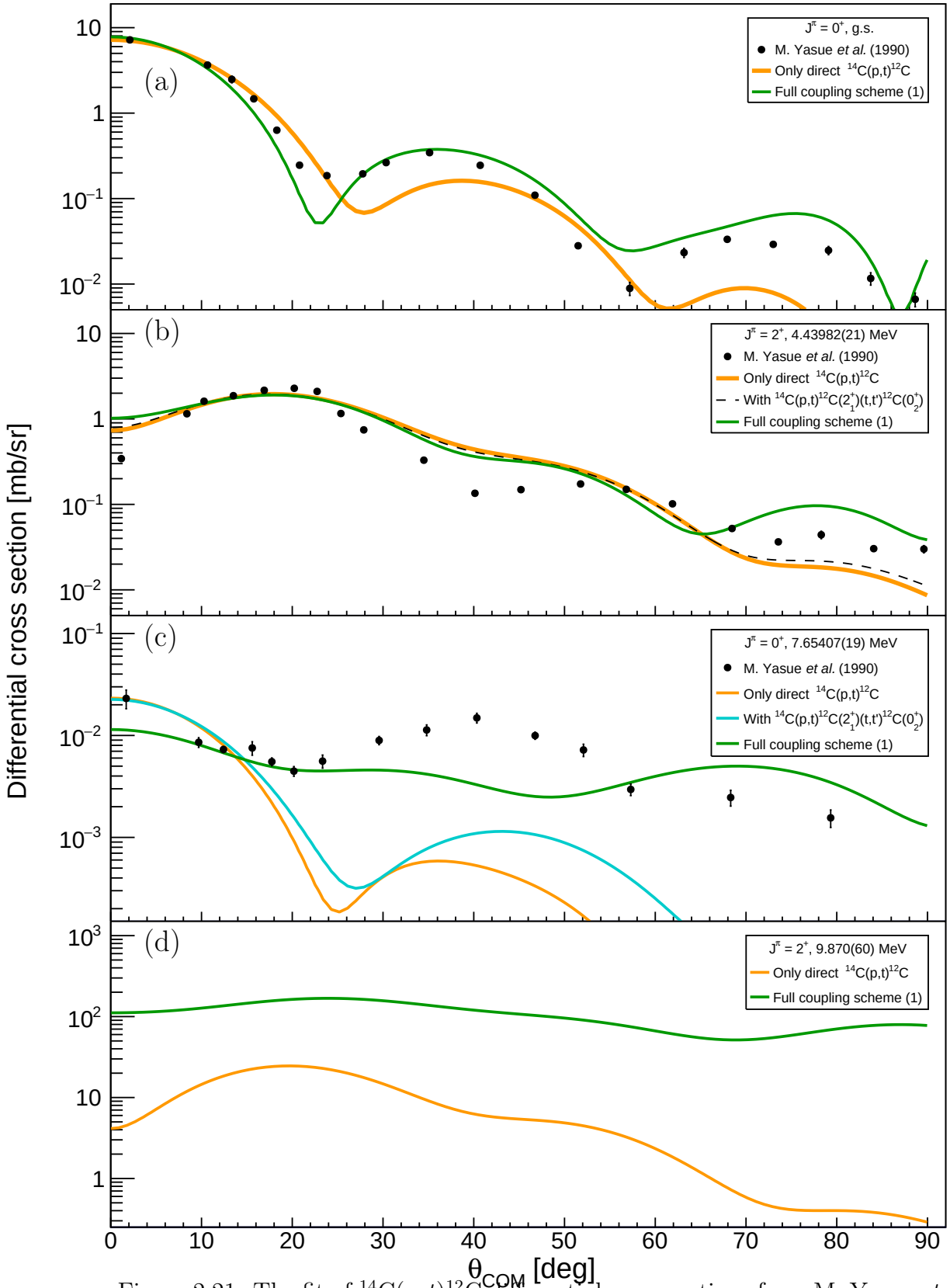

Figure 2.21: The fit of $^{14}\mathrm{C}(p,t)^{12}\mathrm{C}$ differential cross sections from M. Yasue *et al.* [73] with coupling scheme 1 (see Table 2.4).

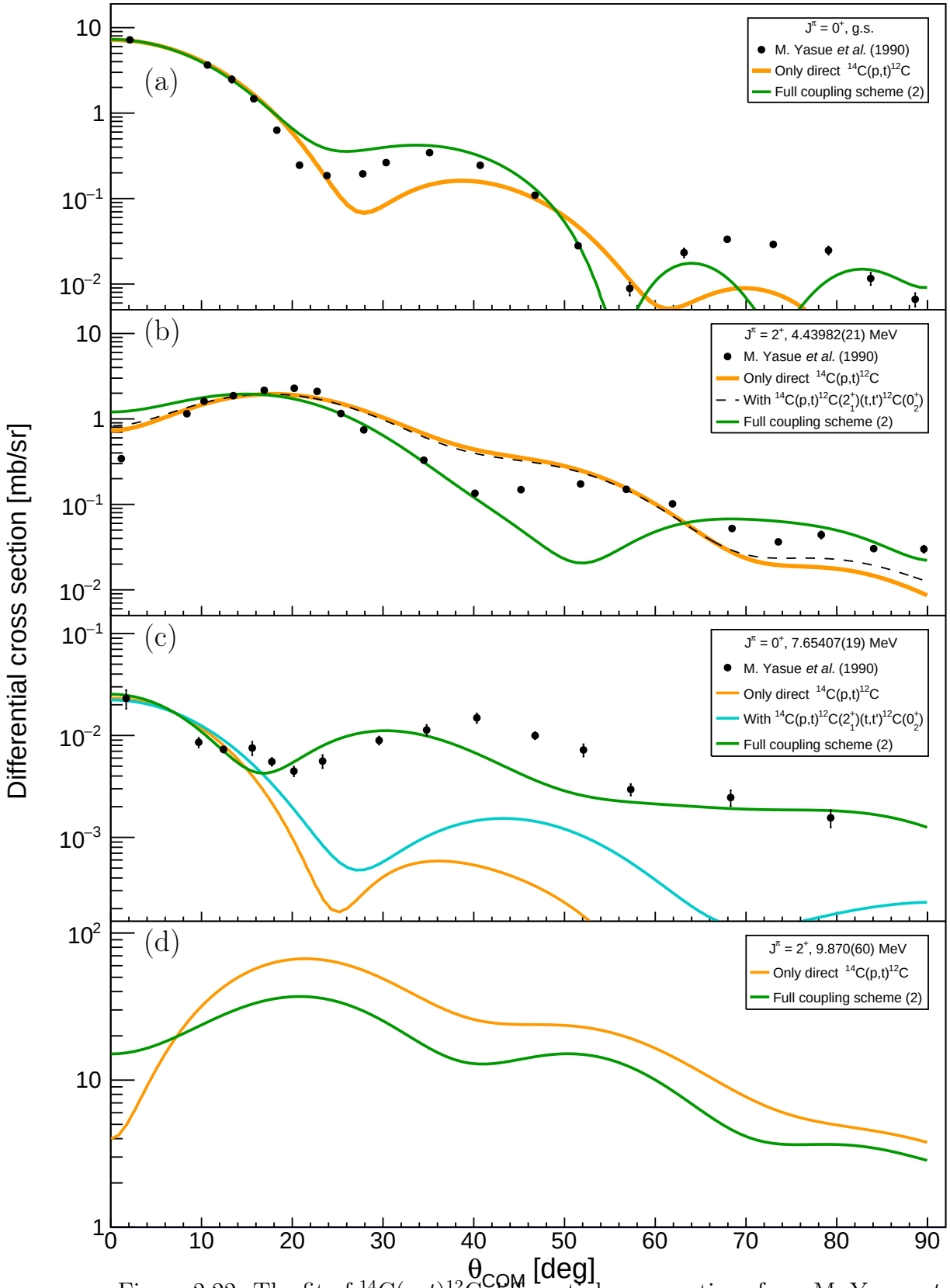

Figure 2.22: The fit of $^{14}\mathrm{C}(p,t)^{12}\mathrm{C}$ differential cross sections from M. Yasue *et al.* [73] with coupling scheme 2 (see Table 2.4).

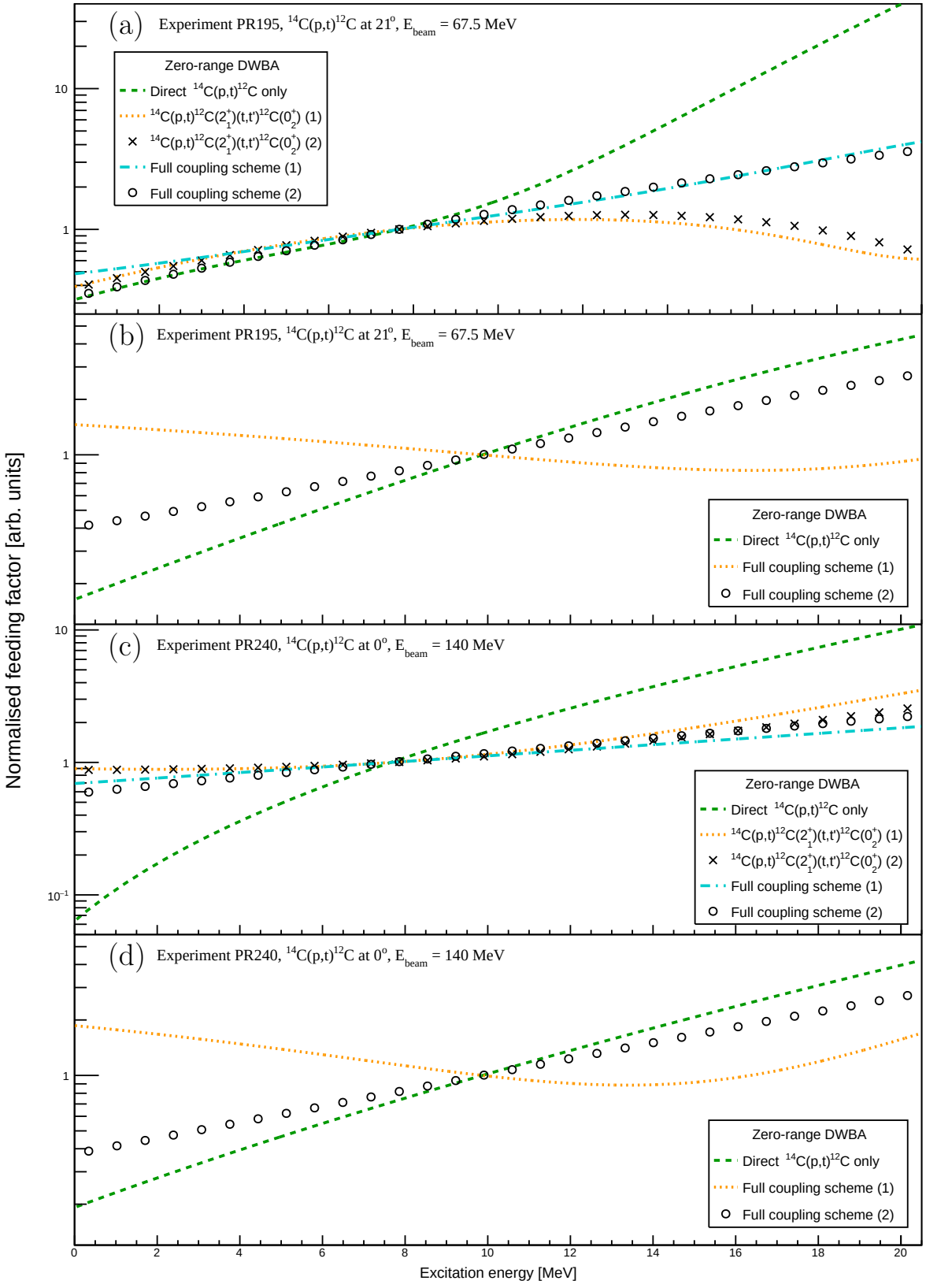

Figure 2.23: The feeding factors for the 0^+_2 Hoyle state of ^{12}C, normalised at $E_x = 7.65407(19)$, are presented for experiments PR195 and PR240 in panels (a) and (c), respectively. The feeding factors for the 2^+_1 state of ^{12}C, normalised at $E_x = 9.870(60)$, are presented for experiments PR195 and PR240 in panels (b) and (d), respectively.

2.8 Decay Channels

2.8.1 Decay Channel Selection Rules

One of the fundamental assumptions of R-matrix theory is the absence or unimportance of all processes in which more than two product nuclei are formed. Consequently, only the angular momentum selection rules for two-body particle decay are relevant. The angular momenta of a parent particle and its decay products are given by

$$j_{parent} = j_1 + j_2 + l, \tag{2.121}$$

where the two decay product nuclei are denoted particles 1 and 2 and l is the orbital angular momentum of the decay. In this context, the channel spin, s, is defined as the coupled intrinsic angular momenta of the reaction products, given by

$$s = |j_1 - j_2|, |j_1 - j_2| + 1, \ldots, j_1 + j_2. \tag{2.122}$$

The possible l-values of decay are restricted to

$$l = |s - j_{parent}|, |s - j_{parent}| + 1, \ldots, s + j_{parent}. \tag{2.123}$$

The parity relation describing the decay is given by

$$\pi_{parent} = \pi_1 \pi_2 (-1)^l. \tag{2.124}$$

The separation energies for α and proton decay from ^{12}C are 7.36659(4) MeV and 15.95668(1) MeV, respectively. The substantially higher proton separation energy dictates that α-decay is the exclusive charged-particle decay mode in the analysed excitation-energy ranges (see Table 3.1). Consequently, proton decay can be ignored for the excitation-energy range of interest of $E_x \approx$ 7-16 MeV.

The angular-momentum selection rules for the α_0 and α_1 decay modes are described in Sections 2.8.1.1 and 2.8.1.2, respectively.

2.8.1.1 The α_0 decay mode

For α decay from the analysed excitation-energy ranges in ^{12}C (see Table 3.1), the α particle remains in its ground state as its first excited state is at over 20 MeV. The angular-momentum selection rules for α_0 decay from natural states in ^{12}C are given by Equations 2.125 and 2.126. The α_0 decay mode cannot occur from unnatural-parity states in ^{12}C as there are no l-values of decay which satisfy parity conservation. In the aforementioned excitation-energy range of interest of $E_x \approx$ 7-16 MeV in ^{12}C, the only possible charged-particle decay mode is α_1 decay.

$$l_\alpha = j_{^{12}\mathrm{C}} \tag{2.125}$$

$$\pi_{^{12}\mathrm{C}} = (-1)^{l_\alpha} \tag{2.126}$$

2.8.1.2 The α_1 decay mode

For α_1 decay mode from ^{12}C, it can be safely assumed that the α-particle decay product remains in its ground state as its first excited state is at over 20 MeV. The angular-momentum selection rules for α_1 decay from natural- and unnatural-parity states in ^{12}C are shown in Tables 2.5 and 2.6, respectively. It is observed that α_1 decay is possible from all combinations of spin and parity in ^{12}C, except for the sole case of α_1 decay from a 0^- state as there is no l-value of decay which satisfies parity conservation.

$j_{^{12}\mathrm{C}}$	$\longrightarrow$	$j_{^{8}\mathrm{Be}}$	+	j_α	+	l_α
0^+		2^+		0^+		2
1^-						1, 3
2^+						0, 2, 4
3^-						1, 3, 5
4^+						2, 4, 6
⋮						⋮

Table 2.5: The angular-momentum selection rules for α_1 decay from natural-parity states in ^{12}C.

$j_{^{12}\mathrm{C}}$	$\longrightarrow$	$j_{^{8}\mathrm{Be}}$	$+$	j_{α}	$+$	l_{α}
0^-		2^+		0^+		-
1^+						2
2^-						1, 3
3^+						2, 4
4^-						3, 5
$\vdots$						$\vdots$

Table 2.6: The angular-momentum selection rules for α_1 decay from unatural-parity states in ^{12}C.

2.9 Hypotheses

The great interest in the 0^+ structure of ^{12}C in the $E_x \approx$ 7-16 MeV excitation-energy region has illicited a myriad of alternative explanations.

Hypothesis H_1

It is postulated that the 0^+ structure of ^{12}C in the $E_x \approx$ 7-16 MeV excitation-energy region of interest can be described solely by the Hoyle state with a single-channel formalism where only the α_0 decay mode contributes. Since the α- and proton-separation energies for ^{12}C are 7.36659(4) MeV and 15.95668(1) MeV, respectively, the α decay mode is dominant in this excitation-energy region.

Results from M. Itoh *et al.* suggest that the broad 0^+ strength at $E_x \approx$ 8-12 MeV is fragmented to exhibit two local maxima [14]. This multipole decomposition analysis (MDA) is independent of the choice of nuclear lineshapes and reveals the strength at $E_x \approx 9$ MeV in ^{12}C to be predominantly 0^+ in nature. Since the penetrability is a monotic function, a single-channel description with the α_0 decay mode cannot produce a high-energy tail with two local maxima. It is nevertheless important to investigate this ill-fated hypothesis as this is the simplest description and the lineshape of the Hoyle state is often presented with such a single-channel approximation [8].

Hypothesis H_2

It is postulated that the 0^+ structure of ^{12}C in the $E_x \approx$ 7-16 MeV excitation-energy region of interest can be described solely by the Hoyle state with a multichannel formalism consisting of the α_0 and α_1 decay modes. As mentioned in hypothesis H_1, the broad 0^+ strength at $E_x \approx$ 8-12 MeV appears to be fragmented to exhibit two local maxima [14].

Whilst the monotonic penetrability of a single-channel description cannot reproduce such a double-peaked structure, With the multichannel approach, since the α_1 width becomes non-negligible at approximately $E_x > 10$ MeV, it is conceivable that the α_1 decay mode could provide a mechanism to produce the aforementioned double-peaked 0^+ structure.

With a vanishing α_1 decay-mode width, this hypothesis reduces to H_1 which therefore corresponds to a nested model. This scenario should therefore provide a better fit of the data with respect to H_1.

Hypothesis H_3

It is postulated that the 0^+ structure of ^{12}C in the $E_x \approx$ 7-16 MeV excitation-energy region of interest can be described by two overlapping but independent resonances: the Hoyle state at 7.65407(19) MeV and a broader resonance at

$E_x \approx 10$ MeV. Whilst overlapping resonances of the same spin and parity should be analysed as a single entity (see H_{5-8}), it is conceivable that the structure of these two resonances are significantly different such that the interference is suppressed. In such a case, these two resonances can therefore be individually treated as single-level approximations. Since the Hoyle state is generally understood to be the archetypal alpha-cluster state with a resonance energy just above the α-separation energy, it is conceivable that its structure may differ significantly from that of a broad state at $E_x \approx 10$ MeV which has approximately 10 times the centre-of-mass decay energy for the α_0 decay mode.

Hypothesis H_4

It is postulated that the 0^+ structure of ^{12}C in the $E_x \approx$ 7-16 MeV excitation-energy region of interest can be described by a two-level approximation (see Equation 2.76) consisting of two resonances: the Hoyle state at 7.65407(19) MeV and a broader resonance at $E_x \approx 10$ MeV. This broader resonances exhibit considerable overlap with the ghost anomaly of the Hoyle state and consequently, the 0^+ structure in this region should be analysed as a single entity. These four hypotheses imply that the unexplained 0^+ strength could possibly be explained by the "interference term" of the two-level approximation, thereby avoiding the need to introduce a new unlisted resonance.

The α- and proton-separation energies for ^{12}C are 7.36659(4) MeV and 15.95668(1) MeV, respectively. Consequently, the α_0 and α_1 decay modes are dominant in the aforementioned excitation-energy region of interest. For the analysis of inclusive measurements in this thesis, alternative decay modes such as proton, γ, pair-production and internal conversion decay are therefore negligible. The only particle-decay widths of interest are for the α_0 and α_1 decays for the pair of resonances, corresponding to four reduced-width ampitudes: γ_{1,α_0}, γ_{1,α_1}, γ_{2,α_0} and γ_{2,α_1}. The relative signs between these reduced widths determine whether the interference between the two resonances is constructive or destructive. Hypotheses 1-4 correspond to the permutations of these interferences, summarised below Table 2.10.

Hypothesis H_5

It is postulated that the 0^+ structure of ^{12}C in the $E_x \approx$ 7-16 MeV excitation-energy region of interest is not fully described by either the two-level approximations of hypotheses 1-4 or the two independent resonances of hypothesis 7. Similar to hypothesis 7, it is presupposed that the structure of the Hoyle state at 7.65407(19) MeV differs sufficiently from that of the broad state at $E_x \approx 10$ MeV such that the interference is suppressed and the two resonances can be individually treated as single-level approximations. This model expands upon the model of hypothesis 7 by introducing a new unlisted 0^+ resonance

Hypothesis	α_0 interference	α_1 interference
H_{4a}	constructive	constructive
H_{4b}	constructive	destructive
H_{4c}	destructive	constructive
H_{4d}	destructive	destructive

Table 2.7: Summary of the α_0 and α_1 constructive/destructive interferences for hypotheses H_{4a}, H_{4b}, H_{4c} and H_{4d}.

at $E_x \approx 9$ MeV which also does not interfere with the neighbouring 0^+ resonances and can therefore be modeled with a single-channel approximation. Such a 0^+ resonance could correspond to an isoscalar giant monopole resonance (ISGMR) predicted by T. Furuta *et al.* [39], as described in Chapter 1. In particular, this resonance could be compatible with the small-amplitude oscillation mode of the ISGMR if the resonance energy is found to be significantly below $E_x \approx 10$ MeV. The spin and parity of such a resonance can be verified through the $^{12}\mathrm{C}(\alpha,\alpha')^{12}\mathrm{C}$ differential cross sections from the PR166 and PR194 experiments analysed for this thesis.

Hypothesis H_6

It is postulated that the 0^+ structure of ^{12}C in the $E_x \approx$ 7-16 MeV excitation-energy region of interest can be described by a two-level approximation (see Equation 2.76) consisting of two resonances: the Hoyle state at 7.65407(19) MeV and a broader resonance at $E_x \approx 10$ MeV. This broader resonances exhibit considerable overlap with the ghost anomaly of the Hoyle state and consequently, the 0^+ structure in this region should be analysed as a single entity. Unlike hypothesis H_4, which assumes that these two resonances an be incoherently summed, the model associated with hypothesis H_6 accounts for the coherent interference between these two resonances. These four hypotheses imply that the unexplained 0^+ strength could possibly be explained by the "interference term" of the two-level approximation, thereby avoiding the need to introduce a new unlisted resonance.

The α- and proton-separation energies for ^{12}C are 7.36659(4) MeV and 15.95668(1) MeV, respectively. Consequently, the α_0 and α_1 decay modes are dominant in the aforementioned excitation-energy region of interest. For the analysis of inclusive measurements in this thesis, alternative decay modes such as proton, γ, pair-production and internal conversion decay are therefore negligible. The only particle-decay widths of interest are for the α_0 and α_1 decays

for the pair of resonances, corresponding to four reduced-width ampitudes: γ_{1,α_0}, γ_{1,α_1}, γ_{2,α_0} and γ_{2,α_1}. The relative signs between these reduced widths determine whether the interference between the two resonances is constructive or destructive. Hypotheses 1-4 correspond to the permutations of these interferences, summarised below Table 2.8.

Hypothesis	α_0 interference	α_1 interference
H_{6a}	constructive	constructive
H_{6b}	constructive	destructive
H_{6c}	destructive	constructive
H_{6d}	destructive	destructive

Table 2.8: Summary of the α_0 and α_1 constructive/destructive interferences for hypotheses H_{6a}, H_{6b}, H_{6c} and H_{6d}.

Hypothesis H_7

It is postulated that the 0^+ structure of ^{12}C in the $E_x \approx$ 7-16 MeV excitation-energy region of interest is described by three distinct, overlapping 0^+ resonances which coherently interfere. Such a structure may require a fit with the formalism of a three-level approximation. Unlike hypothesis H_5, which assumes that these three resonances an be incoherently summed, the model associated with hypothesis H_7 accounts for the coherent interference between these three resonances.

(single channel: α_0) (multichannel: α_0, α_1) (multichannel: α_0, α_1)

Hypothesis	γ_{1,α_0}	γ_{2,α_0}	γ_{3,α_0}	γ_{1,α_1}	γ_{2,α_1}	γ_{3,α_1}
$H_{7\mathrm{a}}$	$-$	$-$	$-$	$-$	$-$	$-$
	$+$	$+$	$+$	$+$	$+$	$+$
$H_{7\mathrm{b}}$	$-$	$-$	$+$	$-$	$-$	$-$
	$+$	$+$	$-$	$+$	$+$	$+$
$H_{7\mathrm{c}}$	$-$	$+$	$-$	$-$	$-$	$-$
	$+$	$-$	$+$	$+$	$+$	$+$
$H_{7\mathrm{d}}$	$-$	$+$	$+$	$-$	$-$	$-$
	$+$	$-$	$-$	$+$	$+$	$+$
$H_{7\mathrm{e}}$	$-$	$-$	$-$	$-$	$-$	$+$
	$+$	$+$	$+$	$+$	$+$	$-$
$H_{7\mathrm{f}}$	$-$	$-$	$+$	$-$	$-$	$+$
	$+$	$+$	$-$	$+$	$+$	$-$
$H_{7\mathrm{g}}$	$-$	$+$	$-$	$-$	$-$	$+$
	$+$	$-$	$+$	$+$	$+$	$-$
$H_{7\mathrm{h}}$	$-$	$+$	$+$	$-$	$-$	$+$
	$+$	$-$	$-$	$+$	$+$	$-$
$H_{7\mathrm{i}}$	$-$	$-$	$-$	$-$	$+$	$-$
	$+$	$+$	$+$	$+$	$-$	$+$
$H_{7\mathrm{j}}$	$-$	$-$	$+$	$-$	$+$	$-$
	$+$	$+$	$-$	$+$	$-$	$+$
$H_{7\mathrm{k}}$	$-$	$+$	$-$	$-$	$+$	$-$
	$+$	$-$	$+$	$+$	$-$	$+$
$H_{7\mathrm{l}}$	$-$	$+$	$+$	$-$	$+$	$-$
	$+$	$-$	$-$	$+$	$-$	$+$
$H_{7\mathrm{m}}$	$-$	$-$	$-$	$-$	$+$	$+$
	$+$	$+$	$+$	$+$	$-$	$-$
$H_{7\mathrm{n}}$	$-$	$-$	$+$	$-$	$+$	$+$
	$+$	$+$	$-$	$+$	$-$	$-$
$H_{7\mathrm{o}}$	$-$	$+$	$-$	$-$	$+$	$+$
	$+$	$-$	$+$	$+$	$-$	$-$
$H_{7\mathrm{p}}$	$-$	$+$	$+$	$-$	$+$	$+$
	$+$	$-$	$-$	$+$	$-$	$-$

Table 2.9: The permutations of signs for the α_0 and α_1 reduced widths for the three-level approximation.

Hypothesis	0_2^+ Hoyle state	0_3^+ $E_x \approx 9$ MeV	0_4^+ $E_x \approx 10$ MeV $\Gamma_{\text{tot}} \approx 3$ MeV	Coherent interference (0_2^+ and 0_4^+)	Coherent interference (0_2^+, 0_3^+ and 0_4^+)
H_1	✓				
H_2	✓				
H_3	✓		✓		
H_4	✓		✓	✓	
H_{4a}				$(\alpha_0 : +, \alpha_1 : +)$	
H_{4b}				$(\alpha_0 : +, \alpha_1 : -)$	
H_{4c}				$(\alpha_0 : -, \alpha_1 : +)$	
H_{4d}				$(\alpha_0 : -, \alpha_1 : -)$	
H_5	✓	✓	✓		
H_6	✓	✓	✓	✓	
H_{6a}				$(\alpha_0 : +, \alpha_1 : +)$	
H_{6b}				$(\alpha_0 : +, \alpha_1 : -)$	
H_{6c}				$(\alpha_0 : -, \alpha_1 : +)$	
H_{6d}				$(\alpha_0 : -, \alpha_1 : -)$	
H_7	✓	✓	✓		✓ †

Table 2.10: Summary of the studied hypotheses. † The various permutations of interference for hypothesis H_7 are summarised in Table 2.9.

Chapter 3

Summary of the Experimental Apparatus

A total of five distinct experiments were analysed for the purposes of this thesis - all of which were performed with the K600 Spectrometer at the Separated-Sector Cyclotron (SSC) facility of iThemba LABS, shown below in Figure 3.1.

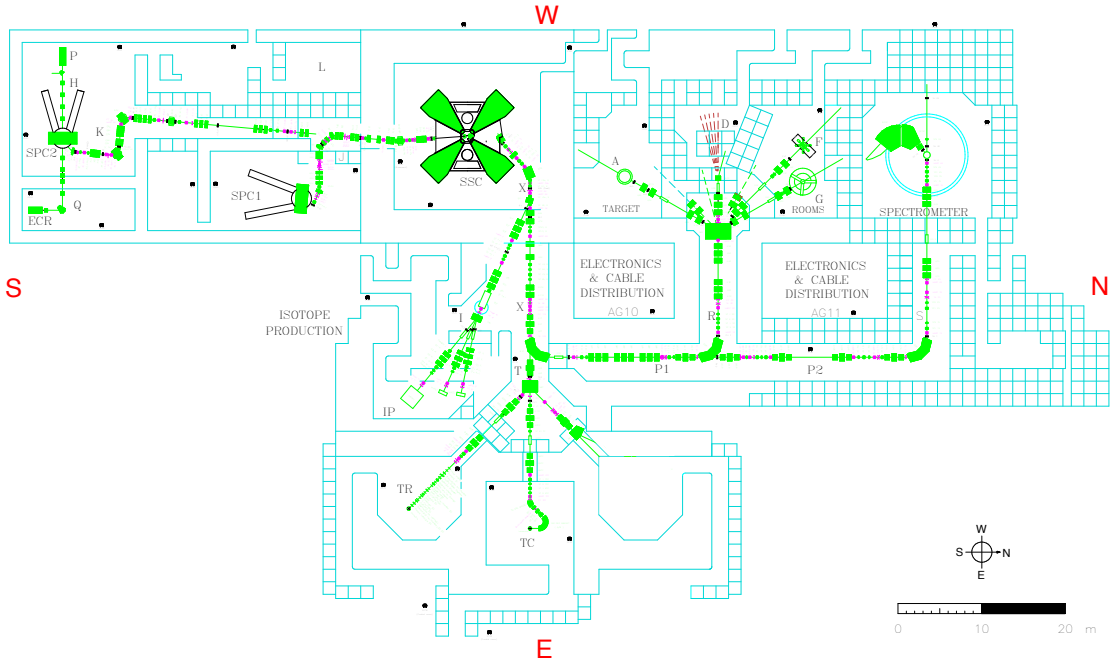

Figure 3.1: Schematic top view of the SSC facility at iThemba Labs.

For convenience, these experiments are referred to by their respective project numbers assigned by the iThemba LABS Programme Advisory Committee (PAC). All of the analysed experiments were performed at the K600 spectrometer vault and the associated detector configurations are summarised in Table 3.1 [81, 82]. The primary experiment of this thesis, PR240, is the sole experiment which was expressly performed for the arguments of this thesis. The other complimentary datasets (PR166, PR194, PR195 and PR251) were repurposed from other experimental projects.

For PR240, an ancillary array of double-sided silicon strip detectors (DSSSDs) known as the CAKE (Coincidence Array for K600 Experiments) was employed. This array detects the charged-particle breakup from excited ^{12}C recoil nuclei, as well as the inherently unstable ^{8}Be daughter nucleus which is produced from α decay. The ancillary detectors employed for the other experiments were not analysed for this thesis and are disclosed solely for completeness.

PAC Code	Year	Reaction	Target (thickness)	E_{beam} [MeV]	Angle* [deg]	E_x range [MeV]	Focal-plane Dispersion	VDC #1, #2	Paddle #1, #2	Ancillary Detectors
PR166	2011	^{12}C(α,α')^{12}C	^{12}C (290 μg/cm^2) ^{12}C (220 μg/cm^2) ^{12}C (290 μg/cm^2)	196 196 196	6 (1.91) 8.5 (1.91) 10 (1.91)	7.0 - 27.3 7.0 - 29.5 7.2 - 28.6	Medium	X , UX	1/4", 1/2"	—
PR194	2012	^{12}C(α,α')^{12}C	^{12}C (300 μg/cm^2)	160	0 (1.91)	7.3 - 20.7	High	XU, XU	1/4", 1/2"	—
PR251	2016	^{12}C(α,α')^{12}C	^{12}C (1053 μg/cm^2)	118	0 (2.0)	5.0 - 14.8	High	XU, —	1/4", —	(8×) CLOVER‡ (2×) $LaBr_3Ce$‡
PR195	2012	^{14}C(p,t)^{12}C	^{14}C (300 μg/cm^2)♭	67.5	21 (1.91)	7.5 - 14.5	Medium	X , X	1/4", —	(2×) W1‡ (3×) YY1‡ (1×) MMM‡
PR240	2017	^{14}C(p,t)^{12}C	^{14}C (unknown)♯	140	0 (2.0)	4.3 - 17.6	Medium	XU, XU	1/4", —	(5×) MMM

Table 3.1: General summary of the experimental setups for all the analysed data. *The bracketed values represent the opening angles for the circular collimator employed for each measurement †The new VDC used in VDC position 2 was inverted so that the U wireplane was upstream with respect to the X wireplane. ‡These ancillary detectors were not analysed for this thesis and are disclosed solely for completeness. ♭The enrichment was approximately 80% ^{14}C and 20% ^{12}C. ♯The enrichment was approximately 87% ^{14}C and 13% ^{12}C.

3.1 The K600

The K600 spectrometer primarily consists of five active elements: two dipole magnets (D1 and D2), two trim coils (the H- and K-coils) and a quadrupole magnet, as shown in Figure 3.2. These magnets work in concert to momentum analyse the ejectile which is then focused at the focal plane. The ejectile is detected by the focal-plane detector system which can be configured at one of three different positions, known as the low, medium and high dispersion focal planes. The unique experimental configurations of each measurement are summarised in Table 3.1. The momentum resolution provided by the dipole magnets is dependent on the the dispersion of the beam, i.e. the correlations

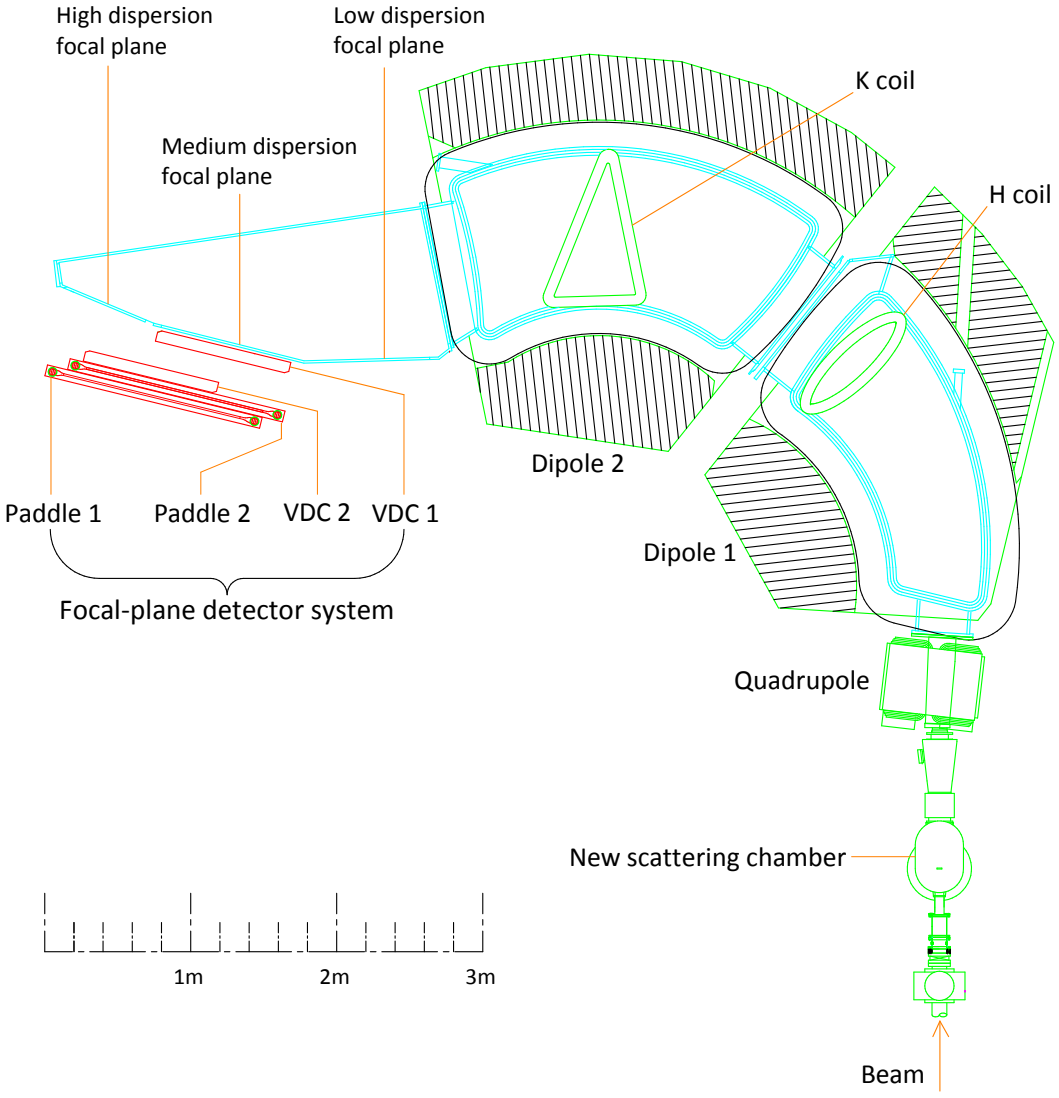

Figure 3.2: Example schematic of the K600 spectrometer setup.

between the kinetic energies and incident angles of the beam particles within a beam packet. To optimise this resolution, a process known as dispersion matching is employed (see Section 3.1). Since magnetic spectrometers separate on the basis of rigidity, a limiting factor for the energy resolution observed at the focal plane is determined by the energy spread of the initial particle beam. Dispersion matching is the process by which the beam characteristics at the target are adjusted to mitigate this energy spread and produce an observed excitation-energy resolution that may even be better than that of the initial beam [83, 84].

For achromatic focus mode (shown in Figure 3.3), the momentum distribution of the beam at the target position is independent of position, thereby leading to a kinematic broadening of the focal plane spectrum.

For lateral dispersion matching (shown in Figure 3.4), the beam profile is generated with the lower momentum ($-\Delta p$) and higher momentum ($+\Delta p$) beam particles upon the inner and outer sides of the bending radius, respectively. By exploiting the fact that the flight path of the $+\Delta p$ particles through the dipole magnetic fields have a larger radius (rigidity) relative to that of the $-\Delta p$ particles, a controlled difference in the exit angles of the ejectiles is obtained. This can be tuned to focus at the focal plane to achieve the aforementioned improved resolution.

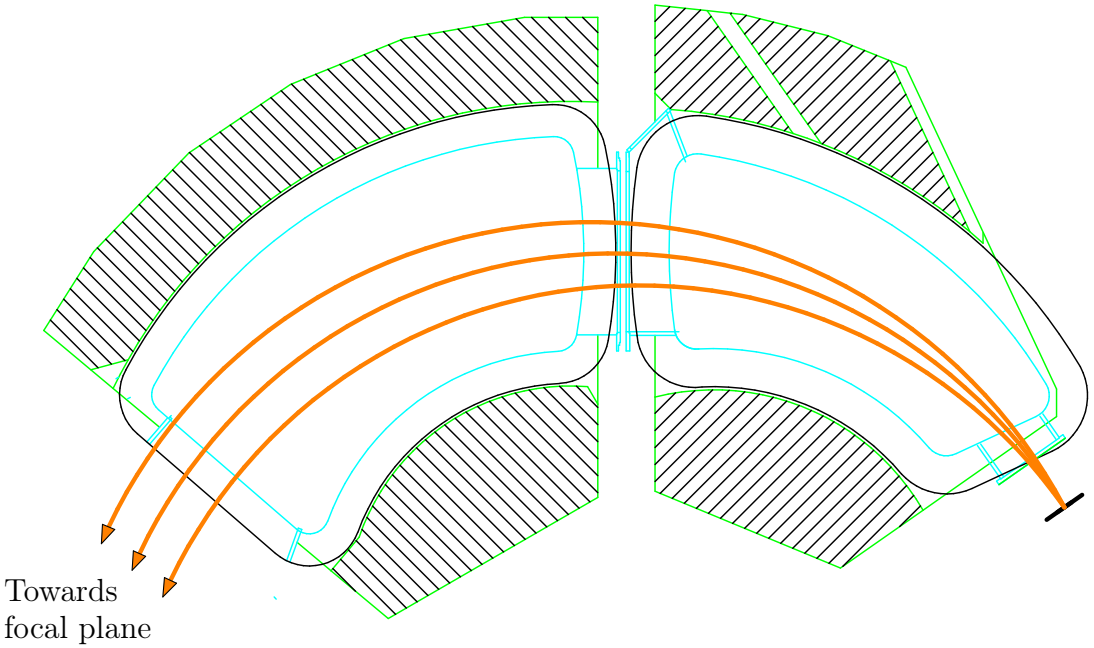

Figure 3.3: Schematic representation of an achromatic focus mode. The momentum distribution of the beam is not well defined at the target (i.e. no positional dependence) which results in a kinematic broadening at the focal plane.

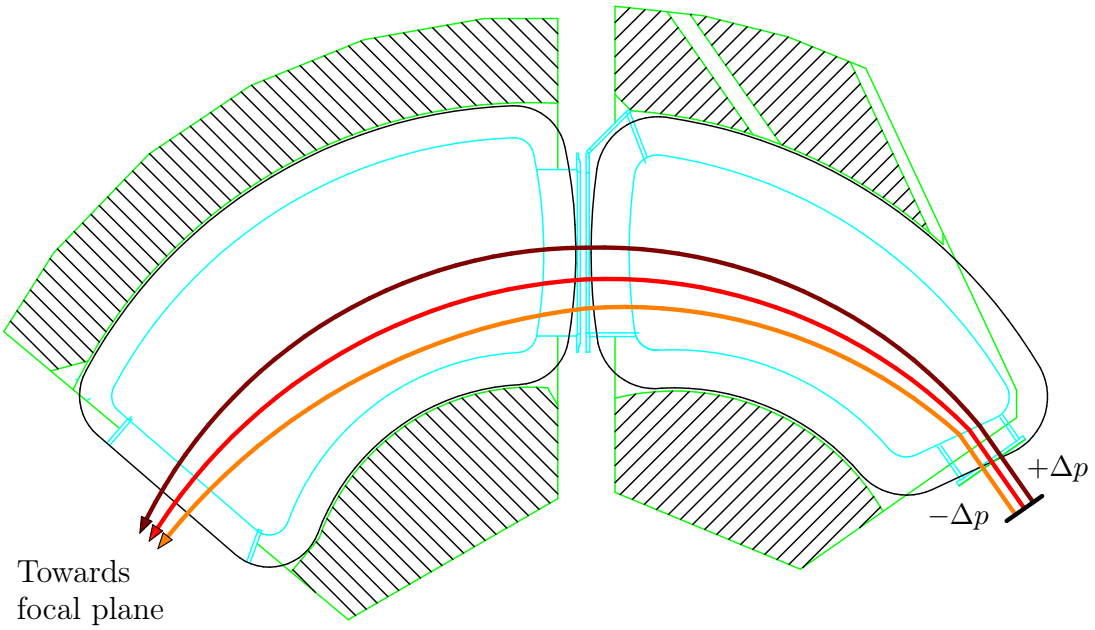

Figure 3.4: Schematic representation of lateral dispersion matching. The lower and higher momentum sides of the beam are indicated by $(-\Delta p)$ and $(+\Delta p)$, respectively. The orange, red and brown particle tracks correspond to particle tracks of lower, moderate and higher momentum, respectively.

3.2 Focal-Plane Detector System

The focal-plane detector system consists of a combination of plastic scintillators (paddles) and vertical drift chambers (VDCs), described in Sections 3.2.1 and 3.2.2, respectively. The most common configuration of this detector system is with two VDCs and two paddles, however this can be tailored for the measurement of interest. This detector system can be configured at three different positions along the exit window of the spectrometer: the low-, medium- and high-dispersion focal planes. The choice of these positions is dictated by the reaction of interest and the measurement constraints. For example, the ^{12}C(α,α')^{12}C measurements at $\theta_{\text{lab}} = 0^{\circ}$ analysed for this thesis were all performed at the high-dispersion focal plane in order to observe the excitation energy range of interest: $E_x \approx$ 7-16 MeV. For the ^{14}C$(p,t)^{12}$C experiment, the same excitation energy range required the use of the medium-dispersion focal plane. Figures 3.5 and 3.6 depict the focal-plane detector system configured for the high- and medium-dispersion focal planes, respectively.

A Kapton exit window is employed at the exit window of the spectrometer to isolate the internal vacuum chamber of the spectrometer from the atmospheric pressure in the vault. VDC 1 is mounted at the focal plane which

is adjacent to this exit window and in the air at atmospheric pressure. This exit window lies between the ejectile and the focal-plane detector system and limits the ejectiles of interest to light ions such as H and He which exhibit a sufficiently low energy loss through the exist window.

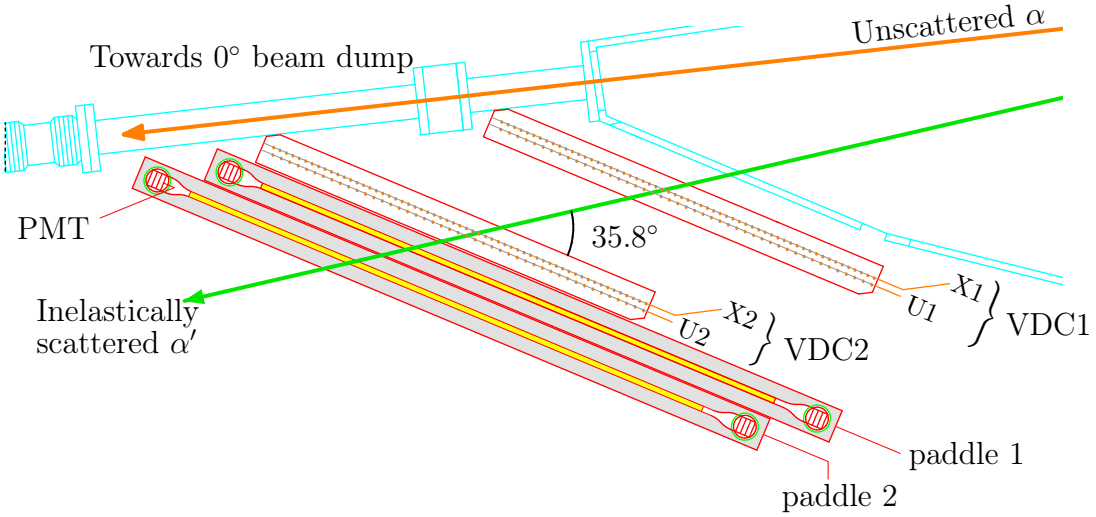

Figure 3.5: Schematic top view of the new focal-plane detector system in high-dispersion focus mode where VDC1 and VDC2 are both configured with XU VDCs.

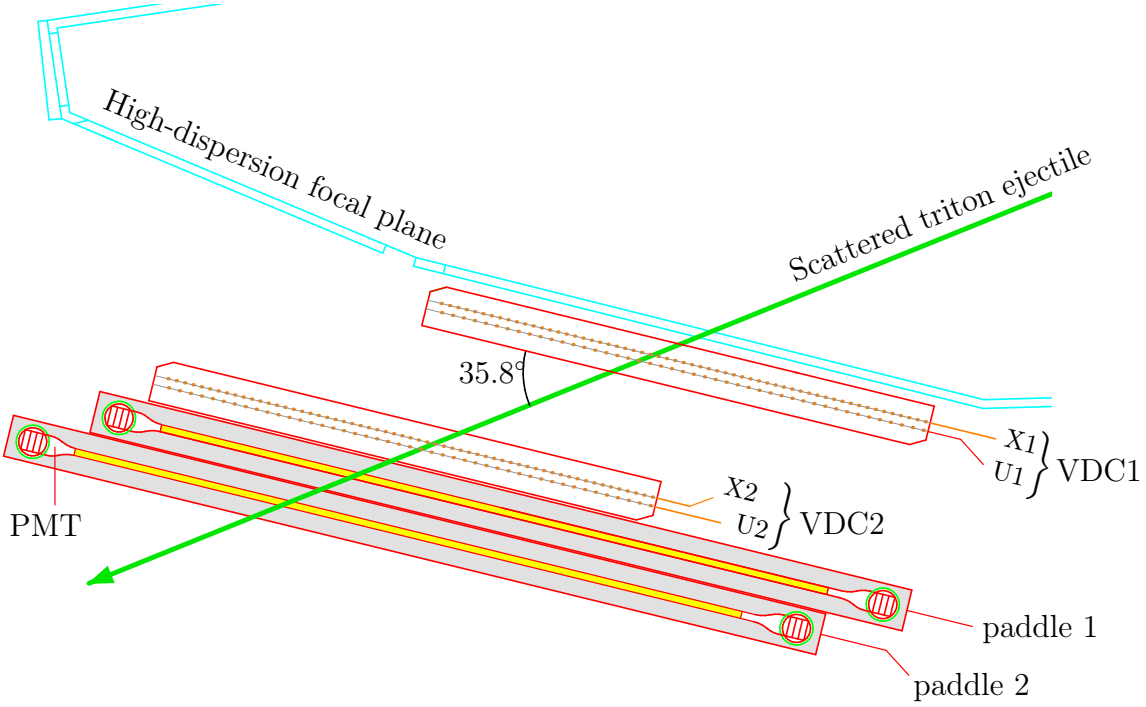

Figure 3.6: Schematic top view of the new focal-plane detector system in medium-dispersion focus mode where VDC1 and VDC2 are both configured with XU VDCs.

3.2.1 Plastic Scintillators (paddles)

The plastic scintillator detectors, which are also referred to as paddles, form an integral component of the focal-plane setup of the K600. They are used to trigger focal-plane events by detecting ejectiles which have traversed through the K600 spectrometer. When such energy deposition occurs, plastic scintillates and light is detected by the two photomultiplier tubes (PMTs) coupled to the ends of each paddle. These PMTs used to detect the light output is sensitive to many factors such as temperature and consequently, often exhibit drifting for their respective detected light outputs. This is mitigated but calibrating the light output per run. In addition, the relationship of the energy deposition in the scintillator to the time-of-flight (TOF) of the ejectile provides particle identification (PID) capability [82, 81]. There are currently paddles of three different thicknesses at the K600: 1/8", 1/4" and 1/2". The paddles are typically used either individually or in a pair configuration and the choice of detector thickness is dependent on the measurement.

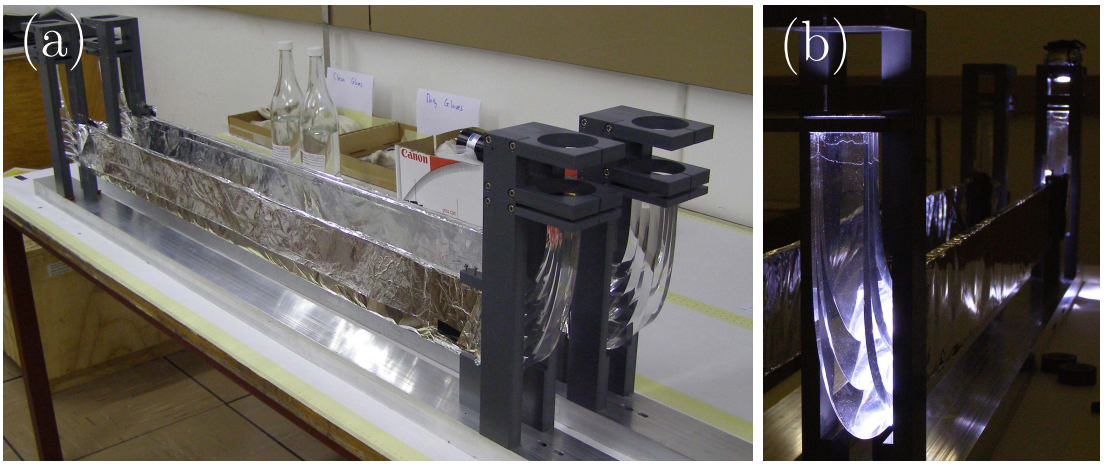

Figure 3.7: Images of the paddles during the construction stages. Image (a) highlights the layer of Mylar around the plastic scintillator material to ensure that the scintillator is insulated from external light sources. Image (b) highlights highlights the light guides which couple the scintillators to the PMTs (which were unattached when this photo was taken). The PMTs are vertically mounted onto the light guides to mitigate the spatial restrictions of the high dispersion focal plane configuration.

3.2.2 Vertical Drift Chambers (VDCs)

The VDCs are gaseous ionisation detectors which are used to track the paths of traversing ejectiles [85]. There are two types of VDC detectors used in the focal-plane detector system of the K600 spectrometer: X and XU. Both types possesses an X wireplane with vertical wires which provide horizontal information, however the XU VDCs have an extra U wireplane with wires that are orientated 50° relative to the horizontal plane to provide a combination of horizontal and vertical information (see Figure 3.8). A cross-sectional schematic showing the construction of a XU VDC is presented in Figure 3.9. By reconstructing the path of the ejectile, the corresponding position of traversal across the wire plane can be determined. This position can be used to infer the excitation energy of the recoil nucleus. Typically, the magnetic optics are optimised for resolution for the X wireplane so the excitation is only calculated from this wire plane whilst the other wire planes enable ancillary measurements such as the projected ejectile scattering angle and vertical focal-plane position (see Sections 4.1.6 and 4.1.5, respectively).

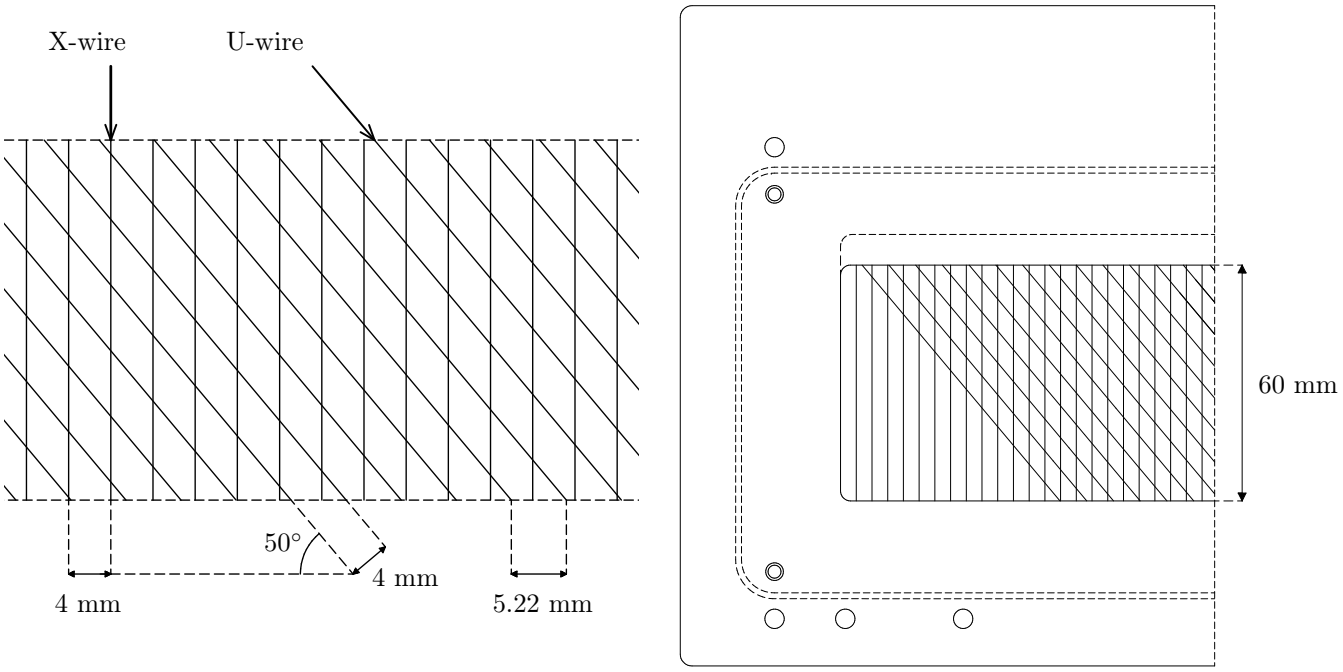

Figure 3.8: Schematic side view of the VDC wire planes (guard wires are excluded for clarity).

3.2.2.1 VDC Operation

The VDC detectors operate through the mechanism of gaseous ionisation. As shown in Figure 3.9, the detector is bounded on both sides by Mylar windows which isolate the internal regions of the VDC from the atmosphere. Each VDC

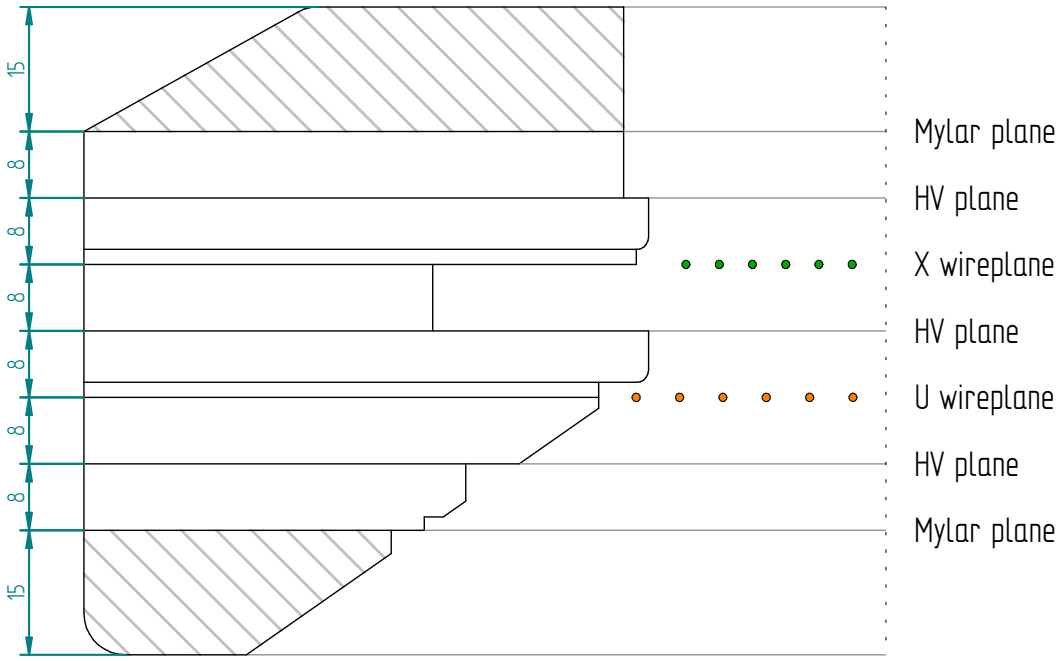

Figure 3.9: Cross-sectional top view of a XU VDC detector. The displayed dimensions are given in mm.

is composed of three high-voltage (HV) planes which are stretched aluminium foil [86]. For the XU VDCs, these HV planes partition the detector into the X- and U- wire chambers. For the detector of α-particle ejectiles, a potential of apprpoximately -2.95 kV is applied to the HV planes. During operation of the VDCs, a combination of Ar and CO_2 gas (in a mass ratio of 90% and 10%, respectively) is continuously flowed through the detector. This gas mixture is the detection medium and occupies the cavities within each VDC that house the wire planes.

If the detector is operated with a sufficiently low potential, the charge collected by the signal wires is directly proportional to the energy deposition in the associated cells. Operation in the Geiger-Müller regime is typified by a relatively higher potential where the electric field is sufficiently high to accelerate liberated electrons such that they impinge upon and further liberate bound electrons. The propagation of these successive ionisations produces a temporary conductive known as a Townsend avalanche near the signal wire where the electric field gradient is largest. This phenomenon produces a larger output signal, however information about the energy deposition in the cells by the ejectile is lost.

A schematic of a VDC event is given in Figure 3.10. An electrical threshold is set for the signal wires of each VDC. If a spectrometer event is triggered by the paddle detector, the drift times of all triggered wires is saved in the data stream. These drift times are used to reconstruct the path of the ejectile through an algorithm known as raytracing.

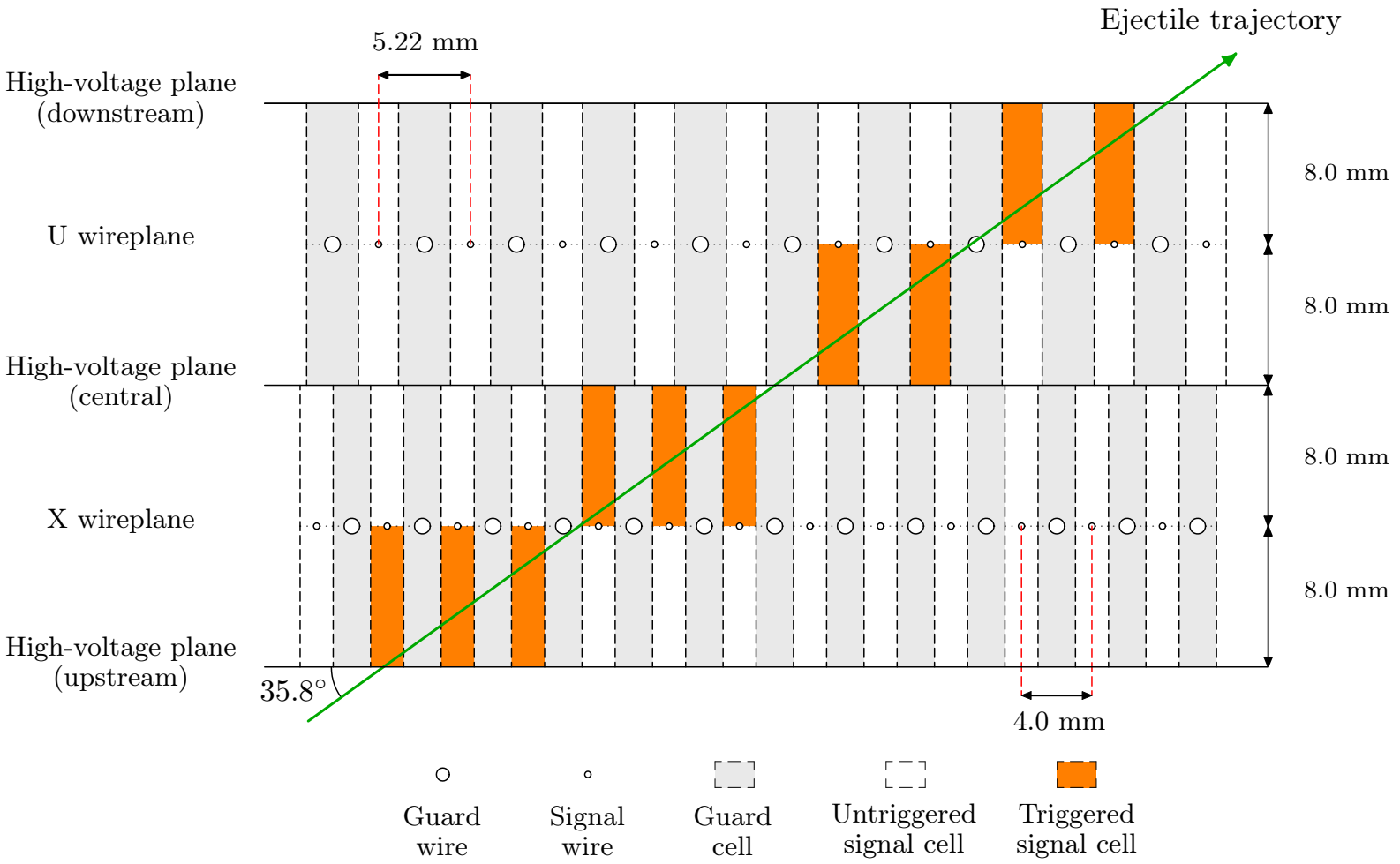

Figure 3.10: Horizontal plane cross section (top view) of the Vertical Drift Chamber operation. The spacing between the wires of the U wireplane is identical to that of the X wireplane, however since the U-wires are at an angle of 50° relative to the vertical X-wires, the U-wires appear to have greater spacing due to the horizontal cross-sectional plane.

3.2.2.2 VDC Configurations

It is shown that for each U wireplane, there is a region on each side which is devoid of wires which therefore cannot provide vertical information. The acceptance range for the X wireplane is therefore larger than for the U wireplane. The VDCs are typically employed in the XU configuration, whereby the X wireplane is upstream with respect to the U wireplane. If acceptance on the high-momentum (low E_x) side is to be prioritised, a UX configuration can be employed whereby the U wireplane is upstream with respect to the X wireplane. Since the average angle of traversal for ejectiles is $\theta_{\text{lab}} \approx 35°$, this UX configuration enables a slightly increased range of X wireplane positions which exhibit full vertical-position acceptance with the U wireplane, as depicted in Figure 3.11.

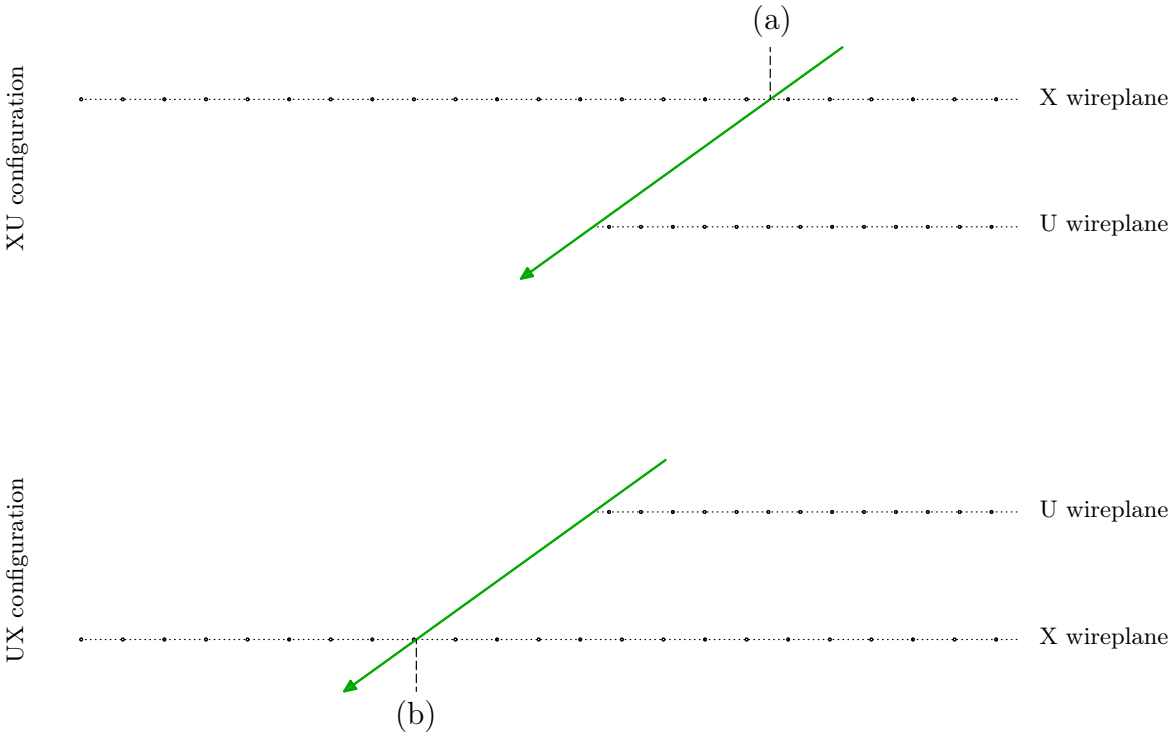

Figure 3.11: Schematic illustrating the difference between XU and UX configurations of a VDC. Only the region of the U wireplane with full vertical-position acceptance is drawn. The largest positions of the X wireplane (equivalent to the lowest E_x of the recoil nucleus) with full vertical-position acceptances are indicated as (a) and (b) for the XU and UX configurations, respectively.

3.3 The CAKE

The Coincidence Array for K600 Experiments (CAKE) is comprised of 5 MMM-type double-sided silicon strip detectors (DSSSDs) which are manufactured by Micron Semiconductor Ltd., as shown in Figure 3.12 [87]. The mounting apparatus for the CAKE was designed with a 3D CAD programme named Solid Edge and enables the array to be mounted at both forward and backward angles with respect to the target.

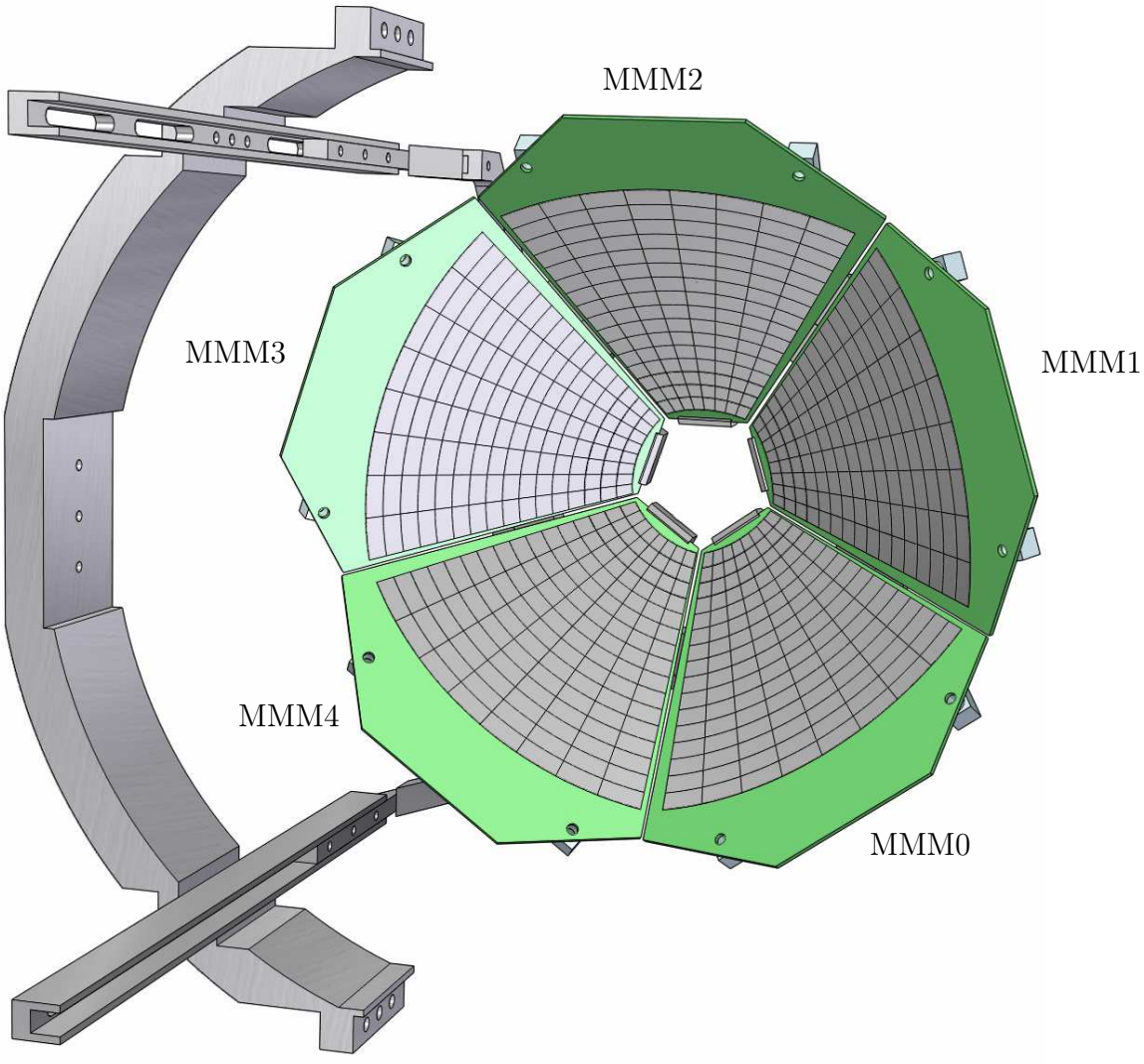

Figure 3.12: 3D rendering of the CAKE, comprised of 5 MMM-type DSSSD detectors. The detector numbering is indicated.

The CAKE is predominantly used to detect at backward angles to maximise the signal-to-background ratio although the array can be accommodated at both forward and backward angles. For experiment PR240, CAKE was mounted at backward angles within the scattering chamber, as shown in Figure 3.13.

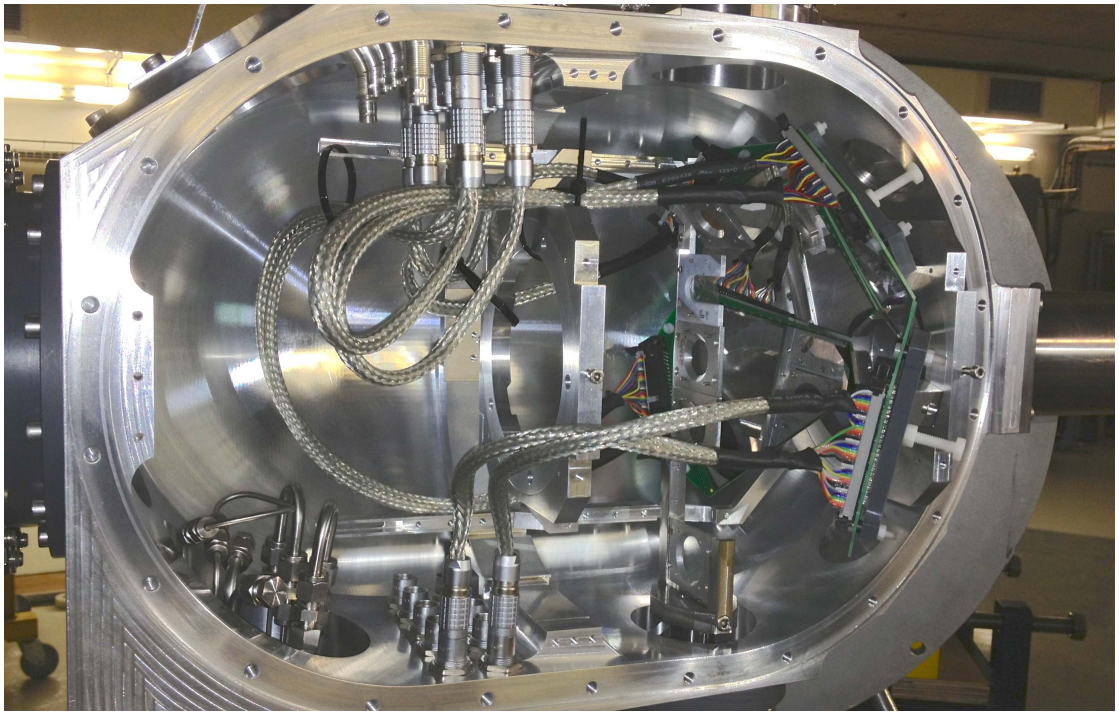

Figure 3.13: Image of the CAKE installed at backward angles within the scattering chamber.

3.3.1 Properties of Silicon semiconductor detectors

The detection mechanism of the MMM-type DSSSDs is achieved through the properties of semiconductors and p-n junctions. Semiconductor materials are defined to exhibit an electrical conductivity between that of a conductor and an insulator. N-type semiconductor materials exhibit electron densities that exceed their hole densities , whilst the converse is true for p-type semiconductor materials. Silicon can be doped with either boron or phosphorous to produce p- or n-type semiconductor materials, respectively, as depicted in Figures 3.14 and 3.15.
When a p-type and an n-type semiconductor are brought into contact, a p-n junction is formed. Electrons in the n-doped silicon material occupy the conduction band, however when these electrons are attracted onto the p-doped silicon material, they occupy the valence band. A region devoid of all mobile

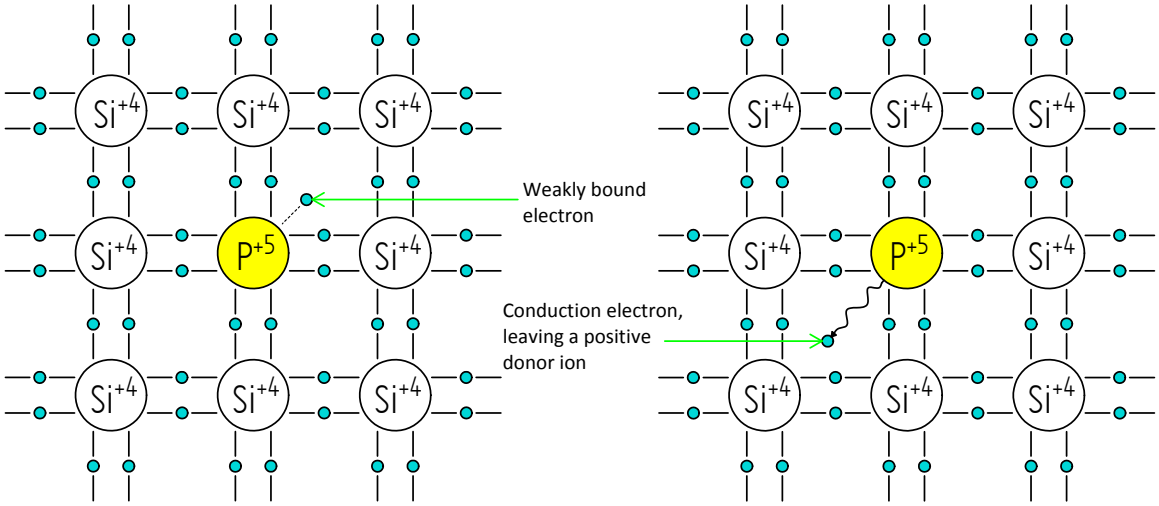

Figure 3.14: Schematic lattice structure of a p-doped silicon material

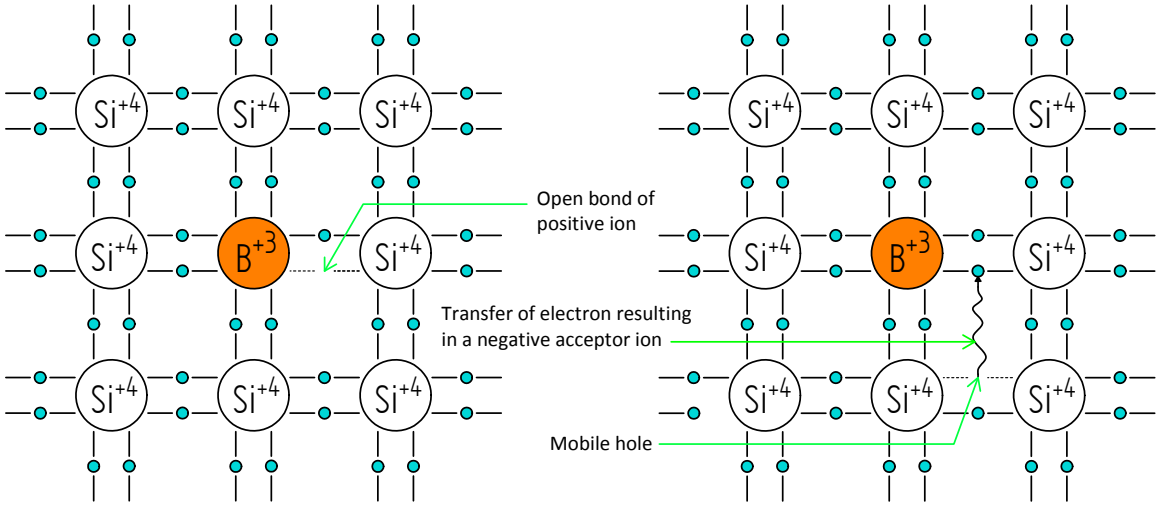

Figure 3.15: Schematic lattice structure of a n-doped silicon material

charge carriers, known as the depletion zone, is formed at this junction and acts as an insulator to prevent drift current flowing across this junction.

Silicon detectors function through reverse biasing: the process through which the p-doped side is supplied with a negative voltage and/or the n-doped side is supplied with a positive voltage (see Figure 3.16). The former method was used to reverse bias the MMMs of the CAKE. This form of biasing attracts the electrons and the electron holes towards n-doped and p-doped sides, respectively, thereby increasing the size of the depletion zone (region with no charge carriers).

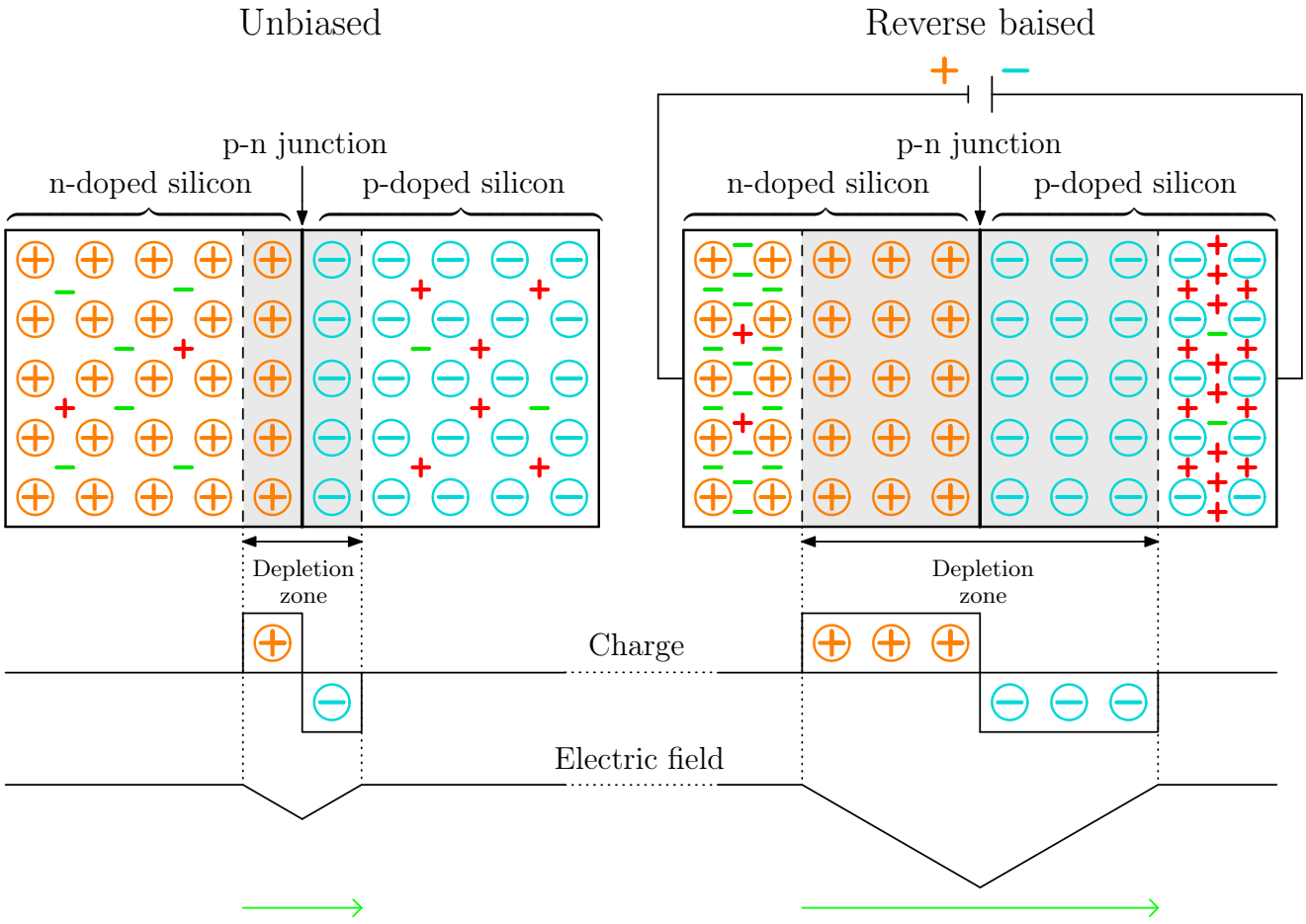

Figure 3.16: Schematic diagram of a p-n junction illustrating the increase of the depletion region with reverse biasing. The encircled orange and blue charges represent the stationary acceptor and donor ions, respectively. The green and red charges represent the electron and hole charge carriers, respectively. The grey regions in the n- and p-doped silicon represent the depletion zone which is devoid of charge carriers. The green arrow indicates the direction of the electric field.

3.3.2 MMM-type DSSSD detectors

The CAKE consists of 5 MMM-type (the design name) double-sided silicon strip detectors manufactured by Micron Semiconductor Ltd. These detectors have 16 ring channels upon the p-side and 8 sector channels upon the n-side, with a channel mapping defined in Figure 3.17. The silicon material of the MMM-type detectors is predominantly n-doped. The mounting apparatus for these detectors is specifically designed for the p-side (ring channels) to face the target: the rationale being that since the electrons move towards the p-side, the energy resolution for this orientation should be superior. The MMM-type detectors were operated in reverse bias mode with a -30 V potential placed on the p-side whilst the n-side was grounded.

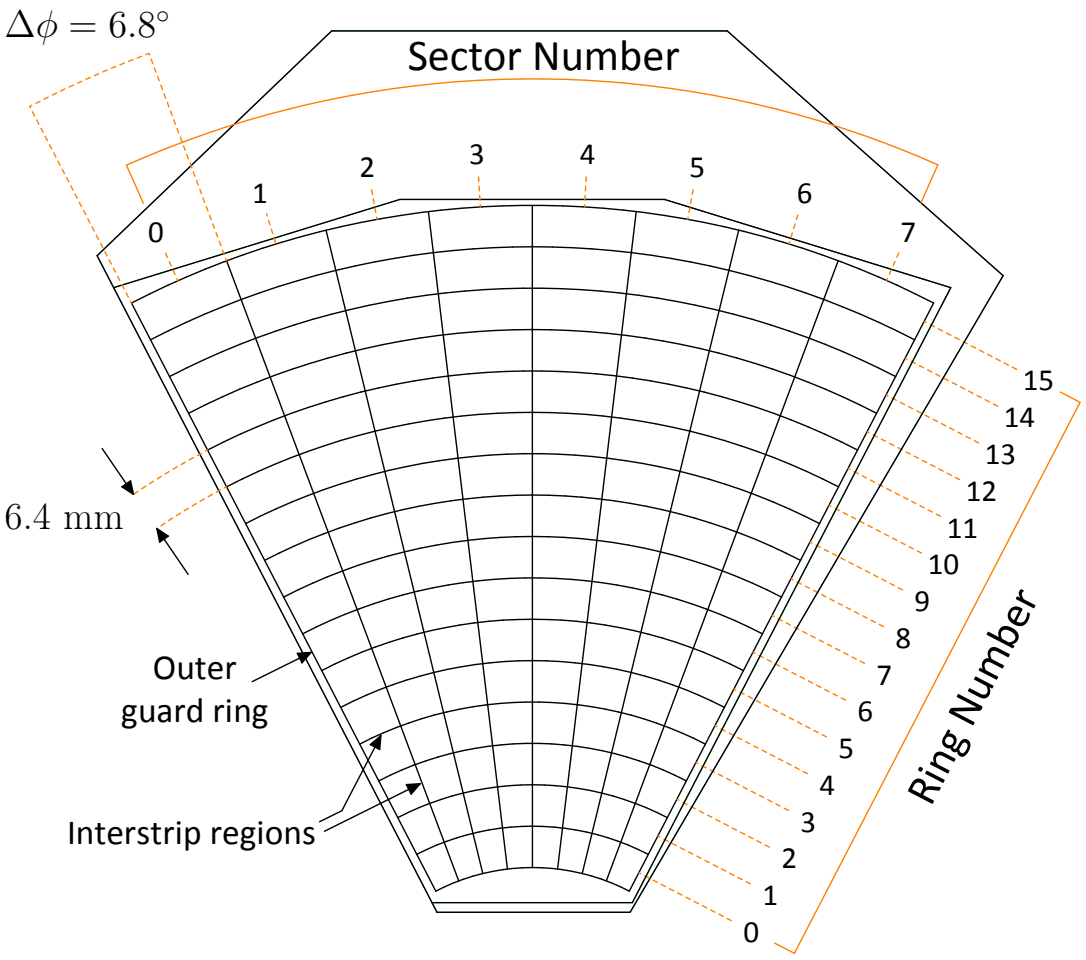

Figure 3.17: Schematic diagram of an MMM-type DSSSD detector manufactured by Micron Semiconductor Ltd.

3.3.3 Electronics

A schematic of the electronics to connect the CAKE to the DAQ is displayed in Figure 3.18. The pairing of MPR-16 and MSCF-16 modules, manufactured by mesytec GmbH & Co. KG, is particularly well suited towards spectroscopy with DSSSDs and as such, the electronics setup for the CAKE is elegantly compact. Energy and timing signals were recorded for each of the 120 channels of the CAKE.

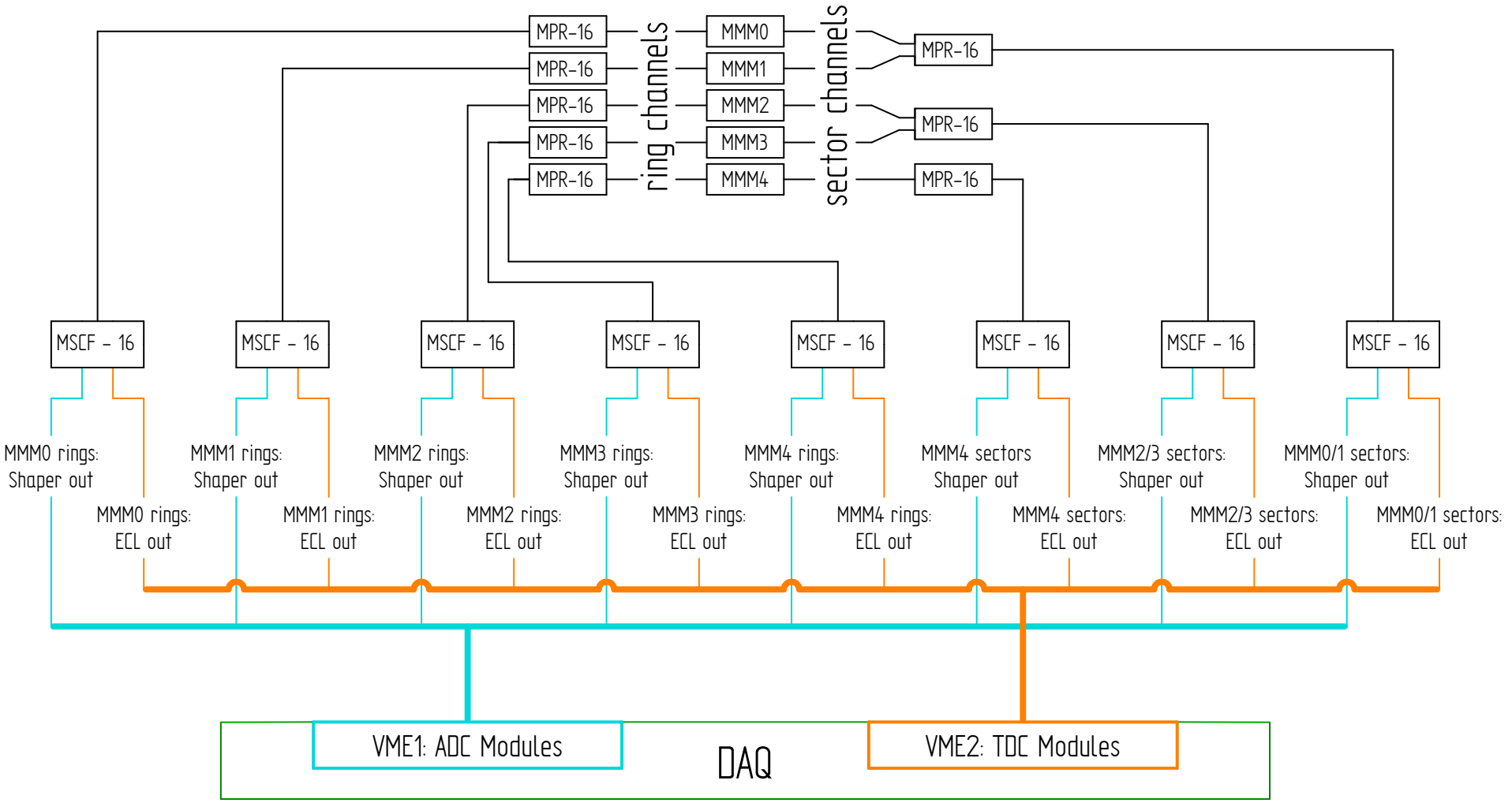

Figure 3.18: Schematic diagram of the CAKE electronics for experiment PR240. MPR-16: a multichannel preamplifier module. MSCF-16: a shaping / timing filter amplifier with constant fraction discriminator and multiplicity trigger.

3.3.4 CAKE GEANT4 simulation

An accurate simulation of the CAKE shown in Figure 3.19 was implemented from the MMM detector design drawings from Micron Semiconductor Ltd [87]. This simulation was used to determine the solid angles of the CAKE relative to the target position, as shown in Figures 3.20 and 3.21. It is observed that the solid angle per ring is shown to be proportional to the yield for isotropic decay which supports the geometrical accuracy of the simulation. The yield for rings 12-15 is slightly below the expected value due to target attenuation effects which are more drastic towards $\theta_{\text{lab}} = 90°$. The ideal total efficiency of the CAKE is 25.6 %, however the malfunctioning channels listed in Table 4.5 yield a lower total efficiency of 22.5 %. This simulation is pivotal for the analysis of angular distributions in Section 4.3.

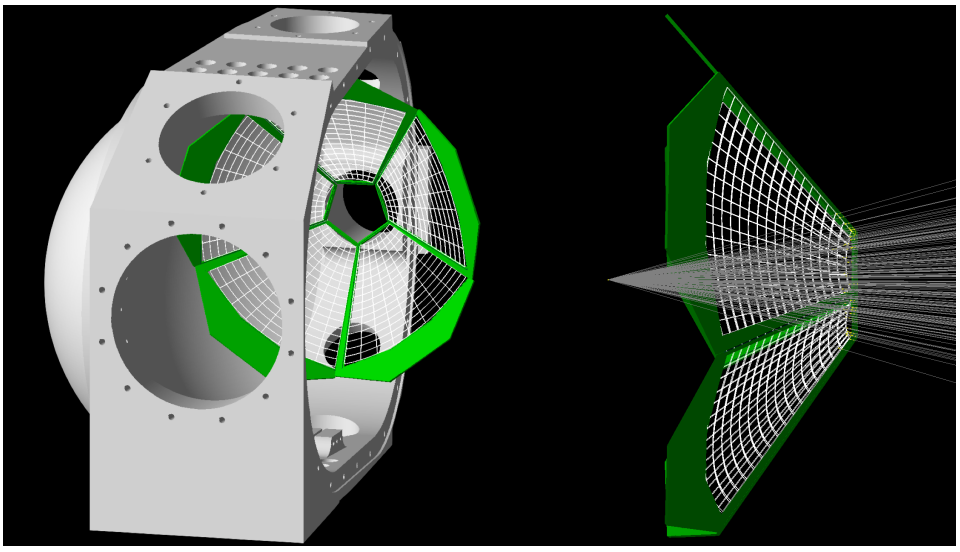

Figure 3.19: Rendering of the CAKE GEANT4 simulation.

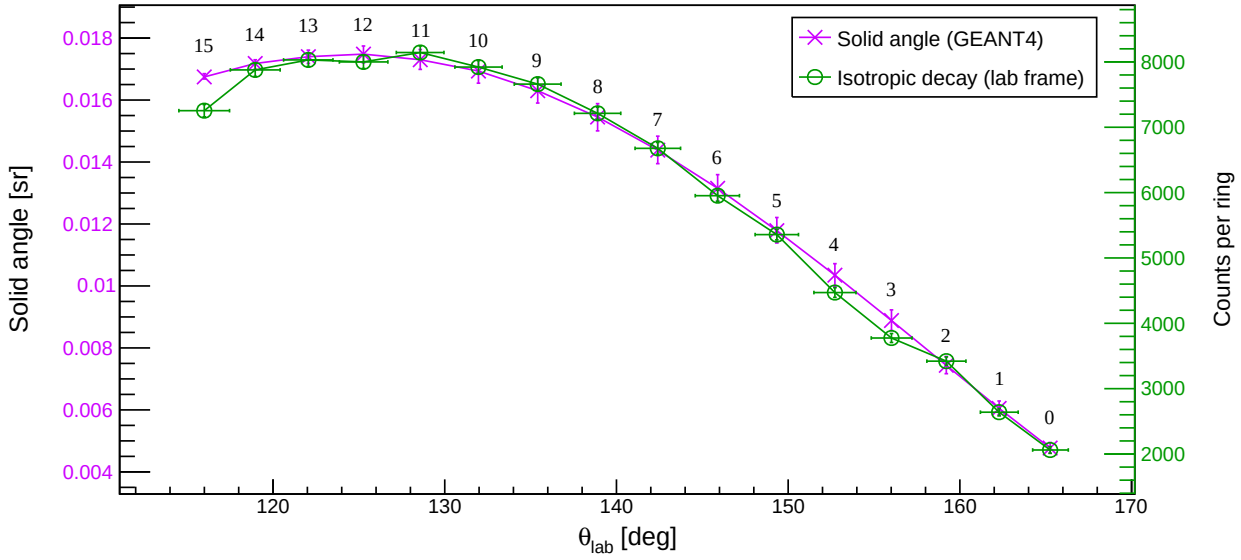

Figure 3.20: The solid angle per ring of the CAKE. The displayed ring numbers correspond to the ring numbers on Figure 3.17. The data for the isotropic decay is from Refs. [87, 88]. The vertical errors for the simulation correspond to a ± 2 mm positional error of the CAKE along the beam axis.

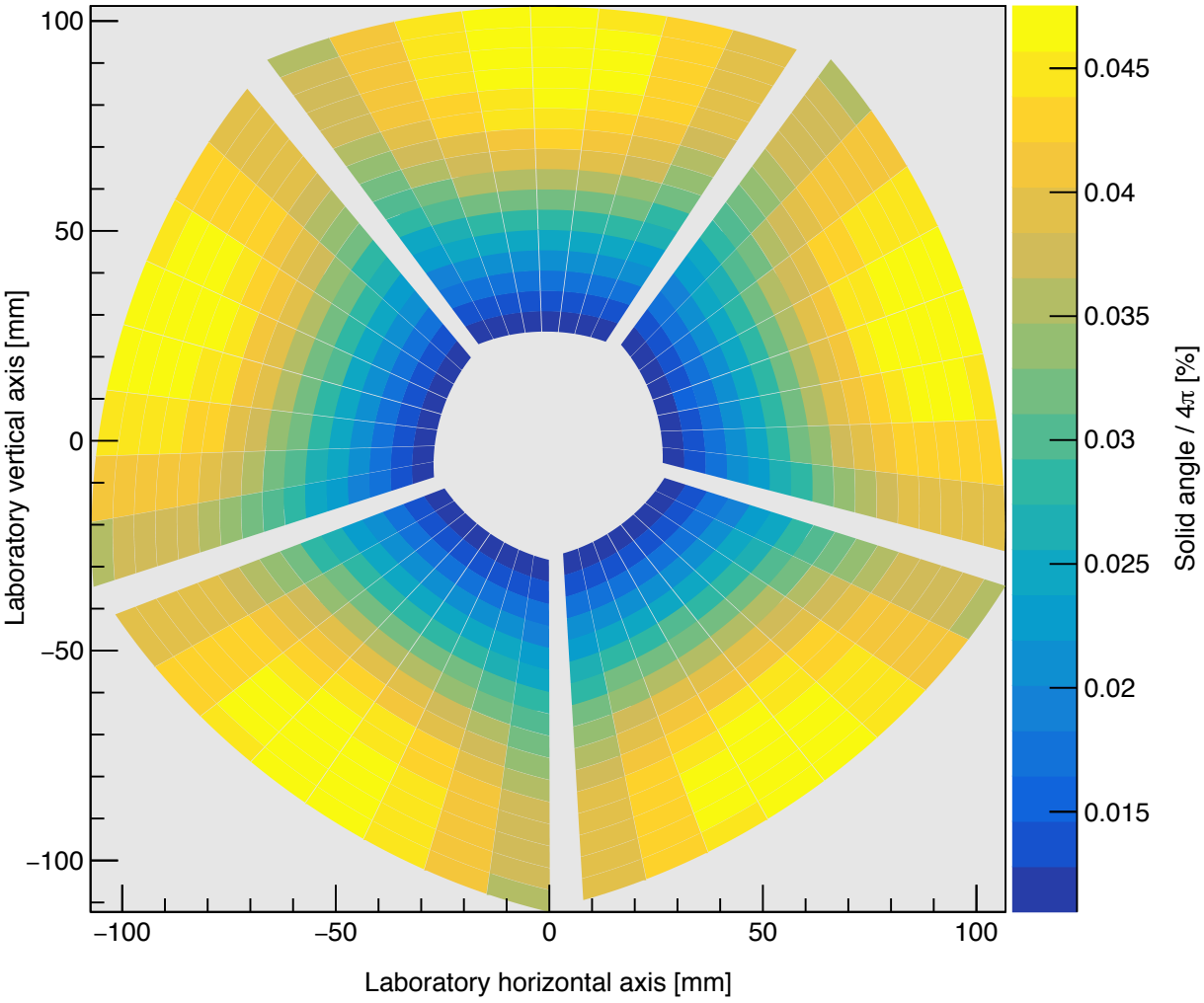

Figure 3.21: The simulated solid angle for each pixel of the CAKE. The CAKE is configured at backward angles and the viewpoint of the spectrum is towards upstream. The active area of each pixel is projected onto the x-y plane with the beam (z) axis coming out of the page.

3.4 Experimental Setup of Experiment PR240, $^{14}\mathrm{C}(p,t)^{12}\mathrm{C}$ at $\theta_{\mathbf{lab}} = 0°$

For the $^{14}\mathrm{C}(p,t)^{12}\mathrm{C}$ reaction with 140 MeV beam energy, the triton ejectile takes approximately 123 MeV - 111 MeV of kinetic energy at $\theta_{\mathrm{lab}} = 0°$ for the $E_x \approx$ 7-16 MeV excitation energy range of interest. The triton ejectiles therefore have a larger rigidity with respect to the unperturbed proton beam particles and the internal beamstop was consequently placed on the beam-left side of the internal vacuum chamber at Dipole 1 (see Figure 3.22). The operating parameters of the K600 magnets are provided in Table 3.2.

A schematic of the focal-plane detector system configuration for experiment PR240 is presented in Figure 3.23. The position of the internal beamstop and the kinematics of the beam necessitated the use of the medium-dispersion focal plane.

Since VDC1 and VDC2 were configured with new and old VDCs, respectively, vertical positional information is only available from VDC1. Given the relatively high stopping power of the tritons from the reaction of interest (at 140 MeV), the tritons do not consistently penetrate a second paddle. Consequently, only a single paddle was used to trigger a K600 event as opposed to a coincidence trigger of two paddles which could bias the analysis.

Figure 3.24 presents the self-supporting ^{14}C target which had an enrichment of approximately 87% ^{14}C and 13% ^{12}C. The tears in the target, which were created through the mounting process, did not affect the measurement. In addition to the ^{14}C target of interest, a viewer, an empty frame and a ^{13}C target were installed which were used for viewing the beamspot and systematic experimental background effects, respectively. Figure 3.25 presents the target ladder and the CAKE (configured at backward angles) installed in the scattering chamber.

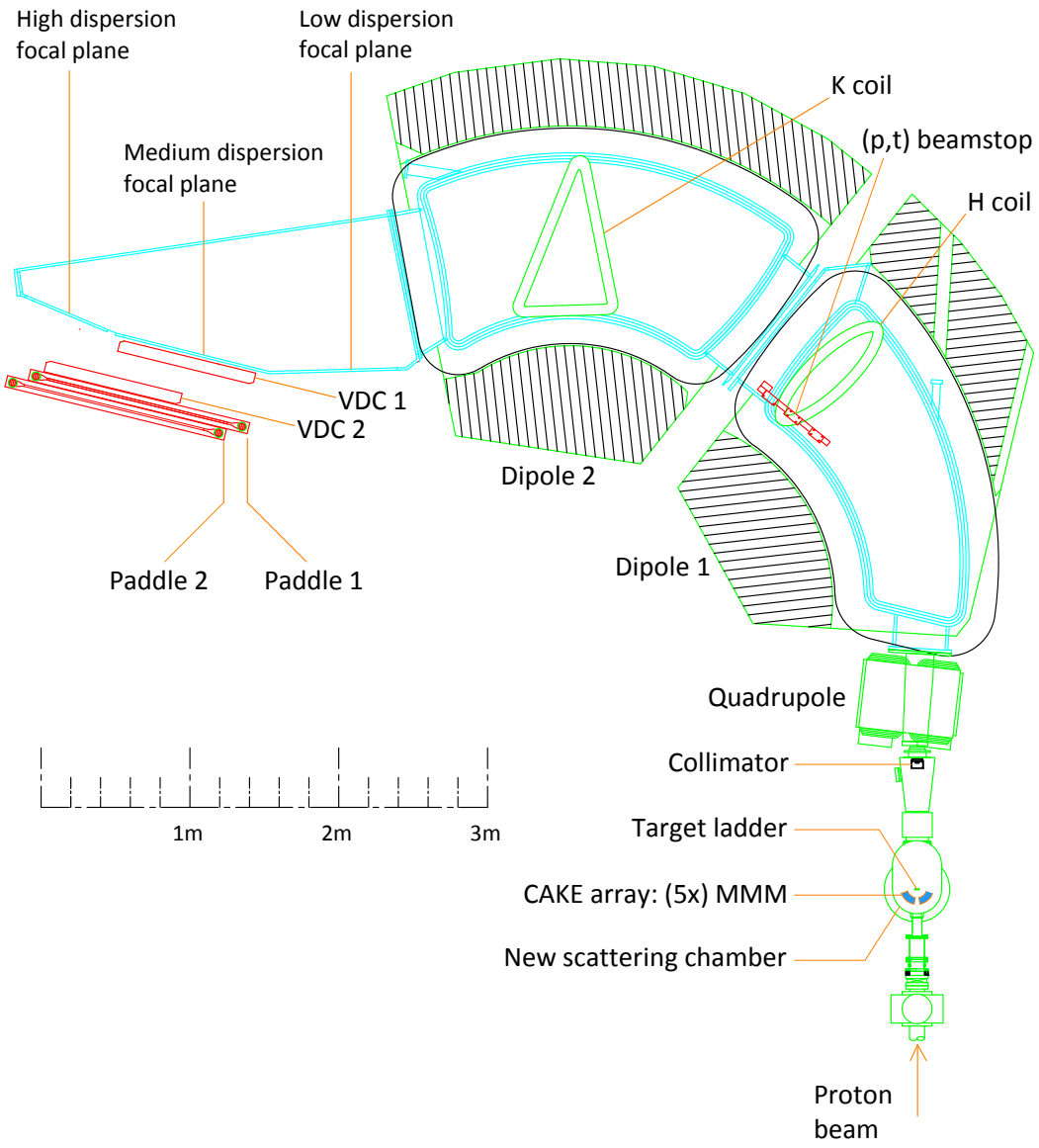

Figure 3.22: Schematic top view of the global K600 spectrometer configuration for experiment PR240.

Magnet	Current [A] (weekend 1)	Current [A] (weekend 2)
Quadrupole	−526.990	−535.869
D1 dipole	426.810	434.000
H-coil	−19.768	−20.101
D2 dipole	424.264	431.412
K-coil	5.931	6.030

Table 3.2: The operating parameters of the K600 spectrometer for experiment PR240 at $\theta_{\text{lab}} = 0°$. The currents are the reference values to which the magnets were set during the experiment.

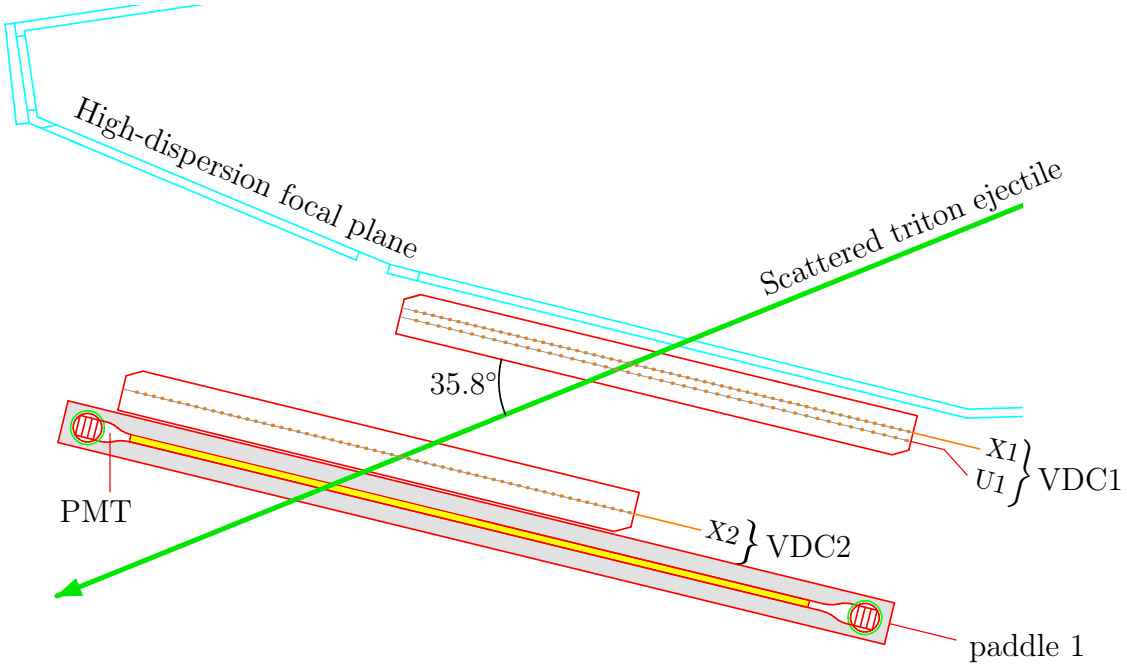

Figure 3.23: Schematic top view of the new focal-plane detector system in medium-dispersion focus mode for experiment PR240. VDC1 and VDC2 were configured with new and old VDCs, respectively. Paddle 1 was chosen to be 1/4" thick.

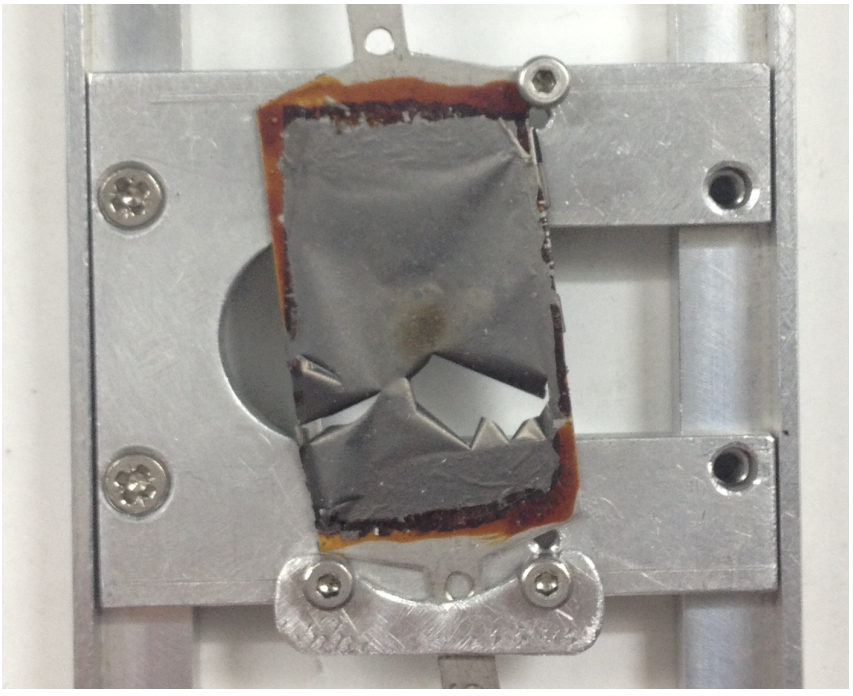

Figure 3.24: The self-supporting ^{14}C target for experiment PR240. The enrichment was approximately 87% ^{14}C and 13% ^{12}C.

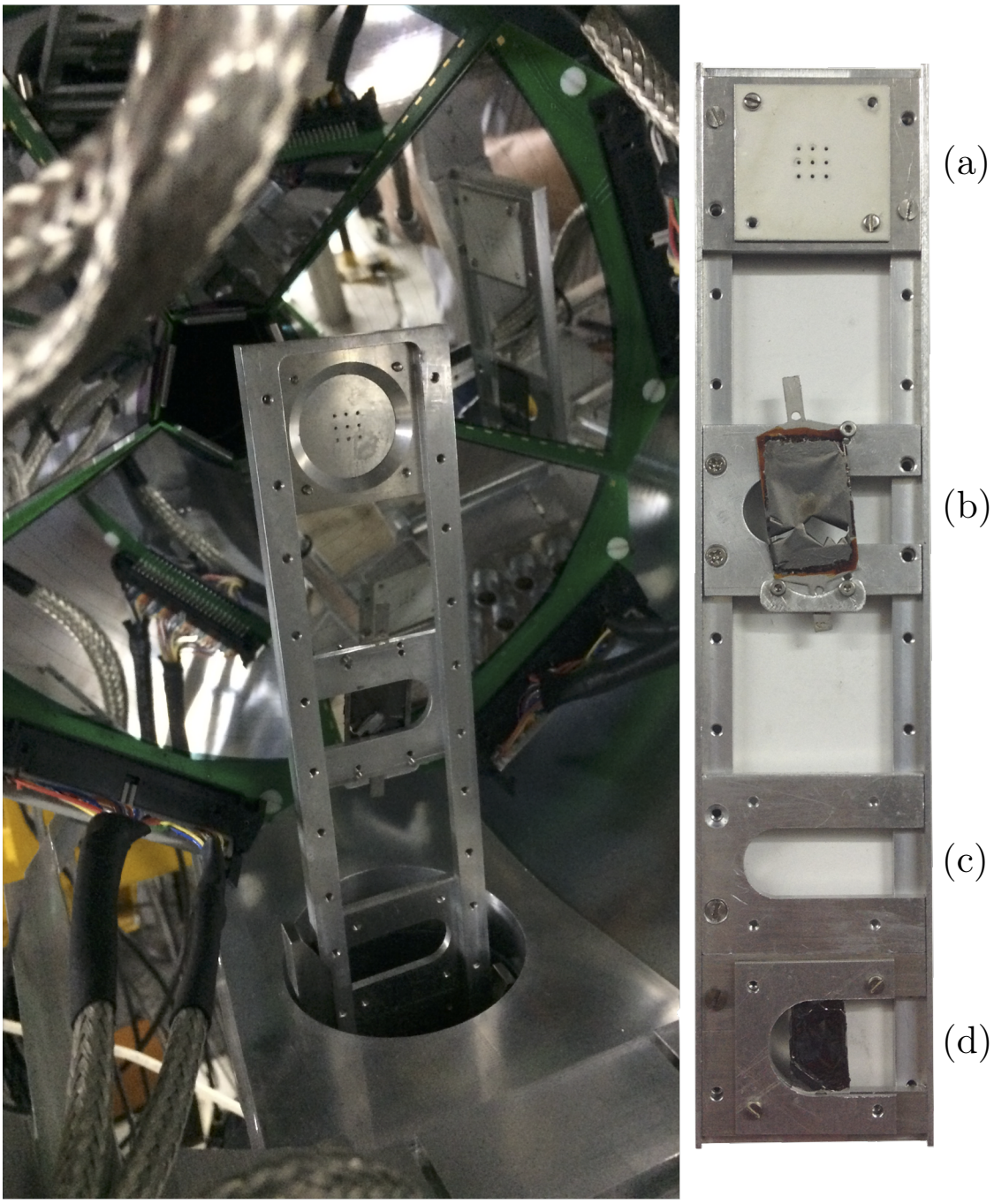

Figure 3.25: Images of the installed target ladder and CAKE setup within the scattering chamber employed for experiment PR240. The target ladder is shown with the (a) viewer, (b) ^{14}C target, (c) empty frame and (d) ^{13}C target.

3.5 Experimental Setup of Experiment PR166, $^{12}C(\alpha,\alpha')^{12}C$ at $\theta_{lab} = 6°, 8.5°$ and $10°$

The data analysed from experiment PR166 corresponds to the measurement of the $^{12}C(\alpha,\alpha')^{12}C$ reaction at $\theta_{lab} = 6°, 8.5° and 10°$ with a beam energy of 196 MeV. The spectrometer and detector configuration for experiment PR166, $^{12}C(\alpha,\alpha')^{12}C$ at $\theta_{lab} = 6°$ is presented in Figure 3.26. The only difference in experimental setup with respect to the measurements at $\theta_{lab} = 8.5° and 10°$ was the spectrometer angle. The target information for experiment PR166 is presented in Table 3.1. The summary of the K600 operating parameters for $^{12}C(\alpha,\alpha')^{12}C$ measurements at $\theta_{lab} = 6°, 8.5°$ and $10°$ are respectively presented in Tables 3.3.

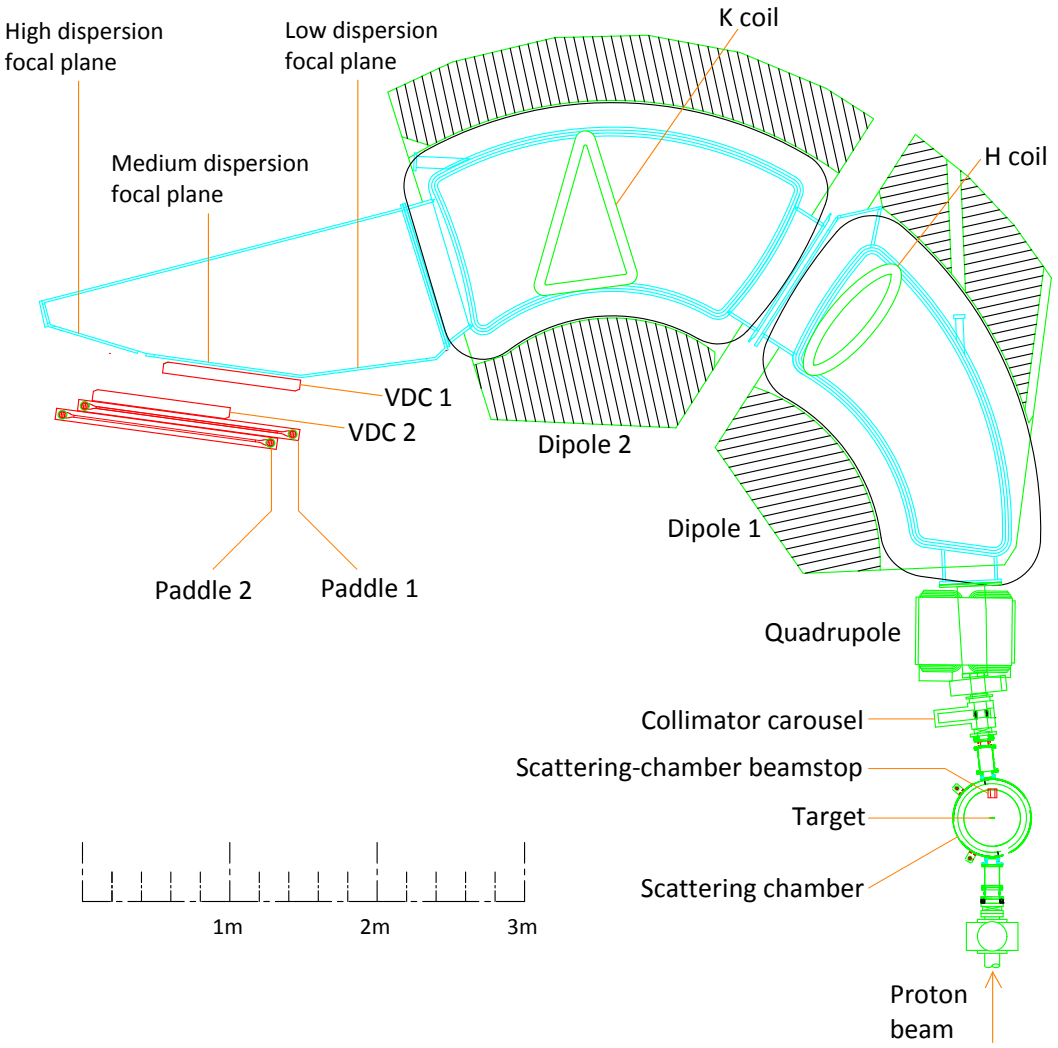

Figure 3.26: Schematic top view of the global K600 spectrometer configuration for experiment PR166, $^{12}C(\alpha,\alpha')^{12}C$ at $\theta_{lab} = 6°$.

A schematic of the focal-plane detector system configuration for experiment PR166 is presented in Figure 3.27. Since VDC1 and VDC2 were respectively configured with X and UX VDCs, vertical positional information is only available from VDC2. As explained in Section 3.11, the UX configuration for a VDC corresponds to the U wireplane being configured upstream of the X wireplane (by rotating the VDC by 180°) in order to maximise the acceptance on the low E_x (high-momentum) side of the VDC.

Angle [deg]	Magnet	Current [A]
6	Quadrupole	−453.604
	D1 dipole	366.920
	H-coil	−84.750
	D2 dipole	364.913
	K-coil	−11.967
8.5	Quadrupole	−443.690
	D1 dipole	366.000
	H-coil	−62.257
	D2 dipole	363.962
	K-coil	−34.000
10	Quadrupole	−443.690
	D1 dipole	366.000
	H-coil	−83.00
	D2 dipole	363.962
	K-coil	−42.000

Table 3.3: The operating parameters of the K600 spectrometer for experiment PR166, ^{12}C(α,α')^{12}C at $\theta_{\text{lab}} = 6°, 8.5°$ and 10°. The currents are the reference values to which the magnets were set during the experiment.

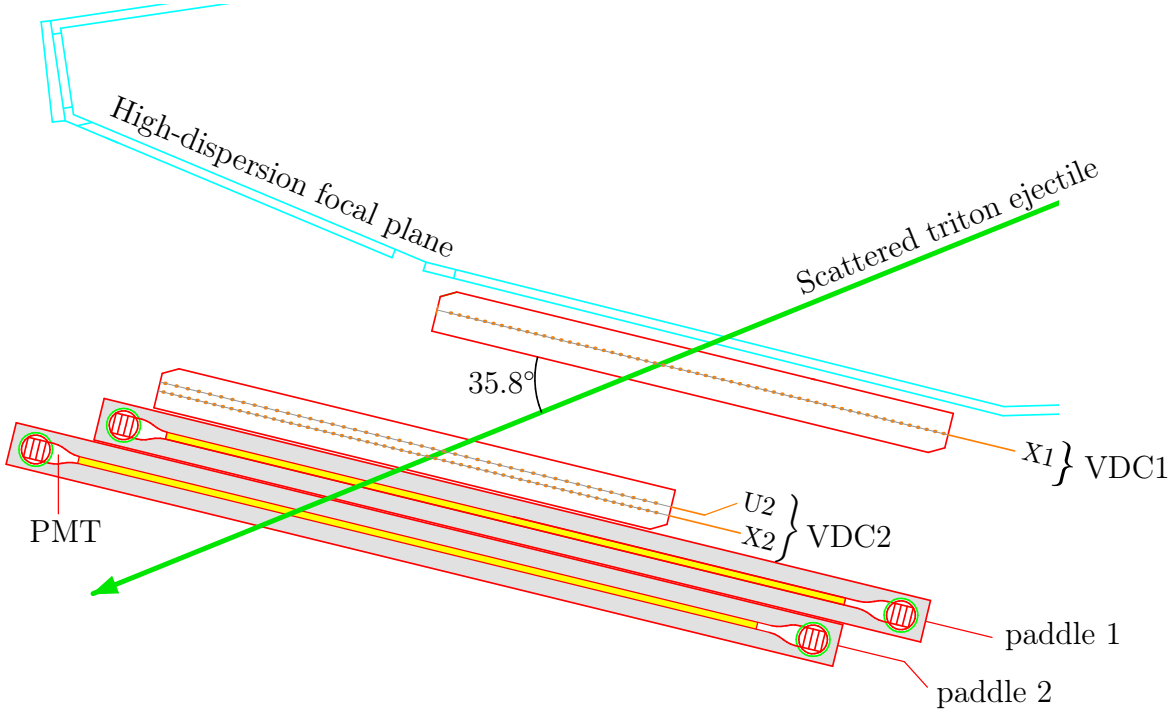

Figure 3.27: Schematic top view of the new focal-plane detector system in medium-dispersion focus mode for experiment PR166. VDC1 and VDC2 were configured with new and old VDCs, respectively. VDC2 was rotated from it's usual configuration by 180° such that U2 wire plane was upstream of the X2 wire plane. Paddles 1 and 2 were both chosen to be 1/4" thick.

3.6 Experimental Setup of Experiment PR194, $^{12}C(\alpha,\alpha')^{12}C$ at 0.0° (160) MeV

The spectrometer and detector configuration for experiment PR194 is presented in Figure 3.28. The summary of the employed targets for experiment PR194 is presented in Table 3.1. The summary of the K600 operating parameters for PR194 is presented in Table 3.4.
A schematic of the focal-plane detector system configuration for experiment PR194 is presented in Figure 3.29. The $\theta_{lab} = 0°$ measurement angle of the K600 spectrometer necessitated the use of the $\theta_{lab} = 0°$ beam dump. VDC1 and VDC2 were both configured with XU VDCs, therefore vertical positional information is available from both VDCs. Since the observed backgrounds for (α,α') measurements at $\theta_{lab} = 0°$ are non negligible, the vertical positional information is crucial for reliable background subtraction. paddles 1 and 2 were chosen to be $^1/_4$" and $^1/_2$" thick, respectively.

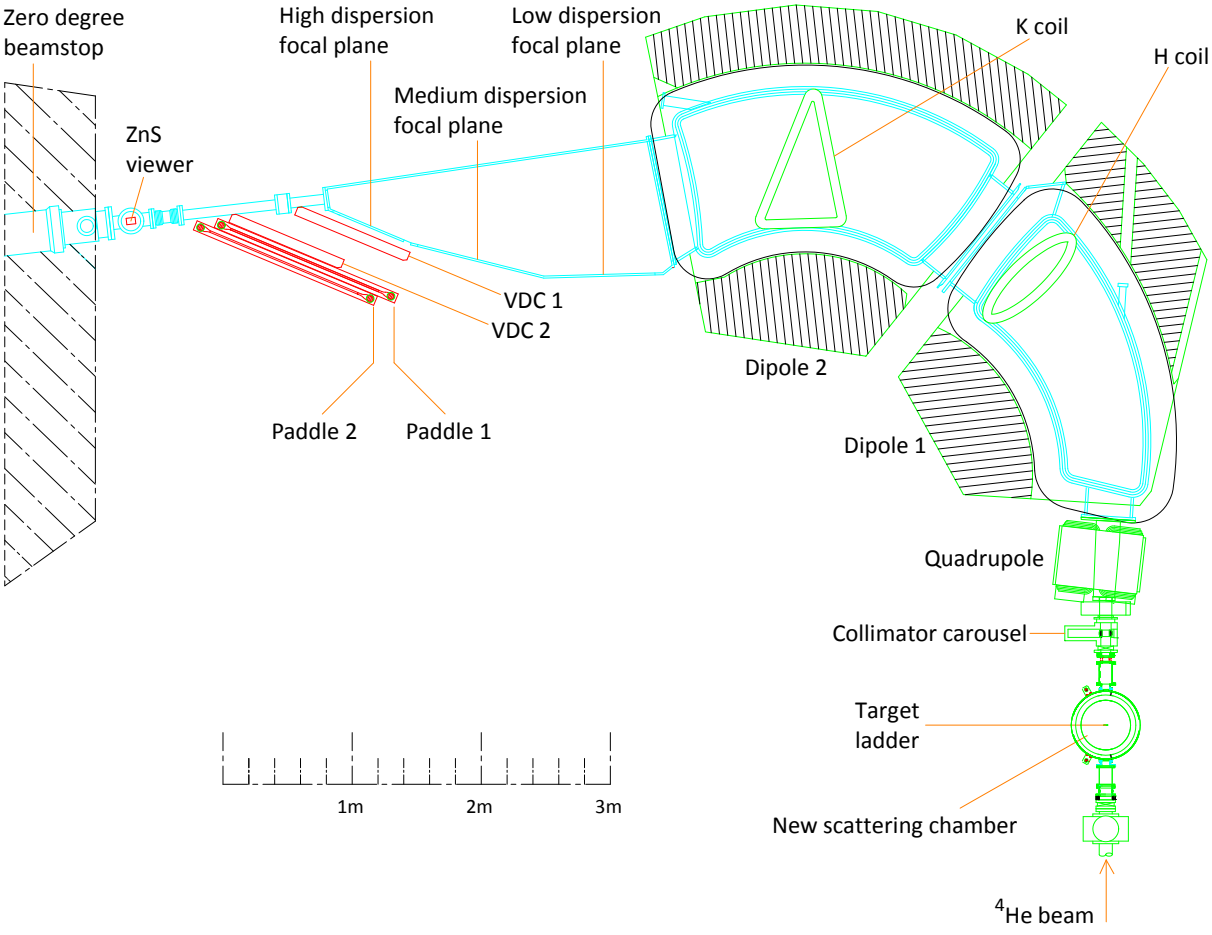

Figure 3.28: Schematic top view of the global K600 spectrometer configuration for experiment PR194.

Magnet	Current [A]
Quadrupole	−403.742
D1 dipole	366.800
H-coil	−40.756
D2 dipole	242.737
K-coil	−19.827

Table 3.4: The operating parameters of the K600 spectrometer for experiment PR194 at $\theta_{\text{lab}} = 0°$. The currents are the reference values to which the magnets were set during the experiment.

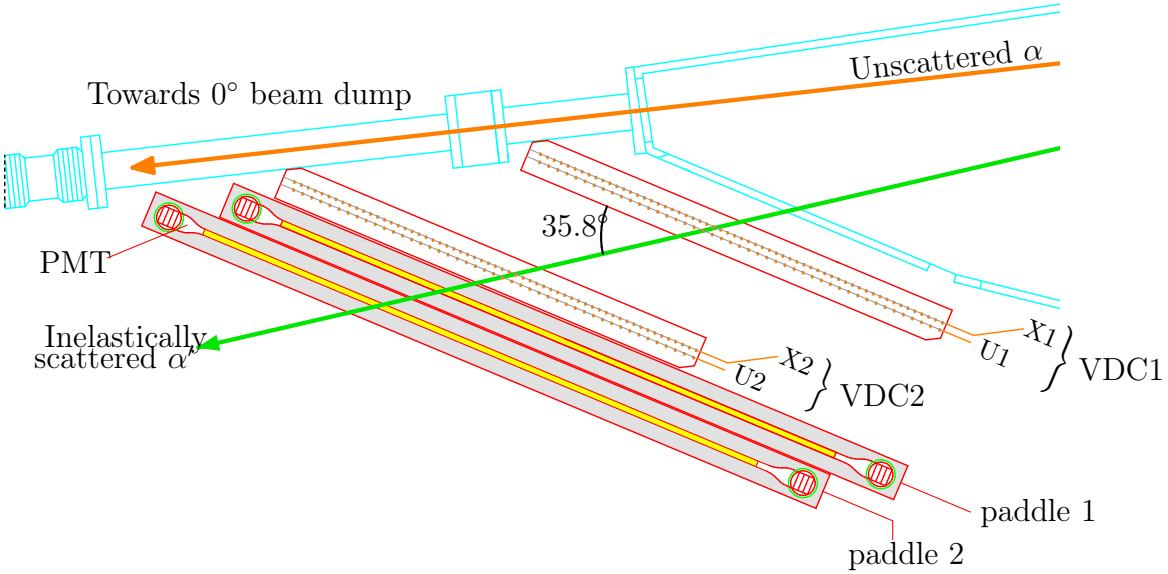

Figure 3.29: Schematic top view of the new focal-plane detector system in high-dispersion focus mode for experiment PR194. VDC1 and VDC2 were both configured with XU VDCs. Paddles 1 and 2 were chosen to be 1/4" and 1/2" thick, respectively.

3.7 Experimental Setup of Experiment PR195, $^{14}\mathrm{C}(p,t)^{12}\mathrm{C}$ at $\theta_{\mathbf{lab}} = 21^{\circ}$

The spectrometer and detector configuration for experiment PR195 is presented in Figure 3.30. The summary of the employed targets for experiment PR195 is presented in Table 3.1. The summary of the K600 operating parameters for PR195 is presented in Table 3.6.

A schematic of the focal-plane detector system configuration for experiment PR195 is presented in Figure 3.31. Since VDC1 and VDC2 were both configured with old VDCs, there is no vertical positional information available from either VDC. Whilst vertical positional information can be useful for background subtraction, the measurement of the $^{14}\mathrm{C}(p,t)^{12}\mathrm{C}$ reaction at a relatively large angle of 21° mitigates this shortfall as the measured background is typically negligible. paddles 1 was chosen to be $^{1}/_{4}$" thick.

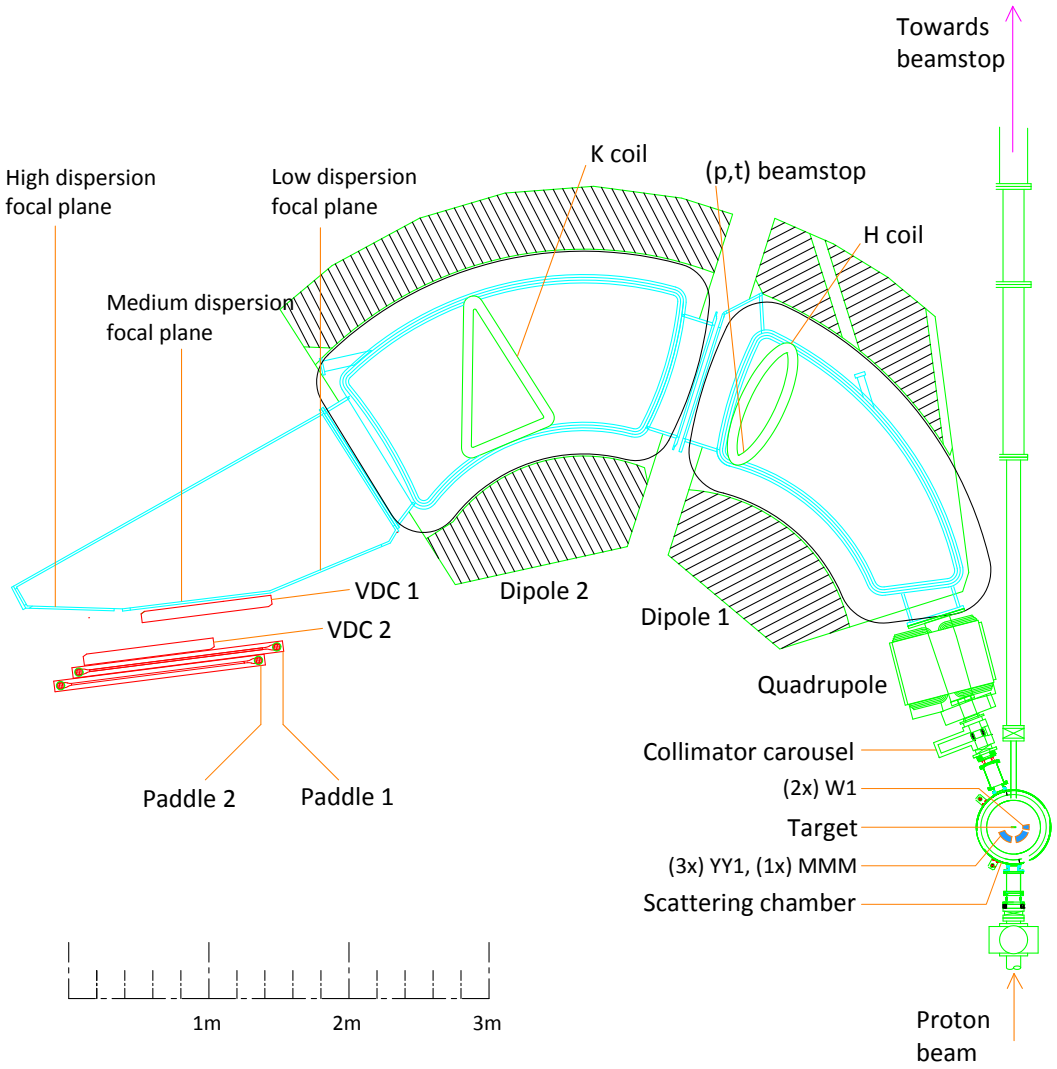

Figure 3.30: Schematic top view of the global K600 spectrometer configuration for experiment PR195.

Magnet	Current [A]
Quadrupole	−401.398
D1 dipole	324.450
H-coil	−66.602
D2 dipole	323.673
K-coil	−5.920

Table 3.5: The operating parameters of the K600 spectrometer for experiment PR195 at $\theta_{\text{lab}} = 21°$. The currents are the reference values to which the magnets were set during the experiment.

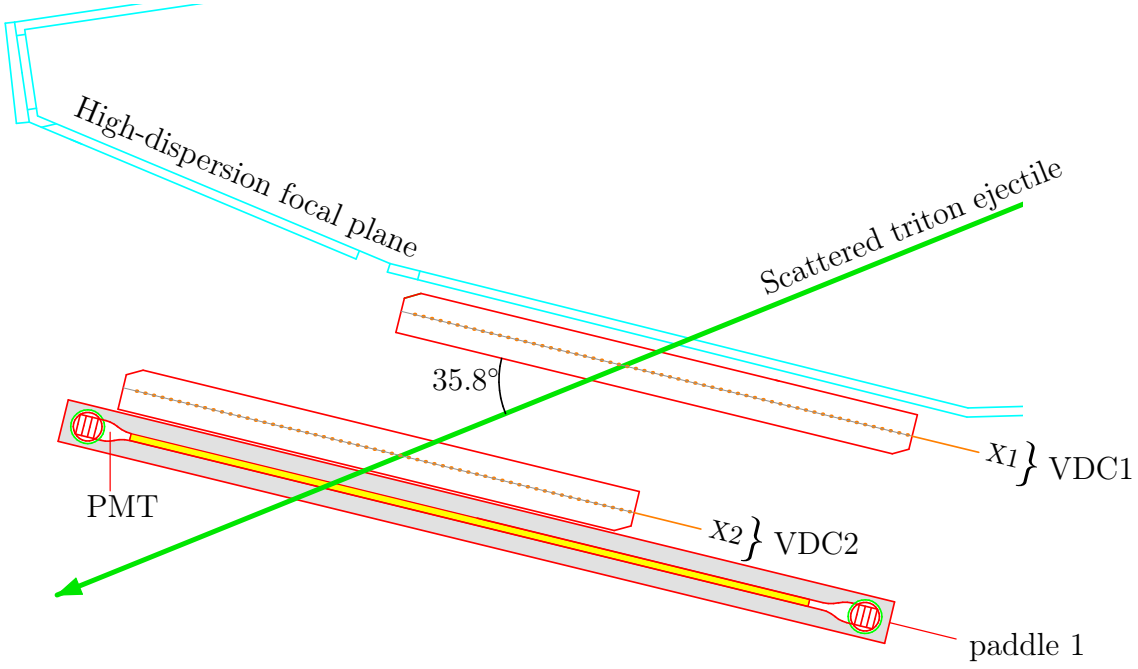

Figure 3.31: Schematic top view of the new focal-plane detector system in medium-dispersion focus mode for experiment PR195. VDC1 and VDC2 were both configured with old VDCs. Paddle 1 was chosen to be 1/4" thick.

3.8 Experimental Setup of Experiment PR251, $^{12}C(\alpha,\alpha')^{12}C$ at 0.0° (118) MeV

The spectrometer and detector configuration for experiment PR251 is presented in Figure 3.32. The summary of the employed targets for experiment PR251 is presented in Table 3.1. The summary of the K600 operating parameters for PR251 is presented in Table 3.6.

A schematic of the focal-plane detector system configuration for experiment PR194 is presented in Figure 3.33. The $\theta_{lab} = 0°$ measurement angle of the K600 spectrometer necessitated the use of the $\theta_{lab} = 0°$ beam dump. Only a single new VDC was employed in the position of VDC1. Since the observed backgrounds for (α,α') measurements at $\theta_{lab} = 0°$ are non negligible, the vertical positional information from the new VDC is crucial for reliable background subtraction. paddle 1 was chosen to be $^1/_4$" thick.

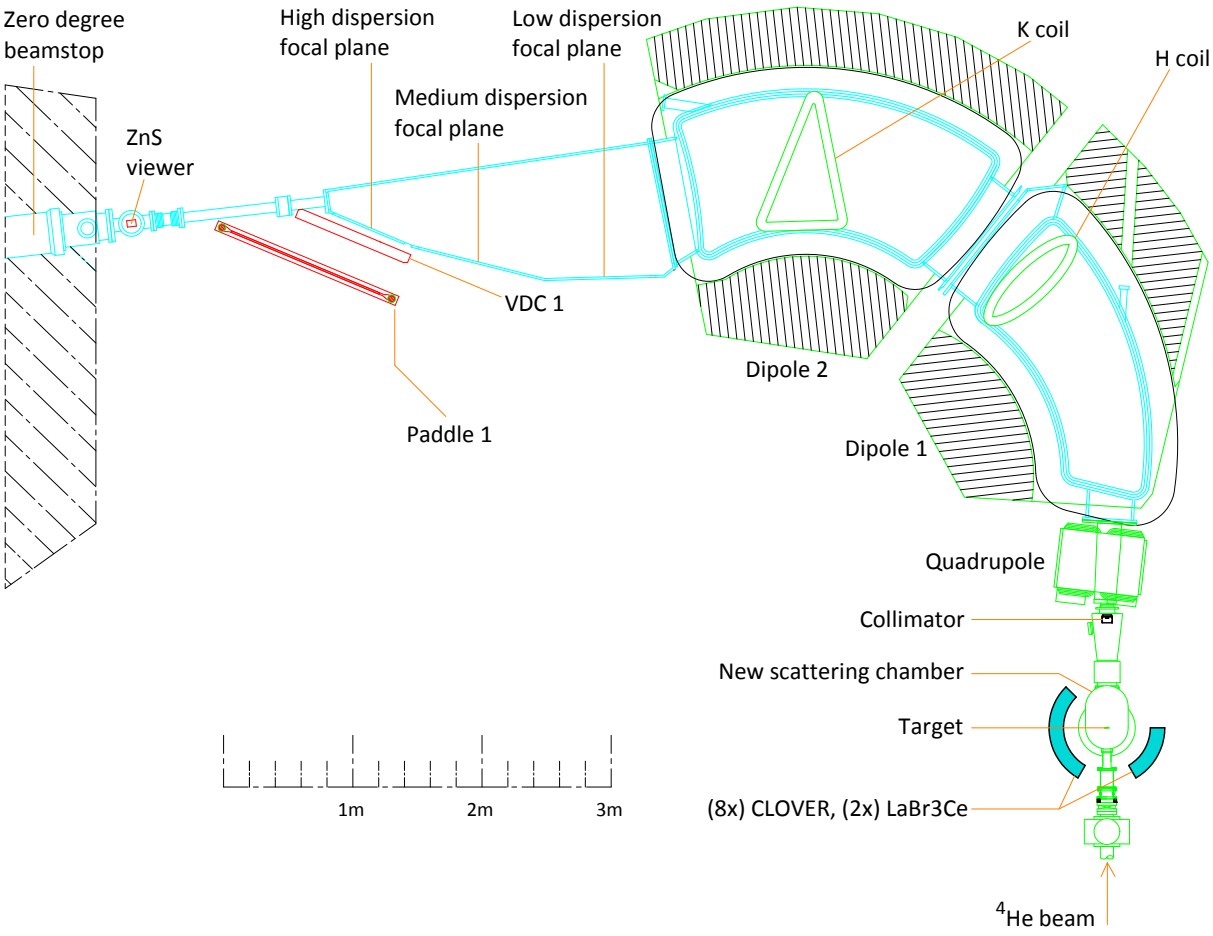

Figure 3.32: Schematic top view of the global K600 spectrometer configuration for experiment PR251.

Magnet	Current [A]
Quadrupole	−349.697
D1 dipole	317.000
H-coil	0.032
D2 dipole	210.282
K-coil	18.218

Table 3.6: The operating parameters of the K600 spectrometer for experiment PR251 at $\theta_{\text{lab}} = 0°$. The currents are the reference values to which the magnets were set during the experiment.

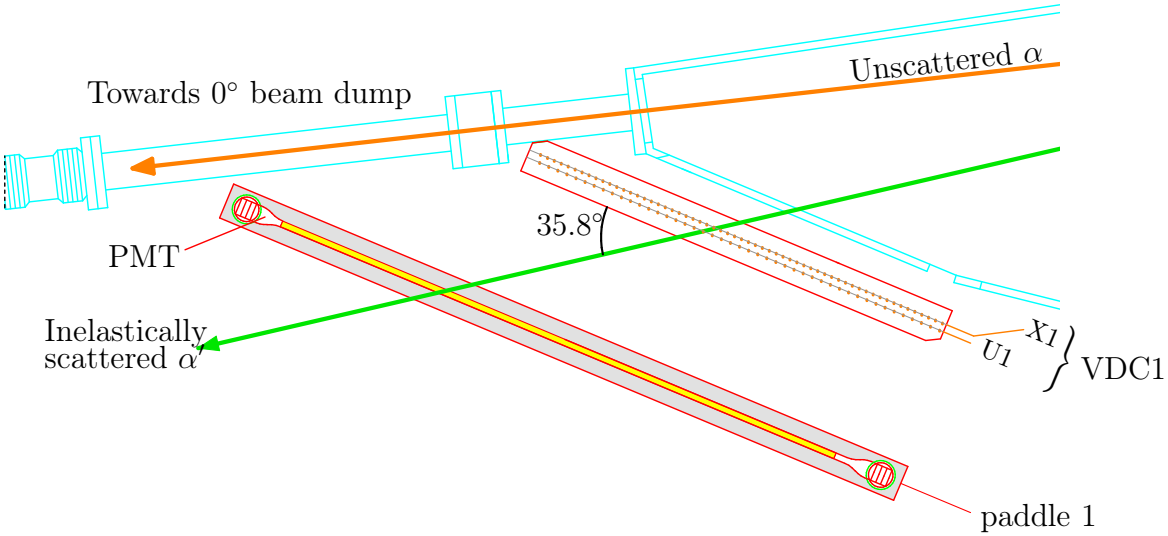

Figure 3.33: Schematic top view of the new focal-plane detector system in high-dispersion focus mode for experiment PR251. VDC1 was configured with an XU VDC. Paddle 1 was chosen to be 1/4" thick.

Chapter 4

Data Analysis

The sole experiment which was expressly performed for the arguments of this thesis is experiment PR240: a $^{14}\mathrm{C}(p,t)^{12}\mathrm{C}$ measurement at $\theta_{\mathrm{lab}} = 0^{\circ}$ with an incident beam energy of $E_{\mathrm{beam}} = 140$ MeV. In this chapter, the general analysis procedures and techniques are presented for experiment PR240. The analyses of all the ancillary experiments are largely analogous and therefore only the final results (excepting notable analysis differences) are presented in Sections 4.4 - 4.8. Detailed analyses of the lineshape corrections for these ancillary experiments are presented in Appendix B. A summary of the different reactions associated with different experiments is presented in Table 4.1.

It is of particular interest to compare the α inelastic-scattering measurements at $\theta_{\mathrm{lab}} = 0^{\circ}$ (PR194, PR251) with the results of PR240 as the population of collective/giant resonances with the $^{14}\mathrm{C}(p,t)^{12}\mathrm{C}$ reaction is purported to be suppressed with respect to the $^{12}\mathrm{C}(\alpha,\alpha')^{12}\mathrm{C}$ reaction [12]. Since $^{12}\mathrm{C}(\alpha,\alpha')^{12}\mathrm{C}$ measurements at $\theta_{\mathrm{lab}} = 0^{\circ}$ are of a similar incident beam energy with respect to PR240, the differences in the spectra should be primarily dependent on this relative suppression of collectivity.

The $^{12}\mathrm{C}(\alpha,\alpha')^{12}\mathrm{C}$ measurements at $\theta_{\mathrm{lab}} = 6^{\circ}$, 8.5° and 10° (PR166) are highly complimentary as resonances with different (natural) spin-parities are populated with varied relative strengths. This may facilitate the discrimination of unresolved resonances with different spins - a particularly helpful tool in resolving the intrinsically broad and overlapping nuclear structure of $^{12}\mathrm{C}$ in $E_x \approx 8$-12 MeV excitation-energy region.

The reanalysis of another $^{14}\mathrm{C}(p,t)^{12}\mathrm{C}$ dataset, experiment PR195, provides a valuable comparison to the data from experiment PR240. Since the single-step two-neutron transfer mechanism can be assumed to be equivalent, the relative differences in the spectra should therefore depend purely on the different measurement angle and incident beam energy for experiment PR195 of 21° and 67.5 MeV, respectively.

PAC Code	Reaction	Beam energy [MeV]	Angle [deg]	E_x range‡ [MeV]
PR166	$^{12}C(\alpha,\alpha')^{12}C$	196	6	6.5 - 27.3
			8.5	7.3 - 29.5
			10	7.2 - 28.6
PR194	$^{12}C(\alpha,\alpha')^{12}C$	160	0	7.3 - 20.7
PR251	$^{12}C(\alpha,\alpha')^{12}C$	118	0	5.0 - 25.0
PR195	$^{14}C(p,t)^{12}C$	67.5	21	7.5 - 14.5
PR240†	$^{14}C(p,t)^{12}C$	140	0	4.3 - 17.6

Table 4.1: General summary of the separate data analyses. †The sole experiment which was expressly performed for the arguments of this thesis. ‡The E_x range is determined by both the momentum range accepted by the K600 spectrometer and the range of positions subtended by the focal-plane detector system.

4.1 Generalised K600 Analysis Procedure

A diagram of the general analysis procedure for all the analysed experiments is shown in Figure 4.1 and each of the processes are discussed below. The CAKE analysis procedures (highlighted in green) are exclusively relevant for experiment PR240.

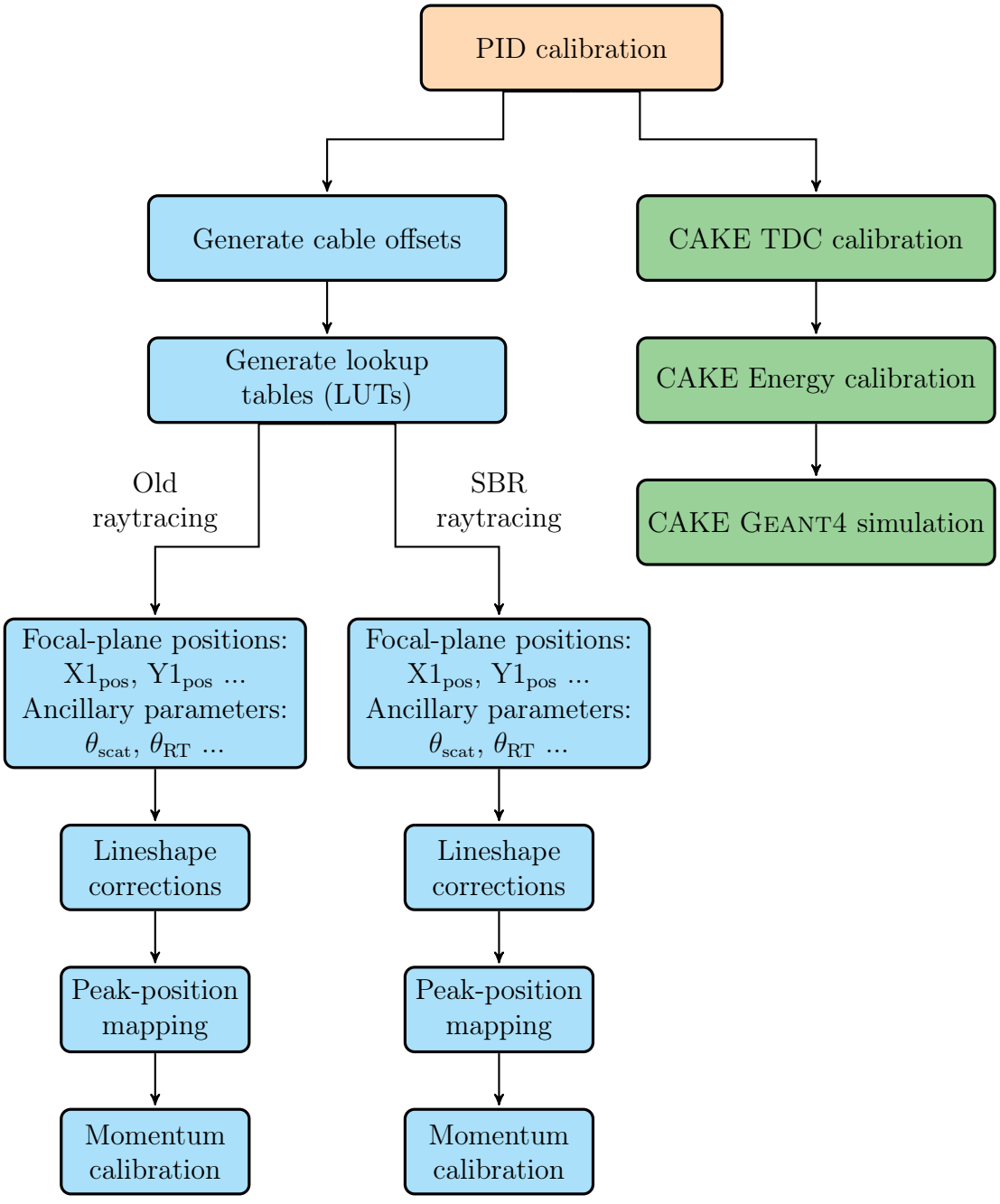

Figure 4.1: The general analysis procedure. The nodes filled in orange, blue and green correspond to data from the paddles, VDCs and CAKE array, respectively. The CAKE analysis procedures are exclusively relevant for experiment PR240.

4.1.1 PID Calibration

The generation of a focal-plane event is triggered by energy deposition within the paddle detectors from impinging particles (see Section 3.2.1). These particles can originate from a myriad of interactions within the target or even target-unrelated sources (e.g. radioactive beamstops and scattering of the beam upstream of the target). To selectively observe the reaction of interest, a gate is placed on the distinguishing characteristics of the corresponding ejectile. By plotting the integrated charge from the PMTs of the paddle(s) against the TOF of the ejectile, the unique locus that corresponds to the reaction of interest.

The first analysis procedure is to calibrate the particle-identification (PID) spectrum to enable an accurate selection of the ejectiles which correspond to the reaction of interest can be identified. The calibration of the detected energy depositions in the paddles for each experimental run is necessary to mitigate the drift of the associated PMTs (see Section 3.2.1). The TOF, measured as the time difference between the paddle trigger and the next RF signal, can undergo slow variations over time as the SSC magnetic fields drift and the beam operators compensate by changing the RF phase. The offsets needed to align both the signal generated by paddles (pad1) and the TOF values are typically determined by measuring the position of the locus of interest for each experimental run (although a different well-defined locus can also be used).

For the $^{14}\mathrm{C}(p,t)^{12}\mathrm{C}$ at $\theta_{\mathrm{lab}} = 0°$ (PR240), the PID spectrum without PID offset corrections is presented in Figure 4.2. It appears that the locus is doubled with a shift in TOF of approximately 20 ns. This shift is corrected in the calibrated PID spectrum presented in Figure 4.3 which shows a locus of interest with a reduced dispersion, thereby enabling a PID gate with an improved signal-to-background ratio.

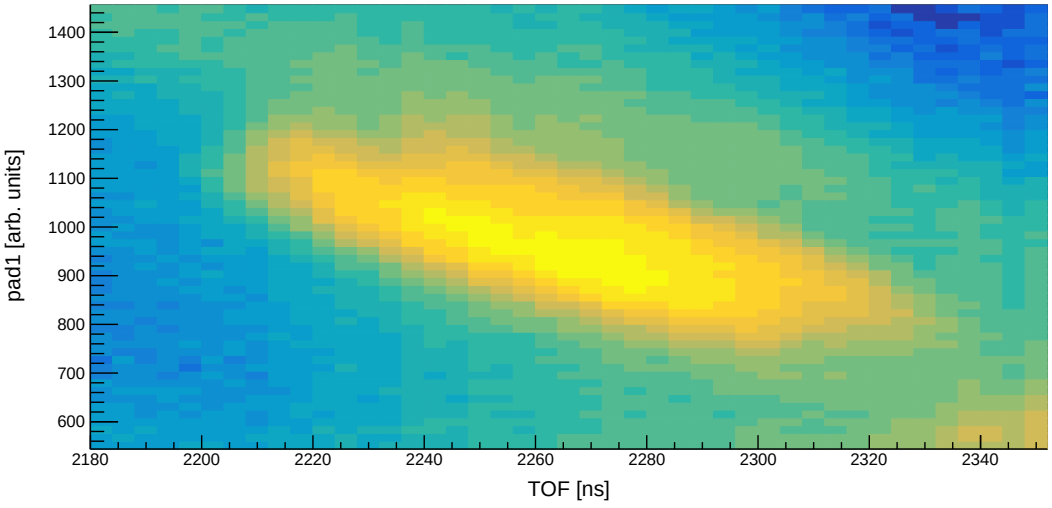

Figure 4.2: PID spectrum for experiment PR240 without PID calibration. The dispersion of the locus is larger with respect to the calibrated PID spectrum in Figure 4.3. Brighter colours inidicate higher counts.

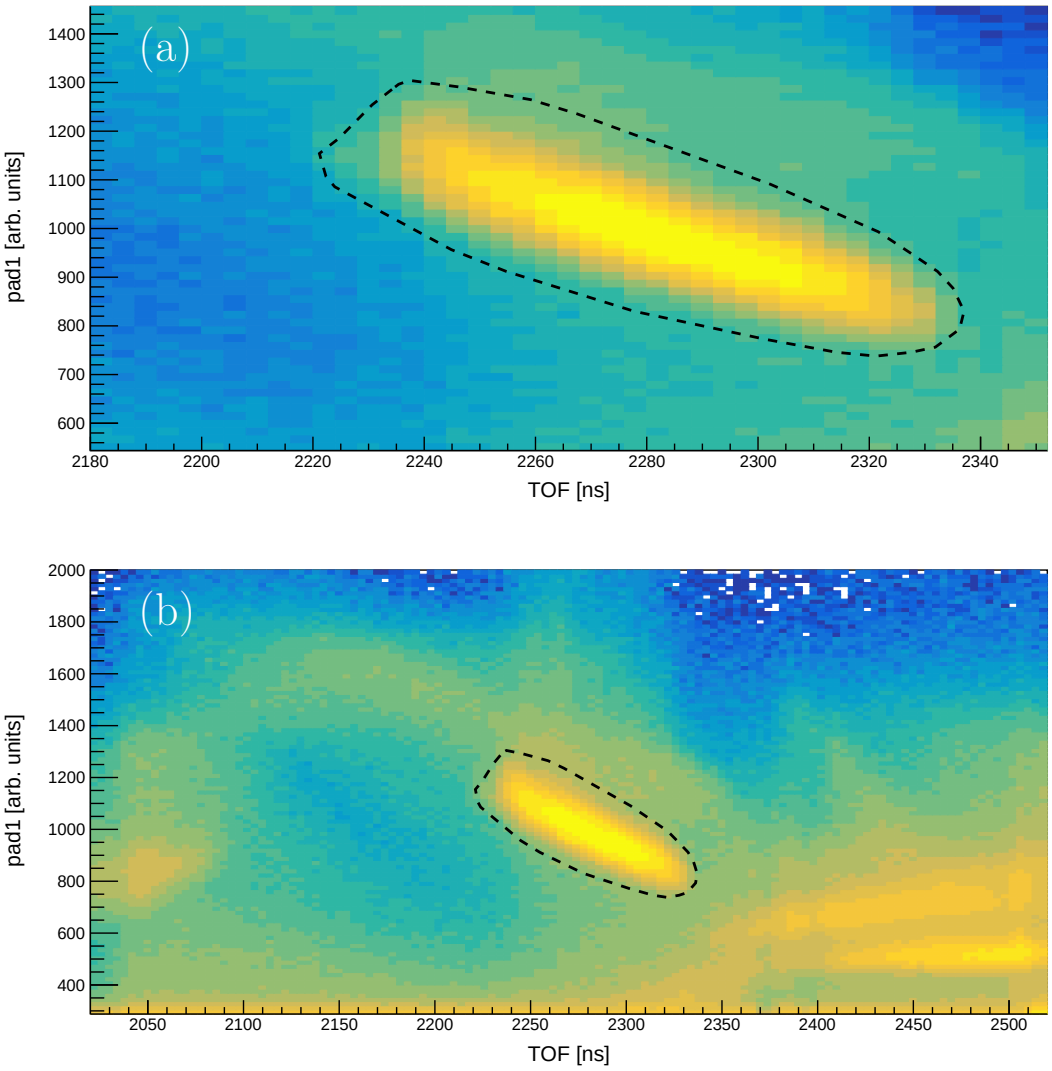

Figure 4.3: PID spectrum for experiment PR240 with PID calibration. Panel (a) is zoomed in on the locus of interest to highlight the reduced dispersion with respect to the uncalibrated PID spectrum in Figure 4.2 and panel (b) shows the full PID spectrum. The dashed line represents the PID gate for the ejectiles corresponding to the $^{14}\mathrm{C}(p,t)^{12}\mathrm{C}$ reaction of interest. Brighter colours inidicate higher counts.

4.1.2 Generate Cable Offsets

The timing of the signals from each wire of a VDC is what ultimately provides the positional information of traversing particles. After a wire is triggered, there is an inevitable delay between the generation of the electrical signal and the reception of this signal by the TDC. In principle, this physical delay is different for each wire and can result from a myriad of possibilities such as different responses between the channels of the VDC preamplifiers and/or TDC modules of the DAQ. In general, the relative differences in the delays are dominated by the differences in the physical cable lengths between the preamplifiers and the TDC modules.

In order to generate a global lookup table (see Section 4.1.3) to map drift time to drift distance, the relative delays between each channel must be corrected. In practice, the wires are calibrated by aligning the trailing edge of their respective drift time distributions.

In the past, a script named "AutoTrim" [82] was used to determine the offsets for each TDC channel. A shortcoming of this basic script is that it does not account for qualitative differences in the trailing edges of the time distributions. An improved algorithm was implemented to more accurately determine these values which iterates a linear fit (where the length of the range was fixed) across the spectrum and the fit with the steepest gradient is used to determine the x-intercept for alignment, as displayed on Figure 4.4.

Figures 4.5 and 4.6 display the spectra of TDC channels versus uncorrected and corrected TDC times, respectively. It is observed that the staggering of the drift time distributions in Figure 4.5 has been removed through the calibration of the TDC times. The fragmented groupings of channels is predominantly due to the custom channel mappings for each VDC (which may also vary between experiments). Whilst there are some missing channels, the raytracing algorithms described in Section 4.1.4 are typically able to mitigate any associated efficiency losses.

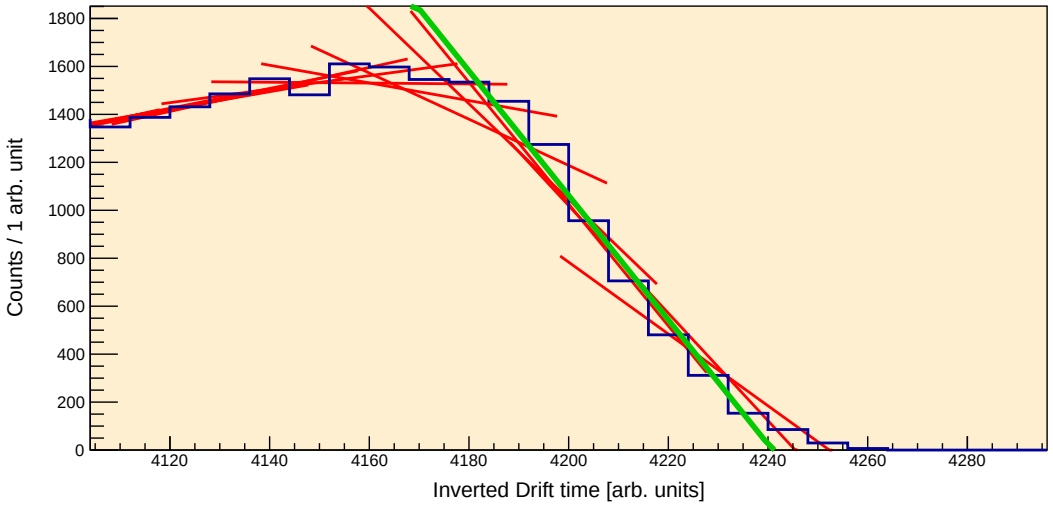

Figure 4.4: The spectrum of uncalibrated drift times of a TDC channel, illustrating the new cable offsets algorithm. The red lines are the suboptimal fits and the green line is the optimal solution with the steepest gradient.

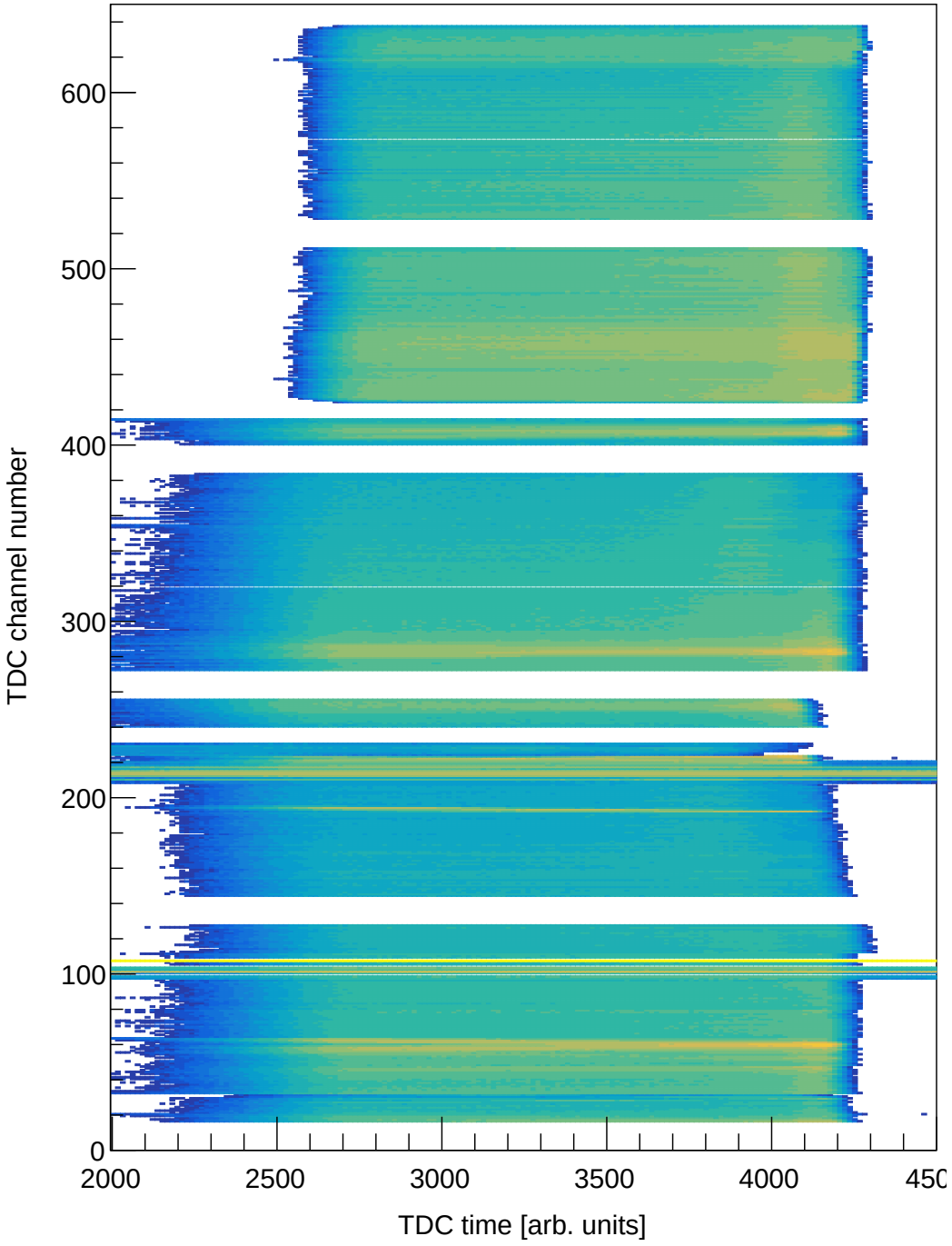

Figure 4.5: Spectrum of TDC channel number versus TDC uncalibrated reference time of the VDC wires for experiment PR240. The lack of TDC alignment produces a staggering between the TDC drift time distributions of the various channels. A display threshold of >50 has been imposed.

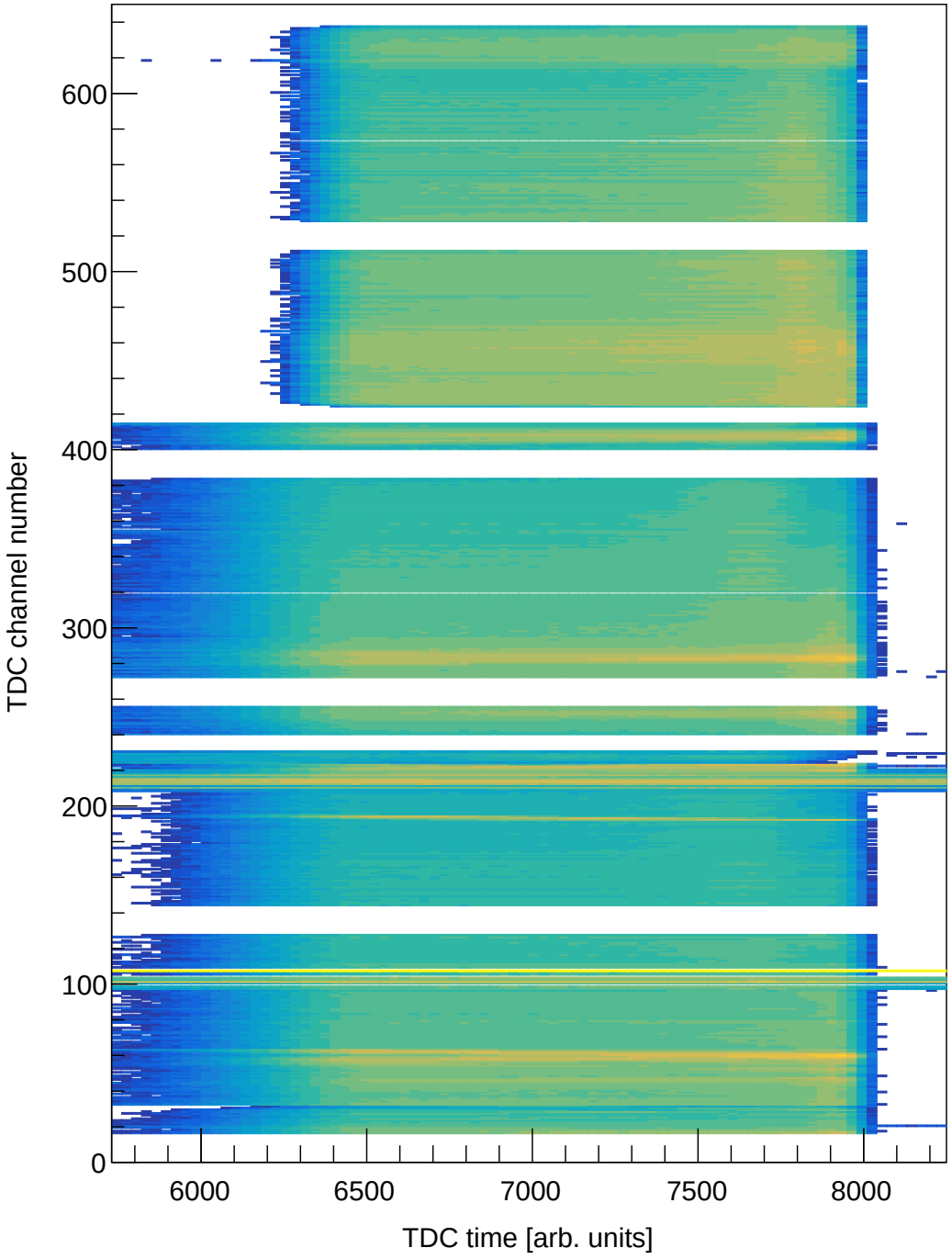

Figure 4.6: Spectrum of TDC channel number versus TDC calibrated reference time of the VDC wires for experiment PR240. The cable offset calibration aligns the trailing edge of the TDC drift time distributions. A display threshold of >50 has been imposed.

4.1.3 Generate Lookup Tables (LUTs)

A lookup table (LUT) is a mapping from the reverse drift time of a wire to drift distance. The reverse drift time is measured from the triggering of a wire to the beginning of the subsequent RF pulse of the cyclotron. Consequently, a larger reverse time corresponds to a shorter drift distance.

The response of each wire plane depends upon a myriad of factors such as design differences (between new and old VDC designs) and operating parameters during an experiment (such as bias voltages and gas flow rates). Consequently, a unique lookup table must be determined for each wire plane for each experiment.

A lookup table is constructed by making the assumption that a homogenous probability distribution function (PDF) of drift distances corresponds to a flat positional distribution on the focal plane. Under such an assumption, a perfectly flat positional spectrum (referred to as an ideal "white spectrum") can be used to map the measured reverse drift times to drift distances. In practice, a smooth slowly-varying region across the focal plane suffices as calibration data. By gating on the focal-plane regions with slowly-varying yields, a distribution of the reverse drift times can be generated. The corresponding cumulative distribution function (CDF) is precisely the LUT (up to normalisation) which provides the drift-time to drift-distance mapping for each wire plane. The distribution of reverse drift times (gated on slowly-varying focal-plane regions) and the associated LUT for the X1 wire plane of experiment PR240 are displayed on Figures 4.7 and 4.8, respectively.

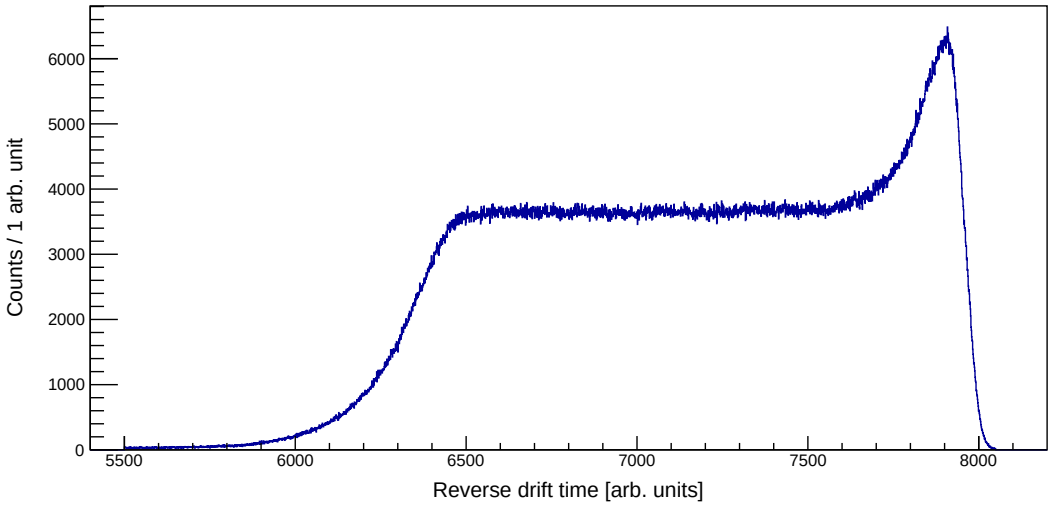

Figure 4.7: Spectrum of reverse drift times of the X1 wire plane, gated on events which form a flat, slowly-varying positional distribution across the focal-plane for experiment PR240.

It is worth noting that a global lookup table for each wire plane assumes that the response of the wires is identical across the wire plane. Whilst this approximation is usually adequate, it has been observed that the response of the wires is indeed dependent on the focal-plane position and therefore the LUTs should also be position dependent. Position-dependent LUTs could be implemented in the future, however they would be inherently limited to experiments with slow-varying yields across large regions of the focal plane. In principle, this could be achieved with an appropriate calibration target which exhibits a smooth excitation function across the focal plane.

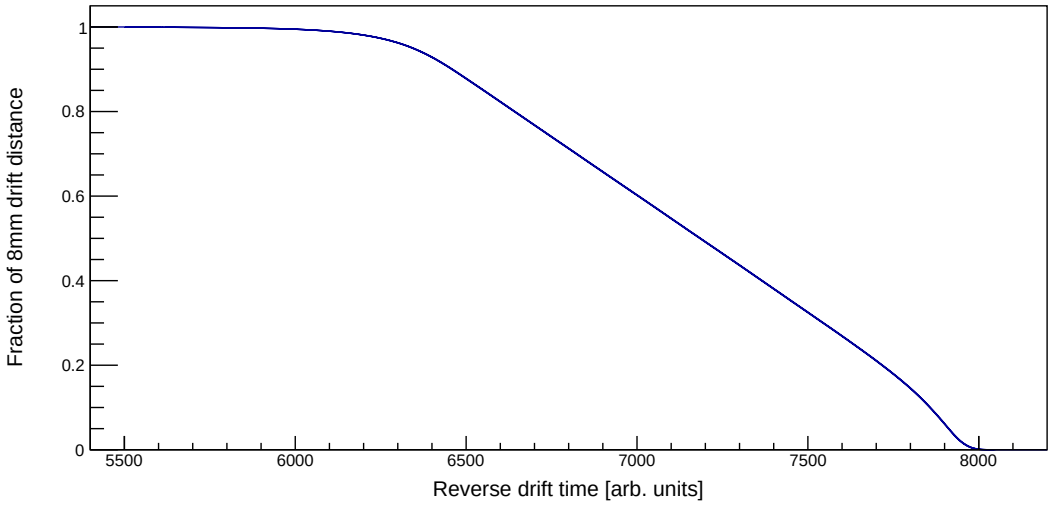

Figure 4.8: The lookup table (LUT) for the X1 wire plane of experiment PR240.

4.1.4 Focal-plane positions

When an ejectile traverses a VDC wire plane, sufficient energy may be deposited in the active area to trigger signal wires. These signal wires can be used to determine a position of traversal across the wire plane through an algorithm known as raytracing. X wireplanes provide horizontal positions of traversals, which in turn can be combined with positions from U wireplanes to determine vertical positions of traversal (see Section 4.1.5). The X1 wire plane of the VDC in position 1 is optimally positioned at the focal plane of the magnetic spectrometer and the associated horizontal position, $X1_{pos}$, is the primary focal-plane position of interest which is used to determine the excitation energy of the recoil nucleus.

4.1.4.1 Least Squares Fit

Raytracing is based on a least squares fit algorithm [89]. Each triggered wire corresponds to a wire-number position (x) and a drift time which corresponds to a calibrated drift distance (y). For each triggered wire and associated calibrated drift distance (y), there corresponds a wire-number position (x) and drift time, respectively. Ideal events produce V-type events as shown in Figure 4.9. Since a single drift time gives no information as to which side of the wire the cell was triggered, a global assumption must be made based on the set of triggered wires for a wire plane. A wire must be chosen such that all wires at equal or higher wire positions are assumed to correspond to energy deposition in the downstream side of the ejectile path. The positions of energy deposition are said to have been inverted after the wire with the shortest drift distance. After this choice of inversion wire has been determined, the first procedure is to calculate the variances σ_x and σ_y and the covariance $cov(x, y)$, defined as

$$\sigma_x^2 = \frac{1}{n}\sum_{i=0}^{n}(x_i - \overline{x})^2, \tag{4.1}$$

$$\sigma_y^2 = \frac{1}{n}\sum_{i=0}^{n}(y_i - \overline{y})^2, \tag{4.2}$$

and

$$\mathrm{cov}(x, y) = \frac{1}{n}\sum_{i=0}^{n}(x_i - \overline{x})(y_i - \overline{y}), \tag{4.3}$$

where $\overline{x}$ and $\overline{y}$ are the average x and y values, respectively. For the linear form

$$\overline{y} = a + b\overline{x}, \tag{4.4}$$

the regression coefficient b and the offset a are given by

$$b = \frac{\mathrm{cov}(x, y)}{\sigma_x^2} \tag{4.5}$$

and

$$a = \overline{y} - b\overline{x}, \tag{4.6}$$

with which the position of traversal (x intercept) across the wire plane can be trivially determined as

$$x' = \frac{-a}{b}. \tag{4.7}$$

The associated r^2 metric indicates the goodness of fit and is defined as

$$r^2 = \frac{[\mathrm{cov}(x, y)]^2}{\sigma_x^2 \sigma_y^2}. \tag{4.8}$$

There is a myriad of possible issues that can result in departures from the ideal V-type event to produce analysis artefacts and worsen resolution. Two such types of anomalous events which depart from this ideal are Z-type and W-type events, as shown in Figures 4.10 and 4.11, respectively. Due to the extra wires that are triggered at the periphery, a direct application of the raytracing algorithm described above would yield an incorrectly reconstructed ejectile path. Current evidence suggests that the extra triggered wires for Z- and W-type events may not be due to spurious electronics and that they possibly correspond to real physical processes which are still to be determined.

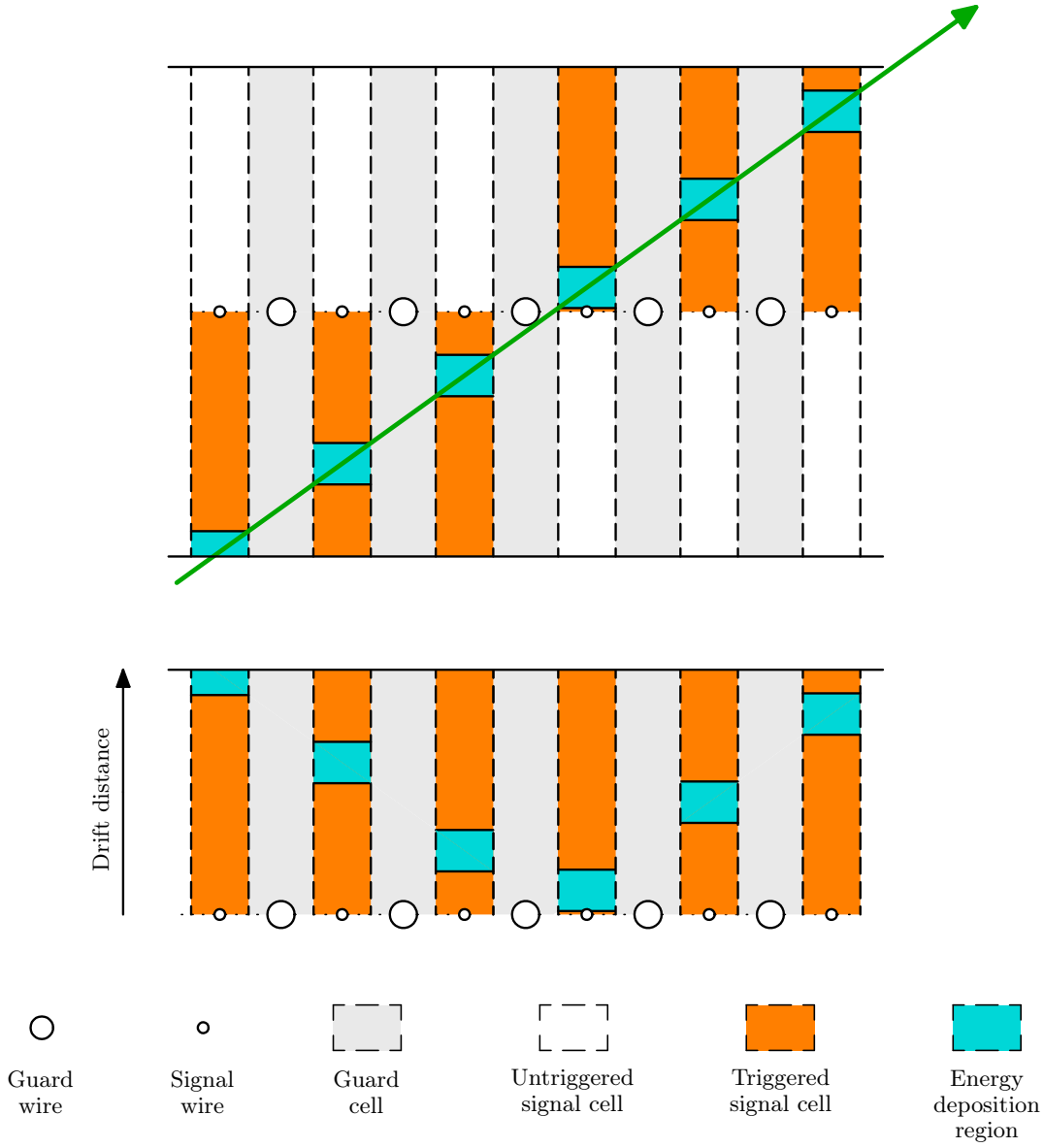

Figure 4.9: The track and drift distances of an ideal event which exhibits a distinct V shape when plotting the drift distance against wire number.

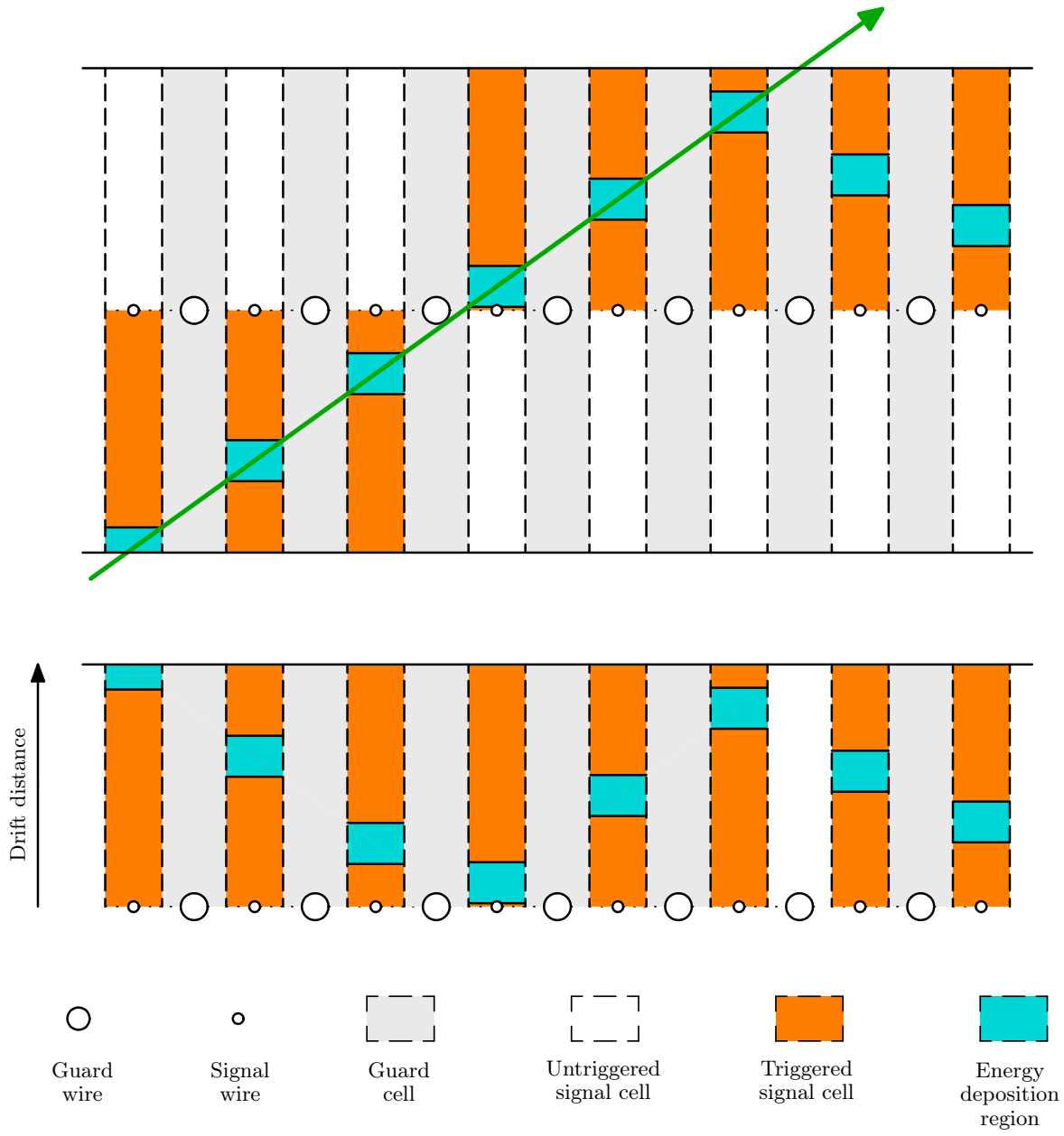

Figure 4.10: The track and drift distances of a Z-type event.

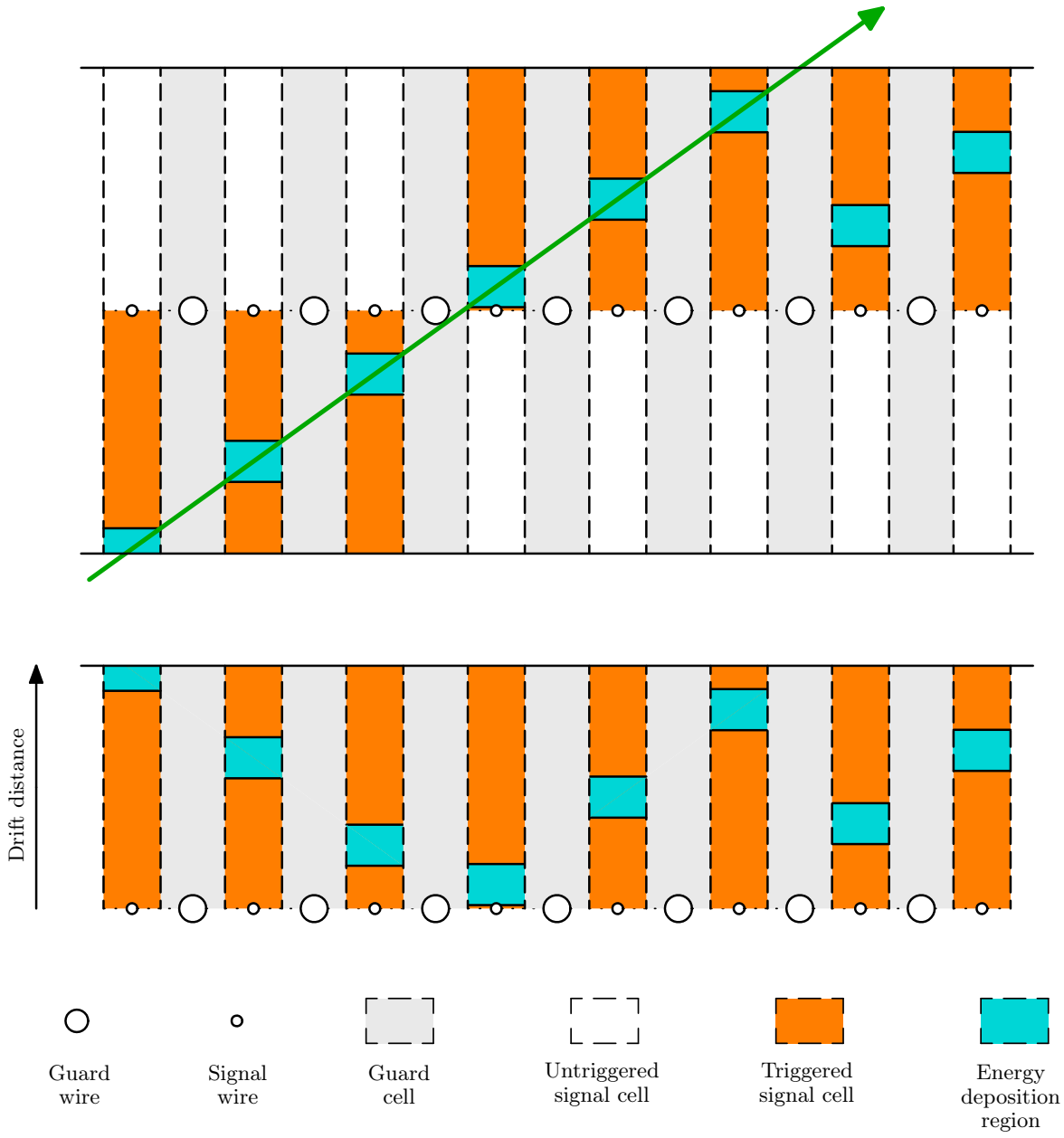

Figure 4.11: The track and drift distances of a W-type event.

4.1.4.2 The new raytracing algorithm

The old raytracing algorithm attempted to eliminate experimental artefacts by first refining the set of triggered wires to be raytraced through a set of explicit conditions. For example, the peripheral wires were tested as to whether they produce Z- or W-type events and if so, they would be rejected for raytracing. After this first refinement of events, it must then be determined for each wire signal whether the corresponding energy deposition occurred upstream or downstream of the wire. It is assumed that there is a triggered wire, known as the wire of inversion, which determines the energy depositions of all preceding/subsequent triggered wires to have occurred upstream/downstream of the wire plane. The old raytracing algorithm also always assumed the wire with the shortest distance to be the wire of inversion and also rejected this wire from the least squares fit as it was always assumed to be bear poor positional information. Additionally, the old algorithm rejected VDC events if the number of missing wires exceeded a user-defined threshold. Missing wires are defined as wire channels which are flanked by triggered wires but do not produce a valid drift time in the event. One of the causes for a missing wire signal is from a faulty electronic channel in a preamplifier of the wire plane. The new SBR algorithm does not explicitly impose a threshold on the number of missing wires. The K600 User Manual [82] and the master's thesis of K.C.W. Li [88] can be referenced for further details on the old raytracing algorithm.

Whilst this old raytracing algorithm has been suitable for past analyses of K600 data, a number of analysis artefacts were discovered through the data analyses for this thesis and an improved algorithm named Silver Bullet Raytrace (SBR) was implemented. The SBR algorithm employs the same basic least squares fitting method, however it is more generalised. Unlike the old raytracing algorithm which is governed by user-defined search patterns and conditions (e.g. the search for Z- and W-type events and the choice of the wire with the shortest drift distance as the inversion wire), the SBR algorithm is designed with the singular goal of determining the maximal linearity within a set of data points. In other words, the SBR algorithm explores all the valid permutations for a set of triggered wires to find the permutation which exhibits the greatest linearity. Each permutation corresponds to a focal-plane position with associated goodness-of-fit metrics which can be used to determine the optimal reconstructed event.

The SBR algorithm uses all n triggered wires, each corresponding to a wire-number position (x) and a drift distance (y). A minimum of 4 wires is imposed for least squares fitting, thus for a set of n total triggered wires, up to $n-4$ wires can be removed to improve the goodness of fit. For n total triggered wires with k raytraced wires ($4 \leq k \leq n$), the number of permutations, p_k, of used wires is given by

$$p_k = \frac{n!}{(n-k)k!}. \tag{4.9}$$

Unlike the old raytracing algorithm, the choice of inversion is crucially not assumed to always be the wire with the shortest drift distance. Since any raytraced wire is permitted to be the inversion wire, for each permutation of k raytraced wires, there are k choices of inversion wire. The algorithm tests each possible inversion wire with a least squares fit to determine the optimal wire. For n total triggered wires with k raytraced wires, the total number of necessary least squared fits is then given by

$$L_k = \frac{kn!}{(n-k)k!}. \tag{4.10}$$

The total number of least squared fits that may be performed for n total triggered wires is therefore given by

$$L_{tot} = \sum_{k=4}^{n} L_k. \tag{4.11}$$

Since this is substantially more computationally intensive than the single least squares fit performed for the old raytracing algorithm, the SBR algorithm is typically only performed for the X1 wire plane as this is the only wire plane which is used to infer the excitation energy of the recoil nucleus.

As the removal of a wire invariably leads to a smaller r^2 value due to the reduced degrees of freedom, this metric is not suitable for comparing between results with different numbers of wires. An appropriate metric for comparison is the adjusted r^2, denoted as r^2_{adj}, which accounts for varying degrees of freedom and is given by

$$r^2_{\text{adj}} = 1 - \frac{(1-r^2)(k-1)}{k-O-1}, \tag{4.12}$$

where k is the number of observations (raytraced wires) and O is the number of independent regressors in the model, which for linear regression is defined as the number of estimated coefficients (i.e. the constant term excluded). A threshold for r^2_{adj} is set such that if a performed raytrace yields a sufficiently high goodness of fit, the SBR algorithm ends without exploring other permutations with more removed wires. This is to protect against an excessive removal of wires when a good least squares fit is found as well as to speed up the computation time of the algorithm.

An example from experiment PR166 is presented in Figures 4.12 - 4.15. In this example, a VDC event from the X1 wire plane with a total of $n = 8$ triggered wires is analysed. Figure 4.12 shows the case where $k = n$ wires are used for the least squares fit and the 5^{th} wire (at 600 mm) was determined to be the optimal wire of inversion, yielding $r^2_{\text{adj}} = 0.907109$. Figure 4.13

shows the case of $k = 7$ wires: the 5^{th} wire (at 600 mm) was rejected and the 6^{th} wire (at 604 mm) was determined to be the optimal wire of inversion, yielding a significantly better goodness of fit of $r^2_{\text{adj}} = 0.964968$. Figure 4.14 shows the case of $k = 6$ wires: the 5^{th} and 8^{th} wires (at 600 and 616 mm, respectively) were rejected and the 6^{th} wire (at 604 mm) was determined to be the optimal wire of inversion, yielding $r^2_{\text{adj}} = 0.974174$. Figure 4.15 shows the case of $k = 5$ wires: the 6^{th}, 7^{th} and 8^{th} wires (at 604, 608 and 616 mm, respectively) were rejected and the 4^{th} wire (at 604 mm) was determined to be the optimal wire of inversion, yielding the highest goodness of fit of $r^2_{\text{adj}} = 0.999275$. This example of a VDC event shows that the highly general objective of SBR to "determine maximal linearity" event out of a given set of wires is highly effective at removing wires which depart from the ideal V-type event. It also shows that the 4^{th} wire with the shortest drift distance (1.27 mm) corresponds to a highly linear data point that should be used for the least squares algorithm. Using the old raytracing algorithm, this wire would have been immediately rejected. In practice, a threshold is sometimes set on the shortest drift distance that is used, typically of the order of ≈ 1 mm. This is based on the geometric argument that given the typical angles of traversal for ejectiles, drift distances below such a threshold must deposit energy directly in the vicinity of the signal wire and/or on both sides of the cell. For such interactions, the mapping of drift time to drift distance is no longer accurate/sensible.

The SBR algorithm solves multiple complex issues in VDC data analyses with its singular objective of determining maximal linearity for a set of triggered wires. Aside from improvements in resolution, the development of the SBR algorithm was motivated by two analysis artefacts, known as the "4 mm structure" and the bifurcation of lineshapes at lower raytrace angles, θ_{RT}. The "4 mm structure" is so named because focal-plane spectra often present with periodic dips in efficiency every 4 mm at the approximate positions of the signal wires, as shown in Figure 4.16. This structure appears to only occur for ejectiles which exhibit relatively higher energy loss such as α-particles and is typically absent for protons, deutrons and tritons. It is observed that the SBR algorithm provides significant improvement to the periodic dips in efficiency, however remnants of the "4 mm structure" persist. The full spectrum of X1_{pos} positions for experiment PR240 is presented on Figure 4.17. It is observed that there is a doubling of the peaks associated with the 2^+_1 and 0^+_2 excited states of ^{12}C, situated at 4.43982(21) and 7.65420(15) MeV, respectively. This is because the raw X1_{pos} focal-plane positions have not yet undergone the lineshape corrections and peak-position mapping described in Sections 4.1.7 and 4.1.8, respectively.

An example of the bifurcation of lineshapes at lower values of θ_{RT} is presented in Figure 4.18. An explanation for this phenomenon is that the old raytracing algorithm does not consistently identify and reject the aforementioned peripheral wires of a VDC event that deviates from the ideal V-type

event. For a given set of a triggered wires, problematic peripheral wires which occur at lower/higher focal-plane positions invariably lead to a lower value of θ_{RT} with a raytraced position that is biased towards lower/higher focal-plane positions. The lineshape from the old raytracing algorithm begins to exhibit smearing/bifurcation at approximately θ_{RT} (old) $\leq 31°$, with a substantial number of events being affected. In contrast, the lineshape with the SBR algorithm appears to only exhibit a weak smearing below a smaller raytrace angle of $\theta_{\mathrm{RT}} \approx 27°$. In mitigating the bifurcation, the SBR algorithm also drastically reduces the number of events with resultant unphysically-low raytrace angles after being affected by such smearing. The remaining affected events are typically rejected with high selectivity by placing a higher threshold on the r^2_{adj} metric.

The mechanism for this bifurcation is presented in Figure 4.19 where the ideal V-type event (blue) corresponds to the ideal raytrace angle θ_{RT} and focal-plane position $\mathrm{X1_{pos}}$. The inclusion of drift distances from problematic peripheral wires at lower focal-plane positions (green) leads to a raytrace angle θ'_{RT} and focal-plane position $\mathrm{X1'_{pos}}$ that are both decreased with respect to their ideal values. Similarly, it is observed that problematic peripheral wires at higher focal-plane positions (red) also lead to a lower raytrace angle θ''_{RT}, resulting in an increased focal-plane position $\mathrm{X1''_{pos}}$.

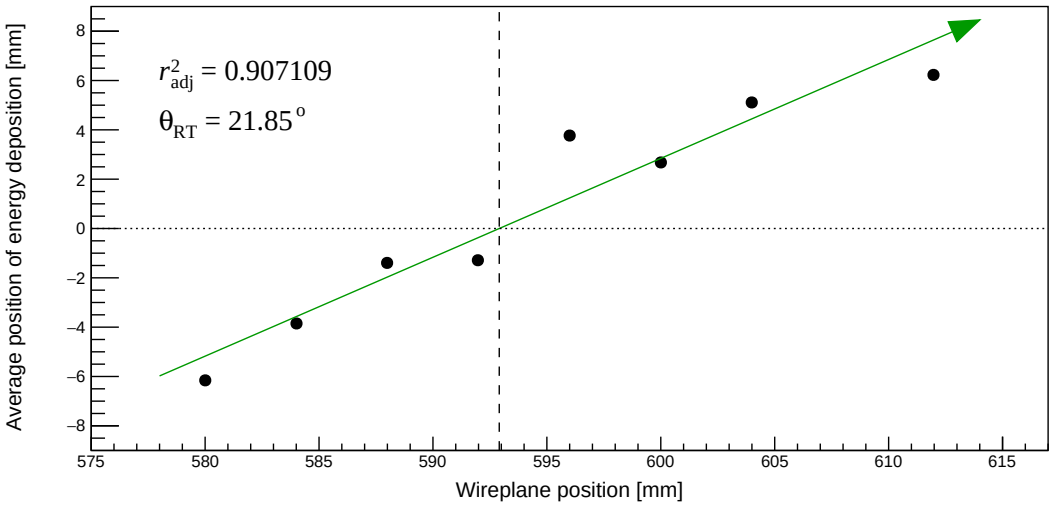

Figure 4.12: An SBR track (green arrow) of the X1 wire plane with no wires removed, from experiment PR166: $^{12}\mathrm{C}(\alpha,\alpha')^{12}\mathrm{C}$ at 6.0°. The vertical dashed line indicates the raytraced position of $\mathrm{X1_{pos}} = 590.03$ mm.

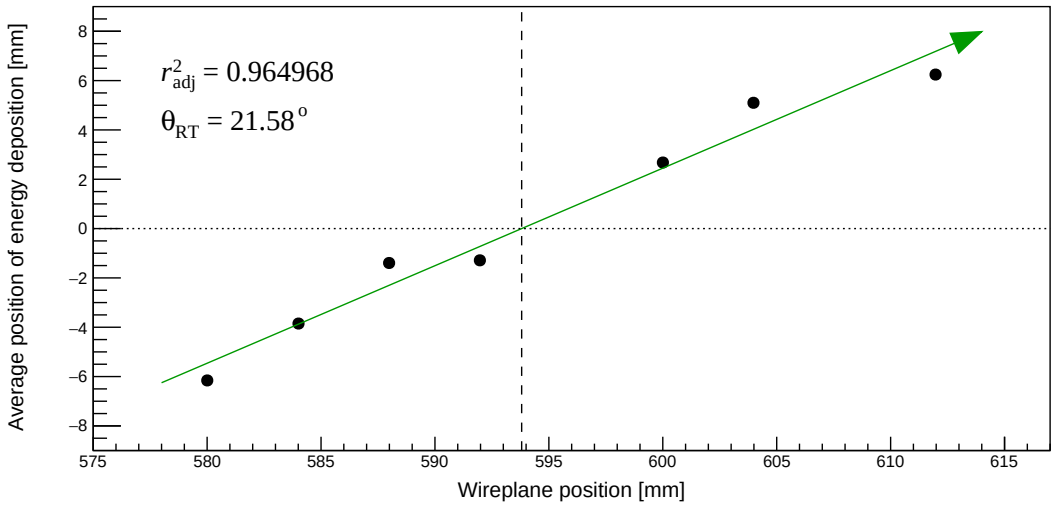

Figure 4.13: An SBR track (green arrow) of the X1 wire plane with 1 wire removed, from experiment PR166: $^{12}C(\alpha,\alpha')^{12}C$ at 6.0°. The vertical dashed line indicates the raytraced position of $X1_{pos}$ = 593.19 mm.

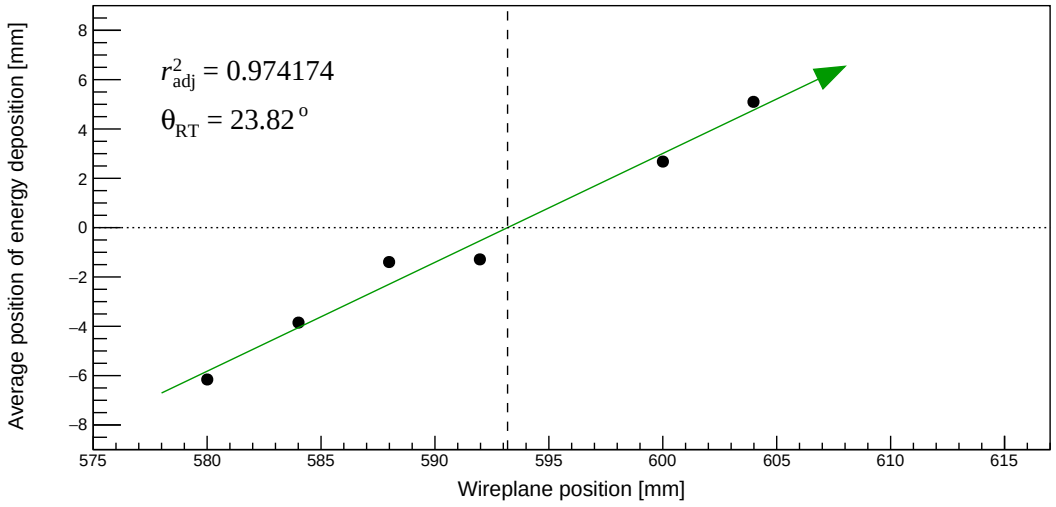

Figure 4.14: An SBR track (green arrow) of the X1 wire plane with 2 wires removed, from experiment PR166: $^{12}C(\alpha,\alpha')^{12}C$ at 6.0°. The vertical dashed line indicates the raytraced position of $X1_{pos}$ = 593.81 mm.

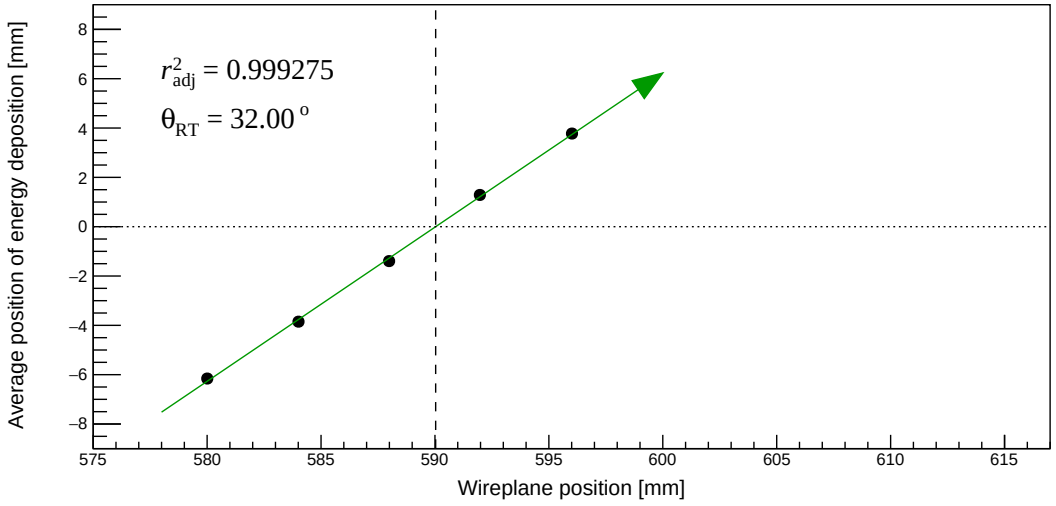

Figure 4.15: An SBR track (green arrow) of the X1 wire plane with 3 wires removed, from experiment PR166: $^{12}C(\alpha,\alpha')^{12}C$ at 6.0°. The vertical dashed line indicates the raytraced position of $X1_{pos}$ = 592.91 mm.

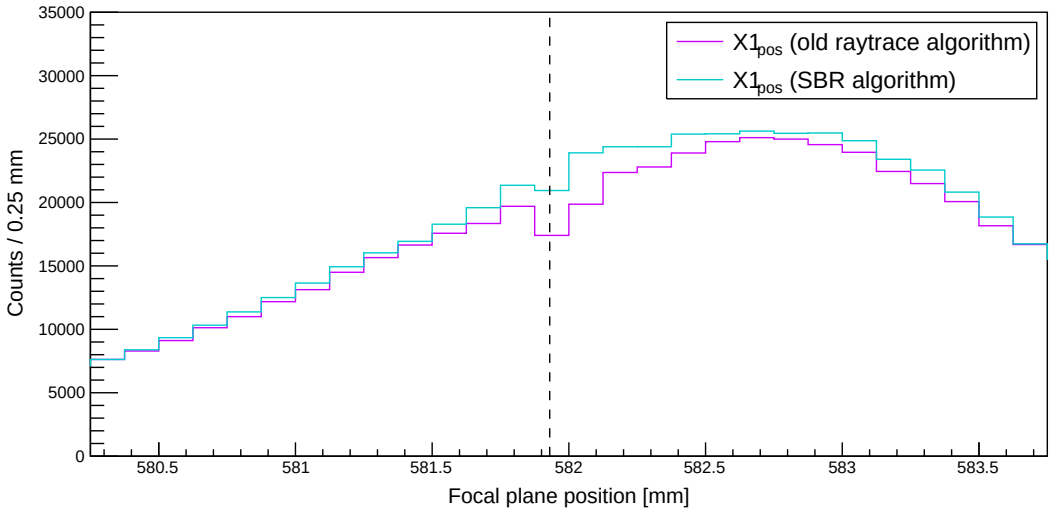

Figure 4.16: Example of the "4 mm structure" analysis artefact for VDC data and the improvement with the SBR algorithm. The vertical dashed line is to guide the eye towards the problematic dip in events.

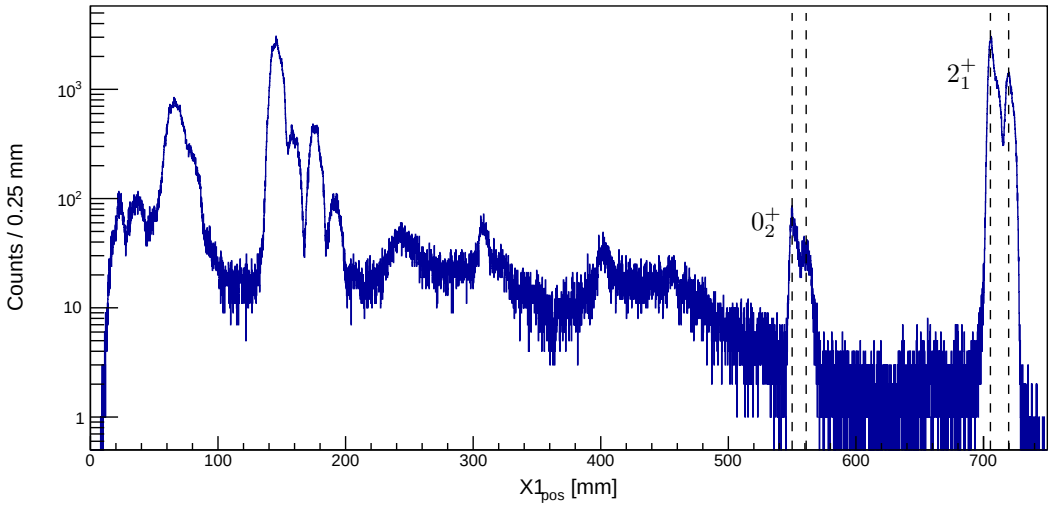

Figure 4.17: The spectrum of $X1_{pos}$ for experiment PR240. The dashed lines indicate the double peaks associated with the 4.43982(21) MeV 2_1^+ and 7.65420(15) MeV 0_2^+ excited states of ^{12}C.

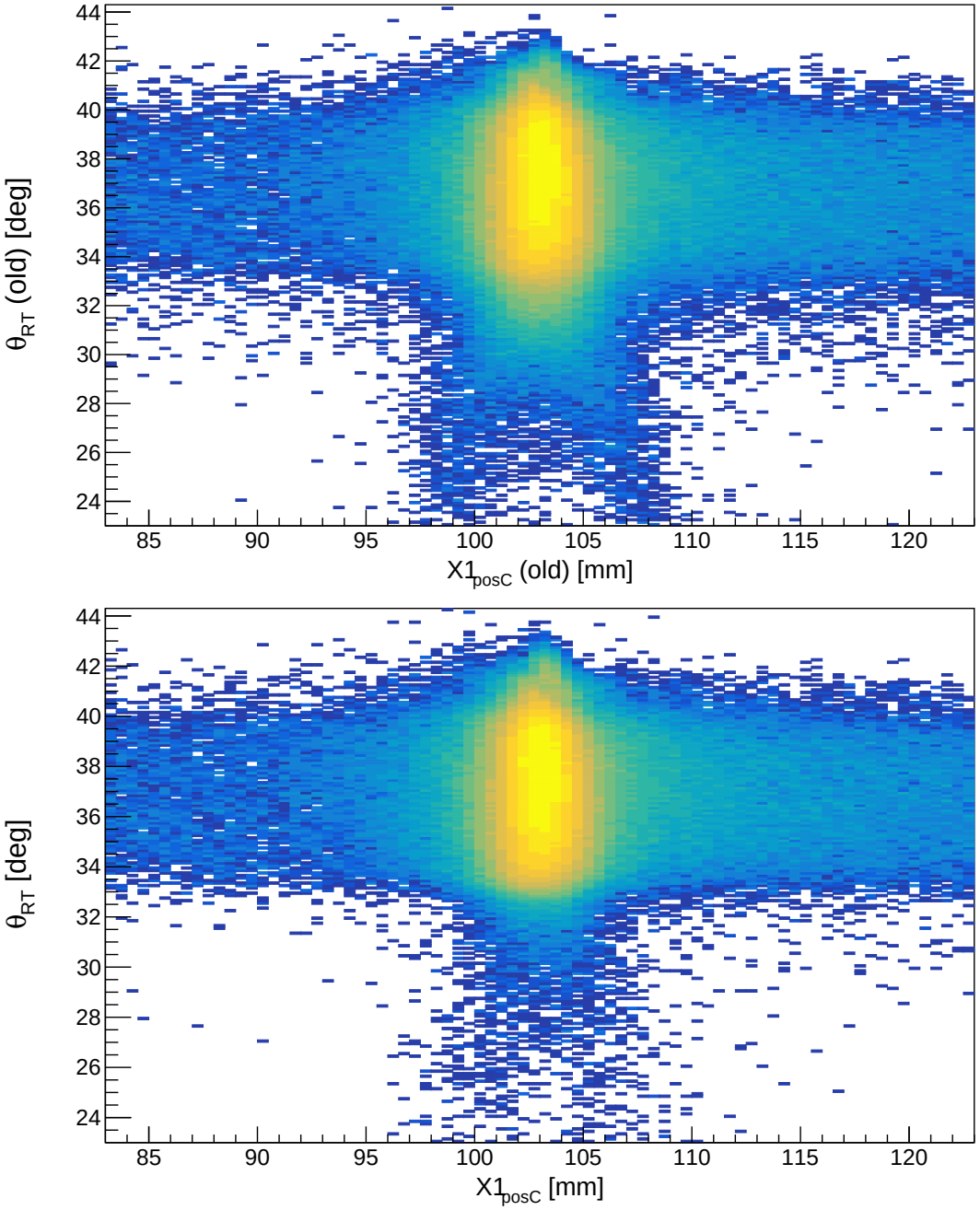

Figure 4.18: Example of the bifurcation of lineshapes at lower values of θ_{RT} with the old raytracing algorithm and its improvement with the SBR algorithm.

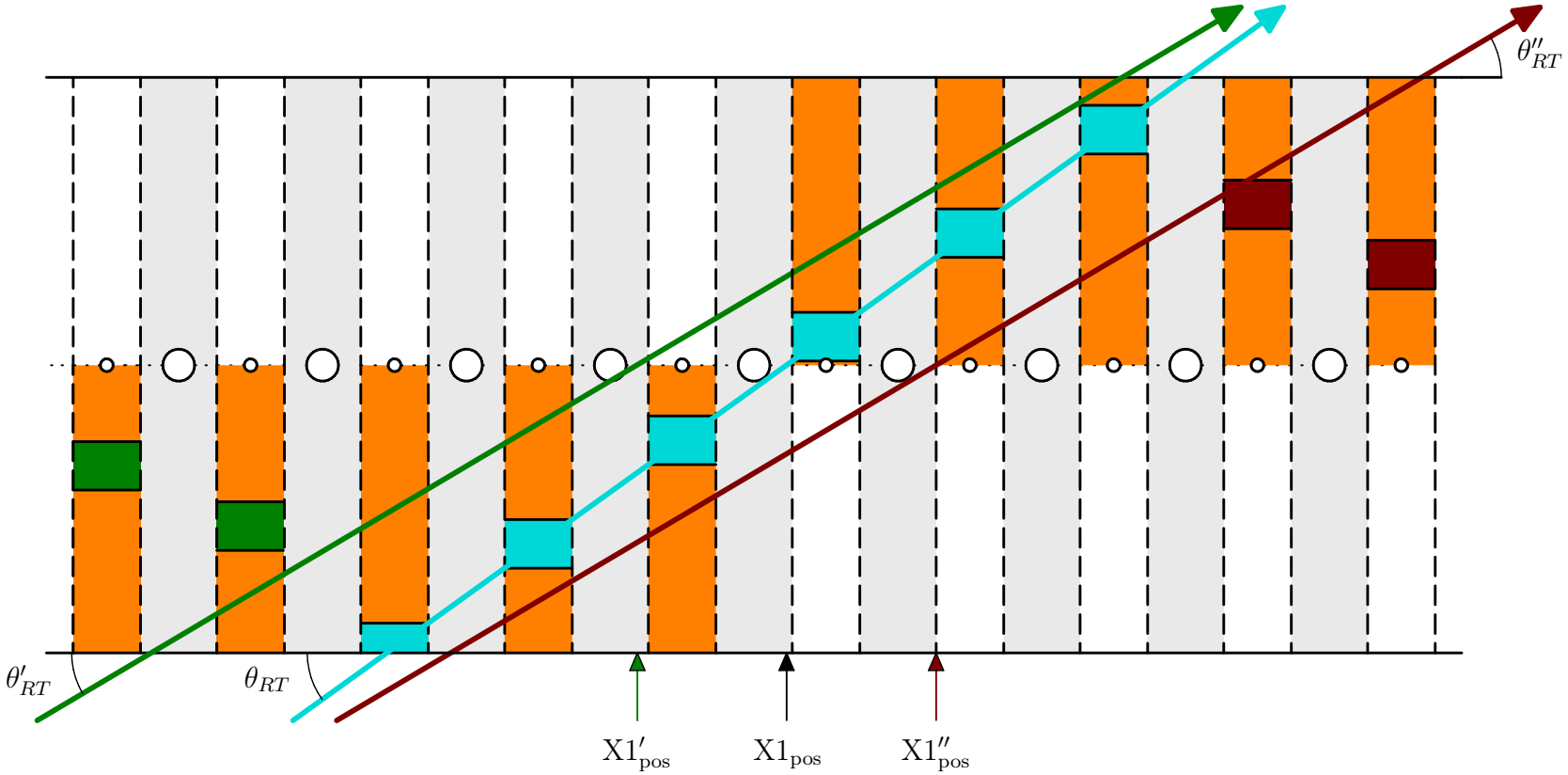

Figure 4.19: Depiction of the mechanism for lineshape bifurcation at lower raytrace angles, θ_{RT}. The ideal V-type track without problematic peripheral wires is shown in blue, corresponding to θ_{RT} and $X1_{pos}$. The energy depositions of problematic peripheral wires at lower focal-plane positions are shown in green, corresponding to θ'_{RT} and $X1'_{pos}$. The energy depositions of problematic peripheral wires at higher focal-plane positions are shown in red, corresponding to θ''_{RT} and $X1''_{pos}$.

4.1.5 Vertical focal-plane position

The U wireplanes provide the vertical information of the ejectile's track. The vertical positions of the ejectile's traversal points, across the X1 and X2 wire planes, are denoted $\mathrm{Y1_{pos}}$ and $\mathrm{Y2_{pos}}$, respectively. The U-wires are obliquely orientated at an angle of $\theta_{\mathrm{Uwire}} = 50°$ relative to the horizontal plane.

$$\mathrm{Y1_{pos}} = -\left(\frac{\mathrm{U1}_{pos}\tan(\theta_{\mathrm{Uwire}}) - g_0\sin(\theta_{\mathrm{Uwire}})}{\sin(\theta_{\mathrm{Uwire}})\tan(\theta_{\mathrm{SCAT}}) - \mathrm{X1_{posC}}}\right)\tan\theta_{\mathrm{Uwire}} + g_1, \tag{4.13}$$

where the constants g_0 and g_1 depend on the configuration of the VDCs (see Section 3.1) and θ_{scat} is the projected polar scattering angle of the ejectile, as described in Section 4.1.6. $\mathrm{Y2_{pos}}$ is similarly calculated.

As mentioned in Section 4.1.6, the magnetic optics of the K600 spectrometer can vertically focus the ejectiles onto the focal plane. This "focus mode" operation enables background-determination which can be crucial for certain experiments, as shown in 4.20. The uniform regions labelled (a) and (c) correspond to background events which correspond to ejectiles which have undergone scattering within the internal cavity of the K600 spectromter and as such, no longer provide viable information about the target-related reactions. It is assumed that the smooth slowly-varying backgrounds in these regions are representative of the background in region (b) and can be therefore used to generate a background spectrum.

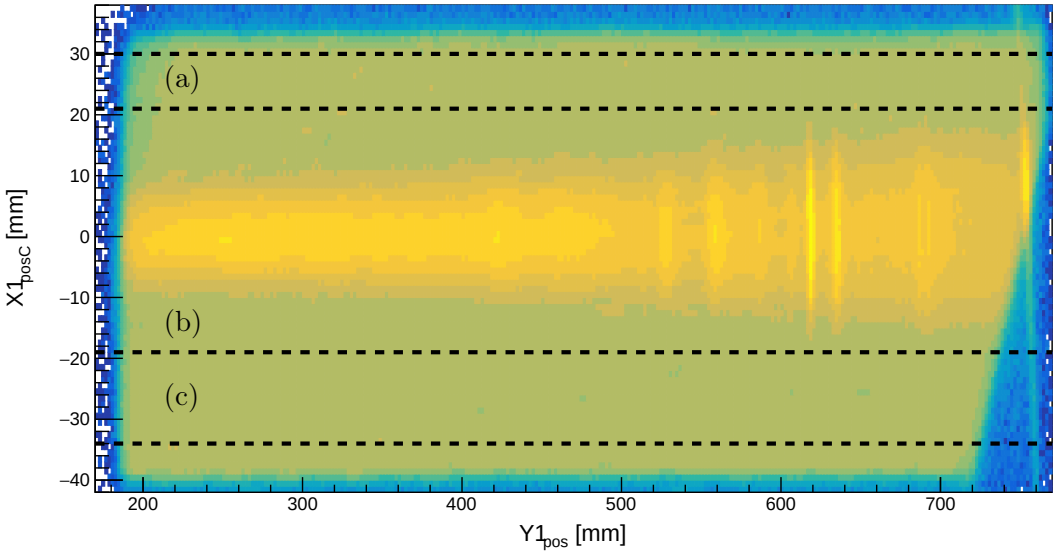

Figure 4.20: Spectrum of $\mathrm{Y1_{pos}}$ versus $\mathrm{X1_{posC}}$ under focus-mode operation from a dataset from another separate thesis and project PR226 [88]. Regions (a) and (c) depict the background regions of $\mathrm{Y1_{pos}}$ whilst region (b) is the focused region of events which carry information about the reaction.

The majority of the experiments analysed for this thesis were not performed in focus mode which is necessary for a reliable background subtraction. This is largely mitigated by the fact that most of the experiments have exceedingly low background due to their reaction/experiment parameters.
In general, ^{14}C$(p,t)^{12}$C measurements (experiments PR240 and PR195) exhibit considerably less background in comparison to ^{12}C$(\alpha,\alpha')^{12}$C measurements at $\theta_{\text{lab}} = 0°$. This stems from the mass exchange of the ^{14}C$(p,t)^{12}$C reaction which means that the radius of curvature (see Equation 4.17) for both the unreacted and elastically-scattered beam particles is usually considerably smaller than that of the ejectiles of interest. The beamstops for ^{14}C$(p,t)^{12}$C reaction measurements are therefore typically placed on the "low-momentum" side within the internal cavity of the K600 spectrometer dipoles. The simultaneous fitting of the backgrounds generated through gates on Y1_{pos} are discussed in Section 4.10.3.

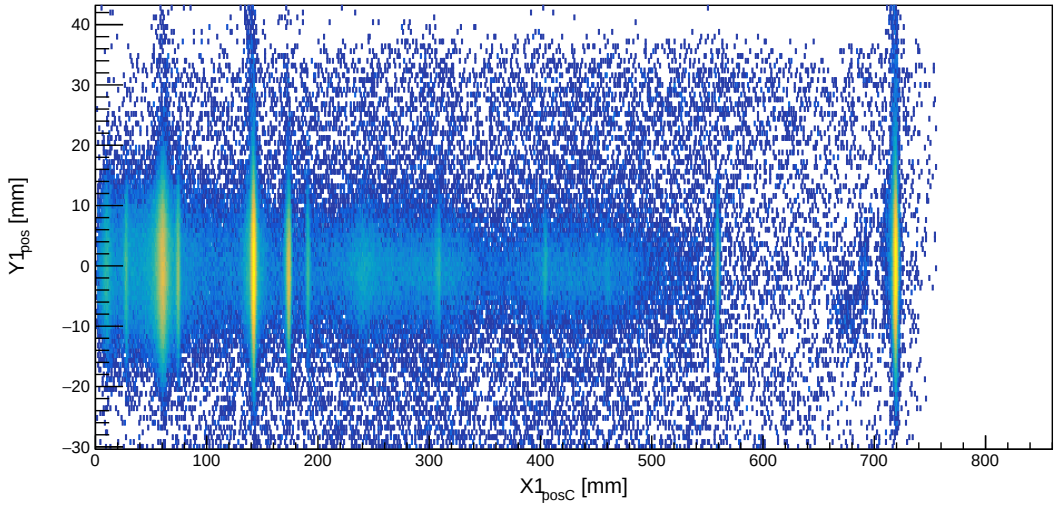

Figure 4.21: Spectrum of Y1_{pos} versus X1_{posC} for experiment PR240.

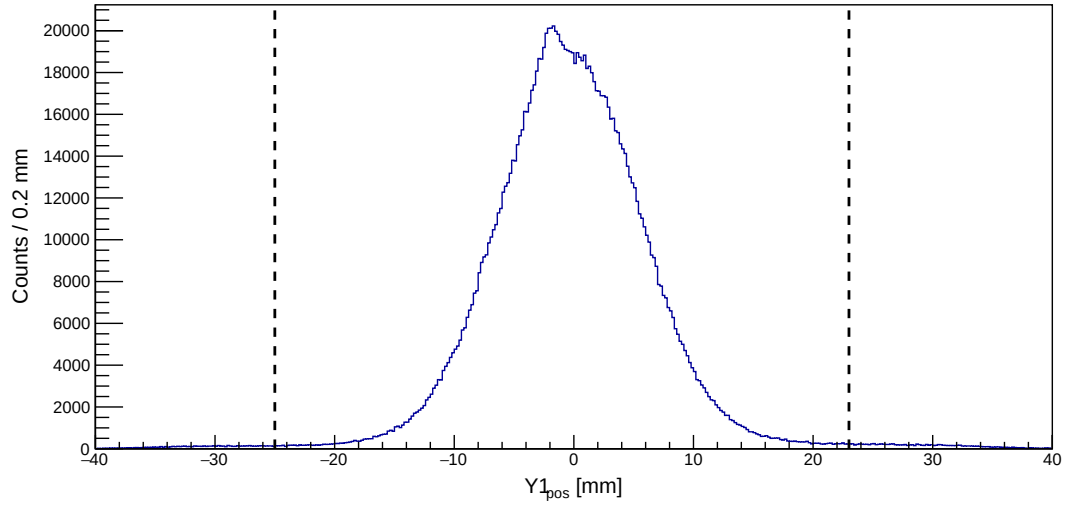

Figure 4.22: Spectrum of Y1_{pos} for experiment PR240. The dashed lines depict the -25.0 mm $< \text{Y1}_{\text{pos}} <$ 23.0 mm gate on the data.

4.1.6 Projected ejectile scattering angle, $\theta_{\mathbf{scat}}$

The magnetic optics of the K600 spectrometer can vertically focus the ejectiles onto the focal plane. This "focus mode" operation enables background-determination which can be crucial for certain experiments. The disadvantage of this mode of operation is the loss of correlation between the vertical position of the ejectile at the focal plane and the ejectile scattering angle relative to the horizontal plane. Even if the magnetic optics are operated in the self-explanatory "unfocused mode", calibration of the vertical position at the focal plane to calculate the polar scattering angle requires a calibration with a specialised collimtor, referred to as a pepperpot, which is not always feasible [82]. Fortunately, there is a component of the polar scattering angle that is always available: θ_{scat}. This angle, depicted below in Figure 4.23, is determined between beam-axis and the projection of the momentum vector of the ejectile onto the horizontal focal-plane. The spectra of θ_{scat} and θ_{scat} vs X1_{posC} are presented in Figures 4.24 and 4.25 respectively. It is observed that the lineshape corrections described in Section 4.1.7 have removed the X1_{posC} dependence of the θ_{scat} lineshapes. Since the $^{14}\text{C}(p,t)^{12}\text{C}$ measurement of experiment PR240 exhibits relatively low background, a gate of $|\theta_{\text{scat}}| < 2.1^\circ$ provides only a small decrease in background events.

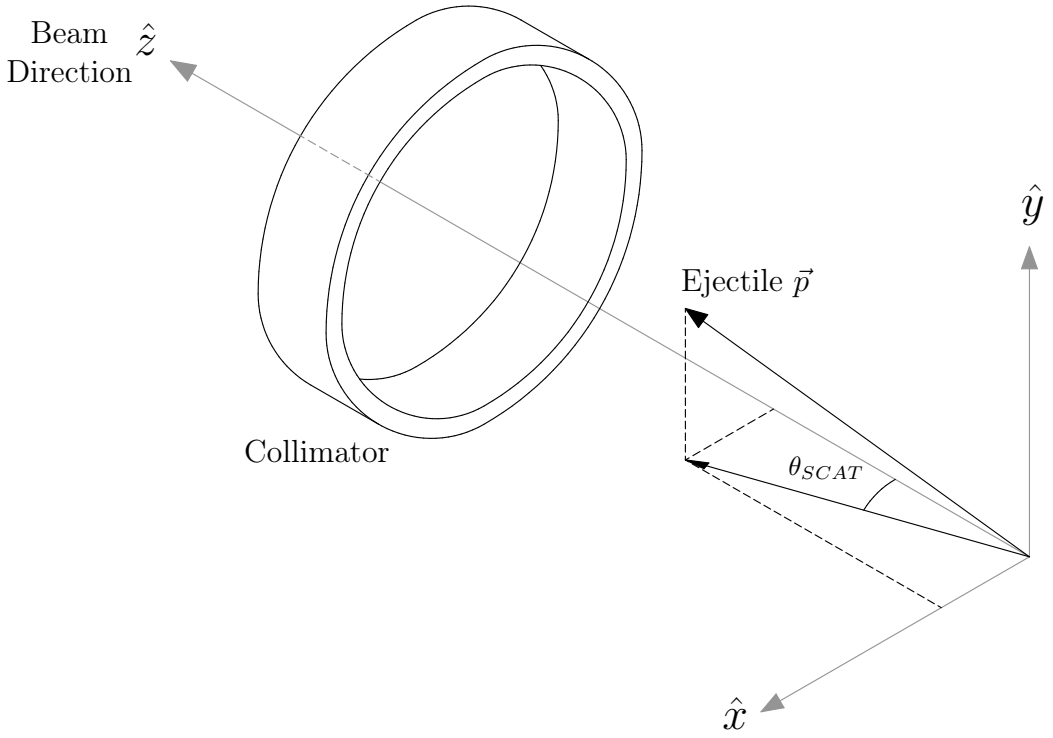

Figure 4.23: Schematic representation of θ_{scat} for experiment PR240, the collimator restricted the polar scattering angle acceptance of the ejectiles to $\theta_{\text{lab}} = 0^\circ \pm 2^\circ$.

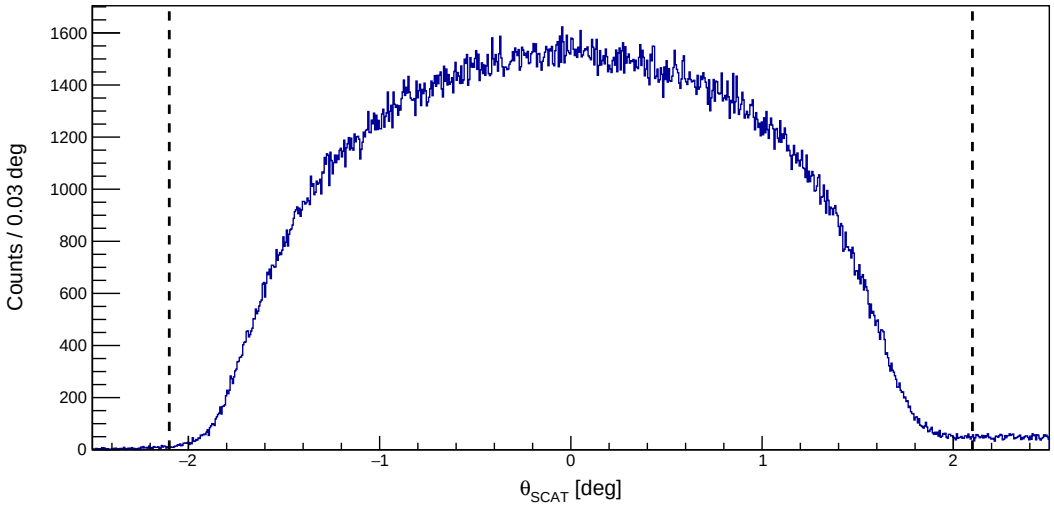

Figure 4.24: Spectrum of θ_{scat} for experiment PR240. The dashed lines depict the $|\theta_{\mathrm{scat}}| < 2.1^{\circ}$ gate on the data.

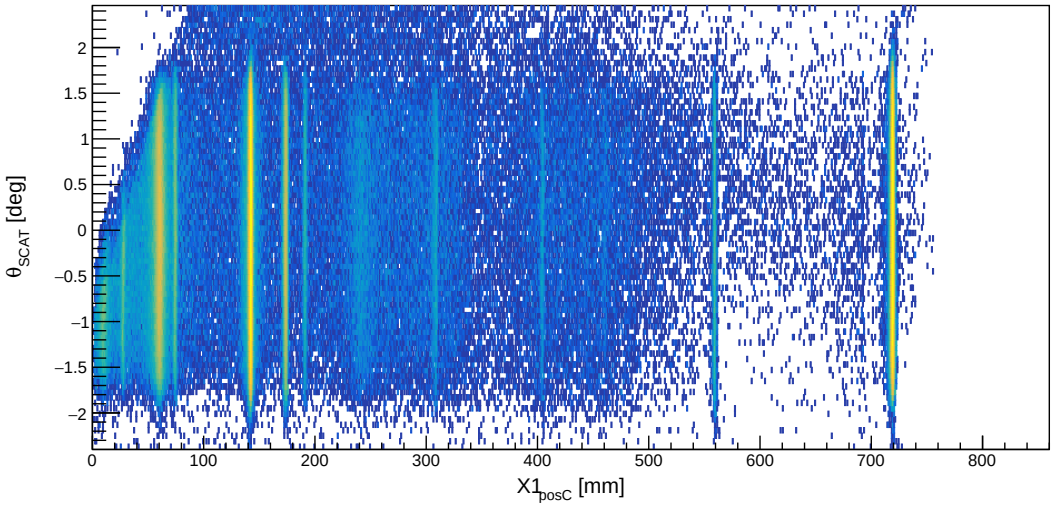

Figure 4.25: Spectrum of θ_{scat} versus $\mathrm{X1}_{\mathrm{posC}}$ for experiment PR240.

4.1.7 Lineshape corrections

A focal-plane lineshape is defined as the locus formed by plotting the focal-plane position against a variable and is an effective method to visualise any correlations, as shown in Figure 4.26. Such correlations, which manifest as aberrations from straight and vertical loci, are detrimental to the resolution of the measured focal-plane position. Due to the inherent ion optics of the K600 spectrometer, the horizontal ejectile position measured at the focal plane ($X1_{pos}$) typically exhibits strong correlations with the ejectile scattering angle as well as the vertical position of traversal through the focal plane ($Y1_{pos}$). For all the analysed experiments, the K600 spectrometer was not configured to allow for a polar scattering angle calibration, however the projected scattering angle onto the horizontal plane (θ_{scat}) can be reliably determined. This projected angle typically exhibits a clear correlation with $X1_{pos}$. The process of removing such correlations is referred to as a lineshape correction.

In the past, the accuracy of such corrections was highly dependent on the judgement of the user as the corrections were performed "by eye". Consequently, it was nearly impossible to provide an accurate correction of complex lineshapes that were valid for the entirety of the focal plane. A new lineshape algorithm and corresponding code named TotalLineshapeCorrection (TLC) was developed (see Appendix A.1). This new algorithm provides several drastic improvements over the old method beyond the obvious benefit of machine accuracy surpassing the visual approximations of a user. Whilst the old algorithm allowed a single lineshape correction to be made with the θ_{scat} and the $Y1_{pos}$ variables, the TLC algorithm allows for an arbitrary number of iterative lineshape corrections. Moreover, correction variables for TLC are completely general so a lineshape correction can be performed with any variable within the data. The drastic improvement to the dispersions of $X1_{posC}$ positions, with respect to the uncorrected $X1_{pos}$ positions, is shown in Figure 4.27.

The lineshape corrections for experiment PR240 summarised in Table 4.2 and the corresponding results are presented in Figures 4.30 - 4.33. The beam-optics for experiment PR240 exhibited substantial changes and as such, the lineshape corrections were run-dependent. The run numbers are listed in Table 4.2 purely for historical reference. The focal-plane resolutions of the various X1 positions for experiment PR240 are presented in Table 4.3.

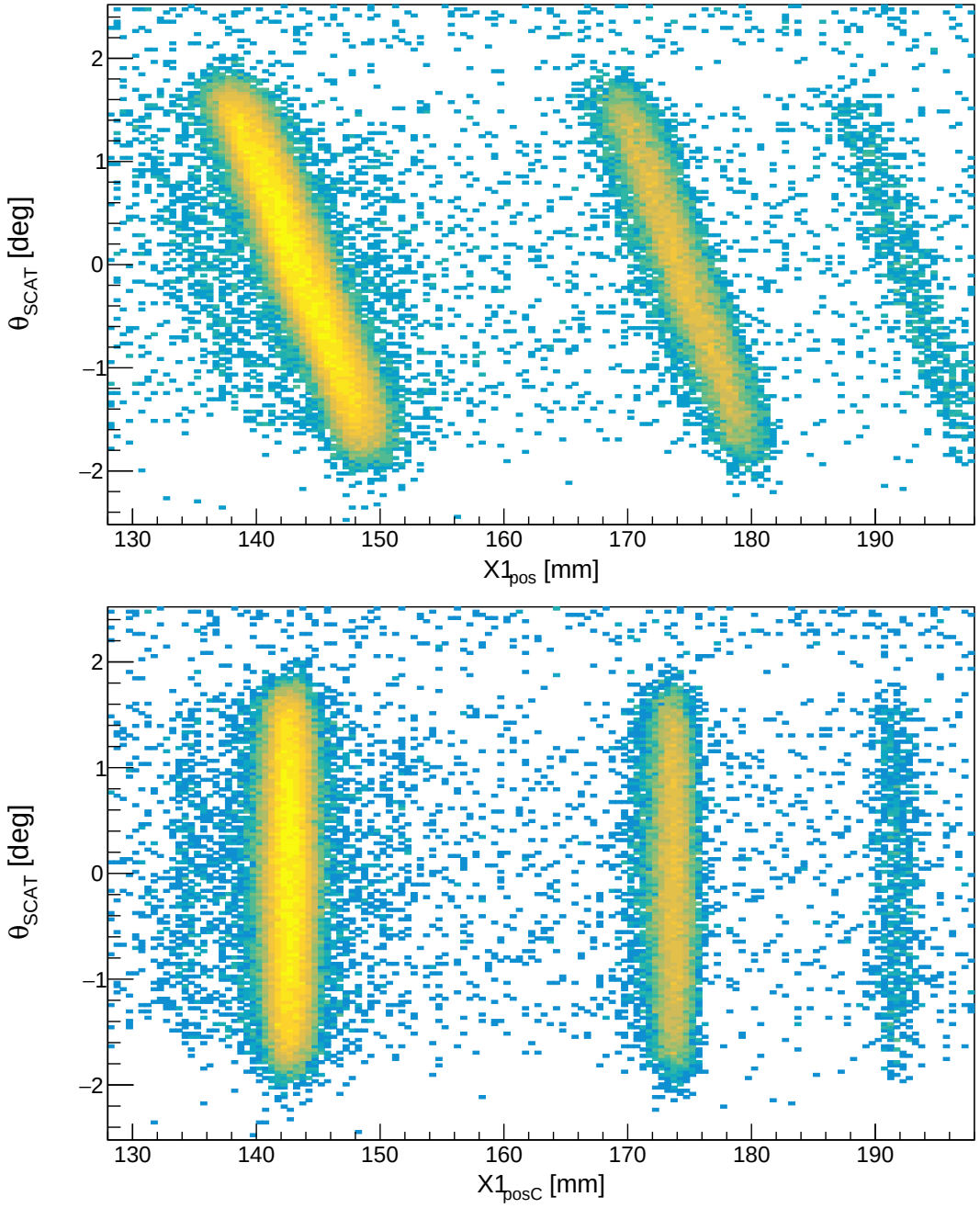

Figure 4.26: Spectra of θ_{scat} versus $\mathrm{X1_{pos}}/\mathrm{X1_{posC}}$, illustrating the effectiveness of lineshape corrections using TLC for a subset of data from experiment PR240. The loci in both spectra correspond to the peaks shown on Figure 4.27.

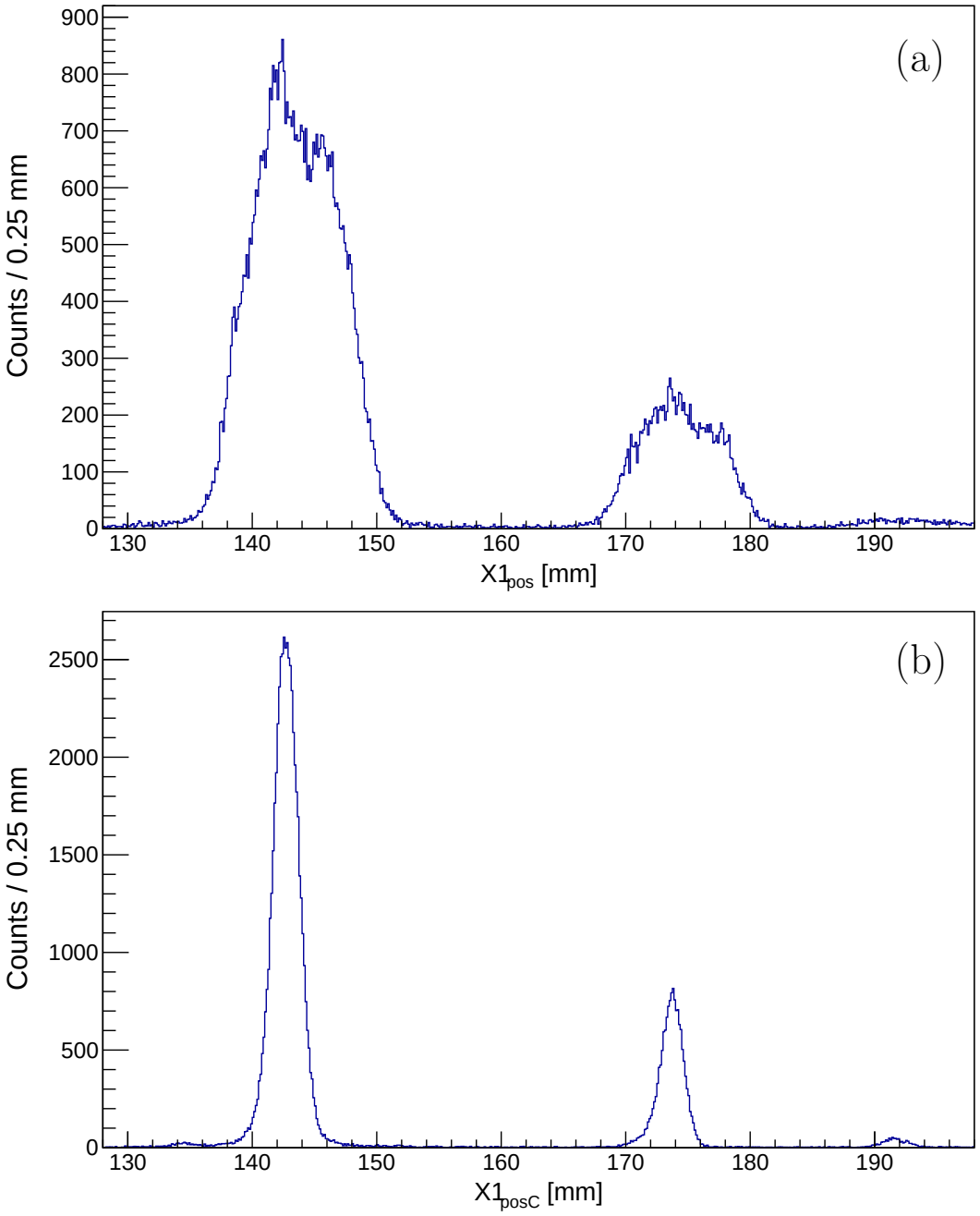

Figure 4.27: The peaks in both spectra correspond to the projection of the loci shown on Figure 4.26. The focal-plane spectrum of $X1_{pos}$ positions shows peaks which do not exhibit the typical Lorentzian form of resonances due to the aberrations of the lineshapes. The lineshape-corrected focal-plane spectrum of $X1_{posC}$ positions shows peaks which are predominantly Lorentzian in form with a significantly lower dispersion.

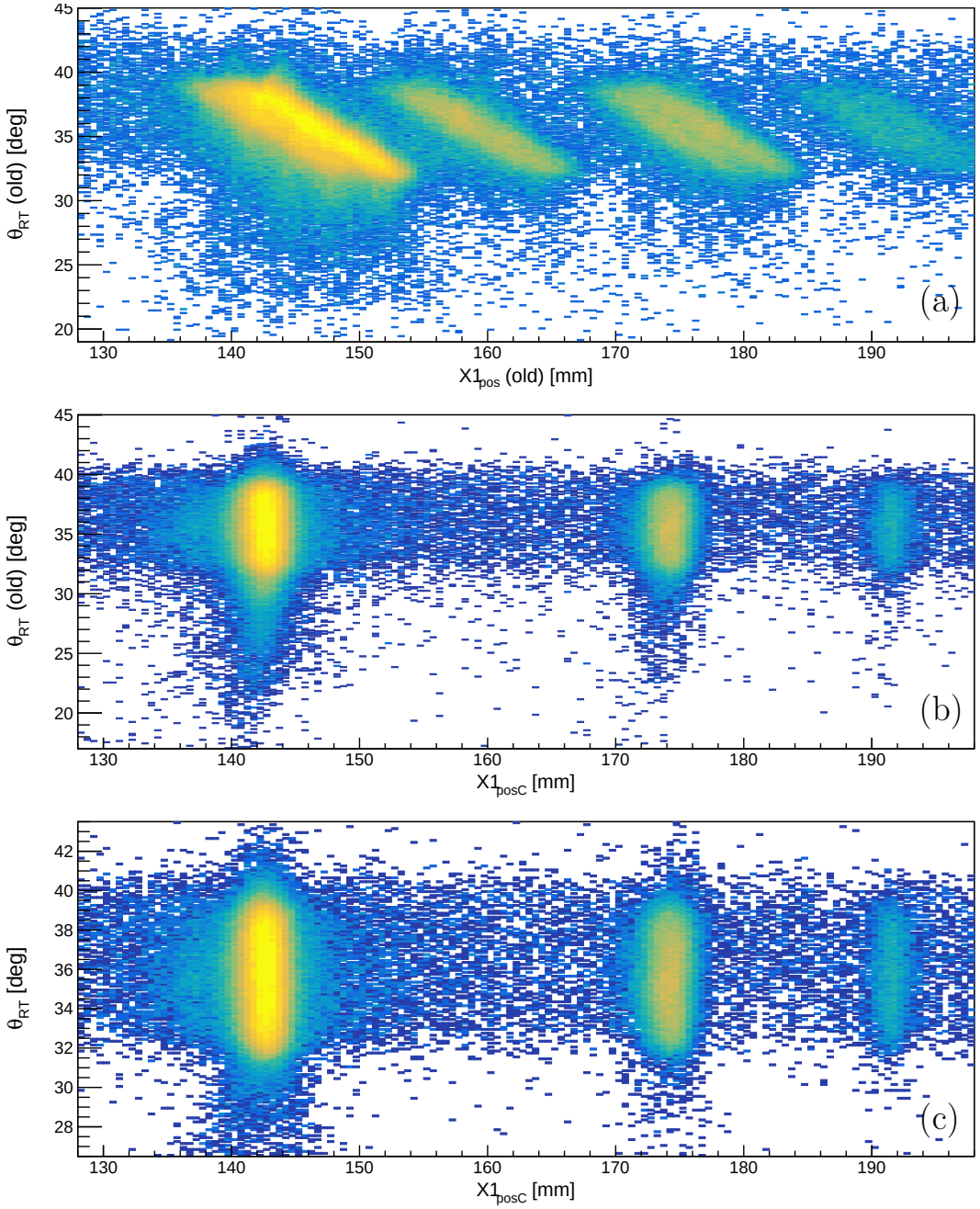

Figure 4.28: Comparison of SilverBulletRaytrace against the old raytrace algorithm for experiment PR240: (a) spectrum of the old raytrace angle (through X1) versus the old uncorrected focal-plane position, (b) spectrum of the old raytrace angle (through X1) versus the new corrected focal-plane position, (c) spectrum of the new raytrace angle (through X1) wire plane versus the new corrected focal-plane position.

Run Numbers	Correction Type	Correction Order
479 - 505	θ_{scat}	4
	Y1_{pos}	4
	θ_{scat}	2
539 - 561	θ_{scat}	3
	Y1_{pos}	3
1016 - 1104	θ_{scat}	3
	Y1_{pos}	3
	θ_{scat}	2
1124 - 1278	θ_{scat}	3
	Y1_{pos}	3
	θ_{scat}	3

Table 4.2: Summary of the lineshape corrections for experiment PR240. The iterative corrections are listed in order of their application.

4.1.8 Peak-position mapping

In general, the focal-plane spectra produced with the K600 spectrometer exhibit drifting in position between runs. The dominant source of this drifting is the changes in the incident beam energy which produces changes in the kinetic energy of the outgoing ejectile and its corresponding trajectory. Whilst the changes in the magnetic fields of the K600 spectrometer do in principle affect the positional drift, this contribution is typically negligible (with respect to the aforementioned beam-fluctuations) if the magnets have been corrected cycled and stabilised.

In the past, simple zeroth-order offsets were used to compensate for this drifting. The well-defined resonances of ^{12}C show that such offsets are insufficient to simultaneously align all the peaks. This implies that the focal-plane spectra are not simply drifting by offsets, but rather that the entire focal-plane is being distorted as time passes. In other words, the ever-present higher-order optics of the spectrometer are revealed through the drifts of the beam conditions.

In order to simultaneously align multiple peaks, a higher order mapping is necessary. For each analysed dataset, a set of n well-defined peaks is selected. For each run of the dataset, a mapping is determined to map the positions of the chosen peaks onto those of the corresponding peaks of a reference run. The mapping is of the form:

$$x' = \sum_{i=0}^{n-1} \alpha_i x^i, \tag{4.14}$$

where x and x' are the original and mapped positions, respectively with the α_i coefficients being the parameters to be determined. In the case where only a single peak is used to compensate for the run-dependent drifting, a basic offset is implemented:

$$x' = x^1 + \alpha, \tag{4.15}$$

where α is the offset to be determined.

The lineshape-corrected focal-plane spectra for experiment PR240, with and without peak-position mapping, are displayed on Figure 4.29. The 0.994 mm dispersion of the mapped $\mathrm{X1_{posC}}$ spectrum (green) exhibits a 15.9% decrease with respect to the 1.18 mm dispersion of the unmapped $\mathrm{X1_{posC}}$ spectrum (blue).

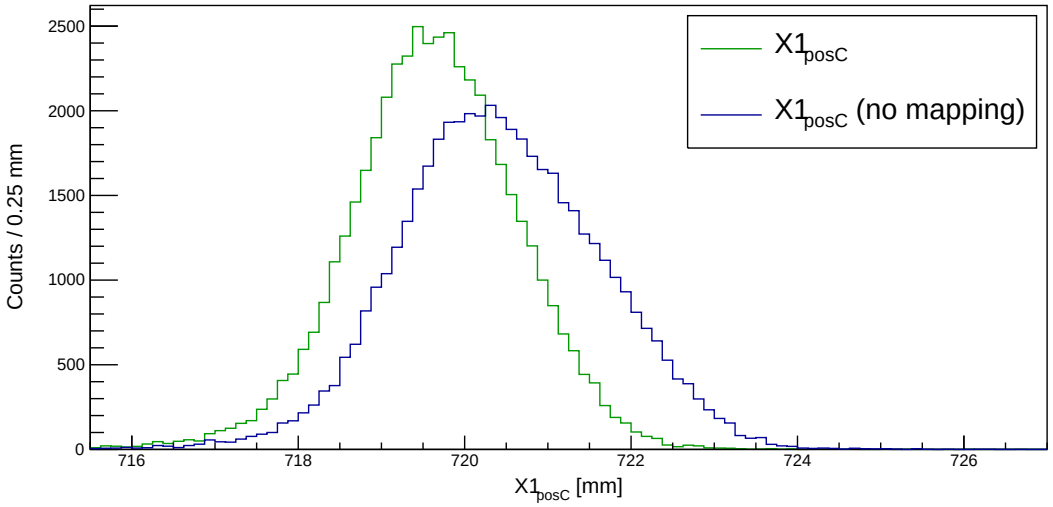

Figure 4.29: The lineshape-corrected focal-plane spectra for experiment PR240, with and without peak-position mapping, are displayed in green and blue, respectively. These spectra correspond to a subset of the data from experiment PR240.

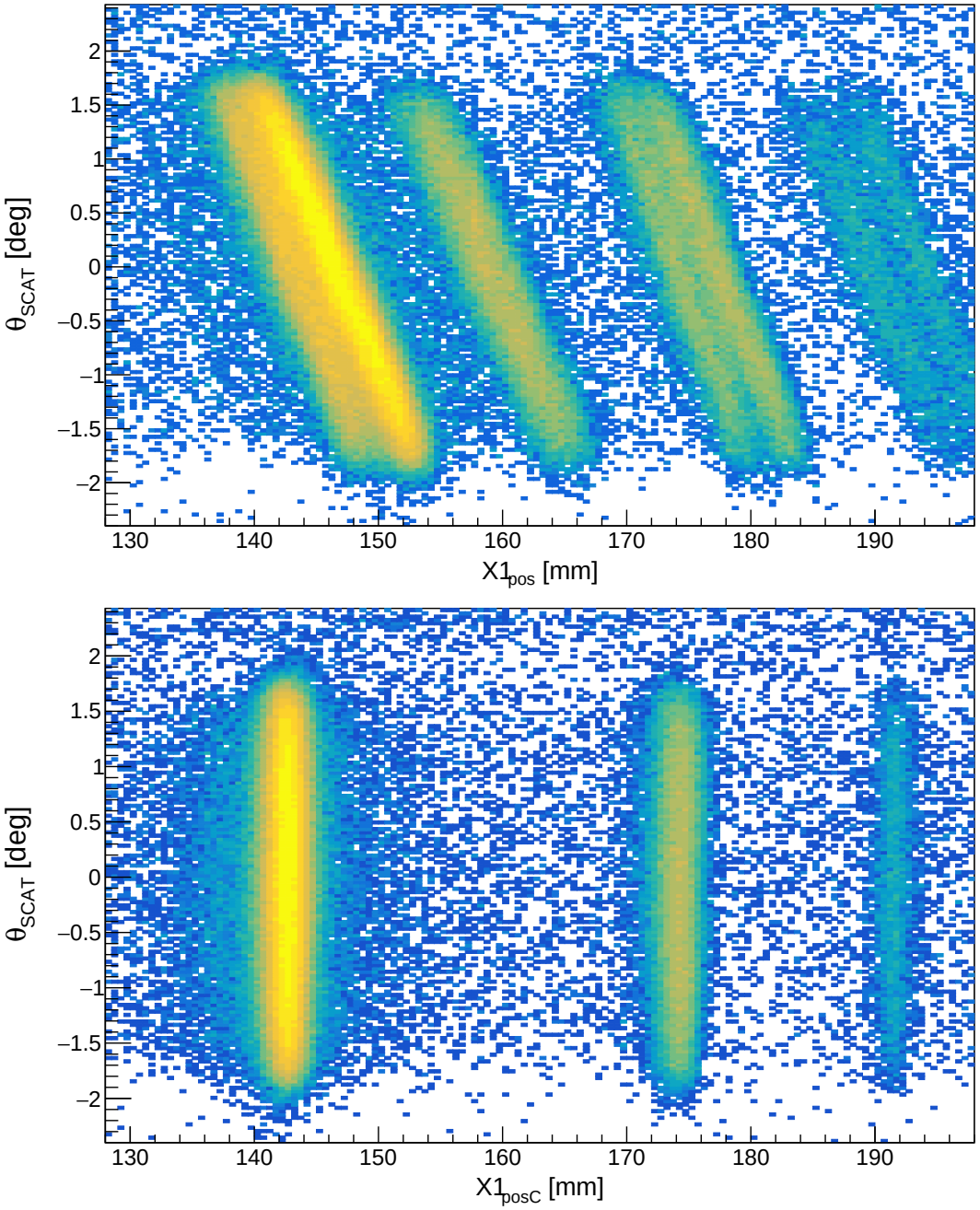

Figure 4.30: The effect of both lineshape corrections and peak-position mapping, illustrated by the difference between the uncorrected (top panel) to the lineshape corrected and peak-position mapped lineshapes (bottom panel).

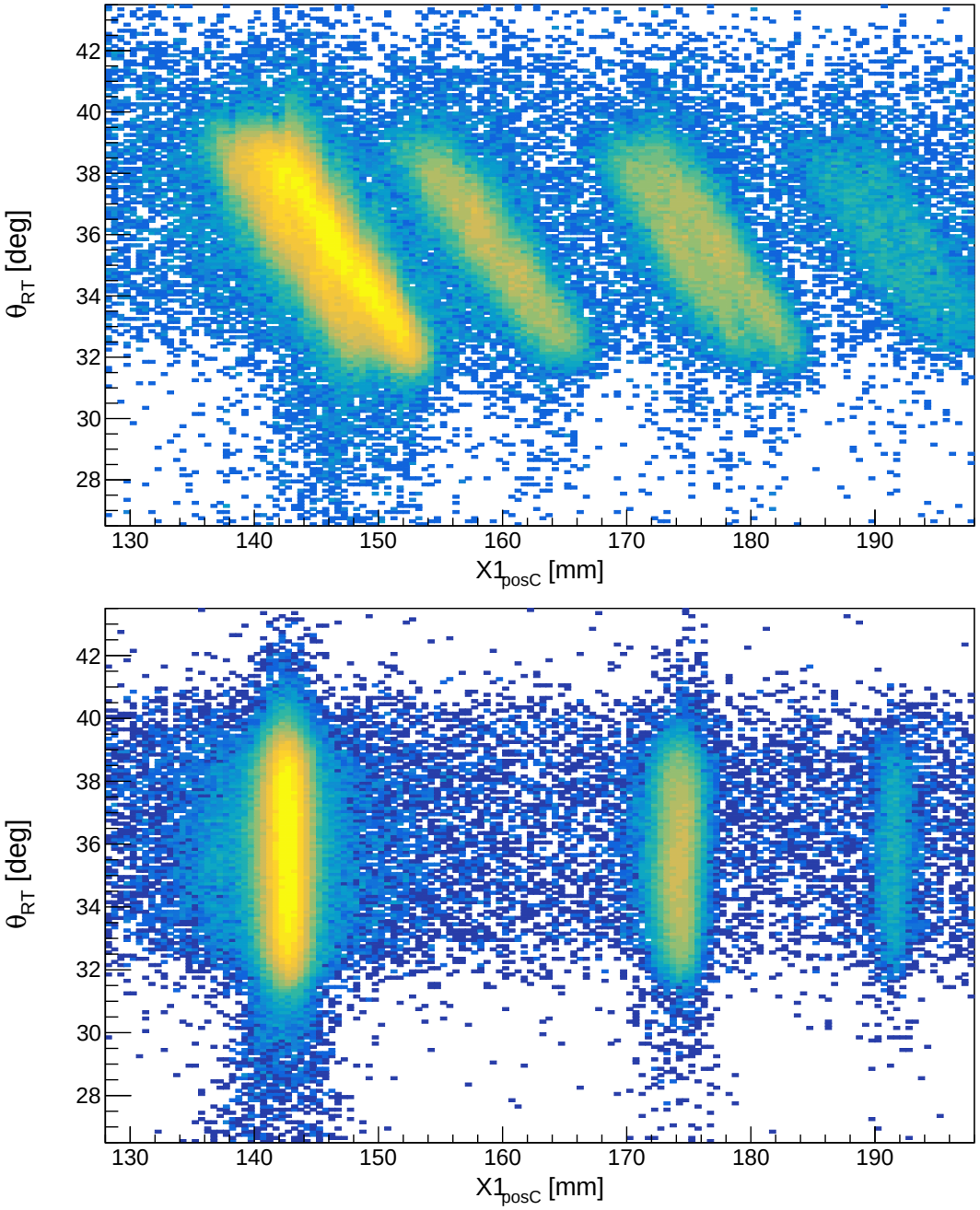

Figure 4.31: The effect of both lineshape corrections and peak-position mapping, illustrated by the difference between the uncorrected (top panel) to the lineshape corrected and peak-position mapped lineshapes (bottom panel).

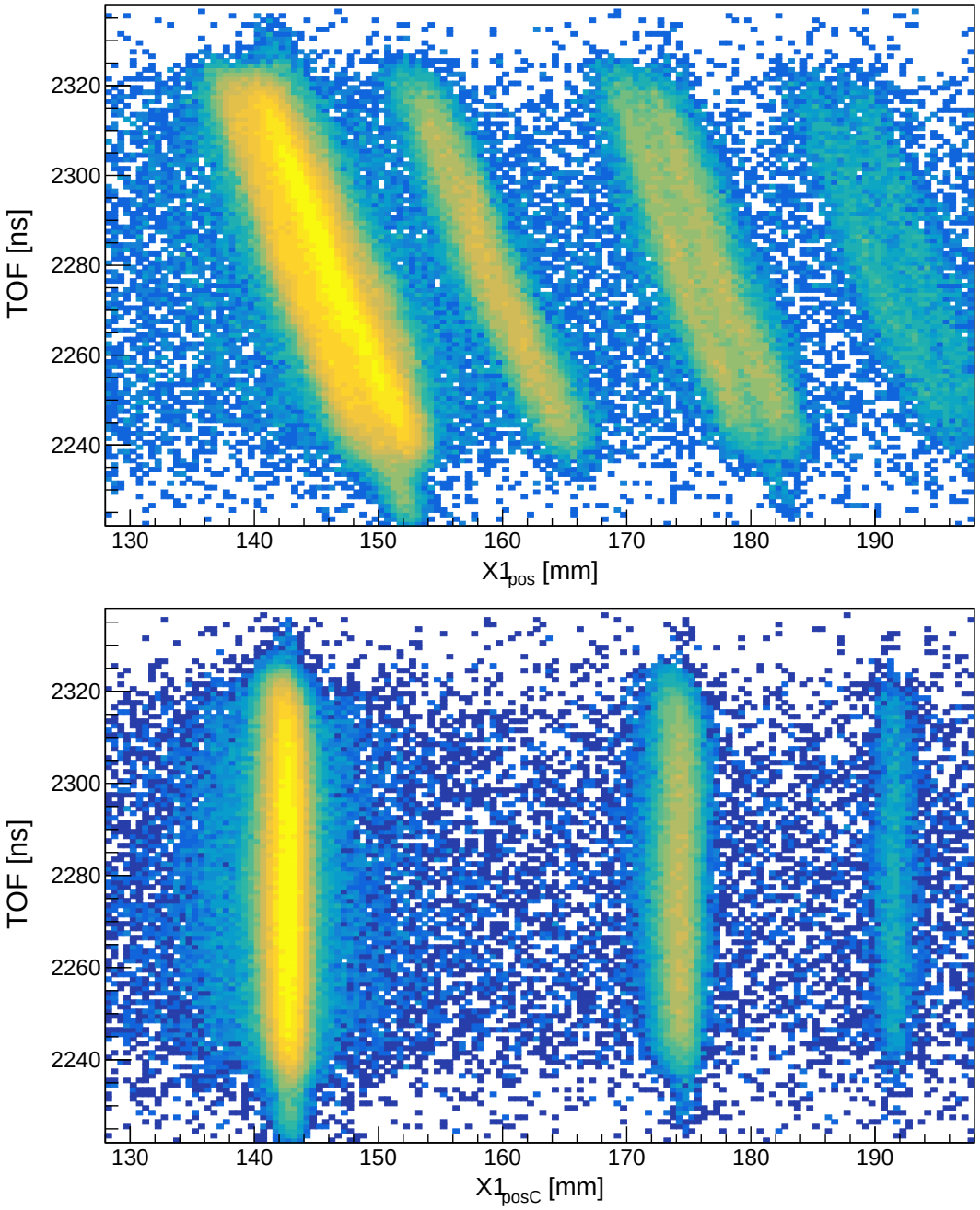

Figure 4.32: The effect of both lineshape corrections and peak-position mapping, illustrated by the difference between the uncorrected (top panel) to the lineshape corrected and peak-position mapped lineshapes (bottom panel).

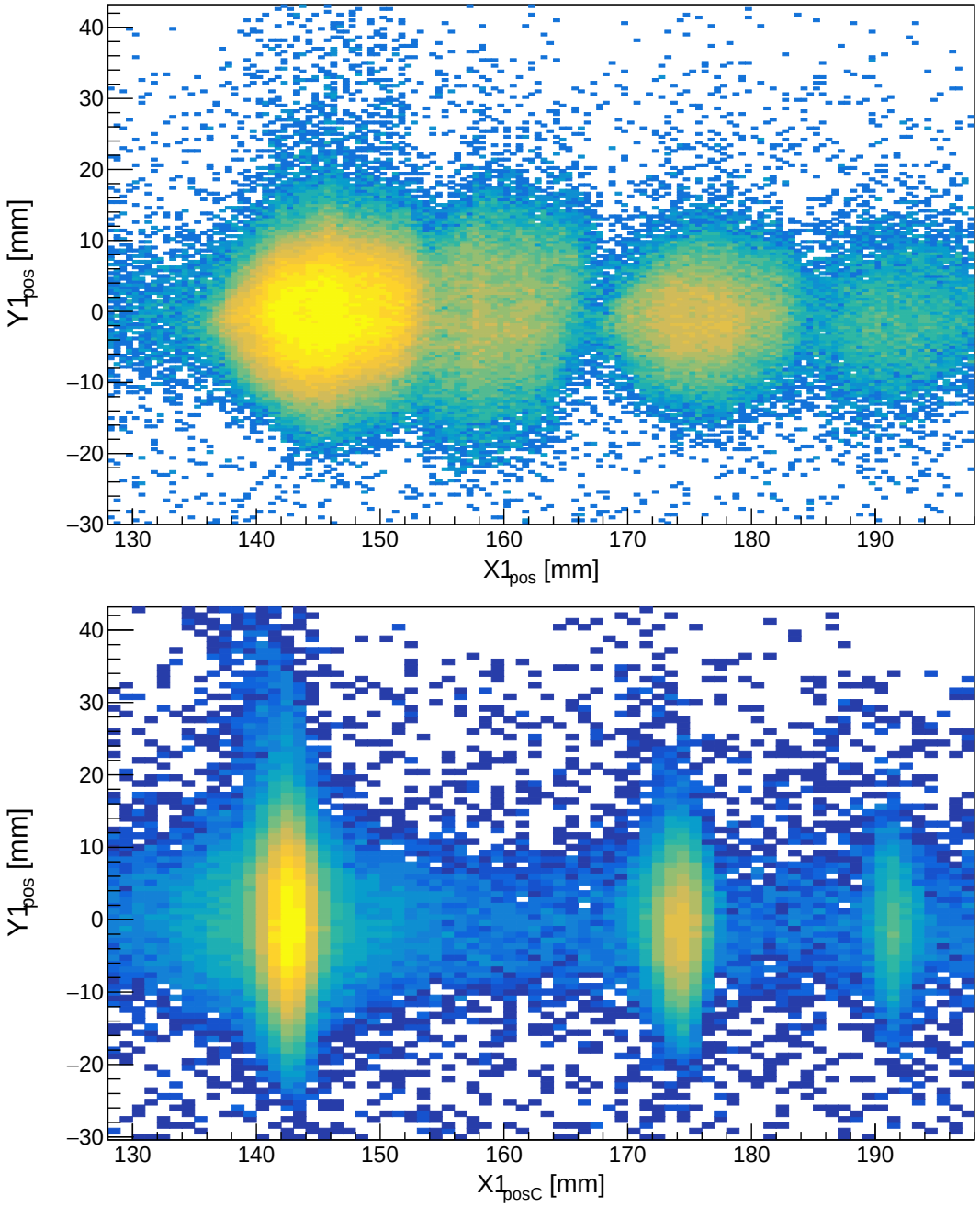

Figure 4.33: The effect of both lineshape corrections and peak-position mapping, illustrated by the difference between the uncorrected (top panel) to the lineshape corrected and peak-position mapped lineshapes (bottom panel).

4.1.9 The improvements of the TLC and SBR algorithms

The improvements of the TLC lineshape correction and the SBR raytracing algorithm are presented in Figure 4.34 and summarised in Table 4.3. The lineshape correction with TLC, which maps $X1_{pos}$ to $X1_{posC}$, yields a 66% decrease in the dispersion. The corrected focal-plane position obtained with the new SBR raytracing algorithm, $X1_{posC}$, exhibits a 3.0(7)% decrease in the dispersion with respect to $X1_{posC}$ (old).

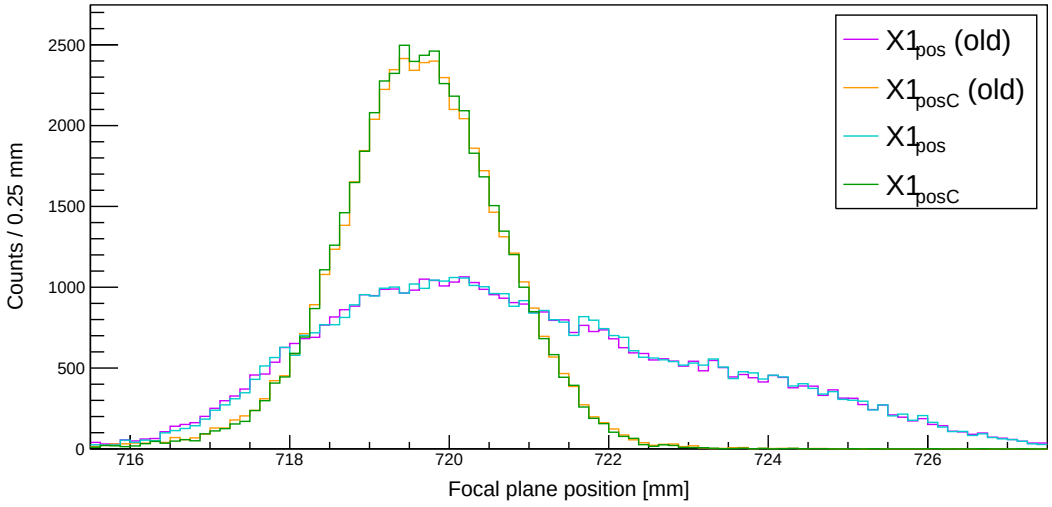

Figure 4.34: Comparison of the focal-plane dispersions of $X1_{pos}$ (old), $X1_{posC}$ (old), $X1_{pos}$ and $X1_{posC}$.

Focal-plane Position	Dispersion [mm]	E_x FWHM [keV]
$X1_{pos}$ (old)	2.36*	221*
$X1_{posC}$ (old)	0.809(4)	75.7(8)
$X1_{pos}$	2.34*	219*
$X1_{posC}$	0.785(4)	73.4(8)

Table 4.3: Summary of the focal-plane dispersions of the X1 wire plane for experiment PR240. *These values were not determined through a fit, but directly from the binned data as the uncorrected focal-plane positions ($X1_{pos}$ and $X1_{posC}$) yield highly irregular lineshapes.

4.1.10 Momentum Calibration

In principle, the ion optics of the spectrometer dictate that the momentum of an ejectile detected by a VDC is related to the associated focal-plane position through a second-order polynomial:

$$p = \alpha_2 x^2 + \alpha_1 x + \alpha_0, \tag{4.16}$$

where x and p and the focal-plane position and relativistic momenta of the ejectile, respectively and α_0, α_1 and α_2 are the mapping parameters to be determined. This momentum is then used to infer the excitation energy of the recoil nucleus. The focal-planes of magnetic spectrometers are often characterised by the radius of curvature of the ejectile with the relation:

$$B\rho = \frac{p}{q} \tag{4.17}$$

where B is the magnetic field strength, ρ is the radius of curvature, p is the ejectile momentum and q is the charge of the ejectile. Since the ejectiles used for the calibration of each dataset all have an identical charge state, a calibration of ρ is equivalent and unnecessary.

Advances in both the new TLC algorithm (see Section 4.1.7) and the new peak-position mapping algorithm (see Chapter 4.1.8) reveal that the second-order mapping of Equation 4.16 is inadequate to describe the ion optics of the spectrometer. TLC shows many cases where more than 3 reference peaks are necessary to remove the correlation with respect to a particular variable. Similarly, the peak-position mapping algorithm shows a significant number of cases where more than 3 reference peaks for peak alignment between runs. This implies that due to the ion optics of the K600 spectrometer, the focal-plane positions exhibit higher-order correlations with the corresponding ejectile momenta. Since the nuclear structure of ^{12}C exhibits many intrinsically narrow and well-separated resonances across the entire excitation-energy range of interest of $E_x \approx$ 7-16 MeV, a higher order mapping is required to map $\mathrm{X1}_{\mathrm{posC}}$ to ejectile momentum. This is confirmed by a test where only second-order momentum calibrations were used for the analysed datasets. Under such conditions, there are non-negligible shifts in excitation energy between equivalent resonances.

For each analysed dataset, the well-defined resonances which correspond to ^{12}C are identified for momentum calibration. For each set of n peaks, the momentum mapping takes the generalised polynomial form of Equation 4.16:

$$p = \sum_{i=0}^{n-1} c_i x^i, \tag{4.18}$$

where x and p are the focal-plane position and relativistic momenta of the ejectile, respectively and the α_i's are the mapping parameters to be determined. Since the aforementioned higher-order components of the beam-optics

can vary between experiments, the momentum calibrations are performed with no degrees of freedom in order to ensure consistent excitation-energy spectra between the various datasets.

Relativistic binary kinematics dictates that if the masses of all the reaction components are known and the kinetic energies of the projectile, target nucleus and ejectile can be determined, the kinetic and excitation energy of the recoil nucleus can be inferred [90]. In the following formalism, the projectile, target, ejectile and recoil nuclei are denoted with indices 0, 1, 2 and 3, respectively. For a stationary target and an incident beam energy of T_0, the total energy of the initial system (E_i) is given by:

$$E_i = E_0 + m_1c^2 = T_0 + (m_0 + m_1)c^2. \tag{4.19}$$

The total energy conservation of the reaction can be expressed as

$$E_i + Q = E_2 + E_3 + E_x = E_{tot.} + E_x, \tag{4.20}$$

where $Q = (m_0 + m_1 - m_2 - m_3)\,c^2$, E_x is the excitation energy of the reaction products and $E_{tot.}$ is the sum of the kinetic and mass energies of the reaction products. E_x can be directly interpreted as the excitation energy of the recoil nucleus as the ejectiles of interest for the experiments relevant to this thesis can be assumed to remain in their respective ground states.

Momentum conservation imposes the following constraints:

$$p_0 = p_2 \cos\theta_2 + p_3 \cos\theta_3 \tag{4.21}$$

and

$$0 = p_2 \sin\theta_2 - p_3 \sin\theta_3, \tag{4.22}$$

where θ_2 and θ_3 are the polar scattering angles of the ejectile and recoil nuclei, respectively. Algebraic manipulation yields a second order equation in E_2:

$$\begin{aligned} E_2^2\left(4p_0^2c^2\cos^2\theta_2 - 4E_{tot.}^2\right) + E_2\left(4E_{tot.}^3 - p_0^2c^2E_{tot.} + 4m_2^2c^4E_{tot.} - 4m_3^2c^4E_{tot.}\right) \\ + \left(2p_0^2c^2E_{tot.}^2 - 2m_2^2c^4E_{tot.}^2 + 2m_2^2c^4p_0^2c^2 + 2m_3^2c^4E_{tot.}^2 - 2m_3^2c^4p_0^2c^2\right. \\ \left. + 2m_3^2c^4m_2^2c^4 - E_{tot.}^4 - p_0^4c^4 - m_2^4c^8 - m_3^4c^8 - 4m_2^2c^4p_0^2c^2\cos^2\theta_2\right) = 0. \end{aligned} \tag{4.23}$$

which is trivially solved with the general solution of a quadratic equation to determine the total energy of the recoil nucleus, E_3:

$$E_3 = E_{tot.} - E_2. \tag{4.24}$$

The excitation energy of the recoil nucleus, E_x, is thus given by

$$E_x = E_0 + E_1 + Q - E_2 - E_3. \tag{4.25}$$

The momentum calibration of the $X1_{posC}$ focal-plane position for experiment PR240 is displayed in Figure 4.35 and the associated parameters are summarised in Table 4.4.

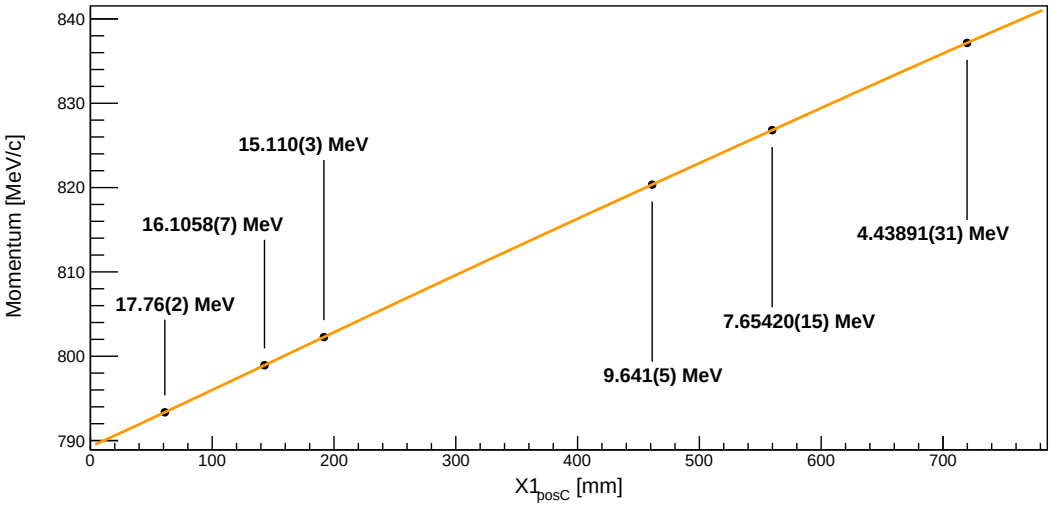

Figure 4.35: Focal-plane momentum calibration for experiment PR240. The momentum (vertical) and focal-plane position (horizontal) error bars are smaller than the symbol size. The reference resonance energies (from the NNDC) are indicated.

Correction parameter	Parameter Value	Unit
c_0	7.89272×10^{2}	MeV/c
c_1	6.56469×10^{-2}	MeV/c/mm
c_2	2.27231×10^{-5}	MeV/c/mm^2
c_3	-7.7232×10^{-8}	MeV/c/mm^3
c_4	1.00555×10^{-10}	MeV/c/mm^4
c_5	-4.83009×10^{-14}	MeV/c/mm^5

Table 4.4: The momentum calibration parameters for experiment PR240 (see Equation 4.18).

4.2 Excitation energy spectra

The excitation-energy spectrum of ^{12}C from experiment PR240 is presented in Figure 4.36 and the valid acceptance range of the measurement, determined by the region with full solid-angle coverage by the focal-plane detector system, is depicted with dashed lines. The $E_x \approx$ 7-16 MeV range of interest is highlighted in Figure 4.37.

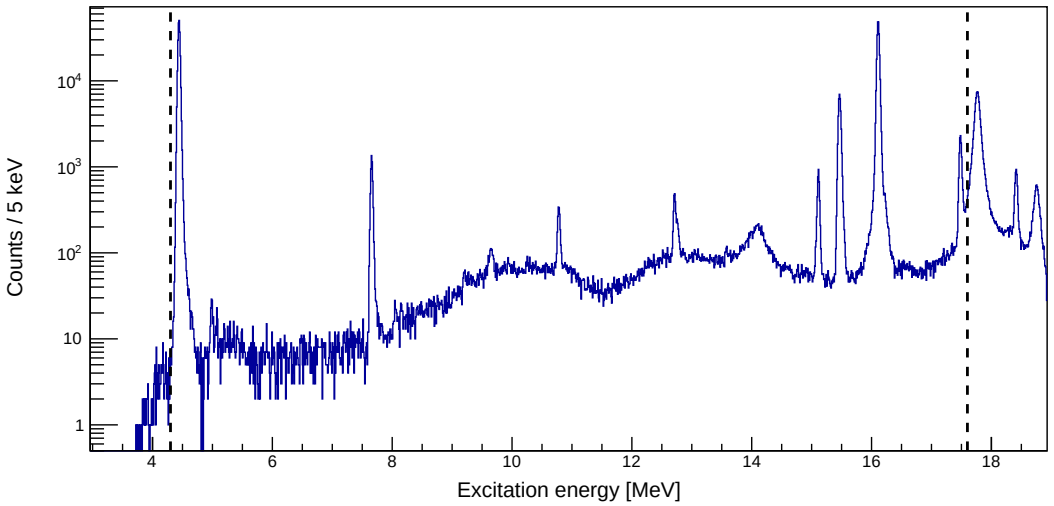

Figure 4.36: The full excitation energy spectrum of ^{12}C from experiment PR240. The dashed lines depict the valid E_x range, determined by the region with full solid-angle coverage by the focal-plane detector system.

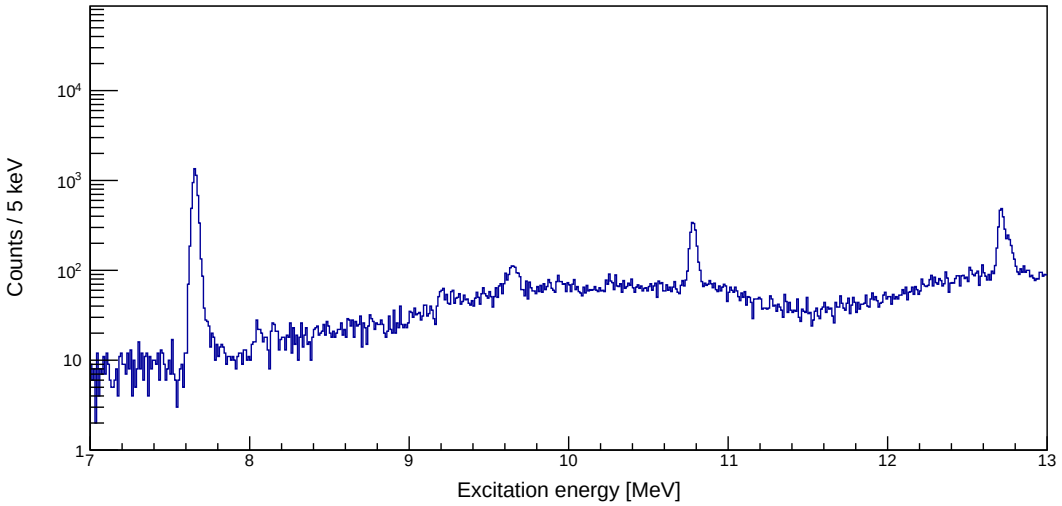

Figure 4.37: The excitation energy spectrum of ^{12}C from experiment PR240, highlighting the $E_x \approx$ 7-13 MeV range of interest.

4.3 CAKE Analysis

The detection of coincident particle decays enables the discrimination between different decay modes if the decay particles exhibit different correlations for the energies deposited in the CAKE (E_{Si}) and/or TOF between the target and the CAKE (T_{Si}). The calibrations of the CAKE TDCs and ADCs are detailed in Sections 4.3.1 and 4.3.2.

4.3.1 CAKE Time (TDC) calibration

When a signal exceeds a certain threshold, an ECL signal for the associated channel is generated and sent to a TDC module of the DAQ. This ECL signal and the subsequent RF pulse form start and stop signals, respectively. The relative difference in time is then recorded for each triggered channel. The uncorrected and corrected CAKE TDC spectra are shown in Figures 4.38 and 4.39, respectively. The missing TDC channels correspond to the damaged/inactive channels of the CAKE, as summarised in Table 4.5. It is observed that the TDC calibration aligns the correlated peaks for each channel. By gating on the correlated peak situated at corrected TDC times of ≈ 0, the correlated CAKE events can be selectively observed. Conversely, by gating on the uncorrelated satellite peaks, the coincident background events can be gauged.

4.3.2 CAKE Energy (ADC) calibration

The uncalibrated ADC channels of the CAKE are presented in Figure 4.40. The CAKE was calibrated with a ^{228}Th source, as shown for a specific channel in Figure 4.42 and the relevant α decays are labelled. It is observed that there are some ADC channels without data which may result from a host of reasons. One common cause is damage to the bonding wires that electrically connect the anode/cathode to the p-/n-doped silicon. The missing ADC channels and their respective detector channels are summarised in Table 4.5. The spectrum for the calibrated ADC channels of the CAKE is presented in Figure 4.41. It is observed that the ADC calibration aligns the observed peaks which correspond to α decays from the ^{228}Th decay chain.

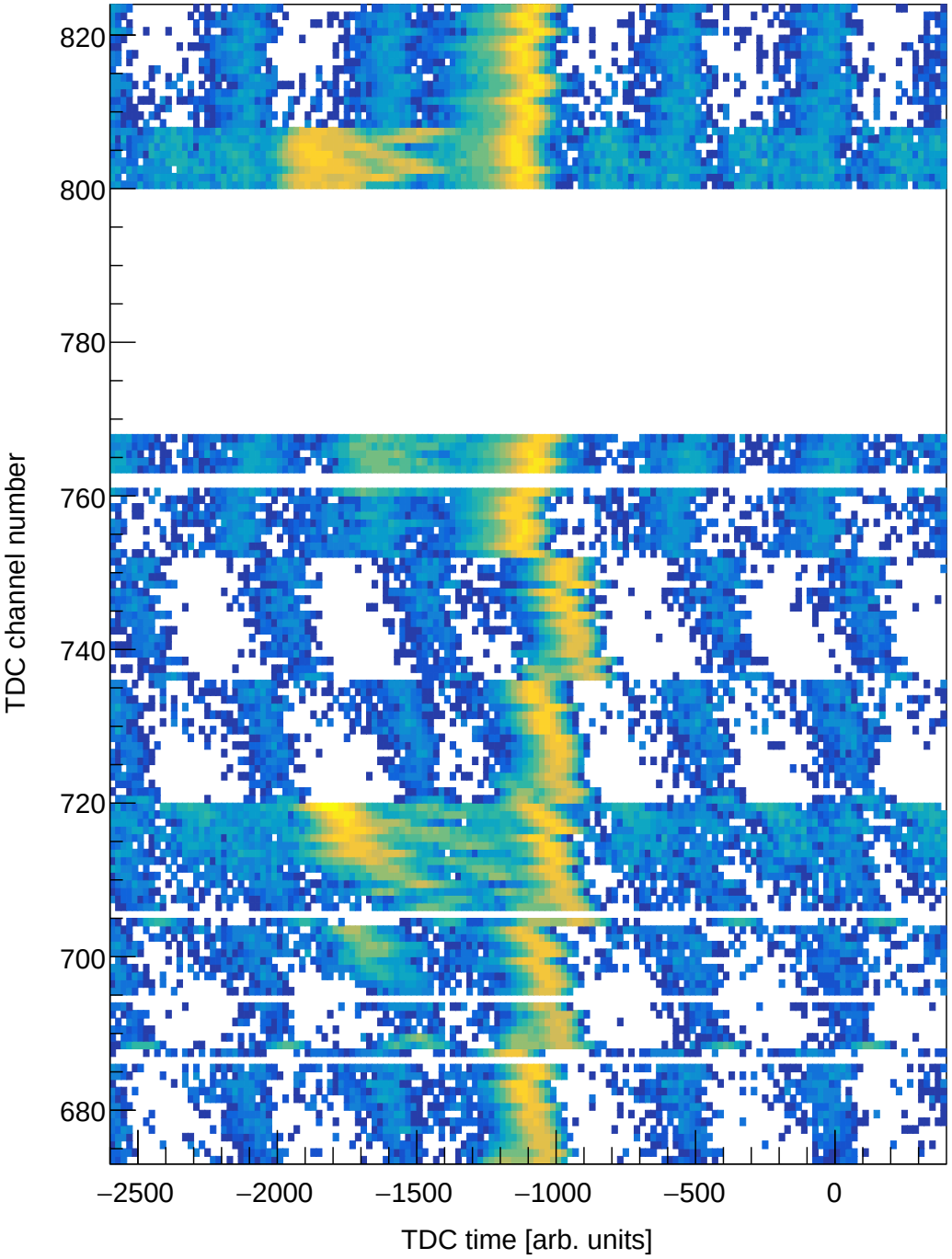

Figure 4.38: Spectrum of TDC channel number versus TDC uncalibrated reference time of the VDC wires for experiment PR240. The lack of TDC alignment produces a staggering between the TDC drift time distributions of the various channels. A display threshold of >50 has been imposed.

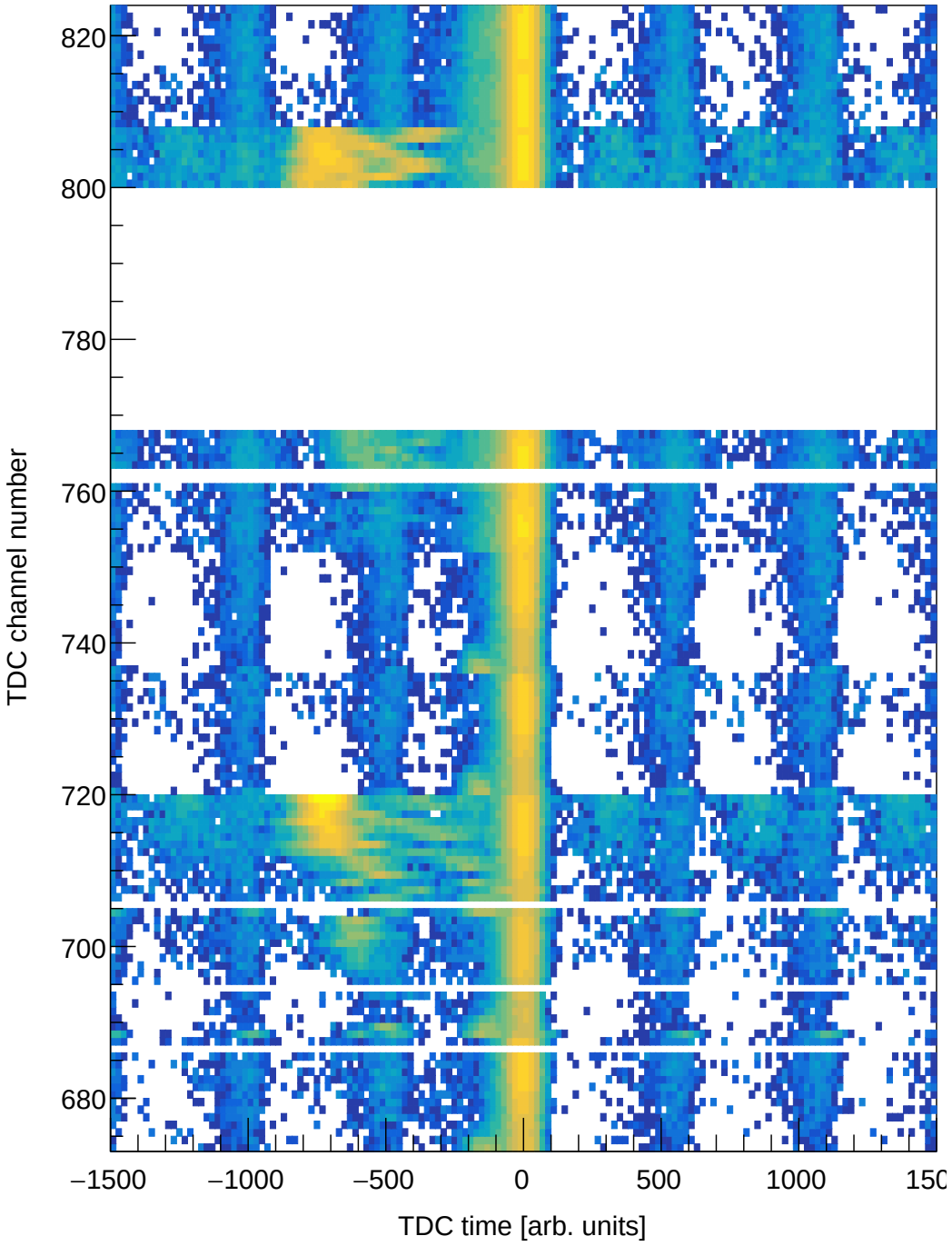

Figure 4.39: Spectrum of TDC channel number versus TDC calibrated reference time of the VDC wires for experiment PR240. A display threshold of >50 has been imposed.

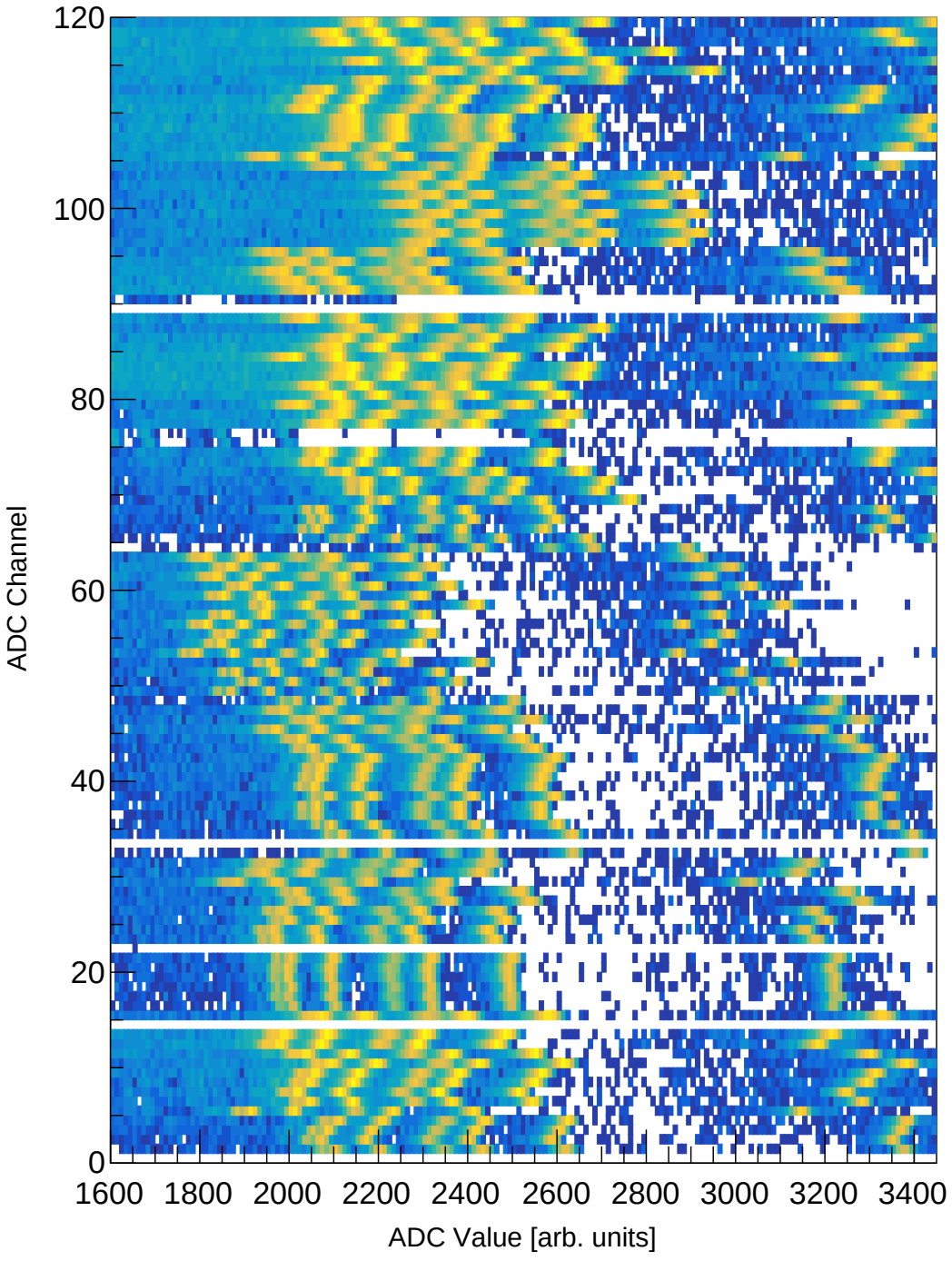

Figure 4.40: Uncalibrated ADC values of all the channels of the CAKE for ^{228}Th source.

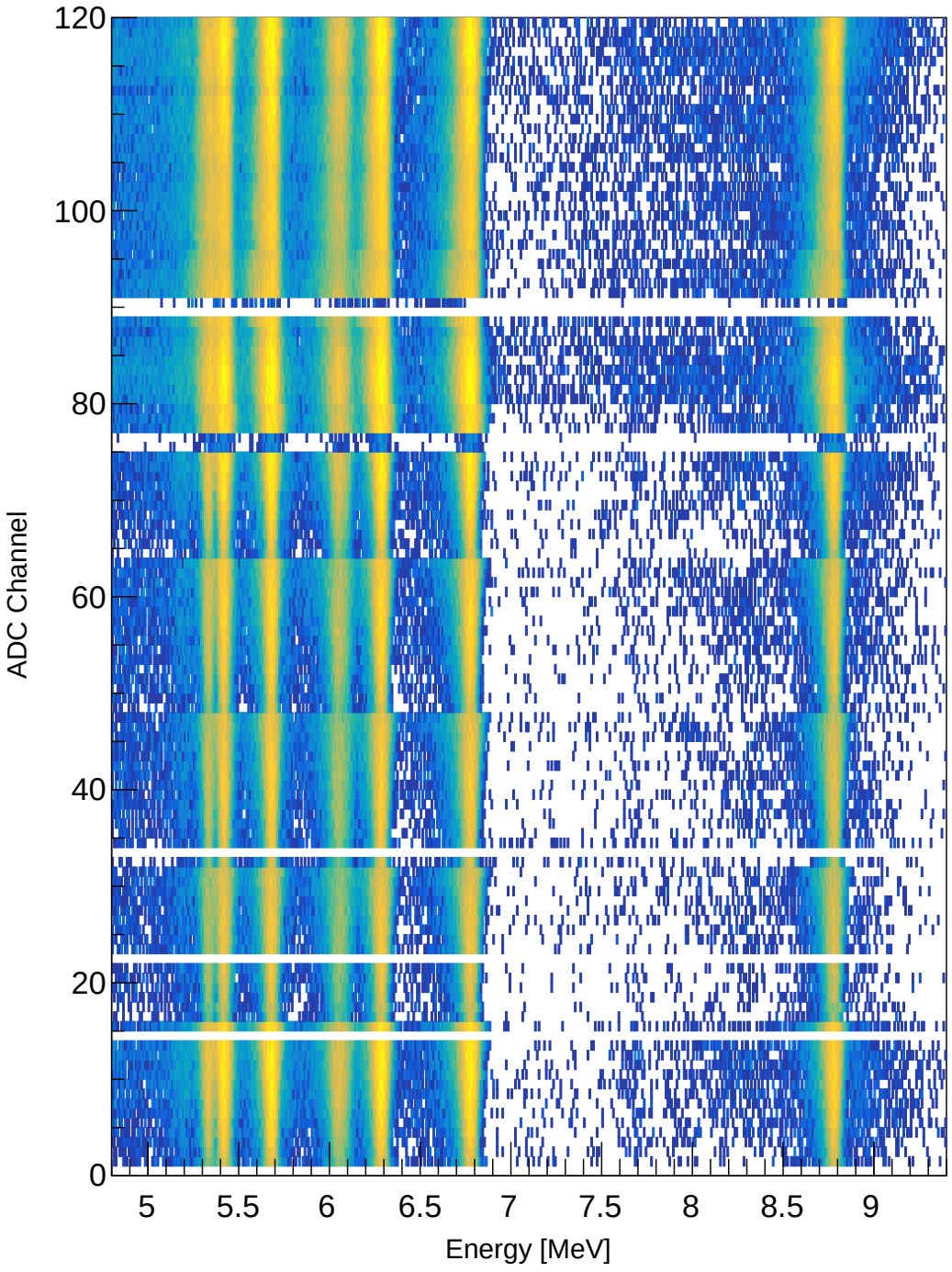

Figure 4.41: Calibrated ADC values of all the channels of the CAKE for ^{228}Th source.

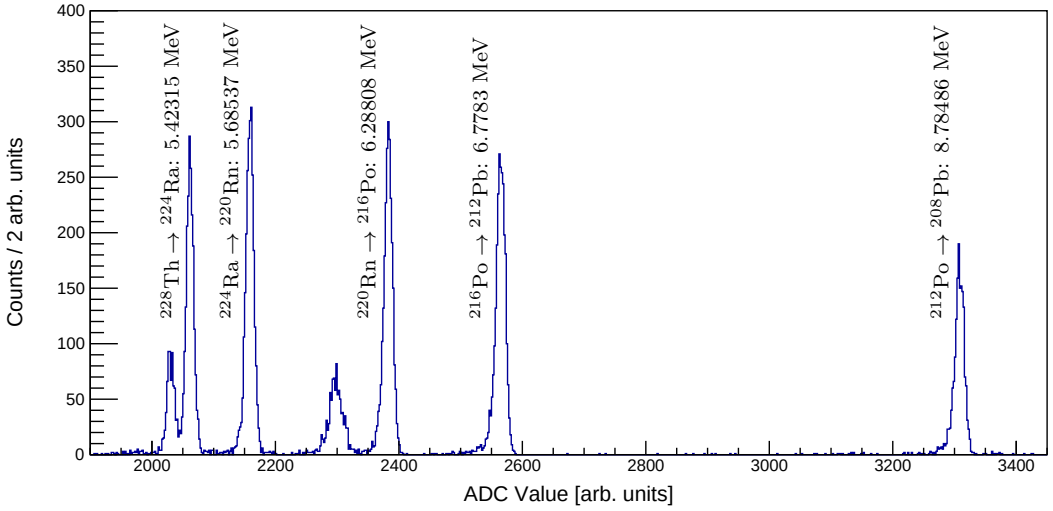

Figure 4.42: ^{228}Th source spectrum of ADC values for a single channel of the CAKE. The α decays used for the calibration are labelled on the corresponding peaks.

4.3.3 CAKE PID

The combination of event times detected by the CAKE and the excitation energy of the recoil nucleus enables particle discrimination. The corresponding PID spectrum with the raw silicon times (T_{Si}) on Figure 4.43 shows distinct but unresolved loci which correspond to α and proton decay particles which exhibit different T_{Si} values given their different masses. The raw silicon times are measured relative to the TOF of the ejectile which is subject to instability in the radio frequency of the cyclotron. An improved particle discrimination can be produced by using the difference between the raw silicon times and the TOF of the ejectile, as shown in Figure 4.44. The dashed lines show the corresponding cuts which can be used to selectively observe α and proton decay particles detected by the CAKE. The improved time resolution shows that the α-particle locus is composed of two separate loci. The locus at lower values of T_{Si} - TOF corresponds to α-particles from 0^+ in ^{12}C situated at 17.760(20) MeV.

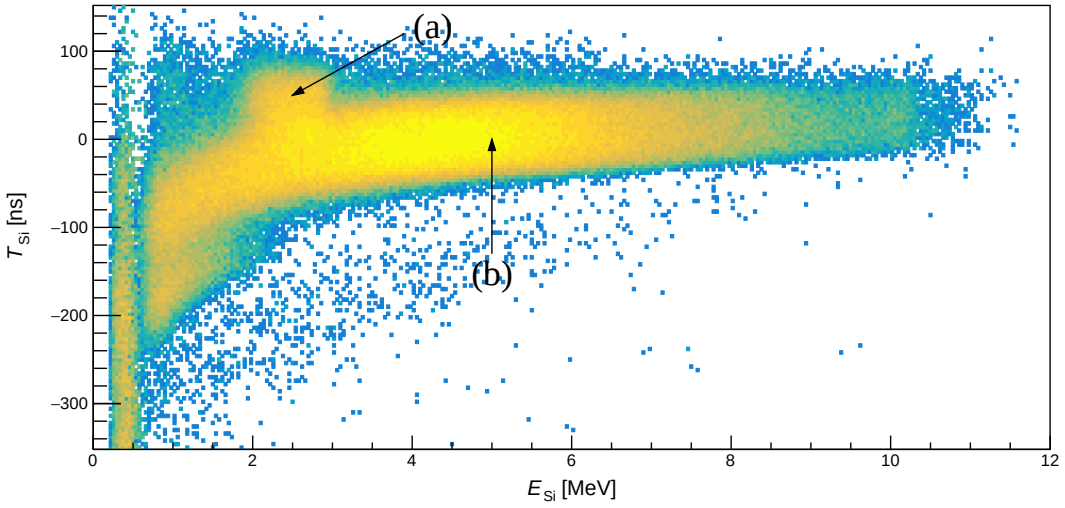

Figure 4.43: CAKE PID matrix of silicon time versus excitation energy.

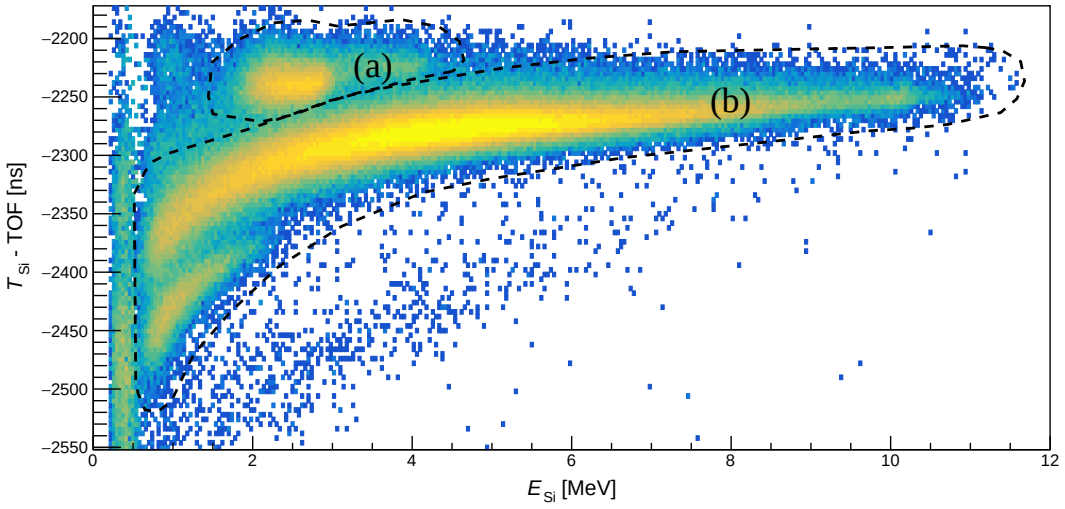

Figure 4.44: CAKE PID matrix of corrected silicon time versus excitation energy. The dashed lines represent the cuts for the p_0 (a) and α (b) decay modes.

4.3.4 CAKE Coincidence Matrices

The coincidence matrix of the silicon energy measured by the CAKE (E_{sil}) versus the excitation energy recoil nucleus determined by the focal-plane detector is presented in Figure 4.45 and the displayed red lines are to guide the eye towards the α_0 (a) and p_0 (c) loci which flank the broad α_1 locus (b). The coincidence matrix enables the discrimination between different charged-particle decay modes. Since the ^{12}C recoil nucleus exhibits a significant kinetic energy of $\approx$ 3.9 MeV for the ^{14}C$(p,t)^{12}$C reaction at $\theta_{\text{lab}} = 0°$ (experiment PR240), the kinetic energies of the subsequent decay particles depend strongly on the polar angle of decay. Consequently, the discrimination between various decay modes can be improved by employing the coincidence matrix for each ring of the CAKE, as presented in Figures 4.46 and 4.47. These cuts are used to generate the excitation-energy spectra for the inclusive (a), α_0 (b), α_1 (c) and p_0 (c) decay modes, as presented on Figure 4.48. It is observed that the α_0 decay mode completely dominates for the primary peak of the Hoyle state at $E_x = 7.654$ MeV which is unsurprising as all of the associated α_1 penetrabilities are negligibly small at this resonance energy (see Figure 2.10). However, the observation of the α_1 decay mode at excitation-energies as low as $E_x \approx 8$ MeV is noteworthy as the α_1 penetrabilities which assume an infinitely-narrow daughter state are all negligibly small below $E_x \approx 9$ MeV and therefore cannot reproduce the associated decay widths (see Figures 2.10 - 2.15). This qualitative result shows that the penetrability with finite-width daughter states, given by Equation 2.94, must be implemented to describe the lineshapes of ^{12}C.

As expected, the p_0 decay mode is only observed at excitation energies greater than $E_x \approx 16$ MeV due to the proton separation energy of 15.95668(1) MeV for ^{12}C. This confirms that only the α_0 and α_1 decay modes are relevant for the $E_x \approx$ 7-16 MeV excitation-energy region of interest for this work.

An unusual observation is that the 1^+_1 12.710(6) MeV state appears to decay through both the α_0 and α_1 decay modes. This should not be possible due to selection rules which prevent unnatural-parity states in ^{12}C from undergoing α_0 decay to the ground state in ^{8}Be, as discussed in Section 2.8.1.1. This shows that the α_0 and α_1 decay mode loci are not sufficiently well resolved, as can be seen for this narrow state in Figures 4.46 and 4.47. The α_0 excitation-energy spectrum presented in Figure 4.51, which is generated through the reconstruction of the ^{8}Be nucleus, is more selective against the α_1 decay mode and consequently, the decay of this 1^+_1 resonance is correctly not observed.

It is worth noting that the α_0 excitation-energy spectrum on panel (b) is the only spectrum analysed for this thesis that exhibits a well-resolved peak for the 1^-_1 ^{12}C state situated at 10.847(4) MeV as it is typically submerged within the adjacent overlapping resonances. This confirms that this resonance must be included in the R-matrix fit of this excitation-energy region.

In summary, the spectra on Figure 4.48 provide a qualitative understanding

of the relative strengths between the widths of the α_0 and α_1 decay modes, however these spectra are not simultaneously fitted with the primary R-matrix analysis of this work as the CAKE efficiency exhibits a complex dependence on the kinematics of the decay particles. Moreover, the calculated efficiencies for anisotropic decays require the calculation/assumption of m-state population ratios. This is beyond the scope of this work which is focused on investigating monopole strengths in ^{12}C.

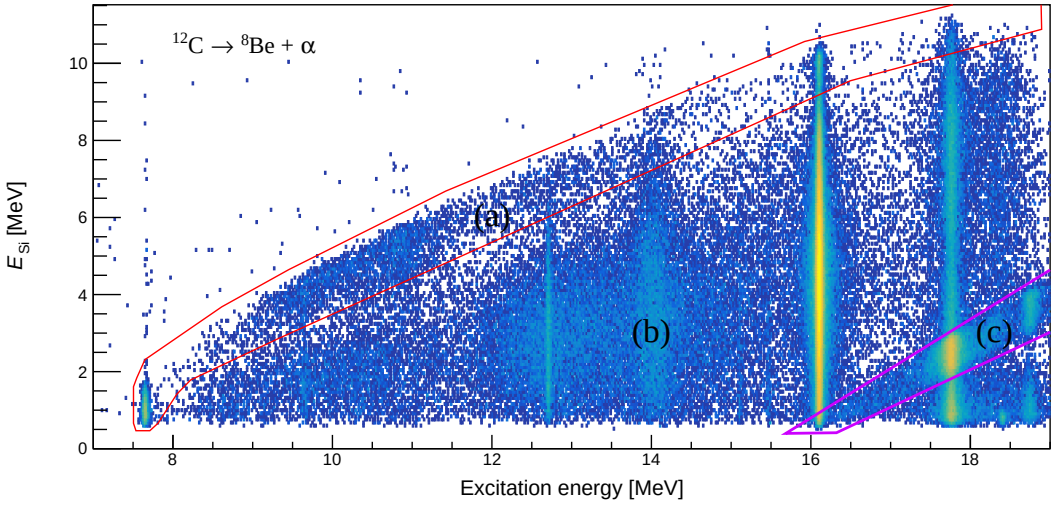

Figure 4.45: The coincidence matrix of silicon energy versus the excitation energy of the recoil nucleus for the entire CAKE. The red and violet lines indicate the α_0 (a) and p_0 (c) decay mode loci, respectively, which flank the broad α_1 (b) locus.

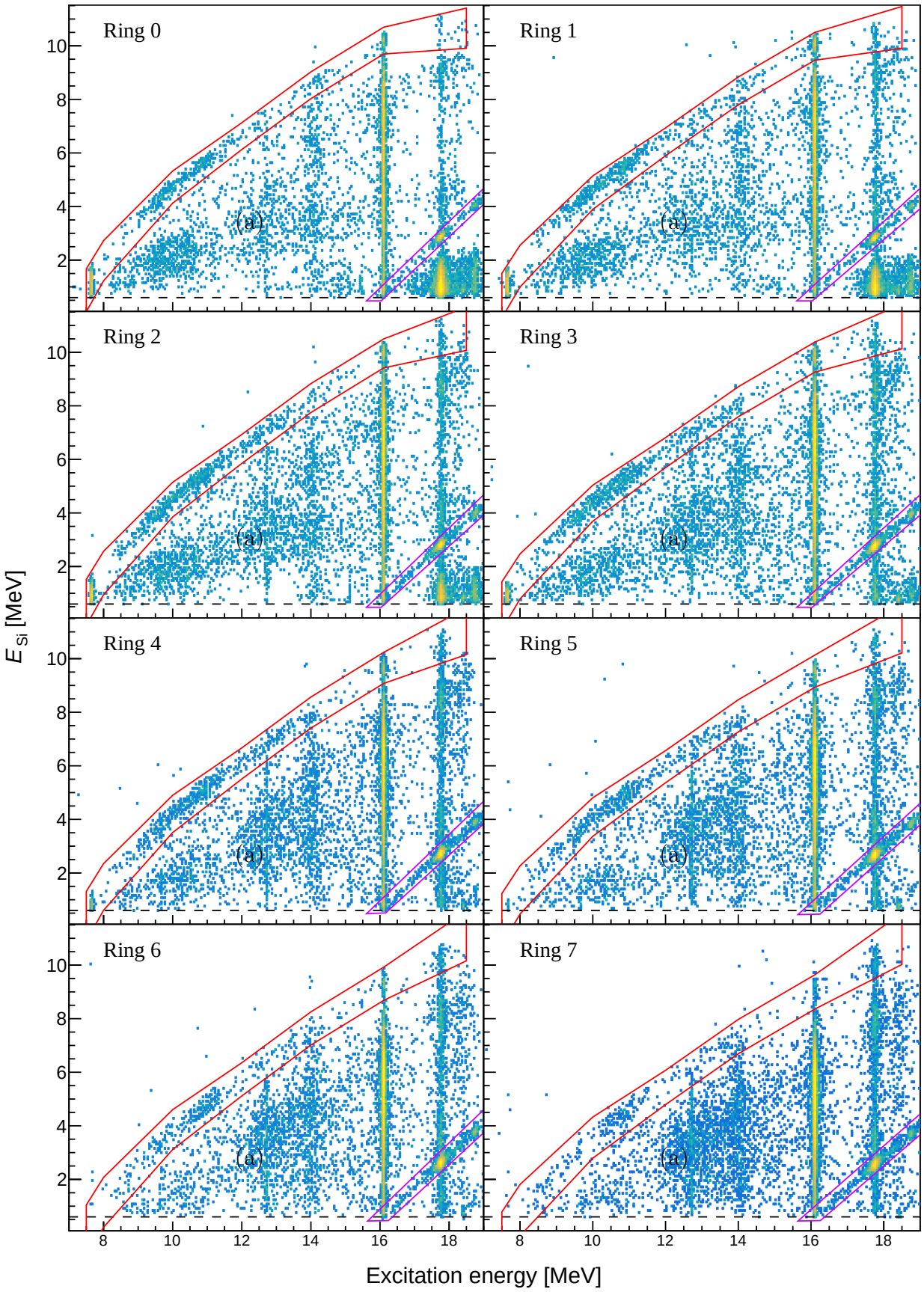

Figure 4.46: The matrix of silicon energy versus excitation energy for rings 0-7 of the CAKE. The red and violet lines indicate the α_0 and p_0 decay mode loci, respectively, which flank the broad α_1 (a) locus. The horizontal dashed lines indicate the 600 keV electronic threshold.

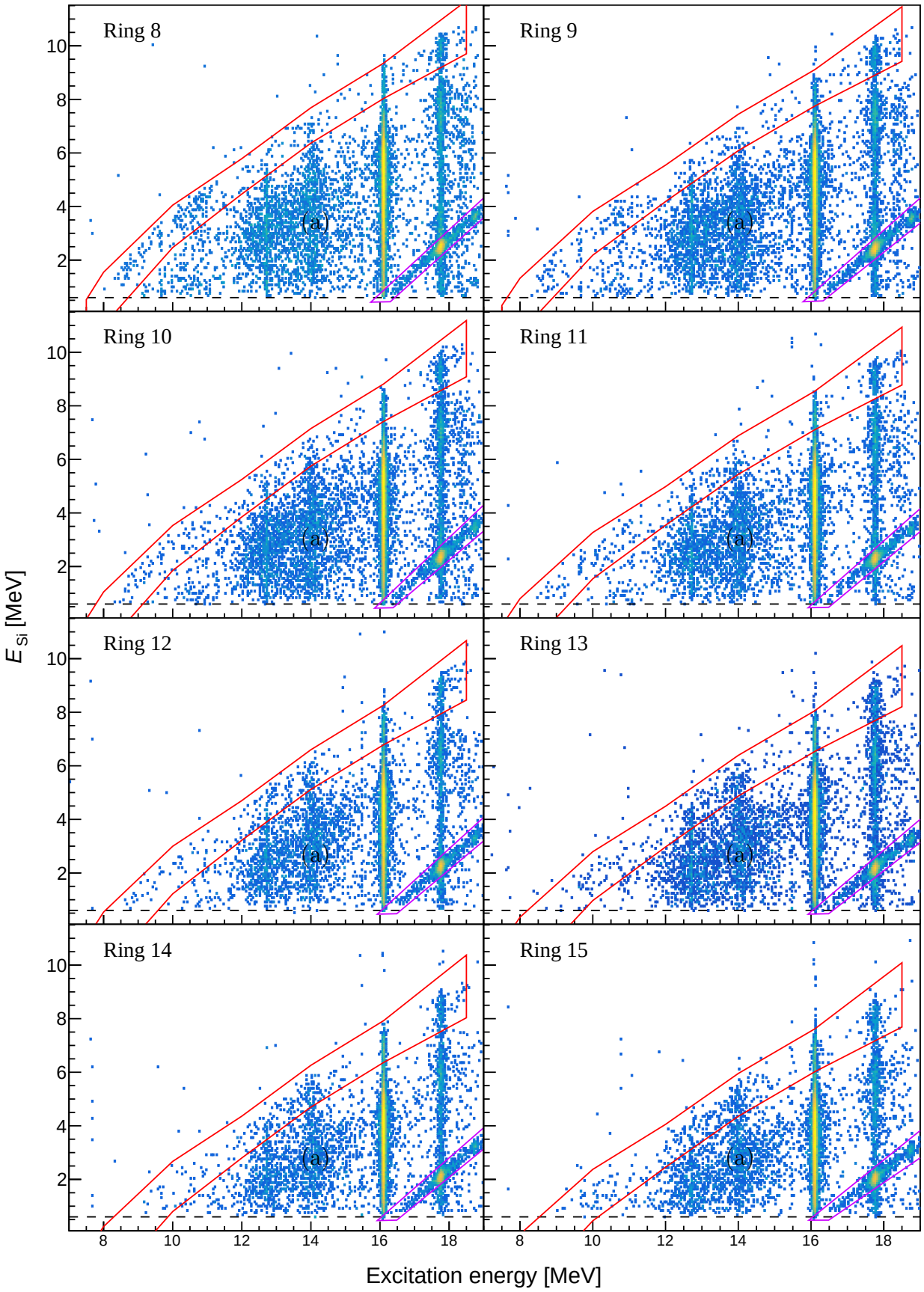

Figure 4.47: The matrix of silicon energy versus excitation energy for rings 8-15 of the CAKE. The red and violet lines indicate the α_0 and p_0 decay mode loci, respectively, which flank the broad α_1 (a) locus. The horizontal dashed lines indicate the 600 keV electronic threshold.

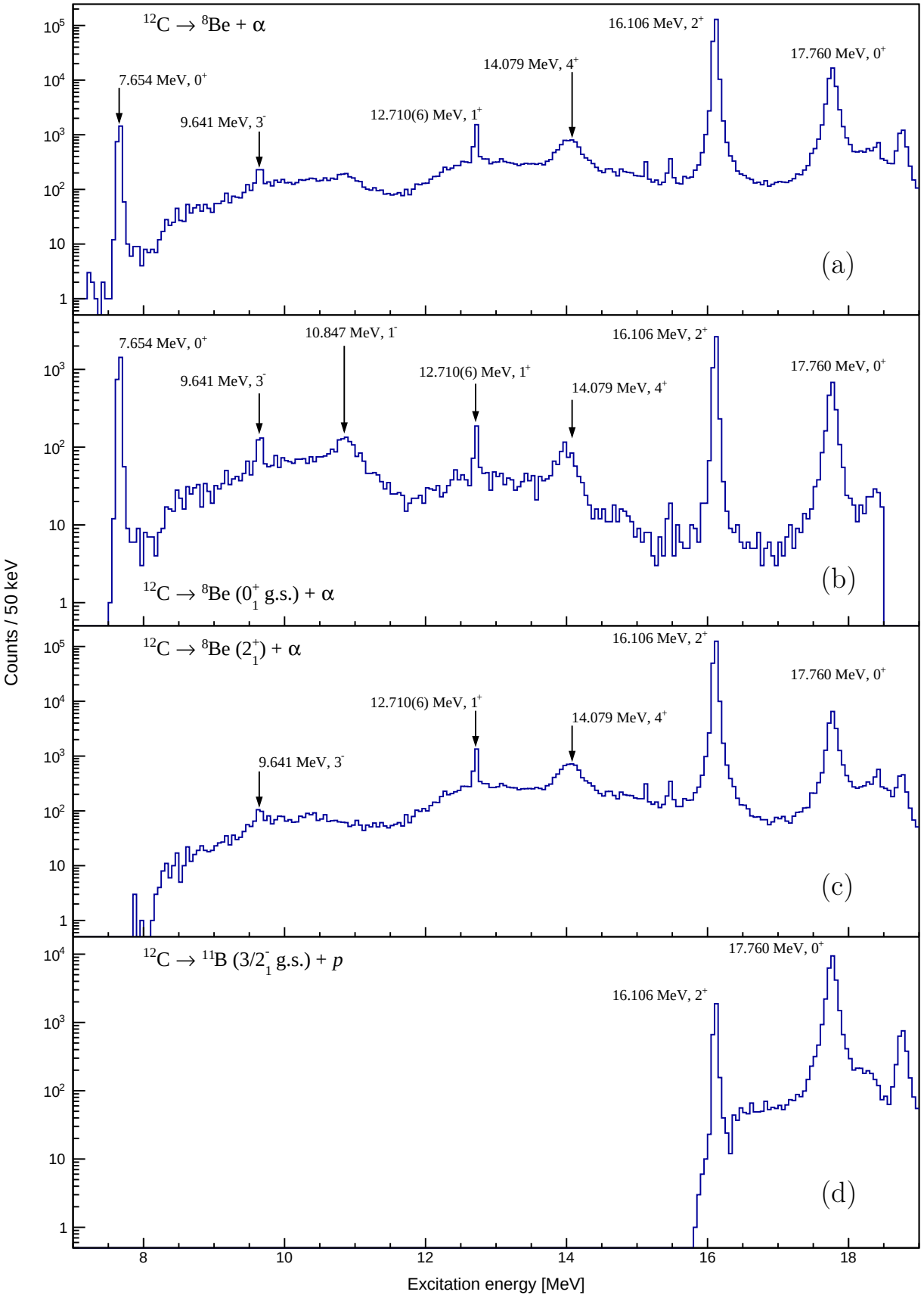

Figure 4.48: The excitation-energy spectra for the inclusive (a), α_0 (b), α_1 (c) and p_0 (d) decay modes detected by the entire CAKE. The ^{12}C states with well-resolved peaks are indicated.

4.3.5 Indirect ^{8}Be measurement

The ground state of ^{8}Be is unbound with respect to α-particle emission with a Q-value of 91.84(4) keV and a width of 5.57(25) eV. Consequently, ^{8}Be is not directly detected but it can be indirectly observed through either missing-energy of relative-momentum reconstruction as described in Sections 4.3.5.1 and 4.3.5.2, respectively. The excitation-energy spectra of ^{8}Be determined with these two methods, presented in Figures 4.49 and 4.50, are found to be equivalent and can be used to determine whether two coincidentally detected α-particles are emitted from the same ^{8}Be parent nucleus.

4.3.5.1 Missing-energy reconstruction

Linear-momentum conservation dictates that for an n-body decay, the momentum vector of the parent nucleus, $\mathbf{P}_{\text{parent}}$, is given by the sum of the momenta of the decay particles:

$$\mathbf{P}_{\text{parent}} = \sum_{i}^{n} \mathbf{P}_i, \tag{4.26}$$

where $\mathbf{P}_i$ is the momentum vector of the i^{th} decay particle. The total energy of the parent particle is given by

$$E_{\text{parent}} = \mathbf{P}^2_{\text{parent}}/2m_{parent}. \tag{4.27}$$

The energy of the decay, which is equivalent to the excitation energy of the parent nucleus is the decay particles can be assumed to be inert, is given by

$$E_{\text{decay}} = \left(\sum_{i}^{n} E_i\right) - E_{\text{parent}}. \tag{4.28}$$

The excitation energy spectrum of ^{8}Be determined with this method is presented in Figure 4.49.

4.3.5.2 Relative-momentum reconstruction

For the case of ^{8}Be which predominantly decays through α emission for excitation energies below $E_x \approx 17$ MeV, the relative momentum between two α decay particles, denoted by 0 and 1, is given by

$$\mathbf{P}_{\text{rel}} = \mathbf{P}_0 - \mathbf{P}_1. \tag{4.29}$$

This relative momentum is Lorentz invariant and therefore the kinetic energy of the two α-particles can be determined in the inertial reference frame of the ^{8}Be nucleus as:

$$E_{\text{decay}} = 2\frac{(\mathbf{P}_{\text{rel}}/2)^2}{2m_\alpha} = \mathbf{P}_{\text{rel}}^2/(4m_\alpha), \tag{4.30}$$

where m_α is the mass of the α-particle. The excitation energy spectrum of ^{8}Be determined with this method is presented in Figure 4.50.

The excitation-energy spectra of ^{8}Be in Figures 4.49 and 4.50 both exhibit the narrow ground state of ^{8}Be located at $E_{\text{decay}} = 92$ keV which corresponds to α_0 decay from ^{12}C. The broad peak located at $E_{\text{decay}} \approx 3$ MeV is the 2_1^+ state in ^{8}Be located at $E_{\text{decay}} = 3.030(10)$ MeV which corresponds to α_1 decay from ^{12}C. By gating on these regions of E_{decay}, the CAKE coincidence matrices and excitation-energy spectra corresponding to α_0 and α_1 decay from ^{12}C can be determined, as presented in Figure 4.51. These α_0 and α_1 spectra, generated by gating on the detection of 2-α breakup from ^{8}Be, do not qualitatively match the corresponding spectra on Figure 4.48. This is because the probability of detecting an α decay particle from ^{12}C exhibits a difference excitation-energy dependence compared to the probability of detecting both α-particles from ^{8}Be. Moreover, it is possible that some α_1 decays to the $J^\pi = 2^+$ state of ^{8}Be may have been misidentified since the α decay particle from ^{12}C cannot be consistently discriminated from α decay from ^{8}Be. As discussed in Section 4.3.4, it is observed that the α_1 decay mode extends towards $E_x \approx 8$ MeV which shows that the finite width of the ^{8}Be daughter state must be accounted for. An interesting observation is that the 1_1^+ 12.710(6) MeV state appears to only decay through the α_1 decay mode. This is in keeping with expectations as selection rules prevent unnatural-parity states in ^{12}C from undergoing α_0 decay to the ground state in ^{8}Be, as discussed in Section 2.8.1.1.

The erroneous observation of α_1 decay from the primary the peak of the Hoyle state is due to the target attenuation of the low-energy α decay particles from this strongly-populated state, leading to a misidentification as α emission from ^{8}Be.

In summary, the spectra on Figure 4.51 provide a qualitative understanding of the relative strengths between the widths of the α_0 and α_1 decay modes, however these spectra are not simultaneously fitted with the primary R-matrix analysis of this work as the CAKE efficiency exhibits a complex dependence on the kinematics of the decay particles. Moreover, the calculated efficiencies for anisotropic decays require the calculation/assumption of m-state population ratios. ANGCOR, a programme that links to the reaction output of CHUCK3 to calculate angular correlations of particle, gamma or fission decay, can be used to calculate the m-state population ratios [91]. This was beyond the scope of this work which is focused on investigating monopole strengths in ^{12}C which invariably decay isotropically in the centre-of-mass inertial reference frame of the parent nucleus.

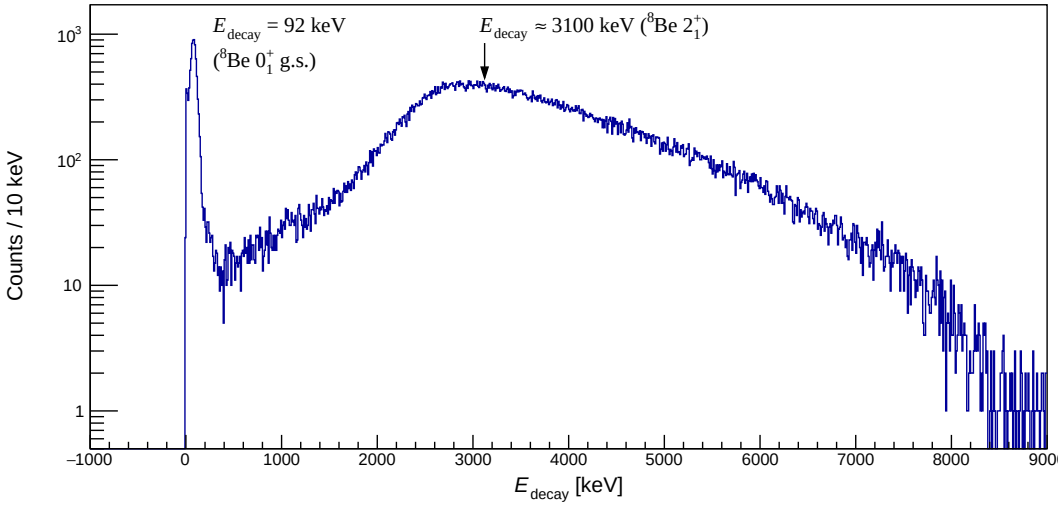

Figure 4.49: The excitation energy of the ^{8}Be nucleus, determined with the missing-energy reconstruction described in Section 4.3.5.1.

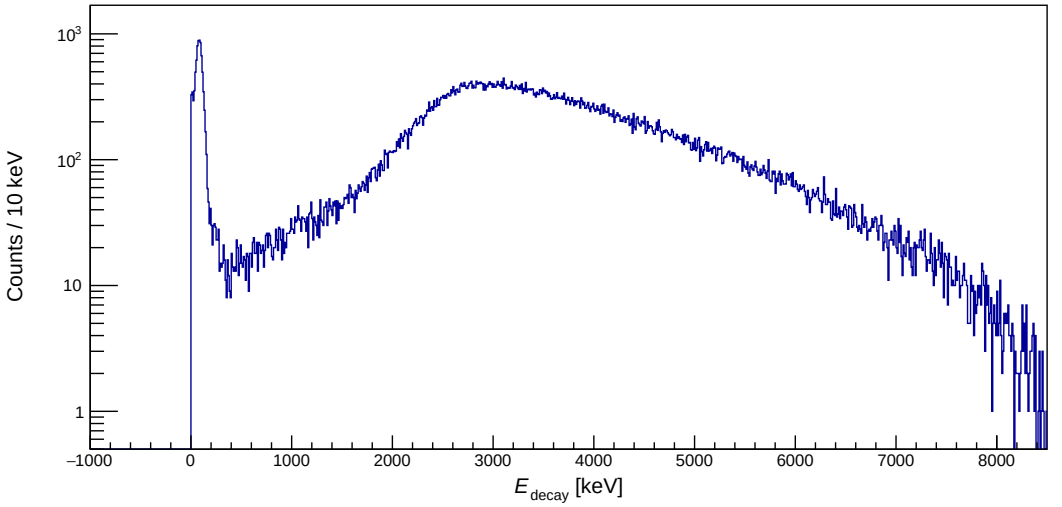

Figure 4.50: The excitation energy of the ^{8}Be nucleus, determined with the relative-momentum reconstruction described in Section 4.3.5.2.

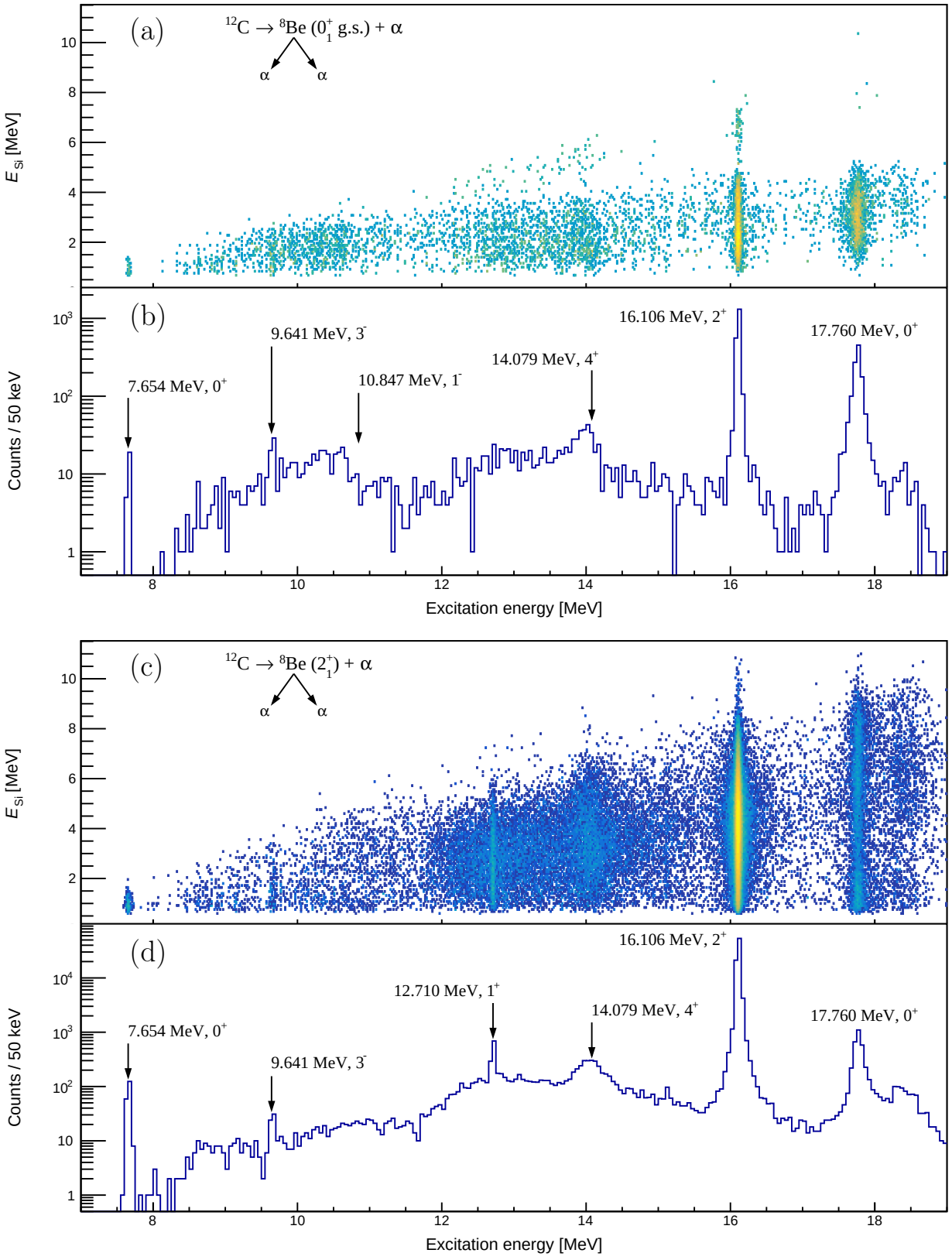

Figure 4.51: The coincidence matrix and projected excitation-energy spectrum for α_0 decay, gated on the narrow peak of the ^{8}Be ground state on Figures 4.49 and 4.50, are presented in panels (a) and (b). The coincidence matrix and projected excitation-energy spectrum for α_1 decay, gated on the broad $J^{\pi} = 2^{+}$ peak of ^{8}Be on Figures 4.49 and 4.50, are presented in panels (c) and (d). The ^{12}C states with well-resolved peaks are indicated.

4.3.6 CAKE Angular Distributions

For the $^{14}C(p,t)^{12}C$ reaction at $\theta_{lab} = 0°$ of experiment PR240, the circular collimator restricts the measurement of the ejectile to be $0° < \theta_{lab} < 2°$, as shown in Figure 2.17. For the incident proton beam energy of $E_{beam} = 140$ MeV, the triton ejectiles detected between 0°-2° correspond to recoil nuclei with kinetic energies between 3.905-3.927 MeV at polar angles of $\theta_{lab} = 174.4° - 180.0°$. The GEANT4 simulation described in Section 3.3.4 is used to simulate the relativistic binary kinematics of both the initial $^{14}C(p,t)^{12}C$ reaction as well as the subsequent particle decays from the excited ^{12}C recoil nucleus. Given the primary purpose of this work to study monopole resonances which inherently decay isotropically, the simulation focused on isotropic α-decay which is the dominant particle decay mode in the $E_x \approx$ 7-16 MeV excitation-energy region of interest. The simulated angular distribution of decay is plotted against the excitation energy of ^{12}C for α_0 decay in Figure 4.52. As expected, the angular distributions begin at the α-separation energy of -7.36659(4) MeV and is highly backward angled. This is due to the significant velocity of the recoil nucleus in the laboratory inertial reference frame which distorts isotropic decay (in the inertial reference frame of the recoil nucleus) to be an anistropic, also known as the headlight effect. For $E_x = 7.654$ and 10.0 MeV, the α-particle from α_0 decay exhibits approximately 5% and 57% of the kinetic energy for recoil nucleus, respectively. This large change of relative kinetic energy in this region results in the angular distribution of decay being strongly dependent on the excitation energy. The excitation-energy dependent efficiencies of the CAKE for the α_0 decay mode from the $^{14}C(p,t)^{12}C$ measurement at $\theta_{lab} = 0°$ (PR240) is presented in Figures 4.53 and 4.54. It is observed that the efficiencies also vary rapidly above the α-separation energy of -7.36659(4) MeV due to the aforementioned headlight effect. As E_x approaches 30 MeV, α_0 decay exhibits approximately 930% of the kinetic energy for recoil nucleus which mitigates the headlight effect, leading to the efficiency asymptotically approaching the 23.7% solid-angle coverage detailed in Section 3.3.4.

The matrix of E_{Si} vs E_x for the entire CAKE is displayed in Figure 4.45. The α_0 (a), α_1 (b) and p_0 (c) decay modes can be observed, however the α_0 and α_1 decay modes are not well resolved. An improved discrimination can be obtained through the matrices of E_{Si} vs E_x for each ring, as presented in Figures 4.46 and 4.47. It is observed that the E_{Si} values of the various loci decrease at lower polar angles (higher ring numbers) due to the aforementioned headlight effect. The angular distributions for the α_0 decay mode can be obtained by gating on the displayed α_0 decay mode cut for each ring. Since the simulated efficiencies for each ring vary drastically over this interval (see Figure 4.54), the calculated angular distributions cannot be accurately determined by evaluating the efficiencies at an average excitation energy. For the i^{th} ring, the expected yield $W_i(\theta)$ can be determined as

$$W_i(\theta) = \int_{E_{\min}}^{E_{\max}} \rho(E')\,\epsilon_i(E')\mathrm{d}E', \tag{4.31}$$

where ϵ is the efficiency for the i^{th} ring of the CAKE and $\rho(E')$ is the lineshape of the binned data which is obtained with a fit. These efficiencies account for the missing channels listed in Table 4.5.

ADC Channel	MMM Number	Detector Channel
0	0	Ring 0
14	0	Ring 14
22	1	Ring 6
33	2	Ring 1
75	4	Ring 11
76	4	Ring 12
89	1	Sector 1
90	1	Sector 2

Table 4.5: The inoperative channels for each MMM-type detector of the CAKE.

4.3.6.1 Isotropic α_0 decay from 0^+ resonances

The primary α_0 angular distribution of interest is that of the broad excitation-energy region at $E_x \approx 9$ MeV which is suggested to be predominantly 0^+ in nature by the MDA analysis of Itoh *et al.* [92, 14]. Since the ground state of ^{8}Be exhibits a spin and parity of 0^+, only a $J^\pi = 0^+$ resonance in ^{12}C can exhibit an isotropic α_0 angular distribution. The α_0 angular distribution from the primary peak of the Hoyle state at 7.654 MeV provides a useful verification for the simulation, as shown in Figure 4.55. Additionally, at high polar angles of decay, the corresponding α_0 locus exhibits high values of E_{Si} which may begin to exceed the dynamic range for the ADCs of the CAKE. Furthermore, at lower polar angles decay, the α_0 locus is not well resolved with respect to the broad α_1 locus. Due to electronic thresholds, the measurement of α decay particles from the primary peak of the Hoyle state with silicon detectors is typically not feasible if the excited ^{12}C nucleus is at rest in the laboratory inertial

reference frame. Additionally, target attenuation effects on the α decay particles may further reduce the possibility of detection. Simulations show that the significant momentum of the ^{12}C recoil nucleus from the ^{14}C$(p,t)^{12}$C measurement (PR240) mitigates these two limitations by boosting the momenta of the α decay particles (See 4.54). Whilst the fit with χ^2_{red} minimisation yields a poor goodness of fit ($\chi^2_{\text{red}} = 44.799$) due to the extension of the α_0 decay mode locus below the electronic threshold of the CAKE ($E_{\text{th}} \approx$600 keV), the calculated angular distribution qualitatively agrees well with the predicted detection with rings 0-4.

The $J^\pi = 0^+$ resonance situated at 17.760(20) MeV also exhibits α_0 decay and the angular distribution is presented in Figure 4.56. The general trend of the data is reproduced by the calculated angular distribution which exhibits the yield fluctuations between neighbouring rings which is caused by the aforementioned missing channels of the CAKE (see Table 4.5). However, the analysis of the α_0 angular distribution of this state is complicated by the prominent α_1 decay mode which contaminates the α_0 gates on Figures 4.46 and 4.47. It is observed that towards higher excitation energies of $E_x \approx 16$ MeV, the separation in E_{Si} values between the α_0 and α_1 loci is decreased. The E_{Si} spectrum of the 17.760(20) MeV resonance is shown in Figure 4.62 and it is observed that the α_0 and α_1 peaks are not fully separated which explains the unsatisfactory goodness of fit. In contrast, the E_{Si} spectrum for the lower excitation energy region of 9.5 MeV $< E_x <$ 10.0 MeV presented in Figure 4.63 exhibits complete separation between the α_0 and α_1 contributions.

The α_0 of the broad excitation-energy region at $E_x \approx 9$ MeV is presented in Figure 4.57. As previously mentioned, for this lower excitation-energy range there is good separation in E_{Si} values between the α_0 and α_1 loci, however the detection of the α_0 decay mode for this range is affected by the electronic threshold of the CAKE for rings 10-15 (see Figures 4.46 and 4.47). Consequently, the data points situated at $\theta_{\text{lab}} < 134^\circ$ were ignored for the analysis. A fit with χ^2_{red} minimisation was performed over rings at $\theta_{\text{lab}} > 134^\circ$ which yielded a satisfactory goodness of fit ($\chi^2_{\text{red}} = 1.532$) which indicates that the strength populated with ^{14}C$(p,t)^{12}$C at $\theta_{\text{lab}} = 0^\circ$ ($E_{\text{beam}} = 140$ MeV) in this excitation energy region is predominantly of 0^+ spin and parity. The calculated yields which are fitted to the data are displayed as filled orange circles whilst the unfilled circles are not fitted and are plotted to give an indication of the expected yield if the aforementioned threshold effects were not present. This result supports the MDA analysis of Itoh *et al.* which indicates that the population of this excitation-energy region with ^{12}C$(\alpha,\alpha')^{12}$C at $\theta_{\text{lab}} = 0^\circ$ ($E_{\text{beam}} = 386$ MeV) is predominantly $L = 0$ in nature [14].

4.3.6.2 Anisotropic α_0 decay from non-0^+ resonances

Since the ground state of ^{8}Be exhibits a spin and parity of 0^+, a non-0^+ resonance in ^{12}C will exhibit anisotropic α_0 decay in the inertial reference frames

of both the recoil nucleus and the laboratory. The quantitative analysis of such decays is more complex as it requires the calculation (or assumption) of m-state population ratios for the excited recoil nucleus (see Ref. [88] for an example). Since this work is focused on the identification and analysis of monopole strength in ^{12}C, the study of α_0 angular distributions from resonances which do not exhibit $J^\pi = 0^+$ spin and parity is only to ensure that the significant kinetic energy of the recoil nucleus (as discussed in Section 4.3.6.1) does not homogenise all angular distributions to be indistinguishable in the laboratory inertial reference frame.

The broad excitation-energy region of 9.8 MeV $< E_x <$ 10.6 MeV is known to be dominated by a broad 0^+ resonance situated at 9.930(30) MeV, however the $J^\pi = 2^+$ resonance situated at 9.870(60) MeV and the $J^\pi = 1^-$ state at 10.847(4) MeV are also expected to contribute. The angular distribution of this excitation-energy region is presented in Figure 4.58 and the calculated angular distributions for isotropic α_0 decay are determined with Equation 4.32. The dips in the calculated angular distribution are due to missing channels of the CAKE (see Table 4.5). It is observed that the fit with the calculated angular distribution yields a poor goodness of fit. Whilst a fit over a smaller range of $\theta_{\text{lab}} < 138°$ yields a much better fit, it is clear that at higher polar angles the data deviates strongly from the expected yield. It is possible that this is predominantly due to the contribution of the aforementioned 2^+ resonance which is known to decay strongly towards backward angles (see Ref. [88]).

The broad excitation-energy regions of 12.9 MeV $< E_x <$ 13.3 MeV and 13.8 MeV $< E_x <$ 14.3 MeV should each be dominated by broad 4^+ resonances situated at 13.3(2) and 14.079(5) MeV, respectively. The angular distributions of these excitation-energy regions are presented in Figures 4.59 and 4.60. It is observed that the calculated angular distribution for isotropic α_0 decay does not reproduce the local minima at $\theta_{\text{lab}} \approx 135°$. The poor goodness of fits indicate that the angular distributions of α_0 decay from 4^+ resonances can be clearly discriminated against isotropic α_0 decay from $J^\pi = 0^+$ resonances.

The well-resolved peak located at $E_x \approx 16.1$ MeV corresponds to the 2^+ ^{12}C resonance situated at 16.1060(8) MeV. The angular distribution of this peak is presented in Figure 4.61 and it is observed that the calculated angular distribution for isotropic α_0 decay does not reproduce the strongly preferential decay towards perpendicular ($\theta_{\text{lab}} = 90°$) and large backward angles ($\theta_{\text{lab}} > 148°$). The poor goodness of fit indicates that the angular distribution of α_0 decay from $J^\pi = 2^+$ resonances can be clearly discriminated against isotropic α_0 decay from $J^\pi = 0^+$ resonances. The observed preferential decay at $\theta_{\text{lab}} > 148°$ for $J^\pi = 2^+$ resonance supports hypothesis that a $J^\pi = 2^+$ resonance contributes to the aforementioned 9.8 MeV $< E_x <$ 10.6 MeV excitation-energy region. However, the rise in intensity towards $\theta_{\text{lab}} = 90°$ is not reproduced as the headlight effect is more drastic at these lower excitation energies and particularly for perpendicular decay angles. In summary, it is clear that anisotropic decays from non-$J^\pi = 0^+$ resonances can be clearly identified and discrim-

inated from isotropic α_0 decay from $J^\pi = 0^+$ resonances and this supports the result that the excitation-energy region of 8.0 MeV $< E_x <$ 8.8 MeV is predominantly of $J^\pi = 0^+$ spin and parity.

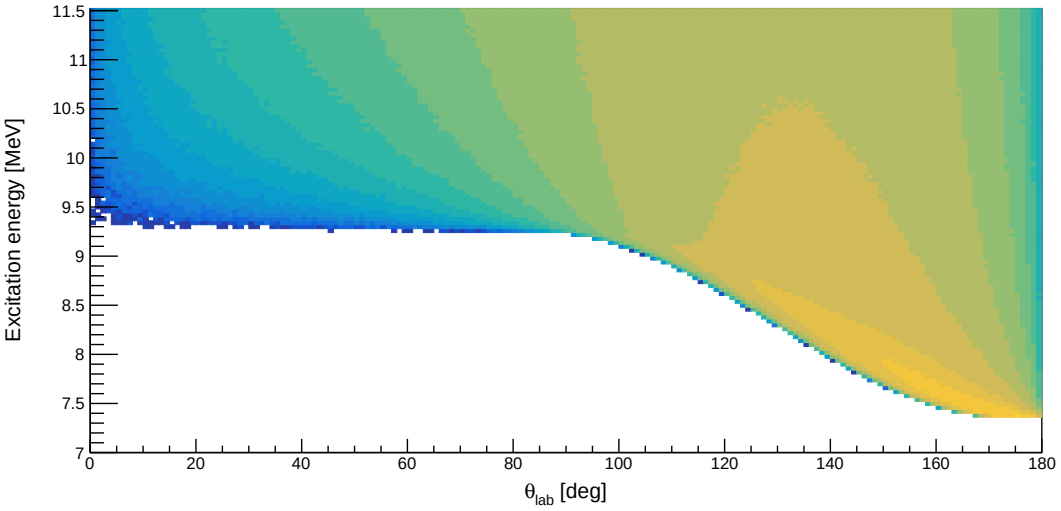

Figure 4.52: The excitation-energy dependent laboratory polar angles for the α-particle from α_0 decay for ^{12}C.

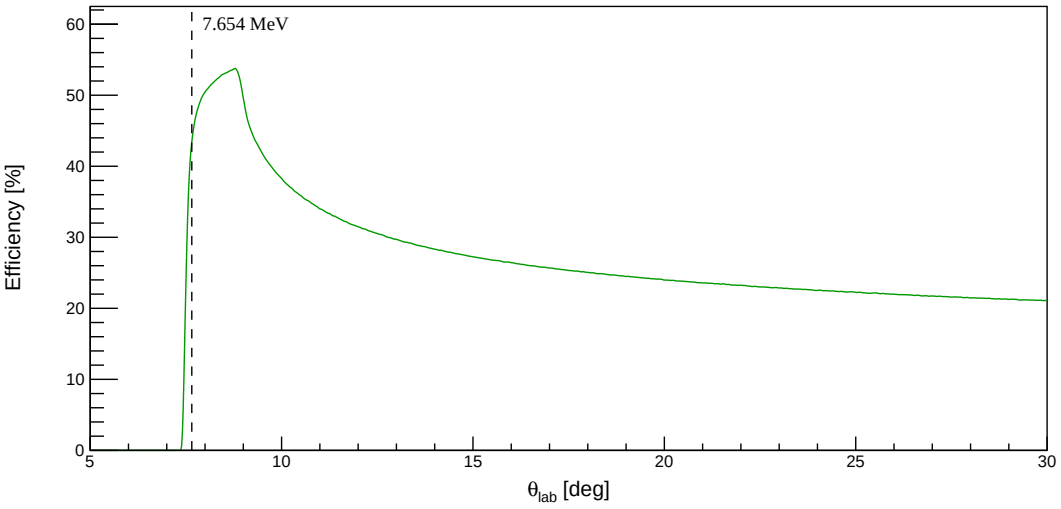

Figure 4.53: The excitation-energy dependent efficiency of the entire CAKE for α_0 decay from ^{12}C. The vertical dashed line indicates the resonance energy of the Hoyle state.

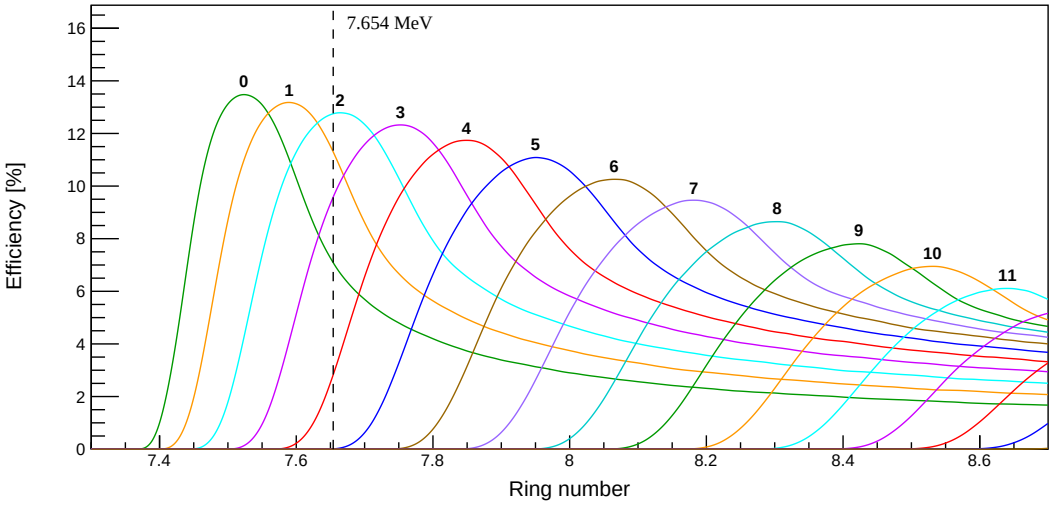

Figure 4.54: The excitation-energy dependent efficiencies for the individual rings of the CAKE for α_0 decay from ^{12}C near the 7.654 MeV resonance energy of the Hoyle state. The ring numbers are indicated at the local maximum of each corresponding efficiency curve.

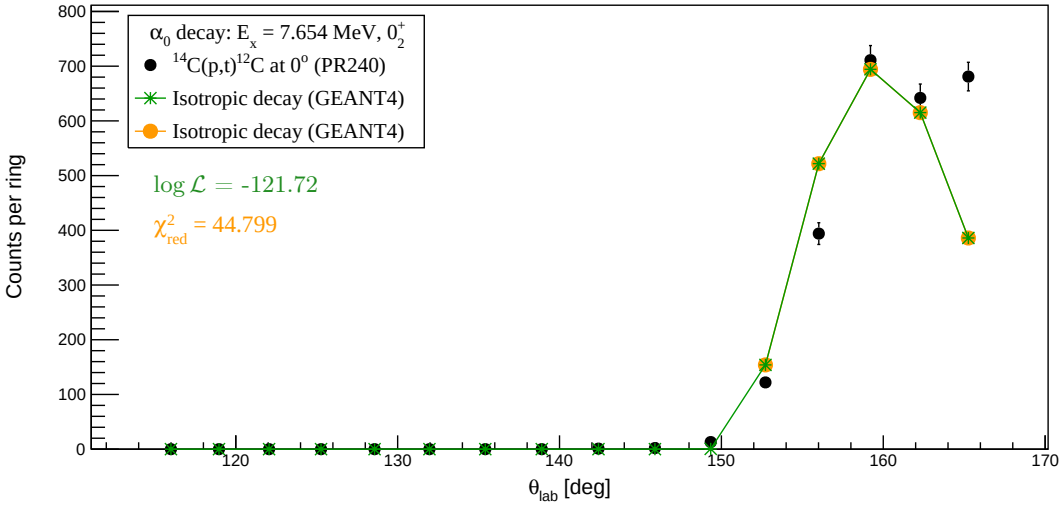

Figure 4.55: The α_0 angular distribution from the primary peak of the 7.65420(15) MeV 0_2^+ Hoyle state in ^{12}C. The orange markers correspond to the predicted isotropic decay fitted over all data points with Chi-square minimisation. The green markers correspond to the predicted isotropic decay fitted to the data from rings 0-4 ($\theta_{\text{lab}} > 152°$) through maximum-likelihood estimation.

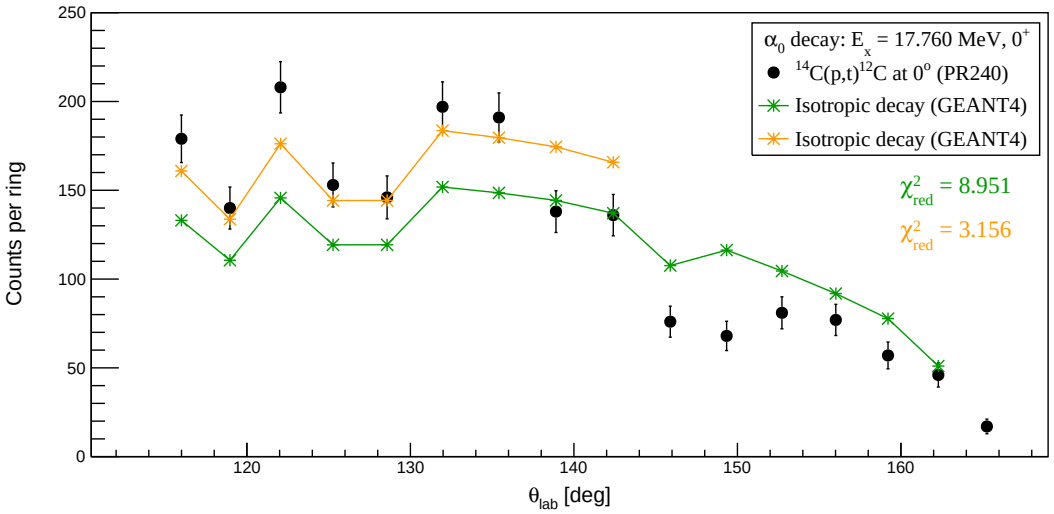

Figure 4.56: The α_0 angular distribution from the 17.760(20) MeV 0^+ state in ^{12}C (experiment PR240). The orange and green markers correspond to the predicted isotropic decay fitted over different ranges of the data points with Chi-square minimisation.

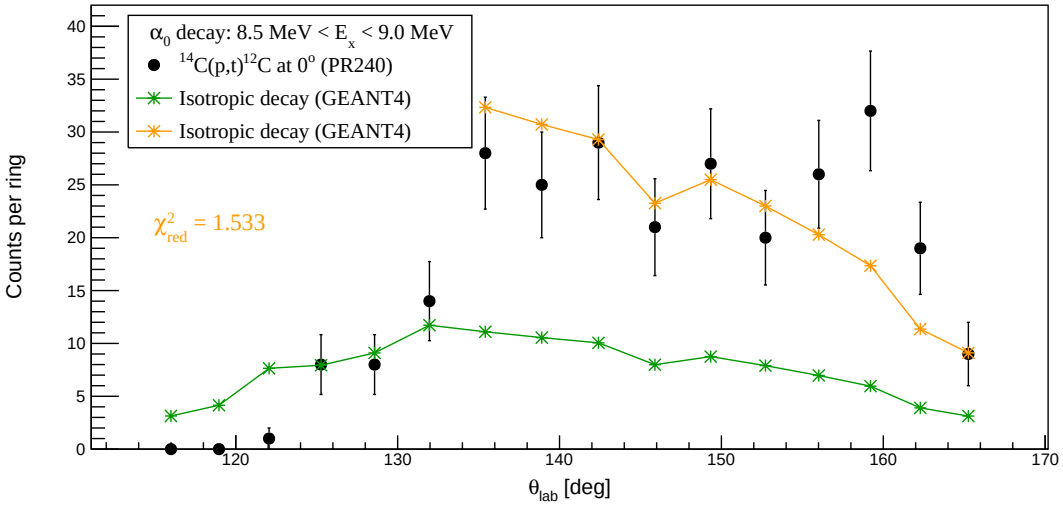

Figure 4.57: The α_0 angular distribution from the 8.5 MeV $< E_x <$ 9.0 MeV excitation-energy region in ^{12}C (experiment PR240). The green markers correspond to the predicted isotropic decay fitted over all data points with Chi-square minimisation. The orange markers correspond to the predicted isotropic decay fitted to the data from rings 0-9 ($\theta_{\text{lab}} > 134°$) through maximum-likelihood estimation.

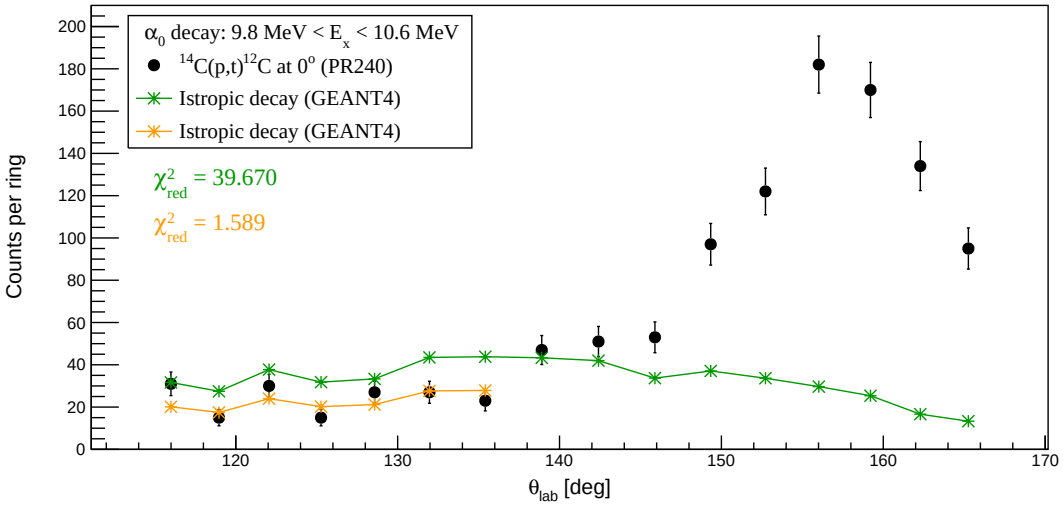

Figure 4.58: The α_0 angular distribution from the 9.8 MeV $< E_x <$ 10.6 MeV excitation-energy region in ^{12}C (experiment PR240). The orange and green markers correspond to the predicted isotropic decay fitted over different ranges of the data points with Chi-square minimisation.

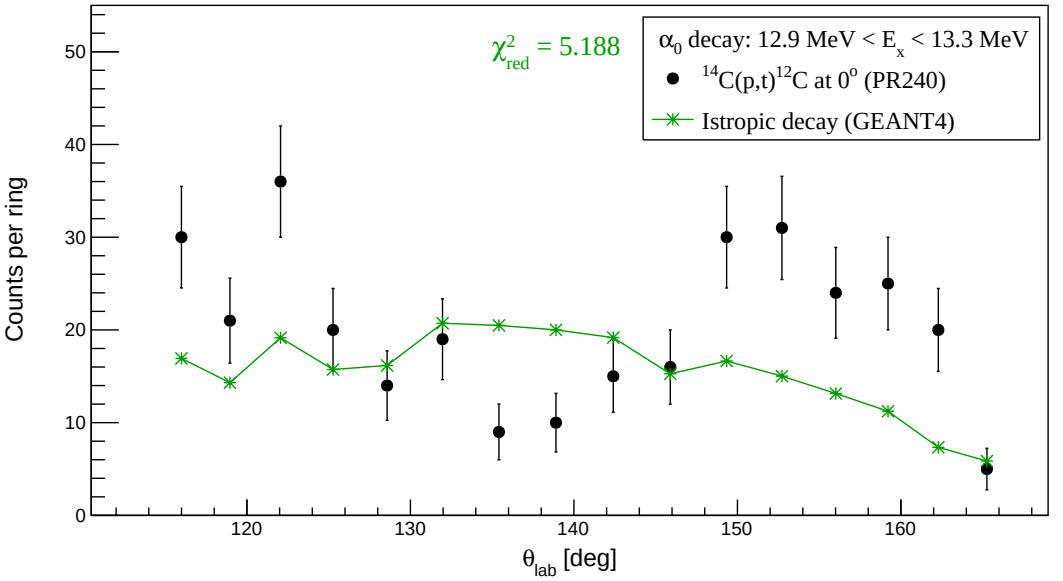

Figure 4.59: The α_0 angular distribution from the 12.9 MeV $< E_x <$ 13.3 MeV excitation-energy region in ^{12}C (experiment PR240).

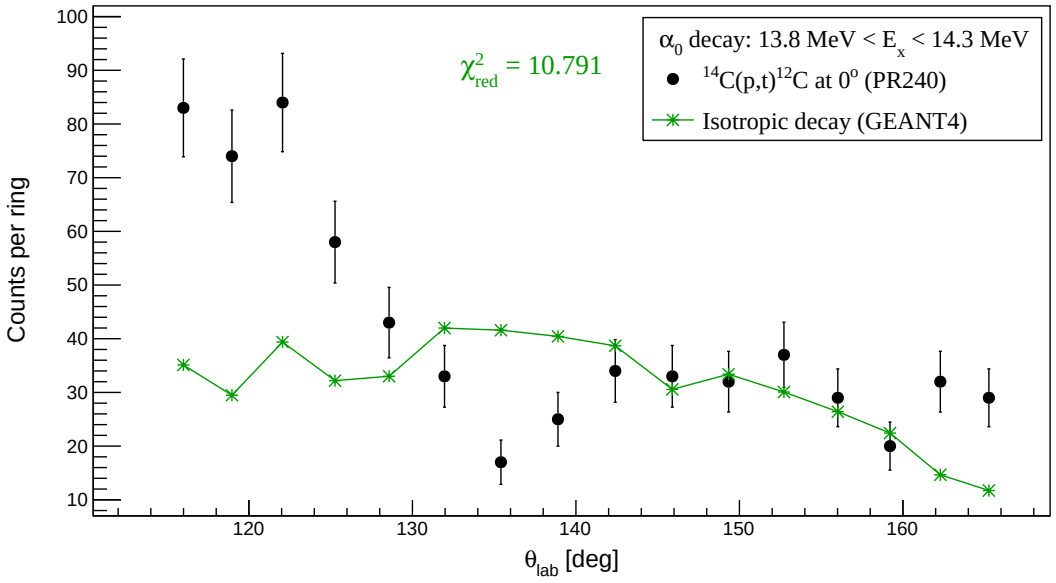

Figure 4.60: The α_0 angular distribution from the 13.8 MeV $< E_x <$ 14.3 MeV excitation-energy region in ^{12}C (experiment PR240).

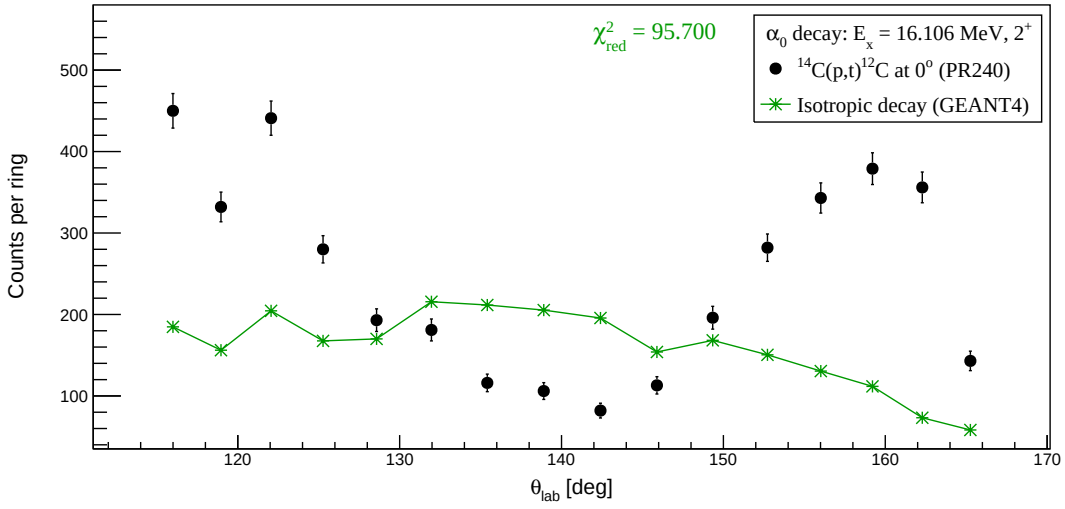

Figure 4.61: The α_0 angular distribution from the 16.1060(8) MeV 2^+ state in ^{12}C (experiment PR240).

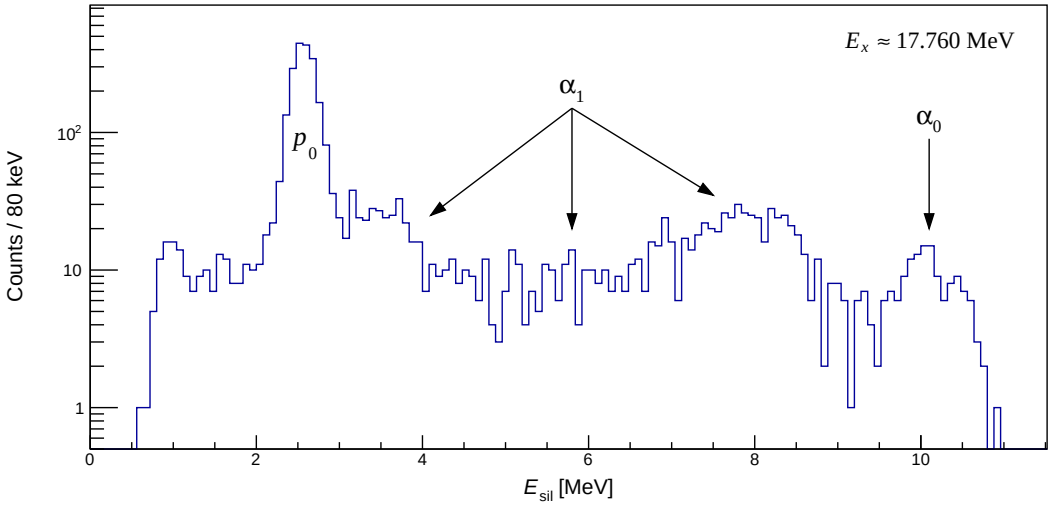

Figure 4.62: The E_{Si} spectrum of ring 7 for the 17.760(20) MeV 0^+ state in ^{12}C. The contributions corresponding to the α_0, α_1 and p_0 decay modes are indicated.

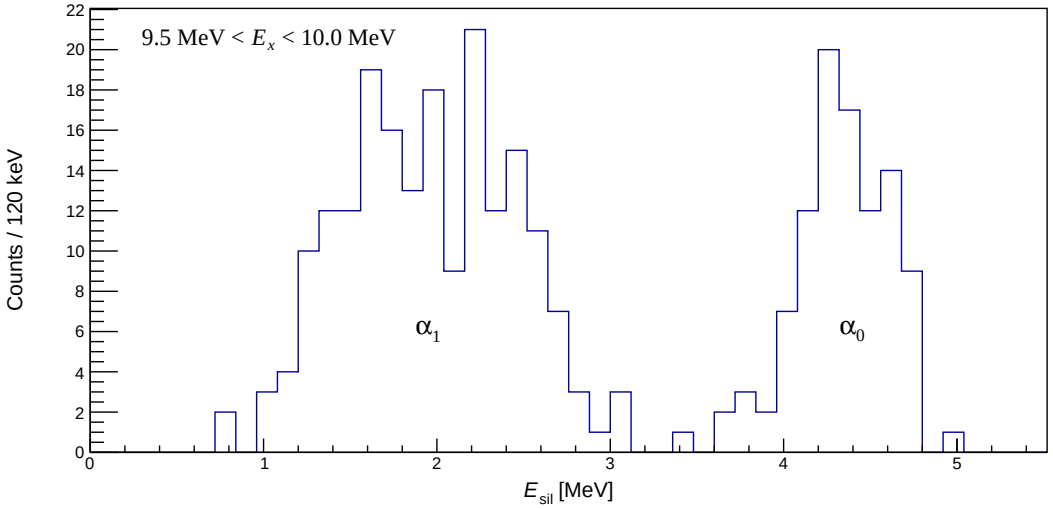

Figure 4.63: The E_{Si} spectrum of ring 2 for the 9.5 MeV $< E_x <$ 10.0 MeV excitation-energy region in ^{12}C. The contributions corresponding to the well-separated α_0 and α_1 decay modes are indicated.

4.4 Abridged Analysis of Experiment PR166, $^{12}C(\alpha,\alpha')^{12}C$ at $\theta_{lab} = 6°$, $E_{beam} = 196$ MeV

The complete PR166 data consists of three different ejectile/spectrometer angles: 6°, 8.5° and 10°, each of which correspond to a distinct analysis. Since the primary experiment that was performed for this thesis is experiment PR240, the analysis for the measurement of the $^{12}C(\alpha,\alpha')^{12}C$ reaction at $\theta_{lab} = 6°$ is presented in an abridged format as the analysis method and descriptions have been detailed in Section 4.1.

The PID spectrum is presented on Figure 4.64 and the dashed line represents the PID gate to selectively isolate the α-particle ejectiles from the $^{12}C(\alpha,\alpha')^{12}C$ reaction.

The spectra of TOF (a), $Y2_{pos}$ (b) and θ_{scat} (c) versus $X1_{posC}$ are presented on Figure 4.65. As mentioned in Section **??**, the X-type VDC was employed in the position of VDC1. Consequently, vertical-positions can only be obtained from VDC2: $Y2_{pos}$. Details of the lineshape corrections can be found in Appendix B.1. It is observed that the lineshape-corrected horizontal focal-plane position, $X1_{posC}$, yields vertically aligned lineshapes with respect to the TOF, $Y2_{pos}$ and θ_{scat} variables.

The spectra of $X1_{posC}$, the associated momentum calibration and the excitation energies are presented on panels (a), (b) and (c) of Figure 4.66, respectively. The momentum calibration parameters are given in Table 4.6.

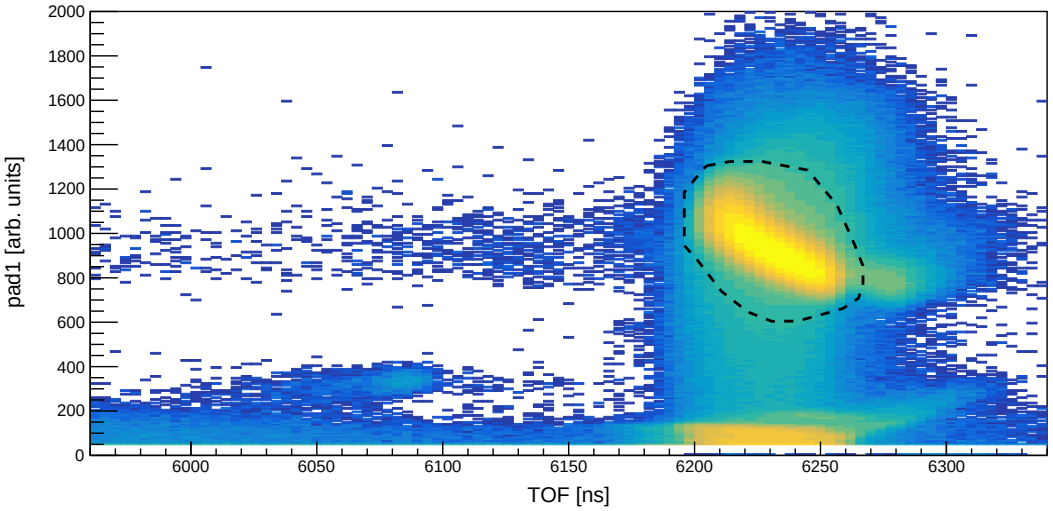

Figure 4.64: PID spectrum for experiment PR166, $^{12}C(\alpha,\alpha')^{12}C$ at $\theta_{lab} = 6°$.

Correction parameter	Parameter Value	Unit
c_0	1.10564×10^{3}	MeV/c
c_1	1.67099×10^{-1}	MeV/c/mm
c_2	-4.73163×10^{-5}	MeV/c/mm^2
c_3	2.14961×10^{-8}	MeV/c/mm^3

Table 4.6: The momentum calibration parameters for experiment PR166, $^{12}C(\alpha,\alpha')^{12}C$ at $\theta_{lab} = 6°$ (see Section 4.1.10 for details).

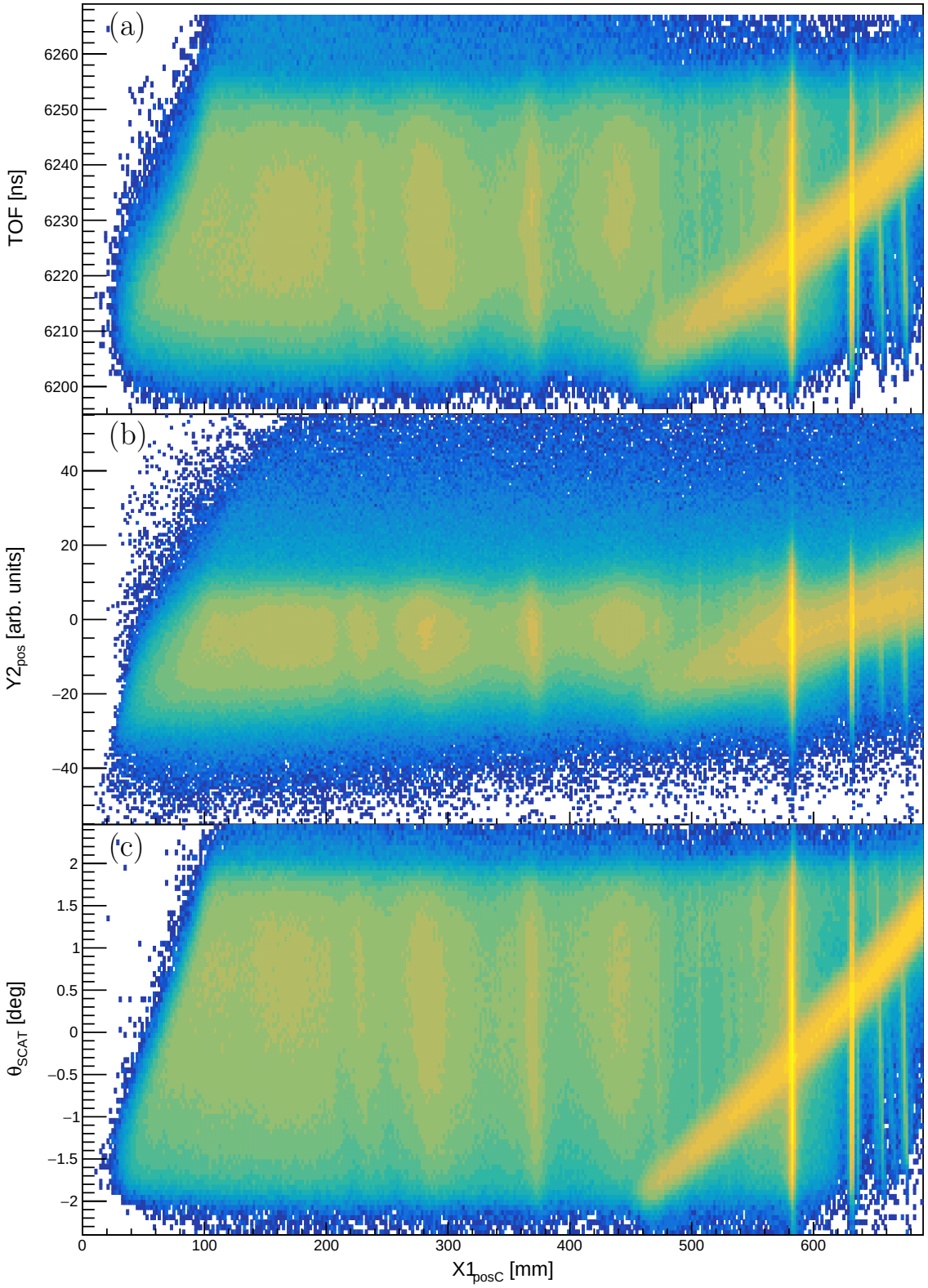

Figure 4.65: The spectra of TOF (a), $\mathrm{Y2_{pos}}$ (b) and θ_{scat} (c) versus $\mathrm{X1_{posC}}$ for experiment PR166, $^{12}\mathrm{C}(\alpha,\alpha')^{12}\mathrm{C}$ at $\theta_{\mathrm{lab}} = 6°$. The broad diagonal locus corresponds to contamination from hydrogen.

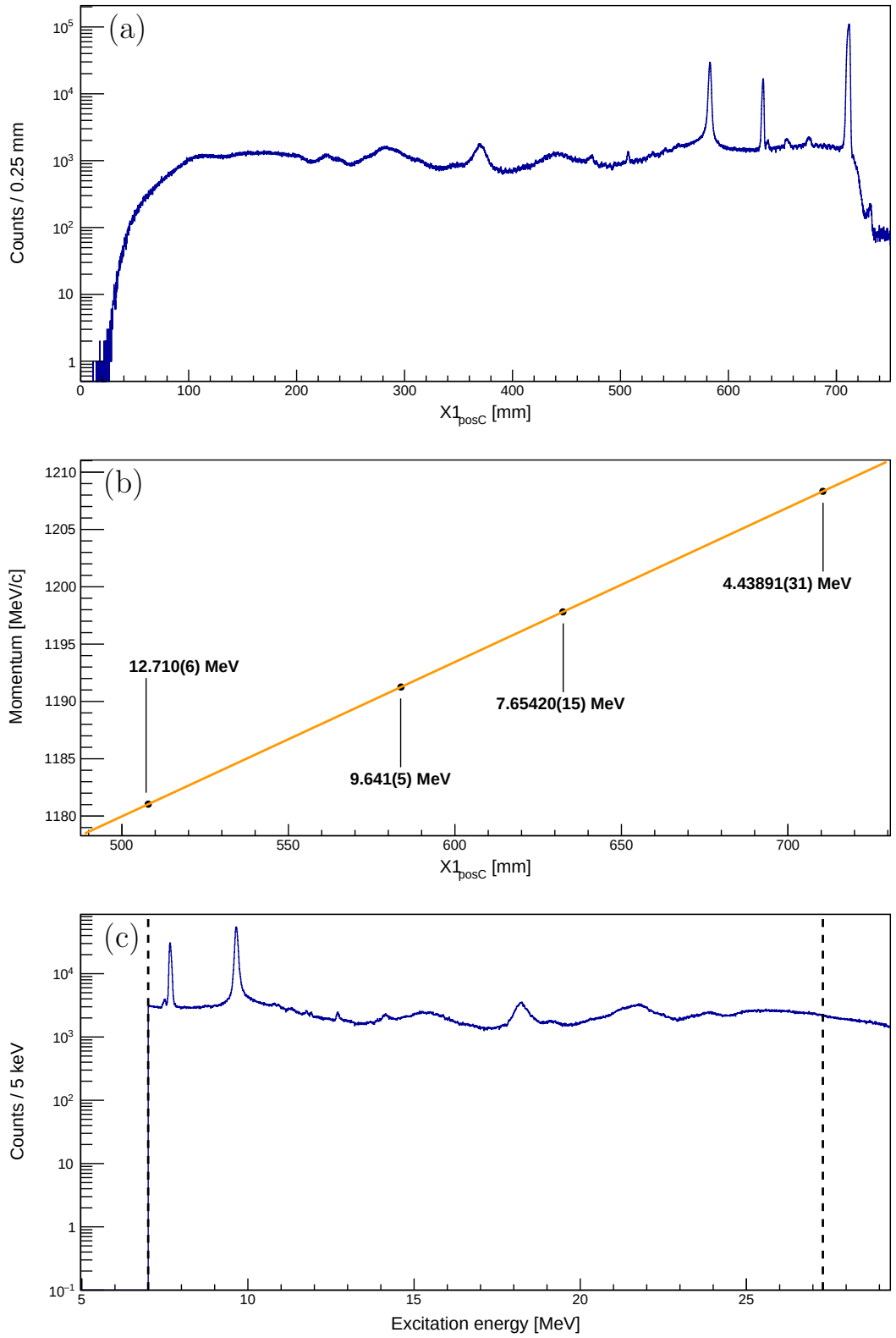

Figure 4.66: The spectra of the corrected focal-plane position $X1_{posC}$ (a), the associated momentum calibration (b) and the excitation energy (c) for experiment PR166, $^{12}C(\alpha,\alpha')^{12}C$ at $\theta_{lab} = 6°$. The vertical dashed lines on panel (c) indicate the excitation-energy range with full acceptance by the K600 spectrometer.

4.5 Abridged Analysis of Experiment PR166, $^{12}C(\alpha,\alpha')^{12}C$ at $\theta_{lab} = 8.5°$, $E_{beam} = 196$ MeV

Since the primary experiment that was performed for this thesis is experiment PR240, the analysis for the measurement of the $^{12}C(\alpha,\alpha')^{12}C$ reaction at $\theta_{lab} = 8.5°$ is presented in an abridged format as the analysis method and descriptions have been detailed in Section 4.1.

The PID spectrum is presented on Figure 4.67 and the dashed line represents the PID gate to selectively isolate the α-particle ejectiles from the $^{12}C(\alpha,\alpha')^{12}C$ reaction.

The spectra of TOF (a), $Y2_{pos}$ (b) and θ_{scat} (c) versus $X1_{posC}$ are presented on Figure 4.68. As mentioned in Section **??**, the X-type VDC was employed in the position of VDC1. Consequently, vertical-positions can only be obtained from VDC2: $Y2_{pos}$. Details of the lineshape corrections can be found in Appendix B.3. It is observed that the lineshape-corrected horizontal focal-plane position, $X1_{posC}$, yields vertically aligned lineshapes with respect to the TOF, $Y2_{pos}$ and θ_{scat} variables.

The spectra of $X1_{posC}$, the associated momentum calibration and the excitation energies are presented on panels (a), (b) and (c) of Figure 4.69, respectively. The momentum calibration parameters are given in Table 4.7.

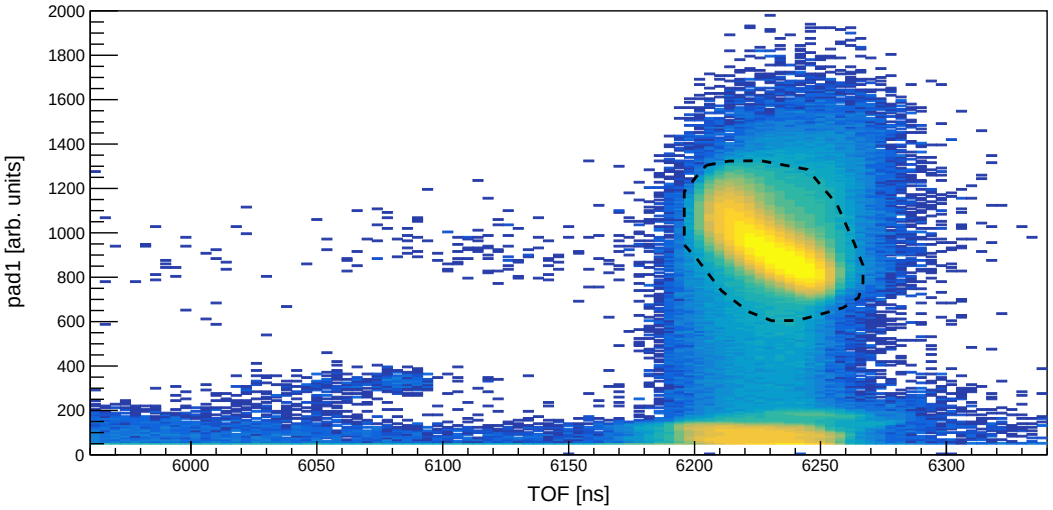

Figure 4.67: PID spectrum for experiment PR166, $^{12}C(\alpha,\alpha')^{12}C$ at $\theta_{lab} = 8.5°$.

Correction parameter	Parameter Value	Unit
c_0	1.09954×10^{3}	MeV/c
c_1	1.77102×10^{-1}	MeV/c/mm
c_2	-6.17806×10^{-5}	MeV/c/mm^2
c_3	2.83217×10^{-8}	MeV/c/mm^3

Table 4.7: The momentum calibration parameters for experiment PR166, $^{12}C(\alpha,\alpha')^{12}C$ at $\theta_{lab} = 8.5°$ (see Section 4.1.10 for details).

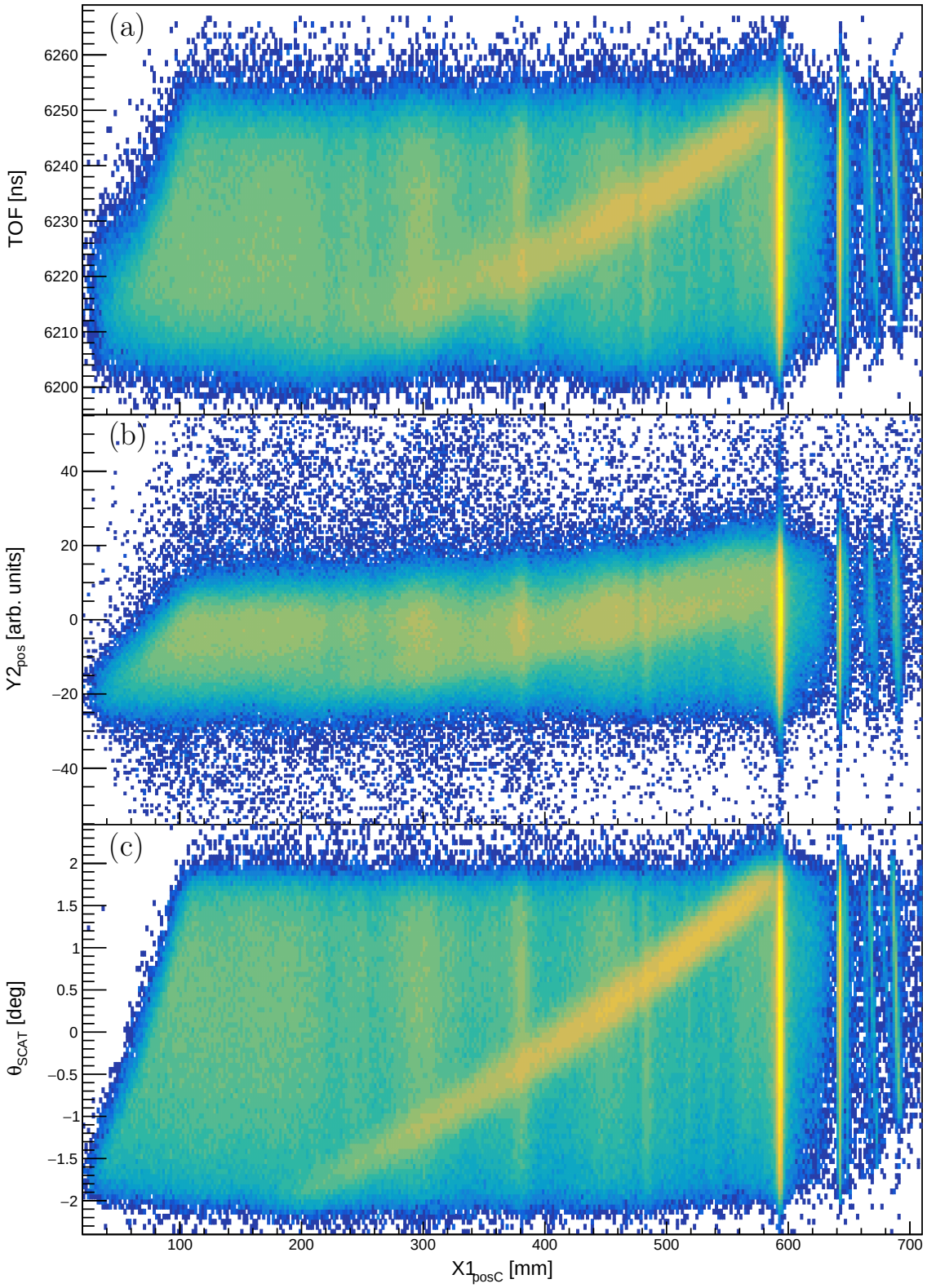

Figure 4.68: The spectra of TOF (a), $Y2_{pos}$ (b) and θ_{scat} (c) versus $X1_{posC}$ for experiment PR166, $^{12}C(\alpha,\alpha')^{12}C$ at $\theta_{lab} = 8.5°$.

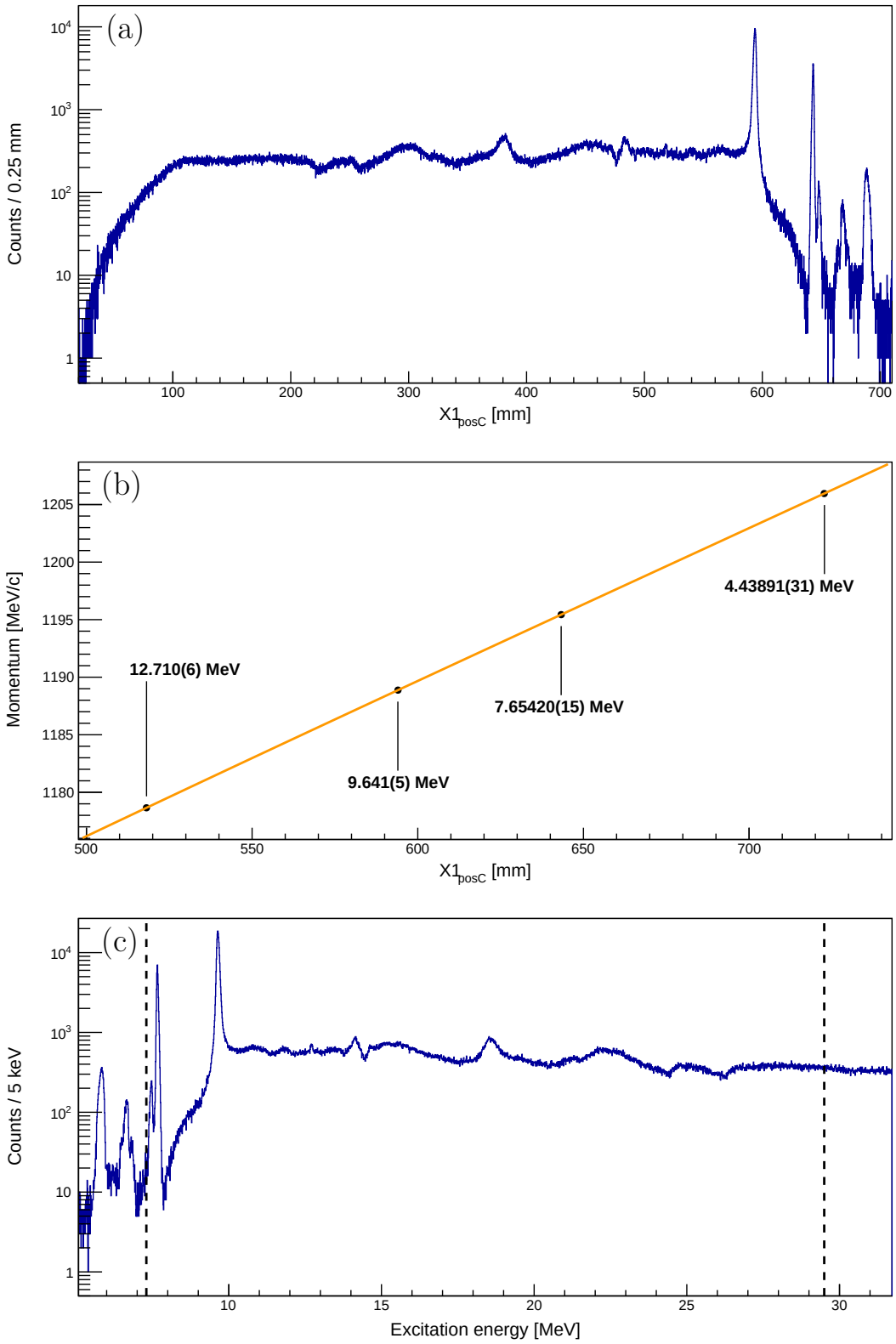

Figure 4.69: The spectra of the corrected focal-plane position $X1_{posC}$ (a), the associated momentum calibration (b) and the excitation energy (c) for experiment PR166, $^{12}C(\alpha,\alpha')^{12}C$ at $\theta_{lab} = 8.5°$. The vertical dashed lines on panel (c) indicate the excitation-energy range with full acceptance by the K600 spectrometer.

4.6 Abridged Analysis of Experiment PR166, $^{12}C(\alpha,\alpha')^{12}C$ at $\theta_{lab} = 10°$, $E_{beam} = 196$ MeV

Since the primary experiment that was performed for this thesis is experiment PR240, the analysis for the measurement of the $^{12}C(\alpha,\alpha')^{12}C$ reaction at $\theta_{lab} = 10°$ is presented in an abridged format as the analysis method and descriptions have been detailed in Section 4.1.

The PID spectrum is presented on Figure 4.70 and the dashed line represents the PID gate to selectively isolate the α-particle ejectiles from the $^{12}C(\alpha,\alpha')^{12}C$ reaction.

The spectra of TOF (a), $Y2_{pos}$ (b) and θ_{scat} (c) versus $X1_{posC}$ are presented on Figure 4.71. As mentioned in Section **??**, the X-type VDC was employed in the position of VDC1. Consequently, vertical-positions can only be obtained from VDC2: $Y2_{pos}$. Details of the lineshape corrections can be found in Appendix B.4. It is observed that the lineshape-corrected horizontal focal-plane position, $X1_{posC}$, yields vertically aligned lineshapes with respect to the TOF, $Y2_{pos}$ and θ_{scat} variables.

The spectra of $X1_{posC}$, the associated momentum calibration and the excitation energies are presented on panels (a), (b) and (c) of Figure 4.72, respectively. The momentum calibration parameters are given in Table 4.8.

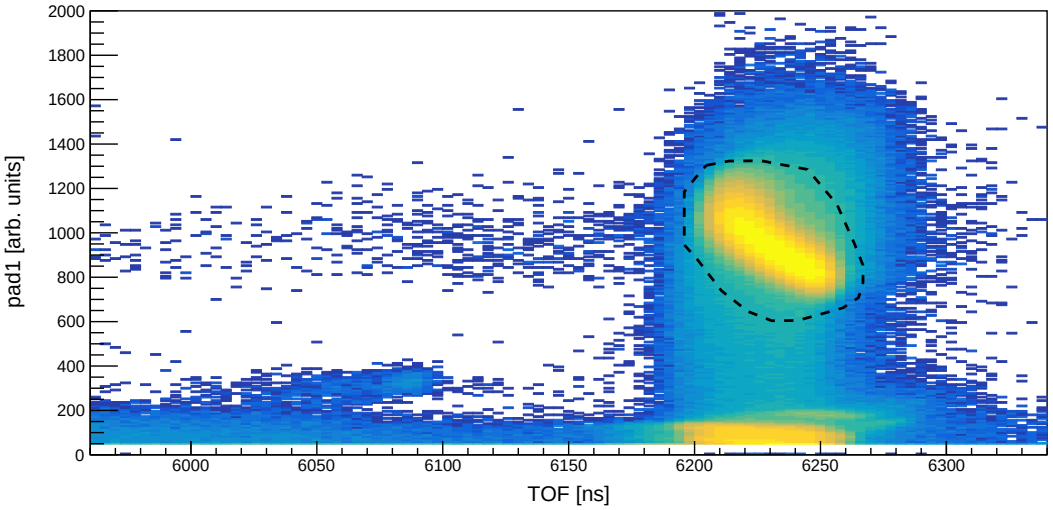

Figure 4.70: PID spectrum for experiment PR166, $^{12}C(\alpha,\alpha')^{12}C$ at $\theta_{lab} = 10°$.

Correction parameter	Parameter Value	Unit
c_0	1.09893×10^{3}	MeV/c
c_1	1.71005×10^{-1}	MeV/c/mm
c_2	-4.9785×10^{-5}	MeV/c/mm^2
c_3	2.19181×10^{-8}	MeV/c/mm^3

Table 4.8: The momentum calibration parameters for experiment PR166, $^{12}C(\alpha,\alpha')^{12}C$ at $\theta_{lab} = 10°$ (see Section 4.1.10 for details).

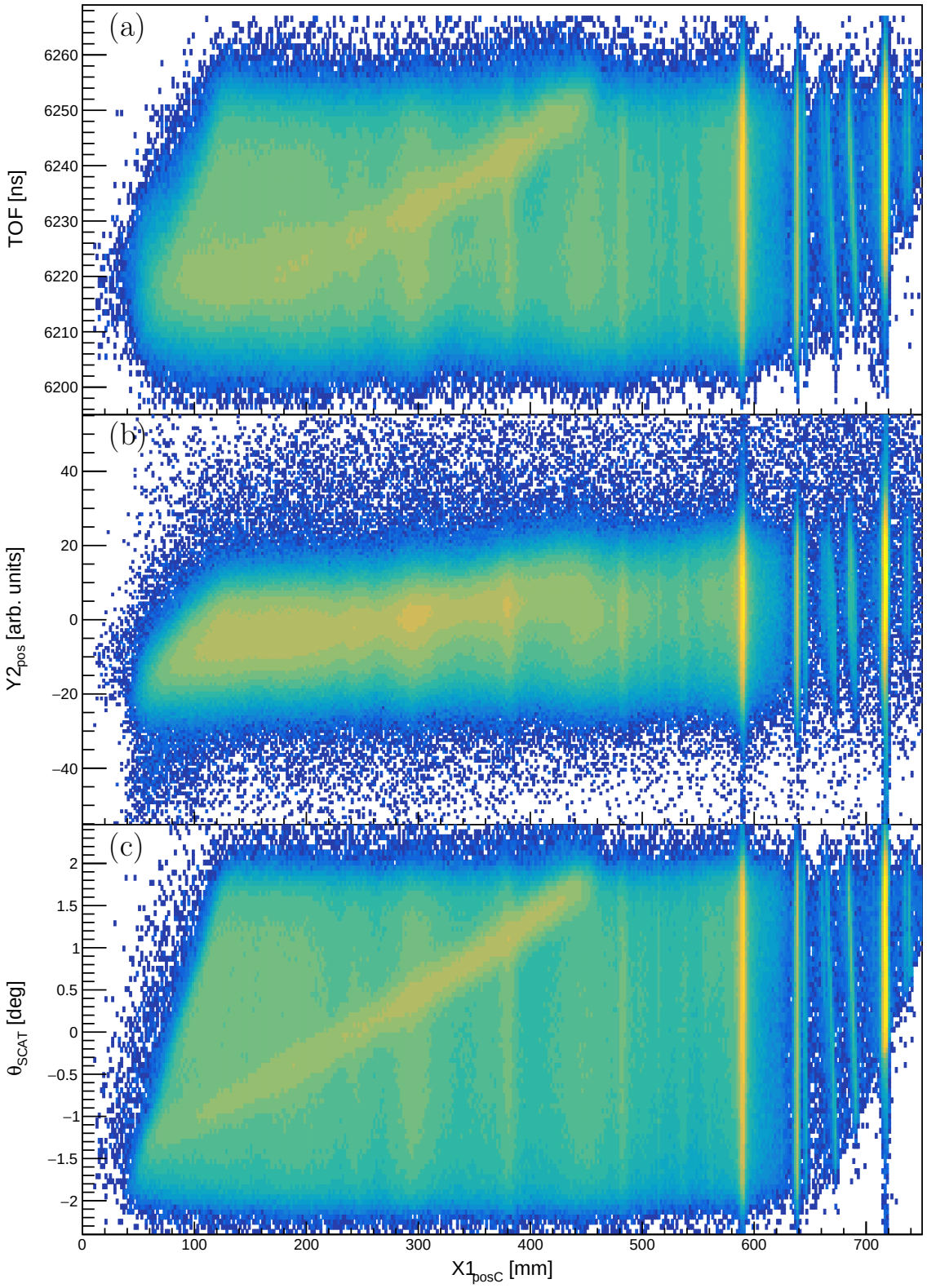

Figure 4.71: The spectra of TOF (a), $Y2_{pos}$ (b) and θ_{scat} (c) versus $X1_{posC}$ for experiment PR166, $^{12}C(\alpha,\alpha')^{12}C$ at $\theta_{lab} = 10°$.

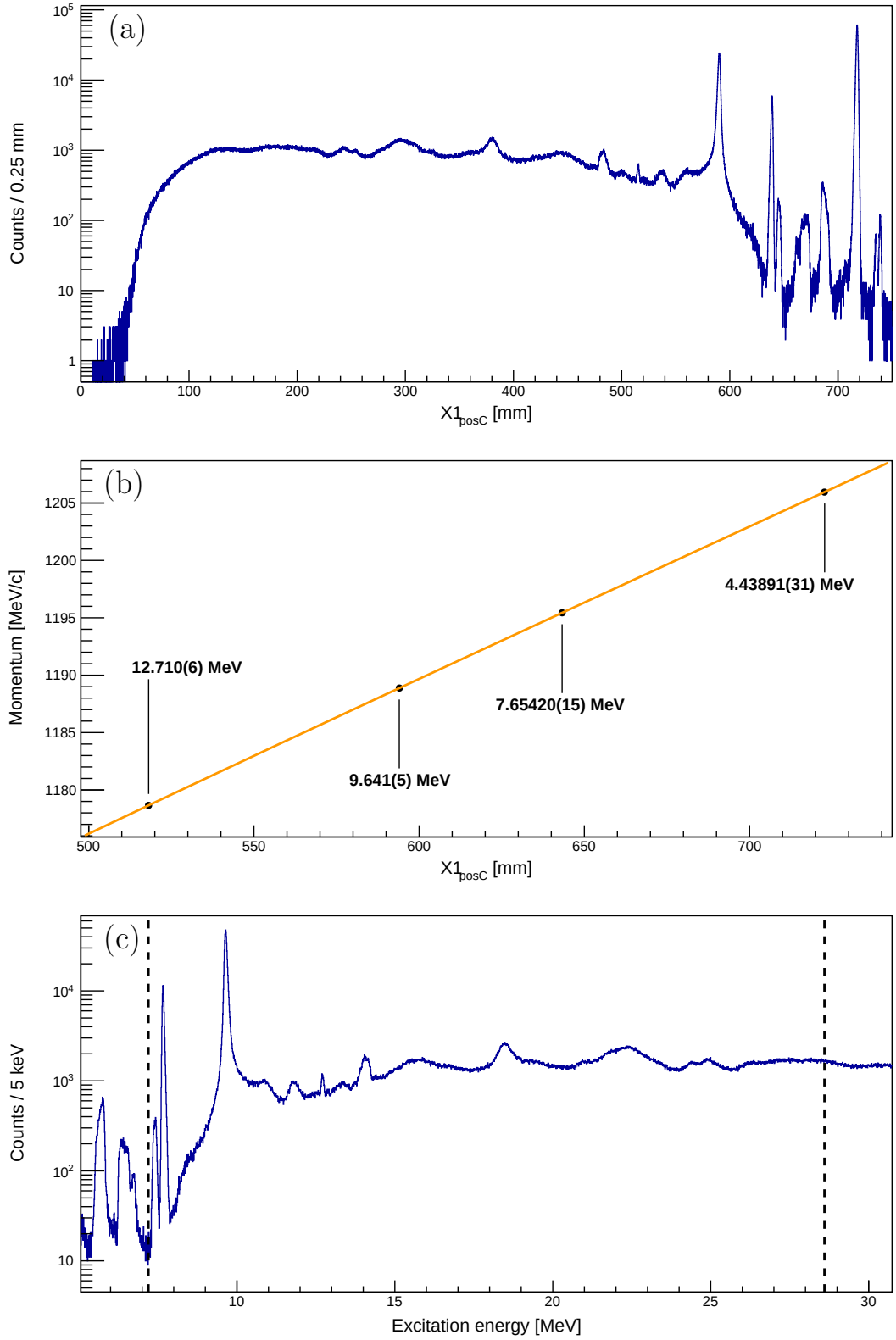

Figure 4.72: The spectra of the corrected focal-plane position $X1_{posC}$ (a), the associated momentum calibration (b) and the excitation energy (c) for experiment PR166, $^{12}C(\alpha,\alpha')^{12}C$ at $\theta_{lab} = 10°$. The vertical dashed lines on panel (c) indicate the excitation-energy range with full acceptance by the K600 spectrometer.

4.7 Abridged Analysis of Experiment PR194, $^{12}C(\alpha,\alpha')^{12}C$ at $\theta_{lab} = 0°$, $E_{beam} = 160$ MeV

Since the primary experiment that was performed for this thesis is experiment PR240, the analysis for the measurement of the $^{12}C(\alpha,\alpha')^{12}C$ reaction at $\theta_{lab} = 0°$ with $E_{beam} = 160$ MeV is presented in an abridged format as the analysis method and descriptions have been detailed in Section 4.1.

The PID spectrum is presented on Figure 4.73 and the dashed line represents the PID gate to selectively isolate the α-particle ejectiles from the $^{12}C(\alpha,\alpha')^{12}C$ reaction.

The spectra of TOF (a), $Y1_{pos}$ (b) and θ_{scat} (c) versus $X1_{posC}$ are presented on Figure 4.74. Details of the lineshape corrections can be found in Appendix B.3. It is observed that the lineshape-corrected horizontal focal-plane position, $X1_{posC}$, yields vertically aligned lineshapes with respect to the TOF, $Y1_{pos}$ and θ_{scat} variables.

The spectra of $X1_{posC}$, the associated momentum calibration and the excitation energies are presented on panels (a), (b) and (c) of Figure 4.75, respectively. The momentum calibration parameters are given in Table 4.9.

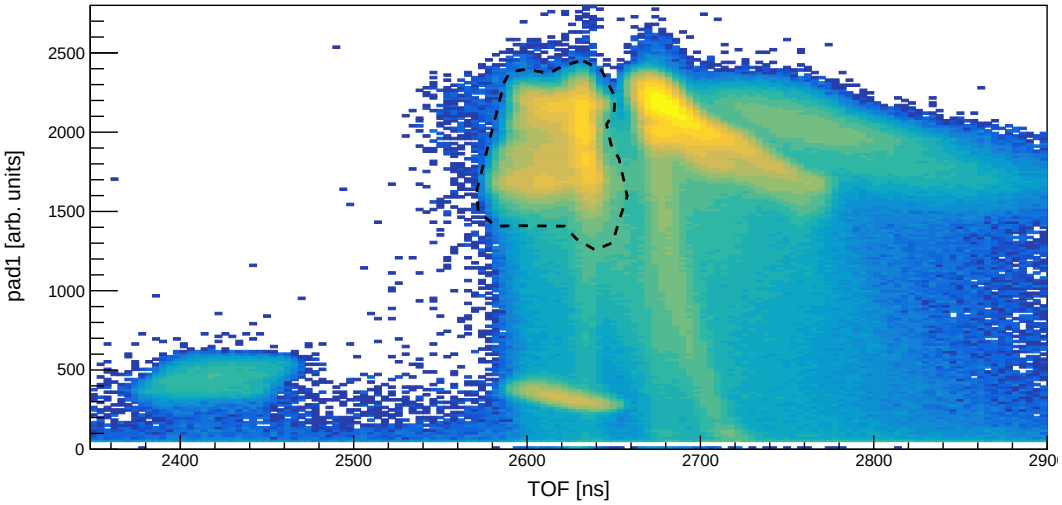

Figure 4.73: PID spectrum for experiment PR194, $^{12}C(\alpha,\alpha')^{12}C$ at $\theta_{lab} = 0°$ with $E_{beam} = 160$ MeV.

Correction parameter	Parameter Value	Unit
c_0	1.00548×10^{3}	MeV/c
c_1	1.07831×10^{-1}	MeV/c/mm
c_2	-1.06216×10^{-5}	MeV/c/mm^2

Table 4.9: The momentum calibration parameters for experiment PR194 (see Section 4.1.10 for details).

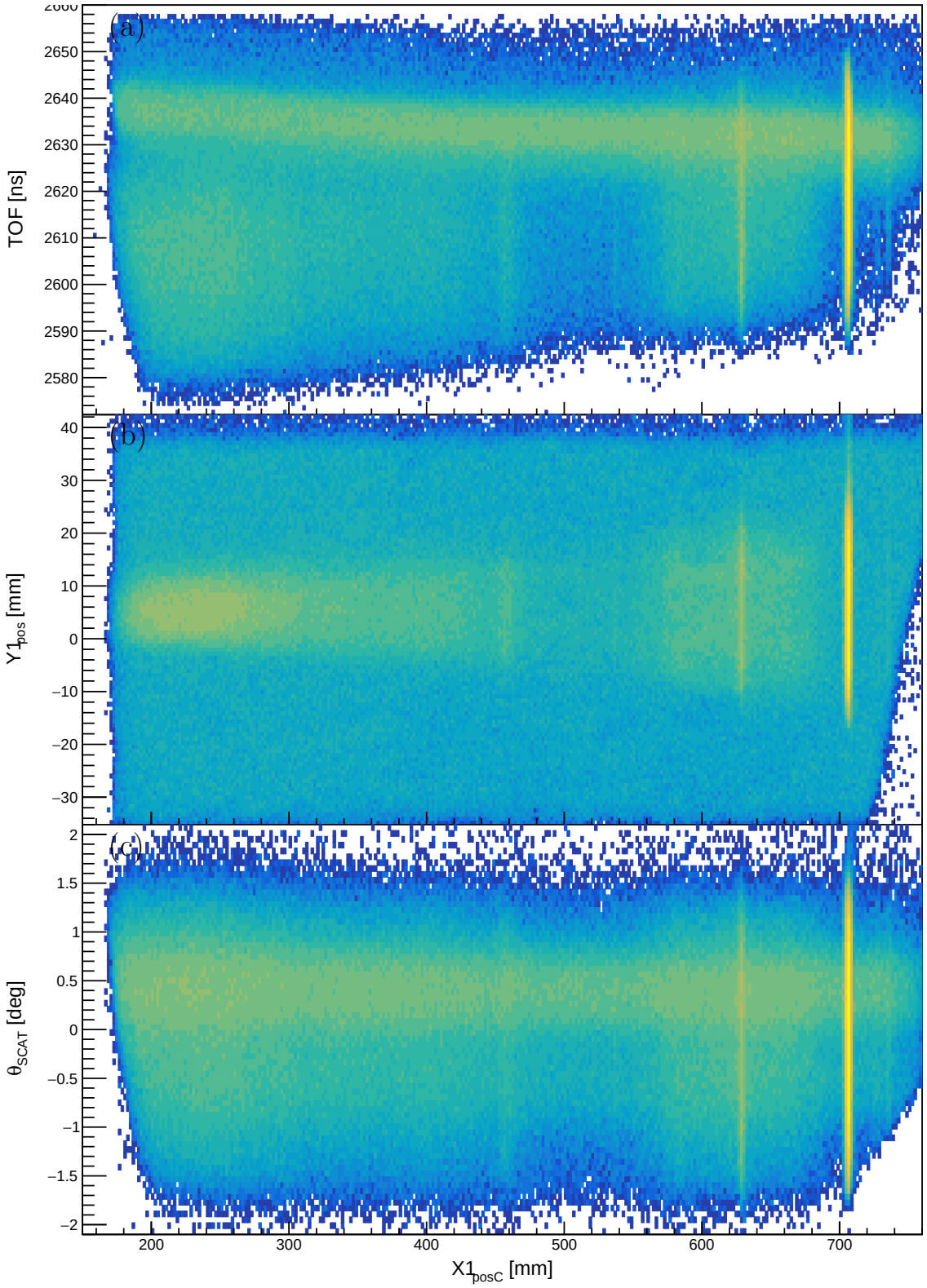

Figure 4.74: The spectra of TOF (a), $\mathrm{Y1_{pos}}$ (b) and θ_{scat} (c) versus $\mathrm{X1_{posC}}$ for experiment PR194, $^{12}\mathrm{C}(\alpha,\alpha')^{12}\mathrm{C}$ at $\theta_{\mathrm{lab}} = 0°$ with $E_{\mathrm{beam}} = 160$ MeV.

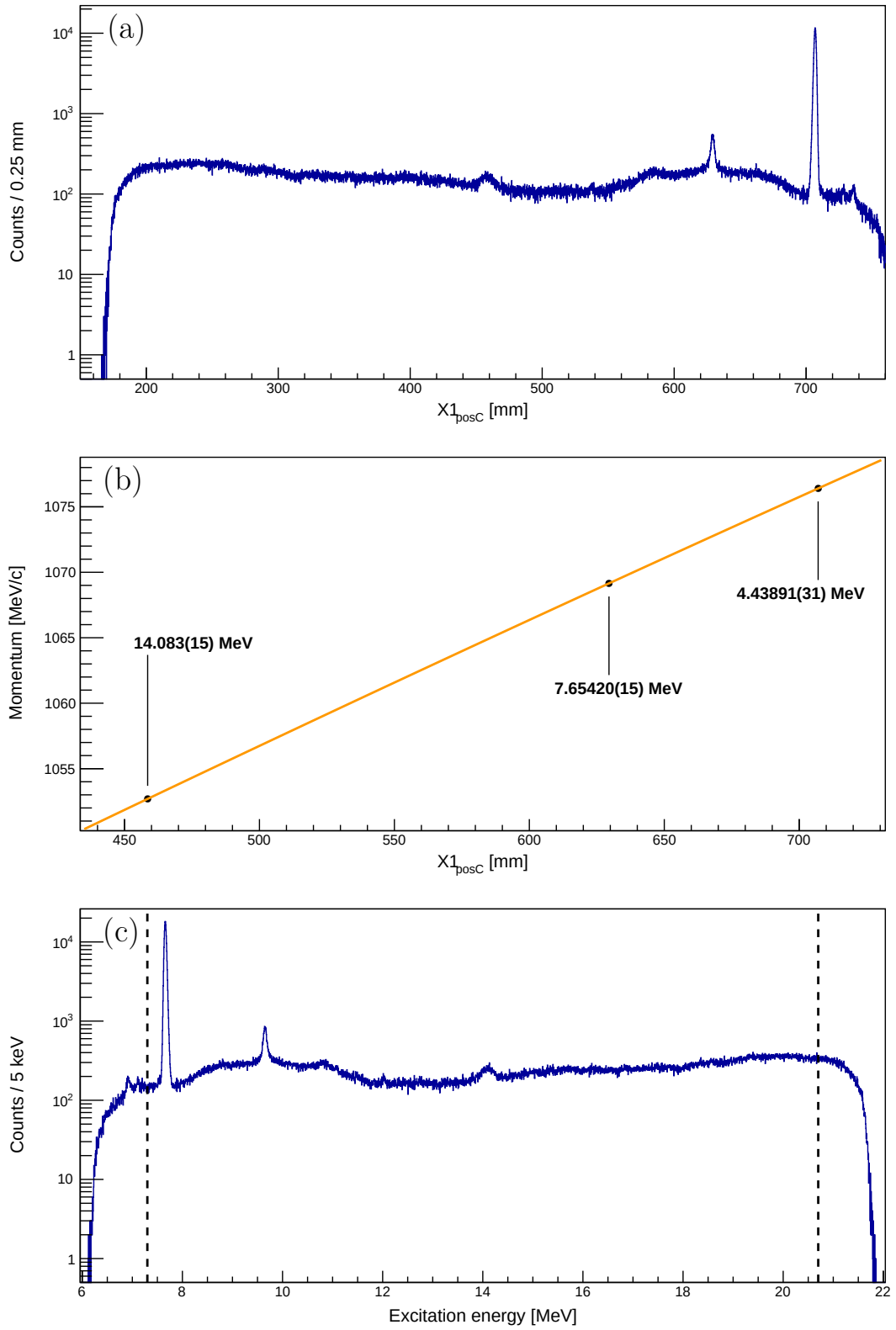

Figure 4.75: The spectra of the corrected focal-plane position $X1_{posC}$ (a), the associated momentum calibration (b) and the excitation energy (c) for experiment PR194, $^{12}C(\alpha,\alpha')^{12}C$ at $\theta_{lab} = 0°$ with $E_{beam} = 160$ MeV. The vertical dashed lines on panel (c) indicate the excitation-energy range with full acceptance by the K600 spectrometer.

4.8 Abridged Analysis of Experiment PR251, $^{12}C(\alpha,\alpha')^{12}C$ at $\theta_{lab} = 0°$, $E_{beam} = 118$ MeV

Since the primary experiment that was performed for this thesis is experiment PR240, the analysis for the measurement of the $^{12}C(\alpha,\alpha')^{12}C$ reaction at $\theta_{lab} = 0°$ with $E_{beam} = 118$ MeV is presented in an abridged format as the analysis method and descriptions have been detailed in Section 4.1.

The PID spectrum is presented on Figure 4.76 and the dashed line represents the PID gate to selectively isolate the α-particle ejectiles from the $^{12}C(\alpha,\alpha')^{12}C$ reaction.

The spectra of TOF (a) and θ_{scat} (b) versus $X1_{posC}$ are presented on Figure 4.77. As mentioned in Section 3.8, the X-type VDCs were employed in the positions of VDC1 and VDC2. Consequently, vertical positions cannot be obtained from the focal-plane detector system. Details of the lineshape corrections can be found in Appendix B.3. It is observed that the lineshape-corrected horizontal focal-plane position, $X1_{posC}$, yields vertically aligned lineshapes with respect to the TOF and θ_{scat} variables.

The spectra of $X1_{posC}$, the associated momentum calibration and the excitation energies are presented on panels (a), (b) and (c) of Figure 4.78, respectively. The momentum calibration parameters are given in Table 4.10.

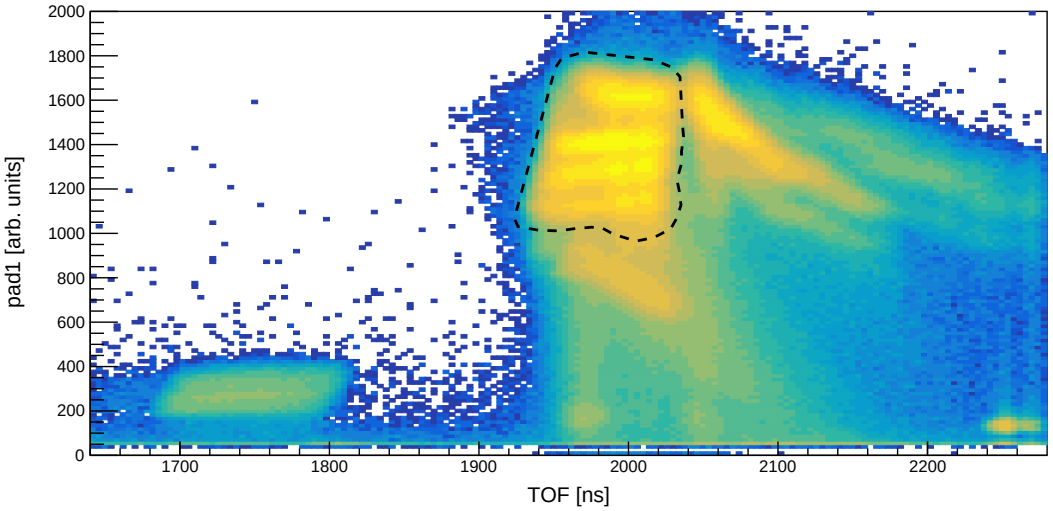

Figure 4.76: PID spectrum for experiment PR251, $^{12}C(\alpha,\alpha')^{12}C$ at $\theta_{lab} = 0°$ with $E_{beam} = 118$ MeV.

Correction parameter	Parameter Value	Unit
c_0	8.63832×10^{2}	MeV/c
c_1	9.53776×10^{-2}	MeV/c/mm
c_2	-2.16144×10^{-5}	MeV/c/mm^2
c_3	1.08406×10^{-8}	MeV/c/mm^3

Table 4.10: The momentum calibration parameters for experiment PR251 (see Section 4.1.10 for details).

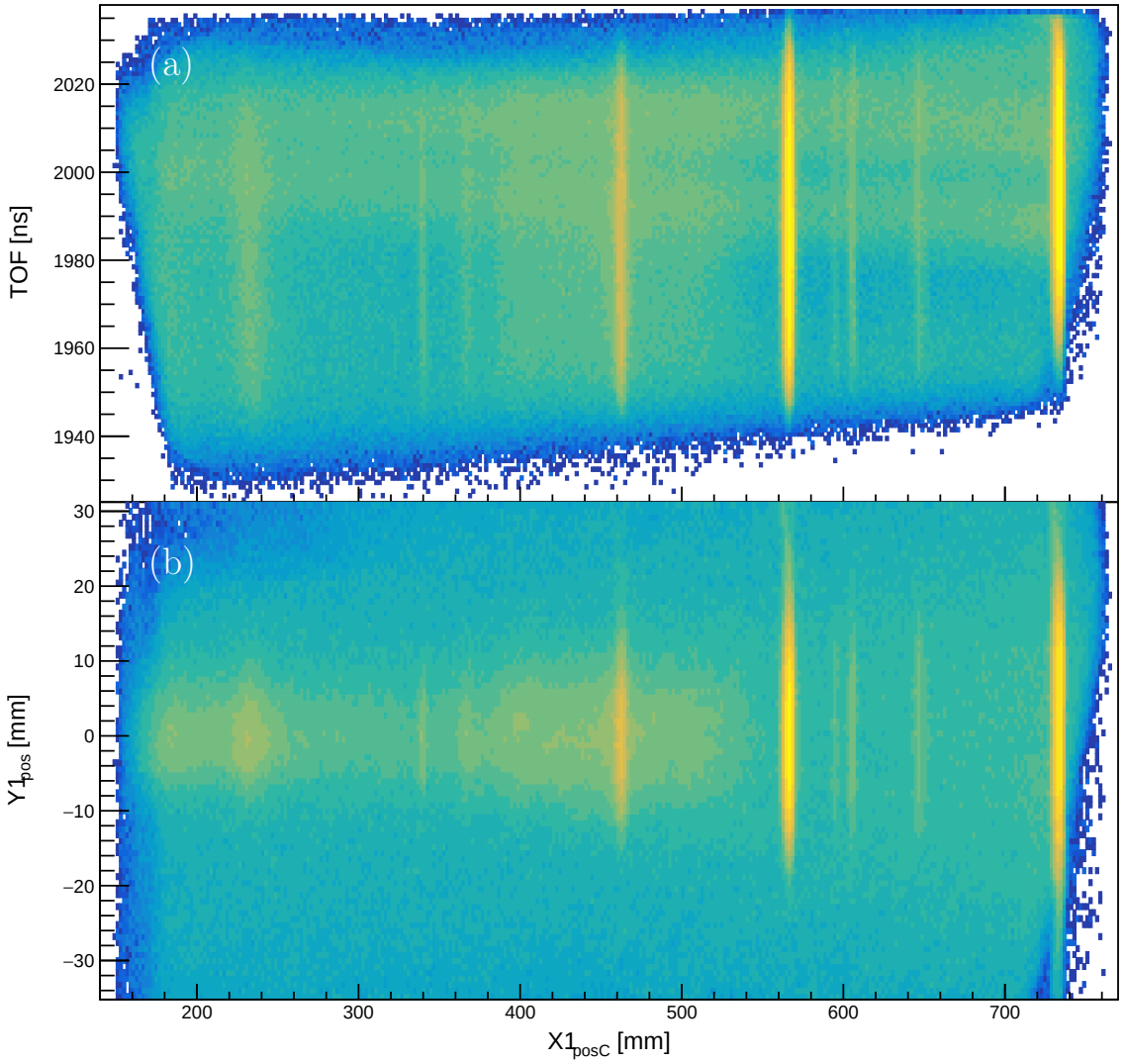

Figure 4.77: The spectra of TOF (a) and θ_{scat} (b) versus $\mathrm{X1_{posC}}$ for experiment PR251, $^{12}\mathrm{C}(\alpha,\alpha')^{12}\mathrm{C}$ at $\theta_{\mathrm{lab}} = 0°$ with $E_{\mathrm{beam}} = 118$ MeV.

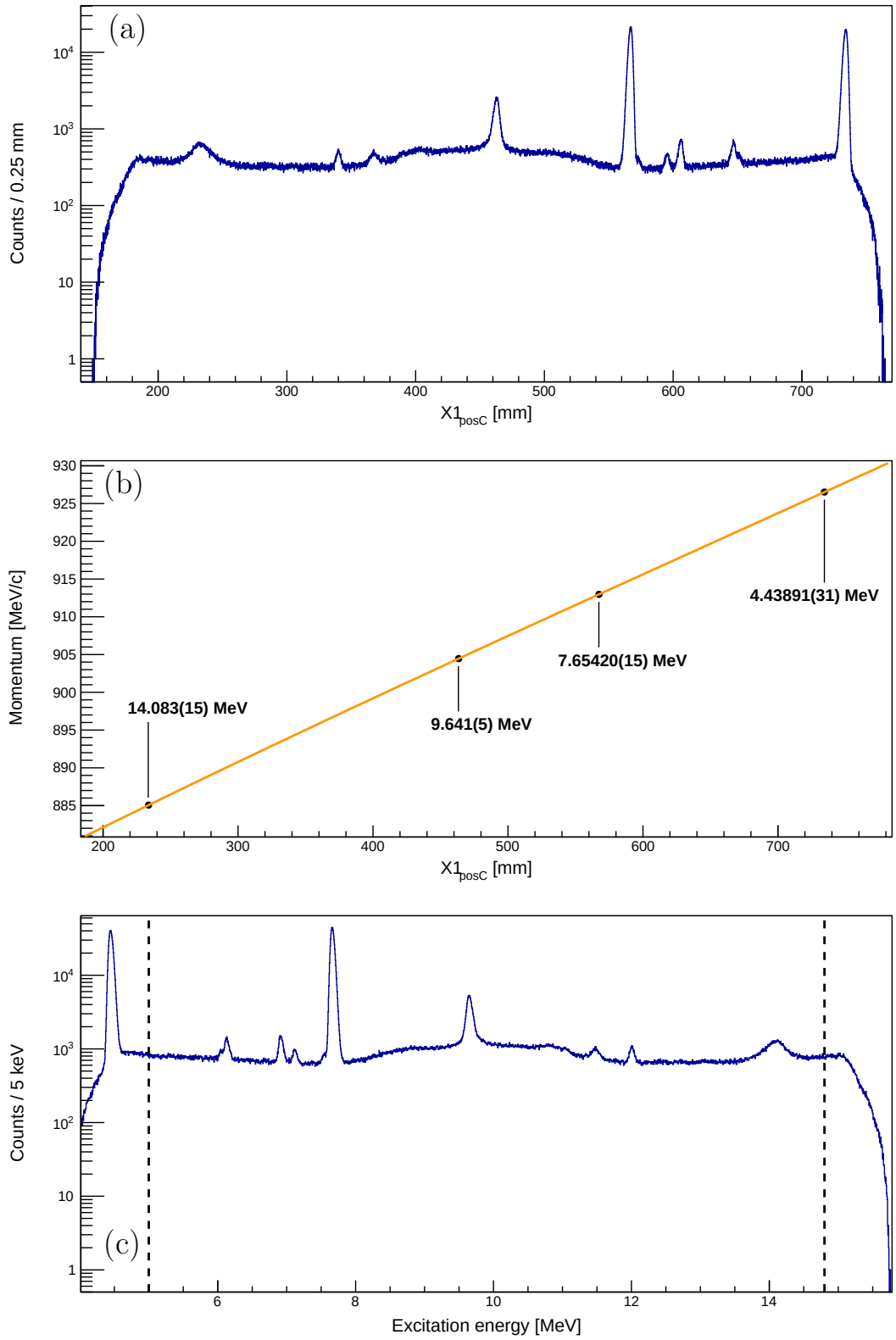

Figure 4.78: The spectra of the corrected focal-plane position $X1_{posC}$ (a), the associated momentum calibration (b) and the excitation energy (c) for experiment PR251, $^{12}C(\alpha,\alpha')^{12}C$ at $\theta_{lab} = 0°$ with $E_{beam} = 118$ MeV. The vertical dashed lines on panel (c) indicate the excitation-energy range with full acceptance by the K600 spectrometer.

4.9 Abridged Analysis of Experiment PR195, $^{14}C(p,t)^{12}C$ at $\theta_{lab} = 21°$, $E_{beam} = 67.5$ MeV

Experiment PR195 consisted of four separate weekends of beam time, with weekend 4 producing viable data for the purposes of this thesis. Since the primary experiment that was performed for this thesis is experiment PR240, the analysis for the measurement of the $^{14}C(p,t)^{12}C$ reaction at $\theta_{lab} = 21°$ is presented in an abridged format as the analysis method and descriptions have been detailed in Section 4.1.

The PID spectrum is presented on Figure 4.79 and the dashed line represents the PID gate to selectively isolate the triton ejectiles from the $^{14}C(p,t)^{12}C$ reaction.

The spectra of TOF (a) and θ_{scat} (b) versus $X1_{posC}$ are presented on Figure 4.82. As mentioned in Section 3.7, the X-type VDCs were employed in the positions of VDC1 and VDC2. Consequently, vertical positions cannot be obtained from the focal-plane detector system. Due to a set of adjacent faulty wires on the X2 wire plane, the raytracing algorithm fails to reconstruct the position of ejectile traversal through the X2 wire plane position. This results in a highly-localised region with $\approx 0\%$ efficiency on the X2 wire plane. Since the ejectile traversal angle, θ_{scat}, is determined from the position of the ejectile at both the X1 and X2 wire planes, this results in a region where θ_{scat} is not calculated, as depicted on Figure 4.80. For the medium-dispersion focal plane setup of this experiment, a set of faulty adjacent wires on the X2 wire plane results in a region of approximately 80 mm on the X1 wire plane where θ_{scat} is not reliably calculated, as shown on Figure 4.81. Consequently, a focal-plane lineshape correction cannot be performed with θ_{scat} as this would result in a localised region of poor efficiency for $X1_{posC}$. The TOF of the ejectile is used an alternative to θ_{scat} for the lineshape correction as the focal-plane dependence of TOF is directly correlated with θ_{scat}. Details of the lineshape corrections can be found in Appendix B.5. It is observed that the lineshape-corrected horizontal focal-plane position, $X1_{posC}$, yields vertically aligned lineshapes with respect to the TOF and θ_{scat} variables.

The spectra of $X1_{posC}$, the associated momentum calibration and the excitation energies are presented on panels (a), (b) and (c) of Figure 4.83, respectively. The momentum calibration parameters are given in Table 4.9.

Correction parameter	Parameter Value	Unit
c_0	4.87368×10^{2}	MeV/c
c_1	6.8687×10^{-2}	MeV/c/mm
c_1	-5.35765×10^{-6}	MeV/c/mm^2

Table 4.11: The momentum calibration parameters for experiment PR195 (see Section 4.1.10 for details).

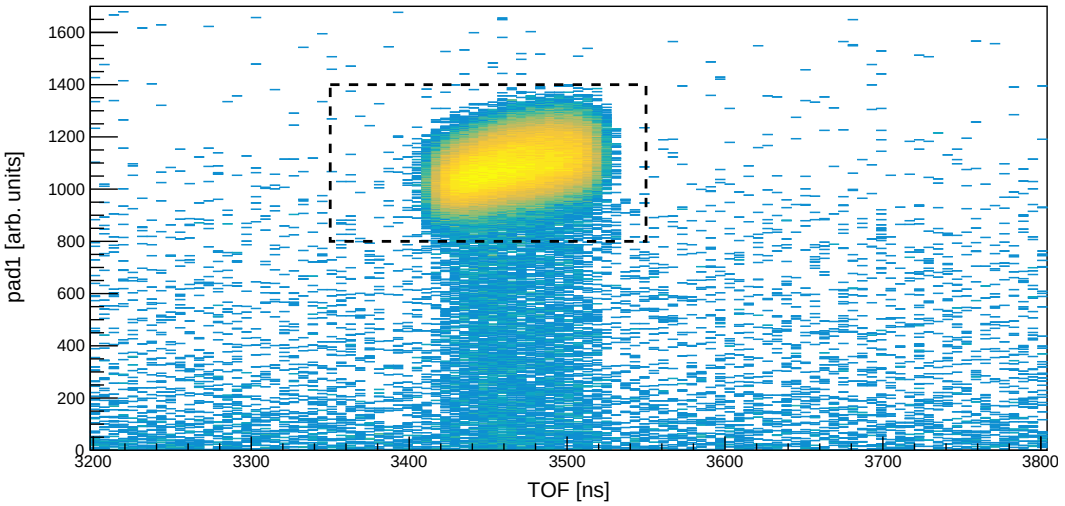

Figure 4.79: PID spectrum for experiment PR195, $^{14}\mathrm{C}(p,t)^{12}\mathrm{C}$ at $\theta_{\mathrm{lab}} = 0°$.

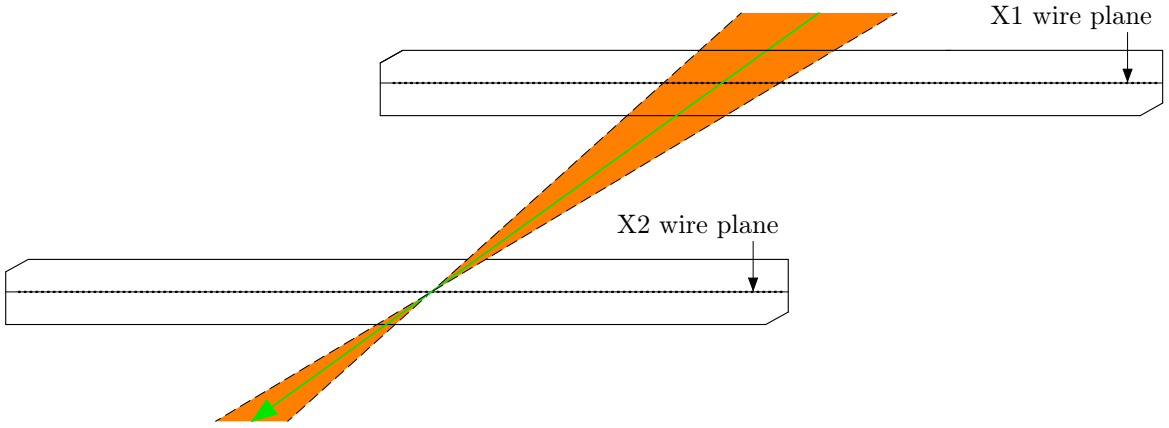

Figure 4.80: Schematic top view of two X-type VDCs illustrating the region of poor θ_{scat} reconstruction for a localised region of poor efficiency in the X2 wire plane.

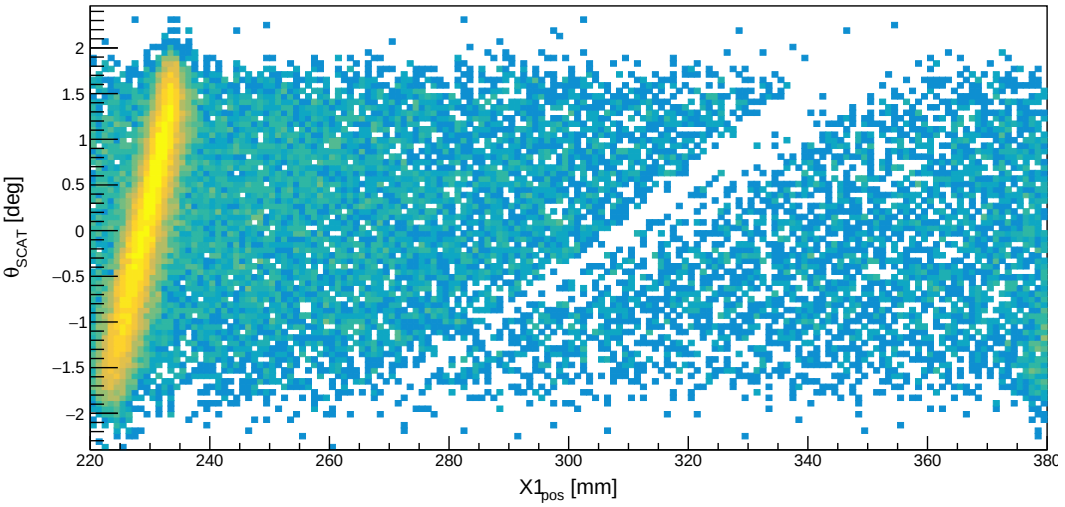

Figure 4.81: Spectrum of θ_{scat} versus $\mathrm{X1}_{\mathrm{pos}}$ for experiment PR195. The region of poor efficiency is clearly observed as a diagonal region with few events.

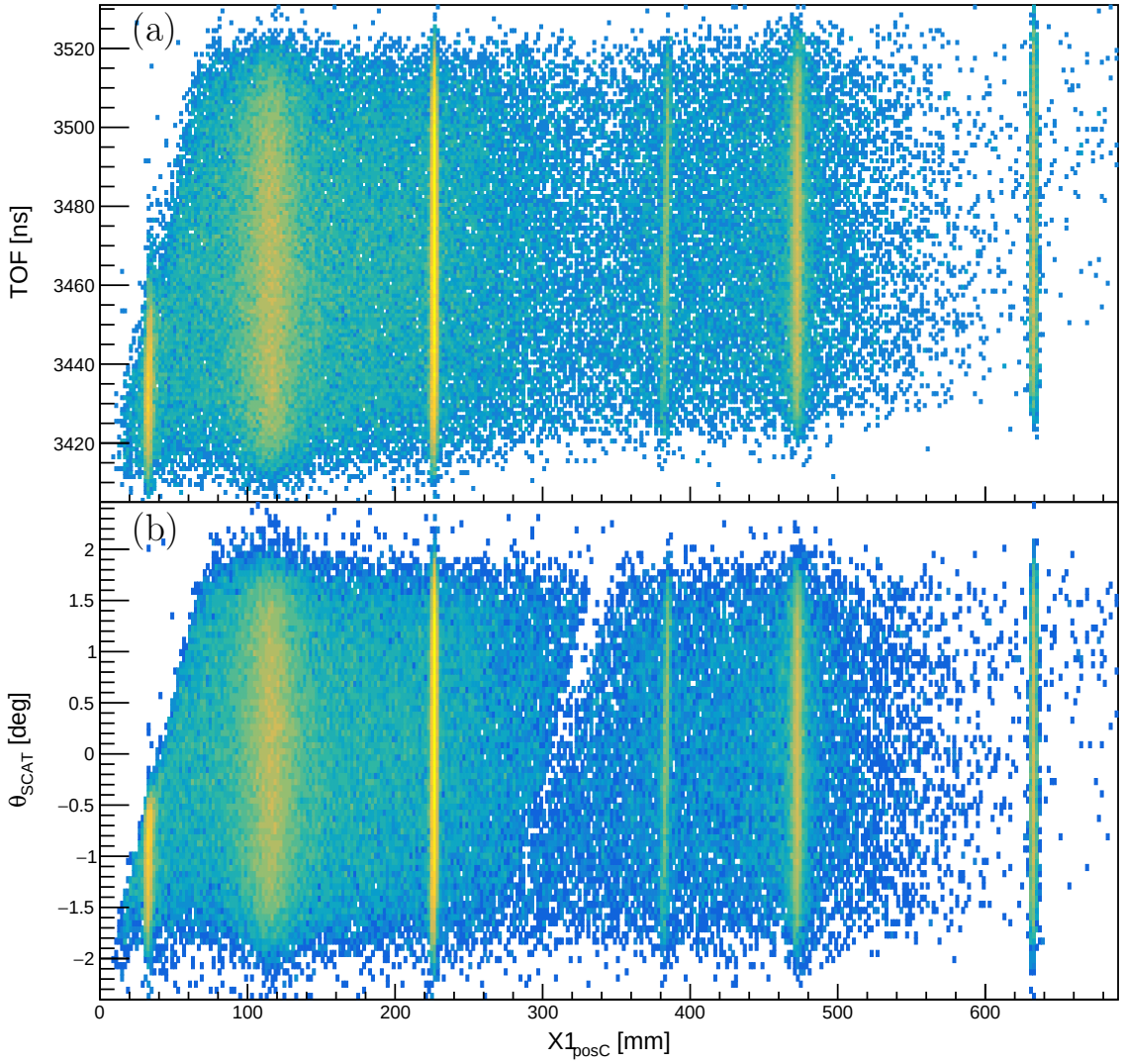

Figure 4.82: The spectra of TOF (a) and θ_{scat} (b) versus $\mathrm{X1_{posC}}$ for experiment PR194, $^{12}\mathrm{C}(\alpha,\alpha')^{12}\mathrm{C}$ at $\theta_{\mathrm{lab}} = 0°$ with $E_{\mathrm{beam}} = 160$ MeV.

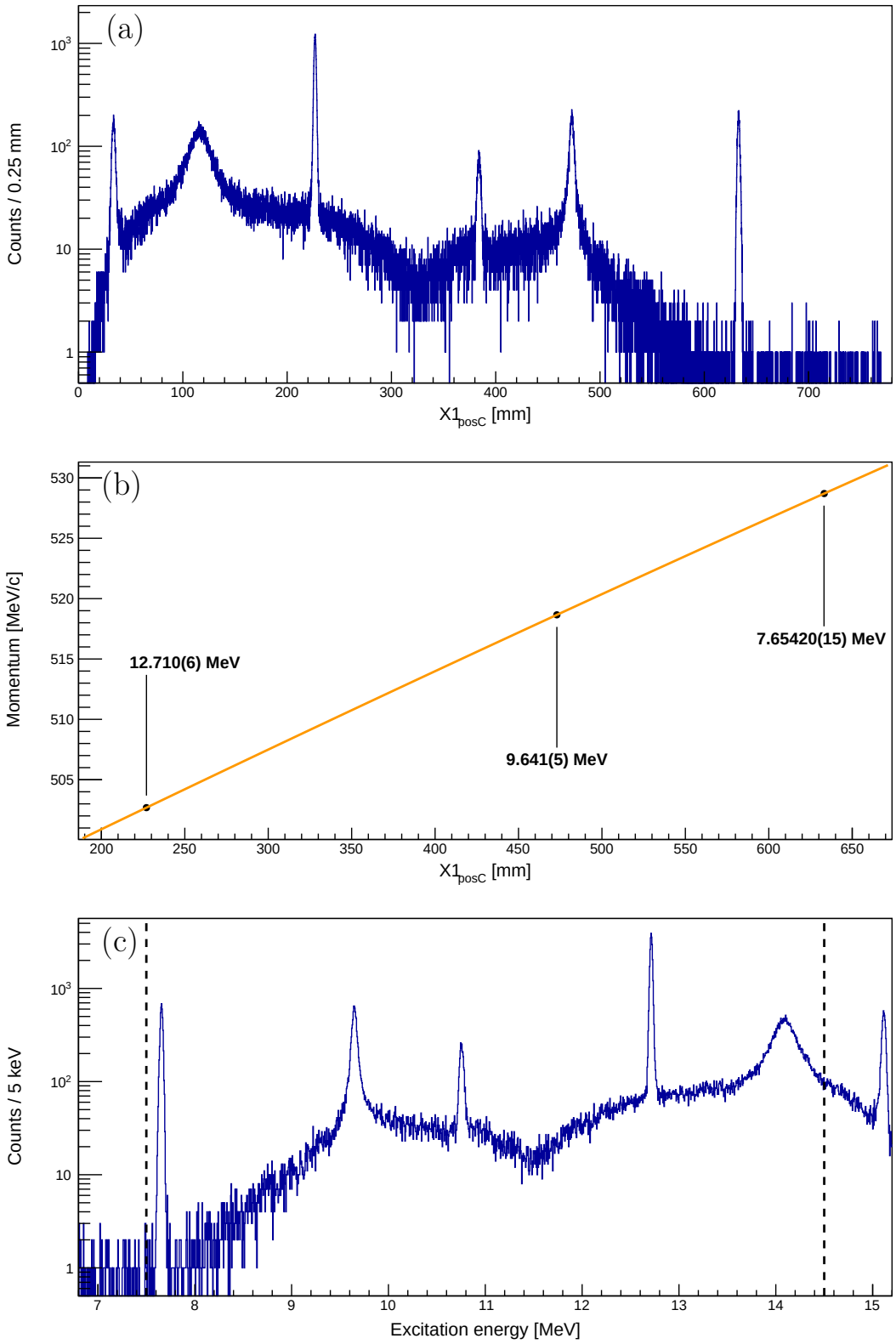

Figure 4.83: The spectra of the corrected focal-plane position $X1_{posC}$ (a), the associated momentum calibration (b) and the excitation energy (c) for experiment PR194, $^{12}C(\alpha,\alpha')^{12}C$ at $\theta_{lab} = 0°$ with $E_{beam} = 160$ MeV. The vertical dashed lines on panel (c) indicate the excitation-energy range with full acceptance by the K600 spectrometer.

4.9.1 Contaminants

Several well-resolved contaminant peaks were observed and these were accounted for in the R-matrix analysis with simplified symmetrical lineshapes.

4.9.1.1 Experiment PR166

For the measurements of $^{12}\mathrm{C}(\alpha,\alpha')^{12}\mathrm{C}$ at $\theta_{\mathrm{lab}} = 6°, 8.5°$ and $10°$ with $E_{\mathrm{beam}} = 196$ MeV, the small satellite peak below the Hoyle state is contaminant that is parameterised by several peaks due to the unusual lineshape. Fortunately, this small contribution is fully separated from the primary peak of the Hoyle state. Additionally for the measurement of $^{12}\mathrm{C}(\alpha,\alpha')^{12}\mathrm{C}$ at $\theta_{\mathrm{lab}} = 10°$, the broad peak at $E_x \approx 11.46$ MeV and the two small, narrow peaks at $E_x \approx 11.76$ and 11.86 MeV are contaminants that are individually parameterised by single peaks. These contaminants are relatively small and should minimally affect the analysis of strongly-populated broad resonances at $E_x \approx 9$ MeV.

4.9.1.2 Experiment PR194

For the measurement of $^{12}\mathrm{C}(\alpha,\alpha')^{12}\mathrm{C}$ at $\theta_{\mathrm{lab}} = 0°$ with $E_{\mathrm{beam}} = 160$ MeV, a contaminant peak was observed at $E_x \approx 11.07$ MeV . This solitary contaminant contribution is accounted for and does not affect the analysis of the broad monopole structure in the $E_x \approx$ 7-16 MeV range of interest.

4.9.1.3 Experiment PR251

For the measurement of $^{12}\mathrm{C}(\alpha,\alpha')^{12}\mathrm{C}$ at $\theta_{\mathrm{lab}} = 0°$ with $E_{\mathrm{beam}} = 118$ MeV, contaminant peaks were observed at $E_x \approx 7.5, 11.07, 11.46$ and 12.0 MeV. These contaminant contributions are accounted for and do not affect the analysis of the broad monopole structure in the $E_x \approx$ 7-16 MeV range of interest.

4.9.1.4 Experiment PR195

For the measurement of $^{14}\mathrm{C}(p,t)^{12}\mathrm{C}$ at $\theta_{\mathrm{lab}} = 21°$ with $E_{\mathrm{beam}} = 67.5$ MeV, no contaminant peaks were observed in the $E_x \approx$ 7-16 MeV range of interest.

4.9.1.5 Experiment PR240

For the measurement of $^{14}\mathrm{C}(p,t)^{12}\mathrm{C}$ at $\theta_{\mathrm{lab}} = 0°$ with $E_{\mathrm{beam}} = 140$ MeV, narrow contaminant peaks were observed at $E_x \approx 8.05, 8.15$ and 9.2 MeV. These well-resolved peaks are accounted for and do not affect the analysis of the broad monopole structure in the $E_x \approx$ 7-16 MeV range of interest.

4.10 Fitting method

The R-matrix theory outlined in Chapter 2 is a prominent phenomenological model with which to interpret resonances in nuclei. Given the relatively recent advances in experimental equipment, excitations in nuclei can now be observed with much greater selectivity. In particular, the advances in silicon detector technology have enabled more precise studies of the decay channels associated with charged-particle emission. This new window of perception necessitates a fitting algorithm that allows not only for the simultaneous fit of an arbitrary amount of spectra (providing self-consisency, i.e. shared parameters for observables which are assumed to be shared amongst the spectra), but is also based on a multichannel formalism since these various particle-decay channels can now be experimentally discriminated.

The purpose of the VeridicalFit fitting toolkit is to provide the following features and goals:

Primary features

- To provide a toolkit to fit spectra with a phenomenological multichannel R-matrix fitting code.
- The ability to simultaneously fit an arbitrary number of spectra with a global minimization.
- The assurance of self-consistent parameters between fitted histograms: the physics of the R-matrix formalism dictates that certain observables are independent of the measurement method. Consequently, the associated parameters of such observables must be shared between the histograms.

  Consider the decay of a resonance: by gating on the detected decay particles at different angles, spectra corresponding to different angular ranges can be analyzed. Whilst the strength of the resonance may exhibit angular dependence, the resonance energy (E_R) parameter does not and consequently must be shared between the fits corresponding to different angular ranges of decay.

  Consider the population of a resonance through two different incoming channels: whilst the population channel may affect the observed lineshape, the resonance energy (E_R) of the resonance must still be identical. The E_R parameter of a resonance is therefore shared across the fits which correspond to different incoming channels.
- The ability to account for the feeding factors for all lineshapes, as described in Section 2.6.1.8.

- The ability to account for the experimental resolution of observed lineshapes. Whilst many approaches use approximations for the associated convolution, such approaches may create a clear logical inconsistency. This toolkit allows for the accurate convolution of intrinsic lineshapes with Gaussian experimental resolutions.

  Consider the population of a resonance in an excitation energy range that allows for particle-decay. In such a regime, the Coulomb interactions associated with such decays can no longer be assumed to be negligible and consequently, the lineshape of the resonance can be modeled with R-matrix theory. The intrinsic lineshape of the resonance is then modeled with a R-matrix Lorentzian profile. An approximation that experimentally observed lineshape can be approximated by a Voigt profile (produced by the convolution of a standard Lorentzian and Gaussian profiles) is completely inconsistent: If the R-matrix formalism is necessary to model the energy dependence of the resonance widths, then the approximation of the observed lineshape to simply be the Voigt profile with an R-matrix width is invalid. Conversely, if the Voigt profile approximation is valid (within experimental error), then the use of the R-matrix formalism is unneccesary to model the observed lineshape of the resonance. Providing a convolution can be crucial when the high-energy tails of resonances and other observed structures are unresolved.

- The ability to calculate observed lineshapes by convolving the intrinsic lineshapes with distributions that stem from experimental artefacts. Typical examples being the Gaussian distribution corresponding to the inherent resolution of the detectors and the Landau distribution corresponding to the target-related energy loss for the ejectile. This is implemented through the TVirtualFFT class (from the ROOT framework), which in turn leverages the FFTW3 library. This class automatically determines whether the ROOT installation has the associated "fftw3" module enabled. If not, a brute force numerical convolution is automatically implemented. VeridicalFit has been written to capitalise on the computational-speed superiority of the FFTW3 library over such a brute force method and consequently, the installation and enabling of this library is strongly recommended.

- The ability to perform the simultaneous fit of spectra with different experimental resolutions and target-related energy losses These experimental factors can be defined to either be uniquely linked to a specific dataset or shared amongst several. When an experimental rfactor is assigned to multiple datasets, the associated parameters are shared between the fits of the respective spectra.

- Parallelization of the fitting code: the level of parallelism must be user definable (the default level is single-threaded). The maximum level of

parallelism is determined by the number of histograms (N_{hist}) to be simultaneously fitted (one thread per histogram).

- Optimization of the parallelization: if the maximum level of parallelism is limited by the hardware constraints to be N_{hard}, the simultaneous fit of N_{hist} histograms is then optimally distributed across the N_{hard} threads.

Ancillary features

- The ability to fit spectra with a variety of lineshapes, e.g. Gaussian, Lorentzian, R-matrix Lorentzian.
- The ability to simultaneously fit nuclear excitations from various nuclei on a single spectrum. One possible benefit is to account for experimental contaminants.

4.10.1 Convolution Of Lineshapes

Experimentally, it is not possible to directly measure the intrinsic lineshape of a nuclear excitation as the very act of measurement inevitably introduces changes to produce the observed lineshape in the form of convolutions. For the Hoyle state, the primary peak (situated at approximately 7.654 MeV) exhibits a Lorentzian-esque intrinsic lineshape with a total width of the order ~ 10 eV which is approximately 6 orders of magnitude smaller than the ~ 2 MeV FWHM of the ghost-anomaly tail (shown in Figure 4.86). The observed lineshape for the primary peak is therefore dominated by experimental factors such as the detector energy resolution and target-related energy loss.

The convolution of two signals $f(x)$ and $g(x)$ is defined by

$$f * g = \int_{-\infty}^{+\infty} f(\tau)\, g(x-\tau)\, d\tau, \tag{4.32}$$

where $*$ denotes the convolution. The convolution theorem states that the Fourier transform of a convolution of two signals is equal to the product of the Fourier transforms of the two individual signals [93]:

$$\mathcal{F}\left(f * g\right) = \mathcal{F}\left(f\right) \cdot \mathcal{F}\left(g\right), \tag{4.33}$$

$\mathcal{F}$ represents the Fourier transform, defined as

$$\mathcal{F}\left(f\right) \equiv F(\xi) = \int_{-\infty}^{+\infty} f(x)\, e^{-2\pi i x \xi}\, dx, \tag{4.34}$$

with the inverse Fourier transform defined as

$$\mathcal{F}^{-1}\left(F\right) \equiv f(x) = \int_{-\infty}^{+\infty} F(\xi)\, e^{2\pi i x \xi}\, d\xi. \tag{4.35}$$

The calculation of a convolution through the Fourier transforms of the base signals is typically more efficient than the direct method of Equation 4.32. Computationally, the Fourier transformation of Equation 4.35 is implemented discretely. The function $f(x)$ is sampled with a sampling interval of Δ to produce a set of N sampled points:

$$\{f_k\} := f_0,\, f_1, \ldots,\, f_{N-1}, \tag{4.36}$$

where

$$f_k = f(k\Delta). \tag{4.37}$$

At the discrete values of ξ_n given by

$$\xi_n \equiv \frac{n}{N\Delta}, \quad \text{and} \quad n = -\frac{N}{2}, \ldots, \frac{N}{2}, \tag{4.38}$$

the Fourier transform can be estimated as

$$F(\xi_n) = \int_{-\infty}^{+\infty} f(x)\, e^{-2\pi i x \xi_n}\, dx \approx \sum_{k=0}^{N-1} f_k\, e^{-2\pi i x_k \xi_n} \Delta = \Delta \sum_{k=0}^{N-1} f_k\, e^{-2\pi i k n/N}. \tag{4.39}$$

The Discrete Fourier Transform (DFT) is defined as

$$F_n = \sum_{k=0}^{N-1} f_k\, e^{-2\pi i k n/N}, \tag{4.40}$$

with the inverse DFT given by

$$f_k = \frac{1}{N} \sum_{n=0}^{N-1} F_n\, e^{2\pi i k n/N}. \tag{4.41}$$

The DFT is related to the continuous Fourier transform as

$$F(\xi_n) \approx \Delta F_n. \tag{4.42}$$

Computationally, the use of DFTs is implemented through a Fast Fourier Transform (FFT) algorithm [94, 95]. Whilst the convolution theorem and DFTs offer a convenient way to calculate convolutions, the direct calculation of DFTs through Equation 4.40 is often too slow as its computation time scales as $O(N^2)$. The computation times of FFT algorithms typically scale as $O(N \log N)$ and are therefore more suited for large-scale fit optimsations.

4.10.1.1 The observed lineshape

Any measurement is always influenced by an inherent experimental resolution, typically assumed to be of a Gaussian distribution.

For scattering experiments where the ejectile is measured to infer the excitation-energy of the recoil nucleus, the ionisation energy-loss of the ejectile through the target can also affect the measurement. Under certain conditions, this energy loss can be well parameterised by a Landau distribution [96].

It is evident that to accurately analyse the scattering data for this thesis, the spectra cannot be directly fitted with intrinsic nuclear lineshapes, but rather with a convolution of the intrinsic, Gaussian and Landau lineshapes. The observed lineshape σ_{obs} is given by

$$\sigma_{obs}(E_x) \propto \int_{-\infty}^{+\infty} \int_{-\infty}^{+\infty} G(y-x) \cdot L(x) \cdot \sigma_{int}(E_x - y)\, dx\, dy, \tag{4.43}$$

where σ_{int} is the intrinsic lineshape of the nuclear excitation, G is the Gaussian distribution given by

$$G(x) = \frac{1}{\sigma\sqrt{2\pi}} e^{-\frac{(x-\mu)^2}{2\sigma^2}} \tag{4.44}$$

and L is the Landau distribution given by

$$L(x) = \frac{1}{\pi c} \int_0^{+\infty} e^{-t} cos\left[t\left(\frac{x-\mu}{c}\right) + \frac{2t}{\pi}\log\left(\frac{t}{c}\right).\right] \tag{4.45}$$

This is implemented in VeridicalFit through the Fourier Transform method:

$$\sigma_{obs}(E_x) \propto \mathcal{F}^{-1}\Big\{\mathcal{F}(G)\cdot\mathcal{F}(L)\cdot\mathcal{F}(\sigma_{int})\Big\}. \tag{4.46}$$

The Landau distribution, which extends to infinite energies, sometimes overestimates the energy loss in the high-energy tail. For certain measurements with significant target-related energy loss, a truncated Landau distribution $L'(x)$ is employed with the following form:

$$L'(x) = \begin{cases} L(x) & \text{if } x < s \\ 0 & \text{if } x \geq s, \end{cases} \tag{4.47}$$

where s is the estimated truncation parameter. An example of the overestimation of the energy loss by the Landau distribution is given by the analysis of the $J^\pi = 2_1^+$ and $J^\pi = 0_2^+$ states of ^{12}C from the ^{12}C$(\alpha,\alpha')^{12}$C data from experiment PR251. Panel (a) of Figure 4.84 presents a fit of the $J^\pi = 2_1^+$ state without Landau truncation which indicates an overestimation of the high-energy tail of the peak at $E_x \approx 4.8$ MeV. Since this state is bound and exhibits an intrinsic width that is several orders of magnitude smaller than the experimental resolution, the experimentally observed lineshape is purely an experimental artefact, largely determined by the experimental resolution and the target-related energy loss. By implementing a truncation parameter of the Landau distribution, as described by Equation 4.47, the fit of the tail of the $J^\pi = 2_1^+$ state is improved, as displayed on panel (b) of Figure 4.84. Similarly for the analysis of the $J^\pi = 0_2^+$ state of ^{12}C from the same dataset, the fit without the Landau truncation parameter is presented in panel (a) of Figure 4.85 and it is observed that the fit overestimates the high-energy tail of the peak at $E_x \approx 7.8$ MeV. By implementing the same Gaussian experimental resolution and Landau truncation optomised for the $J^\pi = 2_1^+$ state on panel (b) on Figure 4.84, the fit of the $J^\pi = 0_2^+$ state on panel (b) of Figure 4.85 is vastly improved. It should be noted that the $J^\pi = 2_1^+$ state from the ^{12}C$(\alpha,\alpha')^{12}$C data from experiment PR251 is not fully accepted by the focal plane and the associated spectra are obtained with additional cuts to ensure uniform acceptance across the displayed range.

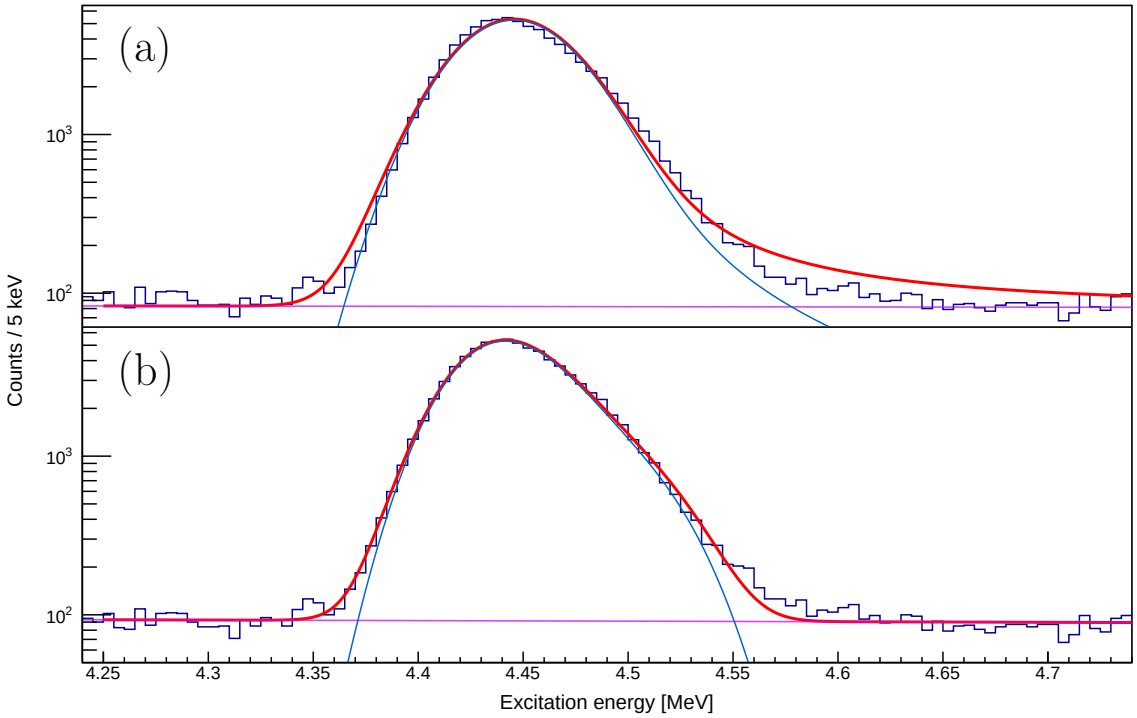

Figure 4.84: Fits of the $J^\pi = 2_1^+$ state of ^{12}C, from the ^{12}C$(\alpha, \alpha')^{12}$C data of experiment PR251, with the convolved lineshape given by Equation 4.46. Panels (a) and (b) correspond to fits with and without the Landau truncation parameter implemented.

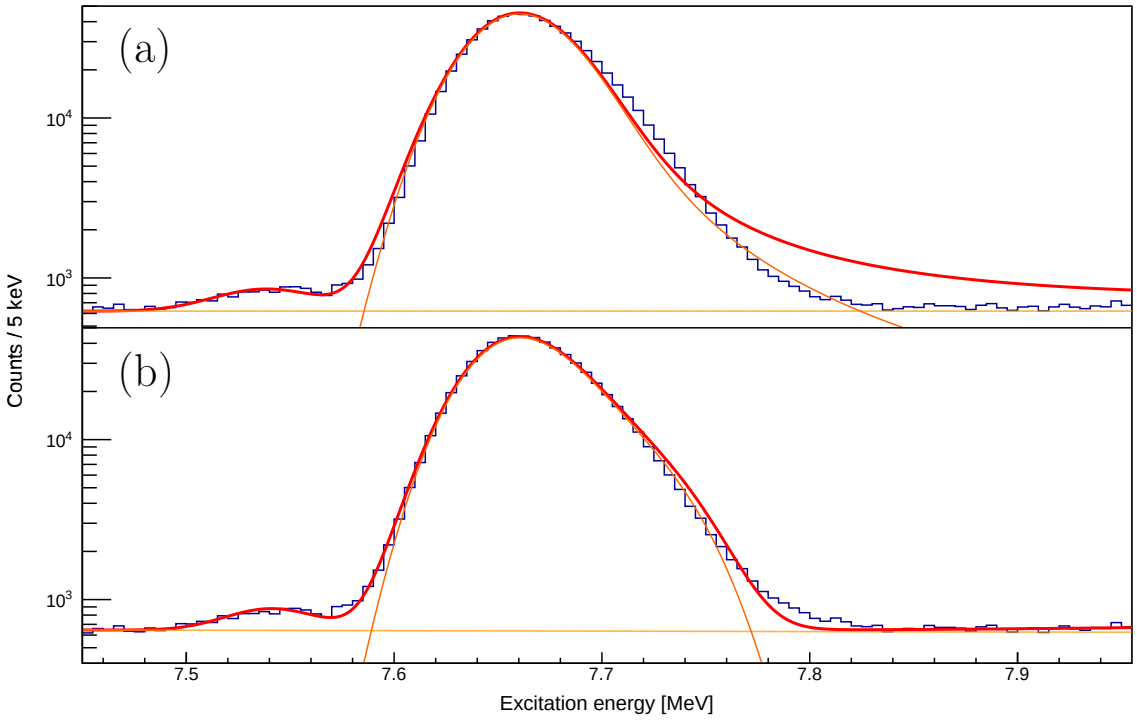

Figure 4.85: Fits of the $J^\pi = 0_2^+$ state of ^{12}C, from the ^{12}C$(\alpha, \alpha')^{12}$C data of experiment PR251, with the convolved lineshape given by Equation 4.46. Panels (a) and (b) correspond to fits with and without the Landau truncation parameter implemented.

4.10.1.2 Compensated DFT Sampling

Numerical convolutions can be computationally taxing and are usually one of the limiting processes when implemented within a fit optimisation. The Fast Fourier Transform (FFT) algorithm is used to efficiently calculate convolutions, the accuracy of which is determined by the number of samples used in the FFT algorithm. The sampling granularity of the "time" spectrum is directly related to the density of the decomposed frequencies. In principle, the sampling interval should be sufficiently smaller than the features of the "time" spectrum. An issue arises when the function to be convolved exhibits structure which are narrower than the sampling interval. An example of such an extremely narrow structure is the primary peak of the Hoyle which exhibits a Lorentzian-esque intrinsic lineshape with a total width of the order ∼10 eV. Due to the circular convolution method, which requires that convolved functions should approach 0 towards the extremes of the sampled range, a large FFT sampling range of ∼100 MeV is chosen. In order to correctly sample the primary peak of the Hoyle state with a sampling interval of ∼1 eV, a prohibitively large dataset with $\sim 10^8$ sampled points must be used which in some cases can be computationally prohibitive.
The sampling interval Δ determines the resolution of the (time) signal, which in turn determines the maximum frequency that can be resolved (see Equation Equation 4.38). The maximum frequency that can be resolved is determined by the highest frequency, known as the Nyquist frequency:

$$f_{\text{Nyquist}} = \frac{1}{2\Delta}, \tag{4.48}$$

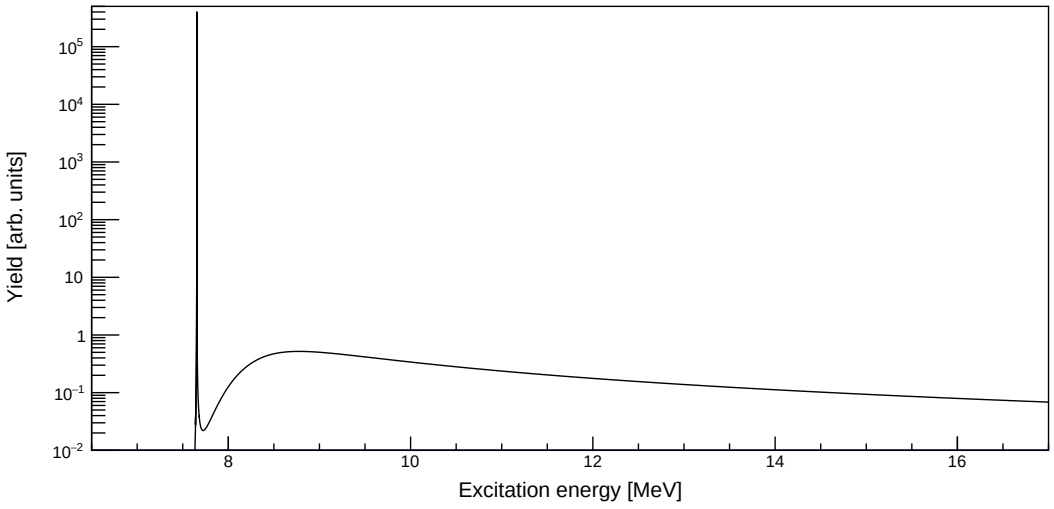

Figure 4.86: The intrinsic lineshape of the Hoyle state with an α_0 single-channel decay mode with a 10 eV width at the resonance energy of $E_x = 7.654$ MeV.

which determines the frequency range of the DFT:

$$-f_{\text{Nyquist}} \leq f_k \leq f_{\text{Nyquist}}. \tag{4.49}$$

For a sampling interval Δ that is significantly larger than 10 eV, the structure of the primary peak is not reliably sampled. A phenomenon known as aliasing occurs whereby the higher-frequency content corresponding to this narrow peak, which lies outside this frequency range, is incorrectly transferred (aliased) into that range. Moreover, the approximation of Equation 4.39 is sensible for a sufficiently small sampling interval such that the function $f(x)$ can be approximated to be linear within each interval. In essence, the energy spectral density (square integral) of the base function $f(x)$ can be approximated as

$$E = \int_{-\infty}^{+\infty} \|f(x)\|^2 \, dx \approx \Delta \sum_{k=0}^{N-1} f_k^2. \tag{4.50}$$

For a 100 eV sampling interval of the Hoyle state, the energy spectral density for the wide ghost peak of the Hoyle state is approximated well by this discrete sum, however the same cannot be said for the narrow primary peak which exhibitis an FWHM of $\approx$ 10 eV. In such a case, the approximation of Equation 4.51 only holds for the broad ghost peak and as such, the ratio of yield (area) between the primary peak and the ghost peak can be miscalculated. The convolution of the intrinsic lineshape of the Hoyle state (with a 10 eV width at the resonance energy and a solitary α_0 decay mode, as shown in Figure 4.86) and a Gaussian lineshape with 1 keV FWHM is presented in Figure 4.87 for different numbers of sampling points. It is observed that the yield ratio be-

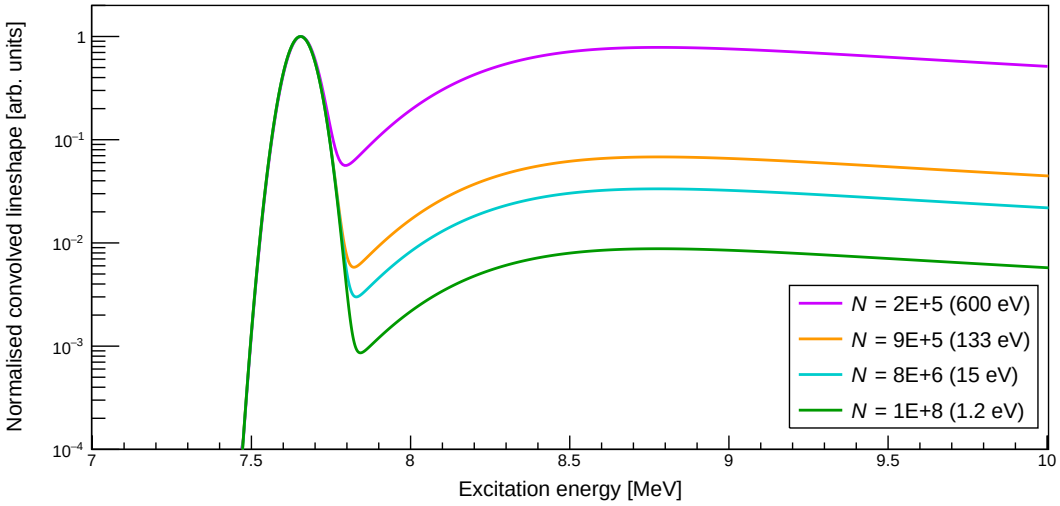

Figure 4.87: The dependence of the convolved lineshape on the number of FFT samples with regular discrete sampling.

tween the primary peak and the ghost peak is dependent on the number of FFT sampling points, but the lineshape of the primary peak is largely independent and is essentially completely determined by the shape of the Gaussian component as the 10 eV width is 2 orders of magnitude smaller than the 1 keV (FWHM) Gaussian resolution. The convolution with 10^8 FFT sampling points (green) reproduces the yield ratio of ~ 2.36 that is determined by directly integrating the intrinsic lineshape. For particularly large sampling intervals, the probability that the intrinsic lineshape is sampled near the maximum of the primary peak is small and therefore the yield ratio is often incorrectly suppressed. There are two simple solutions to such an issue: the first is simply to use a smaller sampling interval, e.g. 1 eV. Computationally, the amount of memory needed for $N \sim 10^8$, coupled with the increased calculation time makes this unfeasible for a large-scale fitting programme. The second solution is to implement a Nonuniform Discrete Fourier Transform (NUDFT): whereas the sampled points for the DFT algorithm are equidistant (see Equation 4.37), the NUDFT algorithm permits arbitrary spacing between the sampled points. In principle, this allows the base signal to be sampled with a smaller intervals in regions which contain high-frequency components and larger intervals for the slowly-varying regions, thereby solving the computation limitations and mitigating aliasing. Some prominent libraries for Nonuniform Fast Fourier Transform (NUFFT) calculations are NUFFT [97] and the more modern FINUFFT [98]. NUFFTs are to NUDFTs as FFTs are to DFTs. Due to the time constraints of this thesis, there was insufficient time to implement such an elegant solution. Instead, a suitable and efficient solution to this undersampling issue was found and implemented with the regular FFT algorithm. This solution is underpinned by the assumption that experimentally, the observed

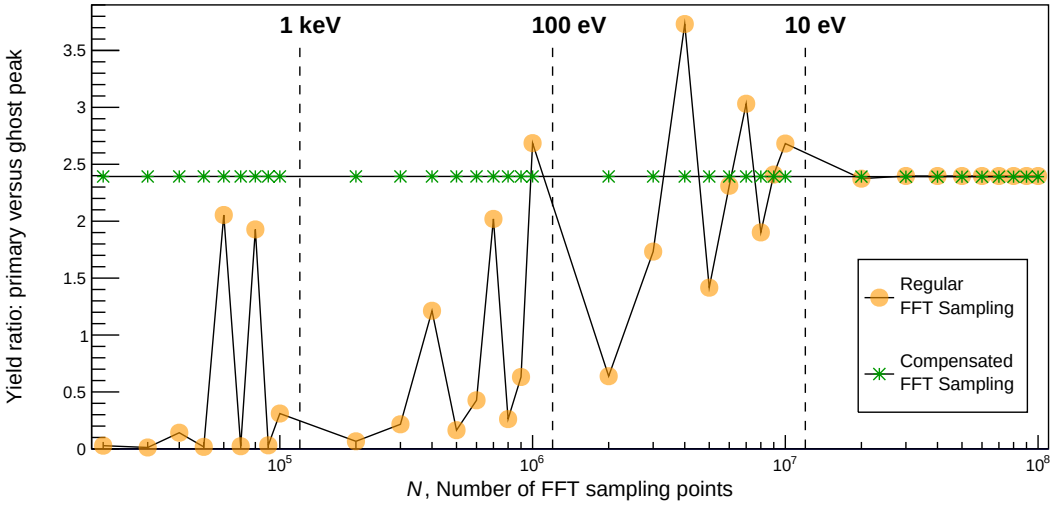

Figure 4.88: The dependence of the yield ratio (between the primary and ghost Hoyle state peaks) on the number of FFT samples.

lineshape of the primary peak of the Hoyle state is indeed completely dominated by the experimental resolution (Gaussian) and target-related energy loss (Landau) components. For the measurements analysed for this thesis, the experimental energy resolution is typically > 50 keV (FWHM). This assumption is therefore well suited for the convolution of narrow peaks of the order 10 eV such as the primary peak of the Hoyle state. Instead of sampling a base function $f(x)$ indiscriminately, regions of high-frequency content (denoted as Λ) must be predetermined. This compensated form of sampling base functions is defined as:

$$f_k = \begin{cases} f(k\Delta) & \text{if } (k\Delta) \notin \Lambda, \\ \dfrac{1}{\Delta} \displaystyle\int_{(k-\frac{1}{2})\Delta}^{(k+\frac{1}{2})\Delta} f(x)\,dx & \text{if } (k\Delta) \in \Lambda. \end{cases} \tag{4.51}$$

In essence, the sampled points f_k are averaged within their respective intervals if $(k\Delta)$ lies within the region(s) of high-frequency content Λ. This compensated sampling satisfies the approximation of Equation 4.39 for the entire sampled range. Whilst it is clear that an extreme case of undersampling and aliasing may still occur, this can be disregarded as the purpose of the Fourier transform is not to reconstruct the original base signal of the intrinsic lineshape. As previously mentioned, the Fourier transform of the intrinsic lineshape serves only to produce the convolved observed lineshape of Equation 4.46. Crucially, this sampling method preserves the yield ratio between the primary and ghost peaks of the Hoyle state. A more rigorous analysis of the dependence of the yield ratio on the number of FFT sampling points is presented in Figure 4.88. It is observed that with the original sampling of Equation 4.37, the convolutions with sampling intervals significantly larger than the 10 eV width do not reliably reproduce the correct yield ratio of ~ 2.36. For FFT sampling intervals smaller than 10 eV, the yield ratio converges to the correct value of ~ 2.36, however as previously mentioned, such large FFT datasets are not computationally feasible for fit optimizations which require many convolutions. The compensated sampling method is shown to reproduce the correct yield ratio for a large range of FFT sampling points N, unlike the regular sampling method which only converges for FFT data sizes $N > 10^7$. The corresponding convolved Hoyle-state lineshapes with compensated sampling are presented for the primary and ghost peaks on Figures 4.89 and 4.90, respectively. It is observed that in contrast to the convolved lineshapes on Figure 4.87, the yield ratio between the primary and ghost peaks of the Hoyle state is independent of the FFT sampling size N. Moreover, the convolved lineshapes of both the primary and ghost peaks are in agreement despite sampling sizes which far exceed the intrinsic width of 10 eV for the primary peak. This confirms the assumption that even a substantially smaller Gaussian width of 1 keV (typical experiments correspond to > 50 keV resolution) completely dominates the convolved line-

shape and only the strength (area) of the primary peak is computationally relevant. The algorithm of compensated DFT sampling is therefore shown to be appropriate for the purposes of VeridicalFit.

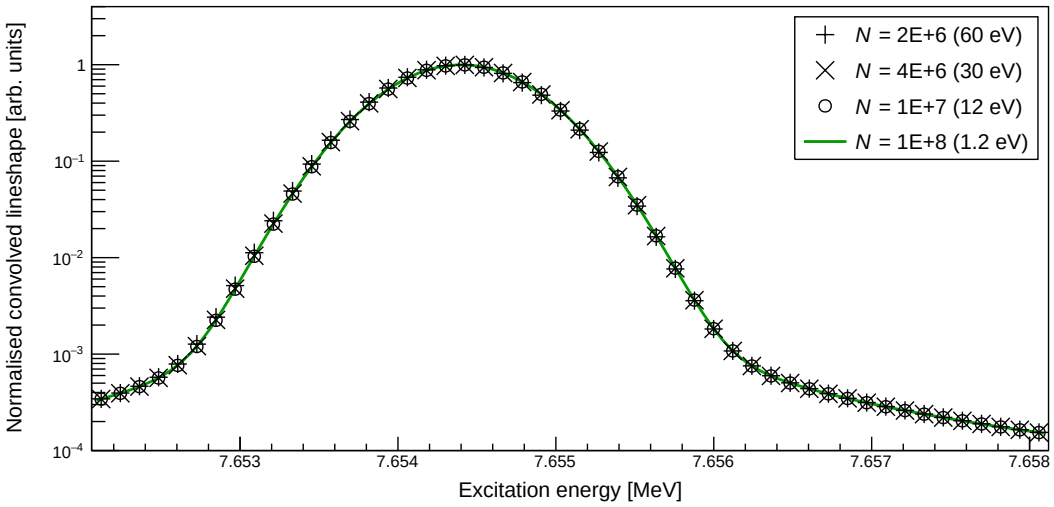

Figure 4.89: The dependence of the convolved lineshape for the primary peak of the Hoyle state on the number of FFT samples. The energy value in brackets (see legend) is the sampling interval for the corresponding FFT data size. See text for further details.

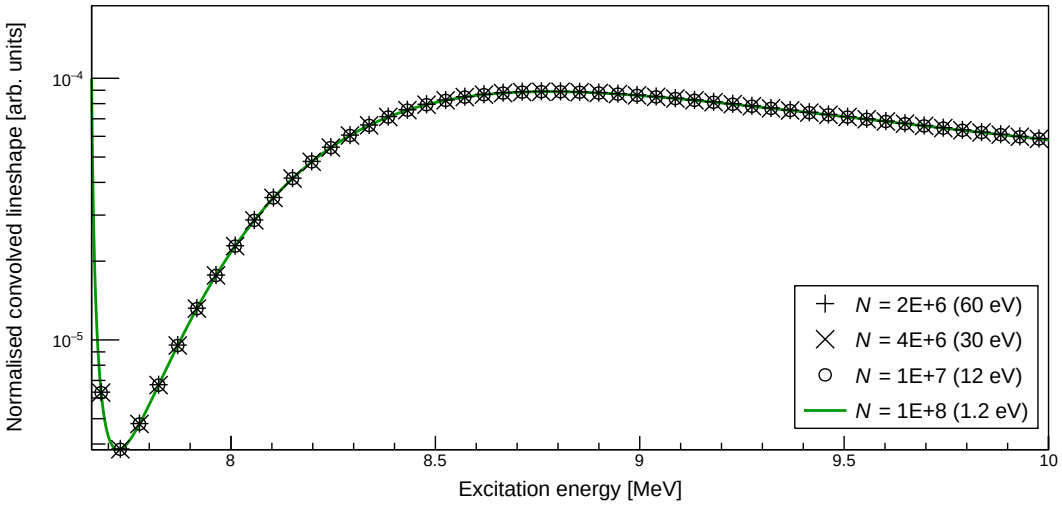

Figure 4.90: The dependence of the convolved lineshape for the ghost peak of the Hoyle state on the number of FFT samples. The energy value in brackets (see legend) is the sampling interval for the corresponding FFT data size. See text for further details.

4.10.2 Fit optimisation Methods

For a fit optimisation, a metric for the goodness of fit is required. There are currently two different such metrics implemented within VeridicalFit: Chi-square and likelihood, denoted χ^2 and $\mathcal{L}$, respectively. The two associated algorithms are described in this Section. The choice of algorithm is dependent on the nature of the observations. Since the data analysed for this thesis consists of histograms with low count observations, maximum-likelihood estimation was employed.

4.10.2.1 Chi-square Test

If data is assumed to be normally distributed, the Chi-square test provides an appropriate metric for fit optimisation [99, 100]. For observations of detector counts, the errors can typically be well modeled with a Poisson distribution, however for large count values, the Poisson distribution can be well approximated by the Gaussian distribution. The χ^2 test is therefore suitable for fitting data which exhibit sufficiently large counts (observation values).

Given n observation values, the χ^2 metric is historically first introduced by K. Pearson [99] as:

$$\chi^2 = \sum_{i=1}^{n} \left(\frac{y_i - \lambda_i}{\lambda_i} \right)^2, \tag{4.52}$$

where y_i and λ_i are the observed and theoretically expected values (corresponding to some density), respectively. Another form of the χ^2 metric is given by

$$\chi^2 = \sum_{i=1}^{n} \left(\frac{y_i - \lambda_i}{\sigma_i} \right)^2, \tag{4.53}$$

where σ_i is the standard deviation [101]. Both forms of the χ^2 metric will be of the order n if there is good agreement between the data and the theoretically expected values. A useful related property that is independent of the n number of observations is the reduced Chi-square, given by

$$\chi^2_\nu = \chi^2/d, \tag{4.54}$$

where d is the number of degrees of freedom. For a model/density with c constraints (parameters), the degrees of freedom with respect to a dataset of n observations is given by

$$d = n - c. \tag{4.55}$$

If there is good agreement between the data and the theoretically expected values, then $\chi^2_\nu \approx 1$. Whilst this can be a highly useful metric for fit optimisation,

it is not appropriate if the associated dispersions cannot be well approximated to be normally distributed. For histograms with low counts, the Poissonian distribution is no longer well approximated by a Gaussian distribution and an alternative metric for fit optimisation is necessary.

4.10.2.2 Maximum-likelihood Estimation

For observations of detector counts, the associated probability mass function (PMF) can typically be well modeled with a Poisson distribution. Whilst the Gaussian distribution can be a useful proxy if the observed counts are sufficiently large, this approximation is unsuitable for low count values. Given the relatively low counts for some of the histograms to be fitted for this thesis, the χ^2 test described in Subsection 4.10.2.1 becomes an unsuitable method of fit optimisation. An alternative metric is the Likelihood. For a given set of n observations (denoted by the vector $\mathbf{y}$), the likelihood is defined as

$$\mathcal{L}(\mathbf{y}, \boldsymbol{\theta}) = p(y_1, \boldsymbol{\theta})\, p(y_2, \boldsymbol{\theta}) \ldots p(y_n, \boldsymbol{\theta}) = \prod_{i=1}^{n} p(y_i, \boldsymbol{\theta}) \tag{4.56}$$

where $p(y_i, \boldsymbol{\theta})$ is the probability density function (PDF) for the i^{th} observation (y_i) given the parameter vector $\boldsymbol{\theta}$. The likelihood $\mathcal{L}(\mathbf{y}, \boldsymbol{\theta})$ gives the probability of observing sample $\mathbf{y}$ given the parameter vector $\boldsymbol{\theta}$. Maximum-likelihood estimation (MLE) is used to determine $\widehat{\boldsymbol{\theta}}$ which is the parameter vector which maximises the likelihood:

$$\mathcal{L}(\mathbf{y}, \widehat{\boldsymbol{\theta}}) = \sup_{\boldsymbol{\theta} \in \boldsymbol{\Theta}} \mathcal{L}(\mathbf{y}, \boldsymbol{\theta}), \tag{4.57}$$

where $\boldsymbol{\Theta}$ is the parameter space. The log likelihood is defined as

$$\ell(\mathbf{y}, \boldsymbol{\theta}) = \ln \mathcal{L}(\mathbf{y}, \boldsymbol{\theta}) \tag{4.58}$$

and is often used for mathematical convenience. Since the natural logarithm is monotonic, the maximisation of $\ell(\mathbf{y}, \boldsymbol{\theta})$ yields the same optimised parameter vector $\widehat{\boldsymbol{\theta}}$:

$$\ell(\mathbf{y}, \widehat{\boldsymbol{\theta}}) = \sup_{\boldsymbol{\theta} \in \boldsymbol{\theta}} \ell(\mathbf{y}, \boldsymbol{\theta}). \tag{4.59}$$

Numerically, the maximisation of $\ell(\mathbf{y}, \boldsymbol{\theta})$ is implemented in the ROOT library used by VeridicalFit through the equivalent minimisation of $-\ell(\mathbf{y}, \boldsymbol{\theta})$:

$$-\ell(\mathbf{y}, \widehat{\boldsymbol{\theta}}) = \inf_{\boldsymbol{\theta} \in \boldsymbol{\Theta}} \big\{ -\ell(\mathbf{y}, \boldsymbol{\theta}) \big\}. \tag{4.60}$$

Given the aforementioned objective of this thesis to fit detector-count histograms, the MLE algorithm implemented within VeridicalFit is therefore performed by determining Equation 4.60 with the associated PDFs in Equation 4.56 being of the Poisson distribution, defined as

$$p(y_i, \boldsymbol{\theta}) = \frac{e^{-\lambda_i} \lambda_i^{y_i}}{y_i!}, \tag{4.61}$$

where λ_i is the theoretically expected value of the model corresponding to the parameter vector $\boldsymbol{\theta}$.

4.10.2.3 Model Comparison

Unlike the χ^2_{red}, the likelihood is dependent on the sample size of observations. The optimised likelihoods for the candidate models consequently have no standalone meaning, only their relative values are of significance. If all the candidate models are nested with respect to one another, i.e. a more complex model can be reduced to a simpler model through modification of the parameters, then the likelihood ratio test (LRT) is appropriate for model comparison [102, 103]. For a set of nested candidate models, there exists an optimal parameter vector $\widehat{\boldsymbol{\theta}}$ that corresponds to entire full parameter space $\boldsymbol{\Theta}$. The relative likelihood of a model with a hypothesis H_0 with a reduced parameter subspace $\boldsymbol{\Theta_0}$ and optimised parameter vector $\boldsymbol{\theta}_0$ is given by

$$W(\boldsymbol{\theta}_0) = -2 \ln RL(\boldsymbol{\theta}_0) = -2\{\ell(\widehat{\boldsymbol{\theta}_0}) - \ell(\widehat{\boldsymbol{\theta}})\}. \tag{4.62}$$

Whilst some of the competing models for this thesis (see Section 2.9) are nested, others are fundamentally different. Consequently, the likelihood ratio test is not appropriate to determine the best model. A metric or criterion is therefore required to compare these competing models whilst accounting for the different number of parameters (to prevent overfitting since an increase of parameters invariably increases the likelihood). One such criterion is the Akaike information criterion (AIC) which is founded on the basis of information theory and represents the loss of information, i.e. the discrepancy between the data and the model [104]. The model with the lowest AIC can therefore be selected as the optimal model. For a model with k estimated parameters, the AIC is defined as:

$$\text{AIC} = -2 \ln\left(\widehat{\mathcal{L}}\right) + 2k, \tag{4.63}$$

where $\widehat{\mathcal{L}}$ is the maximum likelihood estimate of the model. The second term of the AIC penalises the log likelihood for the number of parameters used, however the AIC estimator may still suffer from overfitting when $n/k < 40$ [105]. For such cases, a more appropriate estimator is the AIC_c, defined as

$$\text{AIC}_c = -2 \ln\left(\widehat{\mathcal{L}}\right) + 2k \left(\frac{n}{n-k-1}\right) \tag{4.64}$$

$$= \text{AIC} + \frac{2k^2 + 2k}{n-k-1}, \tag{4.65}$$

which modifies the penalty term of the AIC. A consistent analysis cannot compare between AIC and AIC_c estimators. The choice as to whether the AIC or AIC_c estimator is more suitable is determined by the highest-dimensional candidate model i.e. the model with the highest value of k. For the set of candidate models analysed for this thesis, the total number of observations ($n = 11998$) is approximately 48 times greater than the number of parameters ($k \approx 250$) for the highest-dimensional model. Since the largest ratio for this analysis of $n/k \approx 48$ is not significantly higher than the recommended $n/k < 40$ threshold, both the AIC and AIC_c estimators are to be separately employed for model comparison as both the AIC and AIC_c estimators tend to select the same optimal model for large n/k since the AIC_c reduces to the AIC.

The Bayesian information criterion (BIC) is another criterion which is useful for comparing models which are estimated through the maximum likelihood method and is given by

$$\text{BIC} = -2\ln\left(\widehat{\mathcal{L}}\right) + k\ln(n), \tag{4.66}$$

where n is the number of observations [106]. Similar to both the AIC and AIC_c estimators, a smaller BIC value indicates a better model. The penalising term for parameters is greater for the BIC with respect to the AIC. The BIC estimator is only appropriate for cases where n is much larger than k [107]; a condition which is satisfied by the aforementioned $n/k \approx 48$ value for the highest-dimensional candidate model of this thesis. In summary, the AIC, AIC_c and BIC estimators are all deemed appropriate for the model comparison of this thesis and are thus all employed.

4.10.3 Simultaneous Fit of Backgrounds

The R-matrix analysis method of this work simultaneously analyzes all the relevant excitation-energy spectra. For the implemented maximum-likelihood estimation, the likelihood function employs the Poisson distribution and as such, excitation-energy spectra should not be background subtracted. For some measurements, background excitation-energy spectra can be generated by gating on uncorrelated vertical focal-plane positions ($Y1_{pos}$), as described in Section 4.1.5. These background spectra can be simultaneously fitted from background spectra and scaled to the histogram of interest. The following sections describe all fitted histograms which required a fitted background contribution in the simultaneous R-matrix analysis. These polynomial background parameters were free parameters for the fits of each hypothesis.

The background for the $^{12}C(\alpha,\alpha')^{12}C$ reaction at $\theta_{lab} = 6°$ (PR166) is complex due to the significant hydrogen contamination, as can be seen on Figure 4.65. The background spectrum gated on the uncorrelated ranges of the vertical focal-plane position, $Y1_{pos}$, is presented on Figure 4.91. The orange-filled component is a linear component to fit the hydrogen contamination and the green-filled component is the linear background, as discussed in Section 4.1.5. Since the amount of hydrogen contamination is shown to depend on the gate of for $Y1_{pos}$, only the green-filled linear background is scaled as a background in the excitation-energy spectrum of interest shown in Figure 4.92. The relative size of the gates for the correlated and uncorrelated values of $Y1_{pos}$ can be used to estimate the scaling of the background if the background is assumed to be constant for different values of $Y1_{pos}$. The green-filled linear background is therefore fitted to the excitation-energy spectrum of interest where the scaling parameter is allowed to vary within 20% of this idealised scaling value. The large orange-filled component is the linear hydrogen component and the E_x intercept of this function at approximately $\approx$ 16.5 MeV which matches the end range for the hydrogen locus.

The measurement of the $^{12}C(\alpha,\alpha')^{12}C$ reaction at $\theta_{lab} = 8.5°$ (PR166) did not enable the generation of a background spectrum as the magnetic spectrometer was operated in unfocused mode (see Section 4.1.5), as shown in Figure 4.68. The background for this measurement was therefore assumed to be linear and the R-matrix analyses indicate that the linear background contribution is relatively small, as shown in Figure 4.93.

The $Y1_{pos}$-gated background spectrum for the $^{12}C(\alpha,\alpha')^{12}C$ reaction at $\theta_{lab} = 0°$ with $E_{beam} = 160$ MeV (PR194) is presented on Figure 4.94. Since the K600 spectrometer was operated in unfocused mode (see Section 4.1.5), a background subtraction gated on uncorrelated $Y1_{pos}$ values is not possible, as shown on Figure 4.74. The background for this histogram is therefore assumed to be linear and directly fitted to the excitation-energy histogram of interest. Fortunately, the excitation-energy spectrum of ^{12}C at $E_x \approx 7.6$ MeV is understood to be relatively devoid of smooth background, thus enabling a

reliable estimation of the background.

The $Y1_{pos}$-gated background spectrum for the $^{12}C(\alpha,\alpha')^{12}C$ reaction at $\theta_{lab} = 0°$ with $E_{beam} = 118$ MeV (PR251) is presented on Figure 4.95. The background is simultaneously fitted with a quadratic function in the R-matrix analyses and scaled to the excitation-energy spectrum of interest with a free parameter, as shown in Figure 4.96. The relative size of the $Y1_{pos}$ gate used to generate the background spectrum can be used to estimate the scaling of the background if the background is assumed to be constant for different values of $Y1_{pos}$. The scaling of the quadratic background to the excitation-energy spectrum of interest was permitted to vary within 20% of this idealised scaling value.

The $Y1_{pos}$-gated background for the $^{14}C(p,t)^{12}C$ measurements analysed for this thesis (PR195 and PR240) are minimised since the magnetic optics separate the triton ejectiles of interest from the unscattered proton beam. The $Y1_{pos}$-gated background for the $^{14}C(p,t)^{12}C$ measurements at $\theta_{lab} = 21°$ (PR195) is shown in Figure 4.97. The $^{14}C(p,t)^{12}C$ measurement at $\theta_{lab} = 0°$ (PR240) exhibits a very small but non-negligible background. Since the magnetic spectrometer was operated in unfocused mode for this measurement (see Section 4.1.5 and Figure 4.21), a background spectrum could not be generated. The background for this measurement was fitted directly with a linear polynomial, as shown in Figure 4.98. Fortunately, the combination of the excitation-energy spectrum of ^{12}C below $E_x \approx 7.6$ MeV, which is understood to be relatively devoid of background, and the predominantly linear region at $E_x \approx$ 12-13.5 MeV, enables a relatively reliable estimation of the background.

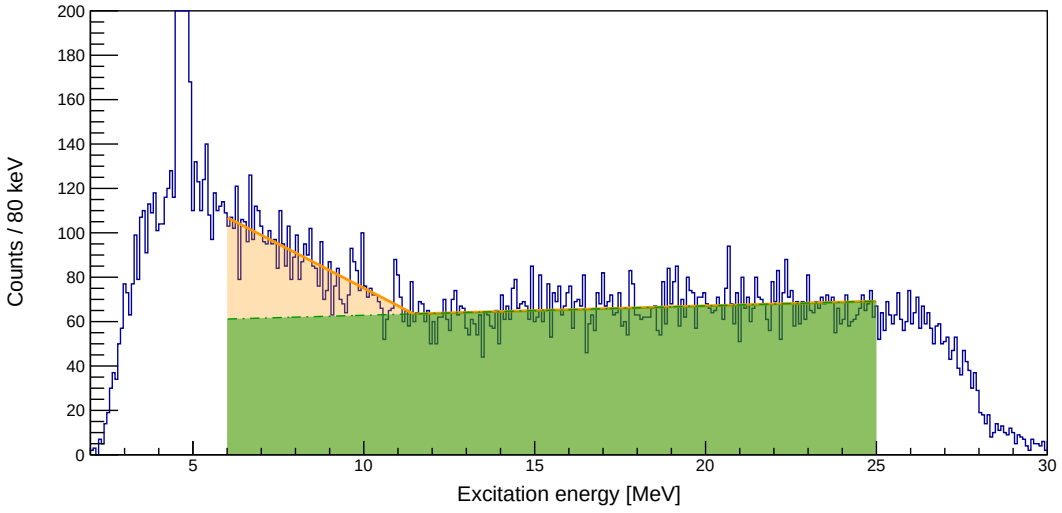

Figure 4.91: The fitted background spectrum for the $^{12}C(\alpha,\alpha')^{12}C$ measurement at $\theta_{lab} = 8.5°$ (PR166). See text for details.

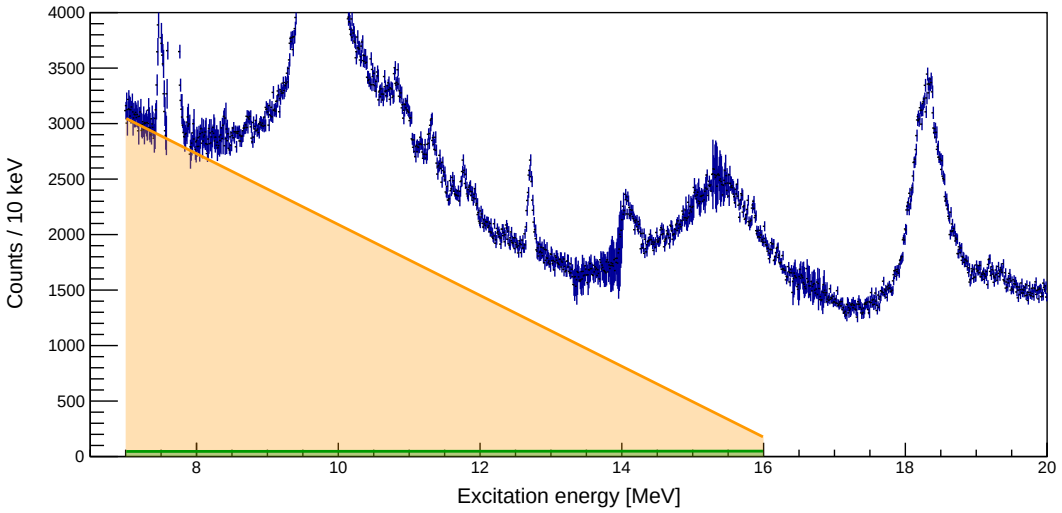

Figure 4.92: The fitted first-order polynomial backgrounds on the excitation-energy spectrum of interest for the ^{12}C$(\alpha,\alpha')^{12}$C measurement at $\theta_{\text{lab}} = 6°$ (PR166). See text for details.

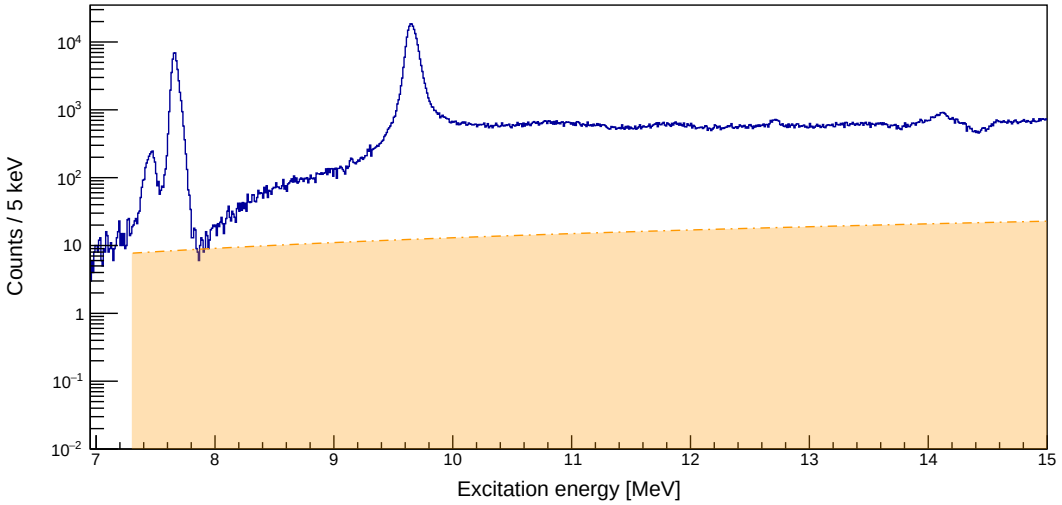

Figure 4.93: The fitted first-order polynomial background on the excitation-energy spectrum of interest for the ^{12}C$(\alpha,\alpha')^{12}$C measurement at $\theta_{\text{lab}} = 8.5°$ (PR166). See text for details.

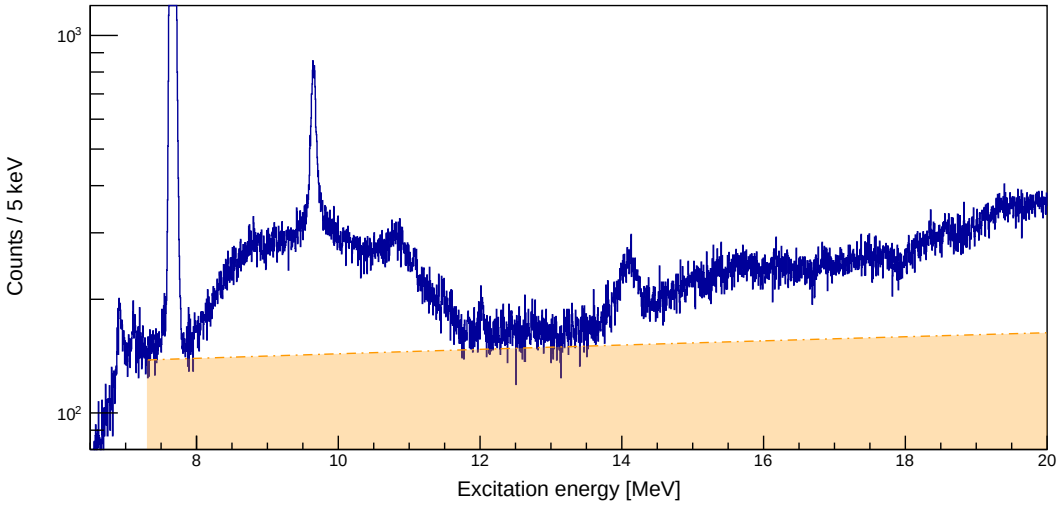

Figure 4.94: The fitted first-order polynomial background on the excitation-energy spectrum of interest for the ^{12}C$(\alpha,\alpha')^{12}$C measurement at $\theta_{\text{lab}} = 0°$ (PR194). See text for details.

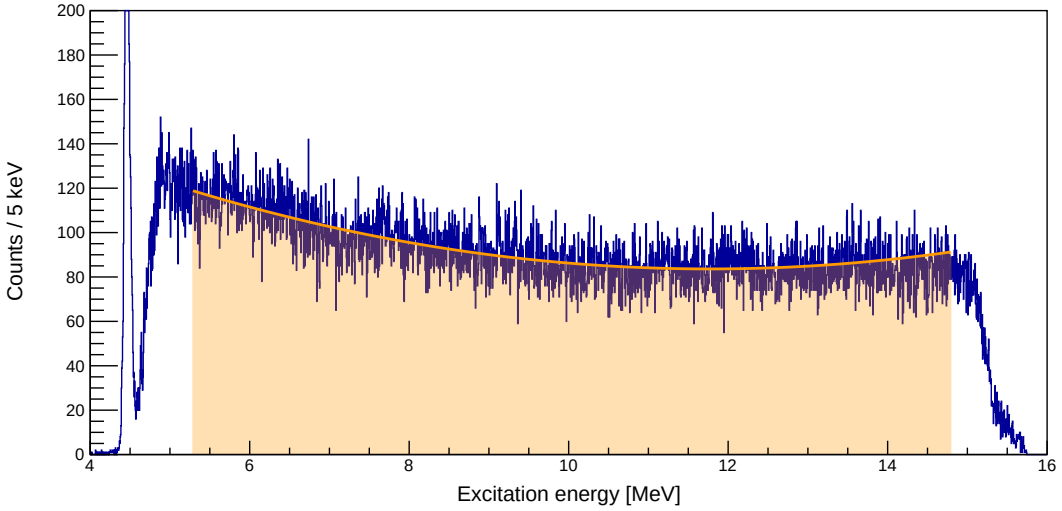

Figure 4.95: The fitted second-order polynomial background spectrum for the $^{12}\mathrm{C}(\alpha,\alpha')^{12}\mathrm{C}$ measurement at $\theta_{\mathrm{lab}} = 0°$ (PR251). See text for details.

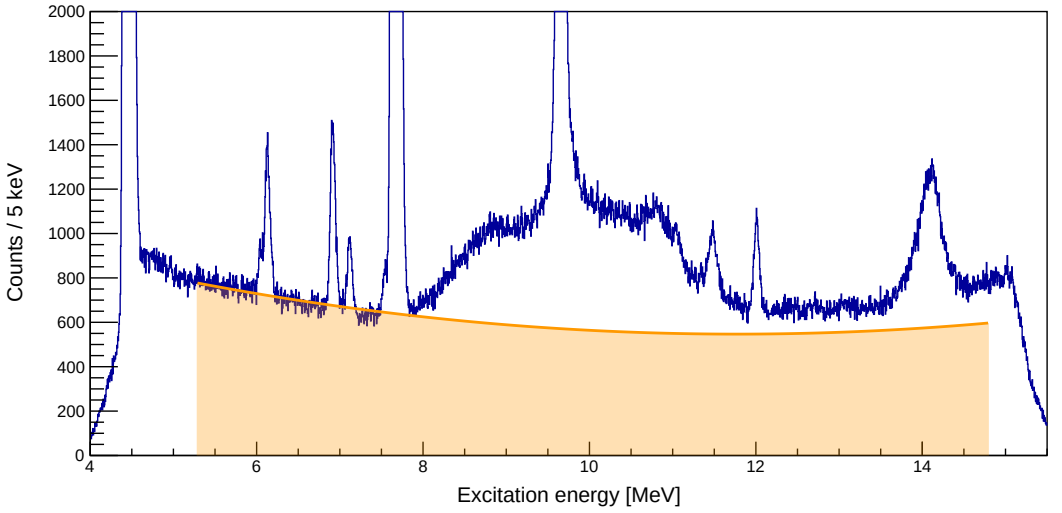

Figure 4.96: The fitted second-order polynomial background on the excitation-energy spectrum of interest for the $^{12}\mathrm{C}(\alpha,\alpha')^{12}\mathrm{C}$ measurement at $\theta_{\mathrm{lab}} = 0°$ (PR251). See text for details.

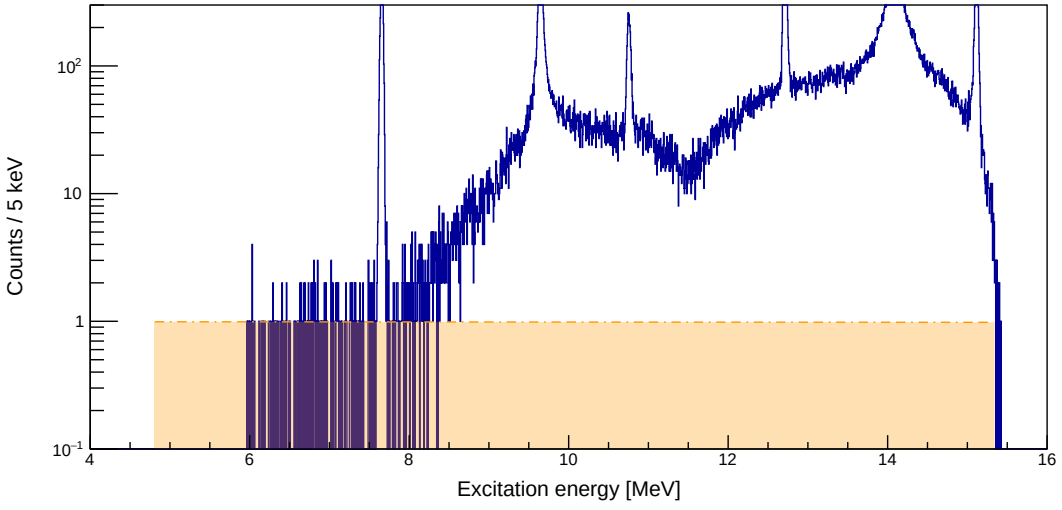

Figure 4.97: The fitted first-order polynomial background on the excitation-energy spectrum of interest for the $^{14}\mathrm{C}(p,t)^{12}\mathrm{C}$ measurement at $\theta_{\mathrm{lab}} = 21°$ (PR195). See text for details.

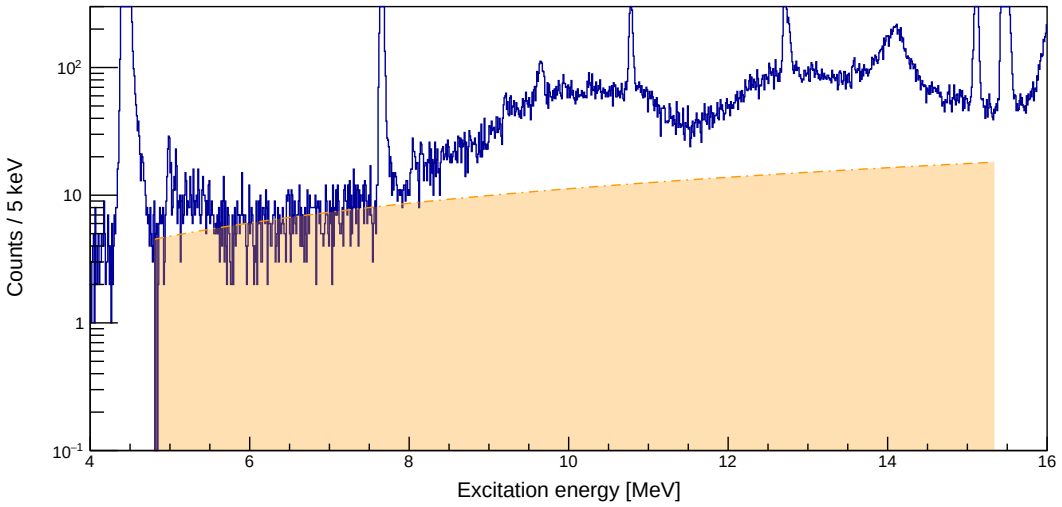

Figure 4.98: The fitted first-order polynomial background on the excitation-energy spectrum of interest for the $^{14}\mathrm{C}(p,t)^{12}\mathrm{C}$ measurement at $\theta_{\mathrm{lab}} = 0^{\circ}$ (PR240). See text for details.

Chapter 5

Results and Discussion

It is postulated that the ^{14}C$(p,t)^{12}$C should suppress collective excitations with respect to the ^{12}C$(\alpha,\alpha')^{12}$C reaction [12]. By comparing data from these reactions at $\theta_{\text{lab}} = 0°$, this selectivity is optimised towards the identification of ISGMRs. The spectra from the ^{14}C$(p,t)^{12}$C and ^{12}C$(\alpha,\alpha')^{12}$C measurements at $\theta_{\text{lab}} = 0°$ (experiments PR194, PR251 and PR240) have been background subtracted (with a constant background as a first approximation) and then normalised to the primary peak of the Hoyle state in Figure 5.1. It is observed that the broad strength at $E_x \approx$ 7-16 MeV appears to be strongly enhanced for the ^{14}C$(p,t)^{12}$C measurement, however such a normalisation yields a biased comparison: since the 0_2^+ Hoyle state is the archetypal α-cluster state, the inelastic scattering of α-particles is expected to strongly enhance the population of the Hoyle state in comparison to the ^{14}C$(p,t)^{12}$C reaction. Since the ISGMR of ^{12}C is postulated to correspond to a strength at $E_x \approx 9$ MeV, a more illuminating normalisation is given by normalising at the broad region between $E_x \approx$ 10.4-10.6 MeV, as shown in Figure 5.2. It is observed that the ^{14}C$(p,t)^{12}$C spectrum exhibits a diminished yield in the broad region at $E_x \approx 9$ MeV with respect to the ^{12}C$(\alpha,\alpha')^{12}$C measurements. Since these are all inclusive measurements, the R-matrix formalism to consistently describe the Hoyle state as an isolated level corresponds to the one-level approximation of Equation 2.68 where the numerator is the total width ($\Gamma_{\text{tot}} = \Gamma_{\alpha_0} + \Gamma_{\alpha_1}$). Since there is no degree of freedom (estimated parameter) to change the relative contributions of the Γ_{α_0} and Γ_{α_1} decay widths for each reaction, the source of the suppression at $E_x \approx 9$ MeV can only originate from the difference in feeding factors of the reaction channels, as discussed in Sections 2.6.1.8 and 2.7. If the difference in feeding factors cannot account for the suppression at $E_x \approx 9$ MeV for the ^{14}C$(p,t)^{12}$C reaction, it suggests that a distinct source of collective monopole strength may manifest in this region.

An indication that the ^{14}C$(p,t)^{12}$C reaction suppresses the population of collective excitations with respect to the ^{14}C$(p,t)^{12}$C is given by the examination of the 3_1^- state situated at 9.641(5) MeV, as listed on the NNDC. Fortunately, the excitation-energy spectrum of ^{12}C at $E_x \approx 6$ to 7 MeV is un-

derstood to be relatively devoid of smooth background, thus enabling a reliable estimation of the background.

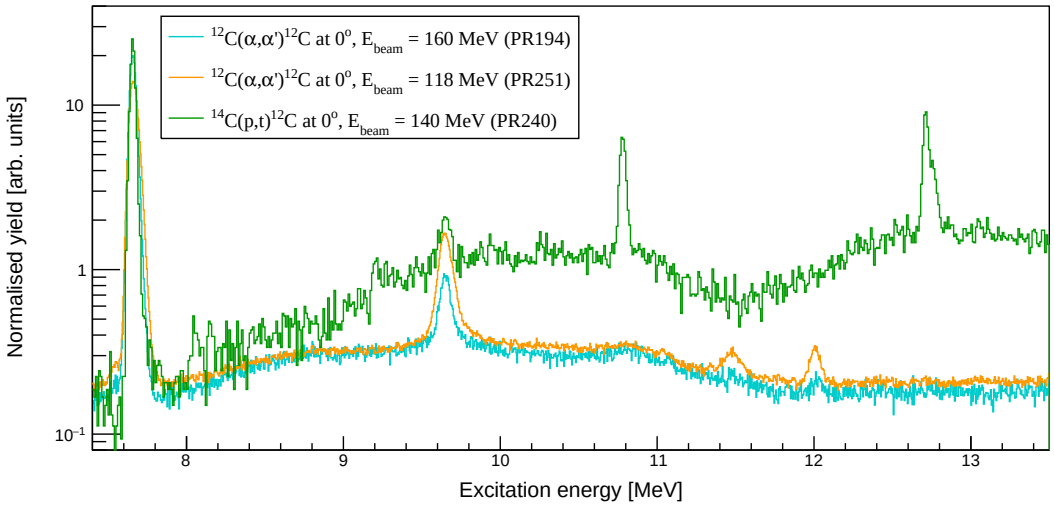

Figure 5.1: Qualitative comparison between the $^{14}\mathrm{C}(p,t)^{12}\mathrm{C}$ and $^{12}\mathrm{C}(\alpha,\alpha')^{12}\mathrm{C}$ measurements at $\theta_{\mathrm{lab}} = 0°$. The spectra are normalised to the area in the Hoyle state.

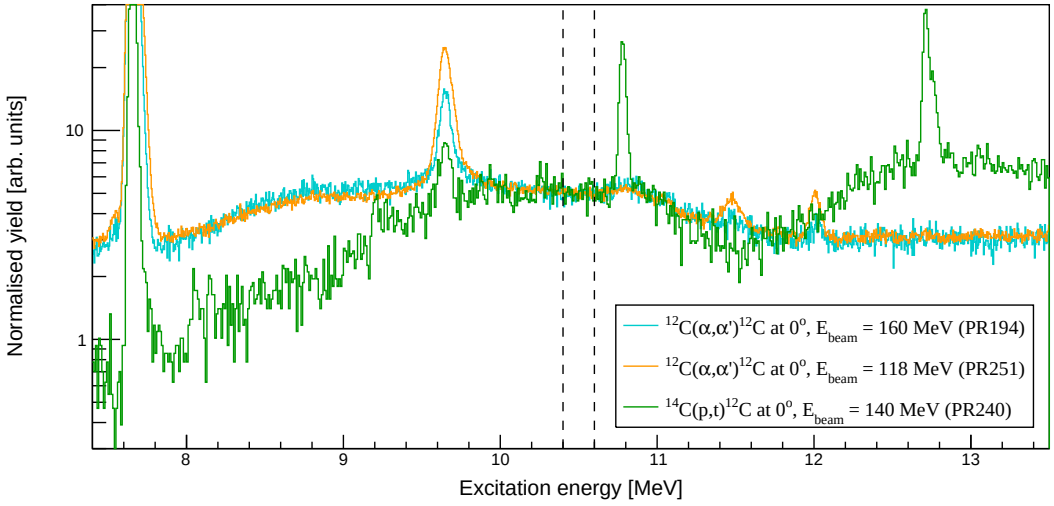

Figure 5.2: Qualitative comparison between the $^{14}\mathrm{C}(p,t)^{12}\mathrm{C}$ and $^{12}\mathrm{C}(\alpha,\alpha')^{12}\mathrm{C}$ measurements at $\theta_{\mathrm{lab}} = 0°$. The spectra are normalised to the area between $E_x \approx 10.4$ and 10.6 MeV, as indicated by the vertical dashed lines.

5.1 Comparison of Hypotheses

The fit results of the observed resonance energies and total widths of the 0_2^+ Hoyle state, ISGMR, 3_1^-, 2_1^+ and broad 0_3^+ states in ^{12}C are summarised in Table 5.1. The model-dependent R-matrix parameters for the primary states of interest are presented in Tables 5.2 - 5.3. The errors for the reduced widths and Wigner ratios are purely from the fit optimisation whilst the resonance energies and observed width errors account for calibration errors. For a particular resonance energy, the calibration errors for all the analysed excitation-energy spectra are considered and the largest error at the particular resonance energy is added in quadrature. To determine the calibration error for the widths, the errors of the momentum-calibration parameters which are 1$^{\text{st}}$ order or higher are considered from all the analysed spectra and the largest width error is added in quadrature.

As described in Section 4.10.2.3, the AIC, AIC$_c$ and BIC estimators enable the comparison of hypotheses which may possess different degrees of freedom. It was found that for the analysed models, the AIC and AIC$_c$ estimators were functionally identical, therefore only the AIC is displayed. Moreover, it was found that the AIC and BIC estimators yielded the same quality ranking for each analysed hypothesis. The simultaneous R-matrix analyses show that hypothesis $H_{6\text{b}}$ yielded the smallest AIC and BIC estimators and is thus the best analysed model to describe the structure of ^{12}C. This hypothesis introduces the an unlisted resonance at $E_x \approx 9$ MeV which is incoherently added to a two-level approximation. The coincident charged-particle decay data from the CAKE shows that the strength at $E_x \approx 9$ MeV decays isotropically and is thus 0^+ in nature (see Figure 4.57).

5.1.1 Hypotheses H_1 and H_2

For hypotheses H_1 and H_2, it is postulated that the 0^+ structure of ^{12}C in the $E_x \approx$ 7-16 MeV excitation-energy region of interest can be described solely by the Hoyle state and the associated ghost anomaly. This implies that the two broad 0^+ resonances listed in the NNDC at $E_r = 9.930(30)$ and 10.3(3) MeV, which are assumed to correspond to one and the same resonance, do not contribute and have been misidentified as distinct 0^+ resonances. Hypothesis H_1 assumed that only the α_0 decay mode contributes whilst hypothesis H_2 corresponds to a multichannel description of the Hoyle state with both α_0 and α_1 decay modes. It was found that for the Hoyle state, the α_1 decay mode is negligible with a vanishingly small reduced width. Since hypothesis H_1 is a nested model of H_2, which reduces to H_1 with $\gamma^2_{\alpha_1} = 0$, the AIC and BIC estimators for these two hypotheses are functionally identical.

The fitted excitation-energy spectra for hypotheses H_1 and H_2 are presented in Figures 5.3 and 5.5, respectively. It was observed that for both fits, the α_0 reduced-width parameters were limited by the α_0 Wigner limit of

$\gamma^2_{W,\alpha_0} \approx 0.6527$ which corresponded to an observed total width of $\Gamma_{\text{tot}} = 11.3(1)$ eV at the fixed resonance energy of 7.65407 MeV. This total width is not in good agreement with the literature value of 9.3(9) eV [10] and is indicative that the omitted broad 0^+ resonance at $E_x \approx 10$ MeV is necessary to describe the ^{12}C spectra.

The associated decomposition of the intrinsic monopole strengths for hypotheses H_1 and H_2 are presented in Figures 5.4 and 5.6, respectively. The vertical dash-dotted lines indicate the positions of local maxima for the ghost of the Hoyle state as well as the positions at higher excitation energy where the high-energy tails decrease to half of their associated maxima. For a particular hypothesis, the differences in these positions arise purely from the unique feeding factors for each measurement as the resonance energy and reduced width parameters are shared for the fitted functions of each histogram. As mentioned in Section 2.7.2, the feeding factors for the ^{12}C$(\alpha,\alpha')^{12}$C measurements all decrease with increasing excitation energy whilst the converse is true for the ^{14}C$(p,t)^{12}$C feeding factors. The aforementioned positions of local maxima and half maxima are therefore at higher excitation energies for the ^{14}C$(p,t)^{12}$C lineshapes. It is observed that the single-channel approximation of hypothesis H_1 is unable to reproduce the double-peaked structure observed by M. Itoh *et al.* in Figure 1.2. This double-peaked monopole structure is also not reproduced by the fit of hypothesis H_2 which yields a negligibly small α_1 decay mode, reducing the multichannel approximation to be functionally identical to the single-channel approximation of hypothesis H_1.

The fits for hypotheses H_1 and H_2 suggest that the α_0 single-channel approximation, which is commonly used to describe the Hoyle state and the associated high-energy tail, is a good approximation if the Hoyle state can be analysed as an isolated level. However, hypotheses H_1 and H_2 yielded the worst AIC and BIC estimators in comparison to the alternative hypotheses which all account for the broad 0^+ resonance at $E_x \approx 10$ MeV. Moreover, both models yielded poor fits for the ^{12}C$(\alpha,\alpha')^{12}$C measurements at $\theta_{\text{lab}} = 6°$ and 8.5° (PR166) at $E_x \approx 11$ MeV, as shown on panels (a) and (b) of Figures 5.3 and 5.5. The evidence suggests that source(s) of 0^+ strength other than the Hoyle state manifest in the $E_x \approx$ 7-16 MeV excitation-energy region of interest of ^{12}C.

5.1.2 Hypothesis H_3

Hypothesis H_3 builds upon the multichannel description for the Hoyle state of hypothesis H_2 with the inclusion of a broad 0^+ resonance at $E_x \approx 10$ MeV. Both hypotheses H_1 and H_2 are nested models of H_3 which yields improved AIC and BIC estimators. The fitted excitation-energy spectra and the associated decomposition of the intrinsic monopole strengths are presented in Figures 5.7 and 5.8, respectively. Similarly to hypotheses H_2 and H_3, the α_0 reduced-width parameter was limited by the α_0 Wigner limit to produce a

large observed total width of $\Gamma_{\rm tot} = 11.3(1)$ eV with respect to the literature value of 9.3(9) eV. The fit yielded a resonance energy of 10.862(16) MeV for the broad 0^+ resonance. Whilst this energy does not agree well with the literature values, it should be noted that the resonance energies from previous measurements are typically extracted with more simplistic analyses. It is observed that even with the augmented width for the Hoyle state and a broad 0^+ resonance at $E_x \approx 10$ MeV, the lineshapes still underestimate the data at $E_x \approx 9$ MeV for all measurements. It is postulated that the origin of this strength may either be from interference effects or a fragment of the ISGMR for ^{12}C.

Panels (a) and (b) of Figure 5.7 show that the broad 0^+ resonance enables a substantially better description of the data at $E_x \approx 10$ MeV for the $^{12}\mathrm{C}(\alpha,\alpha')^{12}\mathrm{C}$ measurements at $\theta_{\rm lab} = 6°$ and 8.5° (PR166). It should however be noted that there is an inconsistency in the extracted monopole strengths for the $^{12}\mathrm{C}(\alpha,\alpha')^{12}\mathrm{C}$ measurements at $\theta_{\rm lab} = 0°$ of experiments PR194 and PR251. As shown in Figure 5.8, the fits produce a strong contribution from the broad 0^+ resonance for experiment PR251 but a vanishingly small contribution for experiment PR194. Since experiments PR194 and PR251 are relatively similar, this drastic difference in contributions does not appear to be realistic as all other explored hypotheses yield similar monopole structures between the two measurements. This indicates that hypothesis H_3 does not yield a consistent description for the total monopole structure.

5.1.3 Hypothesis H_4

Hypothesis H_4 corresponds to four subhypotheses: $H_{4\rm a}$, $H_{4\rm b}$, $H_{4\rm c}$ and $H_{4\rm d}$, each of which correspond to a different permutation of interference between the α_0 and α_1 decay modes. Hypotheses $H_{4\rm a}$ and $H_{4\rm b}$ correspond to constructive α_0 decay modes and yield better AIC and BIC estimators in comparison to $H_{4\rm c}$ and $H_{4\rm d}$ which correspond to constructive α_1 decay modes (see Table 2.10). The fitted spectra for $H_{4\rm a}$-$H_{4\rm d}$ are presented on Figures 5.9 - 5.15, respectively. It is observed that the α_1 reduced width was found to be vanishingly small for all subhypotheses. In comparisons to hypotheses H_1, H_2 and H_3, the constructive $\alpha 0$ interference of $H_{4\rm a}$ and $H_{4\rm b}$ enables a better fit of the data at $E_x \approx 9$ MeV. The α_0 reduced width approaches the Wigner limit for all subhypotheses whilst the α_1 decay mode is vanishingly small. The large observed width values of $\Gamma_{\rm tot} \approx 11.3$ eV for the Hoyle state indicates that the fit optimisation attempted to account for a missing strength at $E_x \approx 9$ MeV with the high-energy tail of the Hoyle state. It is worth noting that the resonance energy of $E_r \approx 11.8$ MeV for the broad 0^+ resonance is substantially larger than the literature values, however this is not a direct disagreement since the complex interference effects of the two-level approximation greatly complicates the interpretation of resonance energies.

The associated decompositions of the intrinsic monopole strengths for H_{4a}-H_{4d} are presented in Figures 5.10 - 5.16, respectively.

5.1.4 Hypothesis H_5

Hypothesis H_5 builds upon the multichannel description for the Hoyle state of hypothesis H_3 by describing the 0^+ structure of ^{12}C in the $E_x \approx$ 7-16 MeV excitation-energy region of interest with three distinct resonances: the 0^+_2 Hoyle state, a broad 0^+ resonance at $E_x \approx 9$ MeV (parameterised by a standard Lorentzian) and an even broader 0^+ resonance at $E_x \approx 10$ MeV. The AIC and BIC estimators indicate that the quality of this model exceeds that of hypotheses H_1-H_4.

5.1.5 Hypothesis H_6

Hypothesis H_6 corresponds to four subhypotheses: H_{6a}, H_{6b}, H_{6c} and H_{6d}, each of which correspond to a different permutation of interference between the α_0 and α_1 decay modes. Hypotheses H_{6a} and H_{6b} correspond to constructive α_0 decay modes and yield better AIC and BIC estimators in comparison to H_{6c} and H_{6d} which correspond to constructive α_1 decay modes (see Table 2.8). The AIC and BIC estimators indicate that the newly-introduced 0^+ strength at $E_x \approx 9$ MeV together with the two-level approximation yield the best description of the data, as can be seen in Figures 5.19 - 5.25. The observed widths of the Hoyle state extracted with these subhypotheses are substantially below the Wigner limit (within error). In particular, the optimal subhypothesis H_{6b} yields $\Gamma_{\rm tot} \approx 9.3(3)$ eV which is in excellent agreement with the literature value of 9.3(9).

Similarly to hypothesis H_4, it is worth noting that the resonance energy for the broad 0^+ strength exhibits a resonance energy of $E_x \approx 11.6$ MeV. As previously mentioned, the complex form of the two-level approximation complicates the interpretation of resonance energies and as such, this resonance energies should not be directly compared to literature values. Indeed, the intrinsic monopole contributions shown on Figures 5.20 - 5.26 show that the total intrinsic monopole strength exhibits local maxima below 11 MeV. In particular, it is observed on panels (d) and (e) that the total intrinsic monopole strength exhibits a broad structure that is vaguely symmetrical and double-peaked. This qualitatively supports the MDA analysis of M. Itoh *et al.* which indicates a local minimum at $E_x \approx 9.7$ MeV for their measurement of the ^{12}C$(\alpha,\alpha')^{12}$C reaction at $E_{\rm beam} = 386$ MeV (see Figure 1.2).

$H_{\#}$	AIC	BIC	0_2^+ Hoyle state		ISGMR		3_1^-, 9.641(5) MeV		2_1^+, 9.870(60) MeV		0_3^+, 9.930(30) MeV	
	($\times 10^4$)	($\times 10^4$)	E_r [MeV]	Γ_{tot} [eV]	E_r [MeV]	Γ_{tot} [keV]	E_r [MeV]	Γ_{tot} [keV]	E_r [MeV]	Γ_{tot} [keV]	E_r [keV]	Γ_{tot} [keV]
H_1	4.369	4.327	7.65407*	11.3(1)†	—	—	9.641(7)	39.2(5)	9.954(8)	1100(12)	—	—
H_2	4.369	4.327		11.3(1)†	—	—	9.641(7)	39.2(5)	9.954(8)	1100(12)	—	—
H_3	2.973	2.928		11.3(1)†	—	—	9.641(7)	40.6(5)	9.816(8)	968(11)	10.862(16)	2649(48)
H_{4a}	2.460	2.416		11.2(2)	—	—	9.641(7)	41.1(5)	9.870(9)	1020(11)	11.830(11)	3562(58)
H_{4b}	2.459	2.415		11.3(1)	—	—	9.641(7)	41.1(5)	9.869(9)	1019(11)	11.831(18)	3570(73)
H_{4c}	3.342	3.298		11.3(1)†	—	—	9.641(7)	38.0(5)	9.876(8)	1026(11)	11.293(21)	2000(61)
H_{4d}	3.343	3.299		11.3(1)†	—	—	9.641(7)	38.0(4)	9.876(7)	1026(11)	11.288(15)	1997(48)
H_5	2.530	2.484		6.6(1)‡	9.046(15)	1484(29)	9.641(7)	41.8(5)	9.964(11)	1110(12)	10.985(13)	2034(45)
H_{6a}	2.362	2.316		8.7(3)	9.172(5)	1584(24)	9.641(7)	41.4(5)	9.931(12)	1079(12)	11.602(27)	2639(76)
H_{6b}	2.358	2.312		9.3(3)	9.270(14)	1581(58)	9.641(7)	41.5(5)	9.941(10)	1088(12)	11.647(22)	2735(73)
H_{6c}	2.527	2.481		11.3(1)†	9.160(13)	1209(25)	9.641(7)	42.1(5)	10.050(6)	1192(13)	11.967(24)	4649(104)
H_{6d}	2.526	2.480		11.3(1)†	9.160(12)	1209(24)	9.641(7)	42.1(5)	10.050(7)	1192(13)	11.965(23)	4647(77)

Table 5.1: Fit results: the observed resonance energies and total widths of the 0_2^+ Hoyle state, ISGMR, 3_1^-, 2_1^+ and broad 0_3^+ in ^{12}C. *The resonance energy of the Hoyle state is fixed at 7.65407 MeV. †These α_0 observed widths for the Hoyle state were restricted by the Wigner limit. ‡The α_0 width of the Hoyle state is restricted by a three-sigma lower limit obtained from the literature value of $\Gamma_{\text{tot}} = 9.3(9)$ eV [10].

0_2^+ Hoyle state, $E_r = 7.65407(19)$ MeV, $\Gamma = 9.3(9)$ eV												
$H_\#$	AIC	BIC		α_0				α_1				
	$(\times 10^4)$	$(\times 10^4)$	E_r [MeV]	$\Gamma_{\alpha_0}(E_r)$ [keV]	$\mathcal{P}_{\alpha_0}(E_r)$ $(l=0)$	$\gamma^2_{\alpha_0^2}$ [keV]	θ^2_{W,α_0}	$\Gamma_{\alpha_1}(E_r)$ [keV]	$\mathcal{P}_{\alpha_1}(E_r)$ $(l=2)$	$\gamma^2_{\alpha_1^2}$ [keV]	θ^2_{W,α_1}	$\Gamma_{\text{tot}}(E_r)$ [eV]
H_1	4.369	4.327	7.65407*	11.3(1)†	8.6869×10^{-6}*	0.65272(6)	≈ 1†	—	—	—	—	11.3(1)†
H_2	4.369	4.327		11.3(1)†		0.6527(1)	≈ 1†	≈ 0	≈ 0	≈ 0	≈ 0	11.3(1)†
H_3	2.973	2.928		11.3(1)†		0.65272(10)	≈ 1†	≈ 0	≈ 0	≈ 0	≈ 0	11.3(1)†
H_{4a}	2.460	2.416		11.3(2)		0.6527(3)	≈ 1†	≈ 0	≈ 0	0.50(2)	0.77(3)	11.3(1)
H_{4b}	2.459	2.415		11.3(1)		0.6527(6)	≈ 1†	≈ 0	≈ 0	0.49(2)	0.77(3)	11.3(1)
H_{4c}	3.342	3.298		11.3(1)†		0.6527(1)	≈ 1†	≈ 0	≈ 0	≈ 0	≈ 0	11.3(1)†
H_{4d}	3.343	3.299		11.3(1)†		0.6527(7)	≈ 1†	≈ 0	≈ 0	0.500(1)	0.766(2)	11.3(1)†
H_5	2.530	2.484		6.6(1)		0.37988(2)	0.58200(3)	≈ 0	≈ 0	≈ 0	≈ 0	6.6(1)
H_{6a}	2.362	2.316		8.7(3)		0.50(2)	0.77(3)	≈ 0	≈ 0	0.50(2)	0.77(3)	8.7(3)
H_{6b}	2.358	2.312		9.3(3)		0.54(1)	0.82(2)	≈ 0	≈ 0	0.48(5)	0.73(8)	9.3(3)
H_{6c}	2.527	2.481		11.3(1)†		0.653(1)	≈ 1	≈ 0	≈ 0	≈ 0	≈ 0	11.3(1)†
H_{6d}	2.526	2.480		11.3(1)†		0.653(2)	≈ 1	≈ 0	≈ 0	≈ 0	≈ 0	11.3(1)†

Table 5.2: Fit results: the model-dependent R-matrix parameters for the 0_2^+ Hoyle state of ^{12}C listed at 7.65407(19) MeV. The errors for the reduced widths and Wigner ratios are purely from the fit optimisation whilst the resonance energies and observed width errors account for a calibration error. *In the R-matrix analyses, the resonance energy of the Hoyle state is fixed, resulting in identical evaluated penetrabilities for $\mathcal{P}_{\alpha_0}(E_r)$ and $\mathcal{P}_{\alpha_1}(E_r)$. †These parameters were restricted by the Wigner limit.

3^-_1, $E_r = 9.641(5)$ MeV, $\Gamma = 46(3)$ keV												
$H_\#$	AIC	BIC		α_0				α_1				
	($\times 10^4$)	($\times 10^4$)	E_r [MeV]	$\Gamma_{\alpha_0}(E_r)$ [keV]	$\mathcal{P}_{\alpha_0}(E_r)$ ($l=3$)	$\gamma^2_{\alpha_0}$ [keV]	θ^2_{W,α_0}	$\Gamma_{\alpha_1}(E_r)$ [keV]	$\mathcal{P}_{\alpha_1}(E_r)$ ($l=1$)	$\gamma^2_{\alpha_1}$ [keV]	θ^2_{W,α_1}	$\Gamma_{\text{tot}}(E_r)$ [keV]
H_1	4.369	4.327	9.641(7)	39.2(5)	0.29982	0.0653(3)	0.0702(3)	≈ 0	≈ 0	≈ 0	≈ 0	39.2(5)
H_2	4.369	4.327	9.641(7)	39.2(5)	0.29982	0.0653(3)	0.0702(4)	≈ 0	≈ 0	≈ 0	≈ 0	39.2(5)
H_3	2.973	2.928	9.641(7)	40.6(5)	0.30002	0.0676(3)	0.0726(3)	≈ 0	≈ 0	≈ 0	≈ 0	40.6(5)
H_{4a}	2.460	2.416	9.641(7)	41.1(5)	0.30000	0.0685(3)	0.0735(3)	≈ 0	≈ 0	0.64(3)	0.69(3)	41.1(5)
H_{4b}	2.459	2.415	9.641(7)	41.1(5)	0.30000	0.0685(3)	0.0735(3)	≈ 0	≈ 0	0.60(3)	0.64(4)	41.1(5)
H_{4c}	3.342	3.298	9.641(7)	38.0(5)	0.29988	0.0633(3)	0.0680(3)	≈ 0	≈ 0	≈ 0	≈ 0	38.0(4)
H_{4d}	3.343	3.299	9.641(7)	38.0(4)	0.29988	0.0633(2)	0.0680(3)	≈ 0	≈ 0	≈ 0	≈ 0	38.0(4)
H_5	2.530	2.484	9.641(7)	41.8(5)	0.29996	0.0696(3)	0.0748(3)	≈ 0	≈ 0	≈ 0	≈ 0	41.8(5)
H_{6a}	2.362	2.316	9.641(7)	41.4(5)	0.29998	0.0690(3)	0.0742(3)	≈ 0	≈ 0	0.78(5)	0.84(5)	41.4(5)
H_{6b}	2.358	2.312	9.641(7)	41.5(5)	0.29999	0.0691(3)	0.0742(3)	≈ 0	≈ 0	0.68(5)	0.73(6)	41.5(5)
H_{6c}	2.527	2.481	9.641(7)	42.1(5)	0.29995	0.0701(3)	0.0753(3)	≈ 0	≈ 0	≈ 0	≈ 0	42.1(5)
H_{6d}	2.526	2.480	9.641(7)	42.1(5)	0.29995	0.0701(3)	0.0753(3)	≈ 0	≈ 0	≈ 0	≈ 0	42.1(5)

Table 5.3: Fit results: the model-dependent R-matrix parameters for the 3^-_1 state of ^{12}C listed at 9.641(5) MeV. The errors for the reduced widths and Wigner ratios are purely from the fit optimisation whilst the resonance energies and observed width errors account for a calibration error.

2_1^+, $E_r = 9.870(60)$ MeV, $\Gamma = 850(85)$ keV												
$H_\#$	AIC	BIC		α_0				α_1				
	$(\times 10^4)$	$(\times 10^4)$	E_r [MeV]	$\Gamma_{\alpha_0}(E_r)$ [keV]	$\mathcal{P}_{\alpha_0}(E_r)$ $(l=2)$	$\gamma^2_{\alpha_0}$ [keV]	θ^2_{W,α_0}	$\Gamma_{\alpha_1}(E_r)$ [keV]	$\mathcal{P}_{\alpha_1}(E_r)$ $(l=0)$	$\gamma^2_{\alpha_1}$ [keV]	θ^2_{W,α_1}	$\Gamma_{\text{tot}}(E_r)$ [keV]
H_1	4.369	4.327	9.954(8)	1100(12)	1.1056	0.49757(2)	0.53436(3)	≈ 0	≈ 0	0.931(3)	$\approx 1^\dagger$	1100(12)
H_2	4.369	4.327	9.954(8)	1100(12)	1.1056	0.49757(4)	0.53436(4)	≈ 0	≈ 0	0.931(7)	$\approx 1^\dagger$	1100(12)
H_3	2.973	2.928	9.816(8)	968(11)	0.97274	0.49757(6)	0.53436(7)	≈ 0	≈ 0	0.93(1)	$\approx 1^\dagger$	968(11)
H_{4a}	2.460	2.416	9.870(9)	1020(11)	1.0247	0.49757(8)	0.53436(9)	≈ 0	≈ 0	0.13(13)	0.14(14)	1020(11)
H_{4b}	2.459	2.415	9.869(9)	1019(11)	1.0240	0.49757(5)	0.53436(6)	≈ 0	≈ 0	≈ 0	≈ 0	1019(11)
H_{4c}	3.342	3.298	9.876(8)	1026(7)	1.0310	0.49757(6)	0.53436(6)	≈ 0	≈ 0	≈ 0	≈ 0	1026(11)
H_{4d}	3.343	3.299	9.876(7)	1026(11)	1.0311	0.49757(4)	0.53436(4)	≈ 0	≈ 0	0.931(6)	$\approx 1^\dagger$	1026(11)
H_5	2.530	2.484	9.964(11)	1110(12)	1.1150	0.4976(2)	0.5344(2)	≈ 0	≈ 0	0.931(8)	$\approx 1^\dagger$	1110(12)
H_{6a}	2.362	2.316	9.931(12)	1079(12)	1.0840	0.4976(3)	0.5344(3)	≈ 0	≈ 0	0.51(20)	0.54(21)	1079(12)
H_{6b}	2.358	2.312	9.941(10)	1088(12)	1.0930	0.49757(9)	0.53436(9)	≈ 0	≈ 0	0.40(16)	0.43(18)	1088(12)
H_{6c}	2.527	2.481	10.050(7)‡	1192(13)	1.1977	0.4976(1)	0.5344(1)	≈ 0	≈ 0	0.32(18)	0.35(19)	1192(13)
H_{6d}	2.526	2.480	10.050(6)‡	1192(13)	1.1977	0.4976(1)	0.5344(1)	≈ 0	≈ 0	0.30(15)	0.32(16)	1192(13)

Table 5.4: Fit results: the model-dependent R-matrix parameters for the 2_1^+ state of ^{12}C listed at 9.870(60) MeV. The errors for the reduced widths and Wigner ratios are purely from the fit optimisation whilst the resonance energies and observed width errors account for a calibration error. †These parameters were restricted by the Wigner limit. ‡The is restricted by a three-sigma lower limit obtained from the literature value of the resonance energy of $Ex = 9.870(60)$ MeV [10].

0^+, $E_r = 9.930(30)$ MeV, $\Gamma = 2710(80)$ keV / 0^+, $E_r = 10.3(3)$ MeV, $\Gamma = 3.0(7)$ MeV												
$H_\#$	AIC	BIC		α_0				α_1				
	($\times 10^4$)	($\times 10^4$)	E_r [MeV]	$\Gamma_{\alpha_0}(E_r)$ [keV]	$\mathcal{P}_l(E_r)$ ($l=0$)	$\gamma^2_{\alpha_0}$ [keV]	θ^2_{W,α_0}	$\Gamma_{\alpha_1}(E_r)$ [keV]	$\mathcal{P}_l(E_r)$ ($l=2$)	$\gamma^2_{\alpha_1}$ [keV]	θ^2_{W,α_1}	$\Gamma_{\text{tot}}(E_r)$ [keV]
H_1	4.369	4.327	—	—	—	—	—	—	—	—	—	—
H_2	4.369	4.327	—	—	—	—	—	—	—	—	—	—
H_3	2.973	2.928	10.862(16)	2649(48)	2.7934	0.4741(7)	0.509(7)	≈ 0	≈ 0	≈ 0	≈ 0	2649(48)
H_{4a}	2.460	2.416	11.830(11)	3562(58)	3.4743	0.513(3)	0.785(7)	≈ 0	0.16051	≈ 0	≈ 0	3562(58)
H_{4b}	2.459	2.415	11.831(18)	3562(73)	3.4744	0.513(6)	0.786(12)	8(5)	0.16064	0.025(46)	0.039(22)	3570(73)
H_{4c}	3.342	3.298	11.293(20)	2000(61)	3.1118	0.321(8)	0.492(14)	≈ 0	1.2046×10^{-2}	≈ 0	≈ 0	2000(61)
H_{4d}	3.343	3.299	11.289(15)	1981(48)	3.1090	0.319(6)	0.488(10)	15.3(2)	1.1697×10^{-2}	0.6527(6)	$\approx 1^\dagger$	1997(48)
H_5	2.530	2.484	10.985(13)	2034(45)	2.8873	0.352(7)	0.378(7)	≈ 0	5.3323×10^{-4}	≈ 0	≈ 0	2034(45)
H_{6a}	2.362	2.316	11.602(27)	2639(76)	3.3246	0.397(8)	0.608(16)	≈ 0	6.9002×10^{-2}	≈ 0	≈ 0	2639(76)
H_{6b}	2.358	2.312	11.647(22)	2722(73)	3.3542	0.406(7)	0.622(14)	13(5)	8.3205×10^{-2}	0.081(48)	0.124(42)	2735(73)
H_{6c}	2.527	2.481	11.967(24)	4649(104)	3.5610	0.653(7)	≈ 1	≈ 0	2.3707×10^{-1}	≈ 0	≈ 0	4649(104)
H_{6d}	2.526	2.480	11.965(23)	4647(77)	3.5597	0.653(3)	≈ 1	0.020(886)	2.3580×10^{-1}	≈ 0	≈ 0	4647(77)

Table 5.5: Fit results: the model-dependent R-matrix parameters for the broad 0^+ resonance of ^{12}C at $E_x \approx 10$ MeV. The errors for the reduced widths and Wigner ratios are purely from the fit optimisation whilst the resonance energies and observed width errors account for a calibration error. †These parameters were restricted by the Wigner limit.

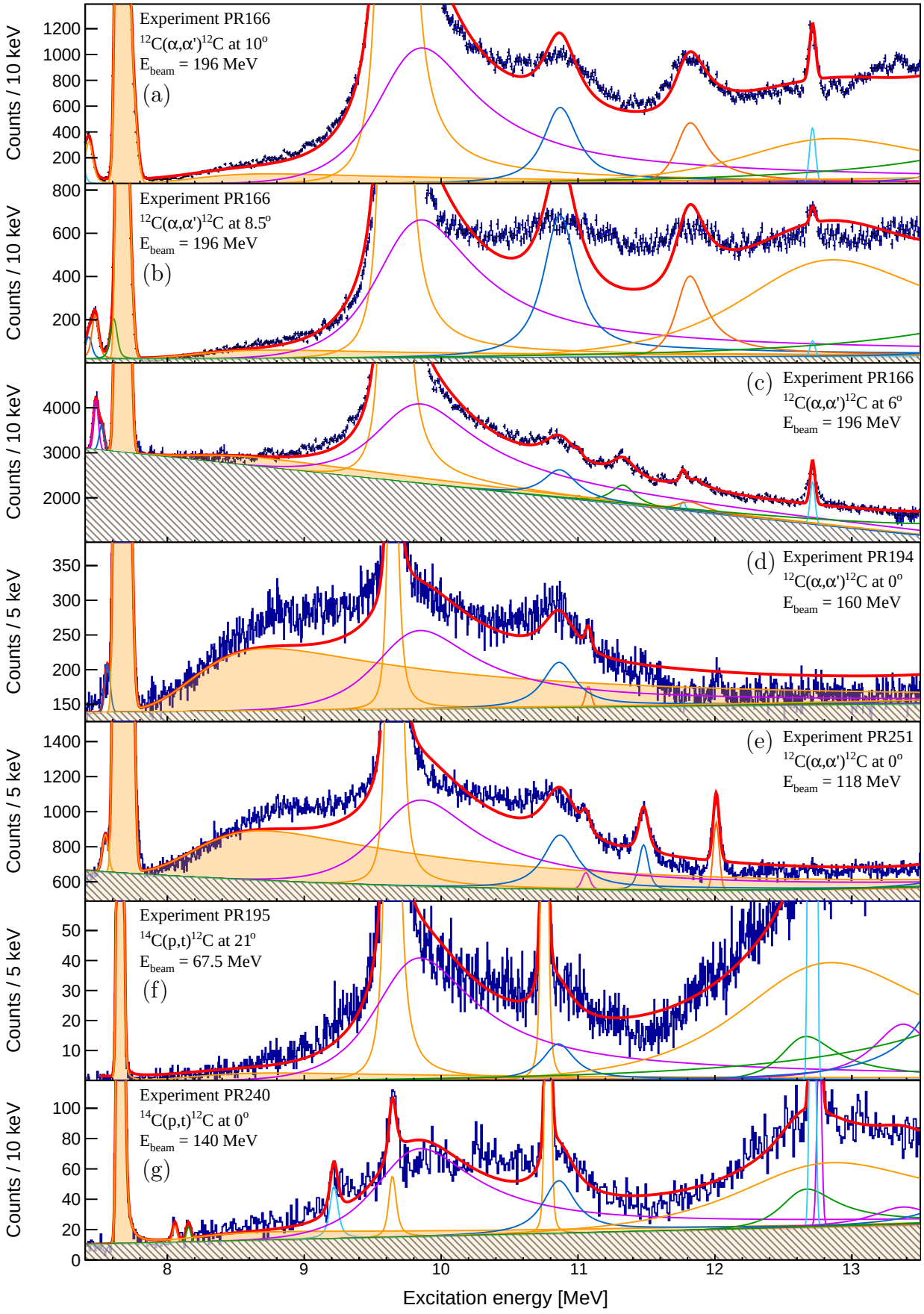

Figure 5.3: Hypothesis H_1: summary of fitted spectra. The contribution of the 0_2^+ Hoyle state is filled in orange. The displayed polynomial backgrounds are filled in translucent white with diagonal gray hatching.

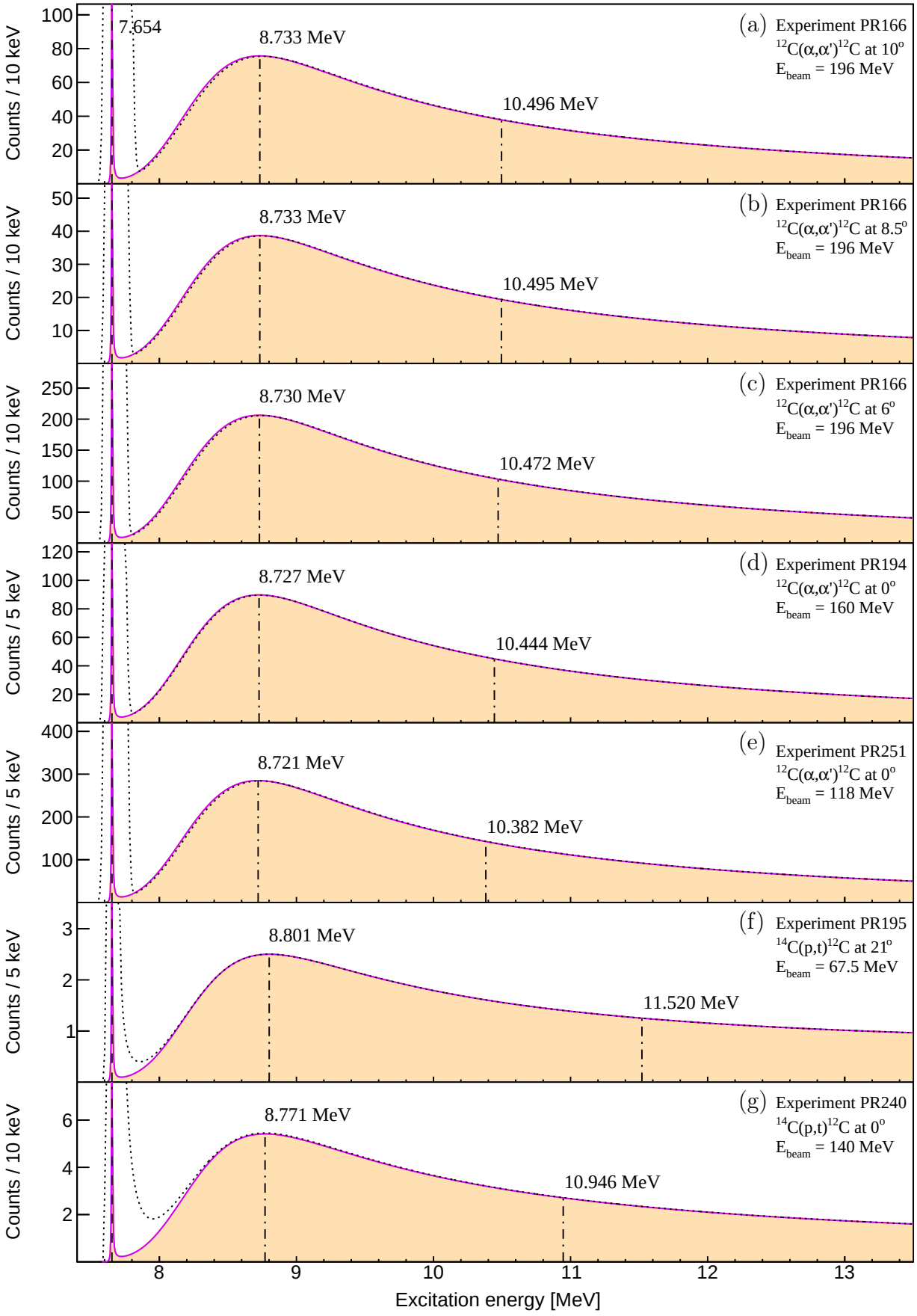

Figure 5.4: Hypothesis H_1: exposition of the populated monopole strength. The intrinsic lineshape of the 0_2^+ Hoyle state is filled in orange. The vertical dashed line indicates the observed resonance energy. The solid violet and dotted black lines represent the total intrinsic and total observed monopole lineshapes, respectively. See Section 5.1.1 for an explanation of the vertical dash-dotted lines.

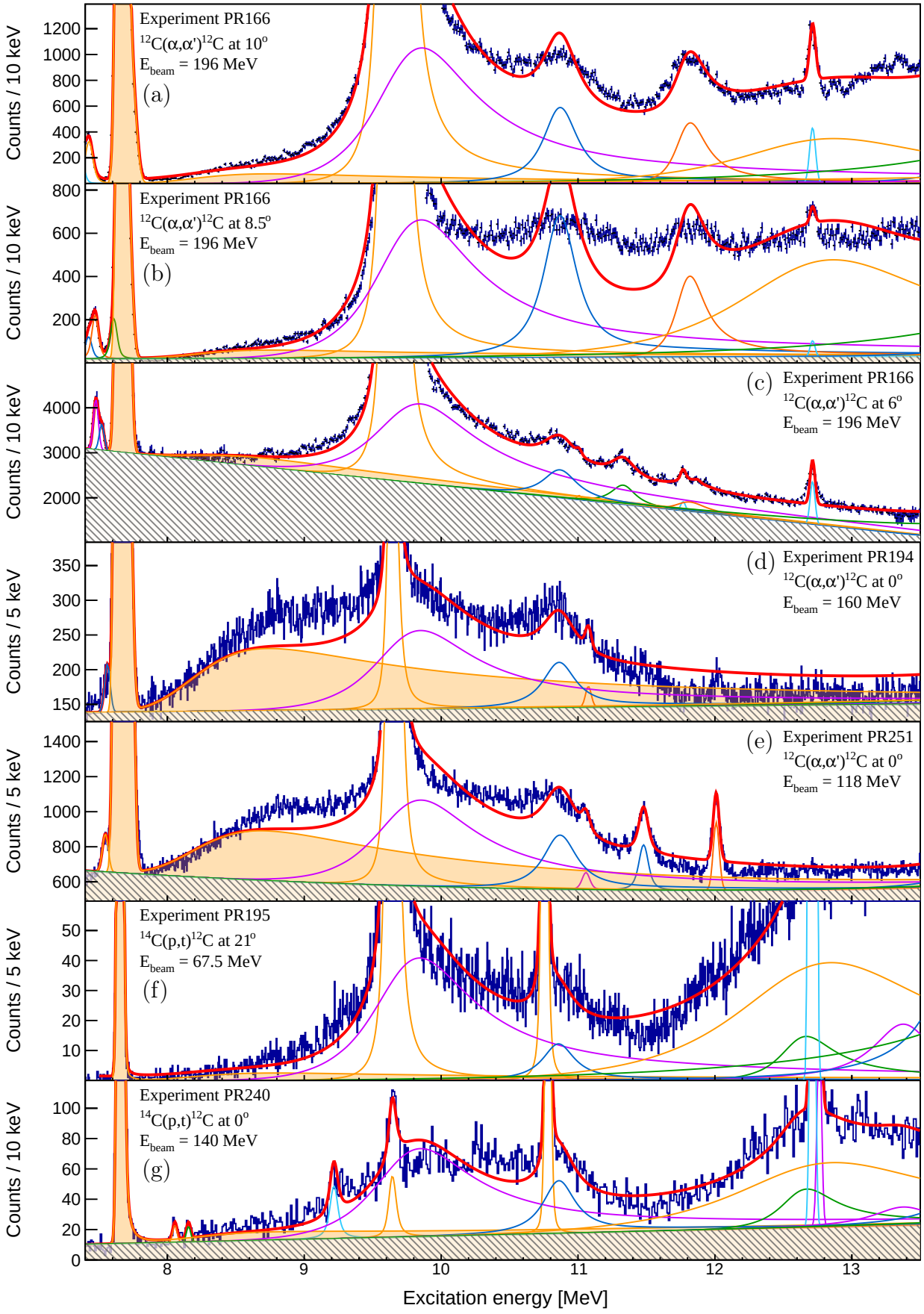

Figure 5.5: Hypothesis H_2: summary of fitted spectra. The contribution of the 0_2^+ Hoyle state is filled in orange. The displayed polynomial backgrounds are filled in translucent white with diagonal gray hatching.

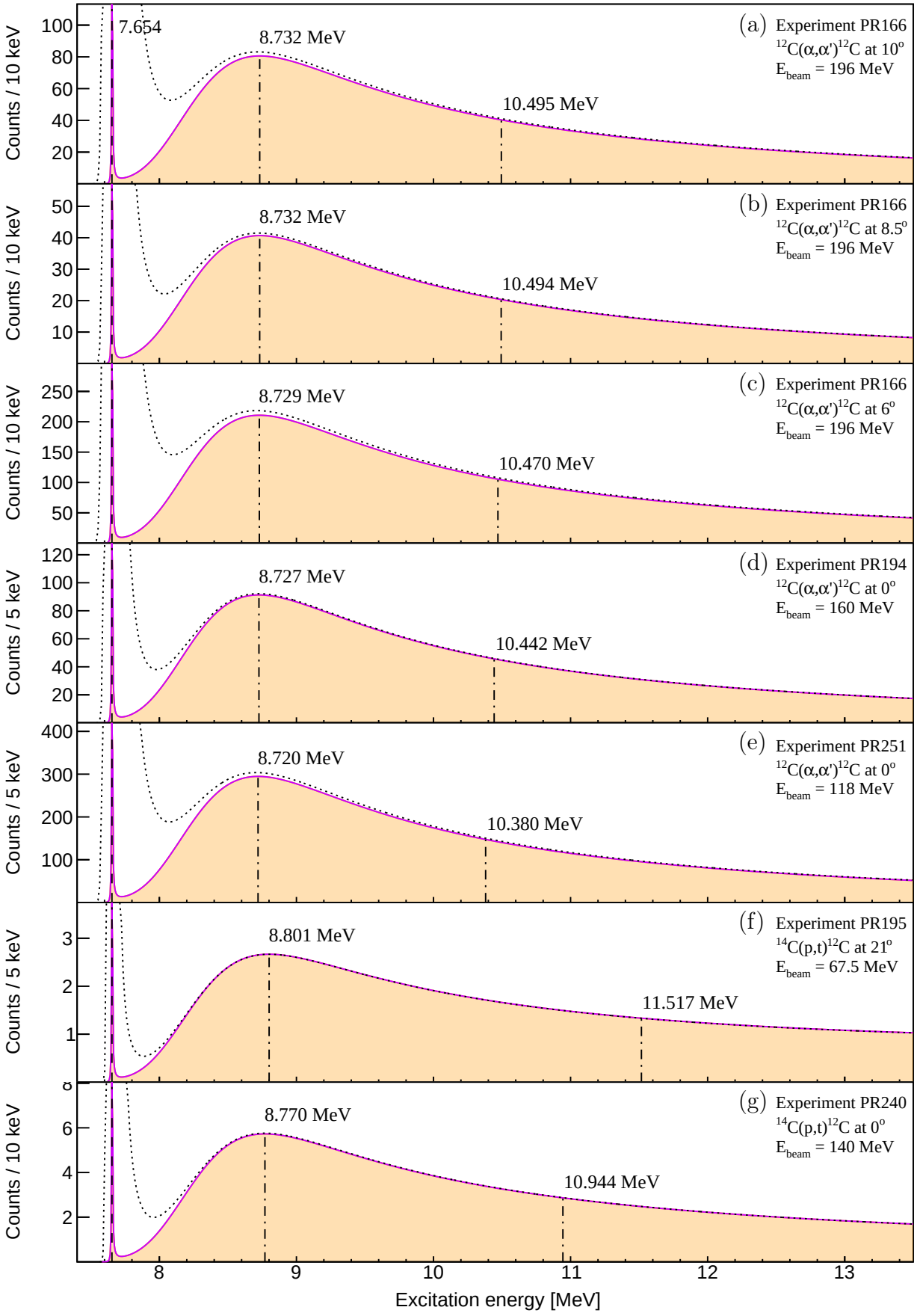

Figure 5.6: Hypothesis H_2: exposition of the populated monopole strength. The intrinsic lineshape of the 0_2^+ Hoyle state is filled in orange. The vertical dashed line indicates the observed resonance energy. The solid violet and dotted black lines represent the total intrinsic and total observed monopole lineshapes, respectively. See Section 5.1.1 for an explanation of the vertical dash-dotted lines.

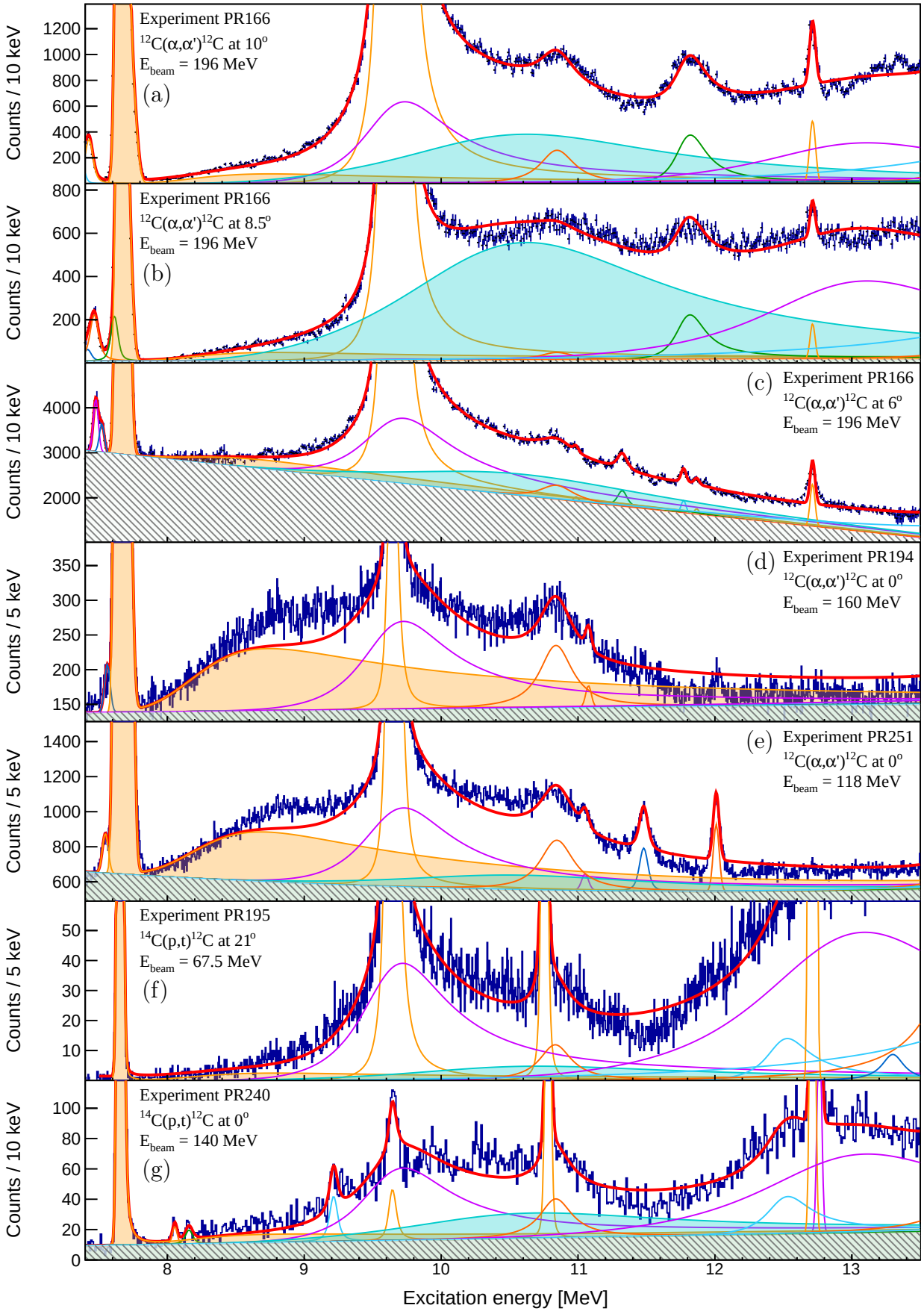

Figure 5.7: Hypothesis H_3: summary of fitted spectra. The incoherent contributions from the 0^+_2 Hoyle state and the broad 0^+ resonance at $E_x \approx 10$ MeV are filled in orange and blue, respectively. The displayed polynomial backgrounds are filled in translucent white with diagonal gray hatching.

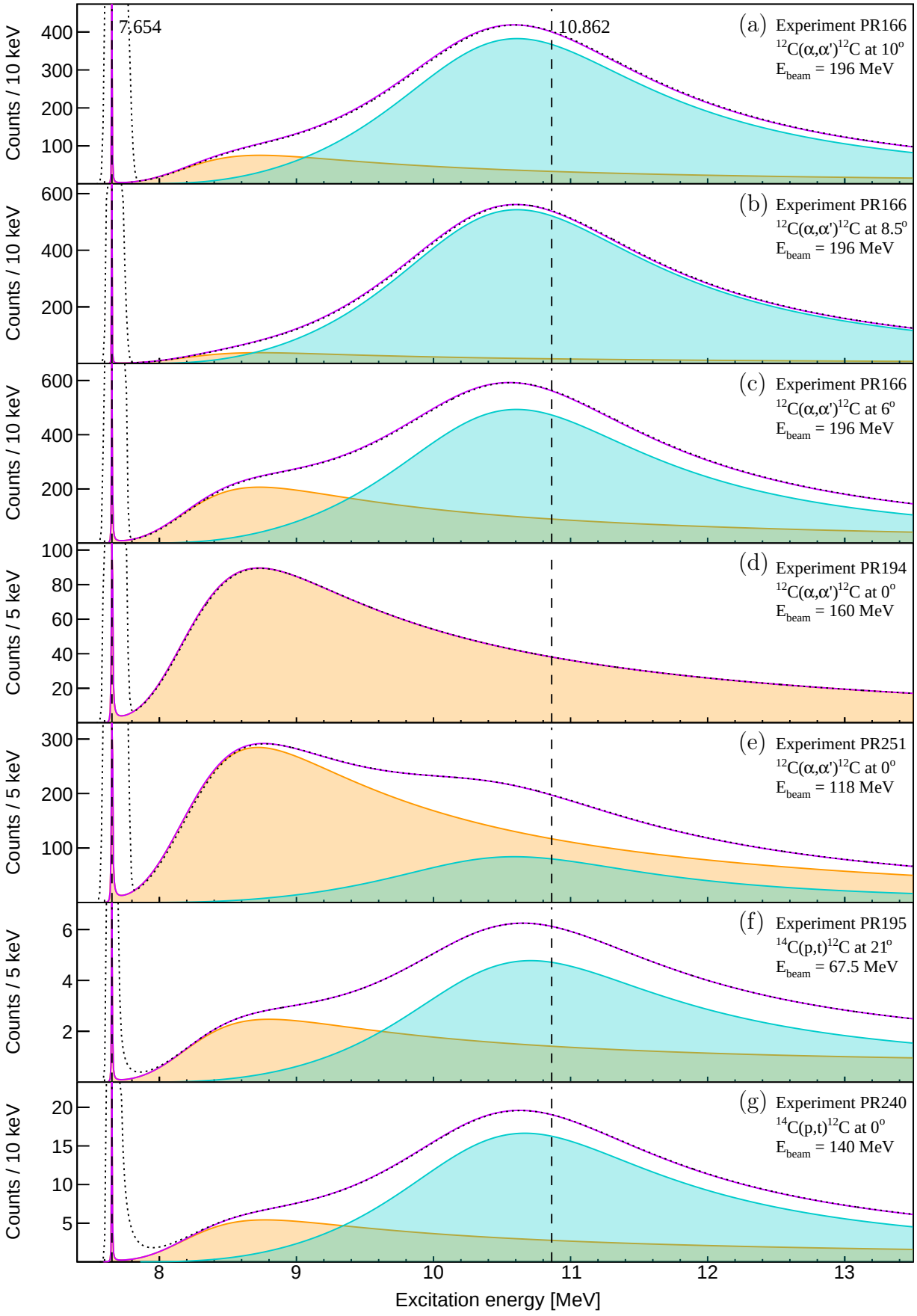

Figure 5.8: Hypothesis H_3: exposition of the populated monopole strength. The intrinsic lineshapes of the 0_2^+ Hoyle state and the broad 0^+ resonance at $E_x \approx 10$ MeV are filled in orange and blue, respectively. The vertical dashed lines indicate the observed resonance energies. The solid violet and dotted black lines represent the total intrinsic and total observed monopole lineshapes, respectively.

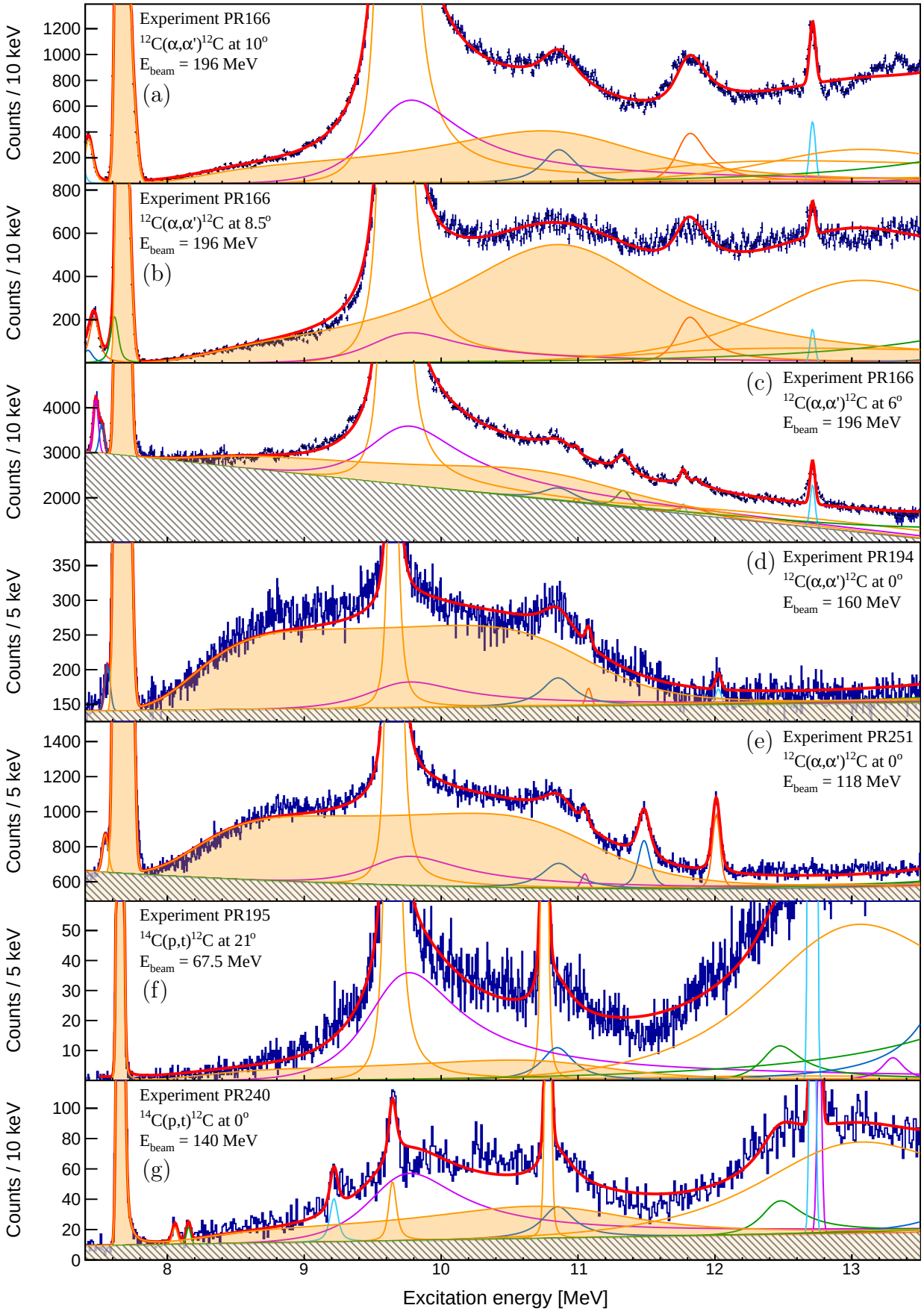

Figure 5.9: Hypothesis H_{4a}: summary of fitted spectra. The contribution from the coherent two-level approximation of the 0_2^+ Hoyle state and the broad 0^+ resonance at $E_x \approx 10$ MeV is filled in orange. The displayed polynomial backgrounds are filled in translucent white with diagonal gray hatching.

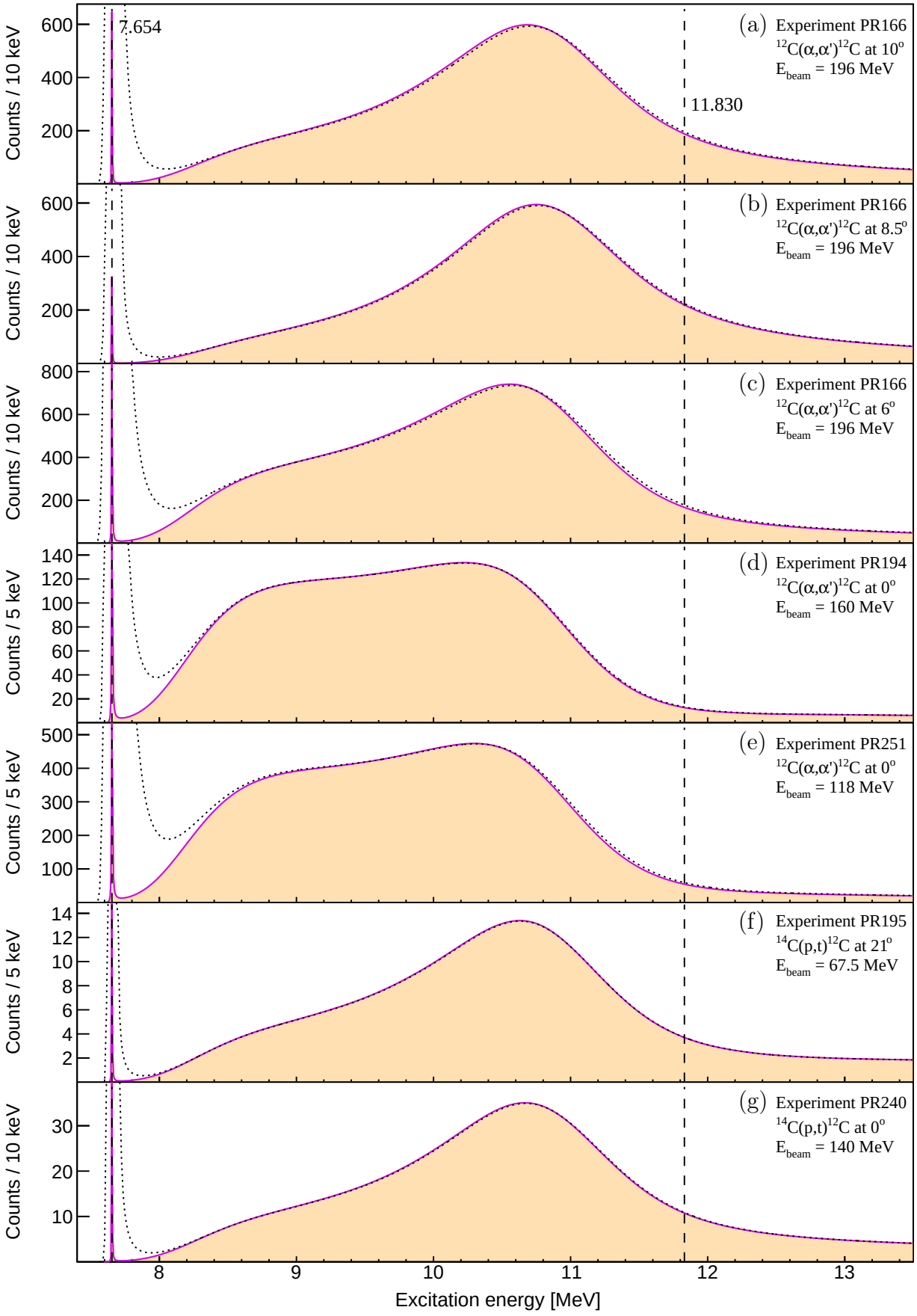

Figure 5.10: Hypothesis H_{4a}: exposition of the populated monopole strength. The intrinsic lineshapes for the coherent two-level approximation of the 0_2^+ Hoyle state and the broad 0^+ resonance at $E_x \approx 10$ MeV is filled in orange. The vertical dashed lines indicate the observed resonance energies. The solid violet and dotted black lines represent the total intrinsic and total observed monopole lineshapes, respectively.

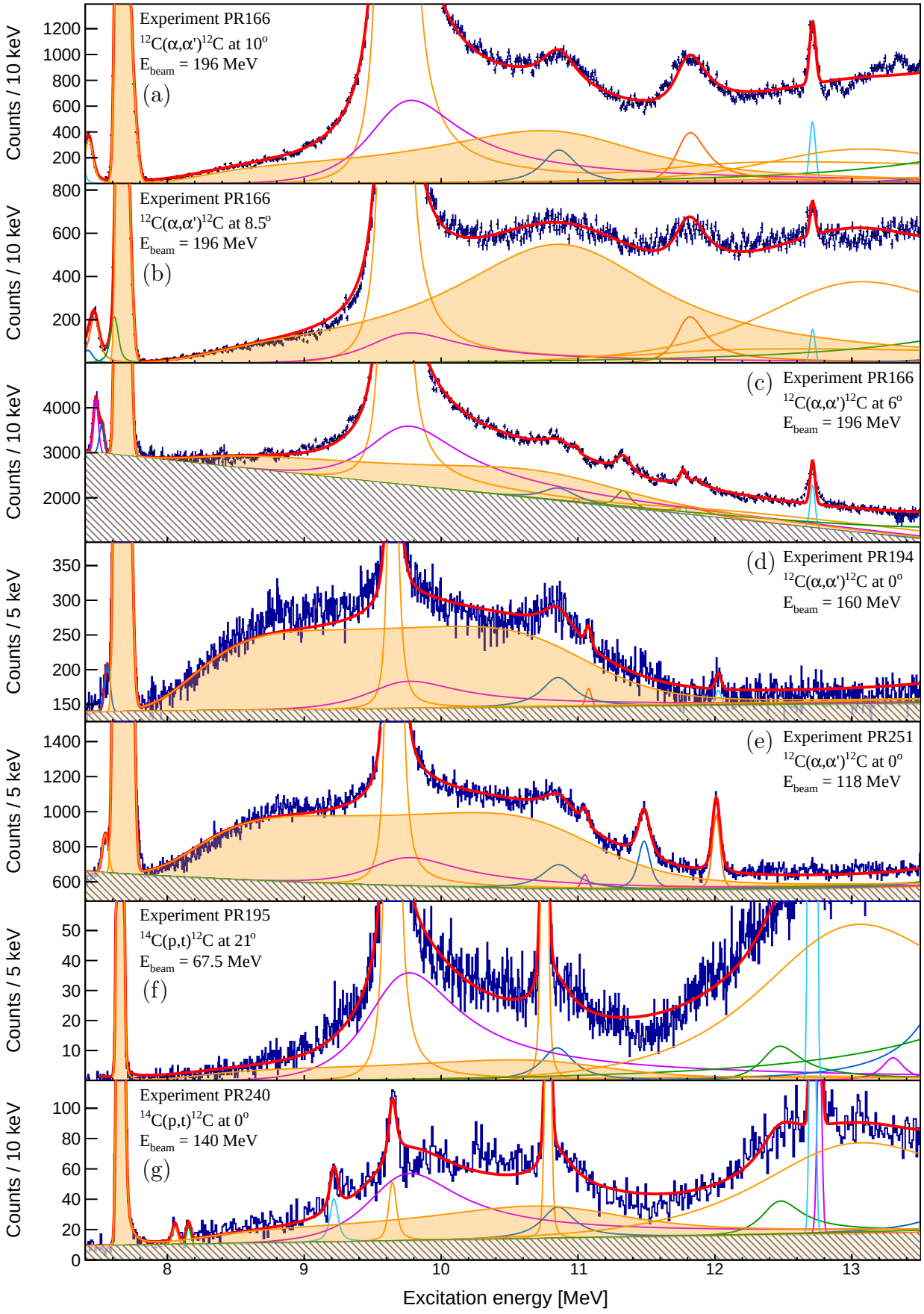

Figure 5.11: Hypothesis H_{4b}: summary of fitted spectra. The contribution from the coherent two-level approximation of the 0_2^+ Hoyle state and the broad 0^+ resonance at $E_x \approx 10$ MeV is filled in orange. The displayed polynomial backgrounds are filled in translucent white with diagonal gray hatching.

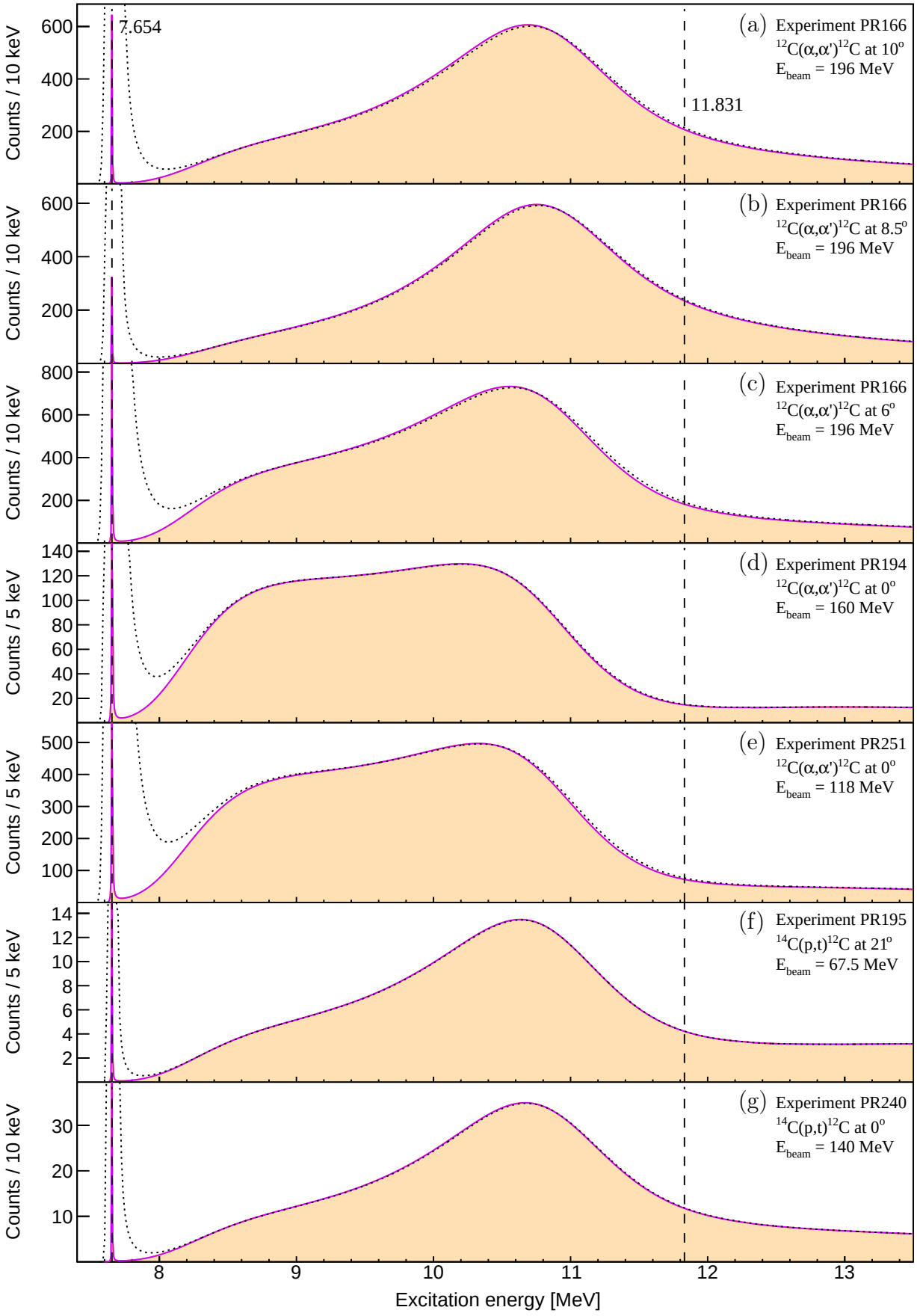

Figure 5.12: Hypothesis H_{4b}: exposition of the populated monopole strength. The intrinsic lineshapes for the coherent two-level approximation of the 0_2^+ Hoyle state and the broad 0^+ resonance at $E_x \approx 10$ MeV is filled in orange. The vertical dashed lines indicate the observed resonance energies. The solid violet and dotted black lines represent the total intrinsic and total observed monopole lineshapes, respectively.

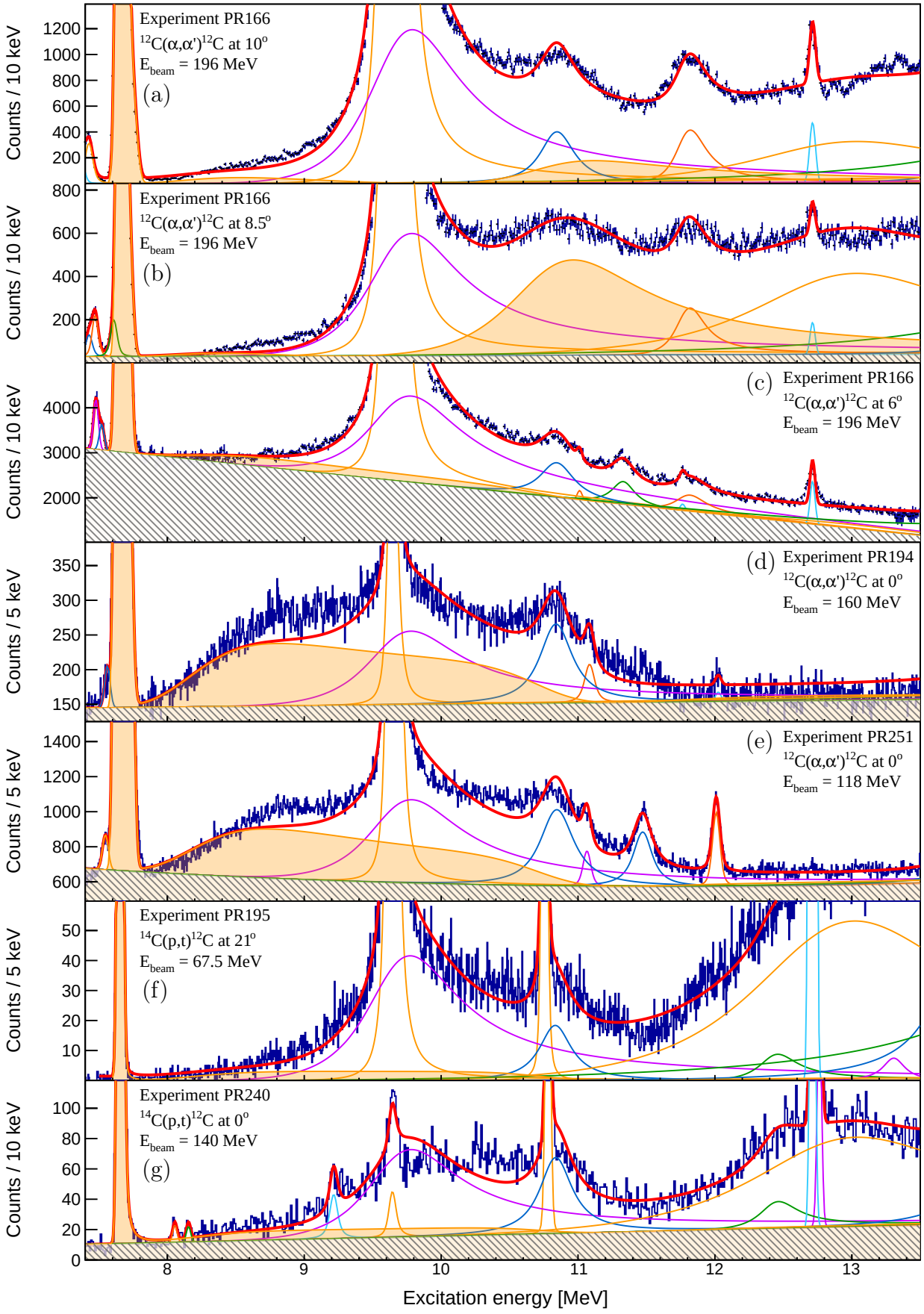

Figure 5.13: Hypothesis H_{4c}: summary of fitted spectra. The contribution from the coherent two-level approximation of the 0_2^+ Hoyle state and the broad 0^+ resonance at $E_x \approx 10$ MeV is filled in orange. The displayed polynomial backgrounds are filled in translucent white with diagonal gray hatching.

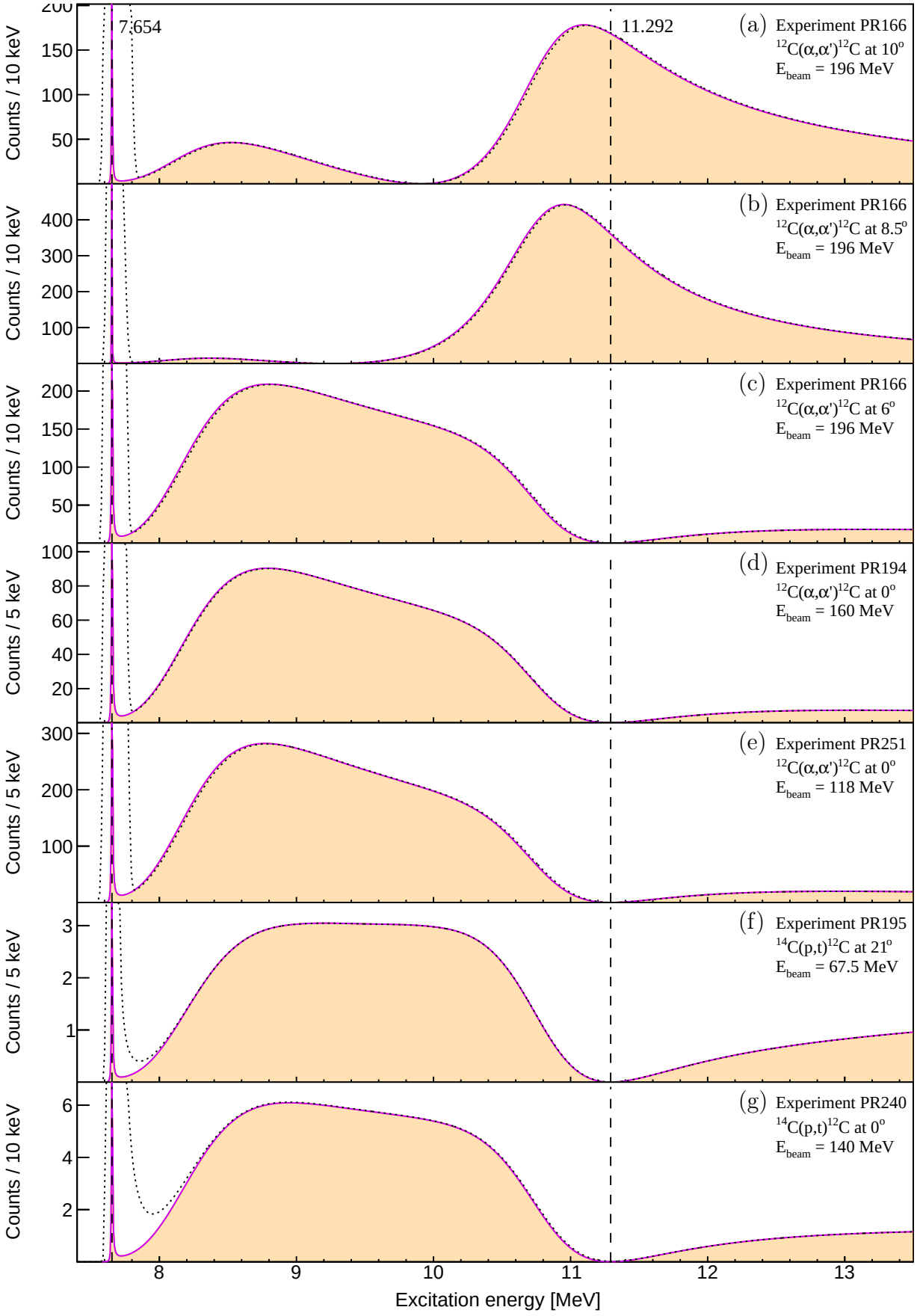

Figure 5.14: Hypothesis H_{4c}: exposition of the populated monopole strength. The intrinsic lineshapes for the coherent two-level approximation of the 0_2^+ Hoyle state and the broad 0^+ resonance at $E_x \approx 10$ MeV is filled in orange. The vertical dashed lines indicate the observed resonance energies. The solid violet and dotted black lines represent the total intrinsic and total observed monopole lineshapes, respectively.

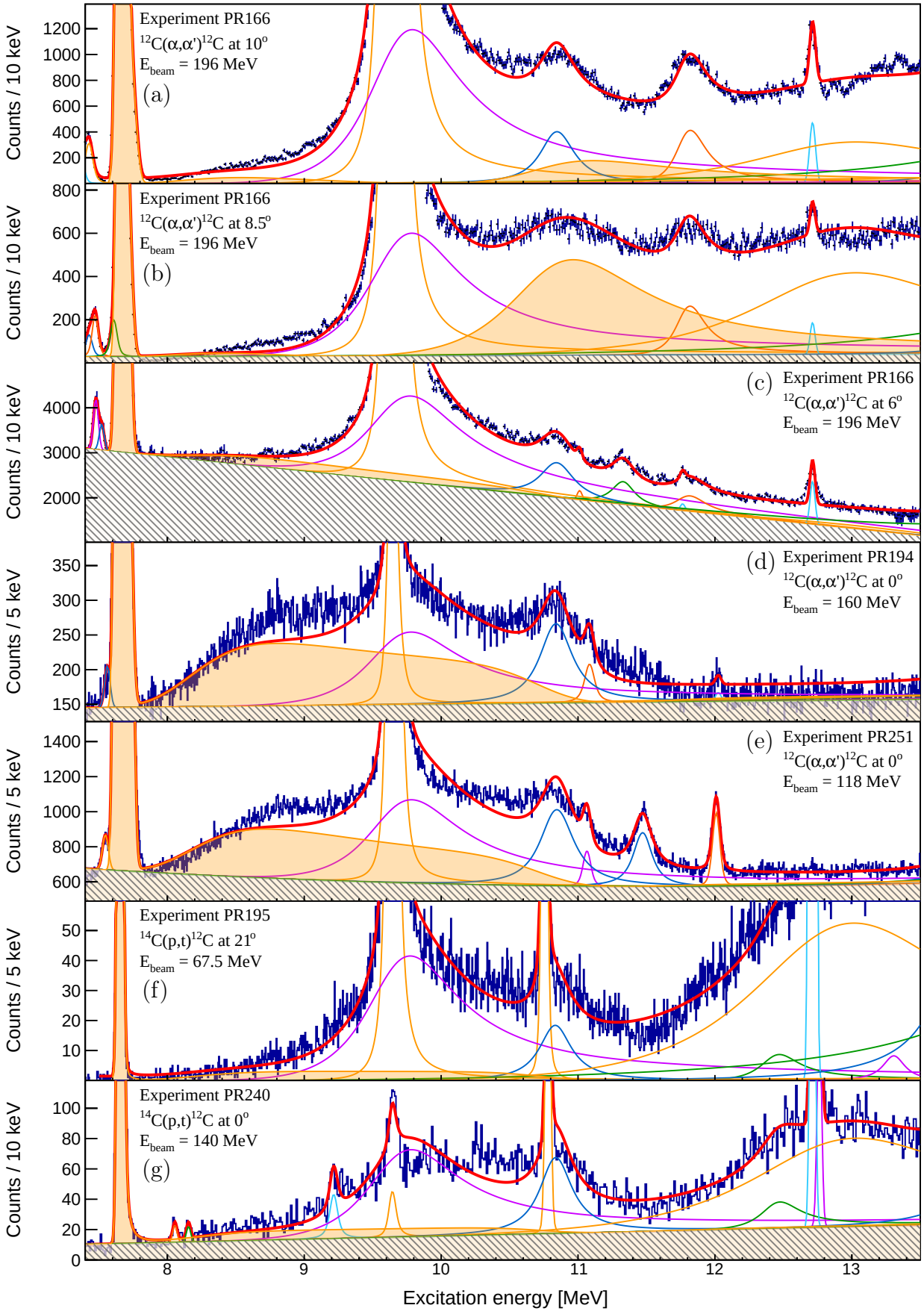

Figure 5.15: Hypothesis H_{4d}: summary of fitted spectra. The contribution from the coherent two-level approximation of the 0_2^+ Hoyle state and the broad 0^+ resonance at $E_x \approx 10$ MeV is filled in orange. The displayed polynomial backgrounds are filled in translucent white with diagonal gray hatching.

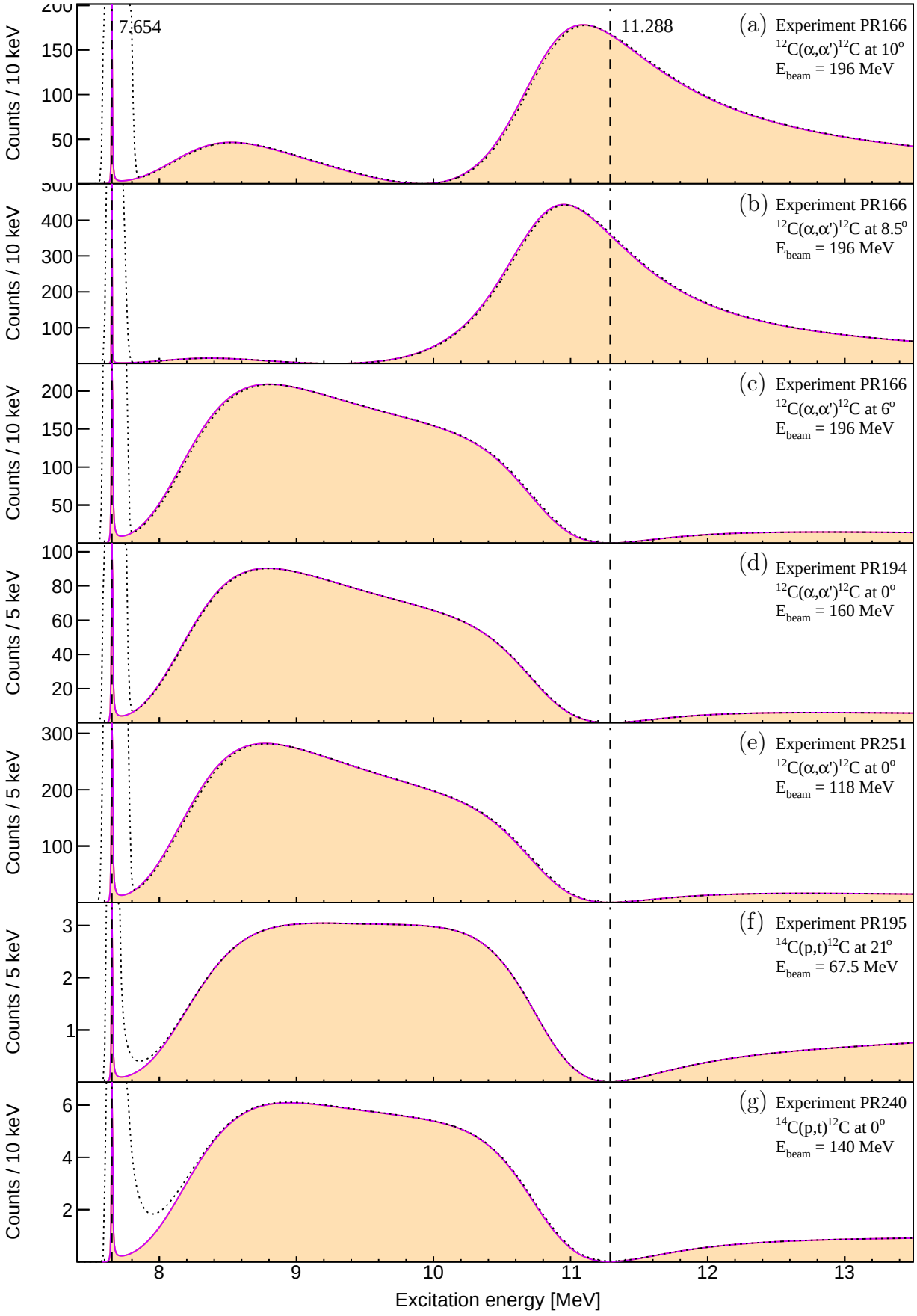

Figure 5.16: Hypothesis H_{4d}: exposition of the populated monopole strength. The intrinsic lineshapes for the coherent two-level approximation of the 0_2^+ Hoyle state and the broad 0^+ resonance at $E_x \approx 10$ MeV is filled in orange. The vertical dashed lines indicate the observed resonance energies. The solid violet and dotted black lines represent the total intrinsic and total observed monopole lineshapes, respectively.

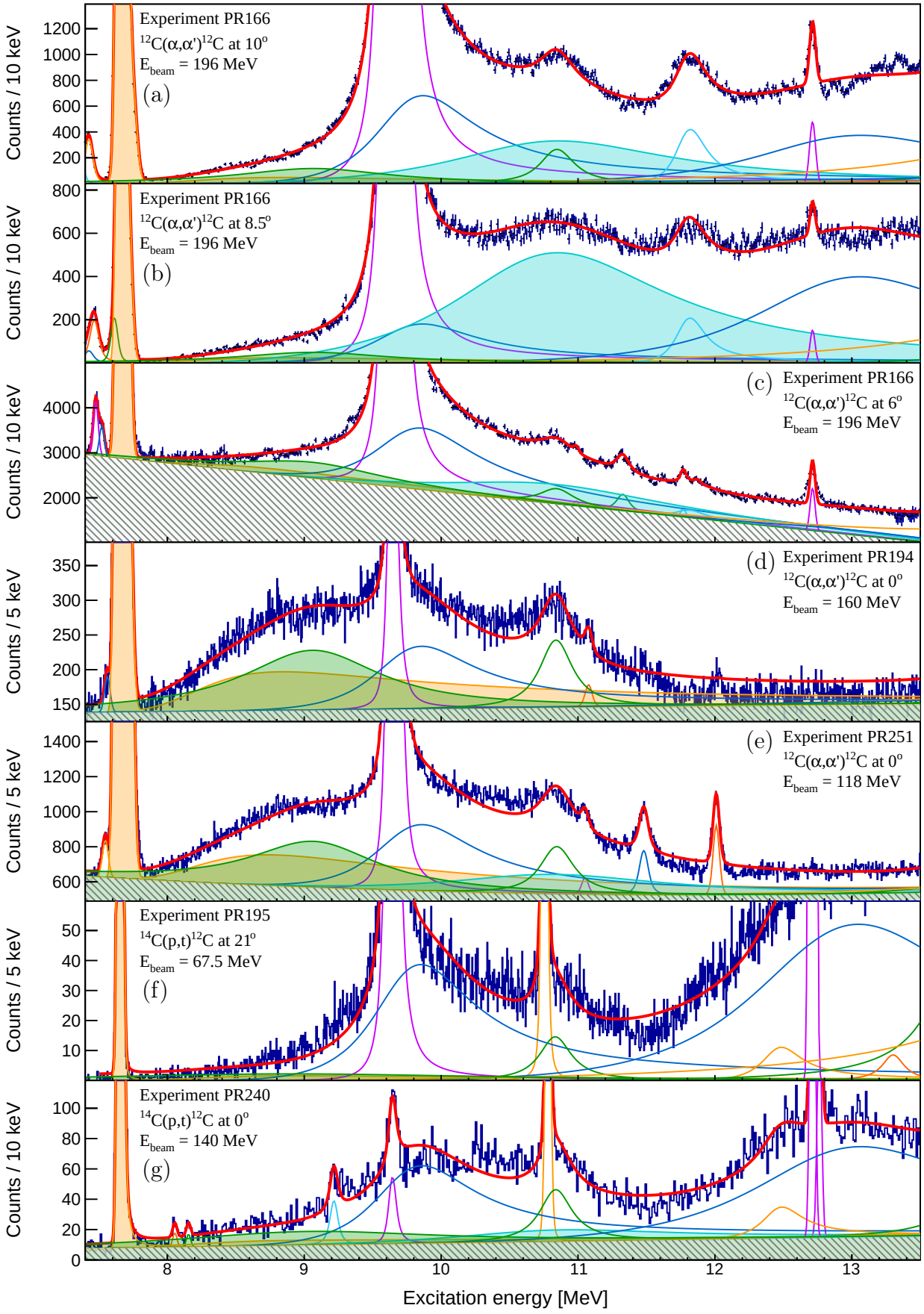

Figure 5.17: Hypothesis H_5: summary of fitted spectra. The incoherent contributions from the 0^+_2 Hoyle state, the ISGMR at $E_x \approx 9$ MeV and the broad 0^+ resonance at $E_x \approx 10$ MeV are filled in orange, green and blue, respectively. The displayed polynomial backgrounds are filled in translucent white with diagonal gray hatching.

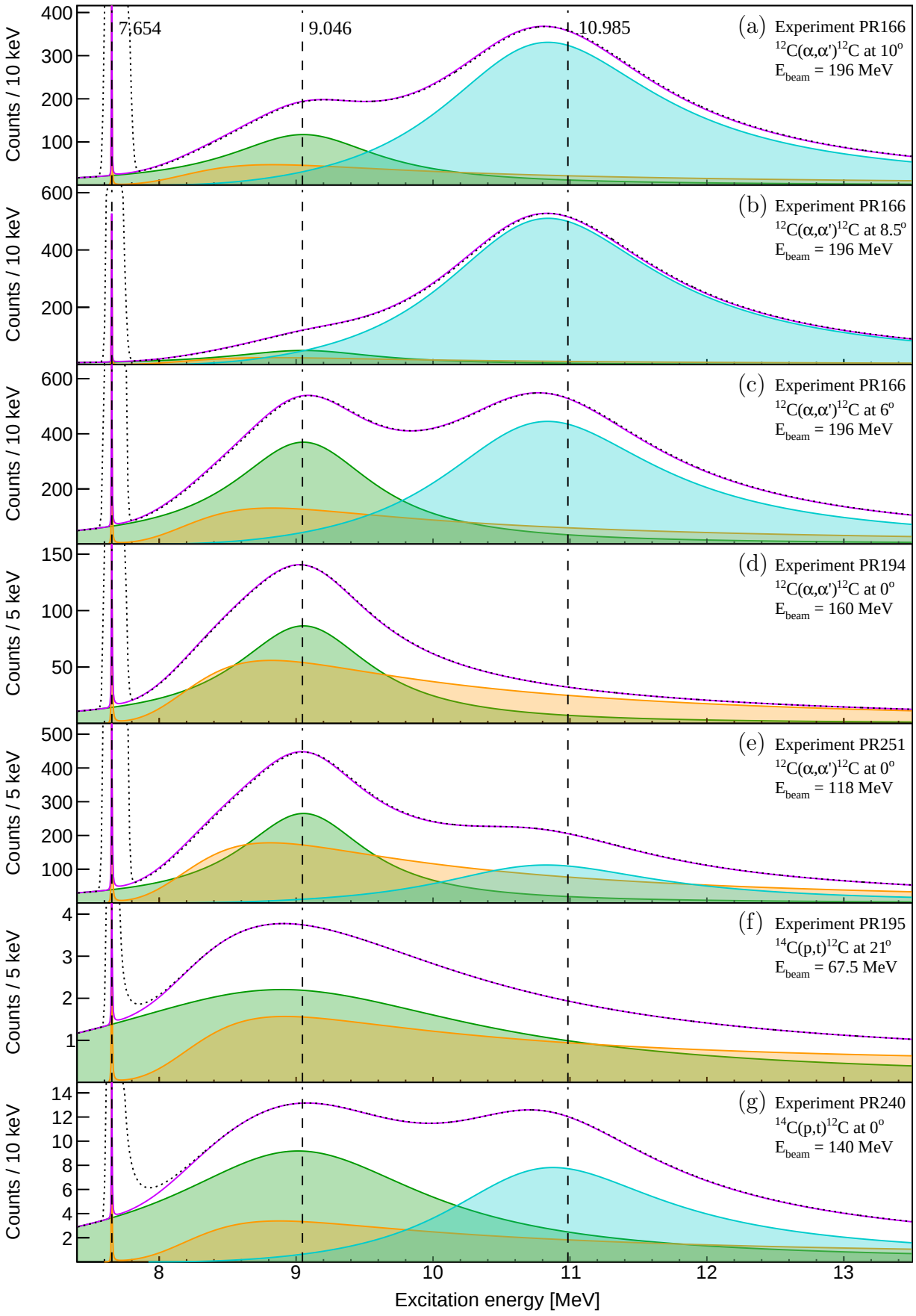

Figure 5.18: Hypothesis H_5: exposition of the populated monopole strength. The intrinsic lineshapes for the 0_2^+ Hoyle state, the ISGMR at $E_x \approx 9$ MeV and the broad 0^+ resonance at $E_x \approx 10$ MeV are filled in orange, green and blue, respectively. The vertical dashed lines indicate the observed resonance energies. The solid violet and dotted black lines represent the total intrinsic and total observed monopole lineshapes, respectively.

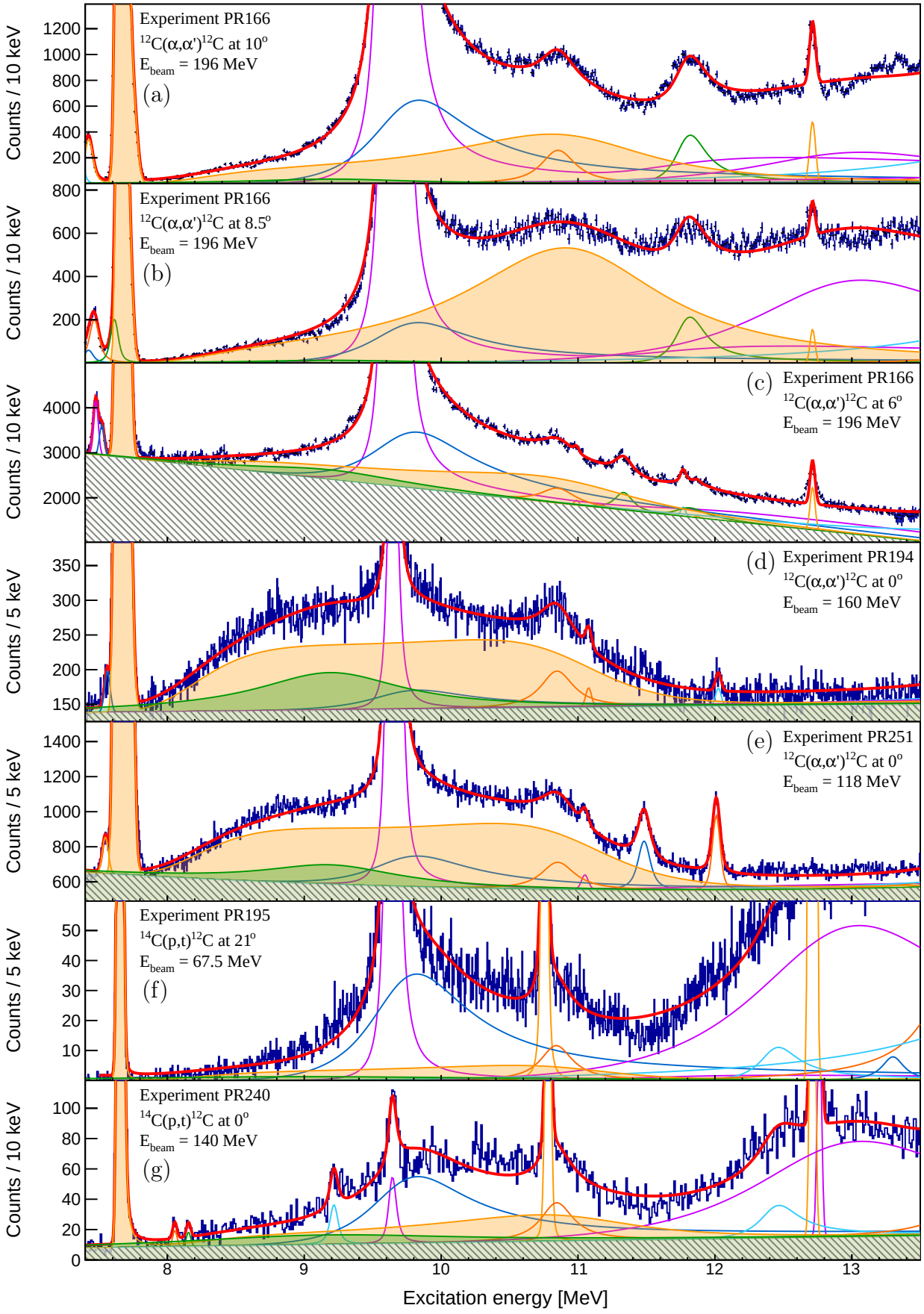

Figure 5.19: Hypothesis H_{6a}: summary of fitted spectra. The contribution from the coherent two-level approximation of the 0_2^+ Hoyle state and the broad 0^+ resonance at $E_x \approx 10$ MeV is filled in orange. The contribution from the ISGMR at $E_x \approx 9$ MeV is filled in green. The displayed polynomial backgrounds are filled in translucent white with diagonal gray hatching.

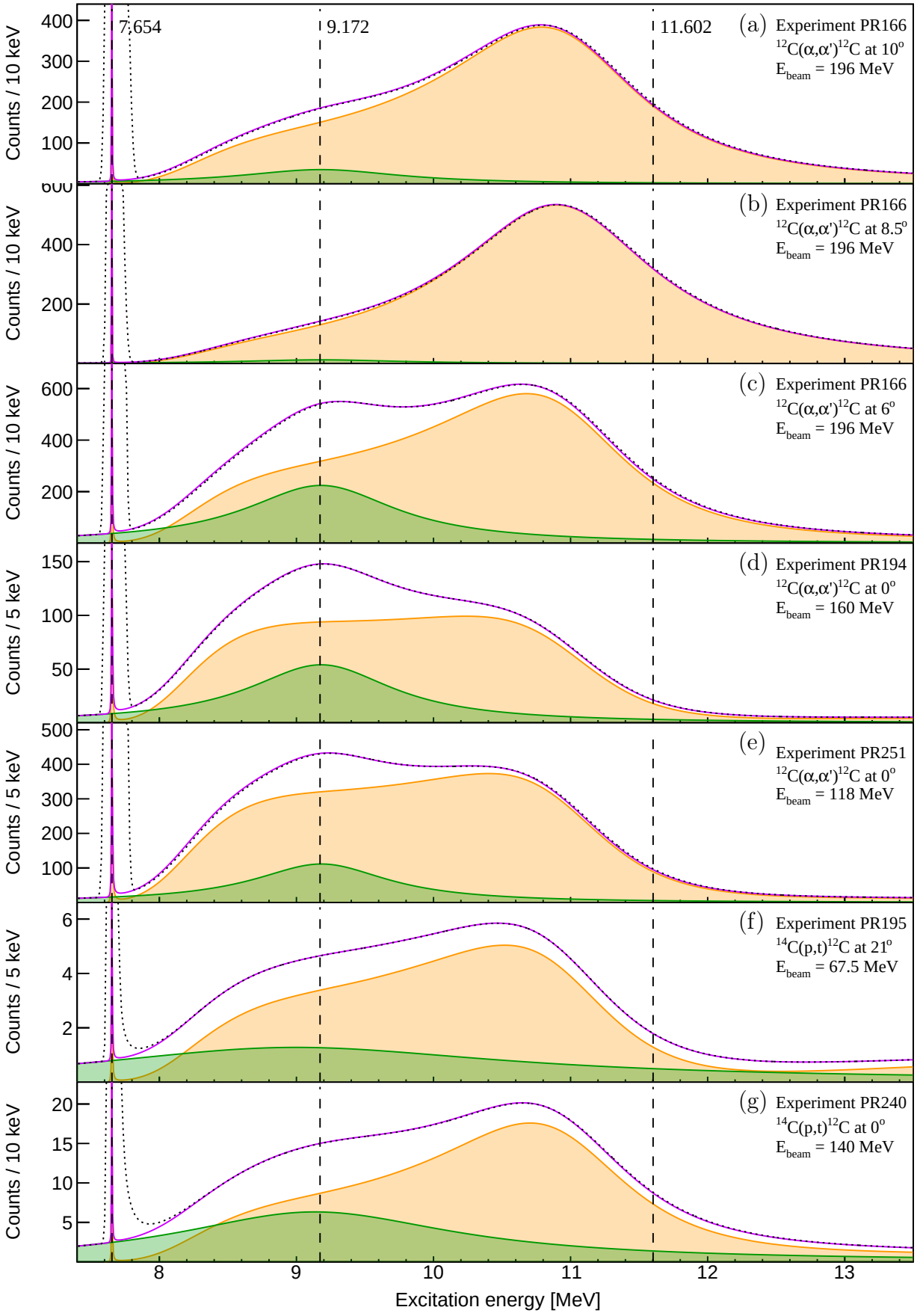

Figure 5.20: Hypothesis H_{6a}: exposition of the populated monopole strength. The intrinsic lineshapes for the coherent two-level approximation of the 0_2^+ Hoyle state and the broad 0^+ resonance at $E_x \approx 10$ MeV is filled in orange. The intrinsic lineshapes for the ISGMR at $E_x \approx 9$ MeV is filled in green. The vertical dashed lines indicate the observed resonance energies. The solid violet and dotted black lines represent the total intrinsic and total observed monopole lineshapes, respectively.

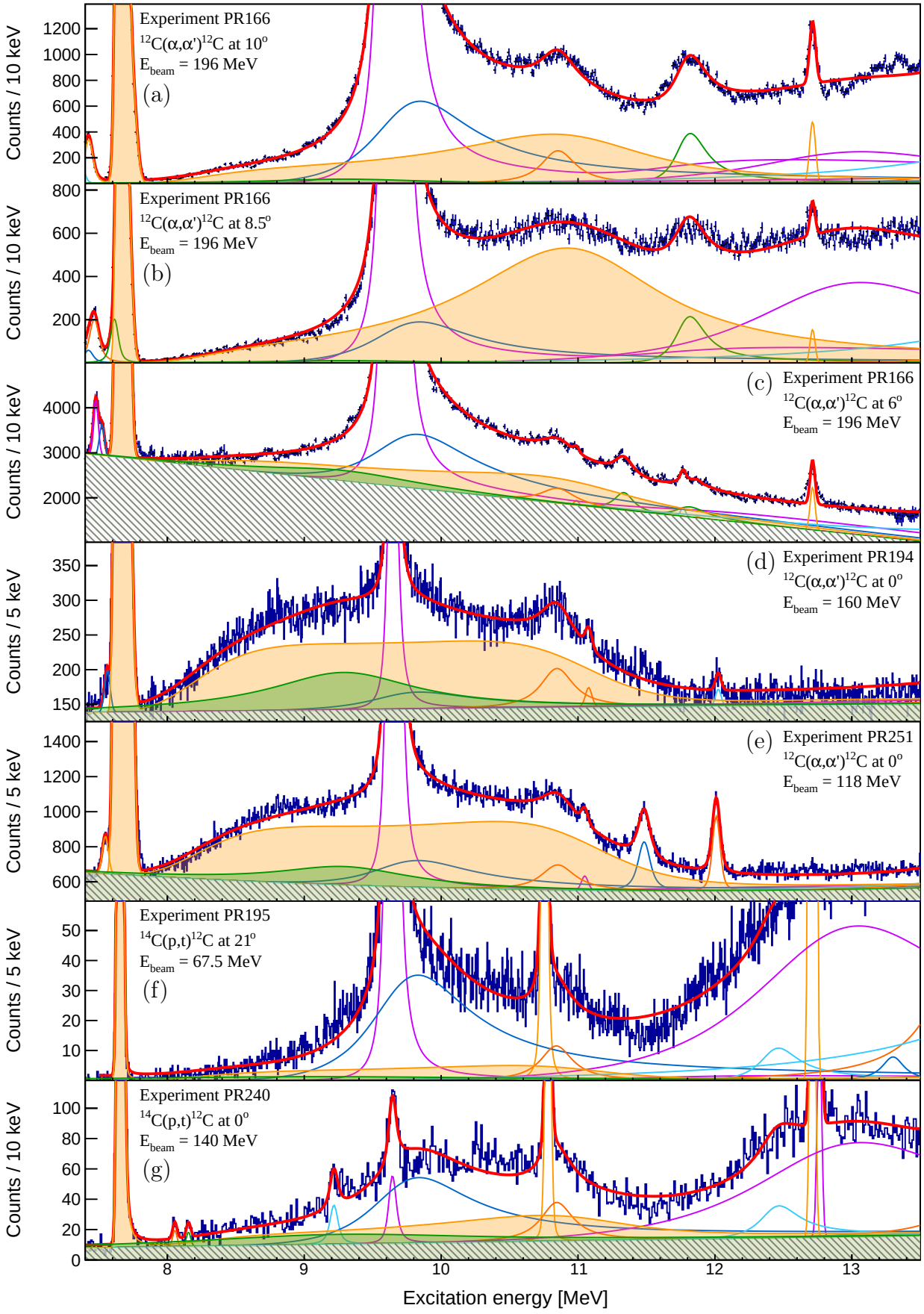

Figure 5.21: Hypothesis H_{6b}: summary of fitted spectra. The contribution from the coherent two-level approximation of the 0_2^+ Hoyle state and the broad 0^+ resonance at $E_x \approx 10$ MeV is filled in orange. The contribution from the ISGMR at $E_x \approx 9$ MeV is filled in green. The displayed polynomial backgrounds are filled in translucent white with diagonal gray hatching.

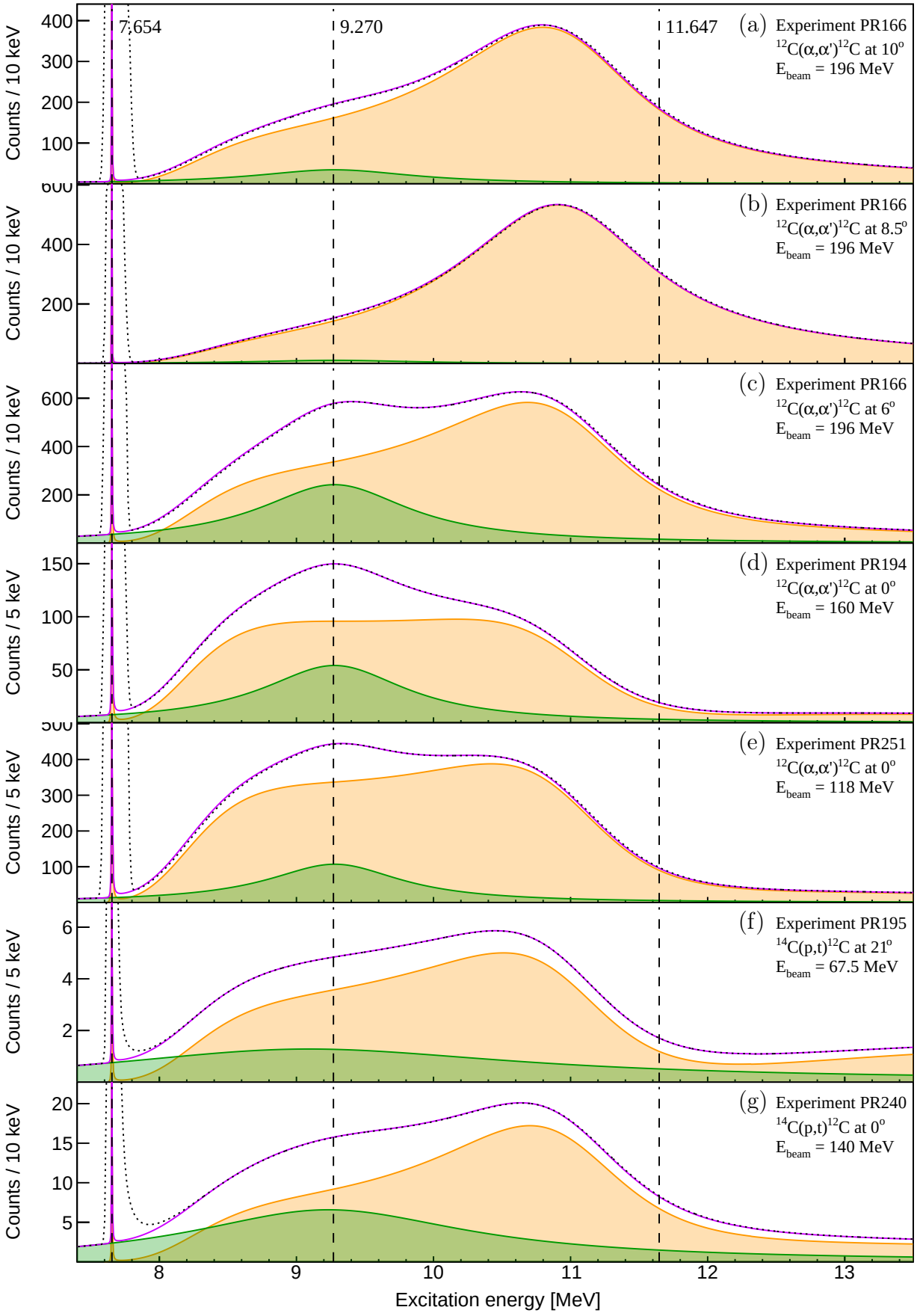

Figure 5.22: Hypothesis H_{6b}: exposition of the populated monopole strength. The intrinsic lineshapes for the coherent two-level approximation of the 0_2^+ Hoyle state and the broad 0^+ resonance at $E_x \approx 10$ MeV is filled in orange. The intrinsic lineshapes for the ISGMR at $E_x \approx 9$ MeV is filled in green. The vertical dashed lines indicate the observed resonance energies. The solid violet and dotted black lines represent the total intrinsic and total observed monopole lineshapes, respectively.

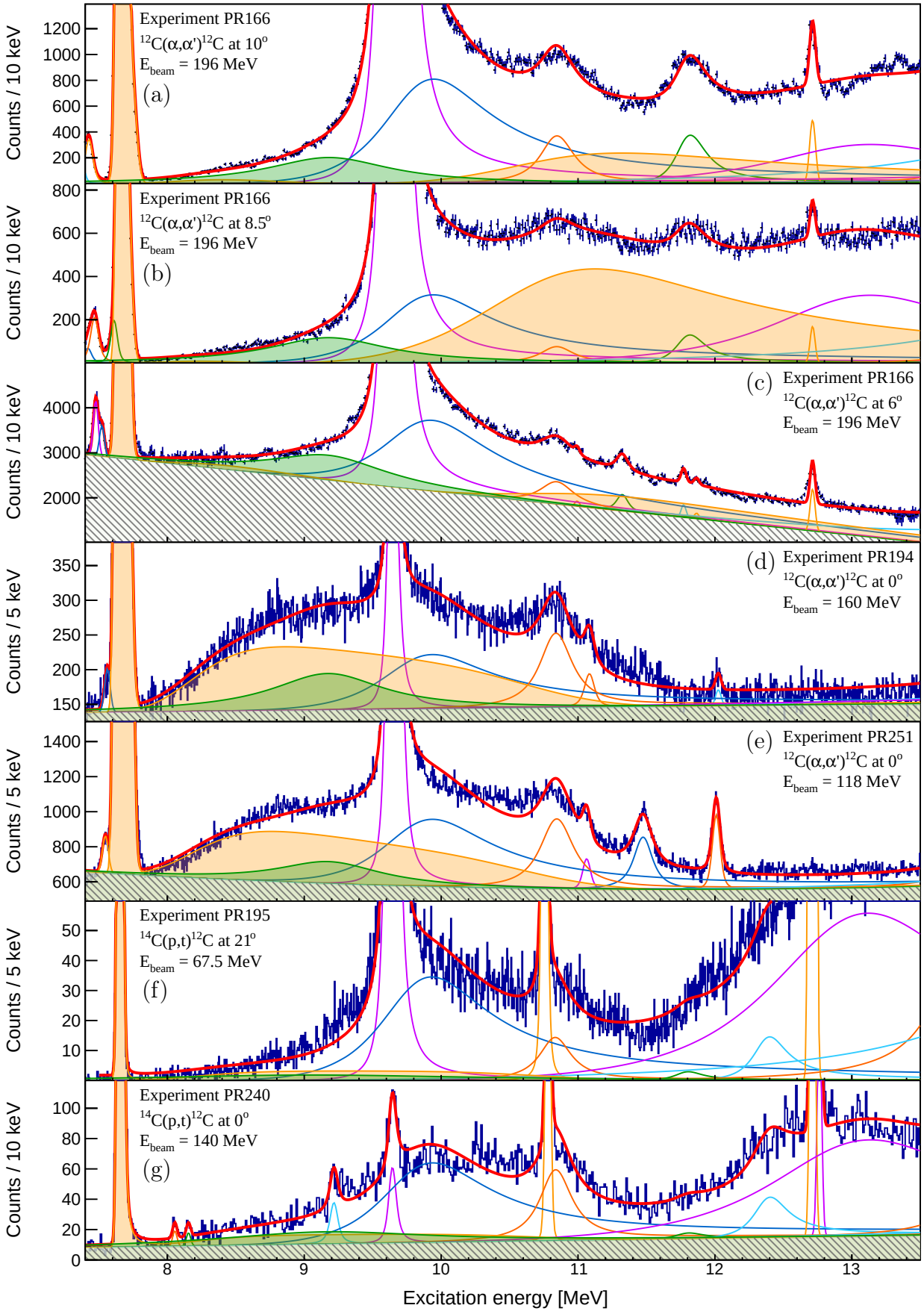

Figure 5.23: Hypothesis H_{6c}: summary of fitted spectra. The contribution from the coherent two-level approximation of the 0_2^+ Hoyle state and the broad 0^+ resonance at $E_x \approx 10$ MeV is filled in orange. The contribution from the ISGMR at $E_x \approx 9$ MeV is filled in green. The displayed polynomial backgrounds are filled in translucent white with diagonal gray hatching.

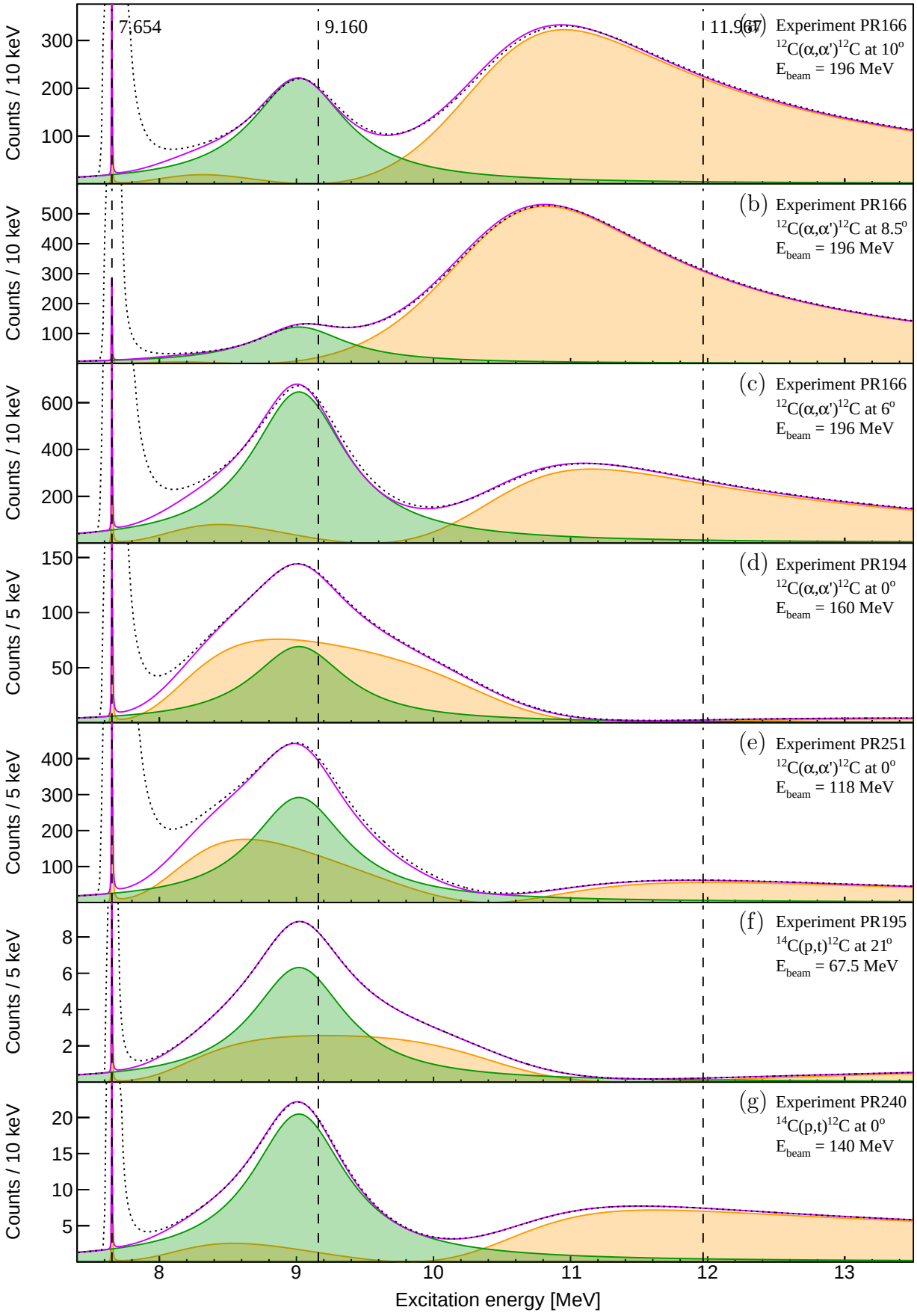

Figure 5.24: Hypothesis H_{6c}: exposition of the populated monopole strength. The intrinsic lineshapes for the coherent two-level approximation of the 0_2^+ Hoyle state and the broad 0^+ resonance at $E_x \approx 10$ MeV is filled in orange. The intrinsic lineshapes for the ISGMR at $E_x \approx 9$ MeV is filled in green. The vertical dashed lines indicate the observed resonance energies. The solid violet and dotted black lines represent the total intrinsic and total observed monopole lineshapes, respectively.

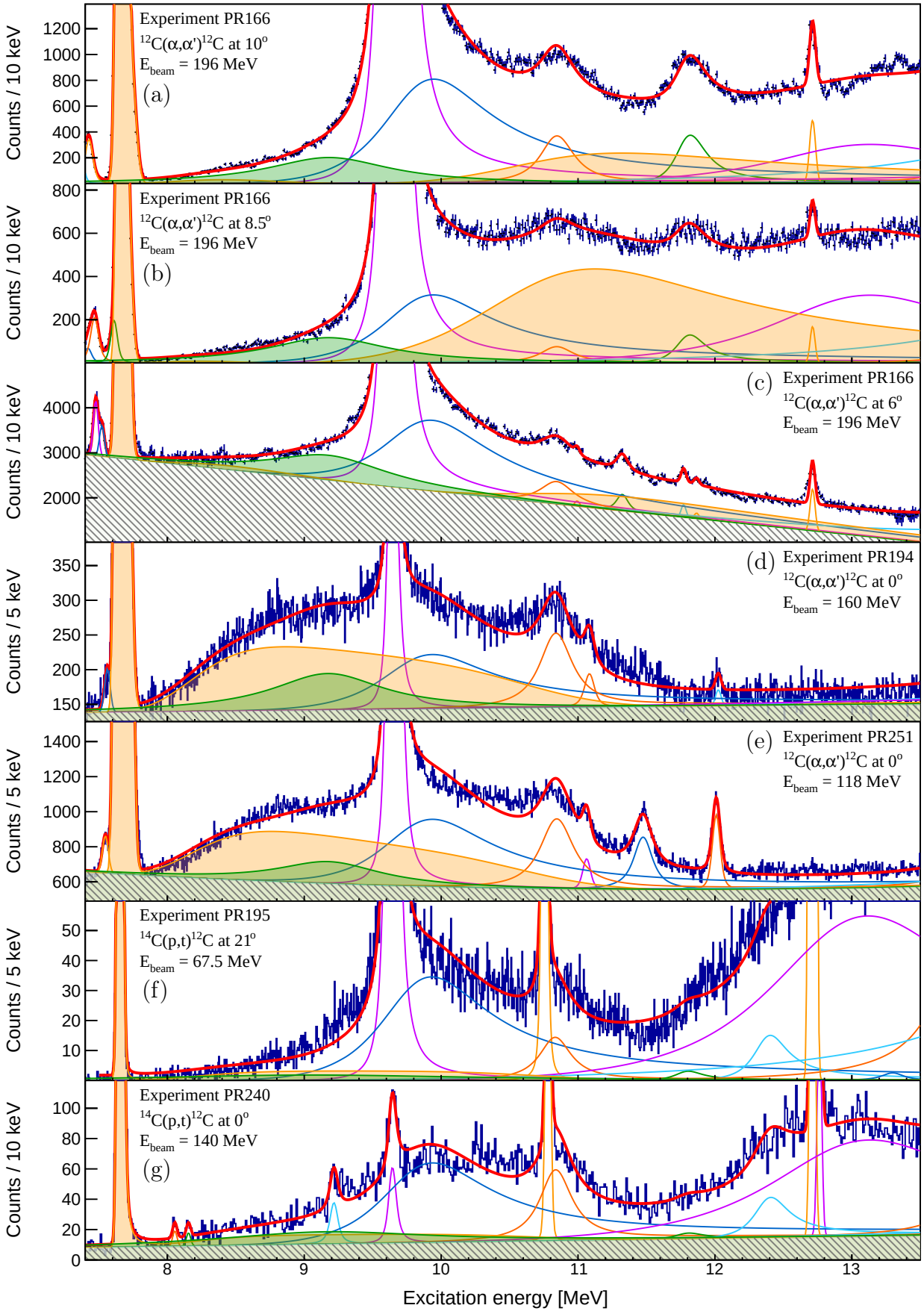

Figure 5.25: Hypothesis H_{6d}: summary of fitted spectra. The contribution from the coherent two-level approximation of the 0_2^+ Hoyle state and the broad 0^+ resonance at $E_x \approx 10$ MeV is filled in orange. The contribution from the ISGMR at $E_x \approx 9$ MeV is filled in green. The displayed polynomial backgrounds are filled in translucent white with diagonal gray hatching.

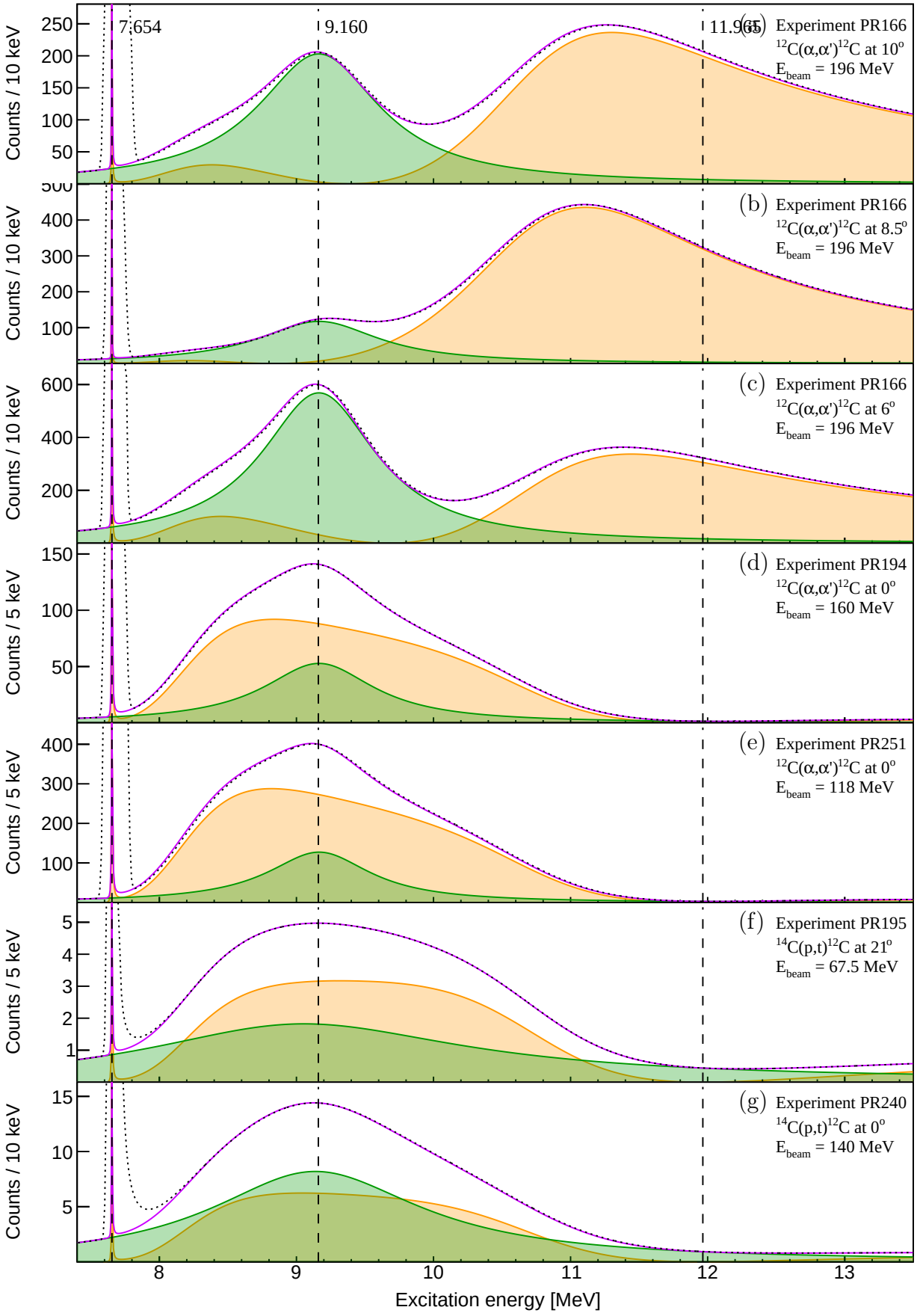

Figure 5.26: Hypothesis H_{6d}: exposition of the populated monopole strength. The intrinsic lineshapes for the coherent two-level approximation of the 0_2^+ Hoyle state and the broad 0^+ resonance at $E_x \approx 10$ MeV is filled in orange. The intrinsic lineshapes for the ISGMR at $E_x \approx 9$ MeV is filled in green. The vertical dashed lines indicate the observed resonance energies. The solid violet and dotted black lines represent the total intrinsic and total observed monopole lineshapes, respectively.

5.2 Experimental factors

As mentioned in Section 4.10.1, experimentally observed lineshapes of nuclear excitations are different to the intrinsic lineshapes since the act of measurement inevitably introduces uncertainty. It is postulated that the excitation-energy spectra measured with the VDCs are affected by two dominating experimental factors: an inherent detector resolution that is presumed to be approximately Gaussian and target-related energy loss for the ejectile that can be described by the Landau distribution. For the ^{12}C$(\alpha,\alpha')^{12}$C measurements, which exhibit considerably larger target-related energy loss with respect to the ^{14}C$(p,t)^{12}$C measurements, a Landau distribution was employed (see Equation 4.47). A summary of the fitted Gaussian and Landau parameters are presented in Table 5.6 and described in Section 4.10.1.1. As expected, the Landau scale parameters for the ^{12}C$(\alpha,\alpha')^{12}$C measurements are greater than those of the ^{14}C$(p,t)^{12}$C measurements as the α-particle ejectiles exhibit greater energy loss in the target with respect to the tritons. The substantial difference in Landau scale parameters between the two ^{12}C$(\alpha,\alpha')^{12}$C measurements at $\theta_{\text{lab}} = 0^{\circ}$ is predominantly due to the ~ 3 times difference in target thickness.

Since the primary peak of the Hoyle state exhibits an observed width of 9.3(9) eV at the resonance energy of 7.65407(19) MeV, the observed lineshape of the primary peak is dominated by the experimental factors such as the detector resolutions and energy-loss effects. The R-matrix fits of the Hoyle state presented on Figures 5.3 - 5.25 present a good test of whether the aforementioned Gaussian and Landau components provide a satisfactory description of the data. It is observed that the convolution between the intrinsic nuclear lineshape with Gaussian and Landau distributions generally yields a good description for the primary peak of the Hoyle state. However, for the fits of the ^{12}C$(\alpha,\alpha')^{12}$C measurements at $\theta_{\text{lab}} = 0^{\circ}$ on panels (d) (PR194) and (e) (PR251), it is observed that the expected value overestimates the tail of the Hoyle at $E_x \approx 7.8$ MeV. For experiments PR194 and PR251, these deviations correspond to approximately $\sim 0.5\%$ and $\sim 1.5\%$ in comparison to the maxima for the corresponding Hoyle state peaks. Whilst these relative deviations are not intolerable, they are indicative that the excitation-energy spectra from these two measurements exhibit a convolved distribution that is neither Gaussian nor Landau in form. This effect is not caused by compounding sources of experimental resolution and/or energy loss as since because both Gaussian and Landau distributions are stable distributions, successive convolutions of Gaussian/Landau distributions must yield a Gaussian/Landau distribution. One possible source of these deviations is energy loss in the Kapton exit window that separates the internal vacuum of the K600 spectrometer from the focal-plane detector system. In comparison to triton ejectiles, α-particle ejectiles are particularly susceptible to scattering interactions at this window since they possess twice the charge of the triton. Preliminary simulations show that the deviated flight paths of such scattered ejectiles induce an asymmetrical

PAC Code	Reaction	E_{beam} [MeV]	Angle [deg]	Target	Target thickness [μg/cm^2]	σ [keV]	c [keV]	s [keV]
PR166	^{12}C$(\alpha,\alpha')^{12}$C	196	6	^{12}C	290	21.9(2)	6.4(1)	146(1)
		196	8.5		220	17.4(5)	6.6(2)	97(1)
		196	10		290	19.0(3)	12.2(2)	89(1)
PR194	^{12}C$(\alpha,\alpha')^{12}$C	160	0	^{12}C	300	20.2(1)	2.2(1)	90(1)
PR251	^{12}C$(\alpha,\alpha')^{12}$C	118	0	^{12}C	1053	21.4(1)	7.4(1)	90(1)
PR195	^{14}C$(p,t)^{12}$C	67.5	21	^{14}C	300	14.3(2)	0.28(7)	none
PR240†	^{14}C$(p,t)^{12}$C	140	0	^{14}C	unknown	15.5(3)	1.3(1)	none

Table 5.6: Summary of the optomised experimental factors (see Section 4.10.1.1).

smearing of the ejectile positions at the focal plane since the ejectiles penetrate the window at an oblique angle. Another possible cause of the deviated lineshape is an imperfect lineshape correction. As explained in Section 4.1.7, the polar angle of the ejectile is not measured and only θ_{scat}, the angle between the projected ejectile vector on the horizontal plane, is able to be determined. Whilst lineshape corrections with θ_{scat} yield substantial increases in resolution for the corrected focal-plane position, X1$_{\text{posC}}$, it is highly possible that a non-negligible correlation between X1$_{\text{posC}}$ and the true polar angle persists. Such a correlation would not be observable on the θ_{scat} versus X1$_{\text{posC}}$ lineshapes and could produce a distortion of the focal-plane spectrum.

5.3 The monopole structure of ^{12}C at $E_x \approx$ 7-16 MeV

A multipole decomposition analysis (MDA) study by M. Itoh *et al.* of the ^{12}C$(\alpha,\alpha')^{12}$C reaction at $\theta_{\text{lab}} = 0^\circ$ with $E_{\text{beam}} = 386$ indicated that an unlisted source of monopole strength may contribute to the broad 0^+ structure in the $E_x \approx$ 7-16 MeV excitation-energy region of interest. The total 0^+ strength appeared to exhibit a double-peaked structure with the central minimum situated at $E_x \approx 9.5$ MeV, as shown in Figure 1.2. Additionally, it is observed that between $E_x = 11$ and 12 MeV, there is a sharp reduction in the monopole strength by $\approx 25\%$ with respect to the local maximum at $E_x \approx 10.5$ MeV. The analysed ^{12}C$(\alpha,\alpha')^{12}$C measurements at $\theta_{\text{lab}} = 0^\circ$ of experiments PR194 and PR251, with respective incident beam energies of $E_{\text{beam}} = 160$ and 118 MeV, provide the closest comparison to the data studied by M. Itoh *et al.* and the corresponding excitation-energy spectra are presented on panels (d) and (e) in Figures 5.3 - 5.25.

The simplest hypotheses that model the monopole structure at $E_x \approx$ 7-16 MeV without interference effects are H_1, H_2, H_3 and H_5. It was observed that H_1 and H_2, which modeled the entire monopole structure with only the Hoyle state and its associated ghost, yielded poor AIC and BIC estimators and could not reproduce the monopole strength at $E_x \approx 9$ MeV, as discussed in Section 5.1.1. Moreover, the intrinsic monopole strengths extracted under H_1 and H_2, could not reproduce the $\approx 75\%$ reduction in the monopole strength between $E_x = 11$ and 12 MeV for the measurements of PR194 and PR251, as shown on panels (d) and (e) of Figures 5.4 and 5.6. Hypothesis H_3 expands upon the Hoyle-state models of H_1 and H_2 with the inclusion of a broad 0^+ resonance at $E_x \approx 10$ MeV, as discussed in Section 5.1.2. Whilst this yielded a significantly better quality model with respect to H_1 and H_2, both the excess monopole strength at $E_x \approx 9$ MeV and the $\approx 75\%$ reduction in the monopole strength between $E_x = 11$ and 12 MeV could not be reproduced for the ^{12}C$(\alpha,\alpha')^{12}$C measurements at $\theta_{\text{lab}} = 0^\circ$ (PR194 and PR251). Hypothesis H_5 expands upon the model of H_3 with the inclusion of an unlisted broad 0^+ resonance at $E_x \approx 9$ MeV, parameterised by a standard Lorentzian lineshape which is modulated by the associated monopole feeding factors calculated for each measurement. This hypothesis yielded the best-quality model for hypotheses which do no not include interference effects. In comparison to hypotheses H_1, H_2 and H_3, the model for hypothesis H_5 provides a better description of the monopole strength at $E_x \approx 9$ MeV, however the $\approx 75\%$ reduction in the monopole strength between $E_x = 11$ and 12 MeV is not reproduced for the ^{12}C$(\alpha,\alpha')^{12}$C measurements at $\theta_{\text{lab}} = 0^\circ$ (PR194 and PR251), as shown on panels (d) and (e) of Figure 5.11.

Hypotheses H_4 and H_6 model the monopole structure at $E_x \approx$ 7-16 MeV with the Hoyle state, the broad 0^+ resonance at $E_x \approx 10$ MeV and the as-

sociated interference effects between these two overlapping contributions, as described by the two-level approximation. Hypothesis H_6 expands on H_4 with the inclusion of an unlisted broad 0^+ resonance at $E_x \approx 9$ MeV. As discussed in Section 2.6.1.6, the constructive/destructive nature of interference between decay modes is determined by the relative signs of the associated reduced width amplitudes. The subhypotheses of H_4 and H_6 correspond to the various permutations of contructive/destructive interference of the α_0 and α_1 decay modes, as summarised in Tables 2.10 and 2.8, respectively. The R-matrix analyses determined that the best quality subhypotheses of H_4 and H_6 are $H_{4\mathrm{b}}$ and $H_{6\mathrm{b}}$, respectively, which both correspond to constructive α_0 and destructive α_1 decay modes.

Detailed decompositions of the intrinsic monopole structures extracted under subhypothesis $H_{4\mathrm{b}}$ are presented on panels (a) and (b) in Figure 5.27 for the $^{12}\mathrm{C}(\alpha,\alpha')^{12}\mathrm{C}$ measurements at $\theta_{\mathrm{lab}} = 0^\circ$ (experiments PR194 and PR251): the solid and dashed grey lines correspond to the resonance terms of the two-level approximation, corresponding to the Hoyle state and the broad 0^+ resonance at $E_x \approx 10$ MeV, respectively (see Section 2.6.1.6). The blue-filled lineshape is the sum of the resonance terms. It is observed that the lineshape of the Hoyle state is suppressed towards $E_x \approx 11$ MeV which is due to the $(\overline{E}_2 - E)$ and $(\overline{E}_1 - E)$ factors in Equation 2.77 which suppress the resonance term of the Hoyle state near the resonance energy of the broad 0^+ resonance at $E_x \approx 10$ MeV and vice versa. The orange line is the total contribution of the total two-level approximation where the area filled in orange corresponds to the effect of the constructive α_0 and destructive α_1 interference terms. The total intrinsic monopole lineshapes extracted from both experiments PR194 (a) and PR251 (b) do exhibit the $\approx 75\%$ reduction in the monopole strength between $E_x = 11$ and 12 MeV, as observed in the aforementioned MDA analysis by M. Itoh *et al.* of the same reaction at $E_{\mathrm{beam}} = 386$ MeV. There are two broad 0^+ resonances listed on the NNDC at $E_x \approx 10$ MeV with resonance energies situated at $E_x = 9.930(30)$ and 10.3(7) MeV with respective total widths of $\Gamma_{\mathrm{tot}} = 2.710(80)$ and 3.0(7) MeV. As discussed in Section 2, these two listed resonances are believed to be one and the same. The resonance energy of the broad 0^+ resonance at $E_x \approx 10$ MeV extracted under subhypothesis $H_{4\mathrm{b}}$ of this work is 11.831(18) MeV, with a total width of $\Gamma_{\mathrm{tot}} = 3.570(73)$ MeV. Whilst the total width is in relatively good agreement with the listed value of 3.0(7) MeV, it must be noted that the various analyses used to determine the literature values do not use R-matrix lineshapes and fewer still use a multichannel formalism. This multichannel formalism may be crucial for such a state as it is situated in a region where both α_0 and α_1 decay modes are possible. For subhypothesis $H_{4\mathrm{b}}$, the α_0 and α_1 widths were extracted $\Gamma_{\alpha_0}(E_r) = 3.570(73)$ MeV and $\Gamma_{\alpha_1}(E_r) = 8(5)$ keV, with associated Wigner ratios of $\gamma^2_{W,\alpha_0} = 0.786(12)$ and $\gamma^2_{W,\alpha_1} = 0.039(22)$. The errors for the resonance energies and observed widths account for calibration errors whilst the errors for the reduced widths and Wigner ratios are purely from the fit optimisation. The Wigner ratios

indicate a significant $\alpha_0 + {}^8\text{Be}$ content to the state and that the $\alpha_1 + {}^8\text{Be}$ contribution may have a non-negligible effect on the lineshape of the resonance, particularly at higher excitation energies where the associated α_1 penetrability becomes considerable. It is noteworthy that one of the best-fitting models from an R-matrix analysis of the β decay from ^{12}N and ^{12}B by S. Hyldegaard *et al.* also yielded a larger resonance energy of $E_x = 11.58$ MeV and a total width of $\Gamma_{\text{tot}} = 2.68$ MeV for the broad 0^+ resonance at $E_x \approx 10$ MeV [18]. Whilst the 11.831(18) MeV resonance energy extracted with hypothesis $H_{4\text{b}}$ is in slightly better agreement with these values, the extracted total width of 3.570(73) MeV is considerably larger. Since many broad overlapping resonances contribute at $E_x \approx 10$ MeV, the extracted resonance energy and width of the this broad 0^+ resonance at $E_x \approx 10$ MeV depends strongly on the model used and the results of S. Hyldegaard *et al.* for this state also exhibit signficant model-dependence. The constructive α_0 decay mode enabled an enhancement of the monopole strength at $E_x \approx 9$ MeV to better fit the $^{12}\text{C}(\alpha,\alpha')^{12}\text{C}$ measurements at $\theta_{\text{lab}} = 0°$ (experiments PR194 and PR251), as shown on panels (d) and (e) on Figure 5.11. However, the $\gamma^2_{\alpha_0}$ parameter is effectively at the upper bound of the Wigner limit and corresponds to a large total observed width of $\Gamma_{\text{tot}} = 11.3(1)$ eV at the resonance energy of the Hoyle state which does not agree well with the literature value of 9.3(9) eV [10]. It is observed that even with the augmented width for the Hoyle state and a broad 0^+ resonance at $E_x \approx 10$ MeV, the lineshapes still underestimate the data at $E_x \approx 9$ MeV on the aforementioned panels, (d) and (e). This suggests the presence of a previously-unlisted broad resonance at $E_x \approx 9$ MeV.

As previously mentioned, subhypothesis $H_{6\text{b}}$ expands upon the two-level approximation formalism of $H_{4\text{b}}$ by introducing a broad resonance at $E_x \approx 9$ MeV which is modeled as a standard Lorentzian lineshape. The fit of subhypothesis $H_{6\text{b}}$, presented on Figure 5.21, yields the lowest AIC and BIC estimators and is therefore deemed the best quality model. It is observed that the newly-introduced broad 0^+ resonance provides an improved description of the excess strength at $E_x \approx 9$ MeV, and in particular, for the $^{12}\text{C}(\alpha,\alpha')^{12}\text{C}$ measurements at $\theta_{\text{lab}} = 0°$ (PR194 and PR251). Detailed decompositions of the intrinsic monopole structures extracted under subhypothesis $H_{6\text{b}}$ are presented on panels (c) and (d) in Figure 5.27 for the $^{12}\text{C}(\alpha,\alpha')^{12}\text{C}$ measurements at $\theta_{\text{lab}} = 0°$ (experiments PR194 and PR251). The solid and dashed grey lines correspond to the resonance terms of the two-level approximation, corresponding to the Hoyle state and the broad 0^+ resonance at $E_x \approx 10$ MeV, respectively and the blue-filled lineshape is the sum of the resonance terms (see Section 2.6.1.6). The orange line is the total contribution of the total two-level approximation where the area filled in orange corresponds to the effect of the constructive α_0 and destructive α_1 interference terms. The green line is the total extracted intrinsic monopole strength where the area filled in green corresponds to the contribution of the newly-introduced broad resonance at $E_x \approx 9$ MeV. The lineshapes for the two-level approximations (orange lines)

are qualitatively similar to those extracted under subhypothesis H_{4b} on panels (a) and (b) and also exhibit the $\approx 75\%$ reduction in the monopole strength between $E_x = 11$ and 12 MeV, as observed in the MDA analysis by M. Itoh *et al.* of the same reaction at $E_{\text{beam}} = 386$ MeV. It is also observed that the total monopole strength extracted under subhypothesis H_{6b} for experiment PR251 (d) reproduces the aforementioned doubled-peaked monopole structure with a local minimum at $E_x \approx 9.7$ MeV that is observed with the MDA analysis.

The detection of coincident charged-particle decay with the CAKE enabled spin and parity assignment by analysing the angular distributions of decay. To determine the spin and parity of the newly-introduced resonance, the angular distribution of α_0 decay for the 8.5 MeV $< E_x <$ 9.0 MeV excitation-energy region was analysed, as shown on Figure 4.57. This limited excitation-energy range was chosen to minimise the contamination from the neighbouring 2_2^+ resonance at 9.870(60) MeV. The angular distribution is shown to decay isotropically, which implies that the strength at $E_x \approx 9$ MeV is predominantly 0^+ in nature.

The observed resonance energies and total widths for this newly-introduced 0^+ resonance are presented in Table 5.1. The resonance energy and width of this state extracted under subhypothesis H_{6b} are $E_x \approx 9.270(14)$ MeV with a width of 1581(58) keV. It is noteworthy that all the hypotheses that account for this unlisted broad resonance yield energies and widths which are in relatively good agreement with these values.

The extracted parameters for this resonance are in excellent agreement with both the measurement by M. Itoh *et al.* as well as the various theoretical predictions, as summarised in Table 5.7. There is particularly good agreement with the work of C. Kurokawa and K. Katō which yielded a resonance energy of $E_x \approx 8.95$ MeV and a width of $\Gamma_{\text{tot}} = 1.48$ MeV [1]. For the 0_4^+, the fit optimisation for the optimal subhypothesis (H_{6b}) yielded a resonance energy of $E_x \approx 11.647(22)$ MeV with a width of $\Gamma_{\text{tot}} = 2735(73)$ MeV. The aforementioned calculation yielded a resonance energy of $E_x \approx 11.87$ MeV with a width of $\Gamma_{\text{tot}} = 1.1$ MeV for the 0_4^+ state. Whilst the resonance energy is in excellent agreement, the width extracted from this work is significantly larger. However, this observed width is in excellent agreement with the literature values of 2.710(80) and 3.0(7) MeV for this resonance [10]. It should be noted that the second-best quality model, corresponding to subhypothesis H_{6a}, also yields parameters for the 0_3^+ and 0_4^+ states which are in similarly good agreement.

Source	Author	E_r [MeV]	Γ [MeV]	E_r [MeV]	Γ [MeV]	AIC	BIC
$^{12}C(\alpha,\alpha')$	M. Itoh *et al.*	9.04(9)	1.45(18)	10.56(6)	1.42(8)		
OCM	S. Ohtsubo *et al.*	8.09	1.68	11.89	1.0		
	C. Kurokawa and K. Katō	8.95	1.48	11.87	1.1		
FMD	B. Zhou *et al.*	9.38	0.92	11.7	0.66		
This work							
H_{6a}		9.172(5)	1584(24)	11.602(27)	2639(76)	2.362	2.316
H_{6b}		9.270(14)	1581(58)	11.647(22)	2735(73)	2.358	2.312

Table 5.7: Summary of the observed and theoretically predicted parameters for the 0_3^+ state of ^{12}C.

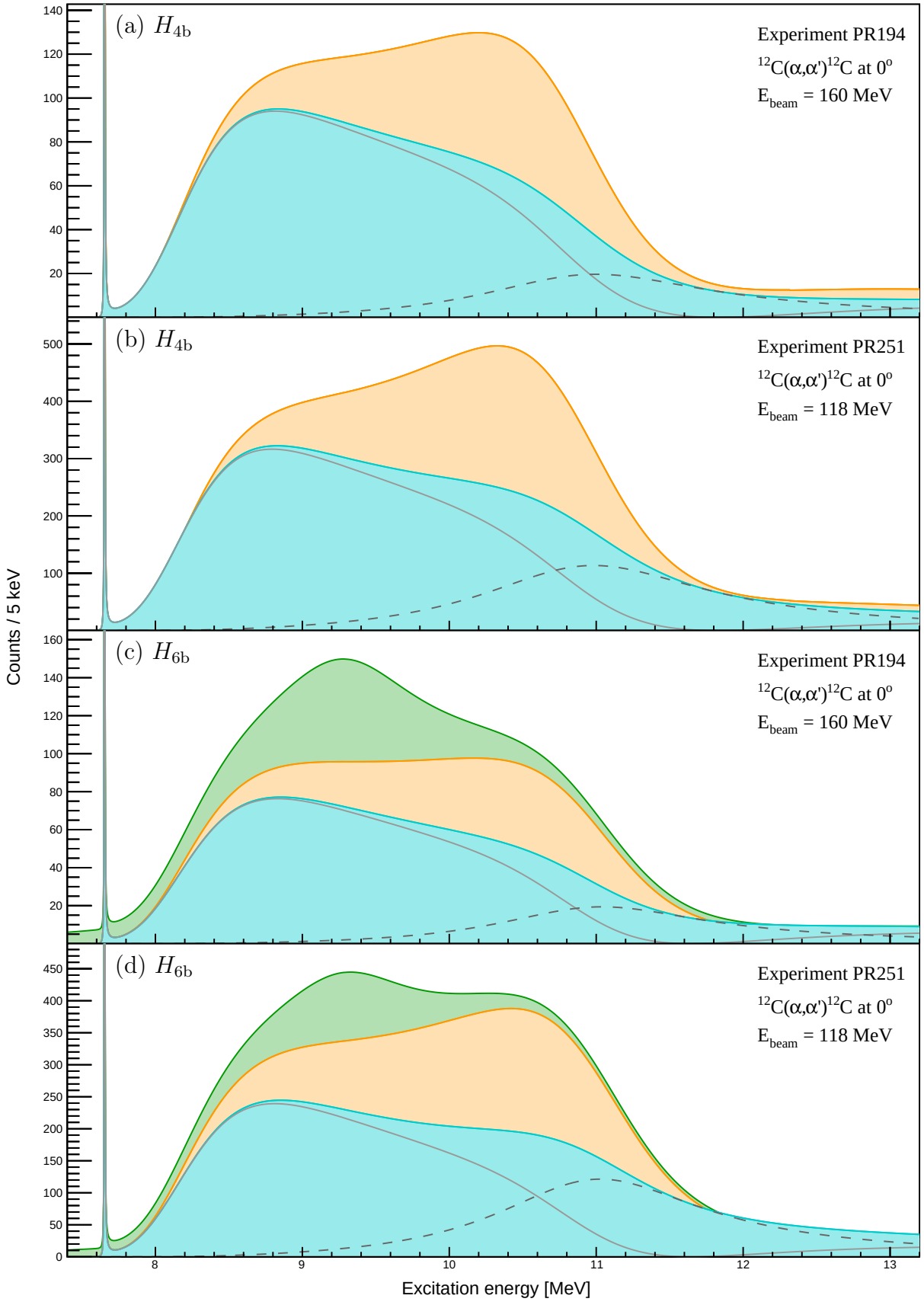

Figure 5.27: Decomposition of the intrinsic monopole structures for the $^{12}\mathrm{C}(\alpha,\alpha')^{12}\mathrm{C}$ measurements at $\theta_{\mathrm{lab}} = 0°$ (experiments PR194 and PR251) with hypotheses H_{4b} and H_{6b}. See text for details.

5.4 The 3_1^- excited state at 9.641(5) MeV

The 3_1^- excited state of ^{12}C is understood to be highly collective, as indicated by its strong population by protons with $E_{\text{beam}} \sim 100$ MeV incident energy which is understood to be a probe that is selective towards collectivity [108]. A study of this state with the $^{12}\text{C}(p,p')^{12}\text{C}$ reaction by Tz. Kokalova *et al.* substantially improved on previous literature value for the width of 34(5) keV with a larger value of 48(2) keV extracted with an R-matrix analysis [109, 10]. It was noted that this extracted width was relatively dependent on the fitted lineshape and that a similar analysis with a standard Lorentzian lineshape yielded a width of 40.4(4) keV. It should be noted that the fitted R-matrix lineshapes for this study were single channel and the α_0 penetrability used did not account for the high-energy tail of the ^{8}Be ground state which also exhibits a ghost anomaly that is similar to that of the Hoyle state, as shown in Figures 2.8 and 2.6. Additionally, whilst a detailed analysis was conducted for energy losses ($\sim$ 10 keV) of the ejectiles and their positional-dependence within the target, the fitted lineshapes did not account for these effects. Whilst protons are not as susceptible to target-related energy losses, the relatively thick 1mg/cm^2 natural carbon target coupled with it was not unreasonable to assume that the target-related energy loss of the singly-charged proton ejectile was not significant. Finally, a Voigt profile approximation was used to describe the observed R-matrix lineshape which may exhibit an incorrect excitation-energy dependence. Whilst this approximation may be valid, the possible deviation from the true numerical convolution was not quantified and may produce a deviation beyond the 2 keV error of the measurement. In comparison, the R-matrix analysis of this work accounts for the finite-width of the daughter states, the target-related energy losses and fits the data with true numerical convolutions for the observed lineshapes.

The extracted R-matrix parameters for this state are summarised in Table 5.3 and it is observed that the extracted total width of this state, evaluated at the fitted resonance energy, is consistently above the previous literature value of 34(5) keV. The optimal subhypothesis of this work, $H_{6\text{b}}$, yields a total width of $\Gamma_{\text{tot}} = 41.5(5)$ which is in relatively good agreement with the previous literature value, however it is significantly smaller than the width of $\Gamma_{\text{tot}} = 48(2)$ measured by Tz. Kokalova *et al.*. It is observed that all hypotheses yield a width of approximately 41 keV for the 3_1^- state. It is possible that the simplified quadratic background used in the study by Tz. Kokalova *et al.* may contribute to the difference in extracted widths Another interesting observation is the considerable α_1 reduced widths and corresponding Wigner ratios that are extracted with hypotheses $H_{4\text{a,b}}$ and $H_{6\text{a,b}}$. The best quality model, $H_{6\text{b}}$, and the hypothesis with the second-lowest AIC and BIC estimators, $H_{6\text{a}}$, yield large Wigner ratios of $\theta^2_{W,\alpha_1} = 0.84(5)$ and $\theta^2_{W,\alpha_1} = 0.73(6)$, respectively. This indicates a significant $\alpha_1 + {}^8$Be content to the state.

A detailed decomposition of the intrinsic lineshape for the 3_1^- lineshape,

populated through $^{12}\mathrm{C}(\alpha,\alpha')^{12}\mathrm{C}$ at $\theta_{\mathrm{lab}} = 0°$ (PR194) and extracted under the hypothesis with the highest-quality model ($H_{6\mathrm{b}}$), is presented in Figure 5.28. Whilst the contribution of the α_1 decay mode does not contribute to the total width at the resonance energy, the α_1 penetrability shown in Figure 2.12 indicates that by accounting for the finite-width of the 2^+_1 ^{8}Be daughter state, the α_1 decay mode may contribute at lower excitation-energies in comparison to the penetrability form that assumes an infinitely-narrow daughter-state width. The blue-filled line is the intrinsic 3^-_1 lineshape and the dashed black line is the corresponding observed lineshape which accounts for the experimental factors (see Section 5.2). The orange-filled line is the α_1 contribution to the total intrinsic lineshape and the $\approx 1\%$ fitting error of the associated $\gamma^2_{\alpha_1}$ parameter does not yield a significant change to the intrinsic lineshape. The green line is the single-channel approximation which only accounts for the α_0 decay mode. It is observed that the α_1 contribution only becomes non-negligible above the resonance energy of 9.641 MeV and therefore does not contribute to the total width evaluated at the resonance energy, $\Gamma_{\mathrm{tot}}(E_R)$. In addition, it appears that the higher-energy tail is dominated by the α_1 contribution and a local maximum is observed at $E_x \approx 12.7$ MeV which is less than 1% of the intrinsic peak maximum. The form of this structure appears to be analagous to the ghost of the Hoyle state, however the origin is somewhat different. The ghost of the Hoyle state arises purely from the proximity of the primary peak to the α_0 separation energy and the rapid increase in the associated penetrability. In contrast, the relatively diminished ghost of the 3^-_1 state is only reproduced in a multichannel formalism with both the α_0 and α_1 decay modes and the occurrence of the local-maximum for the ghost is attributed solely to the latter. Since the α_1 contribution above 12 MeV is smooth and slowly-varying,

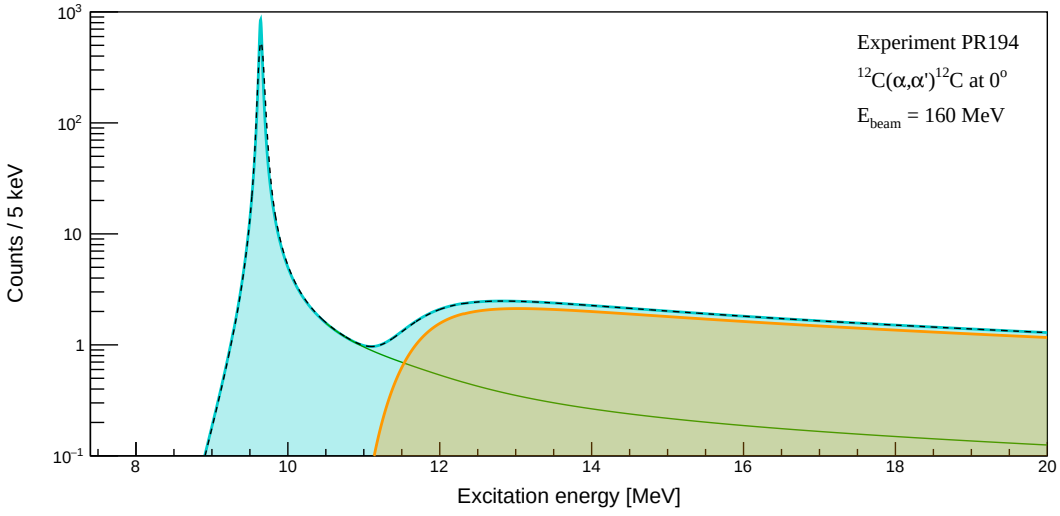

Figure 5.28: Decomposition of the intrinsic lineshape for the 3^-_1 state of ^{12}C extracted under subhypothesis $H_{6\mathrm{b}}$. See text for details.

the size of the contribution extracted with a fit is strongly dependent on the broad overlapping contributions from neighbouring states. This gives rise to the strong dependence of the $\gamma^2_{\alpha_1}$ parameter on the chosen model, as can be observed on Table 5.3. To determine the high-energy tail of the 3^-_1 lineshape more accurately, a better understanding of the neighbouring broad resonances must be established.

5.5 The 2^+_2 excited state at 9.870(60) MeV

The 2^+_2 state of ^{12}C is of great interest as it is understood to be the rotational state of the astrophysically-significant Hoyle state. Currently, the resonance energy is currently listed on the NNDC at $E_x = 9.870(60)$ MeV with an observed width of $\Gamma = 850(85)$ keV. This state is particular hard to measure due to its relatively broad width which typically causes it submerged in the surrounding broad resonances which are dominantly 0^+ in nature. An early indication of this state was provided by the inelastic α scattering measurement by M. Itoh *et al.* which suggested the presence of a 2^+ resonance at $E_x \approx 10$ [110]. The identification of this state was with achieved with multipole decomposition analysis (MDA). A following proton inelastic scattering measurement performed by M. Freer *et al.* also supported the identification of a 2^+ state at $E_x = 9.6(1)$ with a width of $\Gamma = 600(100)$ keV [111]. This data was then combined with data of the $^{12}\mathrm{C}(\alpha,\alpha')^{12}\mathrm{C}$ reaction at $\theta_{\mathrm{lab}} = 0°$ which strongly populates the surrounding broad 0^+ background [112]. A background was extracted from the inelastic α scattering measurement to estimate the background in the aforementioned proton inelastic scattering measurement and the resulting fit indicated the presence of a resonance at $E_x = 9.75(15)$ MeV with a width of 750(150) keV. It is worth noting the R-matrix analysis implemented single-level, single-channel approximations to fit the data and consequently, did not account for possible interference effects. Moreover, the 0^+ background extracted from the $^{12}\mathrm{C}(\alpha,\alpha')^{12}\mathrm{C}$ measurement is obtained with a relatively simplistic fit and the extracted background strength itself contains the 2^+_2 state. These factors may have affected the extracted observed resonance energy and total width. An inelastic α scattering measurement by M. Itoh *et al.* indicated the presence of a 2^+ resonance at $E_x = 9.84(6)$ MeV with a width of $\Gamma = 1.01(15)$ MeV [13]. The identification of this state was with achieved with a combination of peak fitting and MDA. It should be noted that the peak fitting used simplistic Gaussian functions to approximate the broad 0^+ resonance and this may have affected the extracted parameters. This resonance was also studied through photodisintegration by W.R. Zimmerman *et al.* which enabled the unambiguous identification of the 2^+_2 state in ^{12}C at 10.03(11) MeV, with a total α_0-particle width of $\Gamma_{\alpha_0} = 800(130)$ keV [113]. This excitation-energy spectra from the $^{12}\mathrm{C}(\gamma,\alpha_0)^8\mathrm{Be}$ measurement was exclusively for α_0 so the implemented single-channel R-matrix lineshape is suitable.

The 2_2^+ state has also been suggested to manifest at significantly different excitation energies. An example being the multilevel multichannel R-matrix analysis of β decays from ^{12}N and ^{12}B by S. Hyldegaard *et al.* which indicated the presence of a 2^+ resonance at $E_x = 11.1(3)$ MeV with a width of $\Gamma = 1.4(4)$ MeV. A study of the ^{12}C$(p,p')^{12}$C reaction by W.D. Zimmerman *et al.* [114] found no evidence for a 2^+ resonance at $E_x = 11.1(3)$ MeV, but rather supported the excitation energy of $E_x = 9.6(1)$ MeV given in Ref. [111]. A study of the ^{11}B$(^3$He$,d)^{12}$C reaction by G.M. Reynolds *et al.* also indicated the presence of a 2^+ resonance at a considerably higher excitation energy of $E_x = 11.16(5)$. However, a repeat of this measurement by F.D. Smit *et al.* found no evidence for a 2^+ resonance at this location [115].

It is apparent that an accurate consensus for the properties of the 2_2^+ state of ^{12}C has yet to be reached. Moreover, the inability to resolve this state from the surrounding broad background suggests that the background/neighbouring resonances implemented in an analysis may have a sizeable effect on the extracted properties for the 2_2^+ state. The goal of the multilevel multichannel R-matrix analysis of this work is to simultaneously analyse this excitation-energy region, populated with different reactions, whilst minimising the introduction of loosely-approximated backgrounds. Instead, the broad overlapping resonances in this congested region are also consistently analysed for the different reactions. The extracted R-matrix parameters for this state are summarised in Table 5.4. It is observed that the optimal subhypothesis H_{6b} yielded an observed resonance energy at $E_x = 9.941(10)$ MeV which is in good agreement with the literature value of 9.870(60) MeV. The total width of the 2_2^+ state extracted under H_{6b} yields a value of $\Gamma_{\text{tot}}(E_R) = 1088(12)$ keV at the extracted resonance energy.

A detailed decomposition of the intrinsic lineshape for the 2_2^+ lineshape, populated through ^{12}C$(\alpha,\alpha')^{12}$C at $\theta_{\text{lab}} = 0°$ (PR194) and extracted under the hypothesis with the highest-quality model (H_{6b}), is presented in Figure 5.29. The blue-filled line is the intrinsic 2_2^+ lineshape and the dashed black line is the corresponding observed lineshape which accounts for the experimental factors (see Section 5.2). The orange-filled line is the α_1 contribution to the total intrinsic lineshape and it is observed that the corresponding reduced width of $\gamma^2_{\alpha_1} = 0.40(16)$ exhibits a substantial error. Multiple fits for this subhypothesis were conducted with varying initial parameters but the optimised value and large associated error were consistently reproduced. This is indicative that the data is not sufficient to more accurately determine this parameter for this particular model. The α_1 contribution to the intrinsic lineshape is plotted as an orange-filled line and the large error for its strength is propagated to the intrinsic lineshape and shown as violet lines. It is observed that under subhypothesis H_{6b}, the α_1 contribution manifests as a weak, broad contribution to the high-energy tail above $E_x \approx 11$.

The CAKE enabled the detection of coincident charged-particle decay for the ^{14}C$(p,t)^{12}$C measurement at $\theta_{\text{lab}} = 0°$ (experiment PR240). The angular dis-

tribution of α_0 decay for excitation-energy region of 9.8 MeV $< E_x <$ 10.6 MeV is presented in Figure 4.58. It is observed that the angular distribution is distinctly anisotropic and qualitatively matches the highly-backward angle decay for $l = 2$ α_0 decay that is expected from ^{12}C, as discussed in Ref. [88]. This is corroborated by the fit of the inclusive excitation-energy spectrum on panel (g) of Figure 5.21 where it is observed that the 2^+_2 state is dominant in this region. The angular distribution also qualitatively matches that of the well-resolved 2^+ state situated at 16.1060(8) MeV on Figure 4.61, where the difference towards $\theta_{\text{lab}} = 90°$ arises from the variation of the decay kinematics with excitation energy.

Given the many broad, overlapping resonances in this congested excitation-energy region, it is a challenge to fit this high-energy tail with precision. To determine the high-energy tail of the 2^+_2 lineshape more accurately, a better understanding of the neighbouring broad resonances must be established. An improved measurement of this state may be obtained with probes such as the ^{14}C$(p,t)^{12}$C reaction at $\theta_{\text{lab}} = 0°$ which selectively populates the 2^+_2 state relative to the surrounding 0^+ contributions. A quantitative analysis of the angular distributions of α decay for this state may also provide sensitivity towards the lineshape. Specifically, a simultaneous analysis of the CAKE-gated excitation-energy spectra with the inclusive data may enable discrimination of the 2^+_2 state from the surrounding backround. However, the nontrivial kinematics for the recoil nucleus of the ^{14}C$(p,t)^{12}$C measurement complicates the determination of the CAKE efficiency as the m-state population ratios for non-0^+ resonances must be calculated/assumed. This was deemed beyond the scope of this thesis and is reserved for future work.

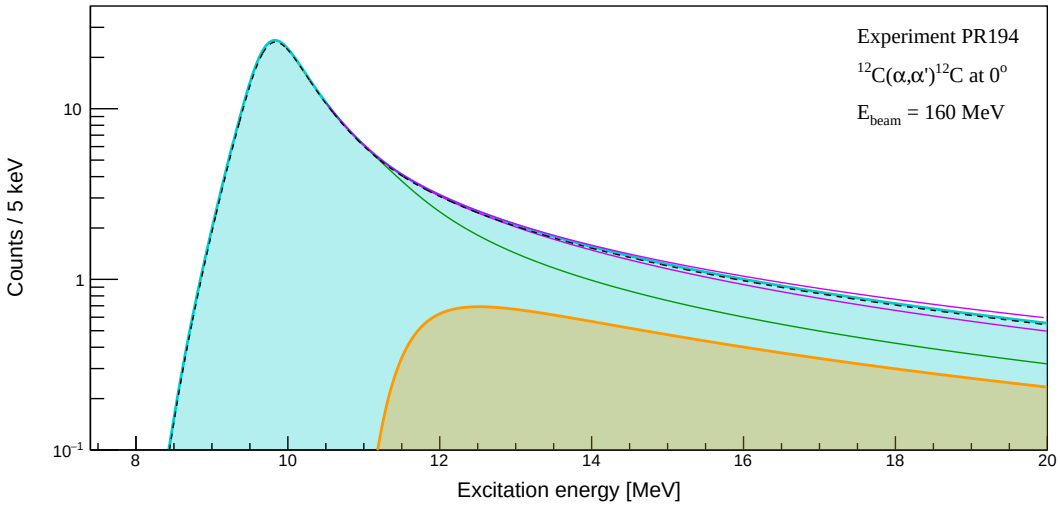

Figure 5.29: Decomposition of the 2^+_2 state of ^{12}C, populated through ^{12}C$(\alpha,\alpha')^{12}$C at $\theta_{\text{lab}} = 0°$ with $E_{\text{beam}} = 160$ MeV (experiment PR194). See text for details.

Chapter 6

Conclusions

The primary objective of this thesis was to attempt to identify new sources of monopole strength in ^{12}C in the excitation-energy region of $E_x \approx$ 7-16 MeV MeV. An inelastic scattering measurement M. Itoh *et al.* found that a $J^\pi = 0^+$ state at $E_x \approx 9$ MeV was necessary to describe the $^{12}\mathrm{C}(\alpha,\alpha')^{12}\mathrm{C}$ data [13]. Several calculations have been performed to describe the broad monopole structure above the Hoyle state, with formalisms such as Antisymmetrized Molecular Dynamics (AMD), Fermionic Molecular Dynamics (FMD), the 3α Orthogonality Condition Model (OCM) and the Generator Coordinate Method (GCM). Some of these calculations yielded two distinct sources of broad monopole strength above the Hoyle state, where the higher-lying 0^+ resonance is postulated to correspond to the broad 0^+ resonance currently listed on the NNDC at $E_x \approx 10.3(3)$ MeV. Notably, several theories indicated that the lower-lying broad monopole strength corresponded to breathing-mode excitation of the Hoyle state. This corresponds to an isoscalar giant monopole resonance (ISGMR) which is microscopically described as a coherent superposition of 1p-1h excitations and in particular, the $1p_{3/2}$-$2p_{3/2}$ and $1p_{1/2}$-$2p_{1/2}$ excitations. Given that the Hoyle state is the archetypal α-cluster state, the challenge of identifying an associated breathing mode is of great interest. Furthermore, the excitation-energy region just above the separation energy is of great astrophysical significance since it plays a major role in the stellar triple-α process [9].

In order to identify a lower-energy fragment of the ISGMR, two contrasting probes were employed: the $^{12}\mathrm{C}(\alpha,\alpha')^{12}\mathrm{C}$ and $^{14}\mathrm{C}(p,t)^{12}\mathrm{C}$ reactions. Five inelastic α scattering measurements were performed at $\theta_{\mathrm{lab}} = 0^\circ(\times 2)$, 6°, 8.5° and 10°. It is understood that inelastic α scattering, particularly at $\theta_{\mathrm{lab}} = 0^\circ$, is the best probe to populate ISGMR strength. In contrast, the $^{14}\mathrm{C}(p,t)^{12}\mathrm{C}$ reaction is understood to be selective against the population of the ISGMR and is rather suggested to be selective towards giant pairing vibrations [15]. For the primary measurement of this thesis, $^{14}\mathrm{C}(p,t)^{12}\mathrm{C}$ at $\theta_{\mathrm{lab}} = 0^\circ$ with $E_{\mathrm{beam}} = 140$ MeV, coincident charged-particle decay was measured with the CAKE to enable the identification of spin and parity for populated excited

states and a detailed GEANT4 simulation of the CAKE was implemented to analyse the data. The combination of these measurements therefore provided an ideal tool to identify new sources of monopole strength and in particular, any lower-lying fragments of ISGMR strength. In order to simultaneously analyse the data, a new multilevel, multichannel R-matrix analysis code was written. This code implemented one-, two- and three-level approximations to be able to accurately account for the interferences between states of the same spin and parity. In order to treat the excitation-energy spectra from the various direct populating reactions on an equal footing, the feeding factors for each reaction were calculated with CHUCK3, a coupled-channels nuclear reactions code written by P.D. Kunz [71]. These feeding factors were input into the R-matrix analysis code. Additionally, a method to accurately account for the different experimental resolutions and target-related energy losses of each experiment was implemented. Finally, a precise treatment of the penetrability was implemented which accounted for the finite width of the ^{8}Be daughter state for α decay from ^{12}C.

A total of 12 dinstinct hypotheses, fitted using the maximum likelihood estimation method and the AIC and BIC estimators, determined that the best-quality model corresponded to hypothesis H_{6b}, which introduced an unlisted broad resonance at $E_x \approx 9$ MeV that was incoherently added to the two-level approximation between the 0^+_2 Hoyle state and the broad 0^+ resonance at $E_x \approx 10$ MeV. For hypothesis H_{6b}, the two-level approximation corresponded to constructive α_0 and destructive α_1 decay modes. The fit optimisation under hypothesis H_{6b} determined this unlisted resonance to be located at $E_x \approx 9.270(14)$ MeV with a width of $\Gamma = 1581(58)$ keV and it should be noted that all the hypotheses that account for this unlisted broad resonance yield energies and widths which are in agreement with these values. The extracted parameters for this resonance are in excellent agreement with both the measurement by M. Itoh *et al.* as well as the various theoretical predictions, as summarised in Table 5.7. There is particularly good agreement with the work of C. Kurokawa and K. Katō which yielded a resonance energy of $E_x \approx 8.95$ MeV and a width of $\Gamma_{\text{tot}} = 1.48$ MeV [1]. From the two-level approximation, the resonance energy of the Hoyle state was fixed at the literature value of 7.65407(19) MeV and the associated total width was determined as $\Gamma_{\text{tot}}(E_R) = 9.3(3)$ eV which is in excellent agreement with the literature value of $\Gamma_{\text{tot}} = 9.3(9)$ eV. The higher-lying broad 0^+ resonance was determined to be situated at $E_x = 11.647(22)$ MeV with a width of $\Gamma = 2.735(73)$ MeV. For the 0^+_4 state, the aforementioned calculation by C. Kurokawa and K. Katō yielded a resonance energy of $E_x \approx 11.87$ MeV with a width of $\Gamma_{\text{tot}} = 1.1$ MeV. Whilst the resonance energy is in excellent agreement, the width extracted from this work is significantly larger. However, this observed width is in excellent agreement with the literature values of 2.710(80) and 3.0(7) MeV for this resonance [10]. Due to the coherent interferences of the two-level approximation, the interpretation of the extracted resonance energy parameters

and observed widths can be complicated. It should be noted that one of the best-fitting models from a multilevel multichannel R-matrix analysis of the β decay from ^{12}N and ^{12}B by S. Hyldegaard *et al.* also yielded a larger resonance energy of $E_x = 11.58$ MeV with a total width of $\Gamma_{\text{tot}} = 2.68$ MeV for the broad 0^+ resonance at $E_x \approx 10$ MeV [18]. In order to determine the spin and parity of the unlisted 0^+ resonance, the angular distribution of the α_0 decay mode for the 8.5 MeV $< E_x <$ 9.0 MeV excitation-energy region was analysed from the ^{14}C$(p,t)^{12}$C measurement at $\theta_{\text{lab}} = 0°$. The α_0 angular distribution for the 8.5 MeV $< E_x <$ 9.0 MeV was determined to be isotropic in nature, thus implying that the strength populated in this region is predominantly 0^+ in nature. It is postulated that this unlisted 0^+ resonance may correspond to a low-lying fragment of the ISGMR strength in ^{12}C and in particular, the breathing-mode excitation built upon the 0^+_2 Hoyle state.

In addition to the confirmation of the unlisted source of monopole strength suggested by M. Itoh *et al.*, precise measurements for the highly-collective $J^\pi = 3^-_1$ state and the $J^\pi = 2^+_2$ rotational excitation of the Hoyle state were obtained. Under the aforementioned optimal hypothesis, the 3^-_1 state was found to be situated at $E_x = 9.641(7)$ MeV with a width of $\Gamma = 41.5(5)$ keV. Notably, several hypotheses yielded a significant Wigner ratio for the α_1 decay channel and in particular, the optimal hypothesis $H_{6\text{b}}$ yielded $\theta^2_{W,\alpha_1} = 0.73(6)$, indicating that the α_1 decay mode may contribute significantly to the high-energy tail of the intrinsic lineshape. The 2^+_2 was found to be situated at $E_x = 9.941(10)$ MeV with a width of $\Gamma = 1088(12)$ keV.

6.1 Future work

It is conceivable that the unlisted source of monopole strength determined in this work to be located at $E_x \approx 9.154(33)$ MeV with a width of $\Gamma = 885(49)$ keV is not a breathing mode excitation of the Hoyle state. If this state is not a highly-collective excitation described by the coherent superposition of 1p-1h excitations, but perhaps rather described by a static α-cluster configuration, then the monopole strength in the excitation-energy region of $E_x \approx$ 7-16 MeV MeV should be analysed with a three-level approximation. Given the many sign permutations for the α_0 and α_1 reduced-width amplitudes (detailed in Section 2.9), the analysis with this formalism was deemed to be beyond the scope of this work and is reserved for future work.

As previously mentioned, the excitation-energy region just above the 0^+_2 Hoyle state in ^{12}C is significant for the stellar triple-α reaction rate, which in turn has direct consequences on other reactions such as the subsequent ^{12}C$(\alpha,\gamma)^{16}$O reaction [9]. The effect of such a newly-introducecd $J^\pi = 0^+$ resonance, coupled with the measured total width for the Hoyle state of $\Gamma_{\text{tot}} = 9.3(3)$ eV, must be explored.

Appendices

Appendix A

Vertical Drift Chamber Analysis

The Vertical Drift Chambers (VDCs), described in Chapter 3.2.2, form a detection system that is integral to the K600 spectrometer setup. The complex nature of drift chambers and the associated analysis produce interesting results/artefacts. These phenomena not only affect the data analyses relevant to this thesis, but most of the experimental work produced with the K600 spectrometer and as such, warrant further investigation.

A.1 Total Lineshape Correction (TLC)

Due to the inherent beam optics of the K600 spectrometer, the horizontal ejectile position measured at the focal plane ($X1_{pos}$) exhibits correlations with the ejectile scattering angle as well as the vertical ejectile position at the focal plane ($Y1_{pos}$). The focal-plane lineshape, defined as the locus formed by plotting the focal-plane position against a variable, is an effective method to visualise any correlations. Such correlations, which manifest as aberrations from straight (constant with respect to the variable) focal-plane lineshapes, are detrimental to the experimental resolution of the focal plane detector. In the past, the accuracy of such corrections was highly dependent on the judgement of the user. Moreover, with this method it is nearly impossible to provide a satisfactory correction of complex lineshapes that are valid for the majority of the focal plane. Consequently, a new lineshape algorithm and corresponding code, named Total Lineshape Correction (TLC), was developed with the following qualities and capabilities:

- To correct the focal plane lineshape, with an algorithm that is easily modifiable to accommodate any correlated variable (θ_{scat} and $Y1_{pos}$ are implemented by default), to produce the corrected horizontal ejectile position: $X1_{posC}$.
- To allow for corrections that are dependent on both the focal plane position $X1_{pos}$ as well the correlated variable in question.

- To be able to correct for an arbitrary ordered aberration in a focal-plane lineshape: an n^{th}-ordered aberration requires $\geq (n+1)$ correction peaks.
- Allow for an arbitrary number iterative corrections, i.e. each successive correction uses the latest corrected position X1_{posC} from all the corrections before.
- Each correction iteration should be customisable by the user to suit the data, i.e. the correction variable (e.g. θ_{scat} or Y1_{pos}) as well as the correction granularity (number of cuts used for the correction variable) should be user-definable.

  Consider the case where there is a complex aberration with respect to the θ_{scat} variable but a smooth linear dependence on Y1_{pos}. Corrections with the θ_{scat} variable may need to have more cuts used for the correction with respect to that of Y1_{pos}.
- The order of the successive corrections and the associated correction variables (e.g. θ_{scat} or Y1_{pos}) should be user-definable.
- To be a relatively user-friendly, TOTALLINESHAPECORRECTION was written in C++ with an attempt to avoid hardcoding by the user. Moreover, it is seamlessly integrated into the k600analyser code (a pre-existing analyser code for the K600 spectrometer data).

Given a focal-plane position x, the corrected position (with respect to α) x' can be expressed in terms of a function f_α:

$$f_\alpha(x) = \sum_{i=0}^{n_o} C_i(\alpha) x^i = x', \tag{A.1}$$

where n_o is the order of the correction (related to the number of correction peaks) and the continuous $C_i(\alpha)$ functions are to be determined. To determine the $C_i(\alpha)$ functions, a choice of n_c cuts (which determines the correction granularity) for the α variable must be made. The $C_i(\alpha)$ prefactors are expressed in terms of α as:

$$C_i(\alpha) = \sum_{j=0}^{n_c-1} D_{i,j} \alpha^j, \tag{A.2}$$

where the $D_{i,j}$ constants are determined through the following procedure:

- Populate n_c focal-plane position spectra - each with a corresponding cut of α. Each spectrum is associated with a mean α value that is determined as the center of the associated cut.

- Populate a focal-plane position spectrum, henceforth referred to as the reference spectrum, with a "centralised" cut which is symmetrical about 0: $-\delta/2 < \alpha < \delta/2$, where δ is by default equal to the widths of the cuts upon the n_c focal-plane position spectra.

- Fit the n_p correction peaks on each of the aforementioned spectra to determine their respective means.

- For a particular spectrum, there is a set of peak means, $\{\mu_l\}$. A polynomial mapping must be determined (by means of a fit) to map $\{\mu_l\}$ onto the set of peak means on the reference spectrum, $\{\mu'_l\}$:

$$\mu'_l = \sum_{i=0}^{n_o} C_i(\alpha)(\mu_l)^i, \tag{A.3}$$

- Each α-gated position spectrum will have its own set of local polynomial mapping parameters $\{C_i(\alpha)\}$. To determine a mapping that is continuous in α, the polynomial mapping parameters across the n_c position spectra are themselves fitted with the form of Equation A.2 to determine the $\{D_{i,j}\}$ prefactors. Each correction is therefore completely determined by specifying the set of $\{D_{i,j}\}$ constants and the choice of correction variable, α.

Given two successive corrections (first with respect to variable α, then with respect to β), the notation for successive corrections is defined as:

$$(f_\beta \circ f_\alpha)(x) = f_\beta\left(f_\alpha(x)\right) = f_\beta\left(x'\right) = x''. \tag{A.4}$$

In general, there is no limitation on the number of successive iterative corrections. Moreover, it is possible (and sometimes necessary) to correct more than once with respect to a particular variable. Consider the experimental case where both θ_{scat} and Y1_{pos} are reliably calculated and there is a particularly strong correlation between X1_{pos} and θ_{scat} whereas the lineshape with respect to Y1_{pos} is relatively constant. It would be sensible to first correct with respect to θ_{scat} - enabling a more sensitive successive correction with respect to Y1_{pos}. In turn, the Y1_{pos} correction may reveal θ_{scat} correlations that the TLC algorithm was not sensitive enough to account for in the initial θ_{scat} correction - thereby necessitating another θ_{scat} correction.

Appendix B

Resolution optimisation for Ancillary Experiments

B.1 Experiment PR166, $^{12}C(\alpha,\alpha')^{12}C$ at 6°

B.1.1 SilverBulletRaytrace algorithm

The newly developed SilverBulletRaytrace algorithm offers improvements with respect to the old raytracing algorithm which has thus far been the standard algorithm for analysing VDC data. In Figure B.1, these improvements are presented for the PR166 $^{12}C(\alpha,\alpha')$ measurement at $\theta_{lab} = 6°$.

In Figure B.1, panel (a) shows the spectrum of the old raytrace angle through the X1 wire plane, θ_{RT} (old), versus the old uncorrected focal-plane position, $X1_{pos}$ (old). It is observed that V-shaped structures extend downwards from the loci of the well-resolved resonances. These V structures are indicative of a raytracing artefact that broadens in the focal-plane spectrum in a non-Gaussian manner which worsens the resolution.

In Figure B.1, panel (b) shows the spectrum of the old raytrace angle through the X1 wire plane, θ_{RT} (old), versus the new corrected focal-plane position, $X1_{posC}$. In comparison to panel (a), the V structures have been eliminated. Moreover, events have been recovered below θ_{RT} (old) $\approx 20°$. These recovered events would have been rejected by the old raytracing algorithm by failing any of the conditions listed in Ref. [82]. The SilverBulletRaytrace algorithm is able to recover some of these events which likely have anomalous wire hit patterns.

In Figure B.1, panel (c) shows the spectrum of the new raytrace angle through the X1 wire plane, θ_{RT}, versus the new corrected focal-plane position, $X1_{posC}$. In general, the events in panels (a) and (b) which extend below $\theta_{RT} \approx 30°$ are not physical. These lower values are a result of the fact that the perturbing wires of anomalous events typically occur on the periphery of a set of triggered wires. These peripheral wires necessarily lead to an incorrectly lowered raytrace angle. Since SilverBulletRaytrace automatically removes these

incorrect peripheral wires from the set of triggered wires that are raytraced, the new raytracing angles are therefore more accurately centered at $\theta_{\mathrm{RT}} \approx 35^{\circ}$ and a large portion of the unphysical values below $\theta_{\mathrm{RT}} \approx 29^{\circ}$ have been remedied.

B.1.2 Lineshape corrections

The lineshape corrections for experiment PR166, $^{12}\mathrm{C}(\alpha,\alpha')^{12}\mathrm{C}$ at $\theta_{\mathrm{lab}} = 6^{\circ}$ are summarised below in Table B.1 and the corresponding results are presented in Figures B.2 - B.5.

Correction Type	Correction Order
θ_{scat}	2
$\mathrm{Y2}_{\mathrm{pos}}$	2
$\mathrm{Y2}_{\mathrm{pos}}$	1
θ_{scat}	2
θ_{scat}	2
$\mathrm{Y2}_{\mathrm{pos}}$	2
θ_{scat}	3

Table B.1: Summary of the lineshape corrections for experiment PR166, $^{12}\mathrm{C}(\alpha,\alpha')^{12}\mathrm{C}$ at $\theta_{\mathrm{lab}} = 6^{\circ}$. The iterative corrections are listed in order of their application.

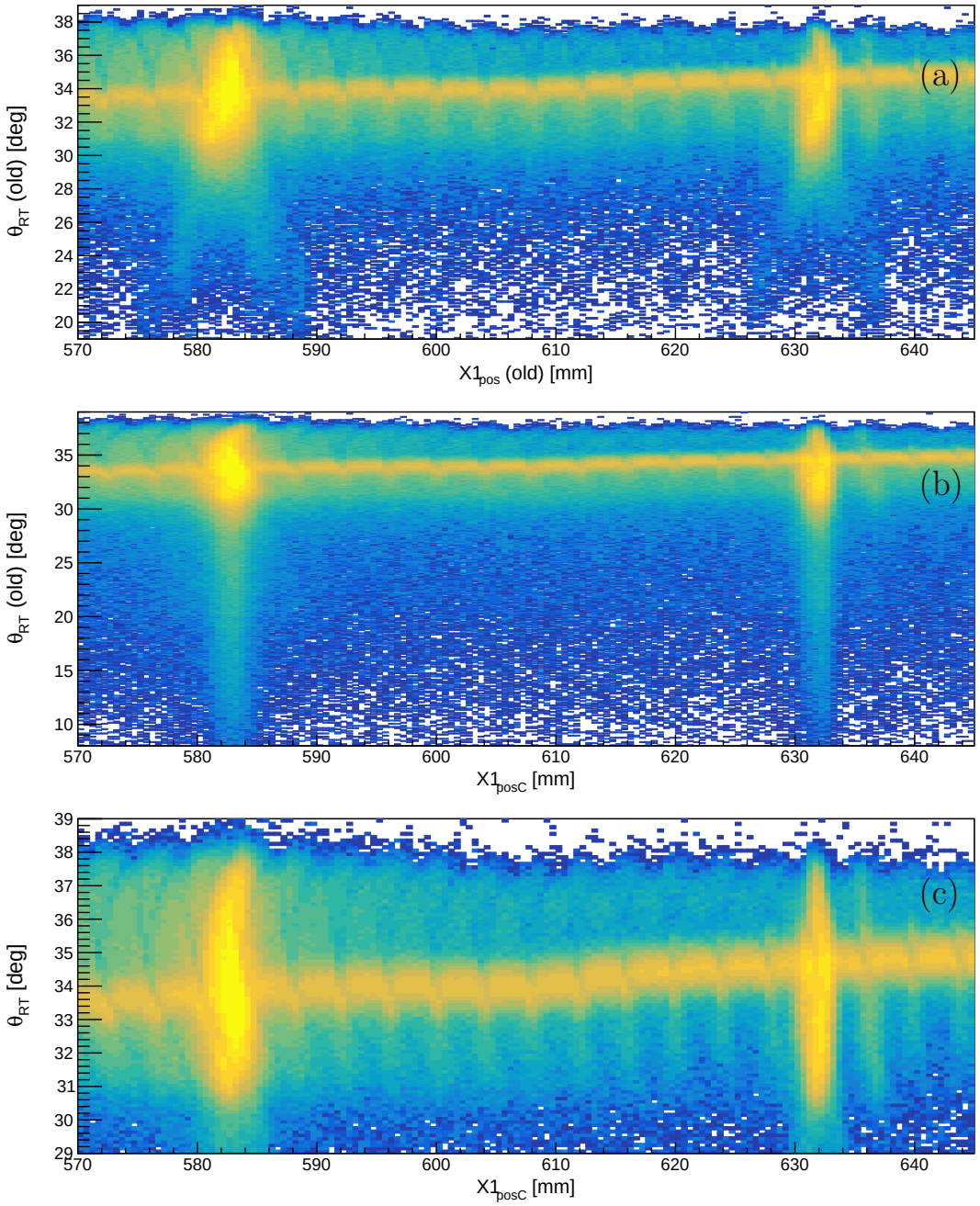

Figure B.1: Comparison of SilverBulletRaytrace against the old raytrace algorithm for experiment PR166, $^{12}\mathrm{C}(\alpha,\alpha')^{12}\mathrm{C}$ at $\theta_{\mathrm{lab}} = 6°$: (a) spectrum of the old raytrace angle (through X1) versus the old focal-plane position, (b) spectrum of the old raytrace angle (through X1) versus the new corrected focal-plane position, (c) spectrum of the new raytrace angle (through X1) wire plane versus the new corrected focal-plane position.

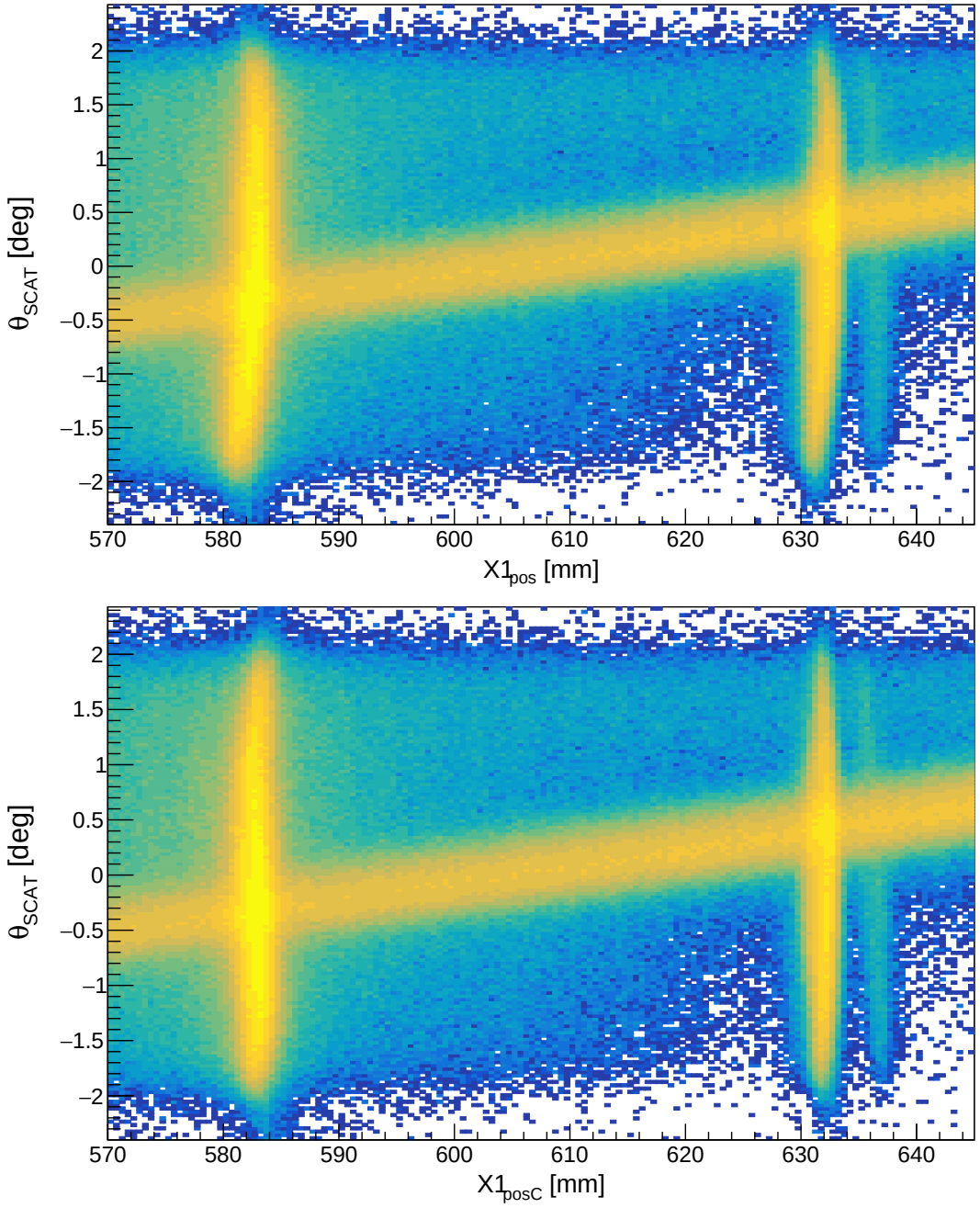

Figure B.2: Lineshape corrections PR166, ^{12}C$(\alpha,\alpha')^{12}$C at $\theta_{\rm lab} = 6°$: $\theta_{\rm scat}$ dependence. The top and bottom panels show the uncorrected and corrected lineshapes, respectively.

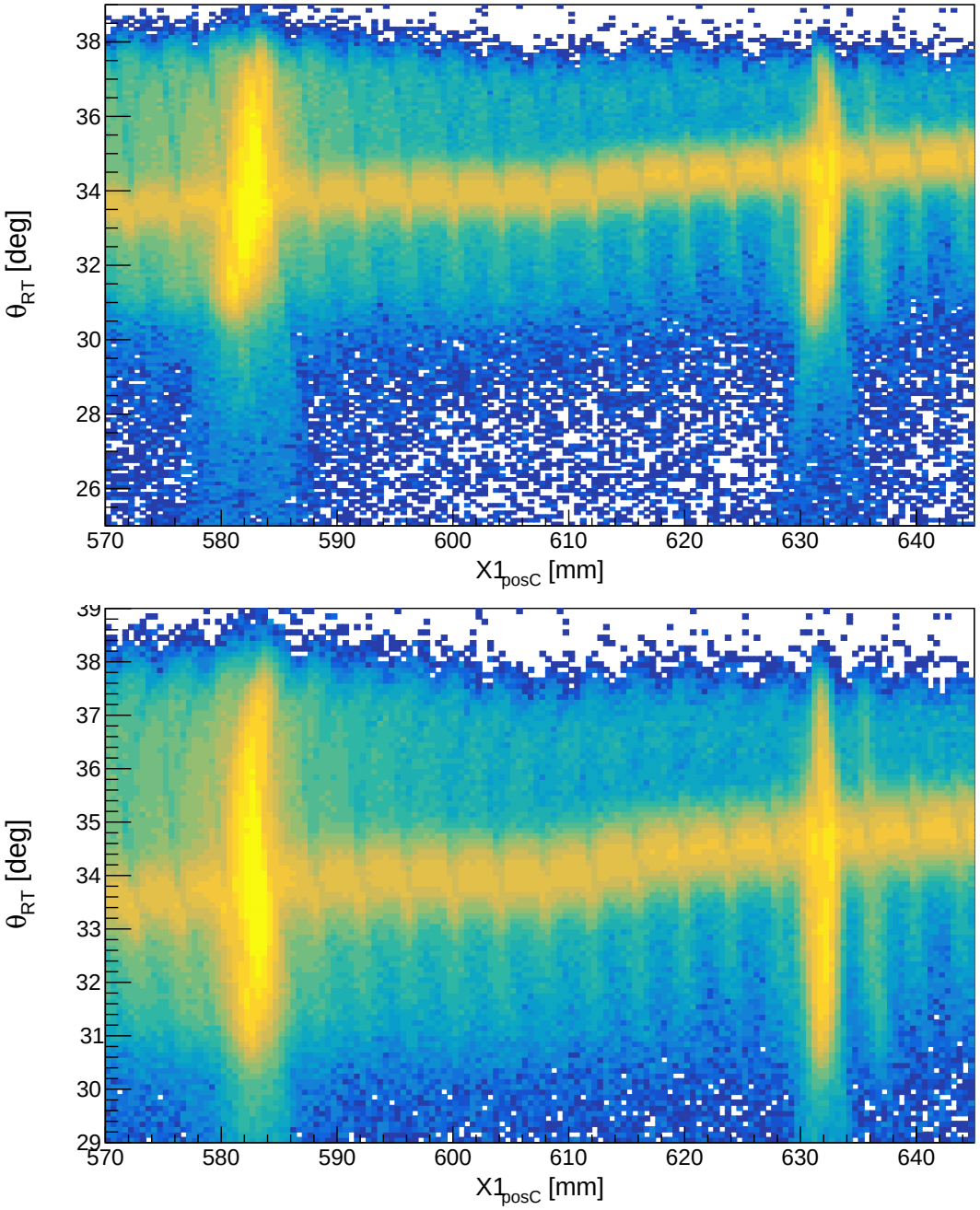

Figure B.3: Lineshape corrections PR166, ^{12}C$(\alpha,\alpha')^{12}$C at $\theta_{\rm lab} = 6°$: θ_{RT} dependence. The top and bottom panels show the uncorrected and corrected lineshapes, respectively.

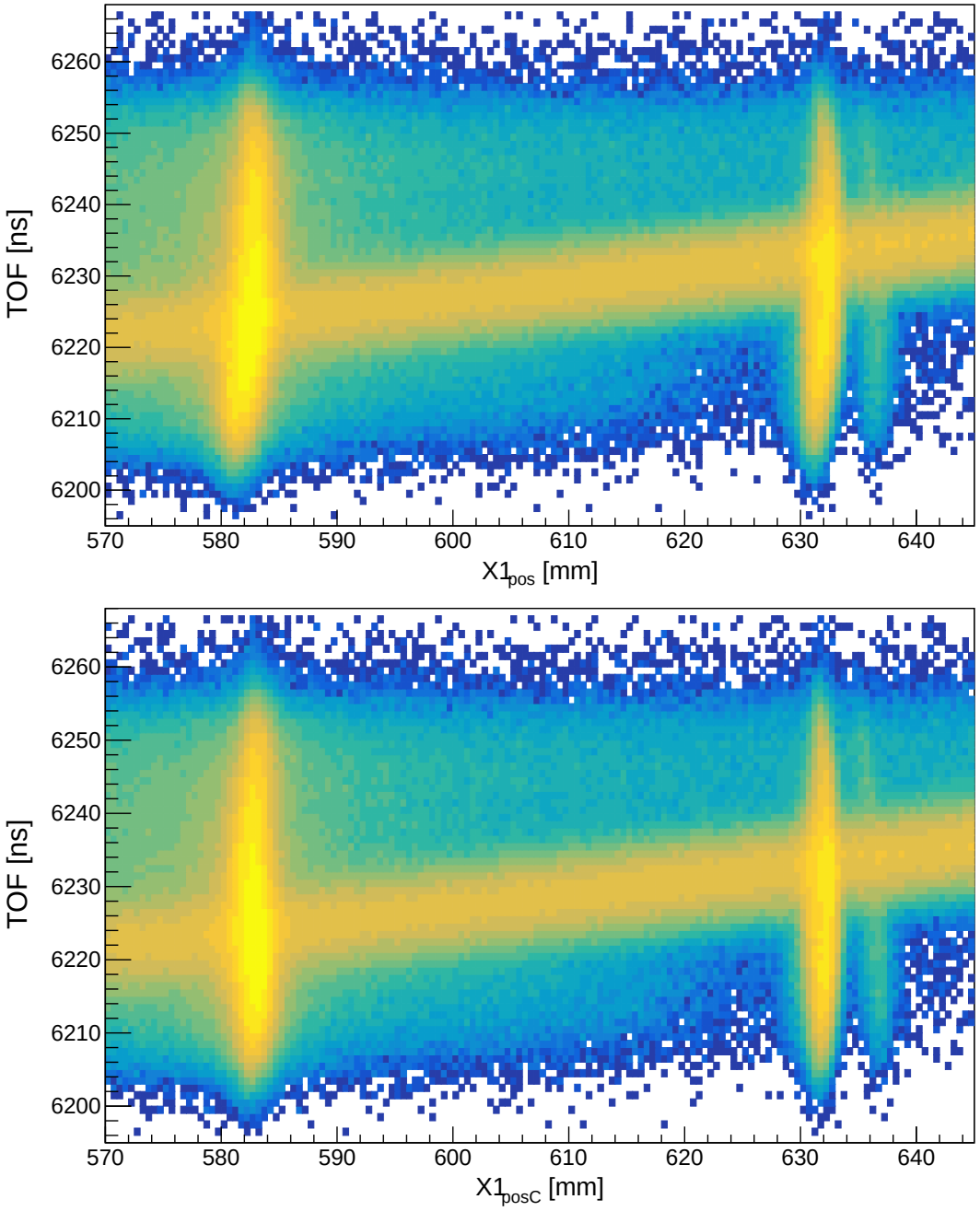

Figure B.4: Lineshape corrections PR166, ^{12}C$(\alpha,\alpha')^{12}$C at $\theta_{\rm lab} = 6°$: TOF dependence. The top and bottom panels show the uncorrected and corrected lineshapes, respectively.

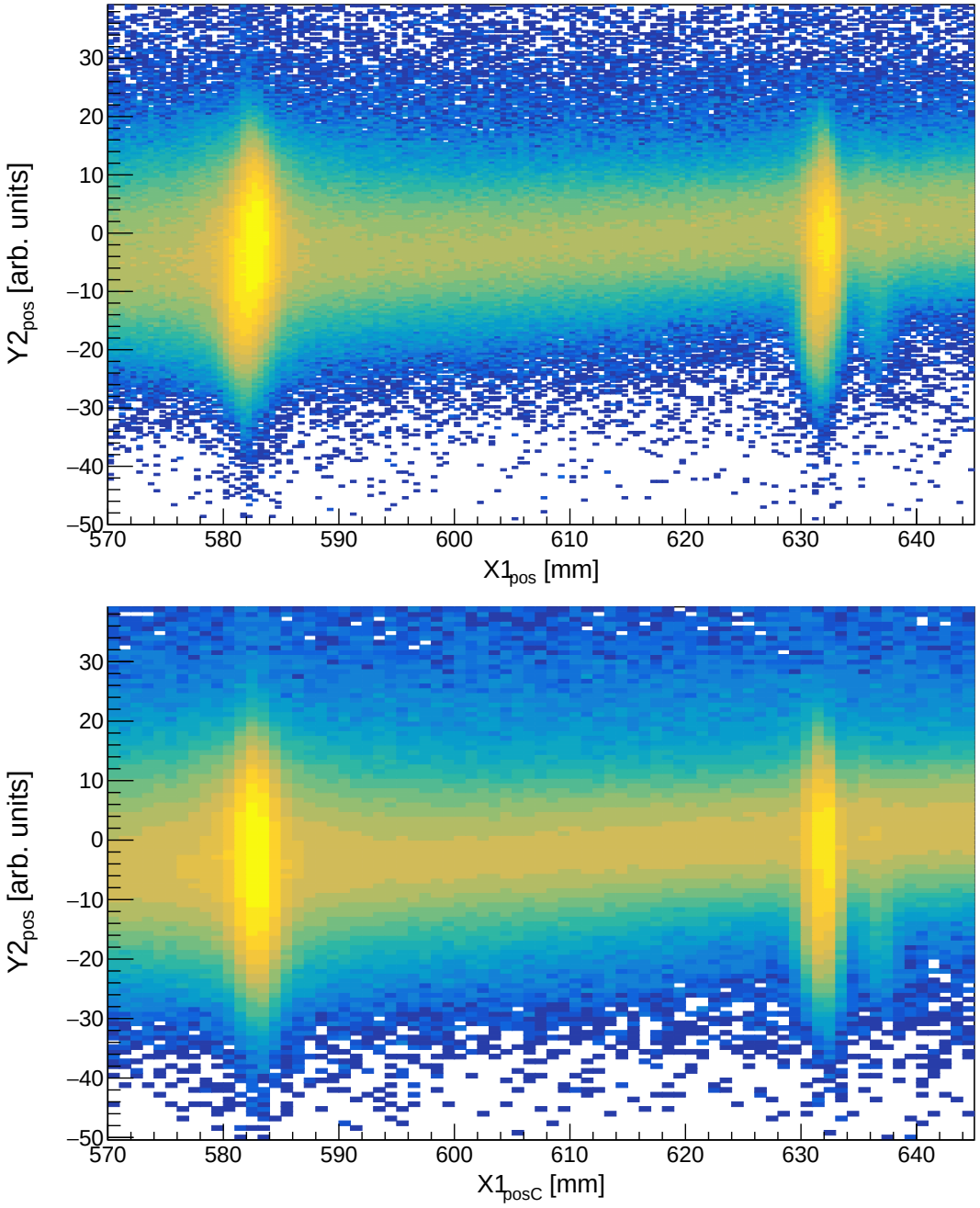

Figure B.5: Lineshape corrections PR166, $^{12}\mathrm{C}(\alpha,\alpha')^{12}\mathrm{C}$ at $\theta_{\mathrm{lab}} = 6°$: $\mathrm{Y2}_{\mathrm{pos}}$ dependence. The top and bottom panels show the uncorrected and corrected lineshapes, respectively.

B.1.3 The improvements of the TLC and SBR algorithms

The improvements of the TLC lineshape correction and the SBR raytracing algorithm are presented in Figure B.6 and summarised in Table B.2. The lineshapes are fitted with a convolution of a Gaussian and a Landau function to model the experimental resolution and target energy-loss components, respectively. The intrinsic width of the peaks can be ignored as the corresponding 7.65420(15) MeV $J^{\pi} = 0^{+}$ resonance has an intrinsic width of $10.8(6) \times 10^{-3}$eV. The lineshape correction with TLC, which maps $\mathrm{X1_{pos}}$ to $\mathrm{X1_{posC}}$, yields a 50(2)% decrease in the dispersion. The corrected focal-plane position obtained with the new SBR raytracing algorithm, $\mathrm{X1_{posC}}$, exhibits an 8(4)% decrease in the dispersion with respect to $\mathrm{X1_{posC}}$ (old).

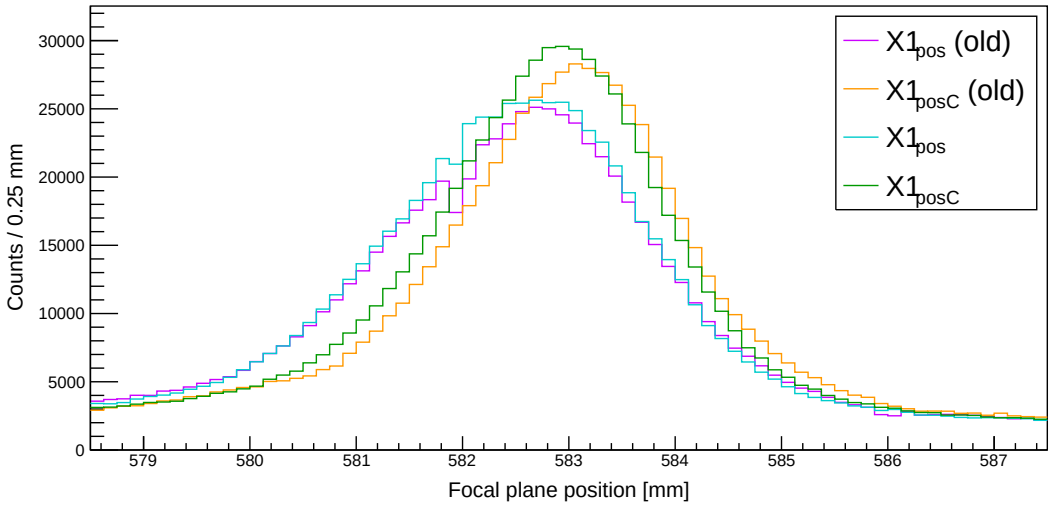

Figure B.6: Comparison of the focal-plane dispersions of $\mathrm{X1_{pos}}$ (old), $\mathrm{X1_{posC}}$ (old), $\mathrm{X1_{pos}}$ and $\mathrm{X1_{posC}}$.

Focal-plane Position	Dispersion [mm]	E_x FWHM [keV]
$\mathrm{X1_{pos}}$ (old)	0.857(7)	165(3)
$\mathrm{X1_{posC}}$ (old)	0.41(1)	79(4)
$\mathrm{X1_{pos}}$	0.752(6)	145(2)
$\mathrm{X1_{posC}}$	0.38(1)	73(5)

Table B.2: Summary of the focal-plane dispersions of the X1 wire plane for experiment PR166, $^{12}\mathrm{C}(\alpha, \alpha')^{12}\mathrm{C}$ at $\theta_{\mathrm{lab}} = 6^{\circ}$.

B.2 Experiment PR166, ^{12}C(α, α')^{12}C at 8.5°

B.2.1 SilverBulletRaytrace algorithm

The newly developed SilverBulletRaytrace algorithm offers improvements with respect to the old raytracing algorithm which has thus far been the standard algorithm for analysing VDC data. In Figure B.7, these improvements are presented for the PR166 ^{12}C(α,α') measurement at $\theta_{\text{lab}} = 8.5°$.

In Figure B.7, panel (a) shows the spectrum of the old raytrace angle through the X1 wire plane, θ_{RT} (old), versus the old uncorrected focal-plane position, X1$_{\text{pos}}$ (old). It is observed that V-shaped structures extend downwards from the loci of the well-resolved resonances. These V structures are indicative of a raytracing artefact that broadens in the focal-plane spectrum in a non-Gaussian manner which worsens the resolution.

In Figure B.7, panel (b) shows the spectrum of the old raytrace angle through the X1 wire plane, θ_{RT} (old), versus the new corrected focal-plane position, X1$_{\text{posC}}$. In comparison to panel (a), the V structures have been eliminated. Moreover, events have been recovered below θ_{RT} (old) $\approx 20°$. These recovered events would have been rejected by the old raytracing algorithm by failing any of the conditions listed in Ref. [82]. The SilverBulletRaytrace algorithm is able to recover some of these events which likely have anomalous wire hit patterns.

In Figure B.7, panel (c) shows the spectrum of the new raytrace angle through the X1 wire plane, θ_{RT}, versus the new corrected focal-plane position, X1$_{\text{posC}}$. In general, the raytrace angles in panels (a) and (b) which extend below θ_{RT} (old) $\approx 30°$ are not physical. These lower values are a result of the fact that the perturbing wires of anomalous events typically occur on the periphery of a set of triggered wires. These peripheral wires necessarily lead to an incorrectly lowered raytrace angle. Since SilverBulletRaytrace automatically removes these incorrect peripheral wires from the set of triggered wires that are raytraced, the new raytracing angles are therefore more accurately centered at $\theta_{\text{RT}} \approx 35°$ and a large portion of the unphysical values below $\theta_{\text{RT}} \approx 2°$ have been remedied.

B.2.2 Lineshape corrections

The lineshape corrections for experiment PR166, ^{12}C(α, α')^{12}C at $\theta_{\text{lab}} = 8.5°$ are summarised below in Table B.3 and the corresponding results are presented in Figures B.8 - B.11.

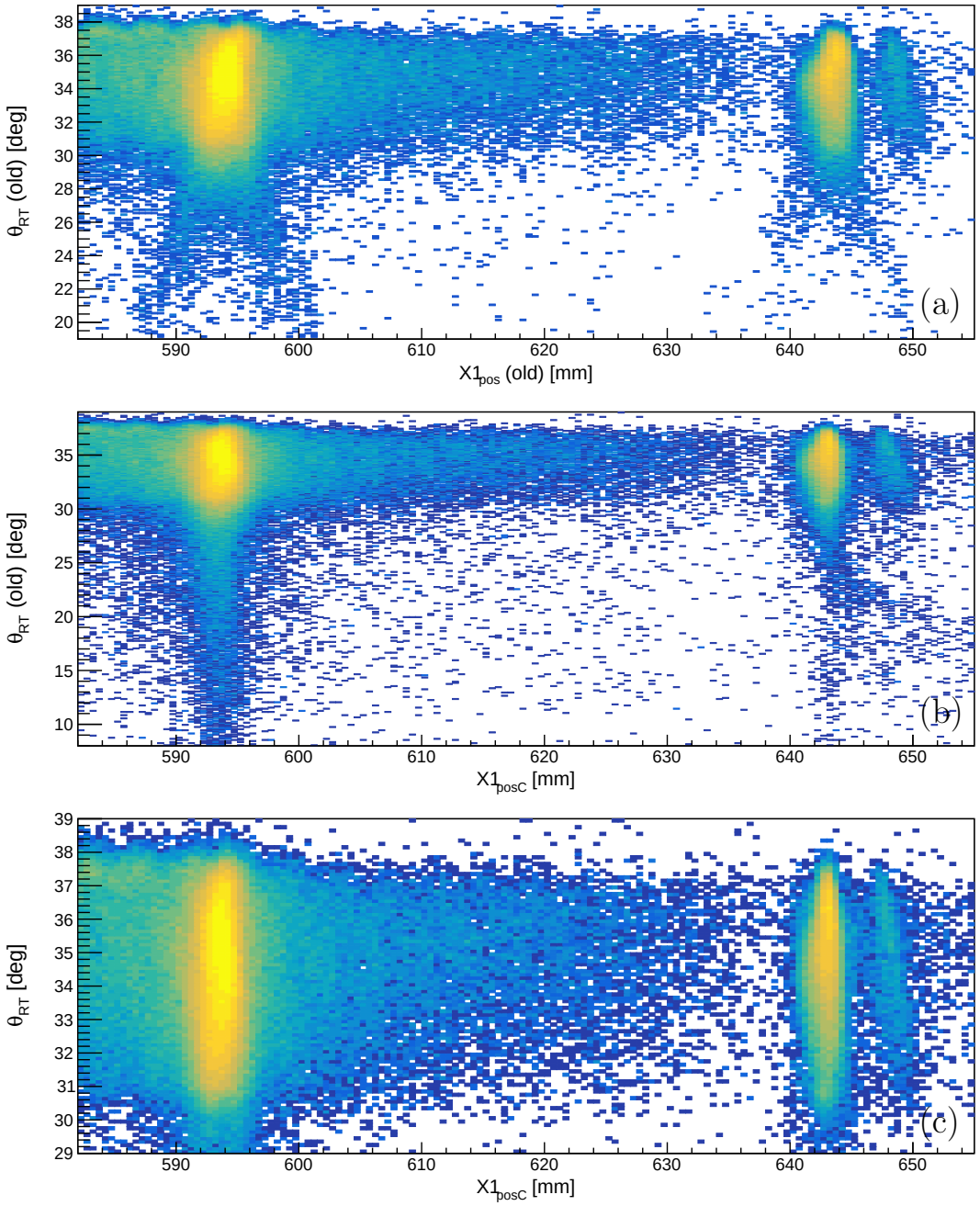

Figure B.7: Comparison of SilverBulletRaytrace against the old raytrace algorithm for experiment PR166, $^{12}\mathrm{C}(\alpha,\alpha')^{12}\mathrm{C}$ at $\theta_{\mathrm{lab}} = 8.5°$: (a) spectrum of the old raytrace angle (through X1) versus the old focal-plane position, (b) spectrum of the old raytrace angle (through X1) versus the new corrected focal-plane position, (c) spectrum of the new raytrace angle (through X1) wire plane versus the new corrected focal-plane position.

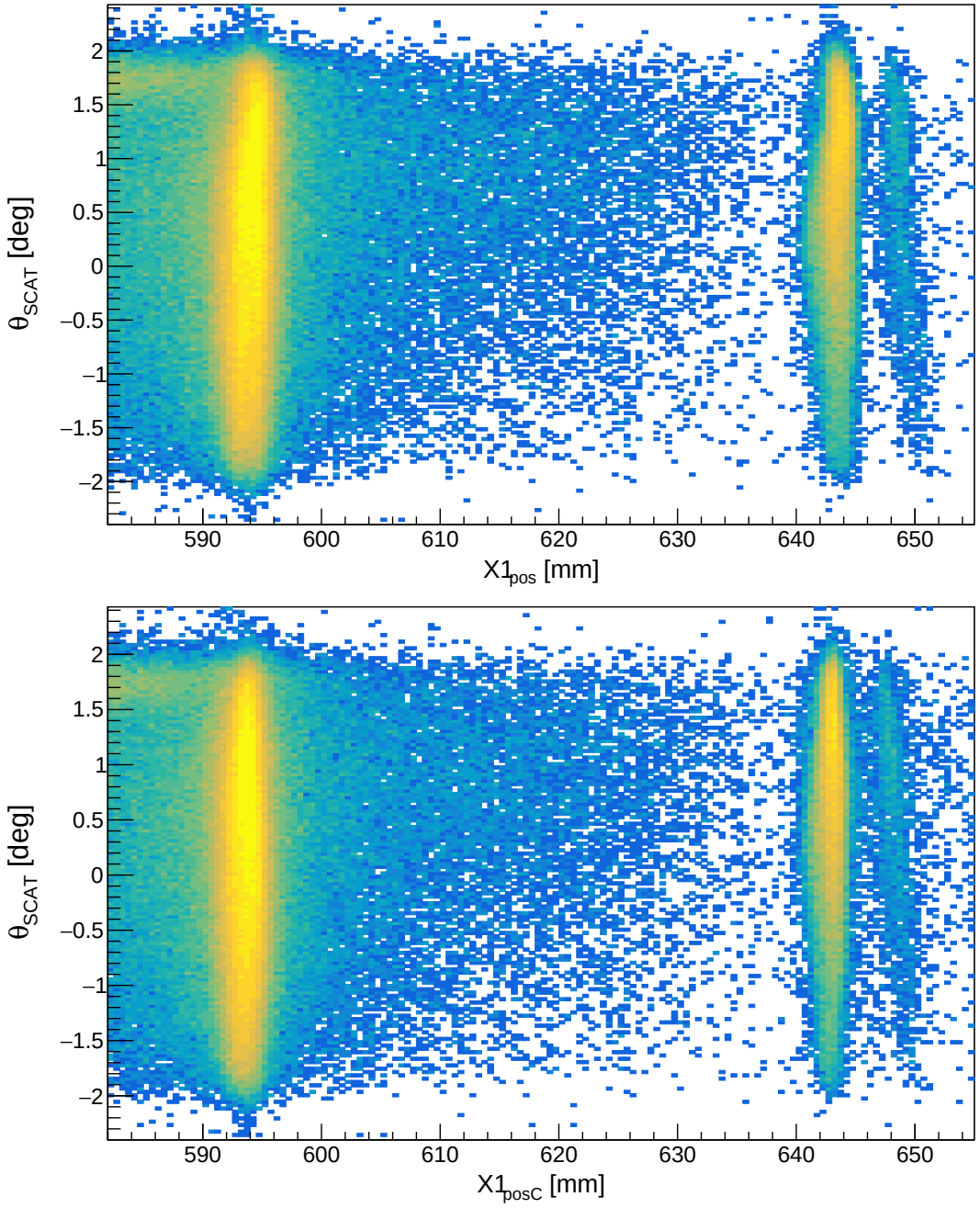

Figure B.8: Lineshape corrections PR166, ^{12}C$(\alpha,\alpha')^{12}$C at $\theta_{\rm lab} = 8.5°$: $\theta_{\rm scat}$ dependence. The top and bottom panels show the uncorrected and corrected lineshapes, respectively.

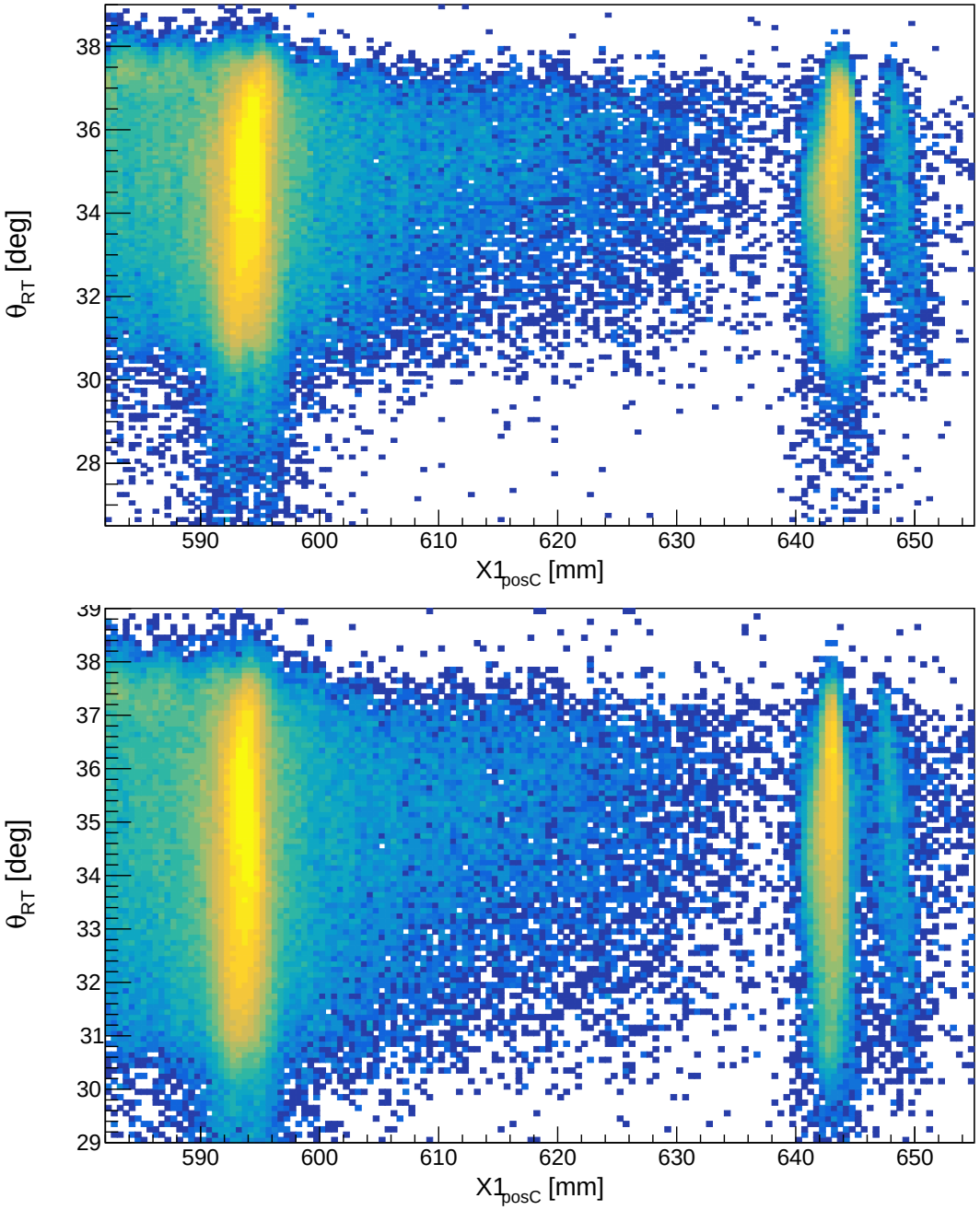

Figure B.9: Lineshape corrections PR166, $^{12}\mathrm{C}(\alpha,\alpha')^{12}\mathrm{C}$ at $\theta_{\mathrm{lab}} = 8.5°$: θ_{RT} dependence. The top and bottom panels show the uncorrected and corrected lineshapes, respectively.

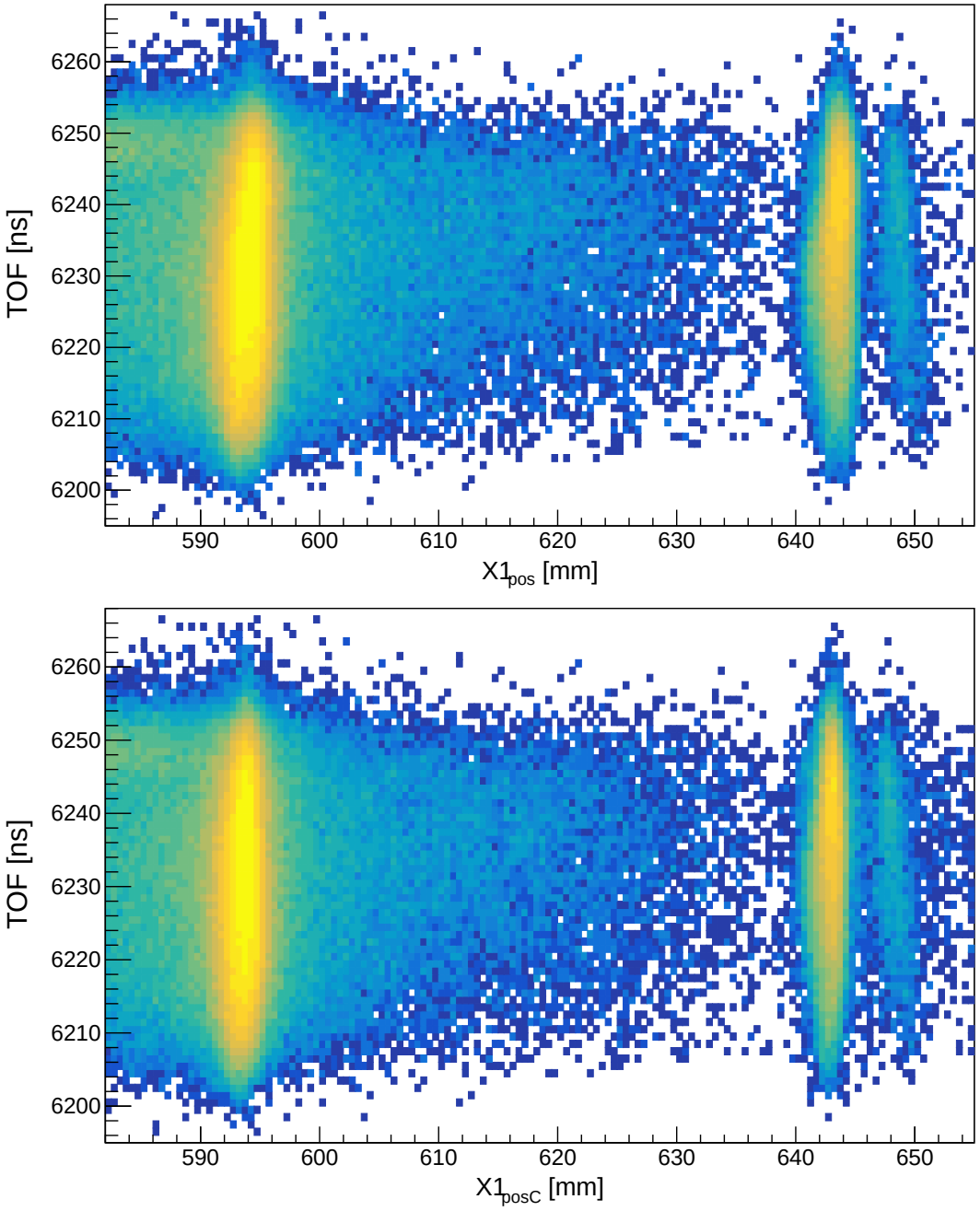

Figure B.10: Lineshape corrections PR166, $^{12}\mathrm{C}(\alpha,\alpha')^{12}\mathrm{C}$ at $\theta_{\mathrm{lab}} = 8.5°$: TOF dependence. The top and bottom panels show the uncorrected and corrected lineshapes, respectively.

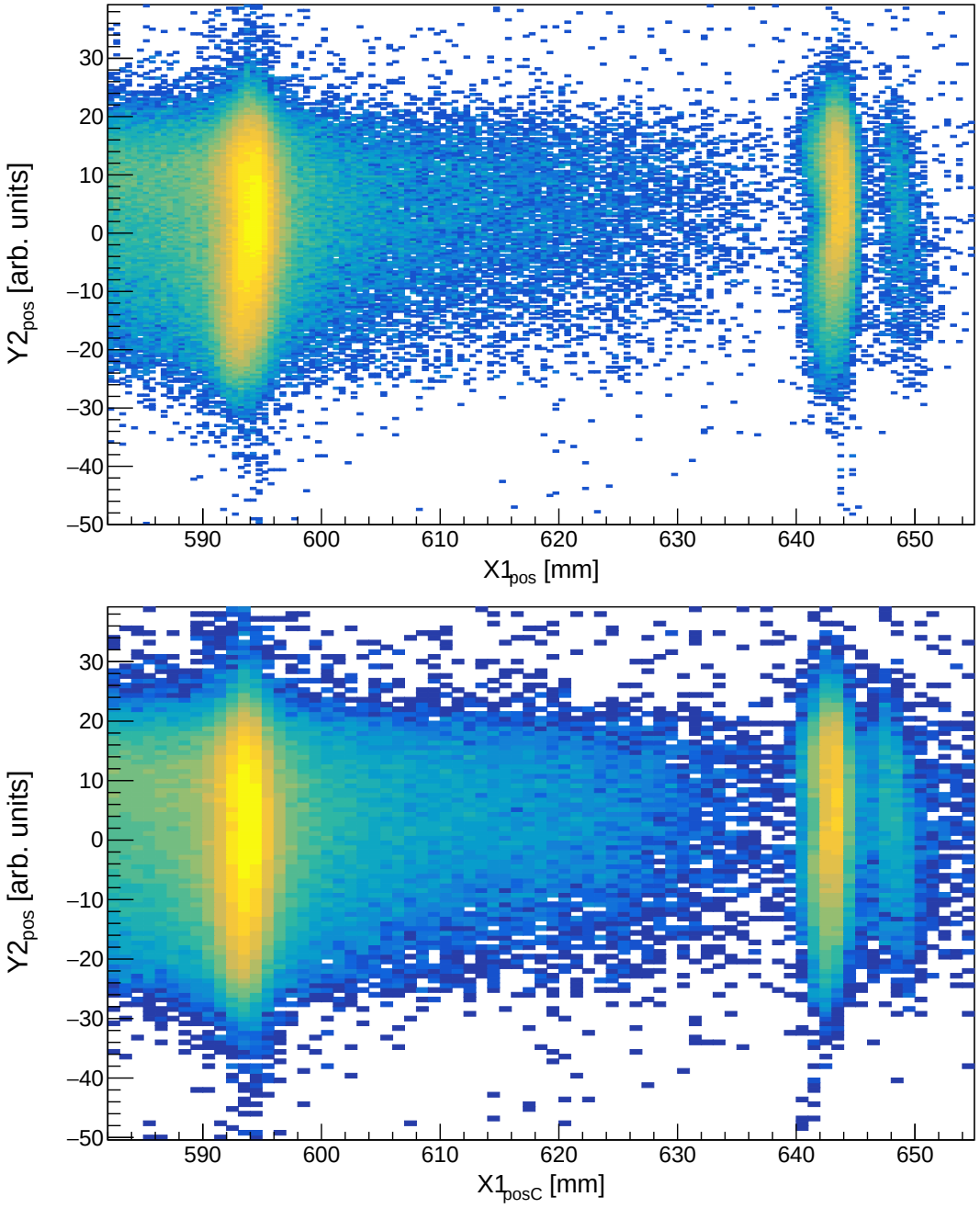

Figure B.11: Lineshape corrections PR166, $^{12}\mathrm{C}(\alpha,\alpha')^{12}\mathrm{C}$ at $\theta_{\mathrm{lab}} = 8.5°$: $\mathrm{Y2_{pos}}$ dependence. The top and bottom panels show the uncorrected and corrected lineshapes, respectively.

Correction Type	Correction Order
θ_{scat}	2
Y1	2
θ_{scat}	2
θ_{scat}	2
θ_{scat}	2
θ_{RT}	3

Table B.3: Summary of the lineshape corrections for experiment PR166, $^{12}\text{C}(\alpha,\alpha')^{12}\text{C}$ at $\theta_{\text{lab}} = 8.5°$. The iterative corrections are listed in order of their application.

B.2.3 The improvements of the TLC and SBR algorithms

The improvements of the TLC lineshape correction and the SBR raytracing algorithm are presented in Figure B.12 and summarised in Table B.4. The lineshapes are fitted with a convolution of a Gaussian and a Landau function to model the experimental resolution and target energy-loss components, respectively. The intrinsic width of the peaks can be ignored as the corresponding 7.65407(19) MeV $J^{\pi} = 0^{+}$ resonance has an intrinsic width of 9.3(9)eV. The lineshape correction with TLC, which maps $\mathrm{X1_{pos}}$ to $\mathrm{X1_{posC}}$, yields a 38(5)% decrease in the dispersion. The corrected focal-plane position obtained with the new SBR raytracing algorithm, $\mathrm{X1_{posC}}$, exhibits an 15(5)% decrease in the dispersion with respect to $\mathrm{X1_{posC}}$ (old).

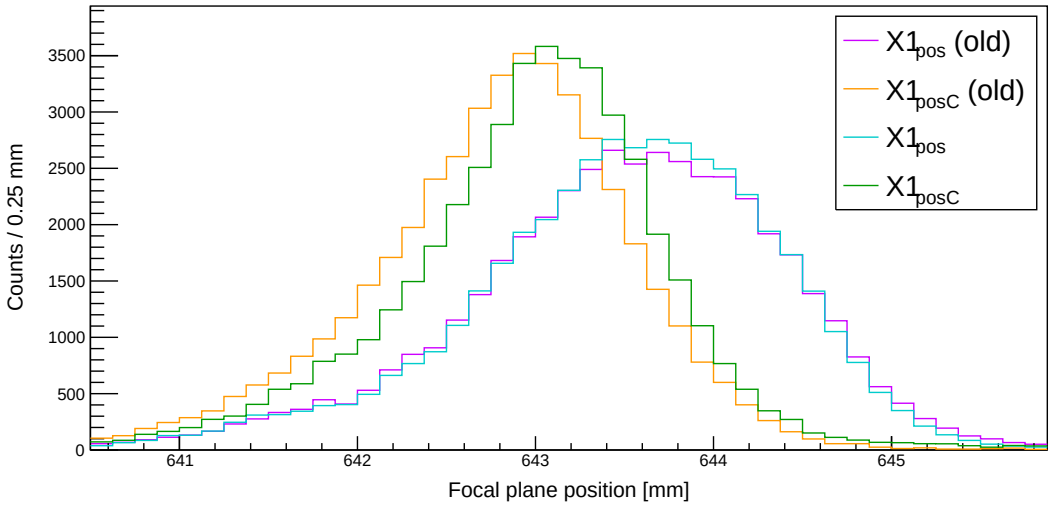

Figure B.12: Comparison of the focal-plane dispersions of $\mathrm{X1_{pos}}$ (old), $\mathrm{X1_{posC}}$ (old), $\mathrm{X1_{pos}}$ and $\mathrm{X1_{posC}}$.

Focal-plane Position	Dispersion [mm]	E_x FWHM [keV]
$\mathrm{X1_{pos}}$ (old)	0.800(9)	152(4)
$\mathrm{X1_{posC}}$ (old)	0.51(1)	96(5)
$\mathrm{X1_{pos}}$	0.70(4)	133(14)
$\mathrm{X1_{posC}}$	0.43(2)	82(8)

Table B.4: Summary of the focal-plane dispersions of the X1 wire plane for experiment PR166, $^{12}\mathrm{C}(\alpha,\alpha')^{12}\mathrm{C}$ at $\theta_{\mathrm{lab}} = 8.5°$.

B.3 Experiment PR166, $^{12}C(\alpha,\alpha')^{12}C$ at 10°

B.3.1 SilverBulletRaytrace algorithm

The newly developed SilverBulletRaytrace algorithm offers improvements with respect to the old raytracing algorithm which has thus far been the standard algorithm for analysing VDC data. In Figure B.13, these improvements are presented for the PR166 $^{12}C(\alpha,\alpha')$ measurement at $\theta_{lab} = 10°$.

In Figure B.13, panel (a) shows the spectrum of the old raytrace angle through the X1 wire plane, θ_{RT} (old), versus the old uncorrected focal-plane position, $X1_{pos}$ (old). It is observed that V-shaped structures extend downwards from the loci of the well-resolved resonances. These V structures are indicative of a raytracing artefact that broadens in the focal-plane spectrum in a non-Gaussian manner which worsens the resolution.

In Figure B.13, panel (b) shows the spectrum of the old raytrace angle through the X1 wire plane, θ_{RT} (old), versus the new corrected focal-plane position, $X1_{posC}$. In comparison to panel (a), the V structures have been eliminated. Moreover, events have been recovered below θ_{RT} (old) $\approx 20°$. These recovered events would have been rejected by the old raytracing algorithm by failing any of the conditions listed in Ref. [82]. The SilverBulletRaytrace algorithm is able to recover some of these events which likely have anomalous wire hit patterns.

In Figure B.13, panel (c) shows the spectrum of the new raytrace angle through the X1 wire plane, θ_{RT}, versus the new corrected focal-plane position, $X1_{posC}$. In general, the raytrace angles in panels (a) and (b) which extend below $\theta_{RT} \approx 30°$ are not physical. These lower values are a result of the fact that the perturbing wires of anomalous events typically occur on the periphery of a set of triggered wires. These peripheral wires necessarily lead to an incorrectly lowered raytrace angle. Since SilverBulletRaytrace automatically removes these incorrect peripheral wires from the set of triggered wires that are raytraced, the new raytracing angles are therefore more accurately centered at $\theta_{lab} \approx 35°$ and a large portion of the unphysical values below $\theta_{scat} \approx 2°$ have been remedied.

B.3.2 Lineshape corrections for $^{12}C(\alpha,\alpha')^{12}C$ at $\theta_{lab} = 10°$

The lineshape corrections for experiment PR166, $^{12}C(\alpha,\alpha')^{12}C$ at $\theta_{lab} = 10°$ are summarised below in Table B.5 and the corresponding results are presented in Figures B.14 - B.17.

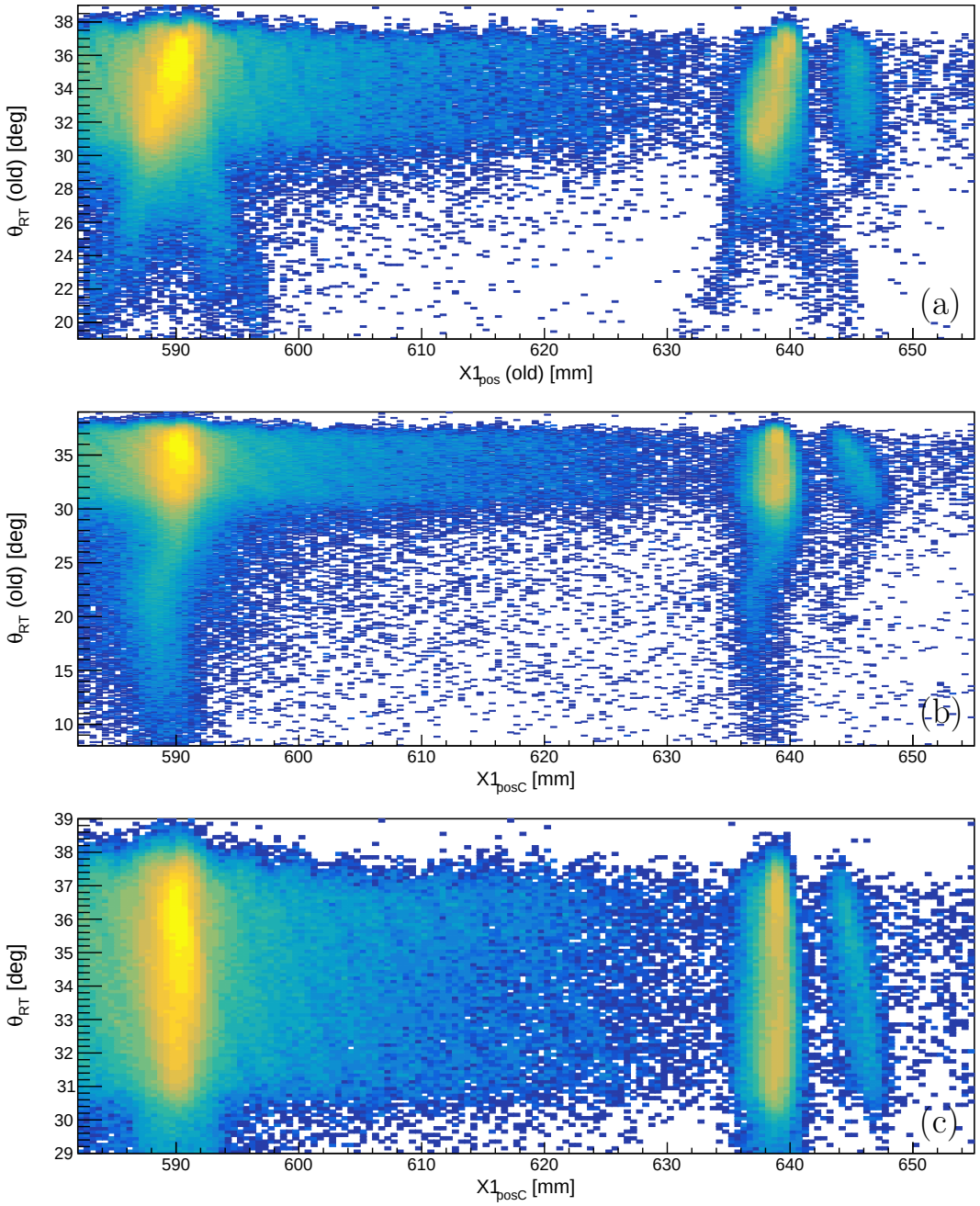

Figure B.13: Comparison of SilverBulletRaytrace against the old raytrace algorithm for experiment PR166, ^{12}C$(\alpha, \alpha')^{12}$C at $\theta_{\text{lab}} = 10°$: (a) spectrum of the old raytrace angle (through X1) versus the old focal-plane position, (b) spectrum of the old raytrace angle (through X1) versus the new corrected focal-plane position, (c) spectrum of the new raytrace angle (through X1) wire plane versus the new corrected focal-plane position.

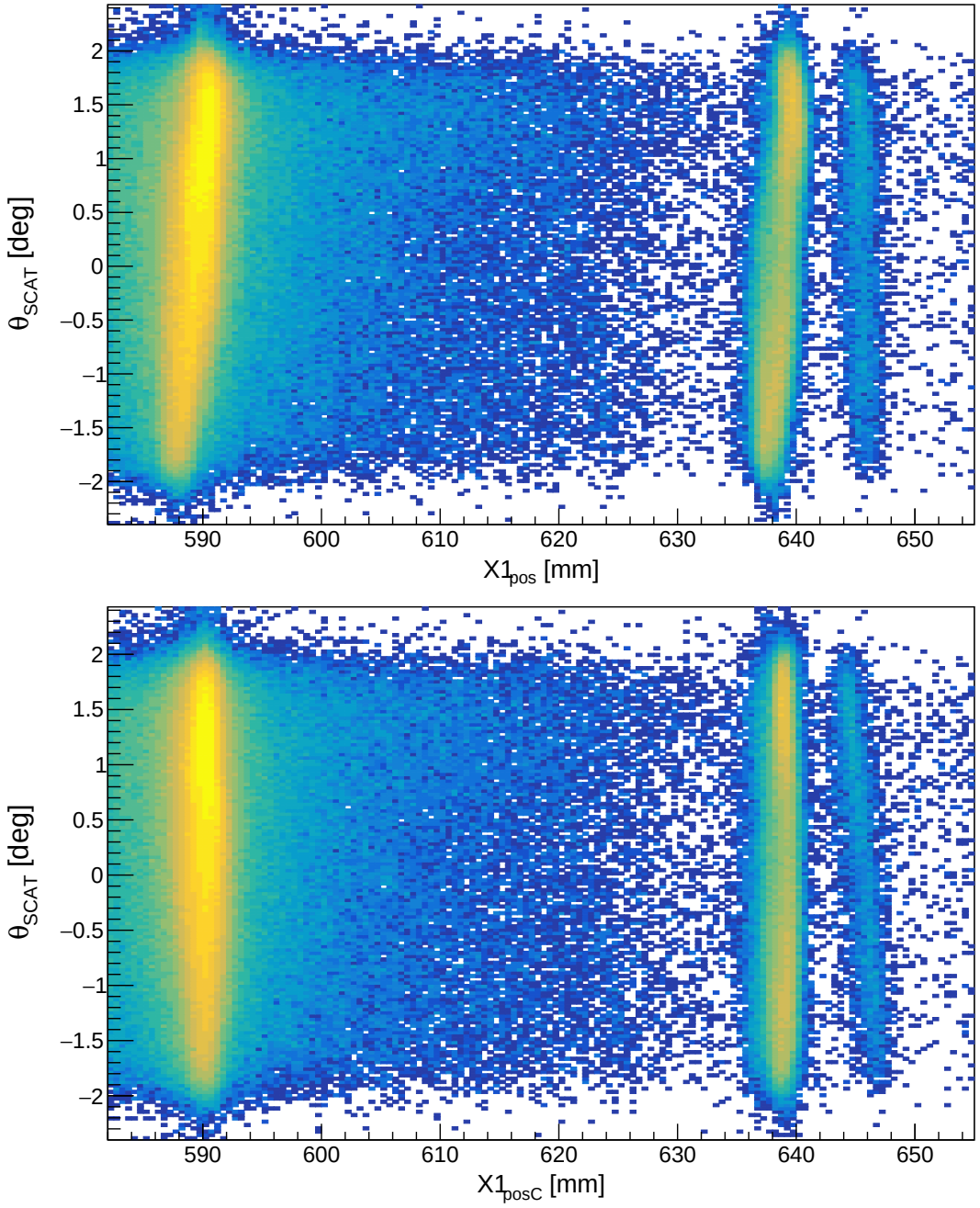

Figure B.14: Lineshape corrections PR166 at $\theta_{\mathrm{lab}} = 10°$: θ_{scat} dependence. The top and bottom panels show the uncorrected and corrected lineshapes, respectively.

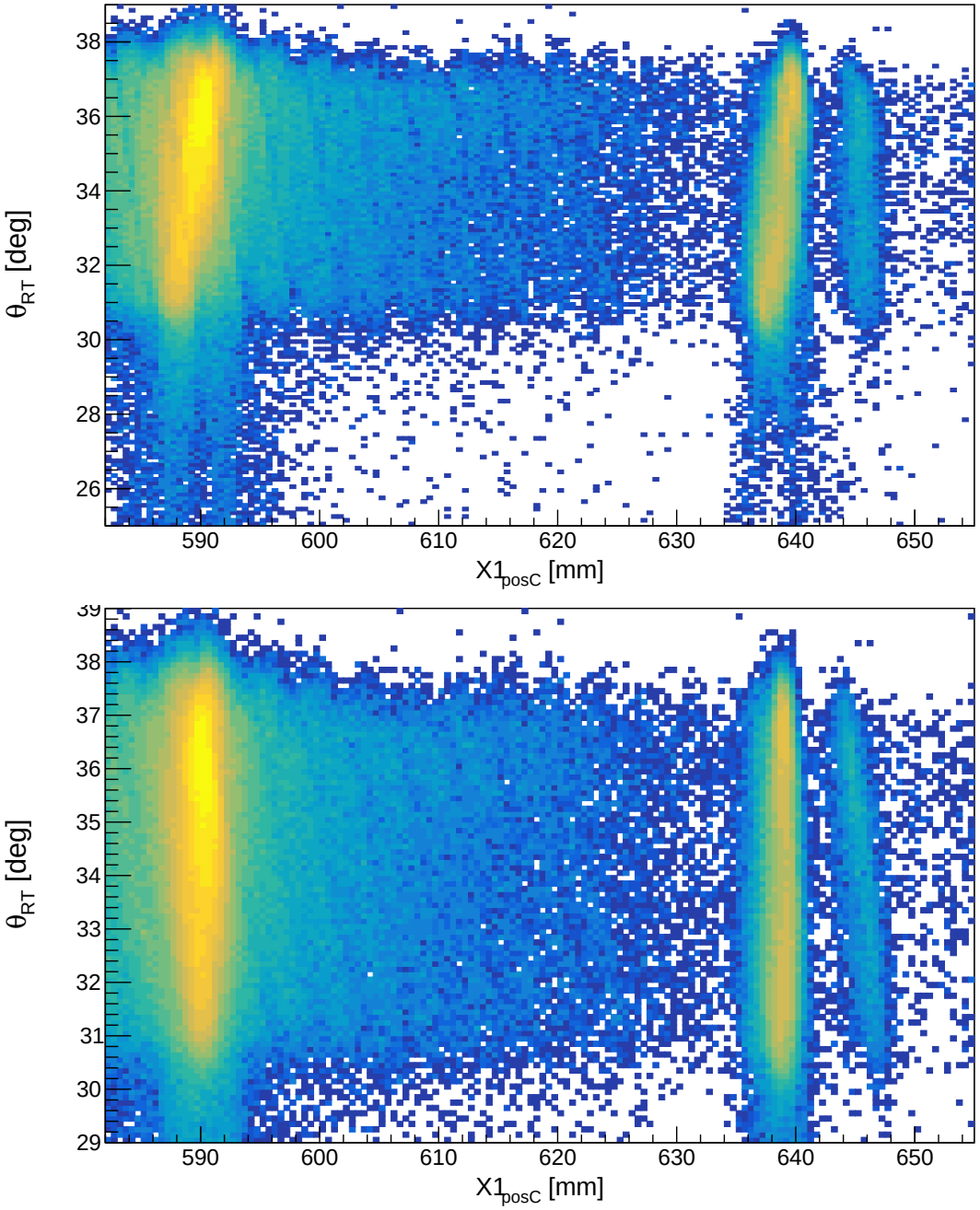

Figure B.15: Lineshape corrections PR166 at $\theta_{\text{lab}} = 10°$: θ_{RT} dependence. The top and bottom panels show the uncorrected and corrected lineshapes, respectively.

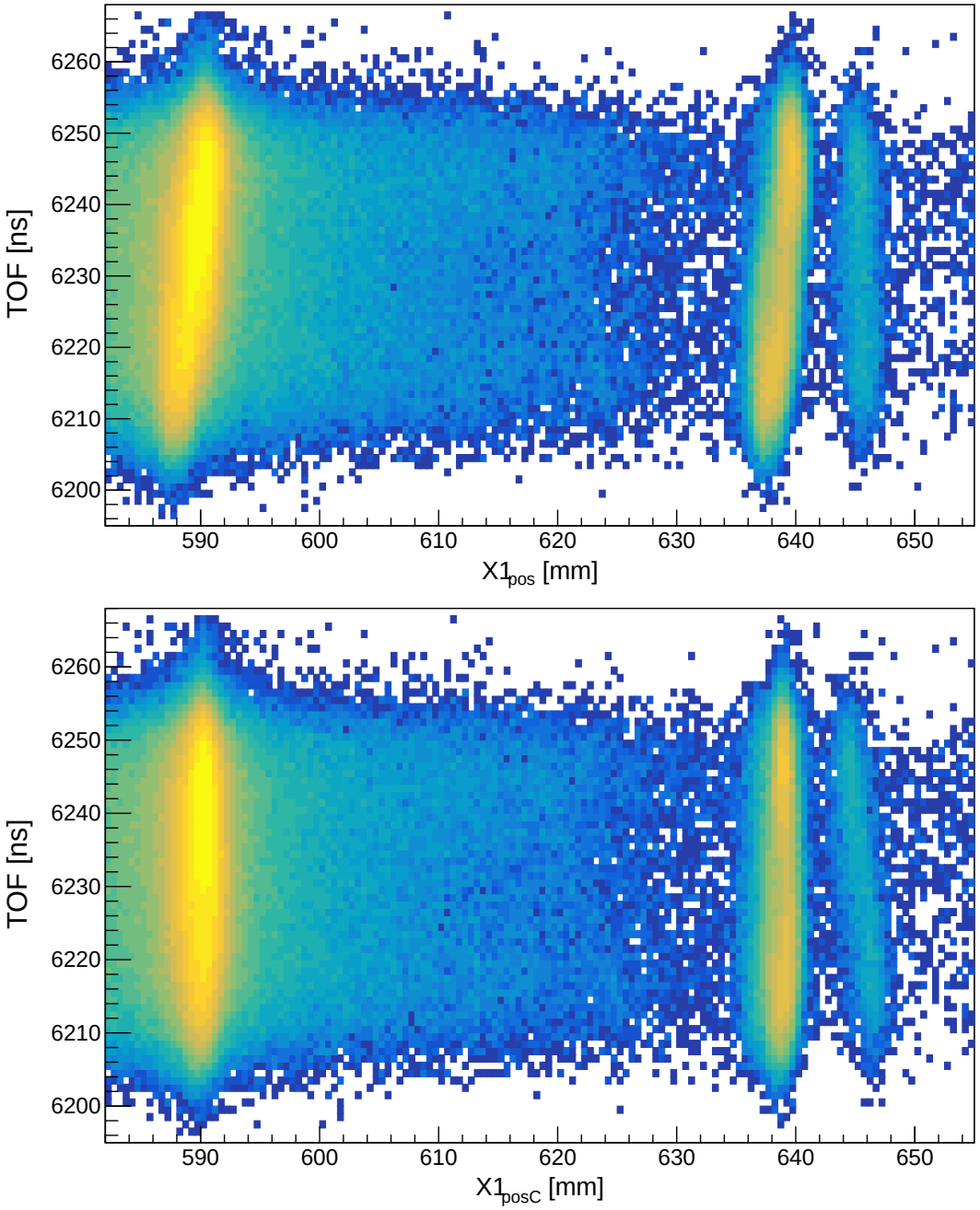

Figure B.16: Lineshape corrections PR166 at $\theta_{\text{lab}} = 10°$: TOF dependence. The top and bottom panels show the uncorrected and corrected lineshapes, respectively.

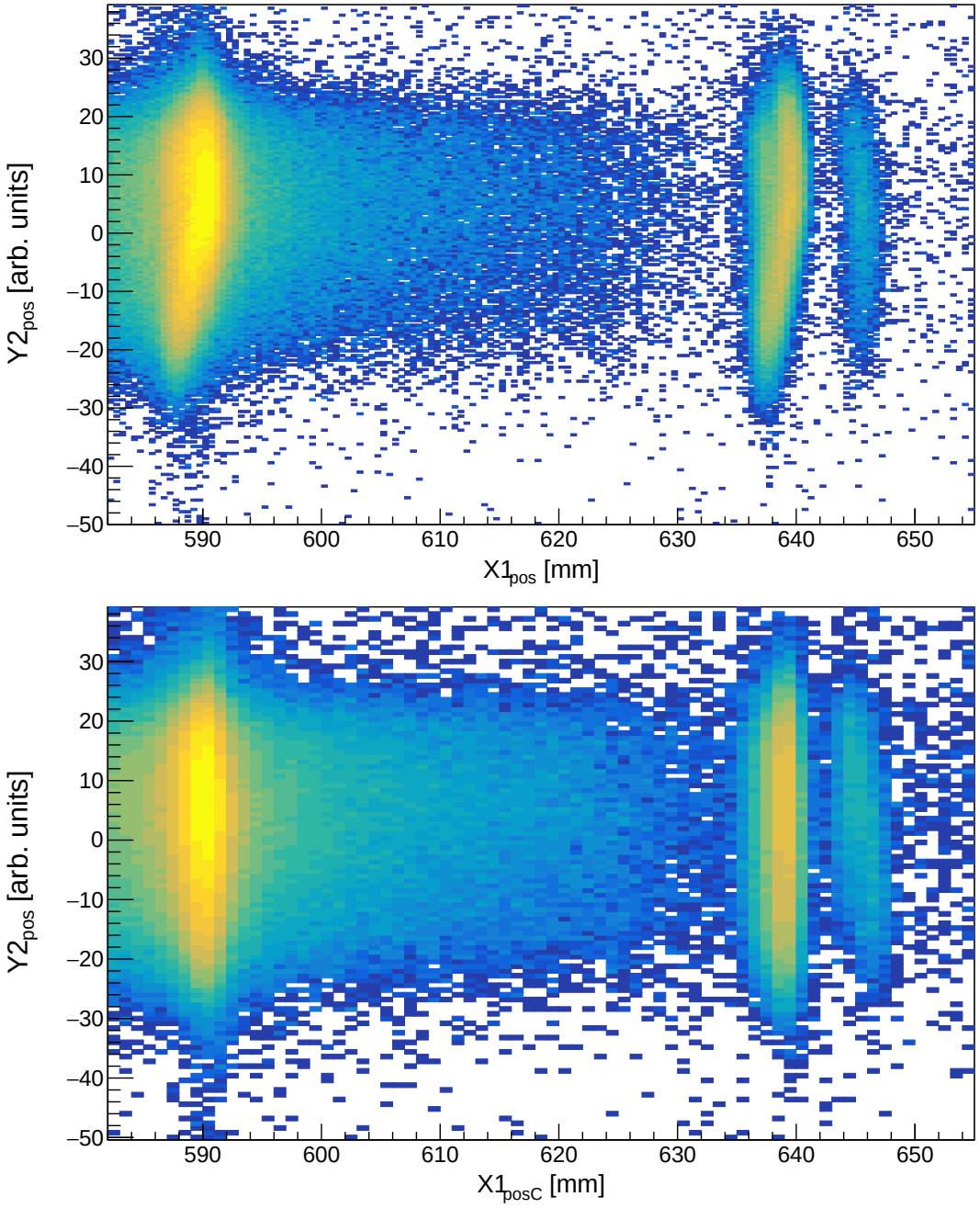

Figure B.17: Lineshape corrections PR166 at $\theta_{\mathrm{lab}} = 10°$: $\mathrm{Y2_{pos}}$ dependence. The top and bottom panels show the uncorrected and corrected lineshapes, respectively.

Correction Type	Correction Order
θ_{scat}	2
θ_{scat}	2
$\mathrm{Y2}_{\mathrm{pos}}$	2
$\mathrm{Y2}_{\mathrm{pos}}$	2
θ_{scat}	2
$\mathrm{Y2}_{\mathrm{pos}}$	2
$\mathrm{Y2}_{\mathrm{pos}}$	2
$\mathrm{Y2}_{\mathrm{pos}}$	1
$\mathrm{Y2}_{\mathrm{pos}}$	2
θ_{scat}	1
θ_{RT}	1

Table B.5: Summary of the lineshape corrections for experiment PR166, $^{12}\mathrm{C}(\alpha,\alpha')^{12}\mathrm{C}$ at $\theta_{\mathrm{lab}} = 10°$. The iterative corrections are listed in order of their application.

B.3.3 The improvements of the TLC and SBR algorithms

The improvements of the TLC lineshape correction and the SBR raytracing algorithm are presented in Figure B.18 and summarised in Table B.6. The lineshapes are fitted with a convolution of a Gaussian and a Landau function to model the experimental resolution and target energy-loss components, respectively. The intrinsic width of the peaks can be ignored as the corresponding 7.65407(19) MeV $J^\pi = 0^+$ resonance has an intrinsic width of 9.3(9)eV. The lineshape correction with TLC, which maps $\mathrm{X1_{pos}}$ to $\mathrm{X1_{posC}}$, yields a 13(6)% decrease in the dispersion. The corrected focal-plane position obtained with the new SBR raytracing algorithm, $\mathrm{X1_{posC}}$, exhibits an 8(4)% decrease in the dispersion with respect to $\mathrm{X1_{posC}}$ (old).

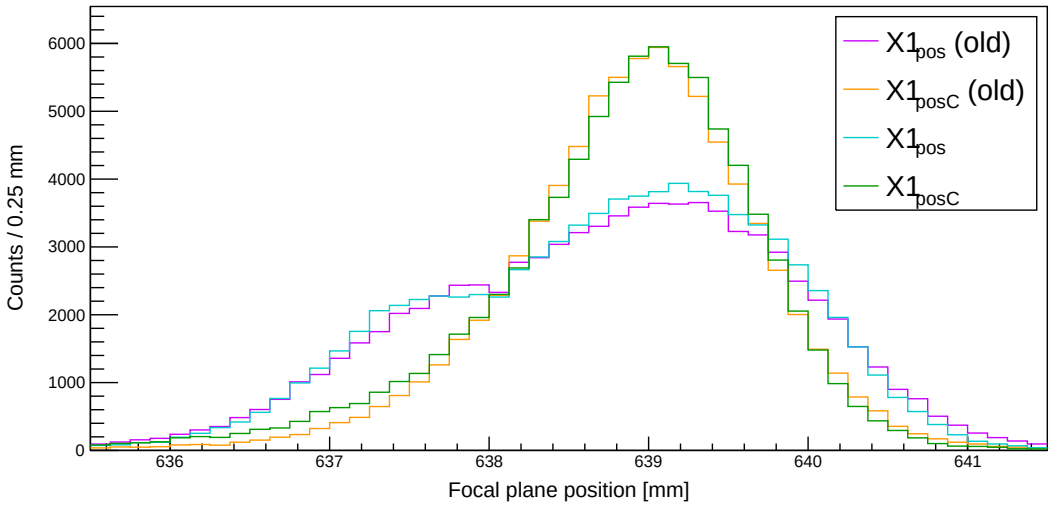

Figure B.18: Comparison of the focal-plane dispersions of $\mathrm{X1_{pos}}$ (old), $\mathrm{X1_{posC}}$ (old), $\mathrm{X1_{pos}}$ and $\mathrm{X1_{posC}}$ for the 4.43982(21) MeV $J^\pi = 2^+$ resonance in ^{12}C.

Focal-plane Position	Dispersion [mm]	E_x FWHM [keV]
$\mathrm{X1_{pos}}$ (old)	*1.14	*218
$\mathrm{X1_{posC}}$ (old)	0.54(1)	103(6)
$\mathrm{X1_{pos}}$	*1.08	*207
$\mathrm{X1_{posC}}$	0.50(1)	95(6)

Table B.6: Summary of the focal-plane dispersions of the X1 wire plane for experiment PR166, $^{12}\mathrm{C}(\alpha,\alpha')^{12}\mathrm{C}$ at $\theta_{\mathrm{lab}} = 10°$. *These dispersions/FWHMs are determined directly from the binned data.

B.4 Experiment PR194, $^{12}C(\alpha,\alpha')^{12}C$ at 0°, $E_{beam} = 160$ MeV

B.4.1 SilverBulletRaytrace algorithm

The newly developed SilverBulletRaytrace algorithm offers improvements with respect to the old raytracing algorithm which has thus far been the standard algorithm for analysing VDC data, as shown in Figure B.19.

Panel (a) in Figure B.19, shows the spectrum of the old raytrace angle through the X1 wire plane, θ_{RT} (old), versus the old uncorrected focal-plane position, $X1_{pos}$ (old). It is observed that V-shaped structures extend downwards from the loci of the well-resolved resonances. These V structures are indicative of a raytracing artefact that broadens in the focal-plane spectrum in a non-Gaussian manner which worsens the resolution.

Panel (b) in Figure B.19, shows the spectrum of the old raytrace angle through the X1 wire plane, θ_{RT} (old), versus the new corrected focal-plane position, $X1_{posC}$. In comparison to the panel (a), the V structures have been eliminated. Moreover, events have been recovered below θ_{RT} (old) $\approx 20°$. These recovered events would have been rejected by the old raytracing algorithm by failing any of the conditions listed in Ref. [82]. The SilverBulletRaytrace algorithm is able to recover some of these events which likely have anomalous wire hit patterns. SilverBulletRaytrace is fundamentally different from the old raytracing algorithm in that specific anomalous structures are not explicitly searched for: fundamentally, the algorithm is a generalised search for linearity in a given set of triggered wires (see Refs. [82, 81, 85]).

Panel (c) in Figure B.19, shows the spectrum of the new raytrace angle through the X1 wire plane, θ_{RT}, versus the new corrected focal-plane position, $X1_{posC}$. In general, the raytrace angles in panels (a) and (b) which extend below $\theta_{RT} \approx 30°$ are not physical. These lower values are a result of the fact that the perturbing wires of anomalous events typically occur on the periphery of a set of triggered wires. These peripheral wires necessarily lead to an incorrectly lowered raytrace angle. Since SilverBulletRaytrace automatically removes these incorrect peripheral wires from the set of triggered wires that are raytraced, the new raytracing angles are therefore more accurately centered at $\theta_{RT} \approx 35°$ as the unphysical values below $\theta_{RT} \approx 30°$ have been remedied.

B.4.2 Lineshape corrections for experiment PR194

The lineshape corrections for experiment PR194 are summarised below in Table B.7 and the corresponding results are presented in Figures B.20 - B.22.

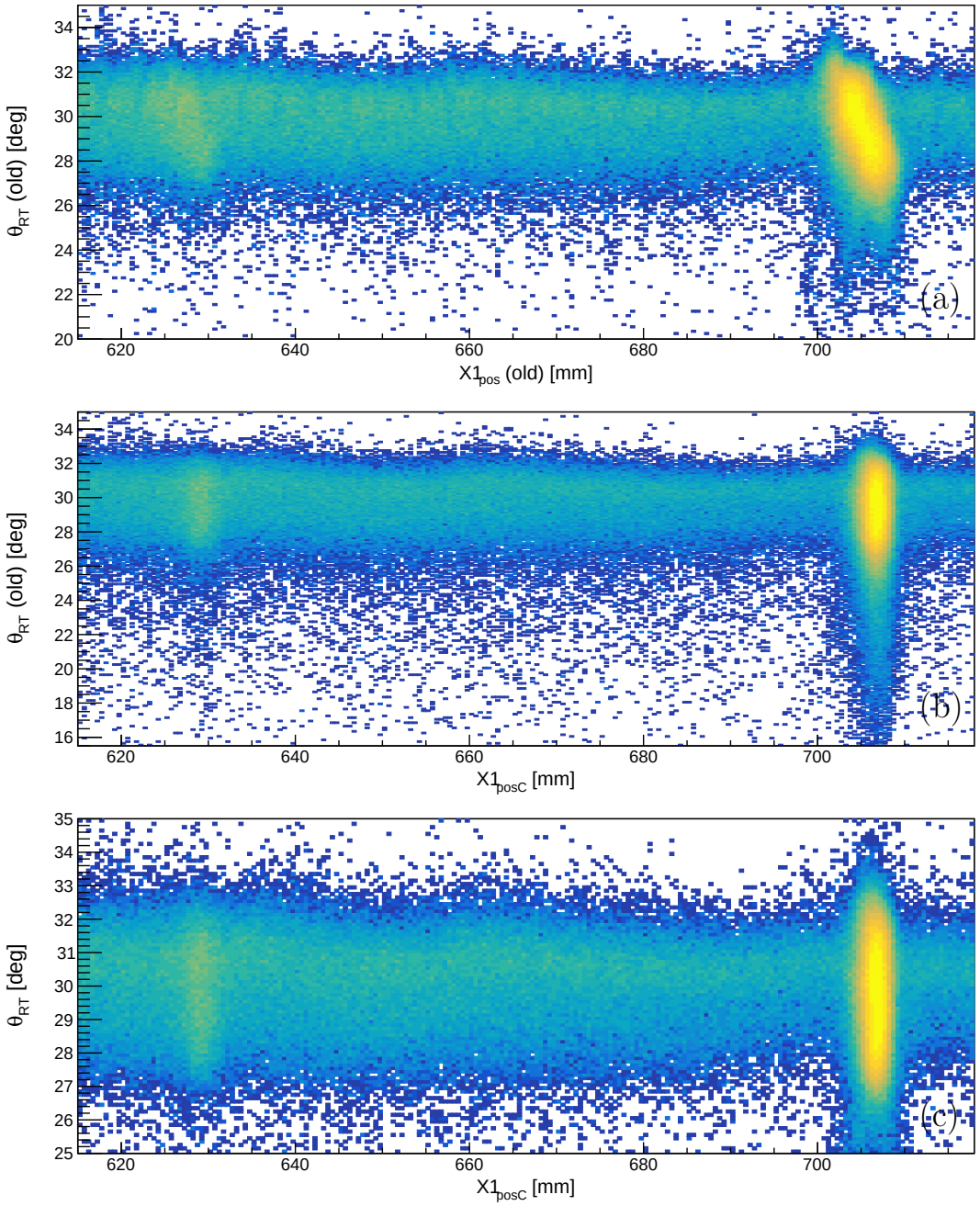

Figure B.19: Comparison of SilverBulletRaytrace against the old raytrace algorithm for experiment PR194: (a) spectrum of the old raytrace angle (through X1) versus the old uncorrected focal-plane position, (b) spectrum of the old raytrace angle (through X1) versus the new corrected focal-plane position, (c) spectrum of the new raytrace angle (through X1) wire plane versus the new corrected focal-plane position.

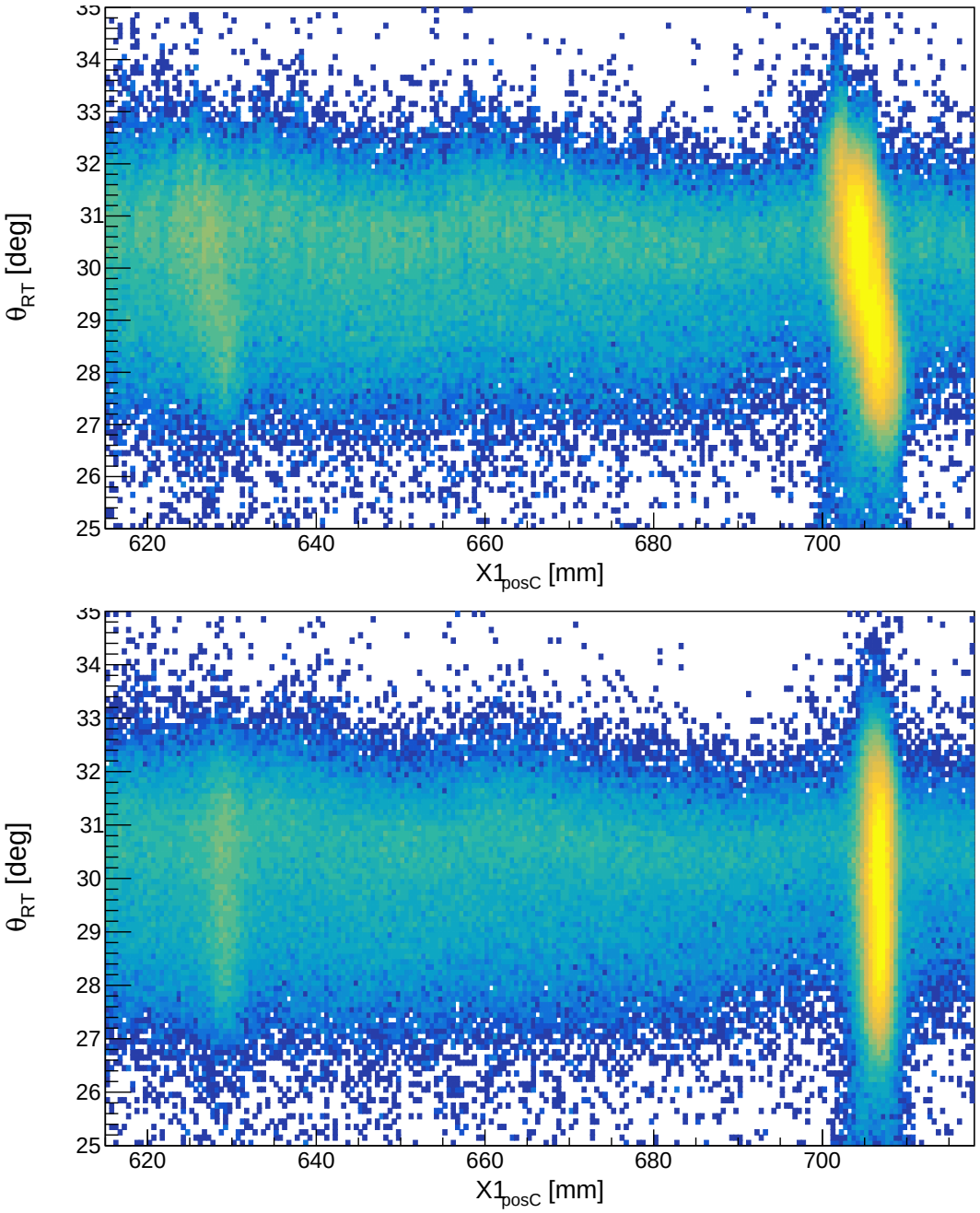

Figure B.20: Lineshape corrections for experiment PR194: θ_{RT} dependence. The top and bottom panels show the uncorrected and corrected lineshapes, respectively.

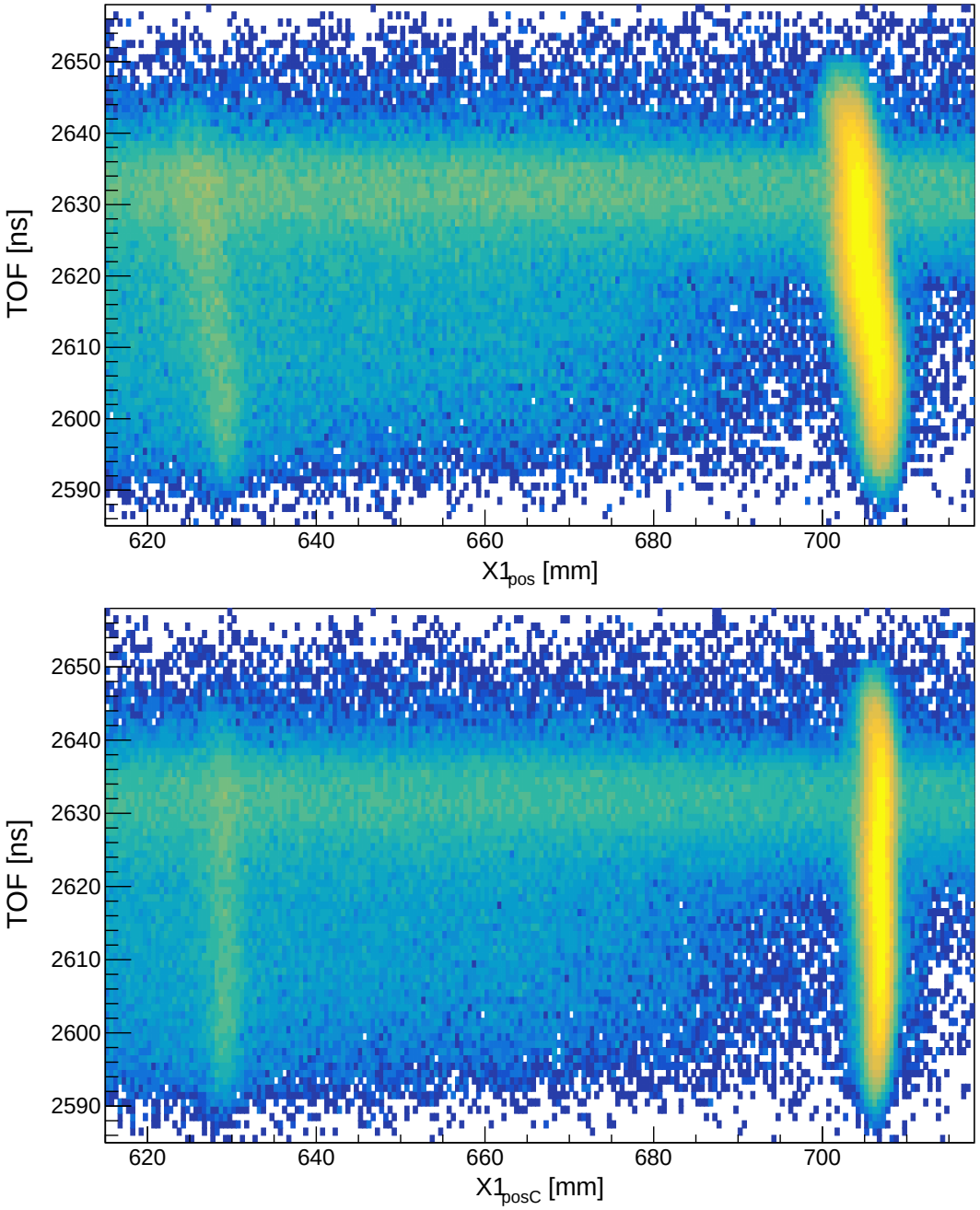

Figure B.21: Lineshape corrections for experiment PR194: TOF dependence. The top and bottom panels show the uncorrected and corrected lineshapes, respectively.

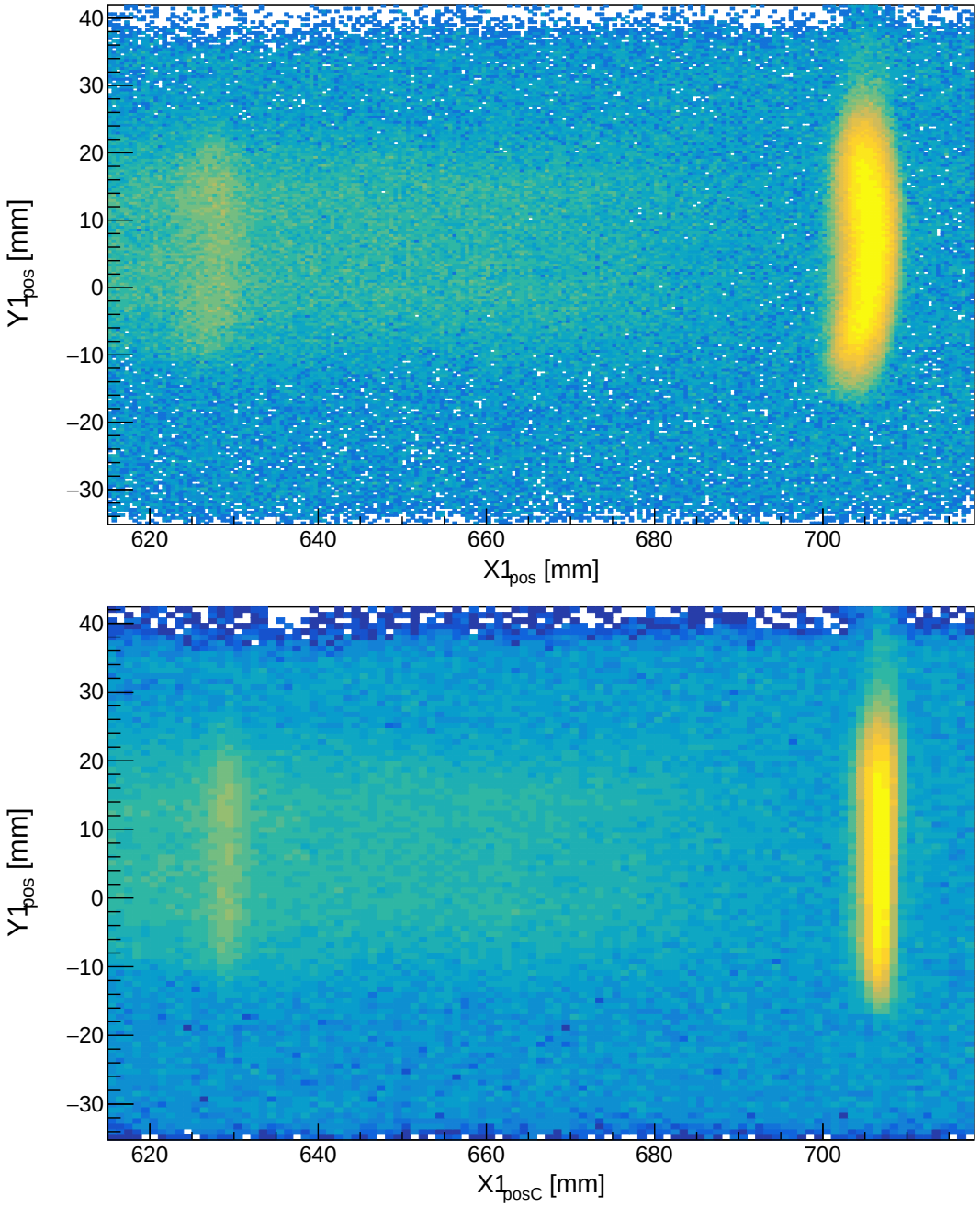

Figure B.22: Lineshape corrections for experiment PR194: $Y1_{pos}$ dependence. The top and bottom panels show the uncorrected and corrected lineshapes, respectively.

Correction Type	Correction Order
θ_{scat}	2
$\mathrm{Y1}_{\mathrm{pos}}$	2
$\mathrm{Y1}_{\mathrm{pos}}$	2
$\mathrm{Y1}_{\mathrm{pos}}$	2
$\mathrm{Y1}_{\mathrm{pos}}$	1
θ_{scat}	2
θ_{scat}	2

Table B.7: Summary of the lineshape corrections for experiment PR194. The iterative corrections are listed in order of their application.

B.4.3 The improvements of the TLC and SBR algorithms

The improvements of the TLC lineshape correction and the SBR raytracing algorithm are presented in Figure B.23 and summarised in Table B.8. The lineshapes are fitted with a convolution of a Gaussian and a Landau function to model the experimental resolution and target energy-loss components, respectively. The intrinsic width of the peaks can be ignored as the corresponding 7.65407(19) MeV $J^{\pi} = 0^{+}$ resonance has an intrinsic width of 9.3(9)eV. The lineshape correction with TLC, which maps $\mathrm{X1_{pos}}$ to $\mathrm{X1_{posC}}$, yields a 60.0(2)% decrease in the dispersion. The corrected focal-plane position obtained with the new SBR raytracing algorithm, $\mathrm{X1_{posC}}$, exhibits an 2.2(8)% decrease in the dispersion with respect to $\mathrm{X1_{posC}}$ (old).

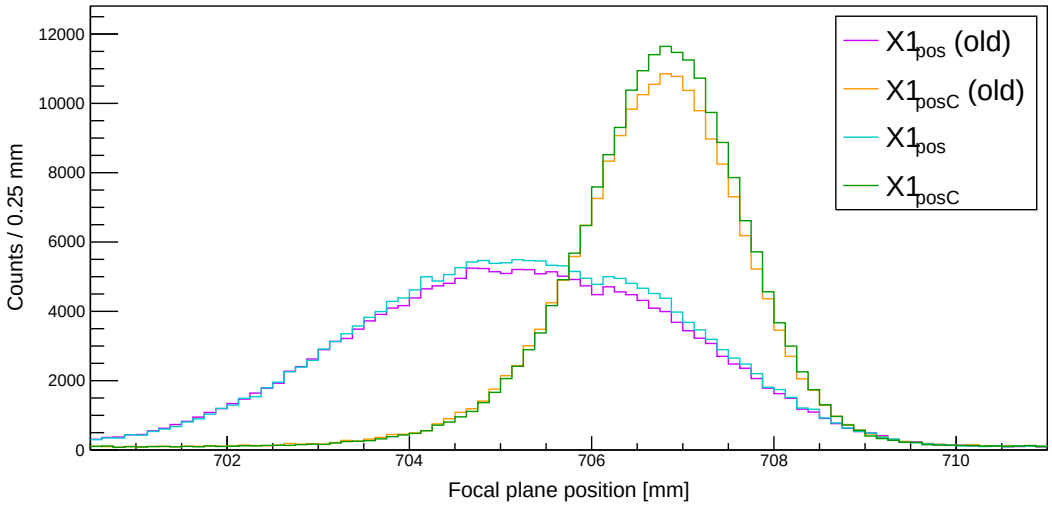

Figure B.23: Comparison of the focal-plane dispersions of $\mathrm{X1_{pos}}$ (old), $\mathrm{X1_{posC}}$ (old), $\mathrm{X1_{pos}}$ and $\mathrm{X1_{posC}}$ for the 4.43982(21) MeV $J^{\pi} = 2^{+}$ resonance in ^{12}C.

Focal-plane Position	Dispersion [mm]	E_x FWHM [keV]
$\mathrm{X1_{pos}}$ (old)	1.910(7)	230(2)
$\mathrm{X1_{posC}}$ (old)	0.768(5)	92(1)
$\mathrm{X1_{pos}}$	1.881(7)	226(2)
$\mathrm{X1_{posC}}$	0.751(4)	90(1)

Table B.8: Summary of the focal-plane dispersions of the X1 wire plane for experiment PR194.

B.5 Experiment PR195, ^{14}C$(p,t)^{12}$C at 21°

B.5.1 SilverBulletRaytrace algorithm

The newly developed SilverBulletRaytrace algorithm offers improvements with respect to the old raytracing algorithm which has thus far been the standard algorithm for analysing VDC data. These improvements are presented in Figure B.24 for weekend 4.

In Figure B.24, the panel labelled (a) shows the spectrum of the old raytrace angle through the X1 wire plane, θ_{RT} (old), versus the old uncorrected focal-plane position, $\mathrm{X1_{pos}}$ (old). The locus at $\mathrm{X1_{pos}}$ (old) ≈ 230 mm exhibits a slight broadening below θ_{RT} (old) $\approx 32°$. In comparison to the ^{12}C$(\alpha,\alpha')^{12}$C reactions in experiments PR166, PR194 and PR251, the tritons from the ^{14}C$(p,t)^{12}$C reaction of this experiment do not induce drastic V structures (see REFERENCE). It is believed that the severity of these V structures is linked to the stopping power of the measured ejectiles which is substantially less for the tritons with respect to the α-particles.

In Figure B.24, the panel labelled (b) shows the spectrum of the old raytrace angle through the X1 wire plane, θ_{RT} (old), versus the new corrected focal-plane position, $\mathrm{X1_{posC}}$. In comparison to the panel labelled (a), the broad structures below θ_{RT} (old) $\theta_{\mathrm{RT}} \approx 32°$ have been eliminated. Moreover, events have been recovered below θ_{RT} (old) 30°. These recovered events would have been rejected by the old raytracing algorithm by failing any of the conditions listed in Ref. [82]. The SilverBulletRaytrace algorithm is able to recover some of these events which likely have anomalous wire hit patterns.

In Figure B.24, the panel labelled (c) shows the spectrum of the new raytrace angle through the X1 wire plane, θ_{RT}, versus the new corrected focal-plane position, $\mathrm{X1_{posC}}$. In general, the raytrace angles in panels (a) and (b) which extend below θ_{RT} (old) $\approx 30°$ are not physical. These lower values are a result of the fact that the perturbing wires of anomalous events typically occur on the periphery of a set of triggered wires. These peripheral wires necessarily lead to an incorrectly lowered raytrace angle. Since SilverBulletRaytrace automatically removes these incorrect peripheral wires from the set of triggered wires that are raytraced, the new raytracing angles are therefore more accurately centered at $\theta_{\mathrm{RT}} \approx 35°$ as the unphysical values below $\theta_{\mathrm{RT}} \approx 32°$ have been remedied.

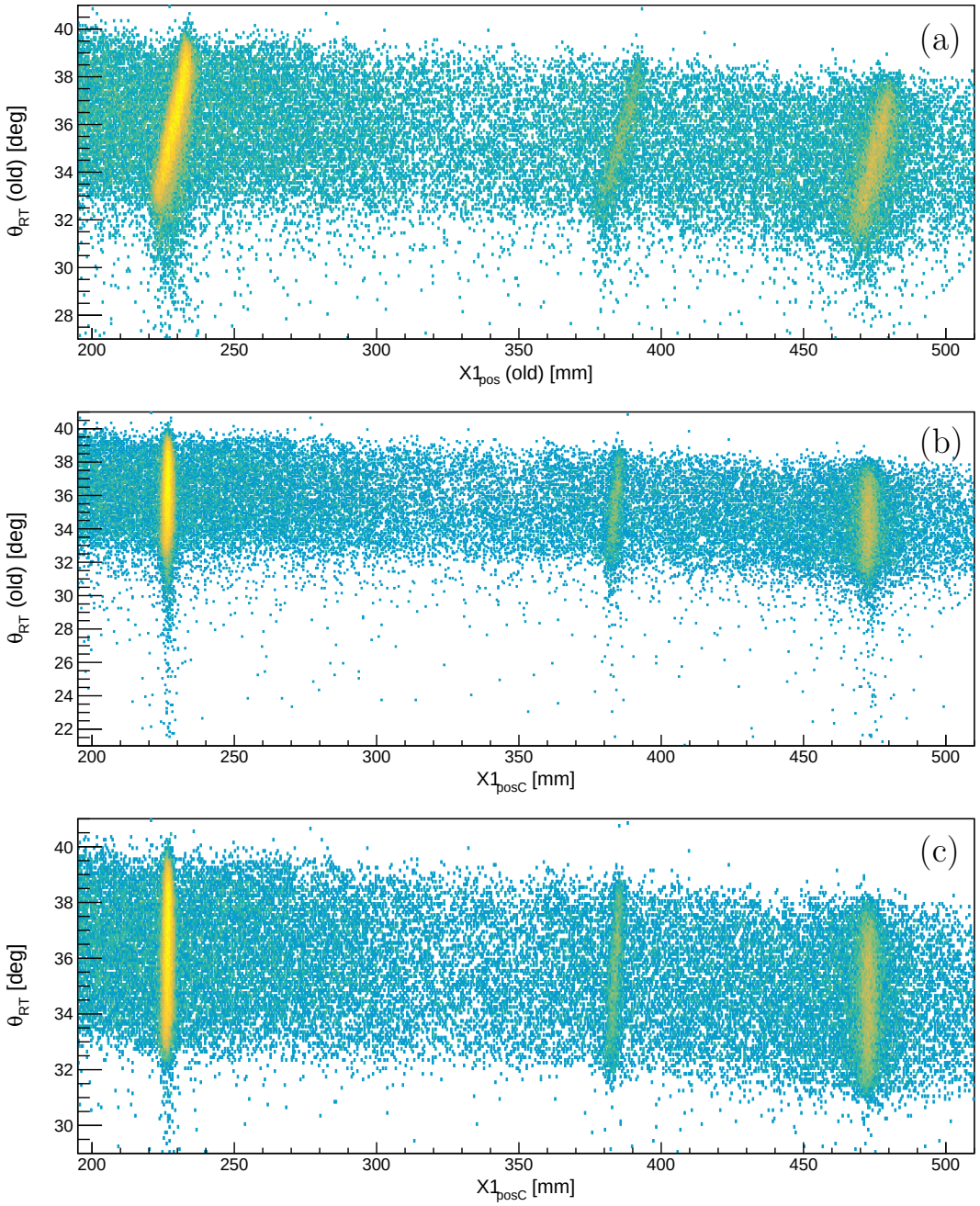

Figure B.24: Comparison of SilverBulletRaytrace against the old raytrace algorithm for weekend 4 of experiment PR195: (a) spectrum of the old raytrace angle (through X1) versus the old uncorrected focal-plane position, (b) spectrum of the old raytrace angle (through X1) versus the new corrected focal-plane position, (c) spectrum of the new raytrace angle (through X1) wire plane versus the new corrected focal-plane position.

Correction Type	Correction Order
TOF	3

Table B.9: Summary of the lineshape corrections for weekend 4 of experiment PR195.

B.5.2 Lineshape corrections for experiment PR195

The lineshape corrections for weekend 4 of experiment PR195 are summarised below in Table B.9 and the corresponding results are presented in Figures B.25 - B.27. The beam-optics for weekend 4 were relative stable and as such, only a single set of lineshape corrections was necessary for this analysis.

As mentioned in section 4.9, the θ_{scat} variable is not directly used for lineshape correction for experiment PR195. The TOF lineshape correction acts as a proxy and Figure B.25 shows that this substitution is effective in removing the θ_{scat} dependence without requiring that a valid θ_{scat} value is determined.

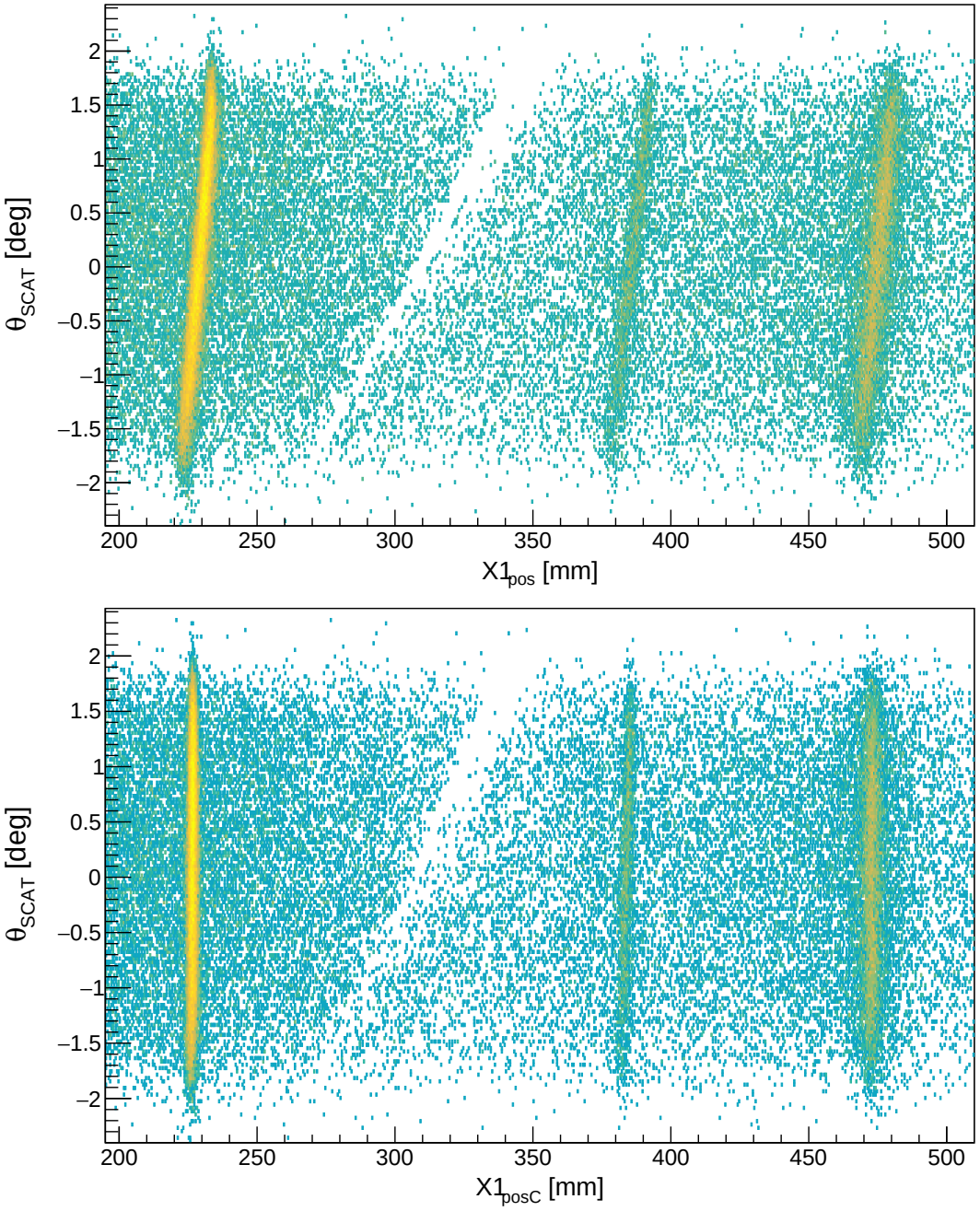

Figure B.25: Lineshape corrections for experiment PR195: $\theta_{\rm scat}$ dependence. The top and bottom panels show the uncorrected and corrected lineshapes, respectively.

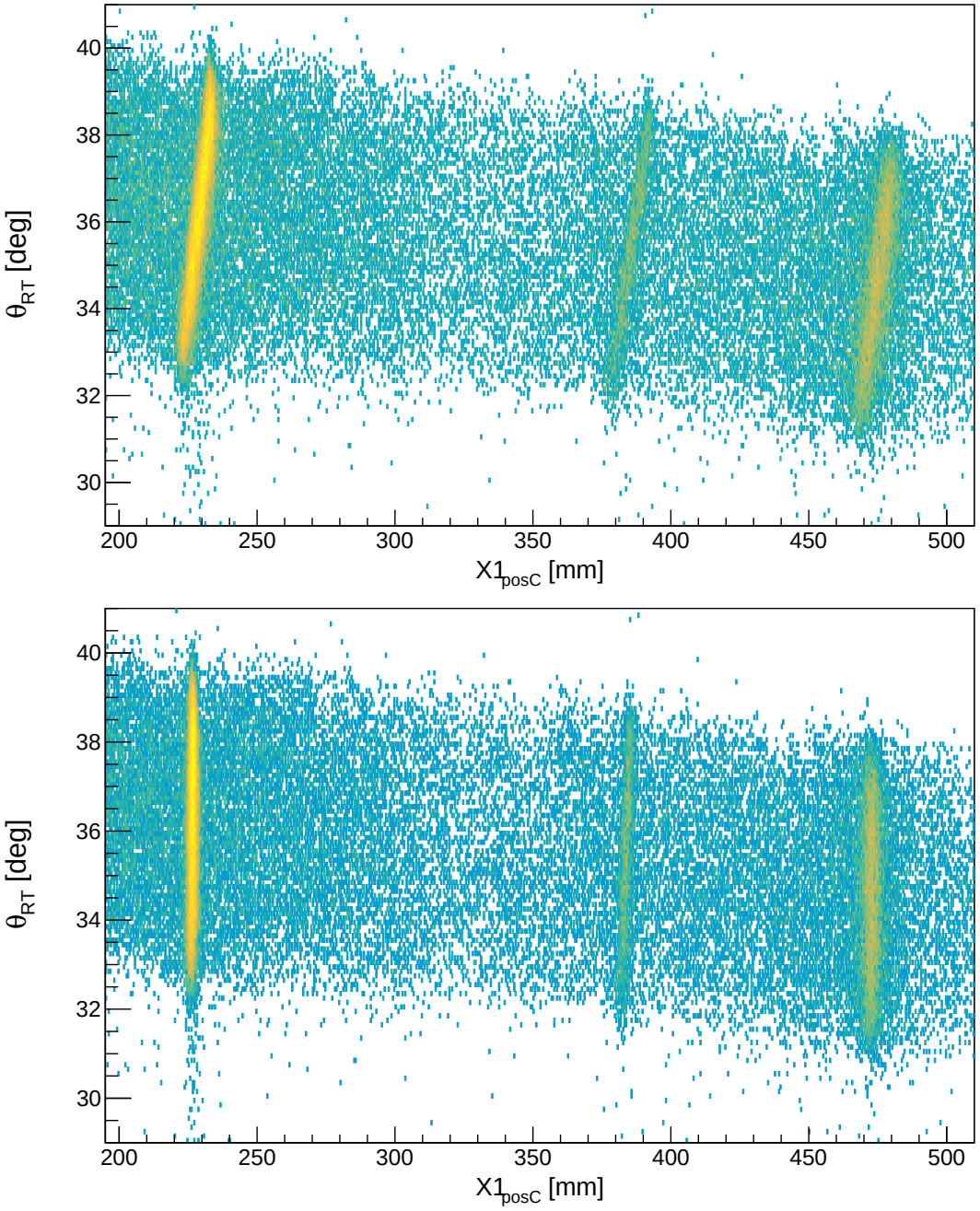

Figure B.26: Lineshape corrections for experiment PR195: θ_{RT} dependence. The top and bottom panels show the uncorrected and corrected lineshapes, respectively.

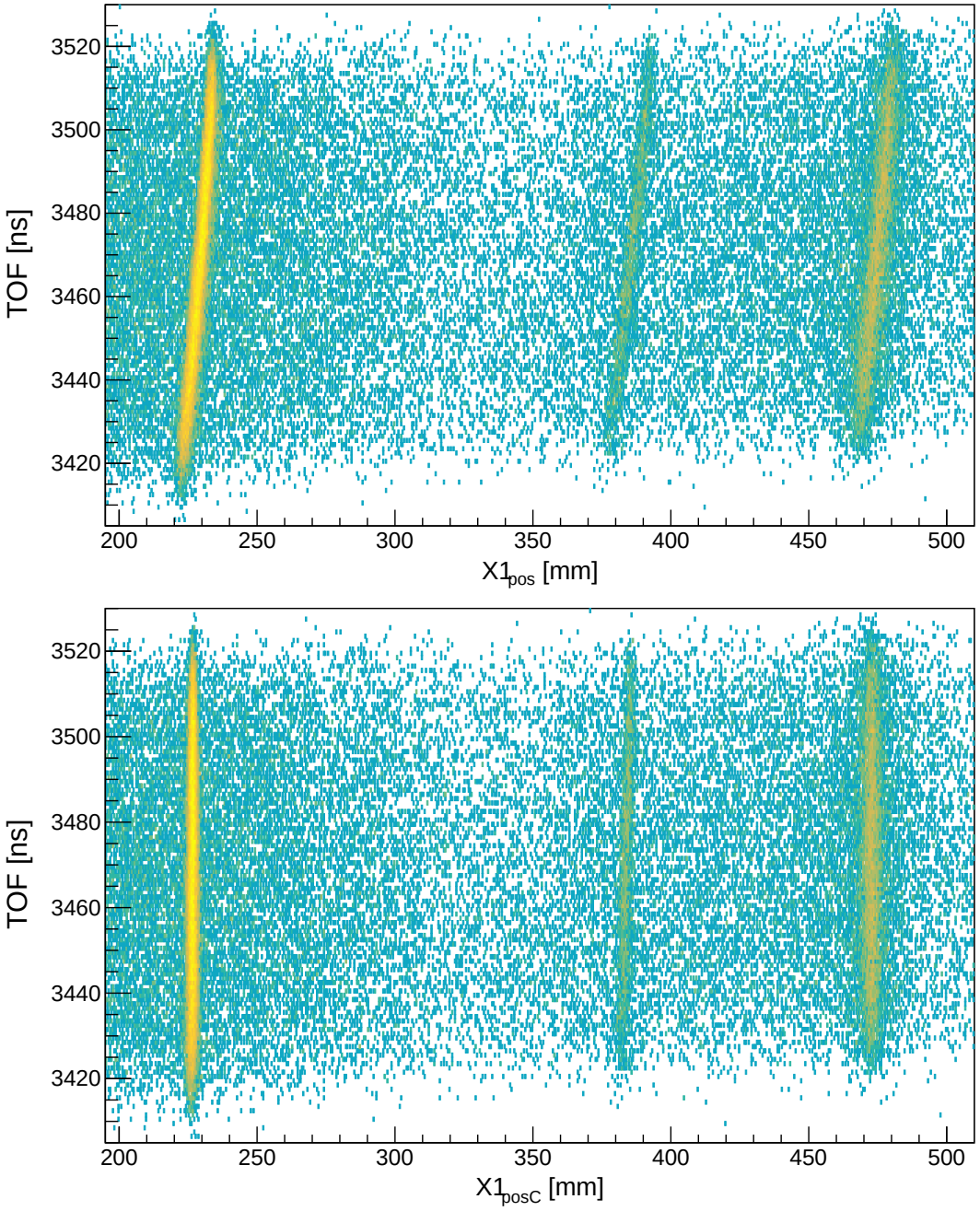

Figure B.27: Lineshape corrections for experiment PR195: TOF dependence. The top and bottom panels show the uncorrected and corrected lineshapes, respectively.

B.5.3 The improvements of the TLC and SBR algorithms for experiment PR195

The improvements of the TLC lineshape correction and the SBR raytracing algorithm are presented in Figure B.28 and summarised in Table B.10. The dispersions are determined directly from the binned data and the intrinsic width of the peaks can be ignored as the corresponding 12.710(6) MeV $J^{\pi} = 1^{+}$ resonance has an intrinsic width of 18.1(28)eV. The lineshape correction with TLC, which maps $X1_{pos}$ to $X1_{posC}$, yields a 71% decrease in the dispersion. The corrected focal-plane position obtained with the new SBR raytracing algorithm, $X1_{posC}$, exhibits an 2% decrease in the dispersion with respect to $X1_{posC}$ (old).

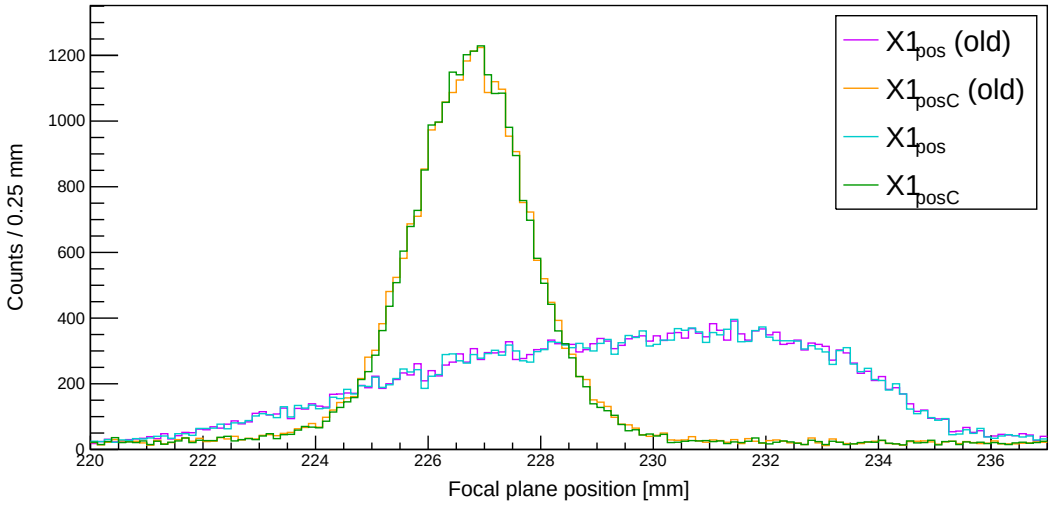

Figure B.28: Comparison of the focal-plane dispersions of $X1_{pos}$ (old), $X1_{posC}$ (old), $X1_{pos}$ and $X1_{posC}$ for the 15.110(3) MeV $J^{\pi} = 1^{+}$ resonance in ^{12}C.

Focal-plane Position	Dispersion [mm]	E_x FWHM [keV]
$X1_{pos}$ (old)	*3.41	*201
$X1_{posC}$ (old)	*1.00	*59.0
$X1_{pos}$	*3.41	*201
$X1_{posC}$	*0.987	*58.1

Table B.10: Summary of the focal-plane dispersions of the X1 wire plane for experiment PR195. *These dispersions/FWHMs are determined directly from the binned data.

B.6 Experiment PR251, ^{12}C$(\alpha,\alpha')^{12}$C at 0°, $E_{\text{beam}} = 118$ MeV

B.6.1 SilverBulletRaytrace algorithm

The newly developed SilverBulletRaytrace algorithm offers improvements with respect to the old raytracing algorithm which has thus far been the standard algorithm for analysing VDC data, as shown in Figure B.29.

Panel (a) in Figure B.29, shows the spectrum of the old raytrace angle through the X1 wire plane, θ_{RT} (old), versus the old uncorrected focal-plane position, X1_{pos} (old). It is observed that V-shaped structures extend downwards from the loci of the well-resolved resonances. These V structures are indicative of a raytracing artefact that broadens in the focal-plane spectrum in a non-Gaussian manner which worsens the resolution.

Panel (b) in Figure B.29, shows the spectrum of the old raytrace angle through the X1 wire plane, θ_{RT} (old), versus the new corrected focal-plane position, X1_{posC}. In comparison to the panel (a), the V structures have been eliminated. Moreover, events have been recovered below θ_{RT} (old) $\approx 20°$. These recovered events would have been rejected by the old raytracing algorithm by failing any of the conditions listed in Ref. [82]. The SilverBulletRaytrace algorithm is able to recover some of these events which likely have anomalous wire hit patterns.

Panel (c) in Figure B.29, shows the spectrum of the new raytrace angle through the X1 wire plane, θ_{RT}, versus the new corrected focal-plane position, X1_{posC}. In general, the raytrace angles in panels (a) and (b) which extend below θ_{RT} (old) $\approx 25°$ are not physical. These lower values are a result of the fact that the perturbing wires of anomalous events typically occur on the periphery of a set of triggered wires. These peripheral wires necessarily lead to an incorrectly lowered raytrace angle. Since SilverBulletRaytrace automatically removes these incorrect peripheral wires from the set of triggered wires that are raytraced, the new raytracing angles are therefore more accurately centered at $\theta_{\text{RT}} \approx 31°$ as the unphysical values below $\theta_{\text{RT}} \approx 26°$ have been remedied.

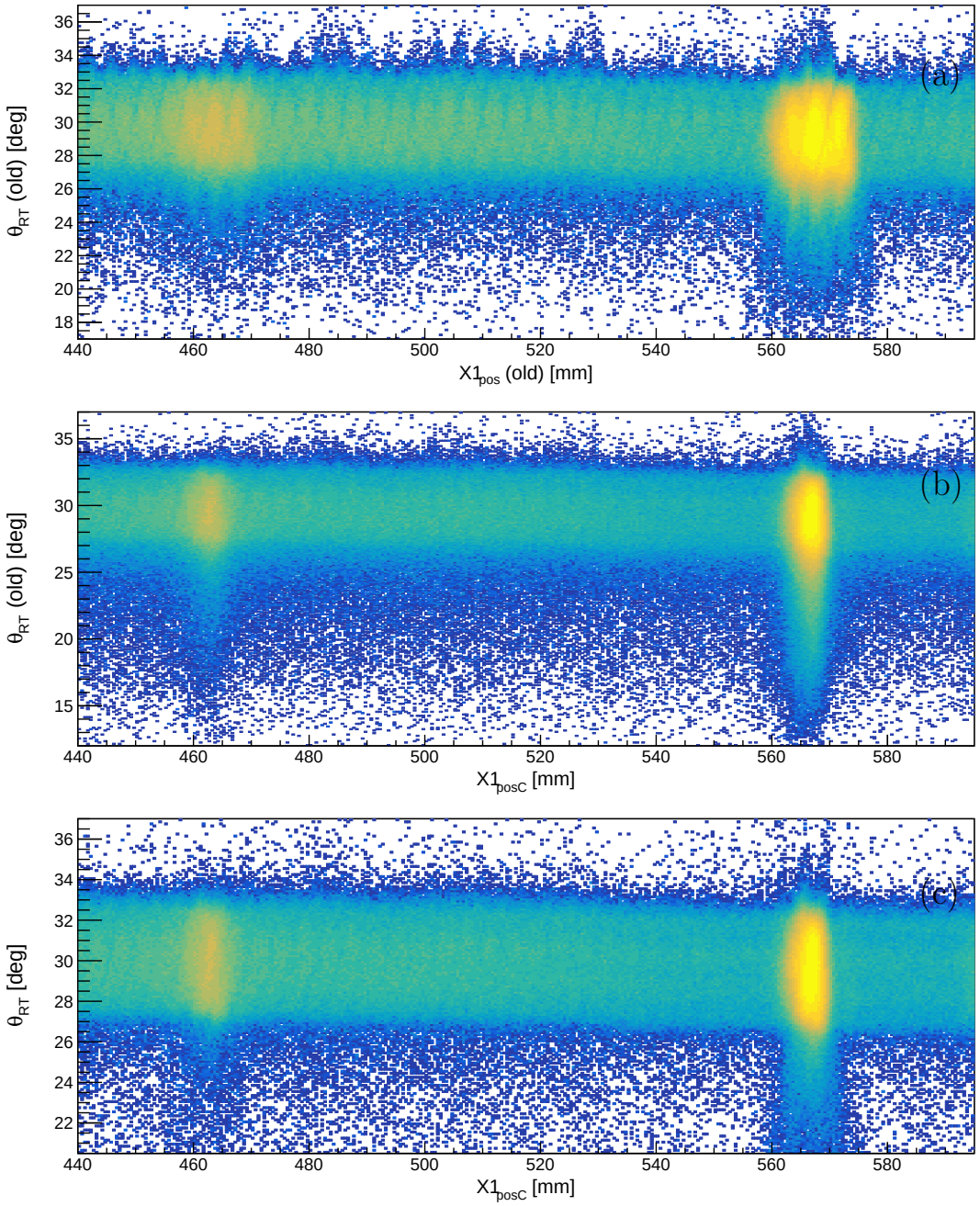

Figure B.29: Comparison of SilverBulletRaytrace against the old raytrace algorithm for experiment PR251: (a) spectrum of the old raytrace angle (through X1) versus the old uncorrected focal-plane position, (b) spectrum of the old raytrace angle (through X1) versus the new corrected focal-plane position, (c) spectrum of the new raytrace angle (through X1) wire plane versus the new corrected focal-plane position.

B.6.2 Lineshape corrections for experiment PR251

The lineshape corrections for experiment PR251 are summarised below in Table B.11 and the corresponding results are presented in Figures B.30 - B.31.

The beam-optics for experiment PR251 exhibited substantial changes and as such, the lineshape corrections were run-dependent. The run numbers are listed in Table B.11 for historical reference.

Run Numbers	Correction Type	Correction Order
2040 - 2056	TOF	2
	TOF	3
	$Y1_{pos}$	1
	$Y1_{pos}$	1
	$Y1_{pos}$	1
2075 - 2076	TOF	2
	TOF	3
	$Y1_{pos}$	1
	$Y1_{pos}$	1
2097 - 2109	TOF	2
	TOF	3
	$Y1_{pos}$	1
	$Y1_{pos}$	1
	TOF	1

Table B.11: Summary of the lineshape corrections for experiment PR251. The iterative corrections are listed in order of their application.

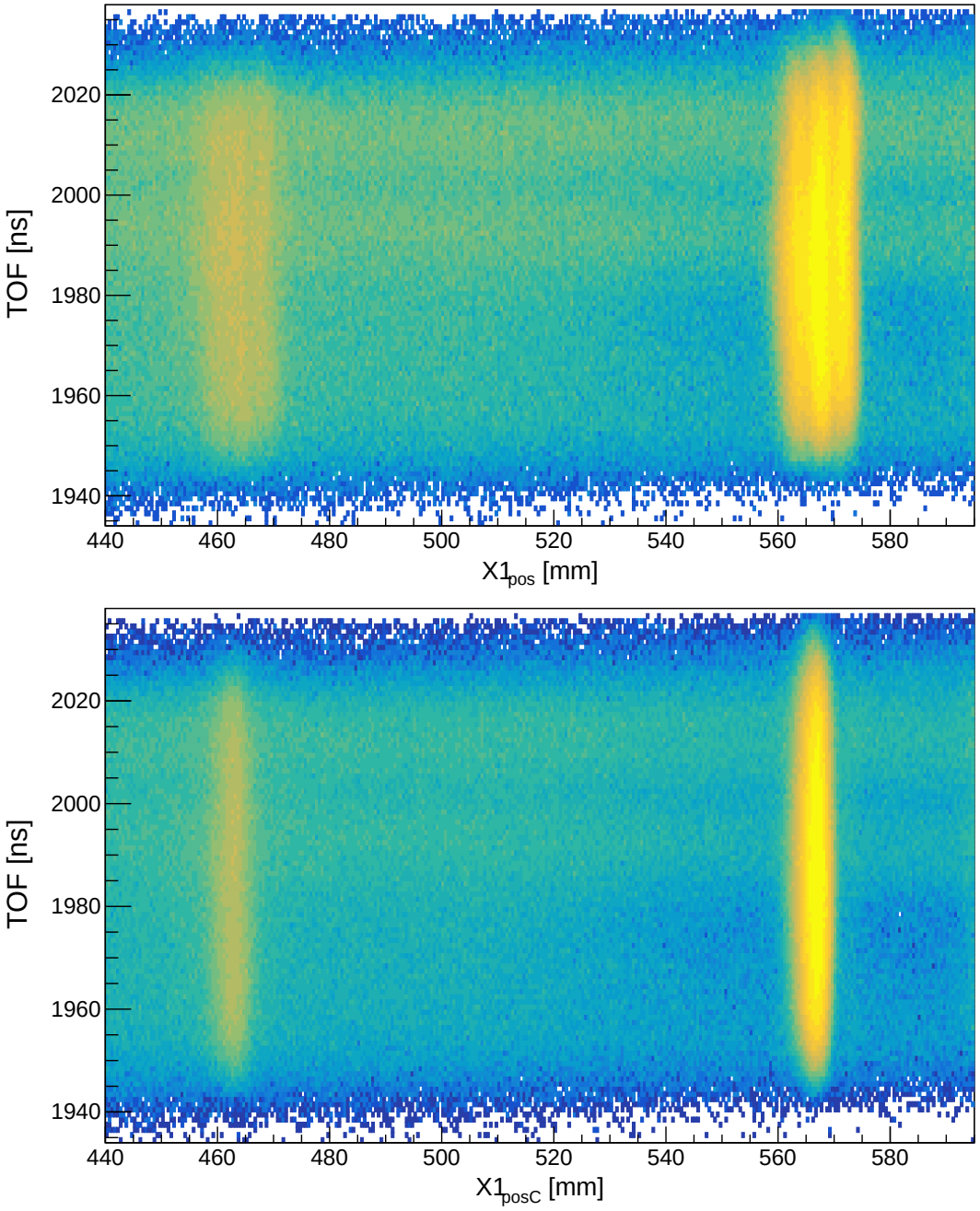

Figure B.30: Lineshape corrections for experiment PR251: TOF dependence. The top and bottom panels show the uncorrected and corrected lineshapes, respectively.

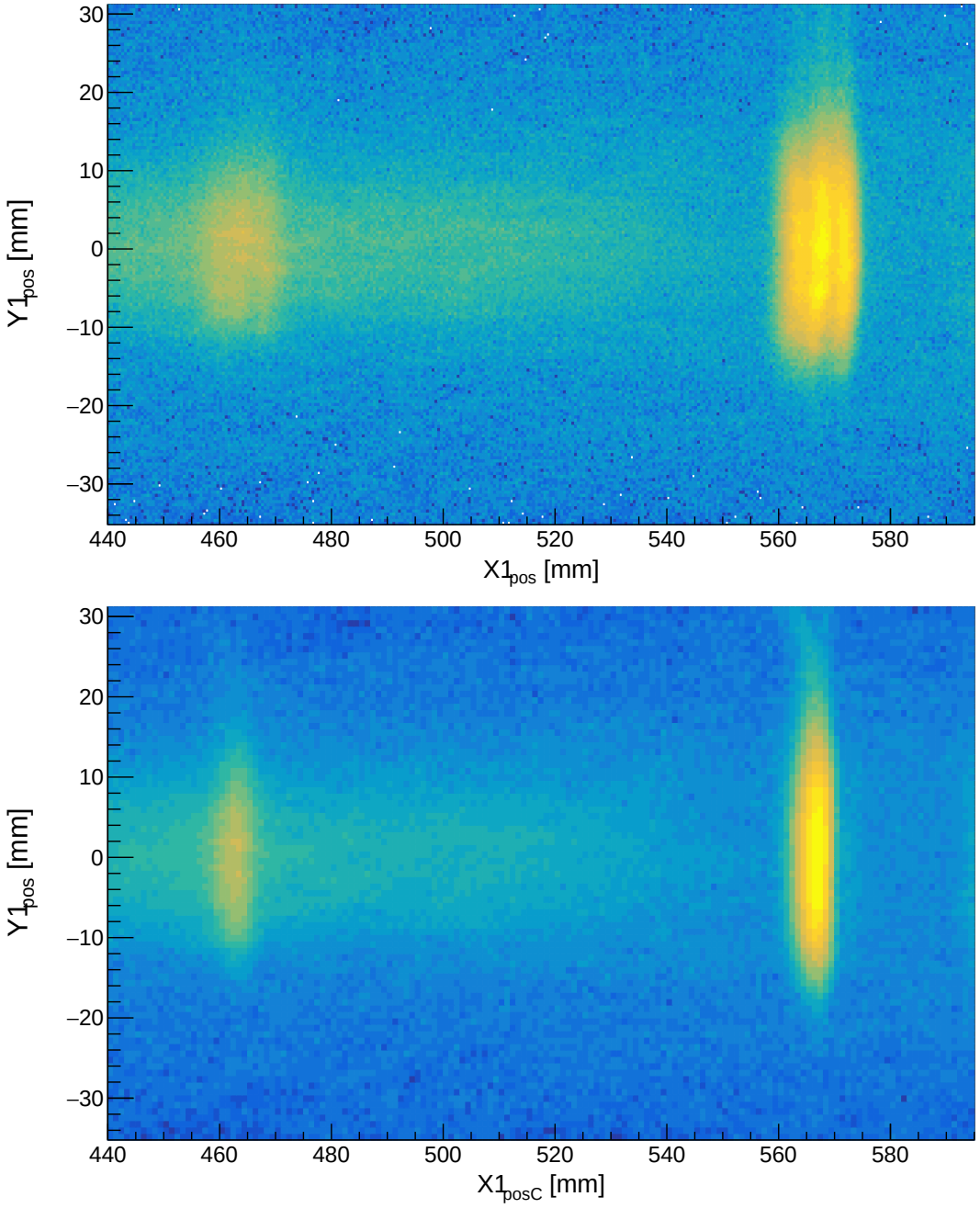

Figure B.31: Lineshape corrections for experiment PR251: $Y1_{pos}$ dependence. The top and bottom panels show the uncorrected and corrected lineshapes, respectively.

B.6.3 The improvements of the TLC and SBR algorithms

The improvements of the TLC lineshape correction and the SBR raytracing algorithm are presented in Figure B.32 and summarised in Table B.12. The lineshape correction with TLC, which maps $X1_{pos}$ to $X1_{posC}$, yields a 73% decrease in the dispersion. The corrected focal-plane position obtained with the new SBR raytracing algorithm, $X1_{posC}$, exhibits a 5(2)% decrease in the dispersion with respect to $X1_{posC}$ (old).

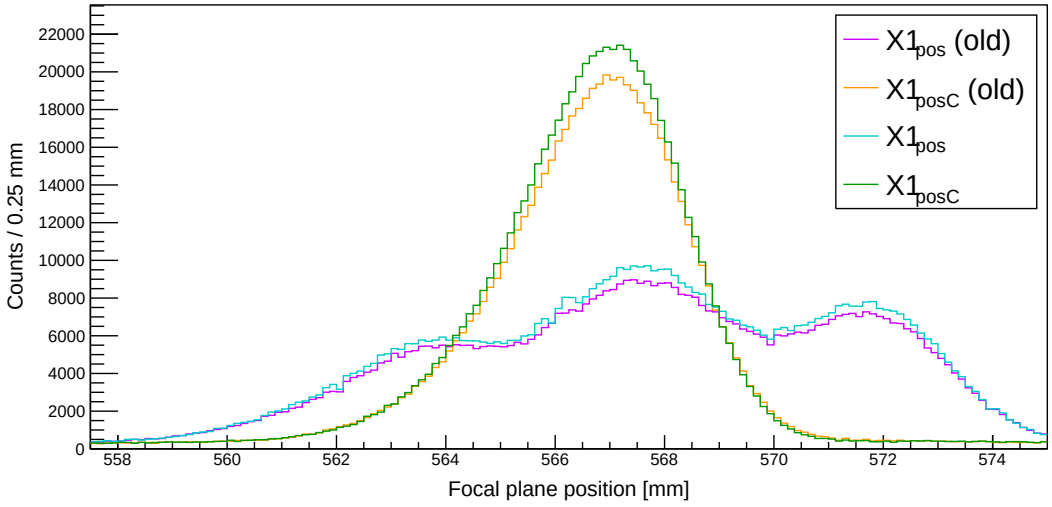

Figure B.32: Comparison of the focal-plane dispersions of $X1_{pos}$ (old), $X1_{posC}$ (old), $X1_{pos}$ and $X1_{posC}$.

Focal-plane Position	Dispersion [mm]	E_x FWHM [keV]
$X1_{pos}$ (old)	3.67*	330*
$X1_{posC}$ (old)	1.05(2)	95(4)
$X1_{pos}$	3.65*	328*
$X1_{posC}$	1.00(2)	90(3)

Table B.12: Summary of the focal-plane dispersions of the X1 wire plane for experiment PR251. *These values were not determined through a fit, but directly from the binned data as the uncorrected focal-plane positions ($X1_{pos}$ and $X1_{posC}$) yield highly irregular lineshapes.

Appendix C

Reaction Calculations

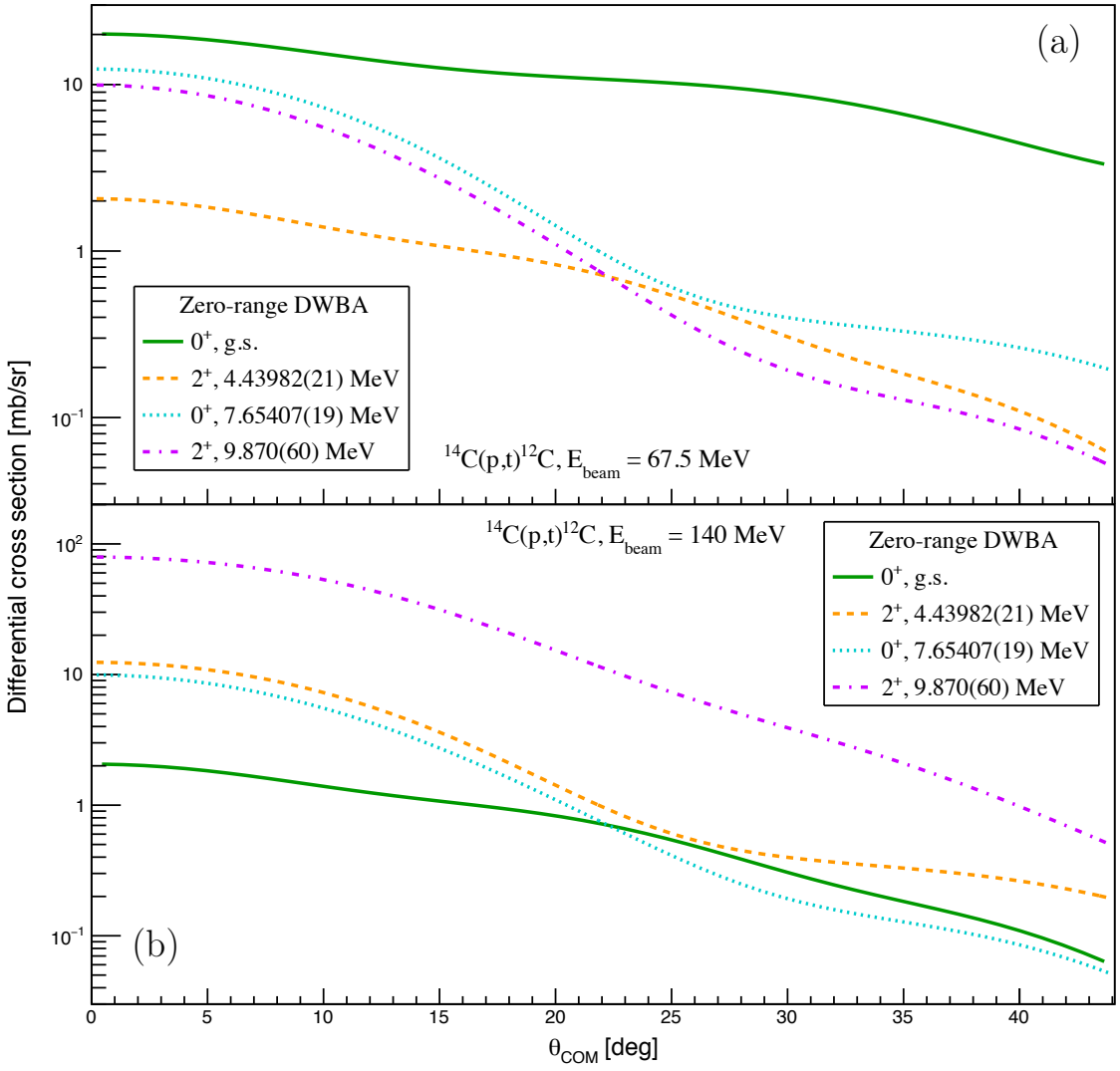

Figure C.1: The differential cross sections for the 0^+_1, 2^+_1, 0^+_2 and 2^+_2 states populated through the $^{14}\mathrm{C}(p,t)^{12}\mathrm{C}$ reaction for experiments PR195 (a) and PR240 (b) with coupling scheme 1.

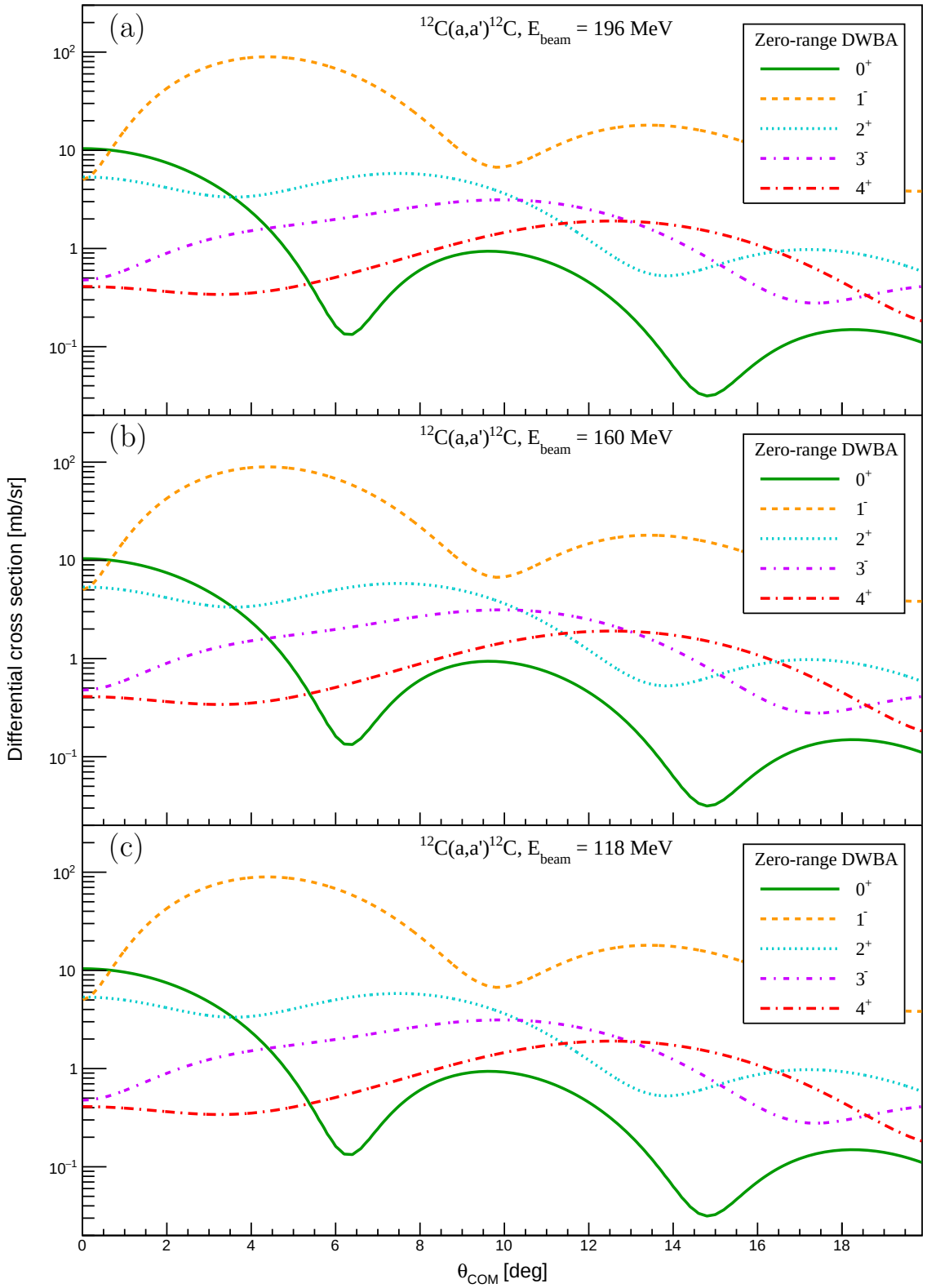

Figure C.2: The differential cross sections for 0^+, 1^-, 2^+, 3^- and 4^+ states populated through the $^{12}C(\alpha, \alpha')^{12}C$ reaction for experiments PR166 (a), PR194 (b) and PR251 (c).

List of References

[1] Chie Kurokawa and Kiyoshi Katō. Spectroscopy of 12c within the boundary condition for three-body resonant states. *Nuclear Physics A*, 792(1):87–101, 2007.

[2] George B. Kaufman. Inorganic chemistry: principles of structure and reactivity, 4th ed. (huheey, james e.; keiter, ellen a.; keiter, richard l.). *Journal of Chemical Education*, 70(10):A279, 10 1993.

[3] F. X. Hu, G. X. Wu, G. X. Song, Q. R. Yuan, and S. Okamura. Orientation of galaxies in the local supercluster: A review. *Astrophysics and Space Science*, 302(1):43–59, Apr 2006.

[4] Bose S.N. Plancks gesetz und lichtquantenhypothese. *Zeitschrift für Physik*, 26:178, (1924).

[5] A. Einstein. Quantentheorie des einatomigen idealen gases. *Sitzungsberichte der Preussischen Akademie der Wissenschaften*, 1:3, (1925).

[6] L.R. Hafstad and E. Teller. The alpha-particle model of the nucleus. *Phys. Rev.*, 54, (1938).

[7] D.M. Brink and E. Boeker. The alpha-particle model of the nucleus. *Nuclear Physics A*, 91, (1967).

[8] M. Freer and H.O.U. Fynbo. The Hoyle state in 12C. *Progress in Particle and Nuclear Physics*, 78:1 – 23, 2014.

[9] Hans O. U. Fynbo, Christian Aa. Diget, Uffe C. Bergmann, Maria J. G. Borge, Joakim Cederkäll, Peter Dendooven, Luis M. Fraile, Serge Franchoo, Valentin N. Fedosseev, Brian R. Fulton, Wenxue Huang, Jussi Huikari, Henrik B. Jeppesen, Ari S. Jokinen, Peter Jones, Björn Jonson, Ulli Köster, Karlheinz Langanke, Mikael Meister, Thomas Nilsson, Göran Nyman, Yolanda Prezado, Karsten Riisager, Sami Rinta-Antila, Olof Tengblad, Manuela Turrion, Youbao Wang, Leonid Weissman, Katarina Wilhelmsen, Juha Äystö, and The ISOLDE Collaboration. Revised rates for the stellar triple-α process from measurement of 12c nuclear resonances. *Nature*, 433:136 EP –, 01 2005.

[10] National Nuclear Data Center. *Nuclear Science References*, version of (2015). Information extracted from the NSR database http://www.nndc.bnl.gov/ensdf.

[11] M.N. Harakeh S. Brandenburg, A.G. Drentje and A. van der Woude. Kvi annual report, monopole excitation in ^{12}C. (1983).

[12] M.N. Harakeh. *Private communications.*

[13] M. Itoh, H. Akimune, M. Fujiwara, U. Garg, N. Hashimoto, T. Kawabata, K. Kawase, S. Kishi, T. Murakami, K. Nakanishi, Y. Nakatsugawa, B. K. Nayak, S. Okumura, H. Sakaguchi, H. Takeda, S. Terashima, M. Uchida, Y. Yasuda, M. Yosoi, and J. Zenihiro. Candidate for the 2^+ excited Hoyle state at $E_x \sim 10$ Mev in ^{12}C. *Phys. Rev. C*, 84:054308, Nov 2011.

[14] M. Itoh, H. Akimune, M. Fujiwara, U. Garg, H. Hashimoto, T. Kawabata, K. Kawase, S. Kishi, T. Murakami, K. Nakanishi, Y. Nakatsugawa, B.K. Nayak, H. Sakaguchi, S. Terashima, M. Uchida, Y. Yasuda, M. Yosoi, and J. Zenihiro. Cluster structure of broad resonances near threshold in 12c and 16o. *Journal of Physics: Conference Series*, 569:012009, Dec 2014.

[15] B. Mouginot, E. Khan, R. Neveling, F. Azaiez, E. Z. Buthelezi, S. V. Förtsch, S. Franchoo, H. Fujita, J. Mabiala, J. P. Mira, P. Papka, A. Ramus, J. A. Scarpaci, F. D. Smit, I. Stefan, J. A. Swartz, and I. Usman. Search for the giant pairing vibration through (p,t) reactions around 50 and 60 mev. *Phys. Rev. C*, 83:037302, Mar 2011.

[16] Martin Freer, Hisashi Horiuchi, Yoshiko Kanada-En'yo, Dean Lee, and Ulf-G. Meißner. Microscopic clustering in light nuclei. *Rev. Mod. Phys.*, 90:035004, Aug 2018.

[17] Evgeny Epelbaum, Hermann Krebs, Dean Lee, and Ulf-G. Meißner. Ab initio calculation of the hoyle state. *Phys. Rev. Lett.*, 106:192501, May 2011.

[18] S. Hyldegaard, M. Alcorta, B. Bastin, M. J. G. Borge, R. Boutami, S. Brandenburg, J. Büscher, P. Dendooven, C. Aa. Diget, P. Van Duppen, T. Eronen, S. P. Fox, L. M. Fraile, B. R. Fulton, H. O. U. Fynbo, J. Huikari, M. Huyse, H. B. Jeppesen, A. S. Jokinen, B. Jonson, K. Jungmann, A. Kankainen, O. S. Kirsebom, M. Madurga, I. Moore, A. Nieminen, T. Nilsson, G. Nyman, G. J. G. Onderwater, H. Penttilä, K. Peräjärvi, R. Raabe, K. Riisager, S. Rinta-Antila, A. Rogachevskiy, A Saastamoinen, M. Sohani, O. Tengblad, E. Traykov, Y. Wang, K. Wilhelmsen, H. W. Wilschut, and J. Äystö. r-matrix analysis of the β decays of ^{12}N and ^{12}B. *Phys. Rev. C*, 81:024303, Feb 2010.

[19] R. Álvarez-Rodríguez, E. Garrido, A. S. Jensen, D. V. Fedorov, and H. O. U. Fynbo. Structure of low-lying 12c resonances. *The European Physical Journal A*, 31(3):303–317, Mar 2007.

[20] M.N. Harakeh and A. van der Woude. *Giant Resonances: Fundamental High-Frequency Modes of Nuclear Excitation.* (2001).

[21] E. Khan. *Giant Resonances and Isospin Asymmetry.* Ecole Joliot-Curie, (2010).

[22] M. Vandebrouck, J. Gibelin, E. Khan, N. L. Achouri, H. Baba, D. Beaumel, Y. Blumenfeld, M. Caamaño, L. Càceres, G. Colò, F. Delaunay, B. Fernandez-Dominguez, U. Garg, G. F. Grinyer, M. N. Harakeh, N. Kalantar-Nayestanaki, N. Keeley, W. Mittig, J. Pancin, R. Raabe, T. Roger, P. Roussel-Chomaz, H. Savajols, O. Sorlin, C. Stodel, D. Suzuki, and J. C. Thomas. Measurement of the isoscalar monopole response in the neutron-rich nucleus ^{68}Ni. *Phys. Rev. Lett.*, 113:032504, Jul 2014.

[23] A. Bracco, E. G. Lanza, and A. Tamii. Isoscalar and isovector dipole excitations: Nuclear properties from low-lying states and from the isovector giant dipole resonance. *Prog. Part. Nucl. Phys.*, 106:360–433, 2019.

[24] J. Piekarewicz. Emergence of low-energy monopole strength in the neutron-rich calcium isotopes. *Phys. Rev. C*, 96:044314, Oct 2017.

[25] D. Vretenar, Y. F. Niu, N. Paar, and J. Meng. Low-energy isovector and isoscalar dipole response in neutron-rich nuclei. *Phys. Rev. C*, 85:044317, Apr 2012.

[26] Umesh Garg and Gianluca Colò. The compression-mode giant resonances and nuclear incompressibility. *Progress in Particle and Nuclear Physics*, 101:55–95, 2018.

[27] R.G.T. Zegers. *Ph.D. thesis, University of Groningen*, 1999.

[28] A. Ono, H. Horiuchi, T. Maruyama, and A. Ohnishi. Fragment formation studied with antisymmetrized version of molecular dynamics with two-nucleon collisions. *Phys. Rev. Lett.*, 68:2898–2900, May 1992.

[29] Akira Ono, Hisashi Horiuchi, Toshiki Maruyama, and Akira Ohnishi. Antisymmetrized Version of Molecular Dynamics with Two-Nucleon Collisions and Its Application to Heavy Ion Reactions. *Progress of Theoretical Physics*, 87(5):1185–1206, 05 1992.

[30] Structure of light unstable nuclei studied with antisymmetrized molecular dynamics. *Progress of Theoretical Physics Supplement*, 142, 2001.

[31] Yoshiko Kanada-En'yo, Hisashi Horiuchi, and Akira Ono. Structure of li and be isotopes studied with antisymmetrized molecular dynamics. *Phys. Rev. C*, 52:628–646, Aug 1995.

[32] Yoshiko Kanada-En'yo and Hisashi Horiuchi. Neutron-rich b isotopes studied with antisymmetrized molecular dynamics. *Phys. Rev. C*, 52:647–662, Aug 1995.

[33] Tadahiro Suhara and Yoshiko Kanada-En'yo. Quadrupole Deformation β and γ Constraint in a Framework of Antisymmetrized Molecular Dynamics. *Progress of Theoretical Physics*, 123(2):303–325, 02 2010.

[34] H. Feldmeier. Fermionic molecular dynamics. *Nuclear Physics A*, 515(1):147 – 172, 1990.

[35] H. Feldmeier, K. Bieler, and J. Schnack. Fermionic molecular dynamics for ground states and collisions of nuclei. *Nuclear Physics A*, 586(3):493 – 532, 1995.

[36] H. Feldmeier and J. Schnack. Fermionic molecular dynamics scv252scv133 v2. *Progress in Particle and Nuclear Physics*, 39:393 – 442, 1997.

[37] T. Neff and H. Feldmeier. Cluster structures within fermionic molecular dynamics. *Nuclear Physics A*, 738:357 – 361, 2004. Proceedings of the 8th International Conference on Clustering Aspects of Nuclear Structure and Dynamics.

[38] M. Chernykh, H. Feldmeier, T. Neff, P. von Neumann-Cosel, and A. Richter. Structure of the hoyle state in ^{12}C. *Phys. Rev. Lett.*, 98:032501, Jan 2007.

[39] T. Furuta, K. H. O. Hasnaoui, F. Gulminelli, C. Leclercq, and A. Ono. Monopole oscillations in light nuclei with a molecular dynamics approach. *Physical Review C*, 82(3), 2010.

[40] Sakae Saito. Effect of Pauli Principle in Scattering of Two Clusters. *Progress of Theoretical Physics*, 40(4):893–894, 10 1968.

[41] Sakae Saito. Interaction between Clusters and Pauli Principle*). *Progress of Theoretical Physics*, 41(3):705–722, 03 1969.

[42] Sakae Saito. *Progress of Theoretical Physics*, 62.

[43] E. Balslev and J.M. Combes. *Commun. Math. Phys.*, 22:280–294, 1971.

[44] I.W. Herbst and J.S. Howland. *Commun. Math. Phys.*, 80:23–42, 1981.

[45] Eiji Uegaki, Yasuhisa Abe, Shigetō Okabe, and Hajime Tanaka. Structure of the Excited States in 12C. II. *Progress of Theoretical Physics*, 62(6):1621–1640, 12 1979.

[46] Bo Zhou, Akihiro Tohsaki, Hisashi Horiuchi, and Zhongzhou Ren. Breathing-like excited state of the hoyle state in ^{12}C. *Phys. Rev. C*, 94:044319, Oct 2016.

[47] A. M. Lane and R. G. Thomas. R-matrix theory of nuclear reactions. *Rev. Mod. Phys.*, 30:257–353, Apr (1958).

[48] R. Imai, T. Tada, and M. Kimura. Real-time evolution method and its application to the 3α cluster system. *Phys. Rev. C*, 99:064327, Jun 2019.

[49] E. P. Wigner and L. Eisenbud. Higher angular momenta and long range interaction in resonance reactions. *Phys. Rev.*, 72:29–41, Jul (1947).

[50] P Descouvemont and D Baye. TheR-matrix theory. *Reports on Progress in Physics*, 73(3):036301, feb 2010.

[51] Niels Bohr. Neutron capture and nuclear constitution. *Nature*, 137(3461):344–348, 1936.

[52] S. N. Ghoshal. An experimental verification of the theory of compound nucleus. *Phys. Rev.*, 80:939–942, Dec 1950.

[53] F.C. Barker. Consistent description of unbound states observed in scattering and reactions. *Australian Journal of Physics*, 41(6):743–764, 1988.

[54] J. H. Kelley, J. E. Purcell, and C. G. Sheu. Energy levels of light nuclei A = 12. *Nucl. Phys.*, A968:71–253, 2017.

[55] D. N. F. Dunbar, R. E. Pixley, W. A. Wenzel, and W. Whaling. The 7.68-mev state in c^{12}. *Phys. Rev.*, 92:649–650, Nov 1953.

[56] Thompson I.J. and Nunes F.M. *Nuclear Reactions for Astrophysics*. Cambridge University Press, New York, (2009).

[57] Iliadis C. *Nuclear Physics of Stars*. Wiley-VCH, Verlag, (2007).

[58] Griffiths D.J. *Introduction to Quantum Mechanics*. Pearson Prentice Hall, Upper Saddle River, NJ, (2005).

[59] G. Breit and M. E. Ebel. Nucleon transfer and virtual coulomb excitation. *Phys. Rev.*, 104:1030–1046, Nov 1956.

[60] M. Abramowitz and Stegun I.A. *Handbook of mathematical functions, with formulas, graphs, and mathematical tables*. Dover Publications, New York, (1965).

[61] Merzbacher E. *Quantum Mechanics*. John Wiley & Sons, New York, (1965).

[62] F.C. Barker. Interference between levels in nuclear reactions. *Australian Journal of Physics*, 20(3):341–344, 1967.

[63] Eugene P. Wigner. Lower limit for the energy derivative of the scattering phase shift. *Phys. Rev.*, 98:145–147, Apr 1955.

[64] L. Eisenbud. *Thesis, Princeton*, (1948).

[65] F. C. Barker, G. M. Crawley, P. S. Miller, and W. F. Steele. The ghost anomaly in the ^{9}Be(p, d)^{8}Be reaction. *Australian Journal of Physics*, 29:245, August 1976.

[66] A. Szczurek and K. Bodek and L. Jarczyk and J. Krug and J. Krug and W. Lübcke and H. Lübcke and H. Rühl and M. Steinke and M. Stephan and D. Kamke and A. Strzałkowski. Ghost anomaly and first excited state of 8Be in the ^{9}Be(d,tα)^{4}He reaction at 7 MeV. *Nuclear Physics A*, 531(1):77 – 92, 1991.

[67] S. Hyldegaard, C. Forssén, C. Aa. Diget, M. Alcorta, F. C. Barker, B. Bastin, M. J. G. Borge, R. Boutami, S. Brandenburg, J. Büscher, P. Dendooven, P. Van Duppen, T. Eronen, S. Fox, B. R. Fulton, H. O. U. Fynbo, J. Huikari, M. Huyse, H. B. Jeppesen, A. Jokinen, B. Jonson, K. Jungmann, A. Kankainen, O. Kirsebom, M. Madurga, I. Moore, P. Navrátil, T. Nilsson, G. Nyman, G. J. G. Onderwater, H. Penttilä, K. Peräjärvi, R. Raabe, K. Riisager, S. Rinta-Antila, A. Rogachevskiy, A. Saastamoinen, M. Sohani, O. Tengblad, E. Traykov, J. P. Vary, Y. Wang, K. Wilhelmsen, H. W. Wilschut, and J. Äystö. Precise branching ratios to unbound ^{12}C states from ^{12}N and ^{12}B β-decays. *Physics Letters B*, 678(5):459 – 464, 2009.

[68] L. Buchmann, E. Gete, J. C. Chow, J. D. King, and D. F. Measday. $\beta-$delayed particle decay of ^{9}C and the $a = 9$, $t = 1/2$ nuclear system: $r-$matrix fits, the $a = 9$ nuclear system, and the stellar reaction rate of ^{4}He$(\alpha n, \gamma)^{9}$Be. *Phys. Rev. C*, 63:034303, Feb 2001.

[69] J. Mabiala, A. A. Cowley, S. V. Förtsch, E. Z. Buthelezi, R. Neveling, F. D. Smit, G. F. Steyn, and J. J. Van Zyl. Analyzing power and cross section distributions of the ^{12}C$(p, p\alpha)^{8}$Be cluster knockout reaction at an incident energy of 100 mev. *Phys. Rev. C*, 79:054612, May 2009.

[70] N.K. Glendenning. *Direct Nuclear Reactions.* (2004).

[71] P.D. Kunz. *CHUCK3, Coupled Channels Programme.* University of Colorado.

[72] M. Nolte, H. Machner, and J. Bojowald. Global optical potential for α particles with energies above 80 mev. *Phys. Rev. C*, 36:1312–1316, Oct 1987.

[73] M. Yasue, M.H. Tanaka, T. Hasegawa, K. Nisimura, S. Kubono, H. Ohnuma, H. Shimizu, K. Ieki, H. Toyokawa, M. Iwase, J. Iimura, H. Yoshida, T. Nakagawa, A. Sato, T. Niizeki, J. Takamatsu, Y. Takahashi, T. Tohei, H. Orihara, T. Suehiro, S.I. Hayakawa, and M. Igarashi. Systematic enhancement for the ^{14}C$(p, t)^{12}$C reaction leading to the $t = 0$ states. *Nuclear Physics A*, 510(2):285 – 300, 1990.

[74] D.G. Madland. Oecd/nea spec. mtg. nucleon-nucleus opt.mod.to 200 mev,paris (1997) p.129.

[75] D. Y. Pang, P. Roussel-Chomaz, H. Savajols, R. L. Varner, and R. Wolski. Global optical model potential for $a = 3$ projectiles. *Phys. Rev. C*, 79:024615, Feb 2009.

[76] M.N. Harakeh. *FORMF.*

[77] C. J. Joachain. *Quantum Collision Theory.* (1983).

[78] R. De Leo, G. D'Erasmo, A. Pantaleo, M. N. Harakeh, E. Cereda, S. Micheletti, and M. Pignanelli. Inelastic proton scattering at 30-40 mev from ^{12}C. *Phys. Rev. C*, 28:1443–1454, Oct 1983.

[79] M. Kumar Raju, J. N. Orce, P. Navrátil, G. C. Ball, T. E. Drake, S. Triambak, G. Hackman, C. J. Pearson, K. J. Abrahams, E. H. Akakpo, H. Al Falou, R. Churchman, D. S. Cross, M. K. Djongolov, N. Erasmus, P. Finlay, A. B. Garnsworthy, P. E. Garrett, D. G. Jenkins, R. Kshetri, K. G. Leach, S. Masango, D. L. Mavela, C. V. Mehl, M. J. Mokgolobotho, C. Ngwetsheni, G. G. O'Neill, E. T. Rand, S. K. L. Sjue, C. S. Sumithrarachchi, C. E. Svensson, E. R. Tardiff, S. J. Williams, and J. Wong. Reorientation-effect measurement of the first 2+ state in 12c: Confirmation of oblate deformation. *Physics Letters B*, 777:250–254, 2018.

[80] A. C. Dreyfuss, K. D. Launey, T. Dytrych, J. P. Draayer, R. B. Baker, C. M. Deibel, and C. Bahri. Understanding emergent collectivity and clustering in nuclei from a symmetry-based no-core shell-model perspective. *Phys. Rev. C*, 95:044312, Apr 2017.

[81] R. Neveling, H. Fujita, F.D. Smit, T. Adachi, G.P.A. Berg, E.Z. Buthelezi, J. Carter, J.L. Conradie, M. Couder, R.W. Fearick, S.V. Förtsch, D.T. Fourie, Y. Fujita, J. Görres, K. Hatanaka, M. Jingo, A.M. Krumbholz, C.O. Kureba, J.P. Mira, S.H.T. Murray, P. von Neumann-Cosel, S. O'Brien, P. Papka, I. Poltoratska, A. Richter, E. Sideras-Haddad, J.A. Swartz, A. Tamii, I.T. Usman, and J.J. van Zyl. High energy-resolution zero-degree facility for light-ion scattering and reactions at ithemba labs. *Nuclear Instruments and Methods in Physics Research Section A: Accelerators, Spectrometers, Detectors and Associated Equipment*, 654(1):29 – 39, 2011.

[82] R Neveling, F D Smit, H Fujita, P Adsley, K.C.W. Li, J.W. Brümmer, D.J Marin-Lambarri, and R T Newman. Guide to the K600 magnetic spectrometer (2017). *K600 User Manual*, 2014.

[83] H. *et al.* Fujita. The alpha-particle model of the nucleus. *Nucl. Instrum. Methods Phys. Res. A*, 484:17–26, (2002).

[84] Y. *et al.* Fujita. The alpha-particle model of the nucleus. *Nucl. Instrum. Methods Phys. Res. B*, 126:274–276, (1997).

[85] W. Bertozzi, M. V. Hynes, C. P. Sargent, C. Creswell, P. C. Dunn, A. Hirsch, M. Leitch, B. Norum, F. N. Rad, and T. Sasanuma. Focal plane instrumentation: A very high resolution mwpc system for inclined tracks. *Nuclear Instruments and Methods*, 141(3):457–476, 1977.

[86] J.A. Swartz. Master's thesis, stellenbosch university. (2010).

[87] P. Adsley et al. CAKE: The Coincidence Array for K600 Experiments. *JINST*, 12(02):T02004, 2017.

[88] K. C. W. Li. *Master's Thesis, Stellenbosch University and iThemba LABS, http://hdl.handle.net/10019.1/97982*, 2015.

[89] F.S Acton. *Analysis of straight-line data.* John Wiley, New York, (1959).

[90] C. Wheldon. Derivations for two-body kinematics (both relativistic and non-relativistic). (2014).

[91] M.N. Harakeh and L.W. Put. *ANGCOR, Angular Correlation Programme*, (1979). KVI-67.

[92] M. Itoh, H. Akimune, M. Fujiwara, U. Garg, H. Hashimoto, T. Kawabata, K. Kawase, S. Kishi, T. Murakami, K. Nakanishi, Y. Nakatsugawa, B.K. Nayak, S. Okumura, H. Sakaguchi, H. Takeda, S. Terashima, M. Uchida, Y. Yasuda, M. Yosoi, and J. Zenihiro. Study of the cluster state at E_x = 10.3 MeV in ^{12}C. *Nuclear Physics A*, 738:268 – 272, 2004. Proceedings of the 8th International Conference on Clustering Aspects of Nuclear Structure and Dynamics.

[93] G. B. Arfken and H. J. Weber. *Mathematical methods for physicists 6th ed.* 2005.

[94] Matteo Frigo and Steven G. Johnson. The design and implementation of FFTW3. *Proceedings of the IEEE*, 93(2):216–231, 2005. Special issue on "Program Generation, Optimization, and Platform Adaptation".

[95] R. Brun and F. Rademakers. ROOT: An object oriented data analysis framework. *Nucl. Instrum. Meth.*, A389:81–86, 1997.

[96] L. Landau. On the energy loss of fast particles by ionization. *J. Phys.(USSR)*, 8:201–205, 1944.

[97] L. Greengard and J. Lee. Accelerating the nonuniform fast fourier transform. *SIAM Review*, 46(3):443–454, 2004.

[98] A.H. Barnett, J.F. Magland, and L. af Klinteberg. A parallel non-uniform fast fourier transform library based on an "exponential of semicircle" kernel. Preprint (2018). math.NA:1808.06736.

[99] Karl Pearson F.R.S. X. on the criterion that a given system of deviations from the probable in the case of a correlated system of variables is such that it can be reasonably supposed to have arisen from random sampling. *The London, Edinburgh, and Dublin Philosophical Magazine and Journal of Science*, 50(302):157–175, 1900.

[100] P. E. Greenwood and M. S. Nikulin. *A Guide to Chi-squared testing.* Wiley, New York, 1996.

[101] John R. Taylor. *An introduction to error analysis.* University Science Books, Sausalito, Calif., 1997.

[102] A. C. Davison. *Statistical Models.* Cambridge University Press, Cambridge, 2003.

[103] Karl-Rudolf Koch. *Parameter Estimation and Hypothesis Testing in Linear Models.* Springer-Verlag, Berlin, Heidelberg, 1988.

[104] Sadanori Konishi and Genshiro Kitagawa. *Information Criteria and Statistical Modeling*. Springer Publishing Company, Incorporated, 1st edition, 2007.

[105] Kenneth P Burnham. *Model selection and multimodel inference: a practical information-theoretic approach*. Springer, New York, 2nd ed. edition, 2002.

[106] Gideon Schwarz. Estimating the dimension of a model. *Ann. Statist.*, 6(2):461–464, 03 1978.

[107] Christophe Giraud. *Introduction to high-dimensional statistics*. Chapman & Hall/CRC Monographs on Statistics & Applied Probability. CRC Press, Hoboken, NJ, 2015.

[108] R. M. Haybron. Scattering of 100 mev protons by 12c. *Nuclear Physics A*, 124(3):662–672, 1969.

[109] Tz. Kokalova, M. Freer, Z. Buthelezi, J. Carter, R. W. Fearick, S. V. Förtsch, H. Fujita, R. Neveling, P. Papka, F. D. Smit, J. A. Swartz, and I. Usman. Precision measurement of the 9.641 mev, 3^- state in ^{12}c. *Phys. Rev. C*, 87:057307, May 2013.

[110] M. Itoh, H. Akimune, M. Fujiwara, U. Garg, H. Hashimoto, T. Kawabata, K. Kawase, S. Kishi, T. Murakami, K. Nakanishi, Y. Nakatsugawa, B. K. Nayak, S. Okumura, H. Sakaguchi, H. Takeda, S. Terashima, M. Uchida, Y. Yasuda, M. Yosoi, and J. Zenihiro. Study of the cluster state at ex=10.3 mev in 12c. *Nuclear Physics A*, 738:268–272, 2004.

[111] M. Freer, H. Fujita, Z. Buthelezi, J. Carter, R. W. Fearick, S. V. Förtsch, R. Neveling, S. M. Perez, P. Papka, F. D. Smit, J. A. Swartz, and I. Usman. 2^+ excitation of the ^{12}C hoyle state. *Phys. Rev. C*, 80:041303, Oct 2009.

[112] M. Freer, M. Itoh, T. Kawabata, H. Fujita, H. Akimune, Z. Buthelezi, J. Carter, R. W. Fearick, S. V. Förtsch, M. Fujiwara, U. Garg, N. Hashimoto, K. Kawase, S. Kishi, T. Murakami, K. Nakanishi, Y. Nakatsugawa, B. K. Nayak, R. Neveling, S. Okumura, S. M. Perez, P. Papka, H. Sakaguchi, Y. Sasamoto, F. D. Smit, J. A. Swartz, H. Takeda, S. Terashima, M. Uchida, I. Usman, Y. Yasuda, M. Yosoi, and J. Zenihiro. Consistent analysis of the 2^+ excitation of the ^{12}c hoyle state populated in proton and α-particle inelastic scattering. *Phys. Rev. C*, 86:034320, Sep 2012.

[113] W. R. Zimmerman, M. W. Ahmed, B. Bromberger, S. C. Stave, A. Breskin, V. Dangendorf, Th. Delbar, M. Gai, S. S. Henshaw, J. M. Mueller, C. Sun, K. Tittelmeier, H. R. Weller, and Y. K. Wu. Unambiguous identification of the second 2^+ state in $^{12}\mathbf{C}$ and the structure of the hoyle state. *Phys. Rev. Lett.*, 110:152502, Apr 2013.

[114] W. R. Zimmerman, N. E. Destefano, M. Freer, M. Gai, and F. D. Smit. Further evidence for the broad 2_2^+ state at 9.6 mev in ^{12}c. *Phys. Rev. C*, 84:027304, Aug 2011.

[115] F. D. Smit, F. Nemulodi, Z. Buthelezi, J. Carter, R. W. Fearick, S. V. Förtsch, M. Freer, H. Fujita, M. Jingo, C. O. Kureba, J. Mabiala, J. Mira, R. Neveling, P. Papka, G. F. Steyn, J. A. Swartz, I. T. Usman, and J. J. van Zyl. No evidence of an 11.16 mev 2^+ state in ^{12}c. *Phys. Rev. C*, 86:037301, Sep 2012.